AFFDL-TR-73-21-Vol. IV

STOL TACTICAL AIRCRAFT INVESTIGATION

VOLUME IV ✦ WIND TUNNEL DATA ANALYSIS

J. Hebert, Jr.
J. C. Ramsey
E. C. Laudeman
N. A. Ponomareff
H. Altman

Convair Aerospace Division of
General Dynamics Corporation

FOREWORD

The Data Analysis Report was prepared by the Convair Aerospace Division of General Dynamics Corporation under USAF Contract F33615-71-C-1754, Project 643A, "STOL Tactical Aircraft Investigation." This contract was sponsored by the Prototype Division of the Air Force Flight Dynamics Laboratory. The USAF Project Engineer was G. Oates (PT) and the Convair Aerospace Program Manager was J. Hebert. J. C. Ramsey, C. A. Whitney, N. A. Ponomareff, E. C. Laudeman, and H. Altman were the principal contributors.

The research reported was conducted during the period from 7 June 1971 through 31 January 1973. This report was submitted by the author on 31 January 1973 under contractor report number GDCA-DHG73-001.

This report has been reviewed and is approved.

E. J. CROSS, JR.
Lt. Col. USAF
Chief, Prototype Division

ABSTRACT

The data analysis report summarizes the force and rake information measured during the 1,087 hours of low speed wind tunnel testing conducted by the Convair Aerospace Division of General Dynamics during the STOL Tactical Aircraft Investigation. Over 2,730 data runs were generated on 242 major configuration variables that covered the following lift/propulsion concepts:

Mechanical Flaps Plus Vectored Thrust
Externally Blown Flaps
Internally Blown Flaps.

The extensive collection of data was reduced to a usable form with an interactive graphic computer program that provided a consistent method of unbiased measurements.

Lift data was reduced into three basic terms.

1. Power-on to power-off lift curve slope ratio, K_{pwr}.
2. Trailing edge flap lift increment at $\alpha = 0$ degrees, $\Delta C'_{L_{TE}}$.
3. Maximum lift coefficient increment due to the application of power, $\Delta C_{L_{max}}\Big)_{c_{\mu_J}}$.

These relationships were evaluated as a function of blowing momentum coefficient for the EBF, IBF, and MF/VT systems. They were then correlated for the effects of configurational variations (wing planform, leading and trailing edges, and nacelle location). A theoretical method of predicting the fully augmented lift parameters as a function of applied power has been compared with the test data.

Drag data was reduced into the form of induced drag factor (e), minimum profile drag ($C_{D_{P_{min}}}$) and thrust recovery (r) and then analyzed as a function of blowing momentum coefficient. Static data was also used in correlation of jet turning efficiency.

The pitching moment data analysis compares the flap pitching moment increment at $\alpha = 0$ among the various configurations. The downwash data was normalized using aerodynamic lift (direct thrust terms removed from total lift) and subsequently analyzed by comparing downwash intensities at various vertical stations. The static lateral-directional stability derivatives were obtained from linear least squares curves fits. Control effectiveness data and effects of asymmetric thrust were also obtained by taking increments between runs with deflected controls and/or symmetric thrust and the undeflected condition.

The lift and drag analysis approach furnished satisfactory results and an improved understanding of the lift/propulsion concepts investigated. The lift coefficients generated by each concept were accompanied as expected by corresponding nose down pitching moments. The downwash associated with powered lift systems was found to be proportional to the aerodynamic lift.

The general trends in the aerodynamic and stability and control data analysis do not indicate either of the lift/propulsion concepts to be significantly superior to the others investigated.

Since large downwash angles and pitching moment are inherent with high lift generation, STOL configurations must be tailored to eliminate these adverse effects. It is recommended that a canard surface CCV design be investigated to fulfill this objective.

TABLE OF CONTENTS

TABLE OF CONTENTS, Contd

TABLE OF CONTENTS, Contd

TABLE OF CONTENTS, Contd

LIST OF ILLUSTRATIONS

LIST OF ILLUSTRATIONS, Contd

LIST OF ILLUSTRATIONS, Contd

LIST OF ILLUSTRATIONS, Contd

LIST OF ILLUSTRATIONS, Contd

LIST OF ILLUSTRATIONS, Contd

LIST OF ILLUSTRATIONS, Contd

LIST OF ILLUSTRATIONS, Contd

LIST OF ILLUSTRATIONS, Contd

LIST OF ILLUSTRATIONS, Contd

LIST OF ILLUSTRATIONS, Contd

LIST OF ILLUSTRATIONS, Contd

LIST OF ILLUSTRATIONS, Contd

LIST OF ILLUSTRATIONS, Contd

LIST OF ILLUSTRATIONS, Contd

LIST OF ILLUSTRATIONS, Contd

LIST OF ILLUSTRATIONS, Contd

LIST OF ILLUSTRATIONS, Contd

LIST OF ILLUSTRATIONS, Contd

LIST OF ILLUSTRATIONS, Contd

NOMENCLATURE

Symbol		Units
AR	Aspect ratio of wing.	
A'	Aspect ratio based on extended wing area.	
b	Wing span.	In.
c	Airfoil section chord, flap and leading edge retracted.	In.
c'	Airfoil chord with leading-and/or trailing-edge flaps extended.	
C_D	Drag coefficient.	
C_{D_H}	Horizontal tail drag coefficient.	
C_{D_o}	Minimum drag coefficient.	
$C_{D_{P_{min}}}$	Minimum profile drag coefficient including loss of thrust recovery.	
C_{D_R}	Ram drag coefficient.	
c_{f_n}	Trailing-edge flap chord. (Subscripts denote different segments of the flap.)	
c'_f	Equivalent skin friction drag coefficient, based on total flap wetted area.	
c_H	Mean aerodynamic chord of horizontal tail.	
C_L	Lift coefficient.	
ΔC_L	Lift coefficient increment.	
$\Delta C_{L_{LE}}$	Lift coefficient increment due to leading-edge device.	
c_{LE}	Leading-edge device chord.	
C_{L_H}	Horizontal tail lift coefficient.	
$C_{L_{H_{max}}}$	Horizontal tail maximum lift coefficient.	
ΔC_{L_H}	Horizontal tail lift coefficient increment.	

NOMENCLATURE, Contd

Symbol		Units
$C_{L_{max}}$	Maximum lift coefficient.	
$C'_{L_{max}})_{LE}$	Maximum lift coefficient with leading-edge device, based on extended wing area.	
$\Delta C'_{L_{max}})_{TE}$	Maximum lift coefficient increment due to deflection and trailing-edge blowing, based on extended wing area.	
$\Delta C'_{L_{max}})_{C_{\mu_J}}$	Trailing-edge flap maximum lift coefficient increment due to engine blowing, based on extended wing area.	
$\Delta C'_{L_{max}})_{C_{\mu_T}}$	Trailing-edge flap maximum lift coefficient increment due to blowing, based on extended wing area	
C_{L_o}	Wing lift coefficient at zero angle of attack.	
ΔC_{L_o}	Lift coefficient increment at zero angle of attack.	
$\Delta C'_{L_{TE}}$	Lift coefficient increment due to the deflection and trailing-edge blowing, based on extended wing area.	
C_{L_V}	Vertical tail lift coefficient.	
C_{L_α}	Lift curve slope	/Deg.
$C_{L_{\alpha_H}}$	Horizontal tail lift curve slope.	/Deg.
$C_{L_\alpha})_{theory}$	Theoretical lift curve slope.	/Deg.
$C_{L_{\alpha_V}}$	Vertical tail lift curve slope.	/Deg.
$C'_{L_\alpha})_{pwr-off}$	Power-off lift curve slope, based on extended wing area.	/Deg.
$C'_{L_\alpha})_{\alpha=\alpha_{oL}}$	Lift-curve slope evaluated at angle of zero lift, based on extended wing area.	/Deg.
C_ℓ	Rolling moment.	
ΔC_ℓ	Rolling moment increment.	

NOMENCLATURE, Contd

Symbol		Units
C_{ℓ_β}	Rolling moment due to sideslip.	
$C_{\ell_{\beta_V}}$	Vertical tail rolling moment due to sideslip.	
Δc_ℓ	Two-dimensional lift coefficient increment.	
$\Delta c_{\ell_{L.E.\ Flap}}$	Two-dimensional lift coefficient increment due to a leading-edge flap.	
$\Delta_3 c_{\ell_{max}}$	Accounts for effects of RN on section characteristics.	
$\Delta c'_\ell)_{TE}$	$\sum c_{\ell_{\delta_n}} \cdot \delta_{f_n}$	
$c'_{\ell_\alpha})_{pwr\text{-}off}$	Two-dimensional power-off lift curve slope, based on extended chord.	/Deg.
$c'_{\ell_{\alpha_{th}}}$	Two-dimensional theoretical lift curve slope, based on extended chord.	/Deg.
c_{ℓ_δ}	Theoretical flap lift effectiveness.	/Deg.
$C_{m_{.25c}}$	Pitching moment increment.	
$\Delta C_{m_{.25c}})_{\alpha=0}$	Pitching moment increment at zero angle of attack.	
C_{m_H}	Horizontal tail pitching moment	
ΔC_{m_H}	Horizontal tail pitching moment increment	
$\Delta c_{m_{.25c}}$	Two-dimensional pitching moment increment.	
$\Delta c_{m_{LE\ flap}}$	Two-dimensional pitching moment increment due to a leading-edge flap.	
C_n	Yawing moment.	

NOMENCLATURE, Contd

Symbol		Units
ΔC_n	Yawing moment increment.	
C_{n_β}	Yawing moment due to sideslip.	
$C_{n_{\beta_V}}$	Vertical tail yawing moment due to sideslip.	
c_R	Root chord of wing.	In.
c_T	Tip chord of wing.	In.
c_w	Mean aerodynamic chord of wing.	In.
C_y	Side force	
ΔC_y	Side force increment.	
C_{y_β}	Side force due to sideslip.	
$C_{y_{\beta_v}}$	Vertical tail side force due to sideslip.	
C_x	Total axial force coefficient measured parallel to the free stream.	
C_μ	Jet momentum coefficient.	
ΔC_μ	Increment in jet momentum coefficient.	
C_{μ_a}	Aileron blowing momentum coefficient.	
C_{μ_e}	Elevator blowing momentum coefficient.	
$C_{\mu_{LE}}$	Leading-edge blowing momentum coefficient.	
$C'_{\mu_{LE}}$	Leading-edge blowing momentum coefficient, based on extended wing area.	
C_{μ_J}	Blowing momentum coefficient of engine blowing system, $MV/q_o S$ (EBF)	
C'_{μ_J}	Blowing momentum coefficient of engine blowing system, based on extended wing area.	
$C'_{\mu_J}\Big)_{TE}$	Blowing momentum coefficient at the trailing edge flap, based on extended wing area for EBF system.	

NOMENCLATURE, Contd

Symbol		Units
D_o	$-0.08\ C'_{\mu_{TE}}$	
D/T	Drag-to-thrust ratio.	
e	Induced drag factor.	
i_w	Wing incidence angle.	Deg.
K_{b_f}	Partial flap span factor.	
K_{pwr}	Ratio of the power-on lift curve slope to power-off lift curve.	
k_{pwr}	Slope assuming full potential flow factor from Spence Jet Flap Theory.	
L/T	Lift-to-thrust ratio.	
ℓ_H	Distance behind wing quarter chord point in chord lengths.	
M	Mach number.	
MAC	Mean aerodynamic chord.	In.
q	Free-stream dynamic pressure.	Lb./Sq. Ft.
RN	Reynolds number.	
r	Thrust recovery factor.	
S	Theoretical wing planform area.	Sq. Ft.
S_T	Blown wing area for IBF system.	Sq. Ft.
S_{exp}	Exposed wing planform area.	Sq. Ft.
t/c	Airfoil thickness ratio.	
$\bar{V}_H$	Horizontal tail volume.	
X_H	Distance from 0.25 c_w to 0.25 c_H.	In.
Δx	Overlap associated with deflected leading-edge device.	
$Y_{cp})_{roll}$	Roll center of pressure	
Δy	Gap associated with deflected leading-edge device.	
Z_H	Vertical height of horizontal tail.	In.

NOMENCLATURE, Contd

Symbol		Units
α	Angle of attack.	Deg.
α_B	Fuselage angle of attack.	Deg.
$\alpha_{C_{L_{max}}}$	Wing angle of attack at maximum lift coefficient.	Deg.
α_{eff}	Effective angle of attack.	Deg.
α_G	Geometric angle of attack.	Deg.
α_H	Horizontal tail angle of attack.	Deg.
$\alpha_H)_{C_{L_{max}}}$	Horizontal tail angle of attack at maximum lift.	Deg.
α_{oL}	Angle of attack at zero lift coefficient.	Deg.
α_{So}	Power-off angle of attack at $C_{L_{max}}$	Deg.
α_v	Vertical tail angle of attack.	Deg.
α_w	Wing angle of attack.	Deg.
β	Yaw angle.	Deg.
δ_a	Aileron deflection angle.	Deg.
δ_e	Elevator deflection.	Deg.
δ_{eff}	Effective leading edge flap deflection.	Deg.
δ_f	Trailing-edge flap deflections.	Deg.
δ_{f_n}	Trailing-edge flap deflection (subscripts denote different segments of the flap).	Deg.
δ_H	Horizontal tail deflection.	Deg.
δ_J	Deflection angle of the jet sheet or stream measured relative to the wing chord plane (positive deflection downward).	Deg.
δ_{LE}	Leading-edge high-lift device deflection angle.	Deg.
δ_r	Rudder deflection.	Deg.

NOMENCLATURE, Contd

δ_{sp}	Spoiler deflection angle.	Deg.
δ_T	Deflection angle of the engine tailpipes, measured relative to the nacelle centerline.	Deg.
ϵ	Downwash angle.	Deg.
ϵ_α	Downwash gradient.	
η	Wing semi-span station.	
η_H	Horizontal tail efficiency.	
η_S	Static turning efficiency.	
η_V	Vertical tail efficiency.	
$\Lambda c/4$	Sweep of quarter chord line of the wing.	Deg.
Λ	Sweep of the 50 percent chord line of the wing.	Deg.
λ	Wing taper ratio.	
$\phi_{TE})_{Total}$	Airfoil trailing edge angle.	Deg.
$\phi_{TE})_{Upper}$	Upper surface trailing edge angle.	Deg.
$\left(1 + \frac{\partial\sigma}{\partial\beta}\right)$	Sidewash gradient	

SECTION 1

INTRODUCTION

This volume presents the results of an analysis of aerodynamic and stability and control data obtained from a series of wind tunnel tests of a 1/20-scale STOL transport model conducted at the General Dynamics Low Speed Wind Tunnel in San Diego during the summer and fall of 1972. The tests (Reference 1-1) consisted of over 2,700 runs totaling 1,087 hours of testing time. Three lift/propulsion systems designed for use with STOL transport configurations were studied;

1. Externally blown flap (EBF)

2. Internally blown flap (IBF)

3. Mechanical flap plus vectored thrust (MF/VT)

Representative examples of these configurations are shown in Figure 1.0-1. A vast assortment of interchangeable model components permitted testing of over 240 wing, leading edge, trailing edge, and engine nacelle combinations (Figure 1.0-2) for the three lift/propulsion systems. The model was also equipped with three independent air systems for engine, leading edge, and trailing edge blowing simulation. Most of the runs were made with the tail assembly off. A summary of the various systems and configurations tested is shown in Table 1.0-1.

A rake of pressure probes capable of measuring flow velocity and deflection was mounted to the model support system aft of the wing at possible tail locations for all tail-off runs. The rake was maintained in a fixed position relative to the model during pitch or yaw sweeps.

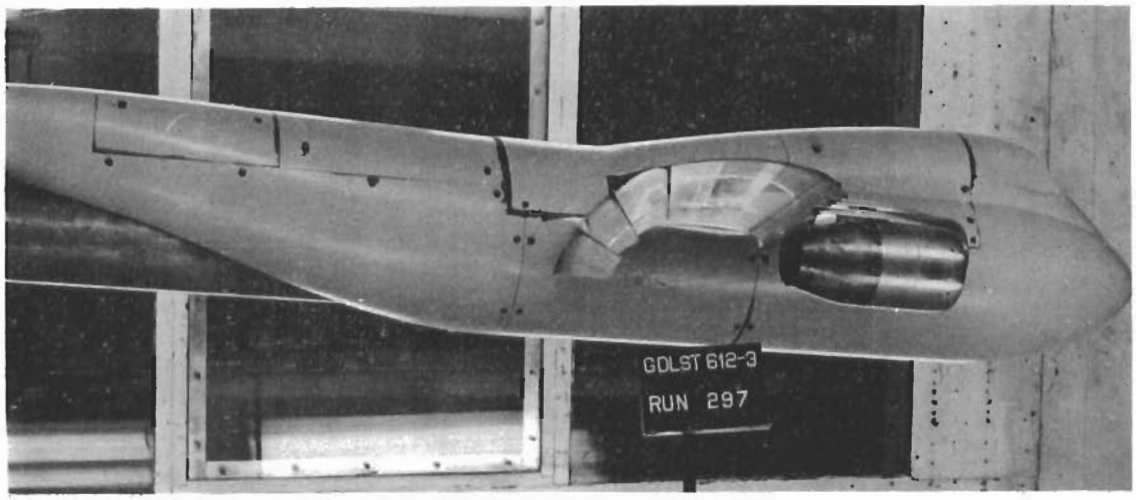

A. Externally Blown Flap

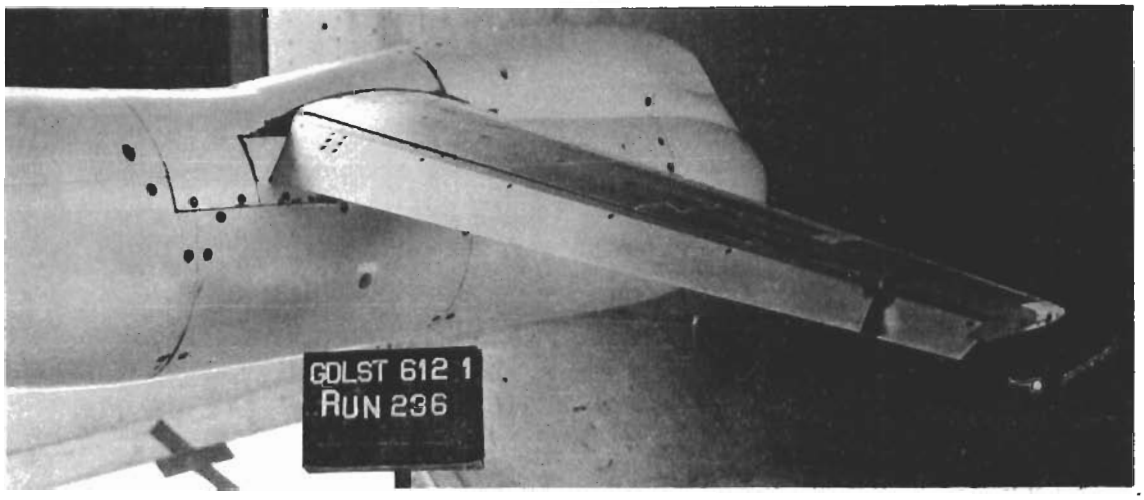

B. Internally Blown Flap

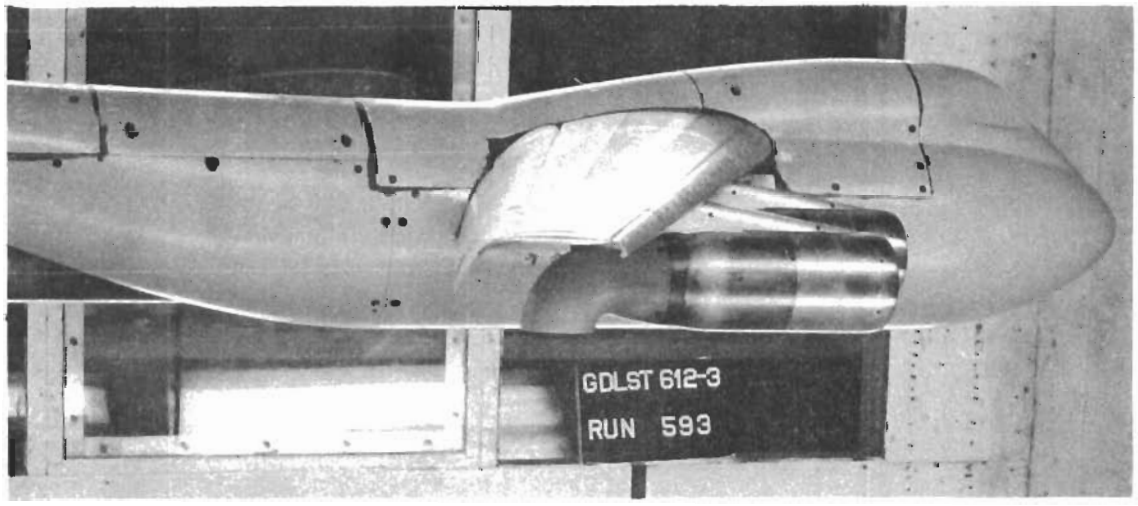

C. Mechanical Flap plus Vectored Thrust

Figure 1.0-1. STOL Transport Lift/Propulsion Concepts

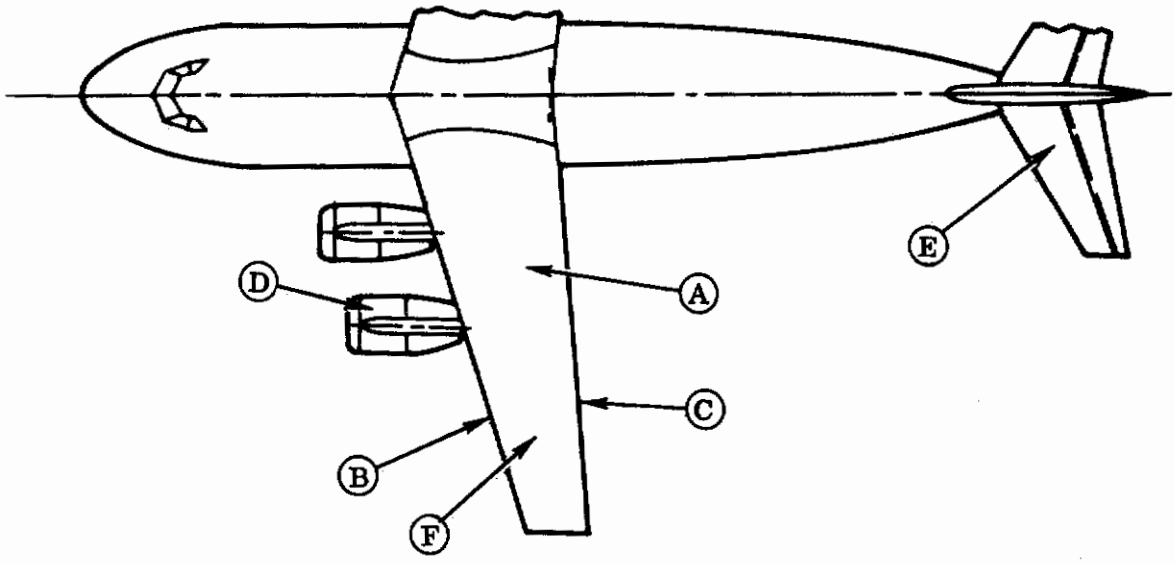

Ⓐ WING PLANFORM
- ASPECT RATIO
- WING SWEEP

Ⓑ LEADING EDGE FLAP SYSTEM
- BLOWN KRUEGER FLAP
- LEADING EDGE SLAT
- VARIABLE CHORD AND DEFLECTION

Ⓒ TRAILING EDGE FLAP SYSTEM
- PLAIN BLOWN FLAP
- SLOTTED FLAPS (SINGLE, DOUBLE, AND TRIPLE)
- VARIABLE CHORD, SPAN, AND DEFLECTION

Ⓓ ENGINE SIMULATORS
- ENGINE BLOWING
- NACELLE LOCATION (SPAN, CHORD, AND HEIGHT)
- THRUST DEFLECTION AND VECTORING
- ONE-ENGINE-OUT SIMULATION

Ⓔ EMPENNAGE
- ON/OFF
- BLOWN ELEVATOR AND RUDDER
- VARIABLE ELEVATOR AND RUDDER DEFLECTION

Ⓕ LATERAL CONTROL DEVICES
- BLOWN AILERON
- SPOILER
- VARIABLE DEFLECTION

Figure 1.0-2. Configuration Variables.

Table 1.0-1. Summary of Flap Configurations Analyzed

Wing No.			W_1	W_3					W_4			W_5			W_6		
AR			8.0	8.0					9.5			7.1			8.0		
Λc/4 (deg)			12.5	25					25			25			35		
Lift/Propulsion Systems □ EBF ○ IBF △ EBF–MF/VT ☆ EBF–IBF–MF/VT		Leading Edge	Clean	Clean	15% c Blown Flap	25% c Blown Flap	15% c Slat	25% c Slat	Clean	15% c Blown Flap	15% c Slat	Clean	15% c Blown Flap	15% c Slat	Clean	15% c Blown Flap	15% c Slat
Trailing Edge Flap																	
Triple-Slotted No. 311																	
100% Span	δ_f = 60 deg		□	□	△	□	□	□	□	□	□	□	□	□	□	△	□
81.6% Span	δ_f = 60 deg			□	□												
Triple-Slotted No. 111																	
100% Span	δ_f = 60 deg				□												
Double-Slotted No. 32																	
100% Span	δ_f = 60 deg		□	□	□	□	□	□	□	□	□	□	□	□	□	□	□
	45 deg			□	□												
	30 deg		△	□	□					□						□	
81.6% Span	δ_f 60 deg				□												
Double-Slotted No. 12																	
100% Span	δ_f = 60 deg			△	△												
	45 deg			□	△												
	30 deg			□	△												
Single-Slotted No. 2																	
100% Span	δ_f = 60 deg			□	□												
	45 deg			□	□												
	30 deg		○	□	□												
	15 deg			□	□												
Plain Blown Flap																	
100% Span	δ_f = 60 deg		○	○	○												
	45 deg			○	○												
	30 deg		○	○	○												
	15 deg			○	○												
81.6% Span	δ_f = 60 deg			○	○												
	30 deg				○												

SECTION 2

MODEL GEOMETRY

The general arrangement of the test model is shown in Figure 2.0-1. The model typifies a four-engine, high-wing, T-tail, subsonic STOL transport. Fan-type engines were simulated by cold air ejectors, and full-span leading and trailing edge blowing systems were incorporated into the wing. The three separately controlled high-pressure air supplies were fed into the model through the sting support system. A six-component strain gage balance was used to measure forces and moments. A tail probe rake was used to measure pressure data above the aft fuselage for all tail-off runs.

Planform geometry for the five wings tested is given in Table 2.0-1. Definitions of geometric parameters associated with the leading- and trailing-edge flaps are shown in Figure 2.0-2. Numerical values of these terms (chord, deflection, gap, and overlap) are given in Tables 2.0-2 and 2.0-3 for the various wing/leading-edge/trailing-edge combinations. Sketches of the leading edge devices are shown in Figure 2.0-3.

The various nacelle locations are shown in Figure 2.0-4. The nacelles have a nominal deflection of -3.5 degrees (upward) relative to the wing chord plane. The vectored thrust configurations have tailpipe deflections (δ_T) of 15, 30, 45, 60, and 90 degrees. However, inefficiencies produce resultant jet deflections (δ_J) of 8.5, 22.5, 37, and 69 degrees, respectively. The nacelle trailing-edge flap orientations for all combinations tested are shown in Figures 2.0-5 through 2.0-9. Flap positions of the plain blown flap are shown in Figure 2.0-10.

The tail probe rake apparatus is shown schematically in Figure 2.0-11, and its various positions are depicted in Figure 2.0-12. The geometry of the horizontal and vertical tail is given in Table 2.0-4.

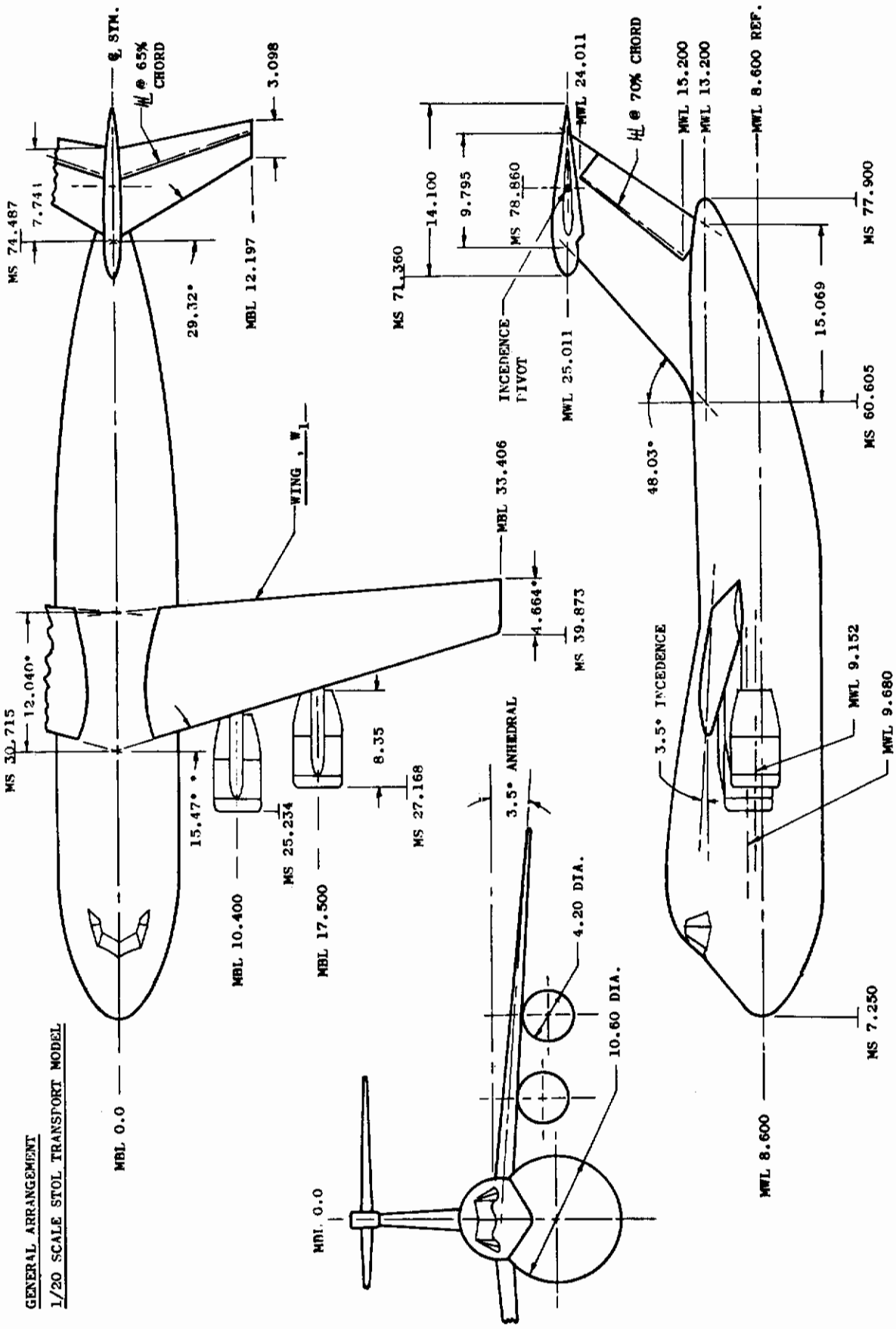

Figure 2.0-1. STOL Transport Model

Table 2.0-1. Wing Geometry

Parameter		Wing W_1	W_3	W_4	W_5	W_6
Span	(in.)	66.8	68.82	77.0	63.7	71.9
Area	(ft^2)	3.875	4.111	4.327	3.945	4.482
Aspect Ratio		8.0	8.0	9.52	7.14	8.0
Taper Ratio		0.387	0.334	0.255	0.384	0.254
Sweep, Λ_{LE}	(deg)		27.9	27.9	27.9	37.8
$\Lambda_{c/4}$	(deg)	12.5	25.0	25.0	25.0	35.0
Dihedral, T.E.	(deg)	- 3.5	- 3.5	- 3.5	- 3.5	- 3.5
Incidence, Root	(deg)	3.5	3.5	3.5	3.5	3.5
Thickness, Root	(%c)	13.7	12.6	12.6	12.6	12.3
MAC	(%c)	13.3	12.5	12.5	12.5	11.4
Tip	(%c)	10.0	10.5	10.0	9.7	9.3
Max. Camber, Root	(%c)	2.1	1.9	1.9	1.9	1.7
MAC	(%c)	2.2	2.0	2.0	2.0	1.7
Tip	(%c)	2.6	2.3	2.4	2.2	2.2
Twist, Root	(deg)	0.0	0.0	0.0	0.0	0.0
MAC	(deg)	- 1.2	- 1.1	- 1.1	- 1.2	- 1.0
Tip	(deg)	- 4.5	- 4.5	- 6.0	- 4.3	- 5.4
Chord, Root	(in.)	12.02	12.05	12.05	12.05	13.30
MAC	(in.)	8.90	9.33	9.04	9.62	10.04
Tip	(in.)	4.66	4.33	3.30	4.97	3.66
ϕ_{TE} (Upper)	(deg)	12.8	12.0	12.0	12.0	11.5
ϕ_{TE} (Total)	(deg)	15.0	14.1	14.0	14.2	13.0

Table 2.0-2. Leading Edge Geometric Data*

Leading Edge Device	δ_{LE} (deg)	c_{LE} (% c)	δ_{LE} (deg)	ΔX (% c)	ΔY (% c)	c'/c
Wing No. 1						
15% c Krueger	55	15.6	53.8	0.45	1.01	1.142
15% c Slat	45	15.3	48.0	-2.37	2.08	1.169
Wing No. 3						
15% c Krueger	50	15.6	45.6	0.4	1.1	1.145
	55	15.5	51.0	0.4	1.1	1.145
	60	15.5	57.5	0.4	1.1	1.147
	65	15.5	63.9	0.4	1.1	1.147
25% c Krueger	55	25.0	51.5	0.4	1.1	1.240
15% c Slat	40	15.4	40.3	-2.5	2.0	1.171
	45	15.0	22.3	-2.5	2.0	1.170
	50	15.4	50.1	-2.5	1.9	1.169
	60	15.3	60.0	-2.5	1.9	1.167
25% c Slat	55	25.0	45.1	-2.5	2.0	1.266
Wing No. 4						
15% c Krueger	55	15.6	51.3	0.4	1.0	1.147
15% c Slat	45	15.3	45.0	-2.5	2.0	1.170
Wing No. 5						
15% c Krueger	55	15.4	51.5	0.4	1.0	1.144
15% c Slat	45	15.3	45.0	-2.6	2.1	1.170
Wing No. 6						
15% c Krueger	55	15.4	48.1	0.5	1.0	1.145
15% c Slat	45	15.4	42.0	-2.7	2.0	1.173

*Sectional Data Measured at Wing MAC.

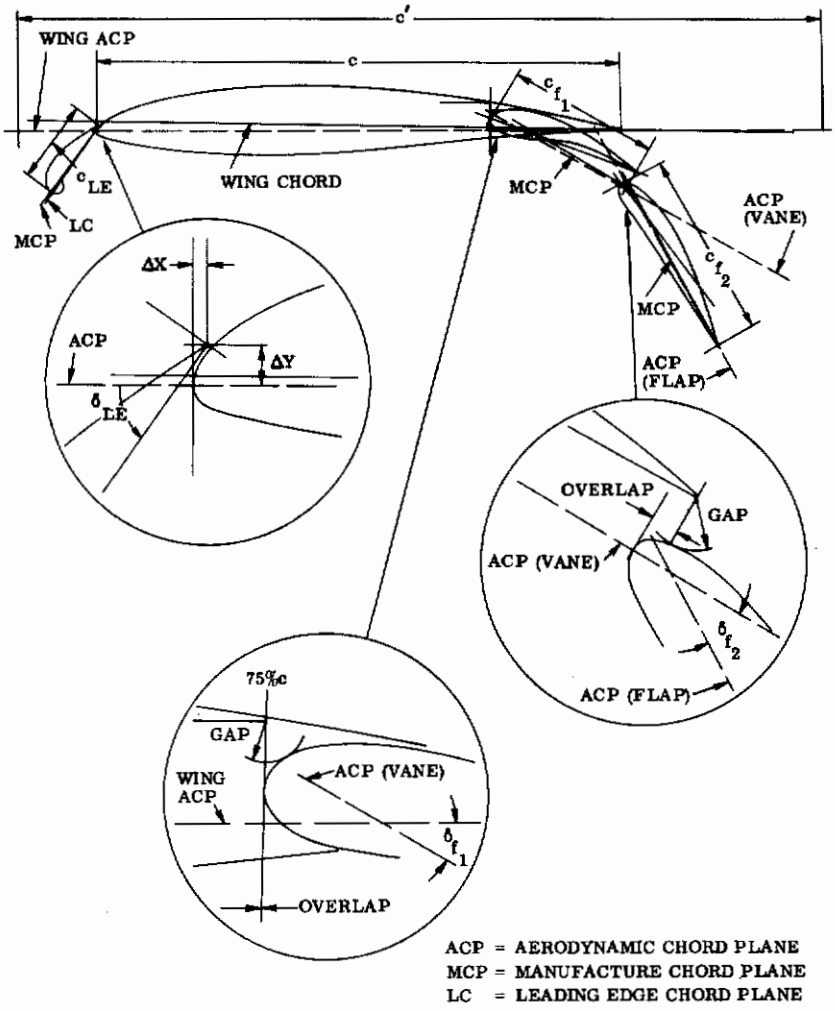

Figure 2.0-2. Leading Edge/Trailing Edge Flap Geometry

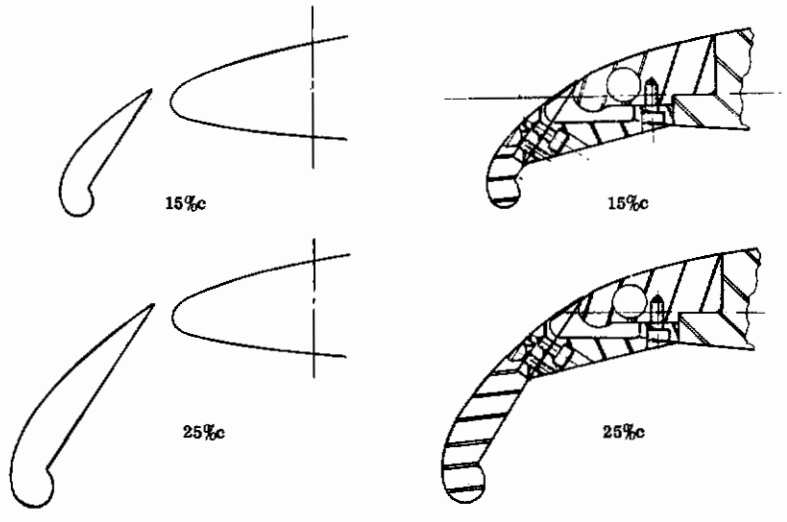

Figure 2.0-3. Leading Edge Device

Table 2.0-3. Trailing-Edge Flap Geometric Data.

Flap System	c_1 (% c)	δ_{f_1} (deg)	Overlap/ Gap (deg)	c_2 (% c)	δ_{f_2} (deg)	Overlap/ Gap (deg)	c_3 (% c)	δ_{f_3} (deg)	Overlap/ Gap (deg)	c'/c
WING NO. 1										
Triple Slotted No. 311										
δ_f = 60 deg	28.7	29.5	0/2.2	24.2	16.5	0.5/2.2	24.4	14.7	0.9/2.2	1.509
Double Slotted No. 32										
δ_f = 60 deg	28.8	29.5	0/2.1	35.9	31.5	1.2/2.2				1.385
45 deg	28.8	17.0	2.1/2.1	35.9	14.0	0.3/2.1				1.373
30 deg										
Single Slotted No. 2										
δ_f = 60 deg	35.3	61.2	0/2.2							1.103
45 deg										
30 deg	34.6	31.2	2.0/2.1							1.076
15 deg										
Plain Blown										
δ_f = 60 deg	32.5	61.0	0/0							1.075
45 deg	30.3	46.0	0/0							1.053
30 deg	28.3	31.0	0/0							1.033
15 deg	26.6	16.0	0/0							1.016
Triple Slotted No. 111										
δ_f = 60 deg										
Double Slotted No. 12										
δ_f = 60 deg										
30 deg										
WING NO. 3										
Triple Slotted No. 311										
δ_f = 60 deg	27.4	28.4	0/2.0	22.3	16.4	0.4/1.9	22.1	15.0	0.8/2.1	1.464
Double Slotted No. 32										
δ_f = 60 deg	27.4	28.5	0/2.0	32.9	31.8	1.2/2.0				1.349
45 deg	27.4	28.5	0/2.0	32.9	16.7	0.4/2.0				1.357
30 deg	27.4	16.5	1.9/2.0	32.9	13.8	0.3/2.0				1.339
Single Slotted No. 2										
δ_f = 60 deg	32.9	60.0	0/2.0							1.087
45 deg	32.9	45.0	0/2.0							1.087
30 deg	32.9	30.0	1.8/2.0							1.069
15 deg	32.9	14.8	1.8/2.0							1.069
Plain Blown										
δ_f = 60 deg	30.3	60.0	0/0							1.061
45 deg	28.5	45.0	0/0							1.043
30 deg	26.9	30.0	0/0							1.027
15 deg	25.5	15.0	0/0							1.013
Triple Slotted No. 111										
δ_f = 60 deg	13.7	28.0	0/2.0	22.3	17.0	0.5/2.0	22.1	15.0	0.8/2.0	1.326
Double Slotted No. 12										
δ_f = 60 deg	13.7	28.0	0/2.0	33.0	32.0	0.7/2.0				1.218
30 deg	13.7	16.0	1.9/2.0	33.0	14.0	0/2.0				1.206
WING NO. 4										
Triple Slotted No. 311										
δ_f = 60 deg	27.4	28.5	0/2.1	22.4	16.0	0.4/2.0	22.1	15.0	0.7/2.1	1.467
Double Slotted No. 32										
δ_f = 60 deg	27.4	28.5	0/2.1	32.9	31.5	1.2/2.0				1.350
45 deg										
30 deg	27.4	16.5	1.9/2.0	33.0	13.5	0.4/2.0				1.340
WING NO. 5										
Triple Slotted No. 311										
δ_f = 60 deg	27.2	28.5	0/2.1	22.2	16.7	0.5/1.9	21.9	14.8	0.8/2.0	1.452
Double Slotted No. 32										
δ_f = 60 deg	27.2	28.5	0/2.1	32.6	31.5	1.2/1.9				1.339
45 deg	27.4	28.5	0/2.0	32.9	16.5	0.4/2.0				1.357
30 deg	27.3	16.8	2.0/1.9	32.6	13.8	0/1.9				1.331
WING NO. 6										
Triple Slotted No. 311										
δ_f = 60 deg	26.1	27.0	0/1.9	20.5	16.0	0.2/1.7	19.8	15.4	0.8/1.8	1.421
Double Slotted No. 32										
δ_f = 60 deg	26.1	27.0	0/1.8	29.6	31.5	1.0/1.7				1.314
45 deg										
30 deg	26.3	15.3	1.9/1.7	30.4	13.2	1.2/1.8				1.314

*Sectional Data Measured From Drawings at Wing MAC.

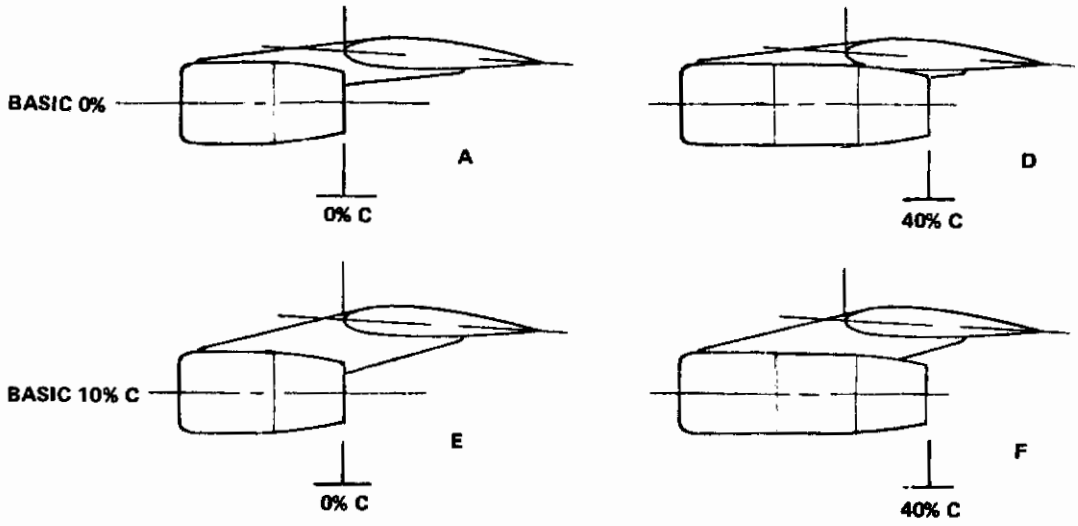

Longitudinal and vertical ejector locations
(Spanwise location A)

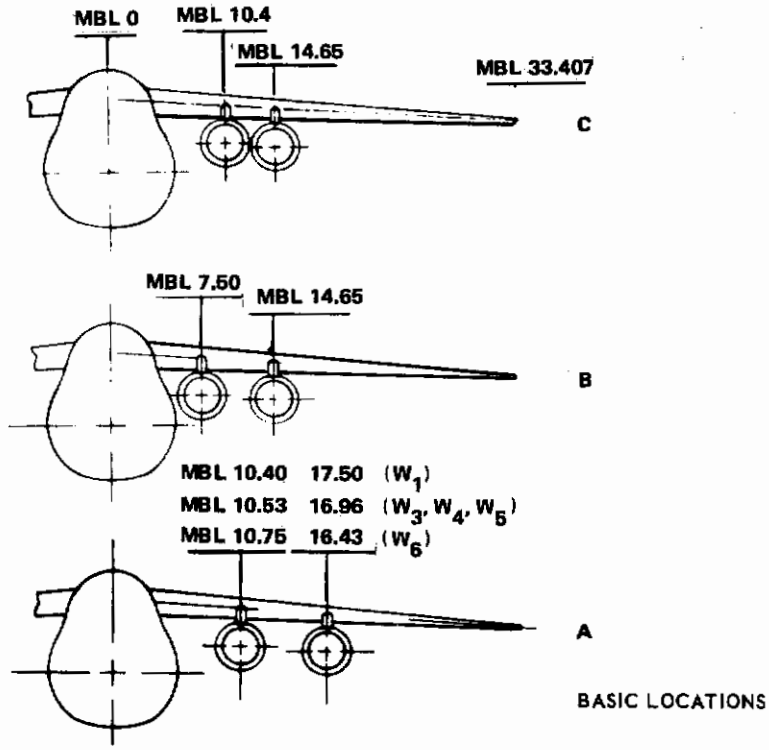

Spanwise ejector locations
(Longitudinal and vertical location A)

Figure 2.0-4. Engine Simulator Locations

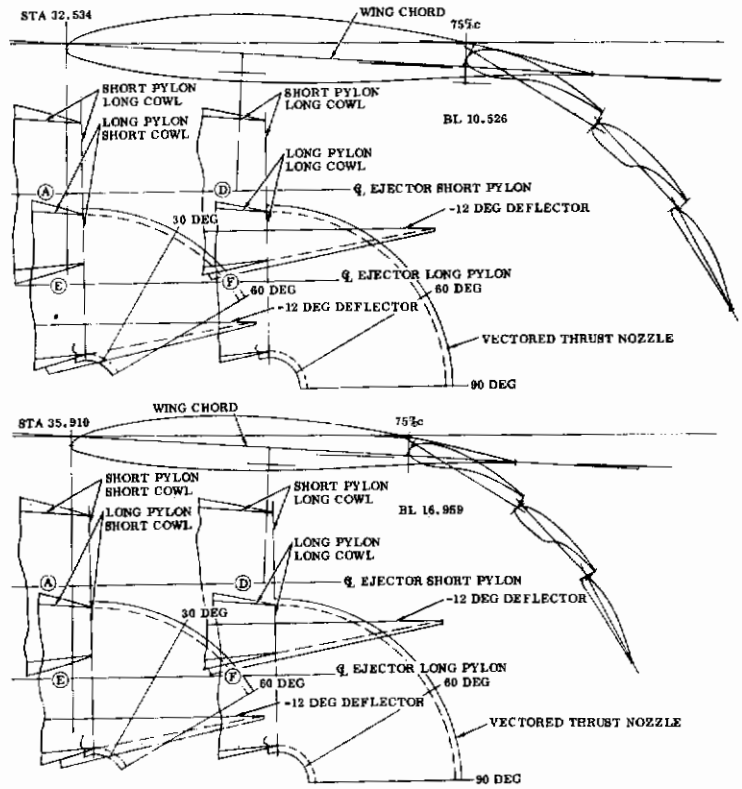

Figure 2.0-5. Airfoil/Nacelle Sectional View, Wing No. 3, Triple-Slotted Flap No. 311 (60 degrees), Nacelle Locations A, D, E, and F

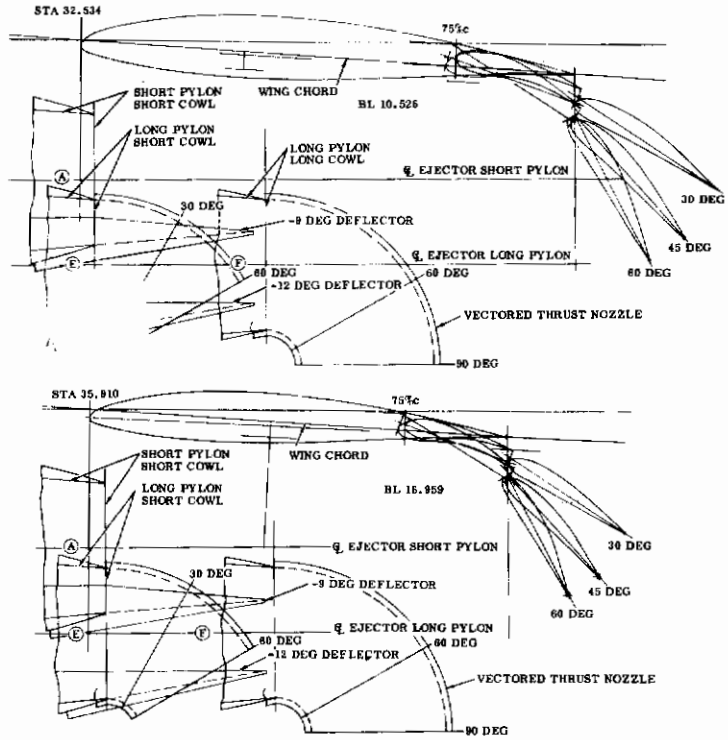

Figure 2.0-6. Airfoil/Nacelle Sectional View, Wing No. 3, Double-Slotted Flap No. 32 (30, 45, and 60 degrees), Nacelle Locations A, E, and F

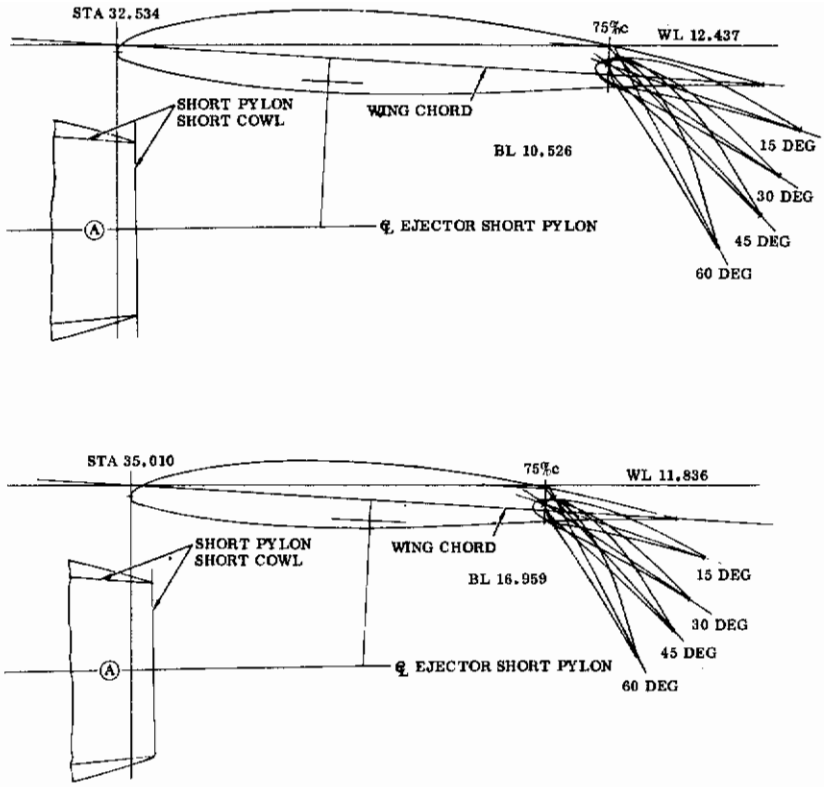

Figure 2.0-7. Airfoil/Nacelle Sectional View, Wing No. 3, Single-Slotted Flap No. 2 (15, 30, 45, and 60 degrees), Nacelle Location A

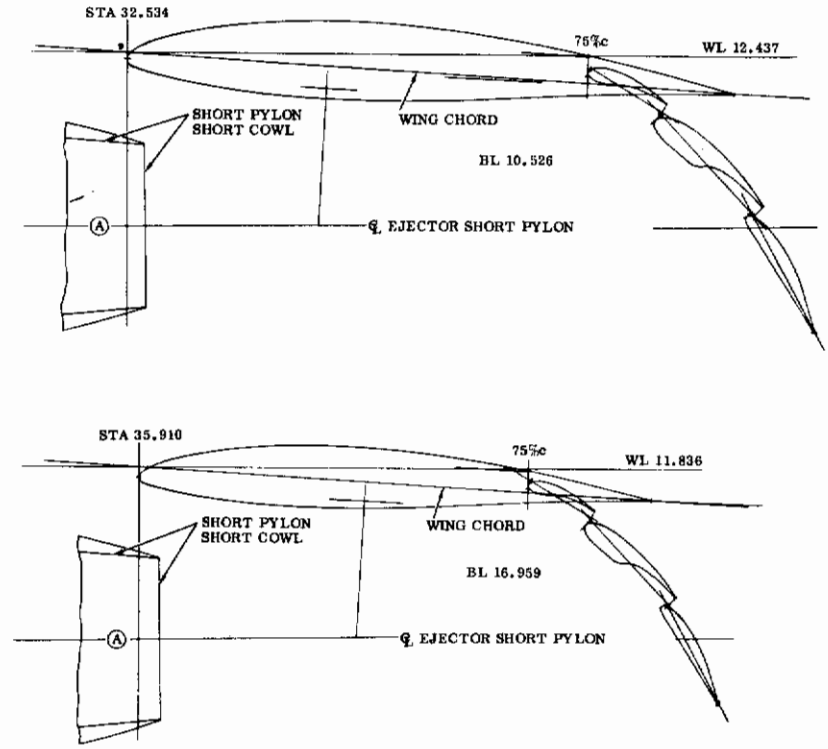

Figure 2.0-8. Airfoil/Nacelle Sectional View, Wing No. 3, Triple-Slotted Flap No. 111 (60 degrees), Nacelle Location A

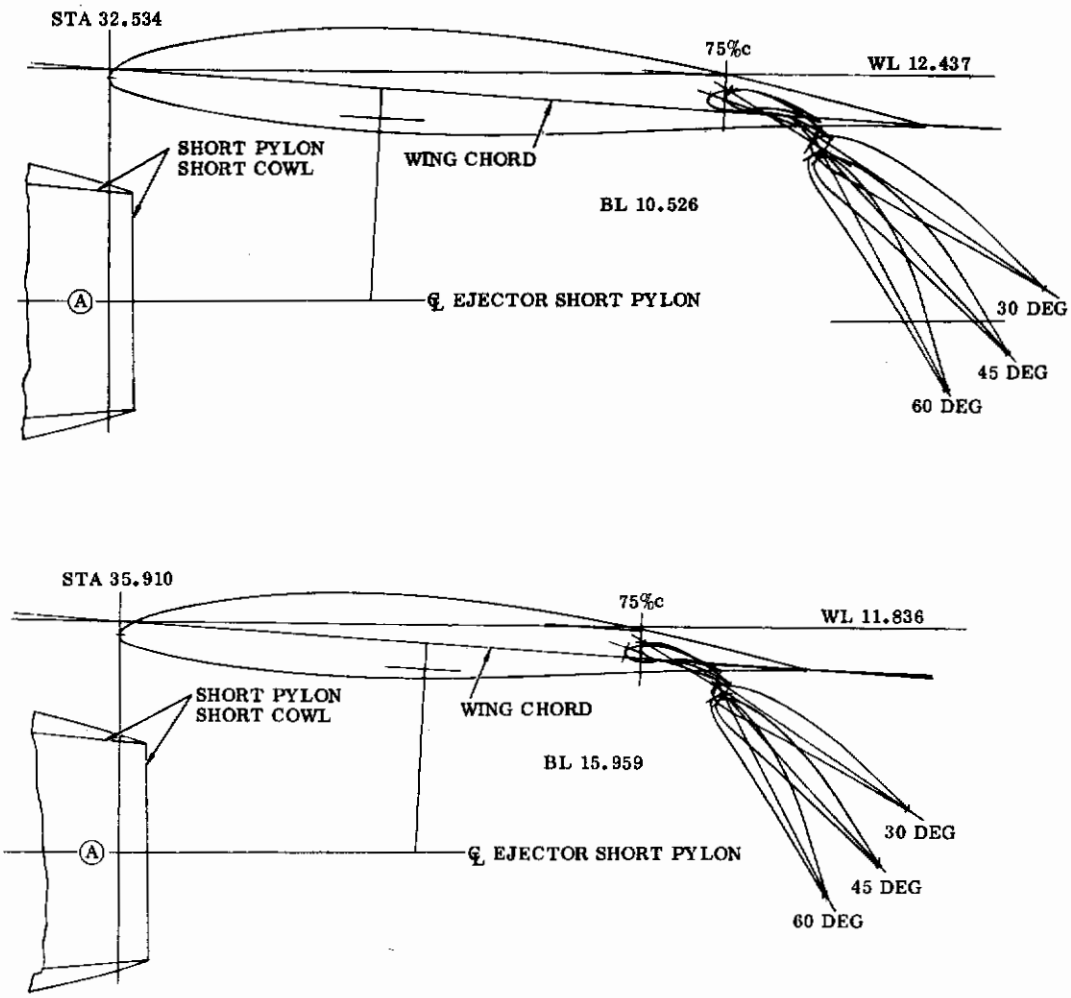

Figure 2.0-9. Airfoil/Nacelle Sectional View, Wing No. 3, Double-Slotted Flap No. 12 (30, 45, and 60 degrees), Nacelle Location A

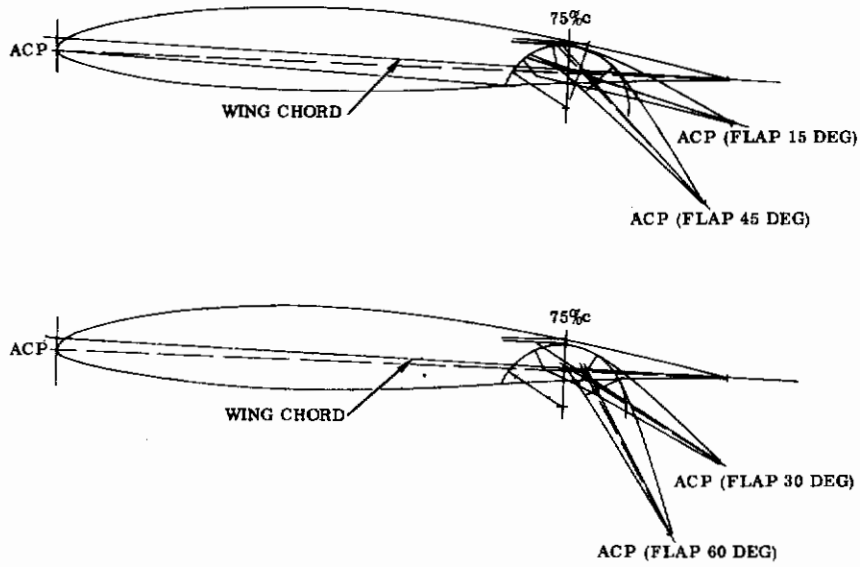

Figure 2.0-10. Airfoil/Plain Blown Flap Sectional View, Wing No. 3

Table 2.0-4. Miscellaneous Model Geometry

Horizontal Tail		
Area	(ft^2)	0.918
Sweepback at c/4	(deg)	25.0
Aspect Ratio		4.50
Taper Ratio		0.40
MAC	(in.)	5.753
Root Section		NACA 0011
Tip Section		NACA 0009
Stabilizer		
Deflection Limits	(deg)	-15 to +5
Elevator		
Chord	(%)	35.0
Span		Full
Deflection Limits	(deg)	±50
Area	(ft^2)	0.3254
Vertical Tail		
Area	(ft^2)	1.020
Sweepback at c/4	(deg)	45
Aspect Ratio		0.95
Taper Ratio		0.65
MAC	(in.)	12.619
Root Section		NACA 0014
Tip Section		NACA 0011
Rudder		
Chord	(%)	30
Span		Full
Deflection Limits	(deg)	±25
Area	(ft^2)	0.2549
Aileron (with BLC)		
Area (per side)	($in.^2$)	7.80
Span (per side)	(in.)	6.343
Chord	(%)	25.0
Deflections	(deg)	+10, 20, 30, and 50

NOTE:
ALL DIMENSIONS ARE IN INCHES MODEL SCALE.

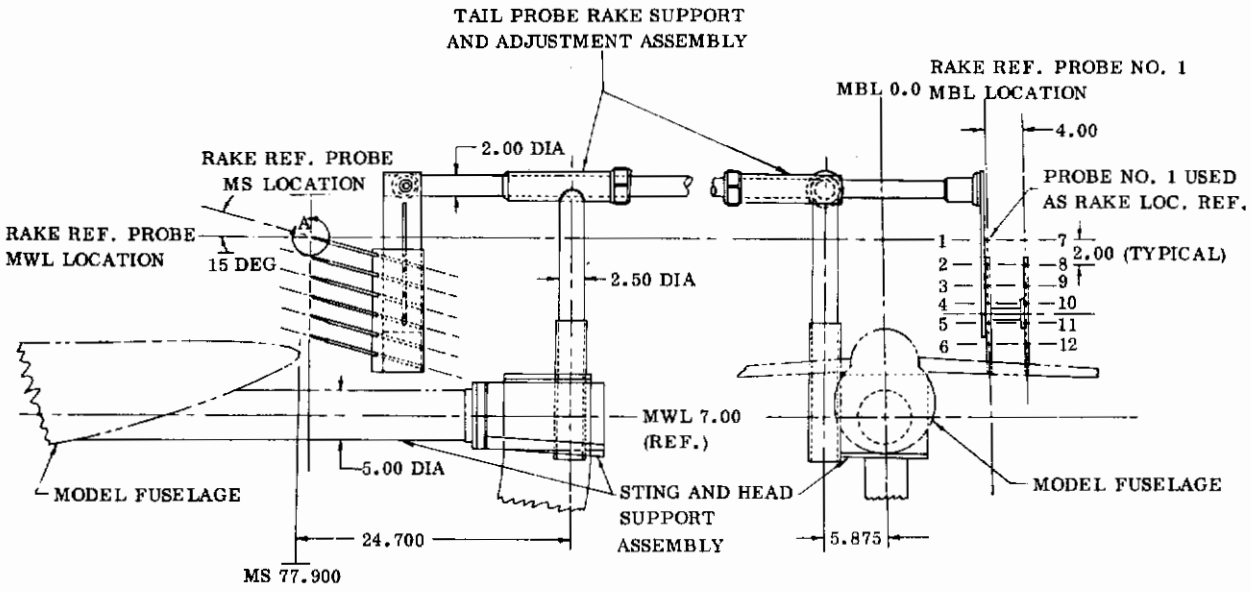

Figure 2.0-11. Trail Probe Rack Assembly

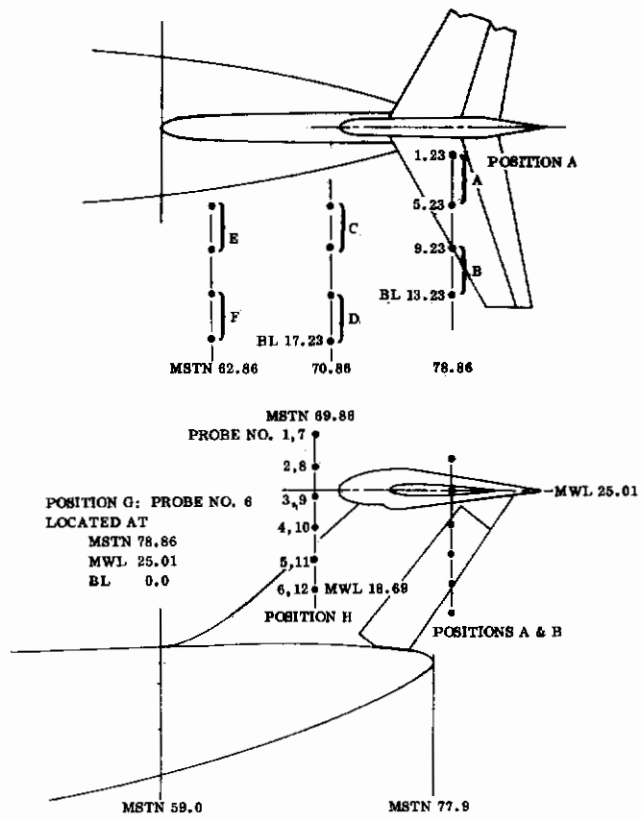

Figure 2.0-12. Trail Probe Positions

SECTION 3

LIFT ANALYSIS

Lift data in the form of lift coefficient based on the reference wing area was obtained from GD/LST 612 wind tunnel tests, Reference 1-1. The lift curve (C_L versus α) was analyzed using an interactive graphic computer program to measure the following aerodynamic parameters.

$\overline{\text{DCL/DALPHA}}$	Lift curve slope measured at an angle of attack near zero where no apparent separation occurs on the wing or high-lift system.
$\overline{\text{CL}\phi}$	Lift coefficient at zero angle of attack obtained as a linear extension of the lift curve slope to $\alpha = 0$.
$\overline{\text{ALPHA}\phi}$	Angle of attack for zero lift coefficient obtained as a linear extension of the lift curve slope to $C_L = 0$.
$\overline{\text{CLMAX}}$	Maximum lift coefficient obtained from a parabolic curve fit of the test data points through wing stall.
$\overline{\text{CUT}}$	Trailing edge blowing coefficient.
$\overline{\text{CJ}}$	Thrust coefficient.

The lift curves for two typical EBF configurations tested are shown in Figures 3.0-1 and 3.0-2. Each figure shows the test data points for lift coefficient plotted against wing angle of attack at several engine power settings. Data for the externally blown triple-slotted flap at 60 degrees of deflection is shown first in Figure 3.0-1. Two identical runs at each power setting are shown, indicating that the data is repeatable. Data for an externally blown, single-slotted flap at 15 degrees of deflection is shown in Figure 3.0-2. Also shown on these figures is the linear curve fit used to evaluate the lift curve slope $\overline{\text{DCL/DALPHA}}$ at low angles of attack. The intercept of this linear curve at $C_L = 0$ and at $\alpha = 0$ are the respective values $\overline{\text{CL}\phi}$ and $\overline{\text{ALPHA}\phi}$.

A quadratic (parabolic) curve fit has been made using the data points around the maximum lift coefficient. The peak value of this curve fit has been taken as the maximum lift coefficient $C_{L_{max}}$. The equations used in the subsequent lift data analysis are summarized in Table 3.0-1.

The numerical values of the terms used in these equations that are not derivable from the test data are tabulated in Table 3.0-2 for each configuration tested.

The test data discussed in this Section has been obtained by assuming that the lift curve is basically a sine curve and is not linear. The large angles of zero lift require that this approximation be made instead of the normal linear approach. The

reference area for the coefficients must be based on the wing area that has been increased due to the extension of flaps and leading edge high-lift devices. The expressions used to make these corrections are given in Table 3.0-1, including corrections to the flap lift increments and maximum lift increments for partial span flaps. This same correction factor is used to account for the fuselage cutout on the flaps. The partial span flap factor curve is shown in Figure 3.0-3.

These lift aerodynamic parameters have been correlated against a jet momentum coefficient, empirically estimated, at the trailing edge of the flap and based on the extended wing area blown by the jet. The estimate of the jet momentum coefficient at the trailing edge of the wing differs between the IBF and the EBF systems. For the IBF system, test data from two sources was used to estimate the momentum coefficient at the flap trailing edge. An equivalent skin friction was obtained from a two-dimensional test, Reference 3-2, of a leading-edge jet nozzle blowing over the top surface of the model to the trailing edge. The variation of the loss in jet momentum with flap chord/nozzle height ratio was obtained from Reference 3-3 and the final results are given in Figure 3.0-4.

For the EBF systems, the loss in momentum due to the jet blowing over the flap is determined by estimating the added skin friction drag due to the jet/flap interaction and assuming this drag to be equal to the loss in jet momentum. Results of this calculation indicated that the loss in jet momentum is equal to 12 percent of the flap chord ratio. Corrections of the wind tunnel blowing coefficient measured at the trailing edge of the flap and based on the extended wing planform that is blown by the jet stream are expressed in Table 3.0-1 for both the IBF and EBF systems.

Test data points on the detailed plots in this section are taken from GDLST 612 (n). The appropriate figure numbers are referenced on the graphs as "W.T. FIG #," with the wing number following in parentheses.

Table 3.0-1. Summary of Equations Used in Analysis of Wind Tunnel Lift Data.

Lift Curve Slope

$$C'_{L_\alpha})_{\alpha = \alpha_{o_L}} = \frac{\overline{DCL/DALPHA}}{\cos(-\alpha_{o_L}) \cdot c'/c}$$

$$K_{pwr} = \frac{C'_{L_\alpha})_{\alpha = \alpha_{o_L}}}{C'_{L_\alpha})_{\substack{PWR \\ OFF}}}$$

Angle of Zero Lift

$$\tan(-\alpha_{o_L}) = \frac{\overline{ALPHA\phi}}{57.29578}$$

Flap Lift Effectiveness at $\alpha = 0$ Degrees

$$\Delta C'_{L_{TE}} = \frac{\overline{CL\phi} - \left[C_{L_o} + \Delta C_{L_{LE}}\right]}{c'/c \cdot K_{bf}}$$

Flap Maximum Lift Increment Due to Blowing

$$\Delta C'_{L_{max}})_{C_{\mu_T}} = \frac{\overline{CLMAX} - \overline{CLMAX})_{C_\mu = 0}}{c'/c \cdot K_{bf}}$$

Blowing Momentum Coefficient-IBF

$$C'_{\mu_T})_{TE} = \frac{\overline{CUT} \cdot (1 - \Delta C_\mu/C_\mu)}{c'/c}$$

Blowing Momentum Coefficient-EBF

$$C'_{\mu_J})_{TE} = \frac{(\overline{CJ} - C_{D_R})(1 - 0.12\, c_f/c)}{c'/c \quad S_{exp}/S}$$

Blowing Momentum Coefficient-MF/VT

$$C'_{\mu_J} = \frac{(\overline{CJ} - C_{D_R})(1 - 0.12\, c_f/c)}{c'/c}$$

Table 3.0-2. Constants Used in Test Data Analysis

		TSF No. 311 δ_f = 60 deg (100% b)					TSF No. 311 60 deg (81.6% b)		DSF No. 32 60 deg (100% b)			
	AR / $\Lambda_{c/4}$	8.0	8.0	9.52	7.14	8.0	8.0	8.0	8.0	9.52	7.14	8.0
	LE	12.5	25.0	25.0	25.0	35.0	25.0	12.5	25.0	25.0	25.0	35.0
c'/c	C	1.510	1.464	1.452	1.452	1.421	1.464	1.385	1.349	1.350	1.339	1.314
$(C_{L_\alpha})_{C_\mu = 0}$	L	0.08004	0.081544	0.07822	0.07822	0.07776	0.81544	0.08263	0.083739	0.08853	0.08055	0.07938
$1 - \Delta C_\mu / C_\mu$	E	0.838	0.915	0.915	0.915	0.915	0.915	0.844	0.928	0.928	0.928	0.928
S_{exp}/S	A	0.855	0.854780	0.8620	0.8487	0.8523	0.82031	0.855	0.85478	0.8620	0.8487	0.8523
K_{bf}	N	0.85	0.858	0.870	0.850	0.864	0.773	0.85	0.858	0.870	0.850	0.864
$\Delta C_{L_{LE}} + C_{L_o}$		0.036	0.04566	0.0764	0.0674	0.0782	0.04566	0.036	0.0469	0.0764	0.0674	0.0782
c'/c	15% c Krueger Flap (55 deg)	1.66	1.609	1.614	1.596	1.566	1.609	1.535	1.494	1.497	1.483	1.459
$(C_{L_\alpha})_{C_\mu = 0}$		0.08004	0.078330	0.08351	0.07490	0.07470	0.078330	0.08763	0.080397	0.08538	0.07708	0.07623
$1 - \Delta C_\mu / C_\mu$		0.838	0.915	0.915	0.915	0.915	0.915	0.844	0.978	0.928	0.928	0.928
S_{exp}/S		0.855	0.85478	0.8620	0.8487	0.8523	0.82341	0.855	0.85478	0.8620	0.8487	0.8523
K_{bf}		0.85	0.858	0.870	0.850	0.864	0.773	0.85	0.858	0.870	0.850	0.864
$\Delta C_{L_{LE}} + C_{L_o}$		-0.023	-0.0167	-0.0164	-0.0174	-0.0130	-0.0167	-0.031	-0.0196	-0.0195	-0.02025	-0.0156
c'/c	15% c Slat (45 deg)	1.66	1.634	1.637	1.636	1.594	1.634	1.535	1.519	1.520	1.519	1.487
$(C_{L_\alpha})_{C_\mu = 0}$		0.08004	0.077795	0.08305	0.07406	0.07413	0.077795	0.08763	0.079840	0.08490	0.07628	0.07565
$1 - \Delta C_\mu / C_\mu$		0.838	0.915	0.915	0.915	0.915	0.915	0.844	0.928	0.928	0.928	0.928
S_{exp}/S		0.855	0.854780	0.8620	0.8487	0.8523	0.82389	0.855	0.85478	0.8620	0.8487	0.8523
K_{bf}		0.85	0.858	0.870	0.850	0.864	0.773	0.85	0.858	0.870	0.850	0.864
$\Delta C_{L_{LE}} + C_{L_o}$		-0.023	-0.0187	-0.01724	-0.0195	-0.0166	-0.0187	-0.031	-0.0217	-0.0204	-0.02258	-0.0193

Table 3.0-2. Constants Used in Test Data Analysis, Cont

		DSF No. 32		DSF No. 32					SSF No. 2			
		δ_f = 60 deg 81.6% b	45 deg 100% b	(30 deg) 100% b					60 deg 100% b	45 deg	30 deg	15 deg
	AR / $\Lambda_{c/4}$ / LE	8.0 25.0	8.0 25.0	8.0 12.5	8.0 25.0	9.52 25.0	7.14 25.0	8.0 35.0	8.0 25.0	8.0 25.0	8.0 25.0	8.0 25.0
c'/c	CLEAN	1.349	1.357		1.339				1.087	1.087	1.069	1.069
$(C_{L_\alpha})_{C_\mu = 0}$	CLEAN	0.083739	0.083584		0.083932				0.088946	0.088946	0.089314	0.089314
$1 - \Delta C_\mu / C_\mu$	CLEAN	0.928	0.928		0.928				0.960	0.960	0.960	0.960
S_{exp}/S	CLEAN	0.82664	0.85478		0.85478				0.85478	0.85478	0.85478	0.85478
K_{bf}	CLEAN	0.773	0.858		0.858				0.858	0.858	0.858	0.858
$\Delta C_{L_{LE}} + C_{L_o}$	CLEAN	0.0469	0.0468		0.0470				0.0498	0.0498	0.0500	0.0500
c'/c	15% c Krueger Flap (55 deg)	1.494	1.502	1.525	1.484	1.487	1.485	1.459	1.232	1.232	1.214	1.214
$(C_{L_\alpha})_{C_\mu = 0}$	15% c Krueger Flap (55 deg)	0.080397	0.080251	0.08334	0.080579	0.08554	0.07704	0.07623	0.085303	0.085303	0.085649	0.085649
$1 - \Delta C_\mu / C_\mu$	15% c Krueger Flap (55 deg)	0.928	0.928	0.844	0.928	0.928	0.928	0.928	0.960	0.960	0.960	0.960
S_{exp}/S	15% c Krueger Flap (55 deg)	0.82937	0.85478	0.855	0.85478	0.8620	0.8487	0.8523	0.85478	0.85478	0.85978	0.85478
K_{bf}	15% c Krueger Flap (55 deg)	0.773	0.858	0.850	0.858	0.870	0.850	0.864	0.858	0.858	0.858	0.858
$\Delta C_{L_{LE}} + C_{L_o}$	15% c Krueger Flap (55 deg)	-0.0196	-0.0194	-0.031	-0.0199	-0.0198	-0.0202	-0.0156	-0.0282	-0.0282	-0.0290	-0.0290
c'/c	15% c Slat (45 deg)	1.519										
$(C_{L_\alpha})_{C_\mu = 0}$	15% c Slat (45 deg)	0.079840										
$1 - \Delta C_\mu / C_\mu$	15% c Slat (45 deg)	0.928										
S_{exp}/S	15% c Slat (45 deg)	0.82979										
K_{bf}	15% c Slat (45 deg)	0.773										
$\Delta C_{L_{LE}} + C_{L_o}$	15% c Slat (45 deg)	-0.0217										

Table 3.0-2. Constants Used in Test Data Analysis, Cont

		TSF No. 111	DSF No. 12			SSF No. 2		PBF			
		δ_f = 60 deg 100% b	δ_f = 60 deg	45 deg	30 deg	δ_f=30 deg	60 deg	60 deg	45 deg	30 deg	30 deg
	AR / $\Lambda_{c/4}$ / LE	8.0 25.0	8.0 25.0	8.0 25.0	8.0 25.0	8.0 12.5	8.0 12.5	8.0 25.0	8.0 25.0	8.0 12.5	8.0 25.0
c'/c	CLEAN	1.326	1.218	1.219	1.206	1.076	1.075	1.061	1.043	1.033	1.027
$(C_{L\alpha})_{C_\mu = 0}$		0.084185	0.086307	0.086288	0.086546	0.09343	0.09343	0.08948	0.08985	0.09450	0.09018
$1 - \Delta C_\mu / C_\mu$		0.932	0.945	0.945	0.945	0.899	0.904	.904	0.9065	0.910	0.909
S_{exp}/S		0.85478	0.85478	0.85478	0.85478	1.000	1.000	1.000	1.00	1.000	1.000
K_{bf}		0.858	0.858	0.858	0.858	0.85	0.85	.858	0.858	0.85	0.858
$\Delta C_{L_{LE}} + C_{L_o}$		0.0471	0.0483	0.0483	0.485	0.040	0.040	0.05050	0.05066	0.040	0.05011
c'/c	15% c Krueger Flap (55 deg)	1.471	1.363	1.364	1.351	1.226	1.225	1.206	1.188	1.183	1.172
$(C_{L\alpha})_{C_\mu = 0}$		0.080817	0.087816	0.082797	0.083041	0.08949	0.08949	0.08580	0.08615	0.09046	0.08646
$1 - \Delta C_\mu / C_\mu$		0.932	0.945	0.945	0.945	0.899	0.904	0.904	0.9065	0.910	0.909
S_{exp}/S		0.85478	0.85478	0.85478	0.85478	1.000	1.000	1.000	1.000	1.000	1.000
K_{bf}		0.858	0.858	0.858	0.858	0.85	0.85	0.858	0.858	0.85	0.858
$\Delta C_{L_{LE}} + C_{L_o}$		-0.0202	-0.0235	-0.0235	-0.0239	-0.039	-0.039	-0.0293	-0.03004	-0.045	-0.03072

Table 3.0-2. Constants Used in Test Data Analysis, Cont

		PBF		
		δ_f = 60 deg 81.6% b	30 deg 81.6% b	15 deg 100% b
	AR / $\Lambda_{c/4}$ / LE	8.0 25.0	8.0 25.0	8.0 25.0
c'/c	C L E A N	1.061	1.027	1.013
$(C_{L_\alpha})_{C_\mu = 0}$		0.08948	0.09018	0.09047
$1 - \Delta C_\mu / C_\mu$		0.904	0.909	0.910
S_{exp}/S		1.000	1.000	1.000
K_{bf}		0.773	0.773	0.858
$\Delta C_{L_{LE}} + C_{L_o}$		0.05050	0.05011	0.05032
c'/c	Krueger Flap (55 deg)	1.206	1.172	1.158
$(C_{L_\alpha})_{C_\mu = 0}$		0.08580	0.08646	0.08674
$1 - \Delta C_\mu / C_\mu$		0.904	0.909	0.910
S_{exp}/S		1.000	1.000	1.000
K_{bf}		0.773	0.773	0.858
$\Delta C_{L_{LE}} + C_{L_o}$		-0.0293	-0.03072	-0.03133

	TSF No. 311		DSF No. 32	
	60 deg 100% b	60 deg 81.6% b	60 deg 100% b	60 deg 81.6% b
AR / $\Lambda_{c/4}$ / LE	8.0 25.0	8.0 25.0	8.0 25.0	8.0 25.0
25% C Krueger Flap (55 deg)	1.704	1.704	1.589	1.589
	0.076325	0.076325	0.078311	0.078311
	0.915	0.915	0.928	0.928
	0.854780	0.82516	0.854780	0.83089
	0.858	0.773	0.858	0.773
	-0.0813	-0.0813	-0.0884	-0.0884
25% C Slat (45 deg)	1.730	1.730	1.615	1.615
	0.075789	0.075789	0.077754	0.077754
	0.915	0.915	0.928	0.928
	0.854780	0.82561	0.85478	0.83128
	0.858	0.773	0.858	0.773
	-0.0748	-0.0748	-0.0814	-0.0814

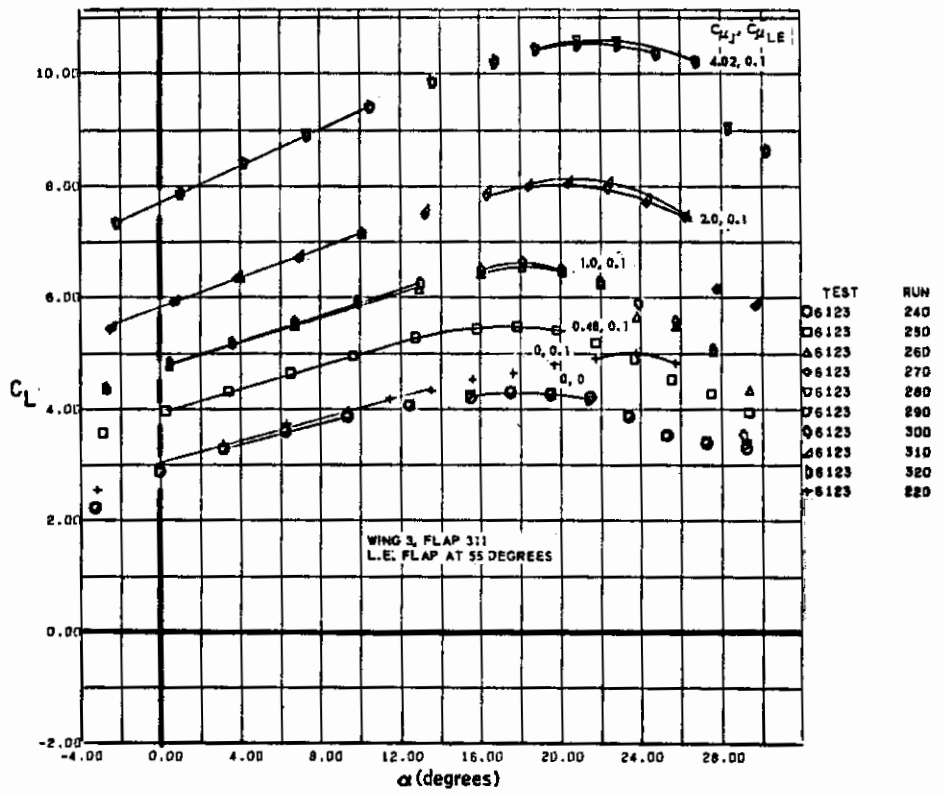

Figure 3.0-1. Typical Lift Curves for EBF Triple-Slotted Flap (60 degrees)

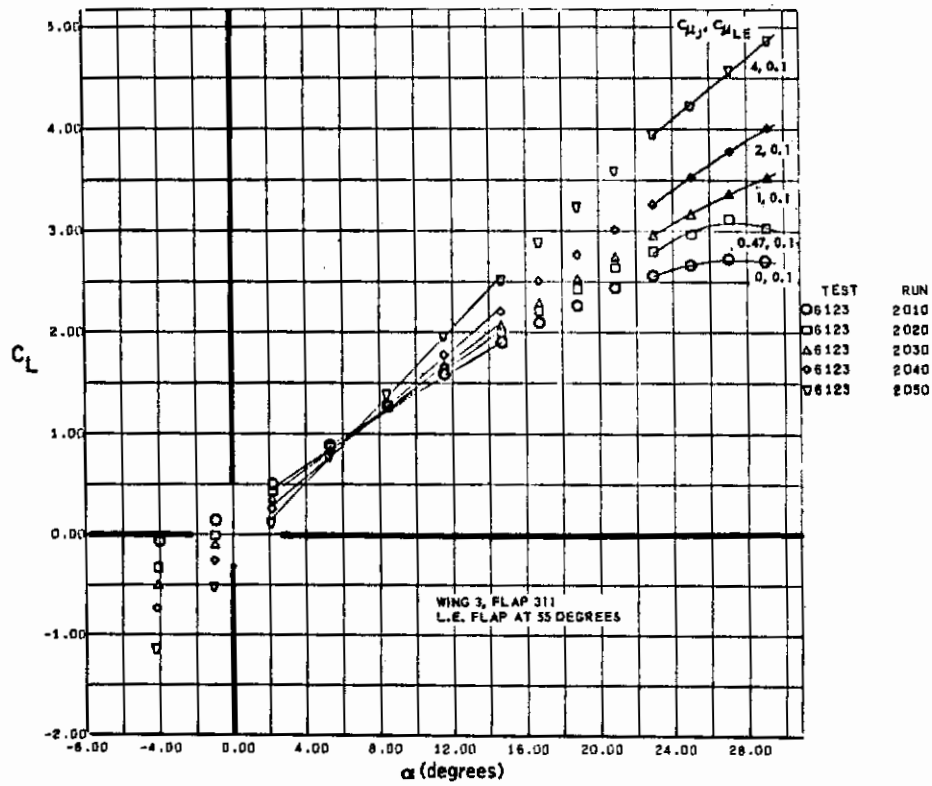

Figure 3.0-2. Typical Lift Curves for EBF Single-Slotted Flap (15 degrees)

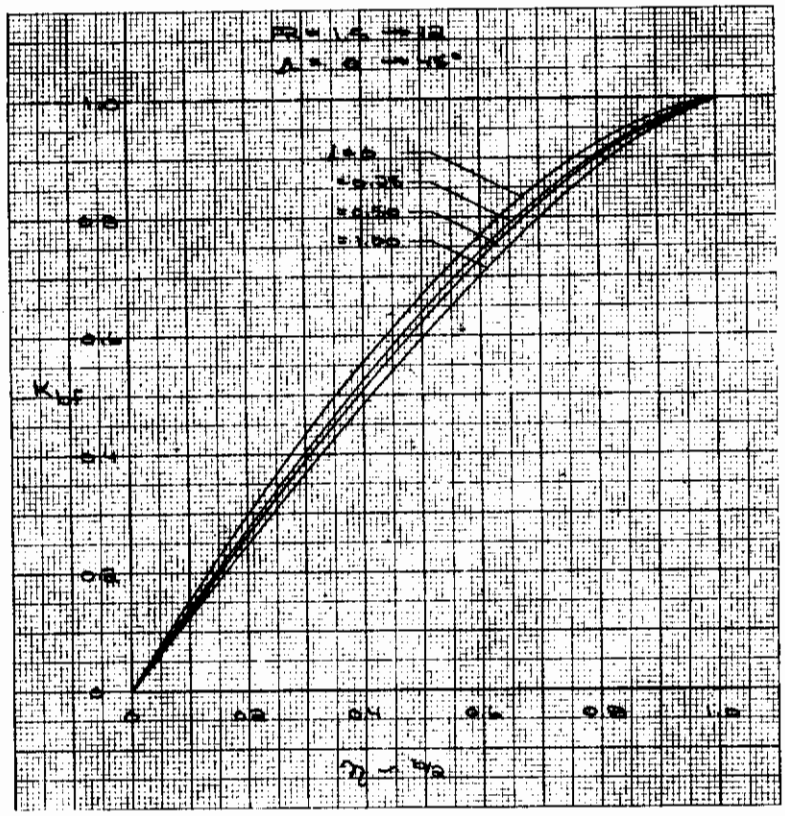

Figure 3.0-3. Partial Span Flap Factors

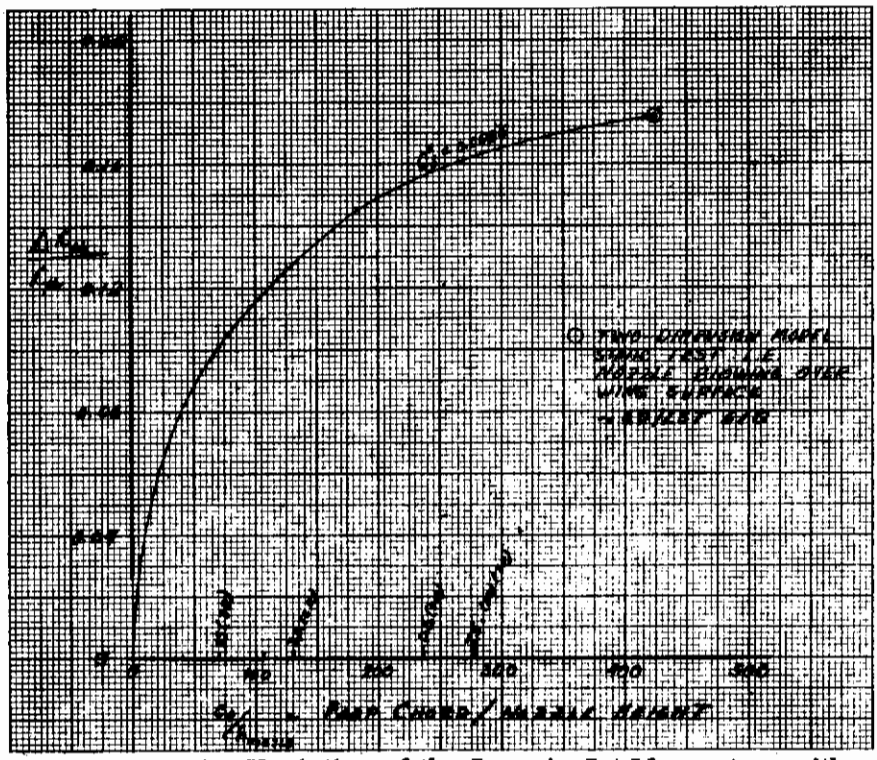

Figure 3.0-4. Variation of the Loss in Jet Momentum with Flap Chord/Nozzle Height

3.1 EBF LIFT CURVE SLOPE ANALYSIS

The analysis of the lift curve slope from wind tunnel test data is presented here as the term K_{pwr}, which is the ratio of the power-on lift curve slope to the power-off lift curve slope assuming full potential flow. This term is presented versus the momentum coefficient $(C\mu'_J)_{TE}$, as estimated at the trailing edge of the flap and based on the blown flap area. The EBF data has been analyzed as it it were IBF data. This EBF/IBF analogy is seen in Figure 3.1-1, which presents a comparison of the lift curve slope ratio, K_{pwr}, for an IBF and EBF triple-slotted flap at 60 degrees of deflection. Test data in this plot shows that there is little difference between K_{pwr} of the two powered lift systems.

On the subsequent data analysis plots appearing in this section, two theoretical lines have been added to show the effects of augmentation. The first line, labeled no augmentation, is simply the power-off lift curve slope ratio plus the effect of the direct thrust vector (Table 3.1-1). The full augmentation line is estimated using the jet flap theory and lifting line theory application by Hartunian from Reference 3-4 (Figure 3.0-3). The full augmentation theory is summarized in Table 3.1-1.

3.1.1 EFFECT OF TRAILING EDGE FLAP CONFIGURATION ON K_{pwr}. Thin airfoil theory has shown that flap deflection does not change the lift curve slope from that of the basic airfoil if flap deflection is not so great that the airfoil stalls. The plots in Figure 3.1-2 show the lift curve slope ratio, K_{pwr}, for several flap configurations on the five wing planforms tested. At zero and low values of momentum coefficient, the lift curve slope ratio is generally below unity. This is caused by flow separation on the aft portion of the flap and is most pronounced for the double-slotted flap at 60 degrees and the single-slotted flap at 45 and 60 degrees. This separation is reduced with the application of power (BLC effect). The small flaps with large deflections show a greater improvement in K_{pwr} than does the large flap configurations at high deflections. This phenomena is shown in the figures. The double-slotted flap at 60 degrees of deflection shown in Figure 3.1-2 shows a comparatively low lift curve slope ratio at $C\mu'_J = 0$. At $C\mu'_J = 0.3$ the lift curve slope ratio has increased and is shown equal to the ratio for the 60-degree, triple-slotted flap, indicating that a BLC effect has reduced some of the separation. At larger momentum coefficients, the lift curve slope ratio for the 60-degree deflection double- and triple-slotted flaps in Figure 3.1-2a is larger than the flaps at 30 degrees. This larger lift curve slope ratio is due to increased flow augmentation of these flaps. The amount of augmentation that will be obtained with a given flap deflection will be a function of the amount of flap immersed in the jet stream.

In Figure 3.1-2b, the single-slotted flap at 30 degrees of deflection shows a high lift curve slope ratio at low values of momentum coefficient (as high as full augmentation); at high values of momentum coefficient, the lift curve slope ratio indicates no augmentation. This characteristic is shown clearly in Figure 3.1-2f. Data shown is for

a single-slotted flap at deflections from 15 through 60 degrees. The 45-degree deflection flap shows the normal EBF trend discussed earlier in this section (i.e., highly separated flap at zero momentum coefficient) becoming unseparated as blowing increases, but showing almost no augmentation at the higher momentum coefficients. At 60 degrees of deflection, the BLC effect does not occur and the flap remains stalled throughout the momentum coefficient range, resulting in low lift curve slopes. At flap deflections of 30 and 15 degrees, the lift curve slope ratio appears to be large at low momentum coefficients but is more normal at the large momentum coefficients. These large lift curve slope ratios at low momentum coefficient are accompanied by little or no flap lift effectiveness at zero angle-of-attack and more normal flap lift effectiveness at the higher momentum coefficients, see Section 3.4. This would suggest that the amount of lift augmentation changes with angle-of-attack at the low momentum coefficients resulting in the large lift curve slopes shown in the data of Figure 3.1-2f.

The effects of varying the flap chord is shown in Figure 3.1-3a for triple-slotted flaps and in Figure 3.1-3b through 3.1-3d for double-slotted flaps at 60, 45, and 30 degrees deflection. There is no effect of flap chord on the lift curve slope ratio other than the augmentation differences due to the different amount of flap immersion in the jet stream.

The effect of flap span is shown in Figure 3.1-4 for triple and double slotted flaps. As would be expected, no major effects on the lift curve slope ratio is shown since the flap span was reduced well outside the influence of the jet stream. It would be expected that a reduction in augmented lift curve slope would occur if the flap span was cut-off in the jet stream.

3.1.2 EFFECT OF LEADING EDGE CONFIGURATION ON K_{pwr}. The effect of blowing from the leading edge Krueger flap is shown in Figure 3.1-5a. The figure shows this effect on K_{pwr} for triple and double-slotted flaps at 60 degree deflection. The data shows that leading edge blowing will have the effect of reducing flap separation with no jet engine blowing but with the leading edge blowing shows little augmentation effect. However, higher leading edge blowing rates may increase the augmentation of the lift curve slope ratio. This effect is also shown in Figures 3.1-5b and 3.1-5c where Krueger-off and Krueger-on, with and without blowing show the same effect at various jet engine blowing rates greater than zero.

The effect of deflection and chord length of leading edge high lift devices is shown in Figures 3.1-6 and 3.1-7. There is little effect on the lift durve slope ratio of these configuration variables. Figure 3.1-8 shows the effect of a blowing leading edge Krueger flap and unblown slat for three other wings.

3.1.3 EFFECT OF NACELLE LOCATION ON K_{pwr}. The effects of the nacelles on the power-off lift curve is shown in Figure 3.1-9. The changes in the increment in lift coefficient with angle-of-attack, shown for several wings with different flap systems, is small; therefore, the nacelles effect on lift curve slope is negligible.

Wind tunnel tests with the nacelles located in different spanwise positions shows that the inboard nacelle position (location B) will have the greatest value of lift curve slope ratio and the nacelles outboard (location A) have the lowest value (see Figure 3.1-10). Due to inaccuracies in measuring slopes from test data, scatter in these measurements tend to mask any real differences due to nacelle spanwise location on the 12.5 degree swept wing.

The chordwise location of the engine nacelles for the two positions tested showed negligible effect on the lift curve slope ratio. Figure 3.1-11 shows this lift curve slope ratio for each of the five wings tested with the triple slotted flap, and for the double-slotted flap on the 12.5 degree swept wing. Chordwise position of the engine nacelle shows very little effect on the lift curve slope ratio of a flap system that has only a small amount of augmentation.

The effect on the lift curve slope ratio of tilting the jet engine thrust line up is also shown throughout the plots in Figure 3.1-11. For the nacelle in this close proximity to the wing, the 3.5 degree tilt built into the model appeared adequate to obtain maximum augmentation for each given flap system. A very slight decrease in lift curve slope would be expected if there were no increase in augmentation due to directing the jet stream upward into the slots of the flap. The most dramatic display of the effect of jet tilt on the lift curve slope augmentation is obtained with the engine nacelle in the lowered position (location E) as shown in Figure 3.1-12a for the wing with the triple-slotted flap. First, it is seen that all lift curve slope augmentation is lost together with some of the BLC effect when the jet stream is lowered away from the wing. This would be expected since the immersion of the flap in the jet stream is reduced. With the engine nacelle in the lower position (location E) and with the jet stream deflected upward toward the slots of the flap, the BLC effect and the augmentation is again regained.

The vertical location of the engine nacelle has a large effect on the augmentation of the lift curve slope ratio. As mentioned above and also in the discussion on the effects of flap chord and deflection the augmentation of the lift curve slope ratio is a function of the amount of flap immersed in the jet stream. Figure 3.1-12a shows this effect with the triple-slotted flap deflected 60 degrees on wing 3. The effect of nacelle vertical location for other flap configurations and deflection on wings 1, 3, and 6 is shown in Figures 3.1-12b through 3.1-12d for the nacelle in the forward position and in Figures 3.1-12e to 3.1-12g for the nacelle in the aft position. For all flap configurations the lift curve slope ratio is less with the nacelle in the lowered position with some configurations showing no augmentation.

3.1.4 EFFECT OF ASPECT RATIO ON K_{pwr}. The effect of wing aspect ratio on the lift curve slope ratio is shown in Figure 3.1-13 for several flap and leading edge configurations. The test data shows that the lift curve slope ratio is the greatest for the wing with an aspect ratio of 9.52 and the least for the wing with an aspect ratio 7.14. The theoretical analysis for full lift augmentation from Hartunian, Reference 3-4, indicates that the lift curve slope ratio has a small variation with wing aspect ratio and over the range of aspect ratios tests this variation would be negligible. This is contrary to the test results indicating that Hartunian does not include all of the aspect ratio effect. It is interesting to note that the no augmentation lift curve slope ratio does have a variation with aspect ratio, Figure 3.1-13, and that even though this variation is about half the variation obtained from the test data, the theoretical variation in lift curve slope ratio does have the same trends as shown in the test data.

3.1.5 EFFECT OF WING SWEEP ON K_{pwr}. The effect of wing sweep is shown in Figure 3.1-14 for several flap and leading edge configurations. The test data show that the lift curve slope ratio is largest for the higher sweep configuration (35 degrees) and smallest for the lower sweep configuration (12.5 degrees). The theoretical analysis from Hartunian, Reference 3-4, has no accountability for sweep on the effect of power. This is apparently contrary to test results. Since Hartunian assumes full spreading of the jet like an IBF system, then wing sweep must have an effect on spreading and therefore on augmentation of the lift curve slope ratio. This is shown in the plots. The effect of sweep on the no augmentation lift curve slope ratio shows the same trend as the test data.

Table 3.1-1. Summary of Theoretical Augmentation Equations Used in Analysis of Wind Tunnel Lift Data.

I. Power-On/Power-Off Lift Curve Slope Ratio

$$K_{pwr} = \frac{k_{pwr}\left[1 + \frac{2C'_{\mu_T}\big)_{TE}}{\pi A'}\right]}{1 + \frac{2}{A'+2}\left[k_{pwr} - 4D_o - 1\right]} \qquad \text{(Full Augmentation)}$$

where

$k_{pwr} = 1 + 0.151\, C'_{\mu_T}\big)_{TE}^{1/2} + 0.219\, C'_{\mu_T}\big)_{TE}$ (Spence Jet Flap Theory)

$D_o = -0.08\, C'_{\mu_T}\big)_{TE}$

A' = Aspect ratio based on extended wing area

$C'_{\mu_T}\big)_{TE}$ = Momentum coefficient at the wing trailing edge of flap, based on extended wing area spanned by blowing

$$K_{pwr} = 1 + \frac{C'_{\mu_T}\big)_{TE}\cos\left(\alpha_{OL} + \delta_J\right)}{C'_{L_\alpha}\big)_{pwr\text{-}off}} \qquad \text{(No Augmentation)}$$

where

α_{OL} = Angle of attack at zero lift

δ_J = Jet deflection angle

$$C'_{L_\alpha}\big)_{pwr\text{-}off} = \frac{2\pi A'}{2 + \left[\left(\frac{A'\beta}{\kappa}\right)^2\left(1 + \frac{\tan^2\Lambda}{\beta^2}\right) + 4\right]^{1/2}}$$

$\beta = (1-M^2)^{1/2}$

$\kappa = c'_{\ell_\alpha}\big)_{pwr\text{-}off} \Big/ \frac{2\pi}{\beta}$

$c'_{\ell_\alpha}\big)_{pwr\text{-}off} = c'_{\ell_{\alpha_{th}}} \cdot \frac{1.05}{\beta}$

$c'_{\ell_{\alpha_{th}}} = 2\pi + 4.7\, t/c' \left[1 + 0.00375\, \theta_{TE}\right]$

Λ = Sweep of the 50% chord line

Table 3.1-1. Summary of Theoretical Augmentation Equations Used in Analysis of Wind Tunnel Lift Data, Cont

II. Trailing Edge Flap Lift Increment at $\alpha = 0$ Degrees

- $$\Delta C'_{L_{TE}} = \frac{C'_{L_\alpha}\Big)_{\text{pwr-off}}}{c_{\ell_\alpha}\Big)_{\text{pwr-off}}} \cdot \frac{K_{\text{pwr}}}{k_{\text{pwr}}} \cdot \Delta c'_\ell\Big)_{TE}$$ (Full Augmentation)

where

$$\Delta c'_\ell\Big)_{TE} = \sum c_{\ell_{\delta_n}} \cdot \delta_{f_n}$$

$c_{\ell_{\delta_n}}$ = Theoretical flap lift effectiveness due to deflection from thin airfoil theory and jet flap theory. (Subscript "n" denotes the different flap segments.)

δ_{f_n} = Trailing edge flap deflection - radians (δ_f of most-aft flap segments includes upper surface angle for IBF only).

- $$\Delta C'_{L_{TE}} = C'_{\mu_T}\Big)_{TE} \cdot \sin(-\delta_J)$$ (No Augmentation)

III. Maximum Trailing-Edge Flap Lift Increment Due to Power

- $$\Delta C'_{L_{max}}\Big)_{C_{\mu_J}} = C'_L\Big)_{C_{\mu_J},\ \alpha_{So}} - C'_L\Big)_{C_{\mu_J}=0,\ \alpha_{So}}$$ (Full Augmentation)

where

α_{So} = Power-off angle of attack at $C_{L_{max}}$

- $$\Delta C'_{L_{max}}\Big)_{C_{\mu_J}} = C'_{\mu_T}\Big)_{TE} \cdot \sin(\alpha_{S_o} - \delta_J)$$ (No Augmentation)

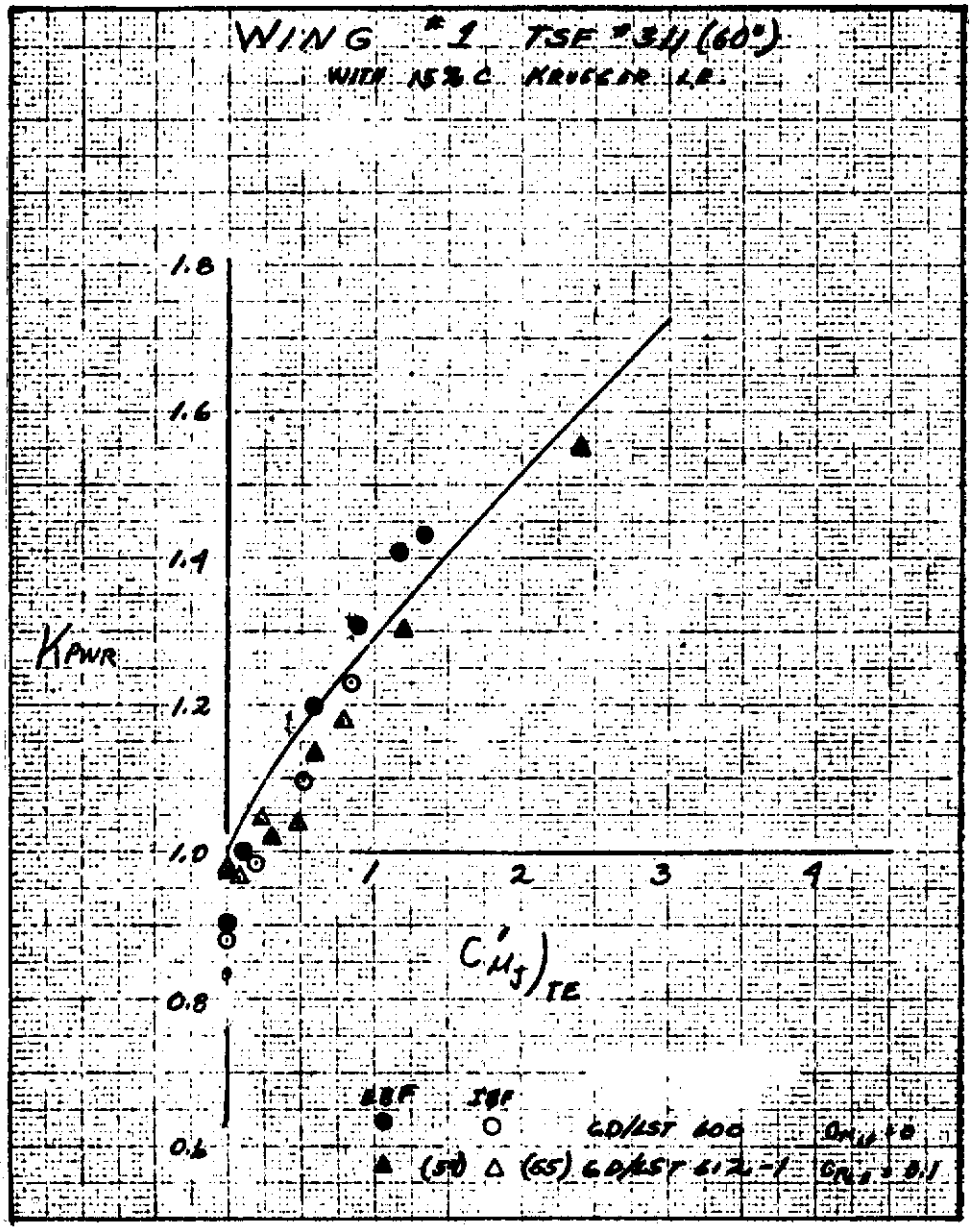

Figure 3.1-1. EBF/IBF Analogy

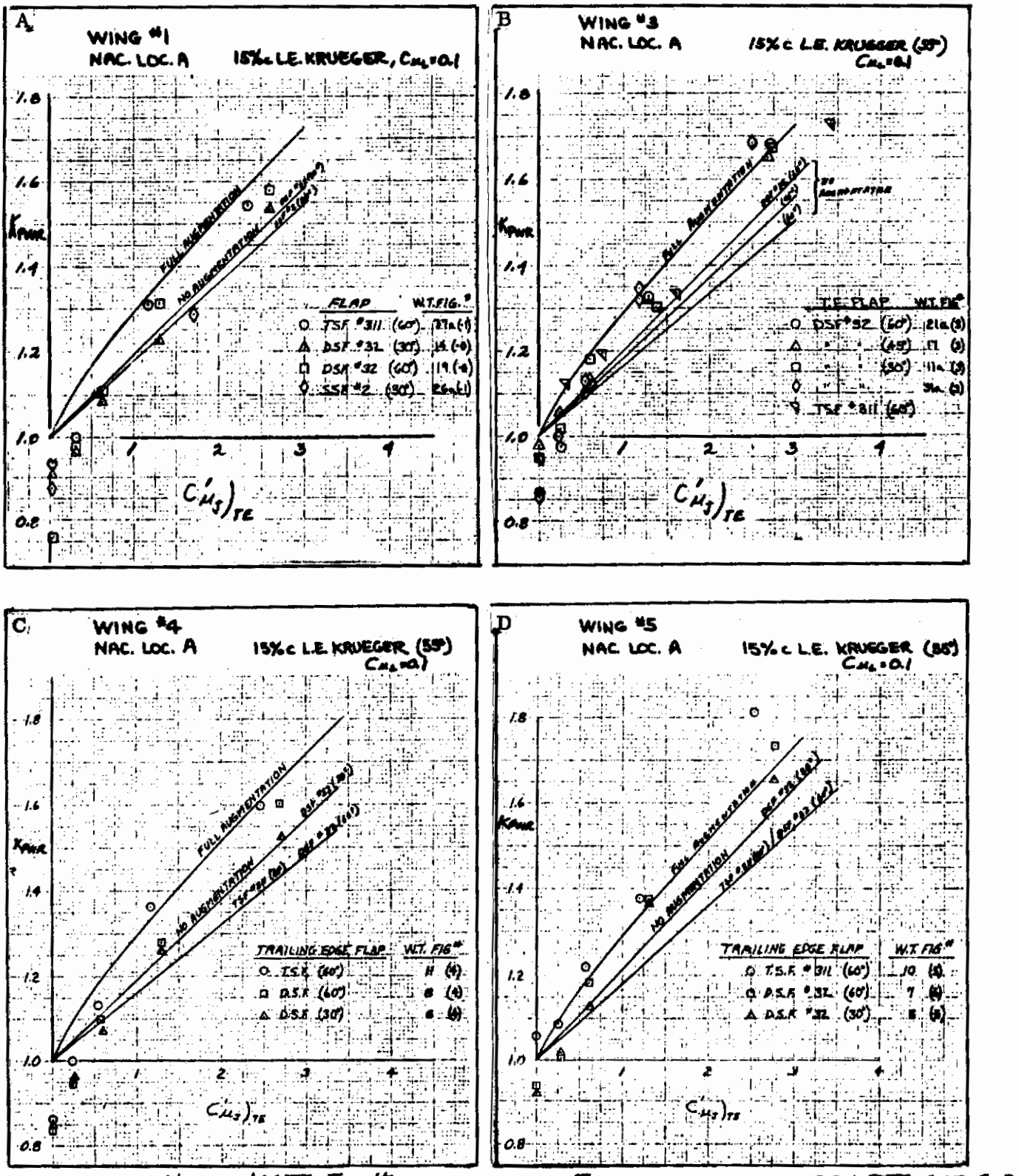

NOTE: W.T. FIG # INDICATES FIGURE ___ FROM GDLST 612( )

Figure 3.1-2. Effect of Trailing Edge Flap Configuration on K_{pwr}

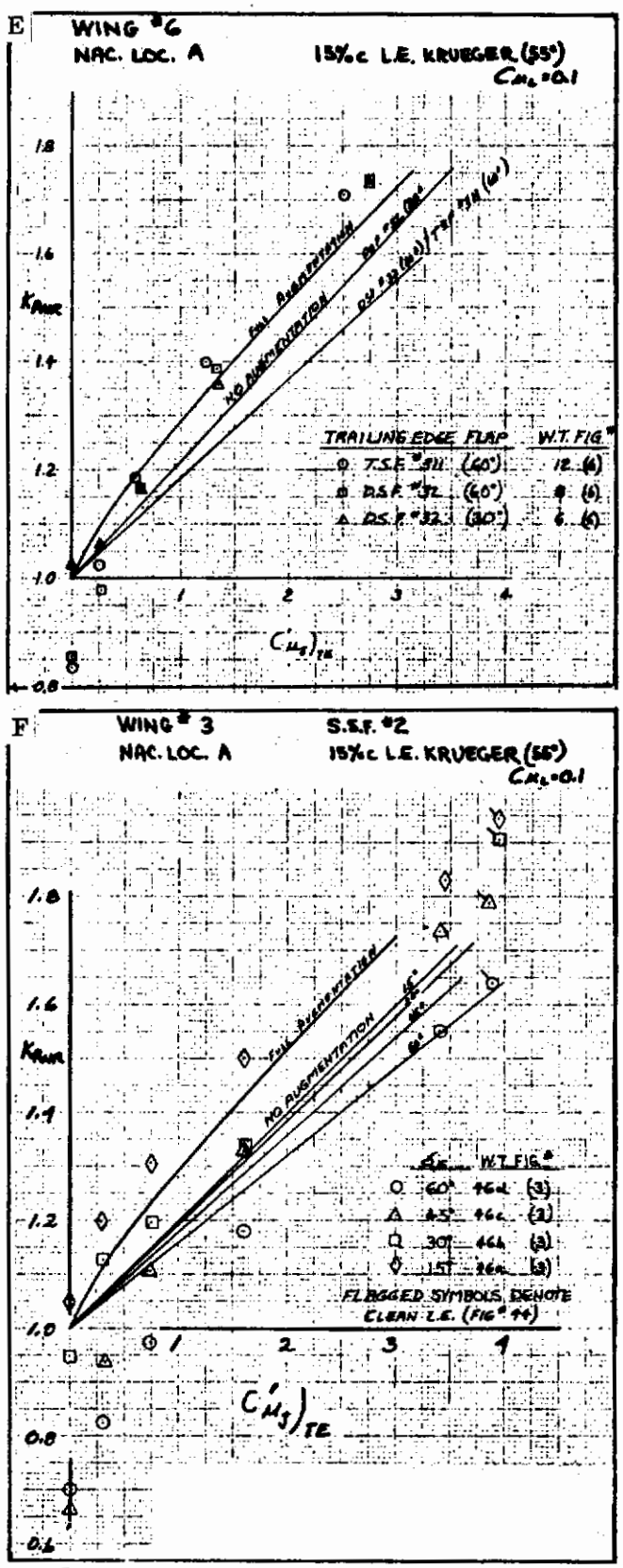

Figure 3.1-2. Effect of Trailing Edge Flap Configuration on K_{pwr}, Cont

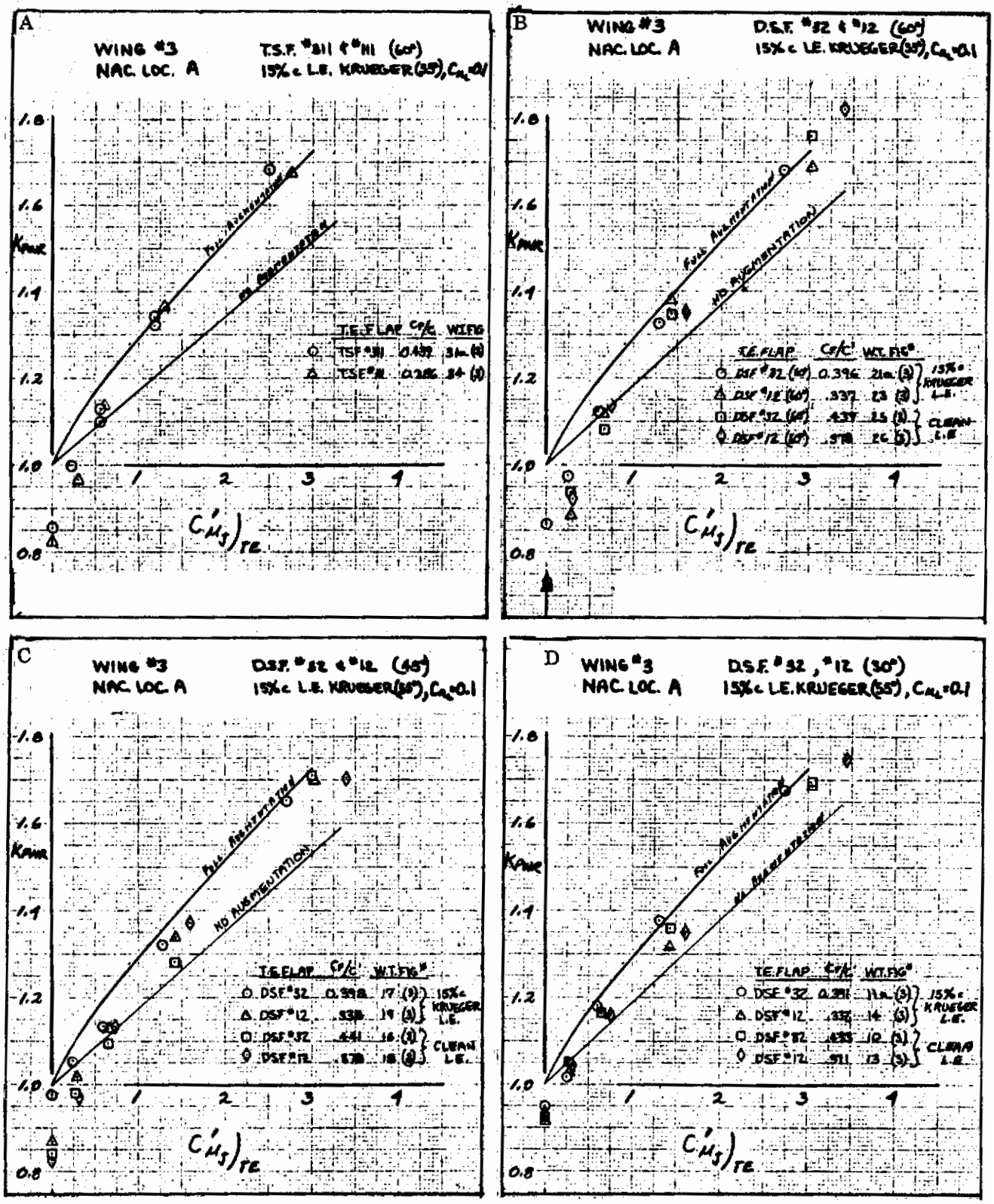

Figure 3.1-3. Effect of Trailing Edge Flap Chord on K_{pwr}

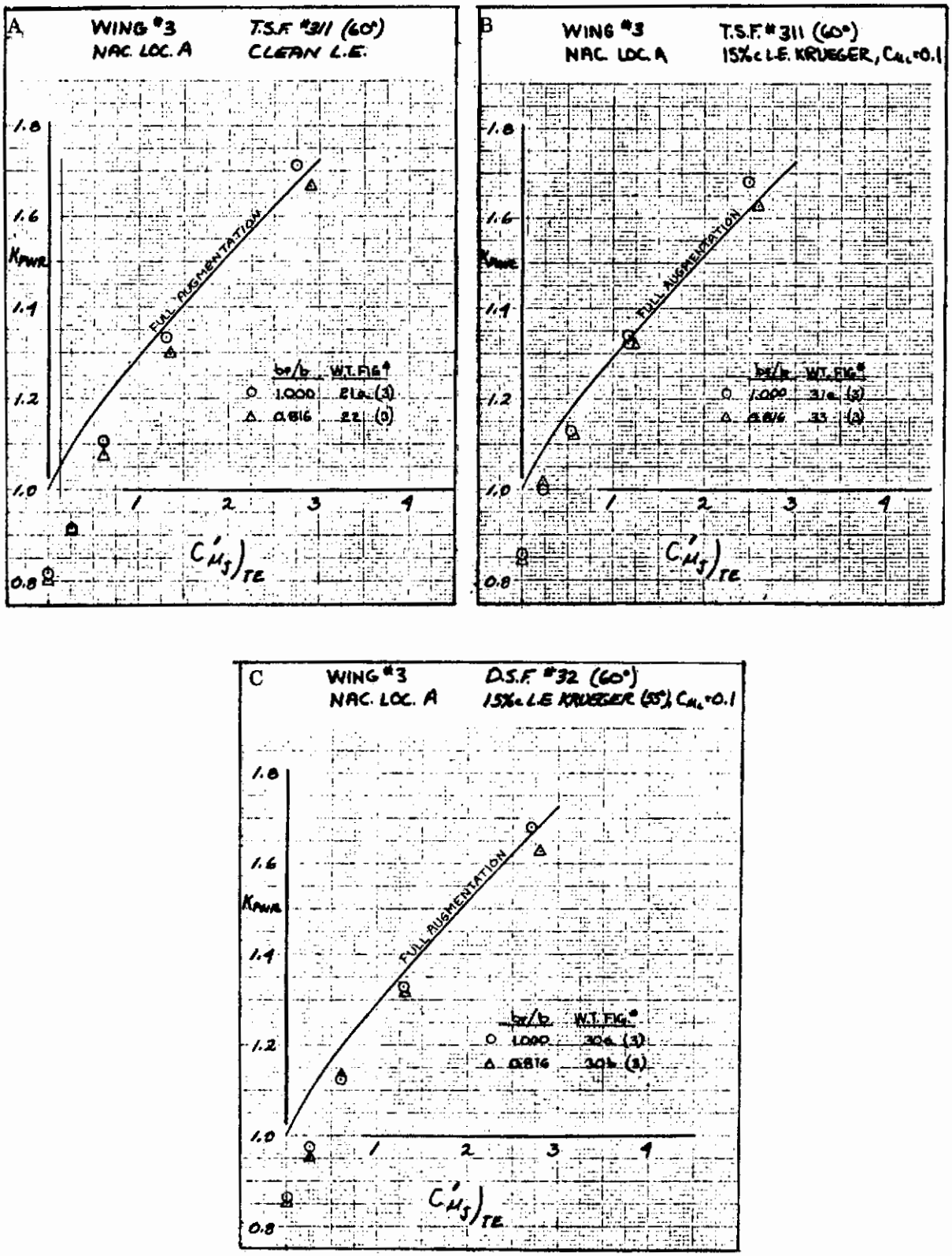

Figure 3.1-4. Effect of Partial Span Trailing Edge Flap on K_{pwr}

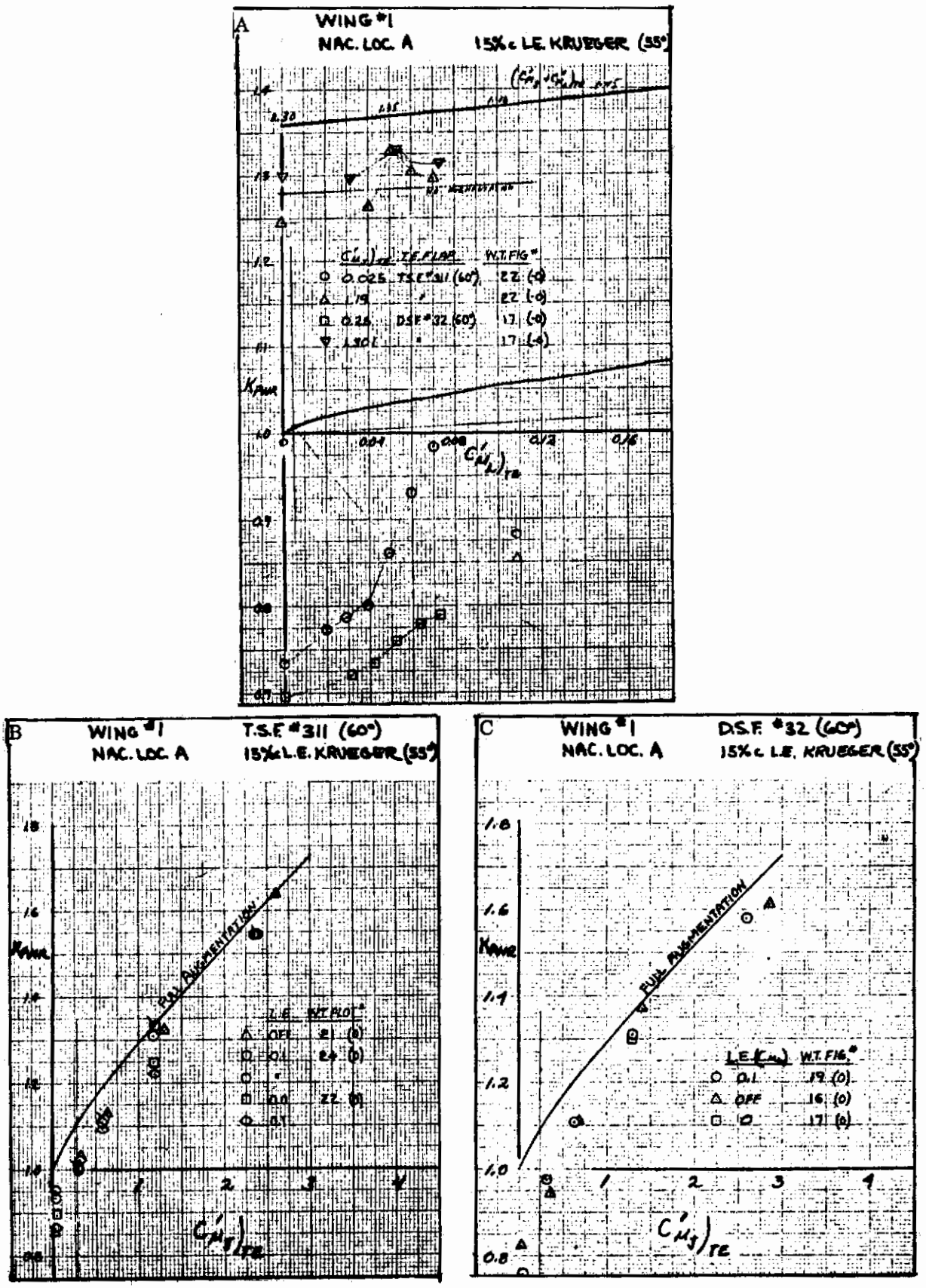

Figure 3.1-5. Effect of Leading Edge Blowing on K_{pwr}

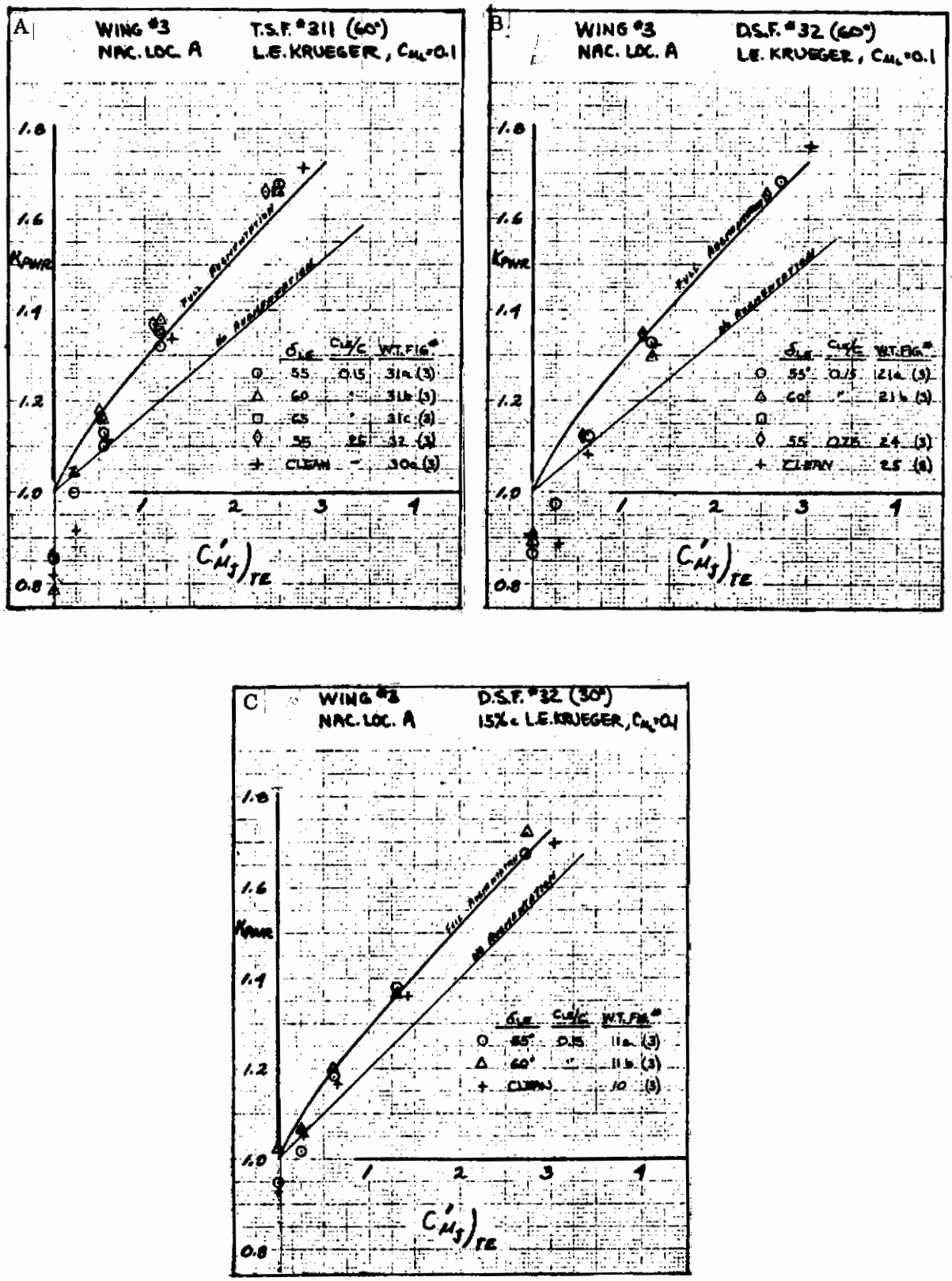

Figure 3.1-6. Effect of Leading Edge Flap Deflection and Chord on K_{pwr}

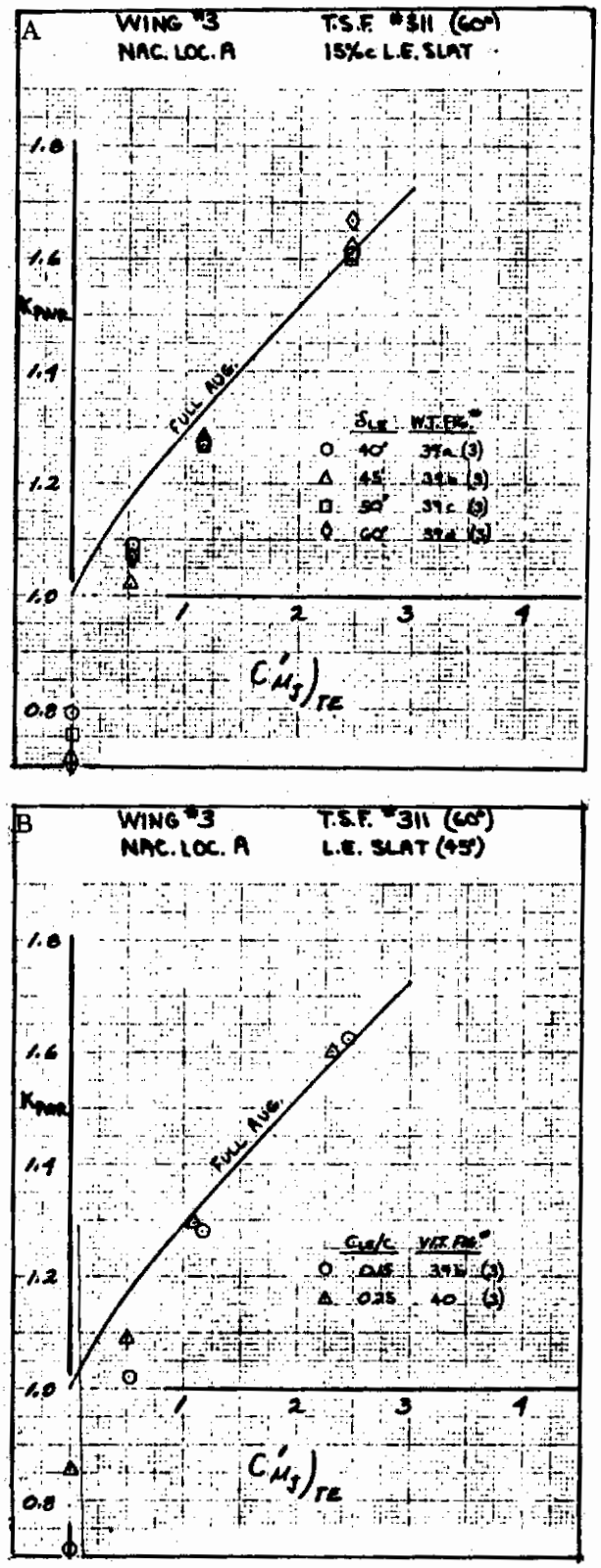

Figure 3.1-7. Effect of Leading Edge Slat Deflection and Chord on K_{pwr}

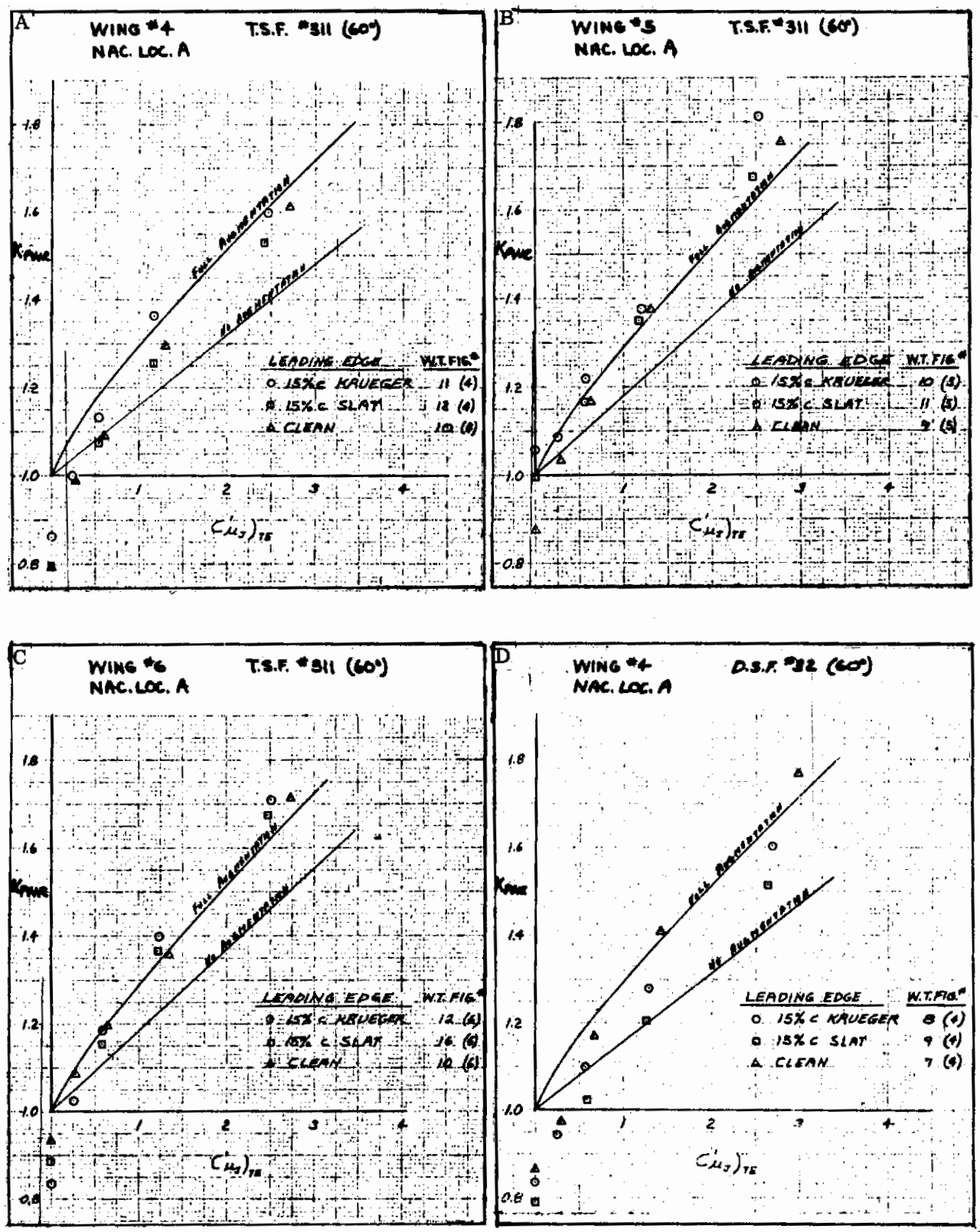

Figure 3.1-8. Effect of Leading Edge Configuration on K_{pwr}

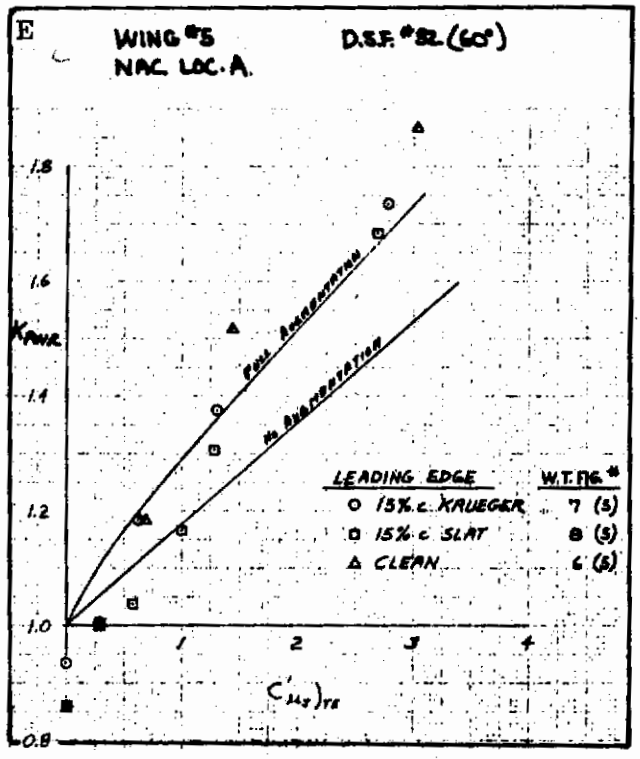

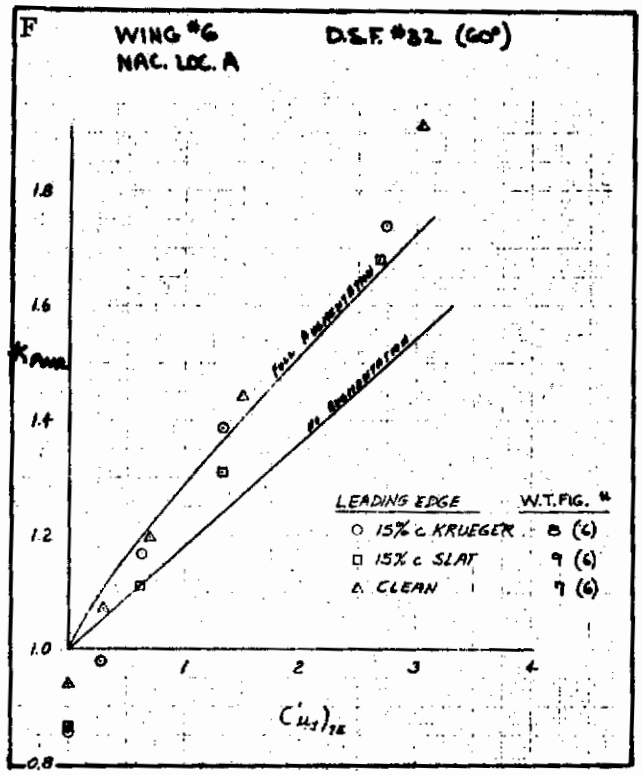

Figure 3.1-8. Effect of Leading Edge Configuration on K_{pwr}, Cont

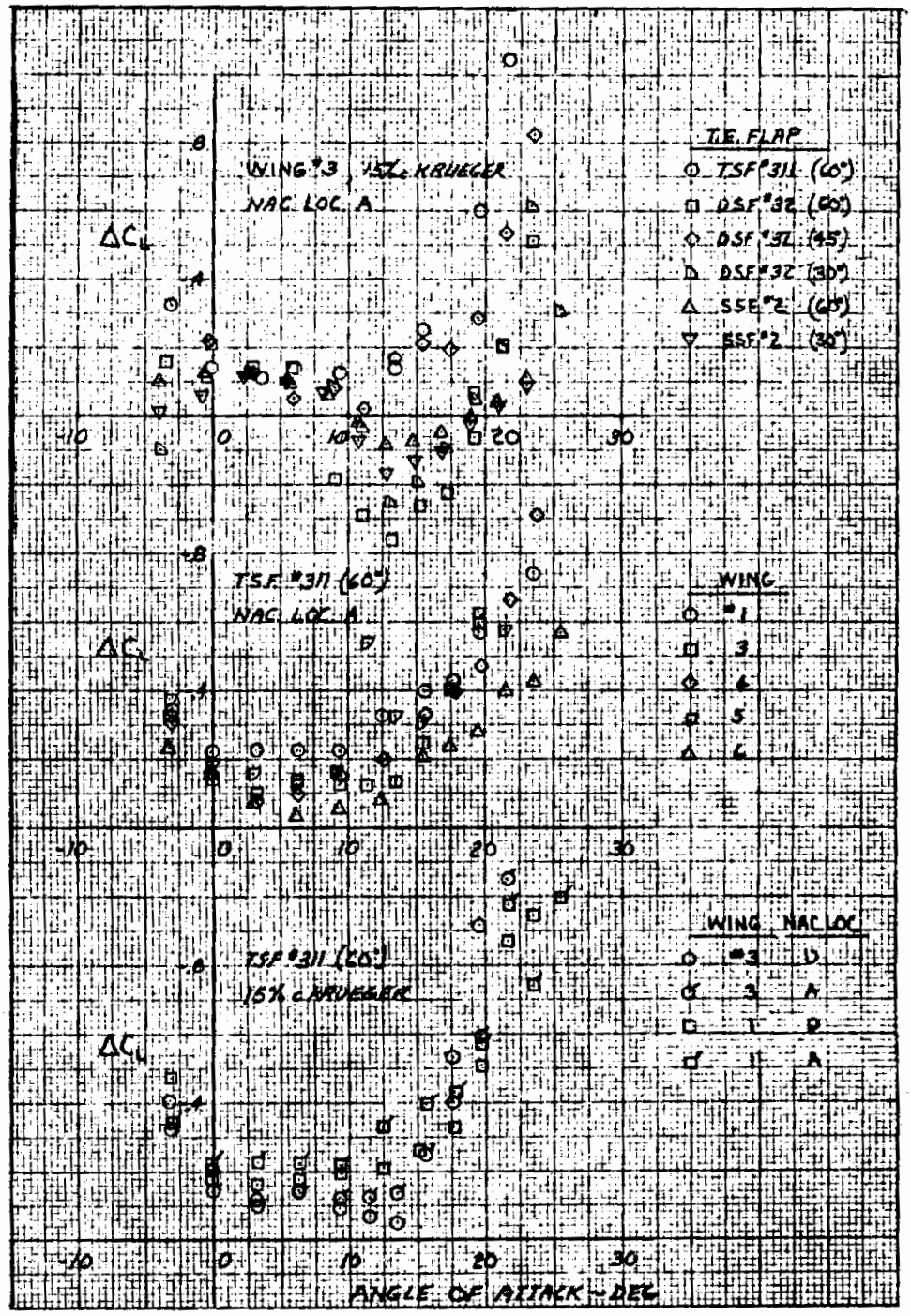

Figure 3.1-9. Incremental Lift Due to Engine Nacelles/Pylons

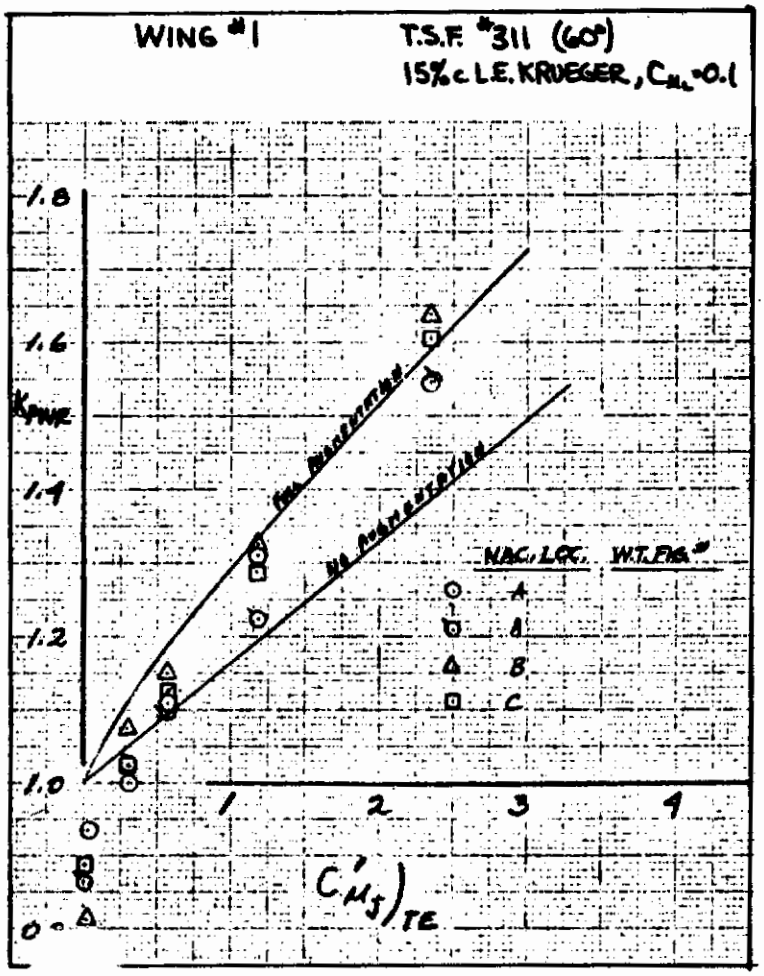

Figure 3.1-10. Effect of Spanwise Nacelle Location on K_{pwr}

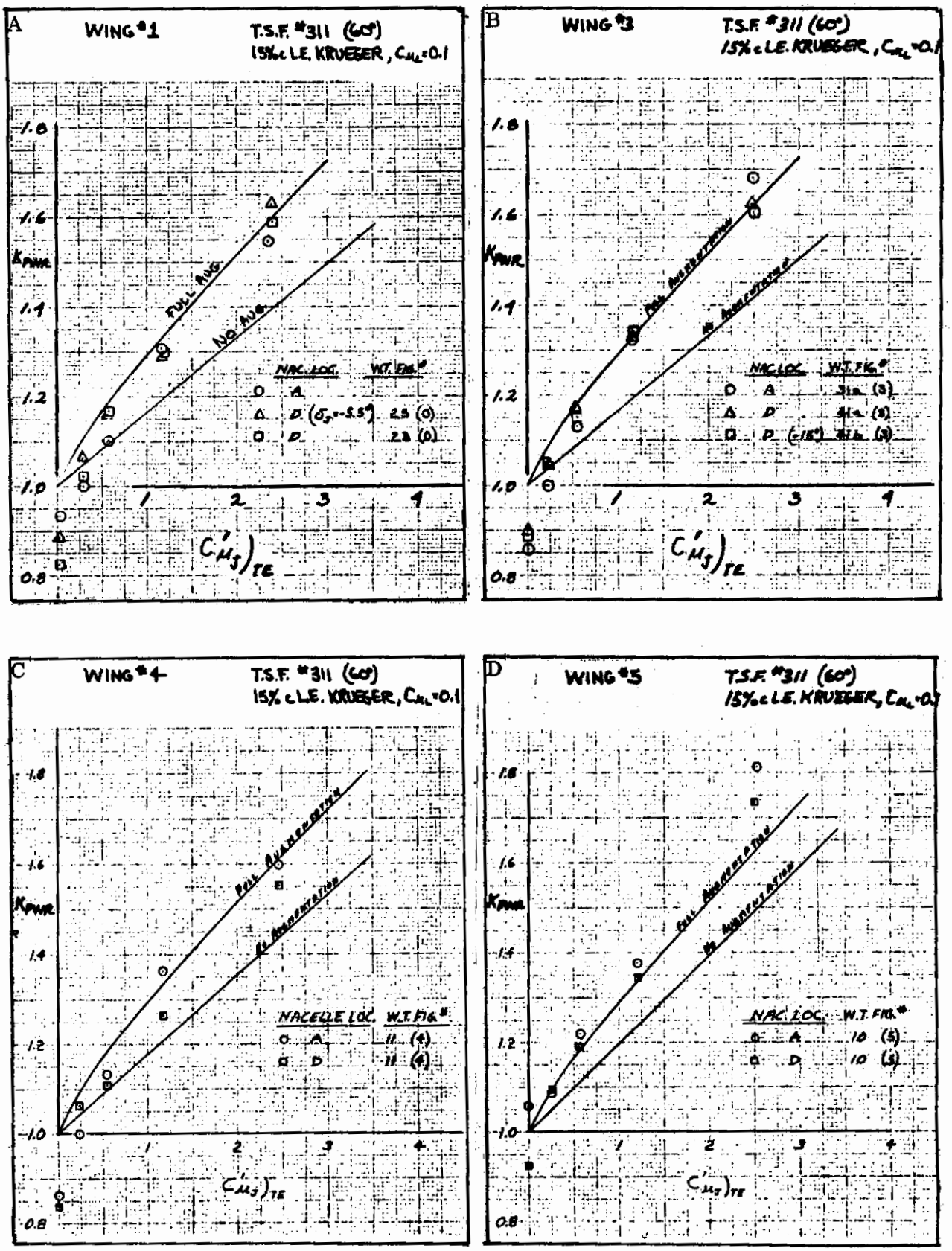

Figure 3.1-11. Effect of Chordwise Nacelle Location on K_{pwr}

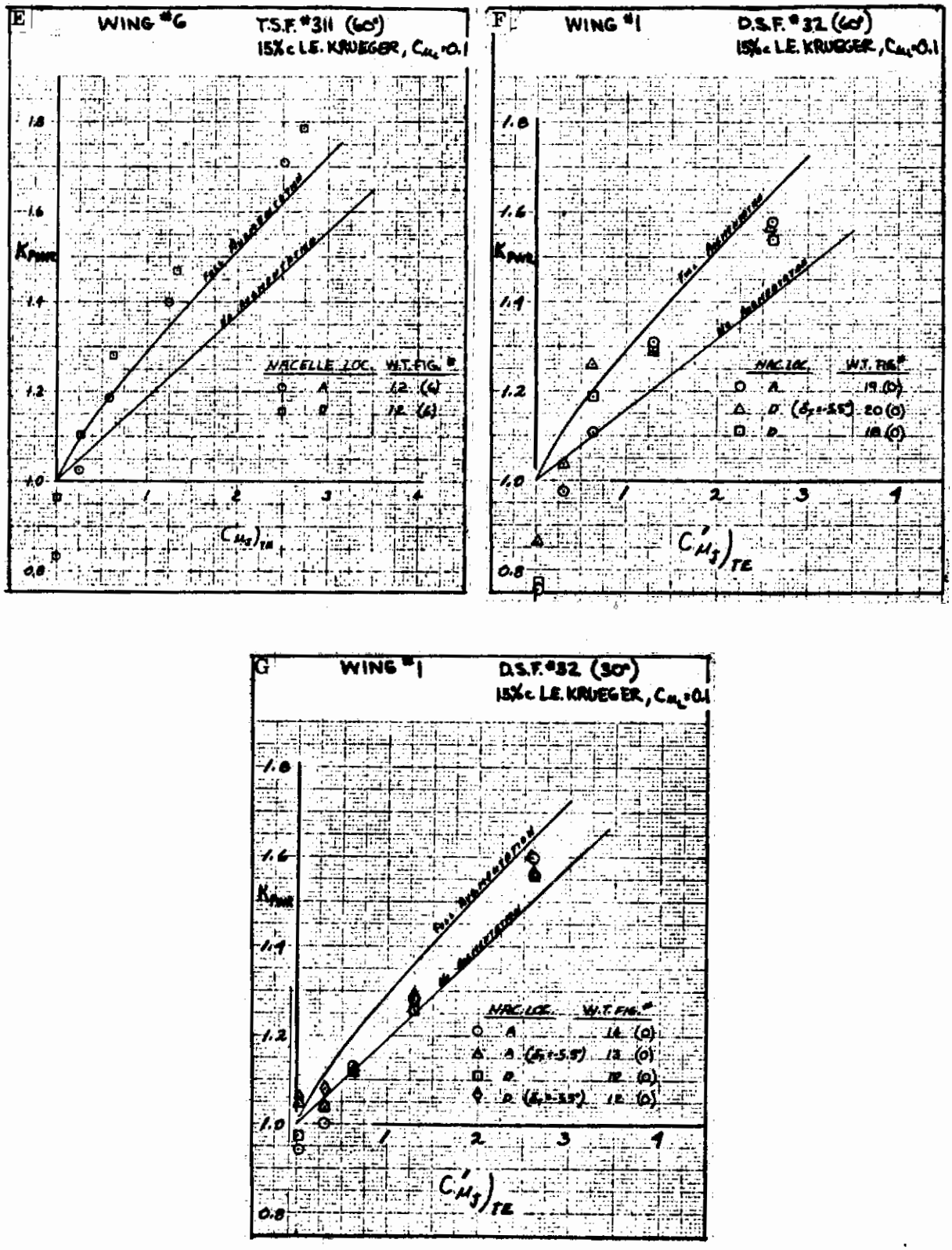

Figure 3.1-11. Effect of Chordwise Nacelle Location on K_{pwr}, Cont

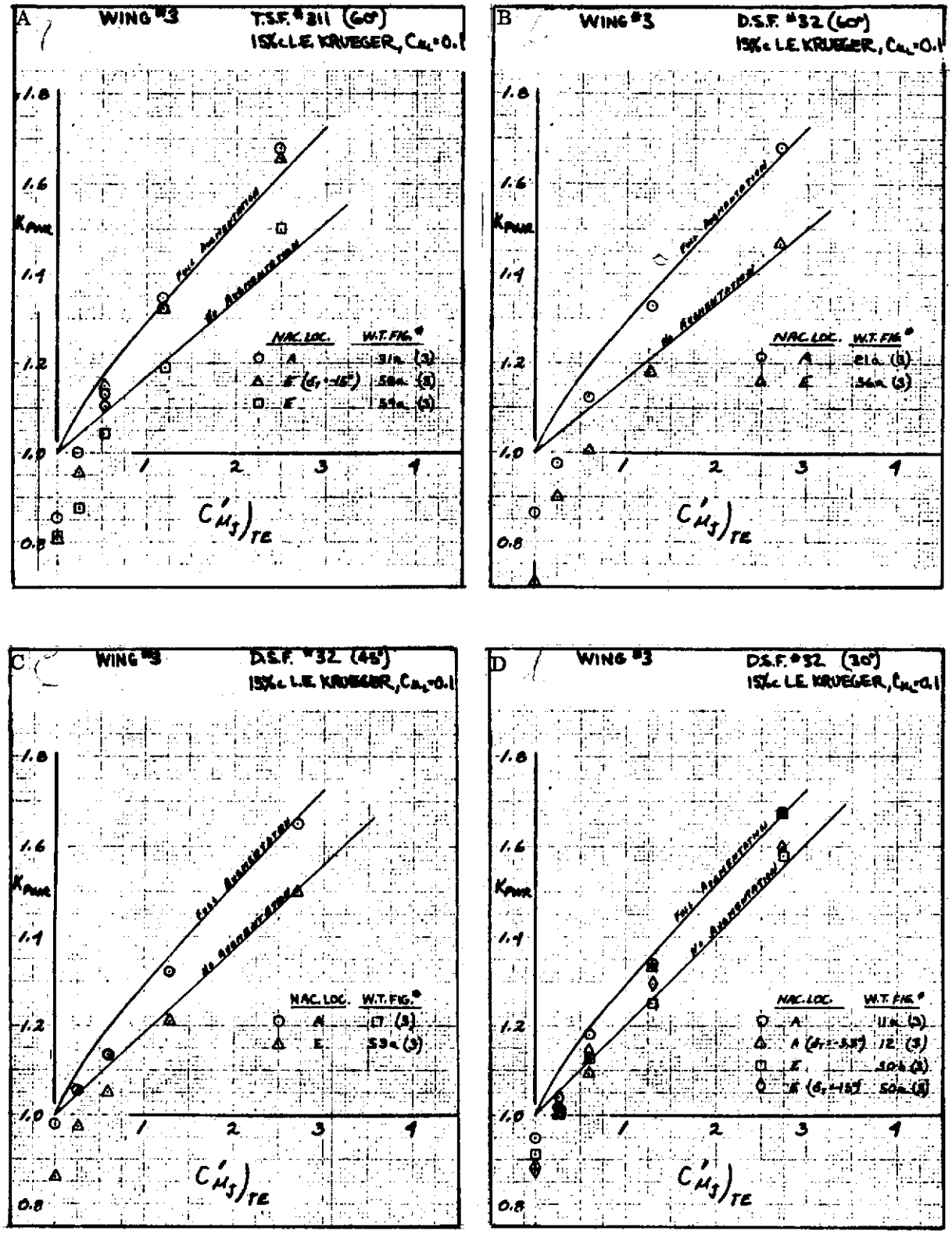

Figure 3.1-12. Effect of Nacelle Height Location on K_{pwr}

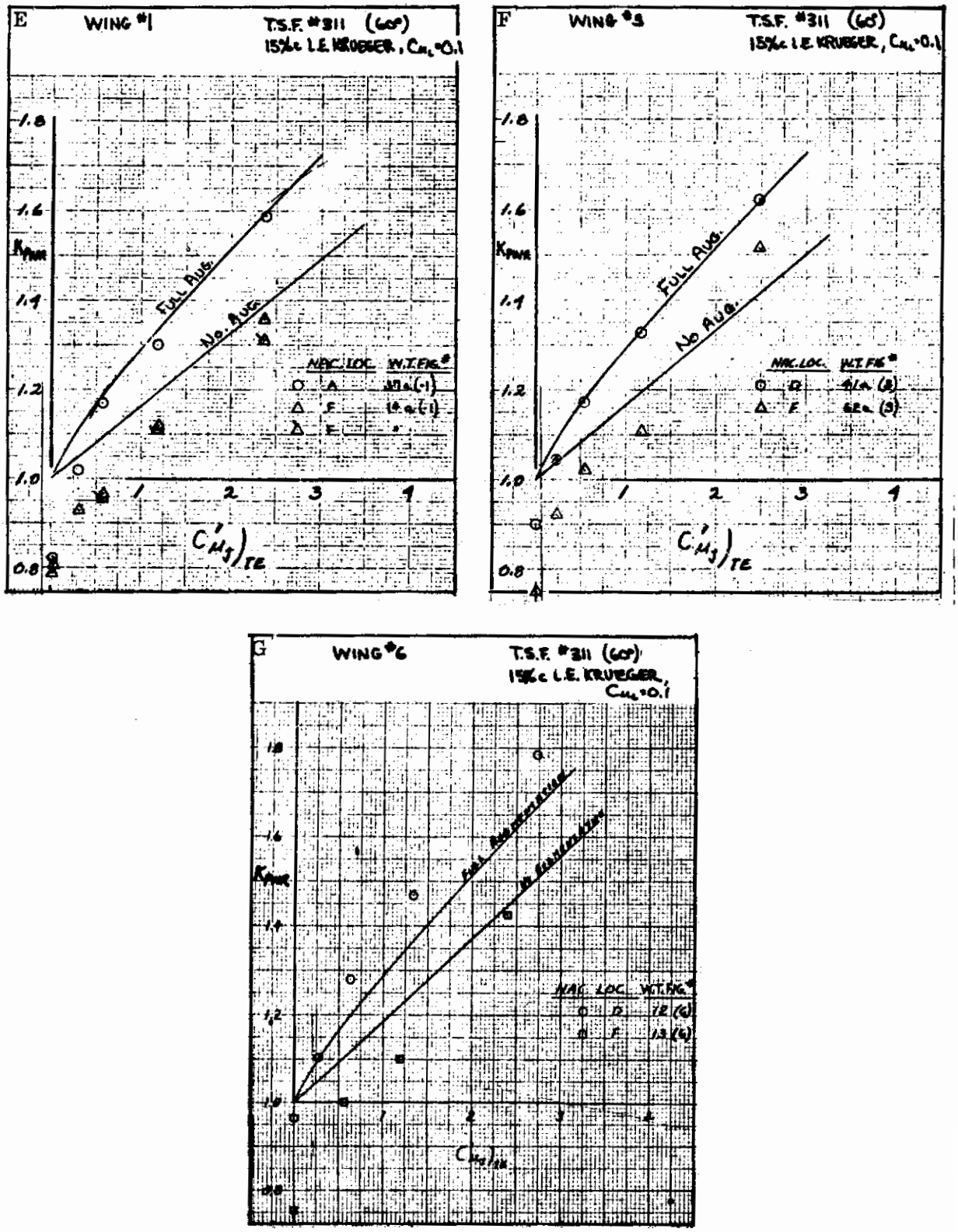

Figure 3.1-12. Effect of Nacelle Height Location on K_{pwr}, Cont

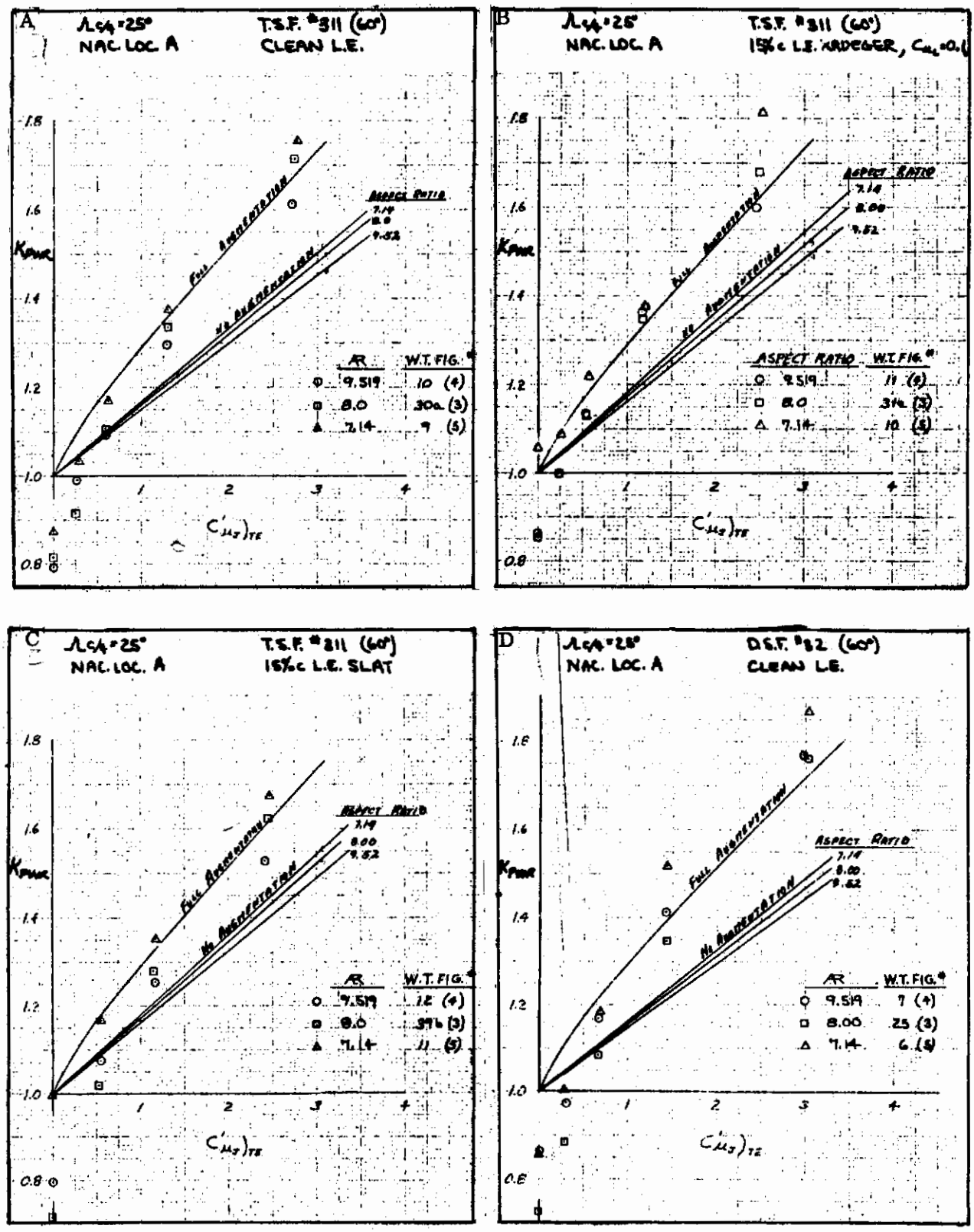

Figure 3.1-13. Effect of Aspect Ratio on K_{pwr}

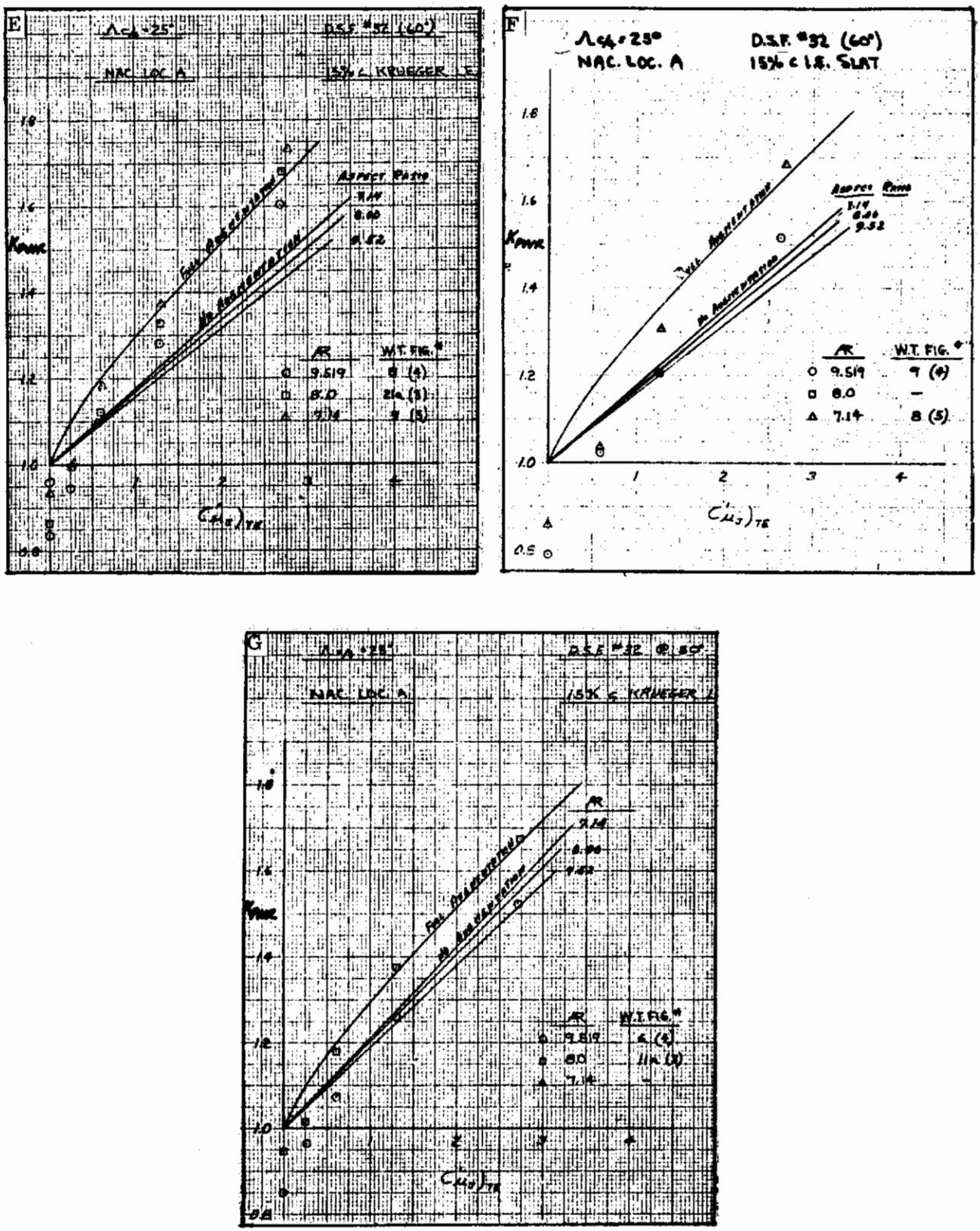

Figure 3.1-13. Effect of Aspect Ratio on K_{pwr} Cont

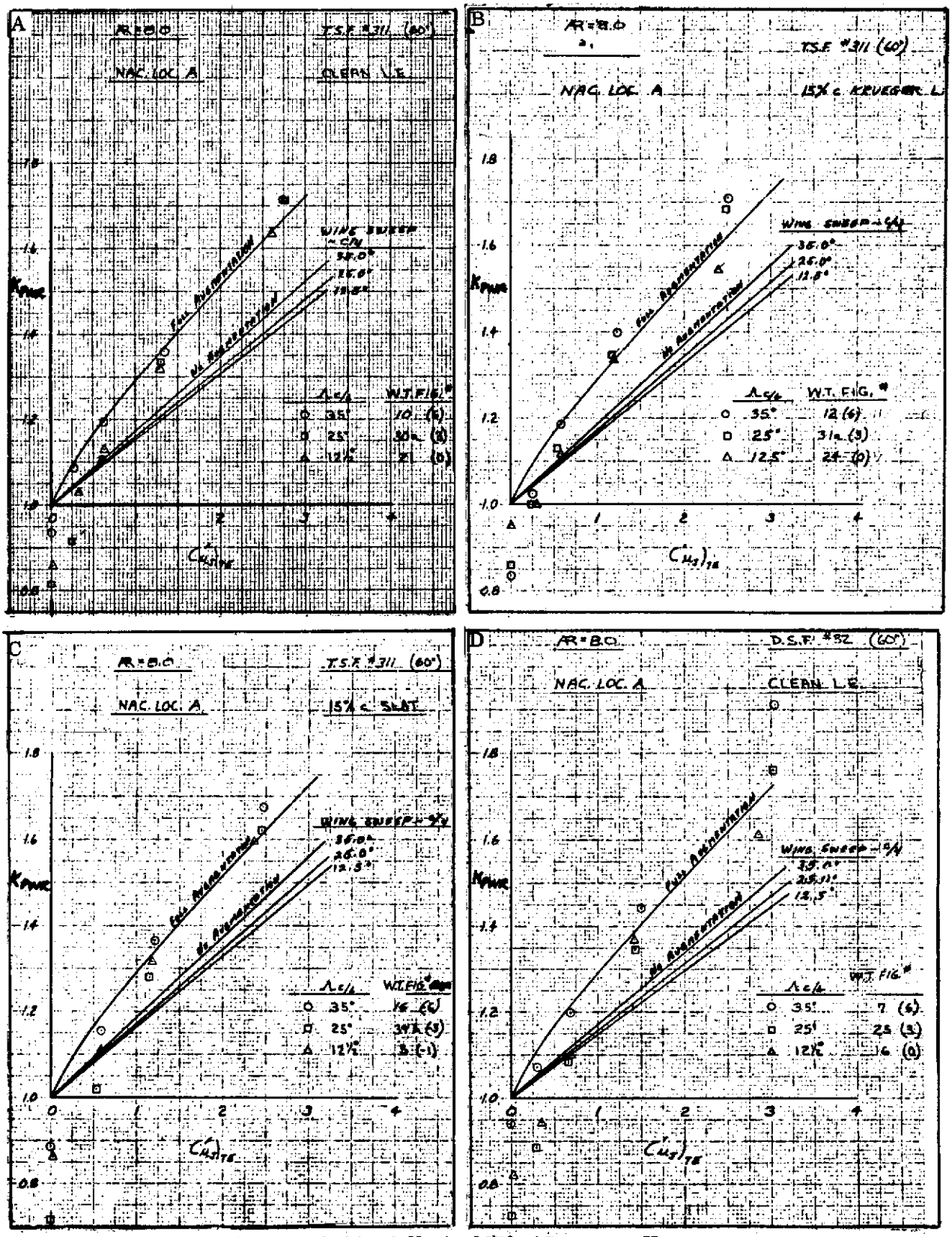

Figure 3.1-14. Effect of Wing Sweep on K_{pwr}

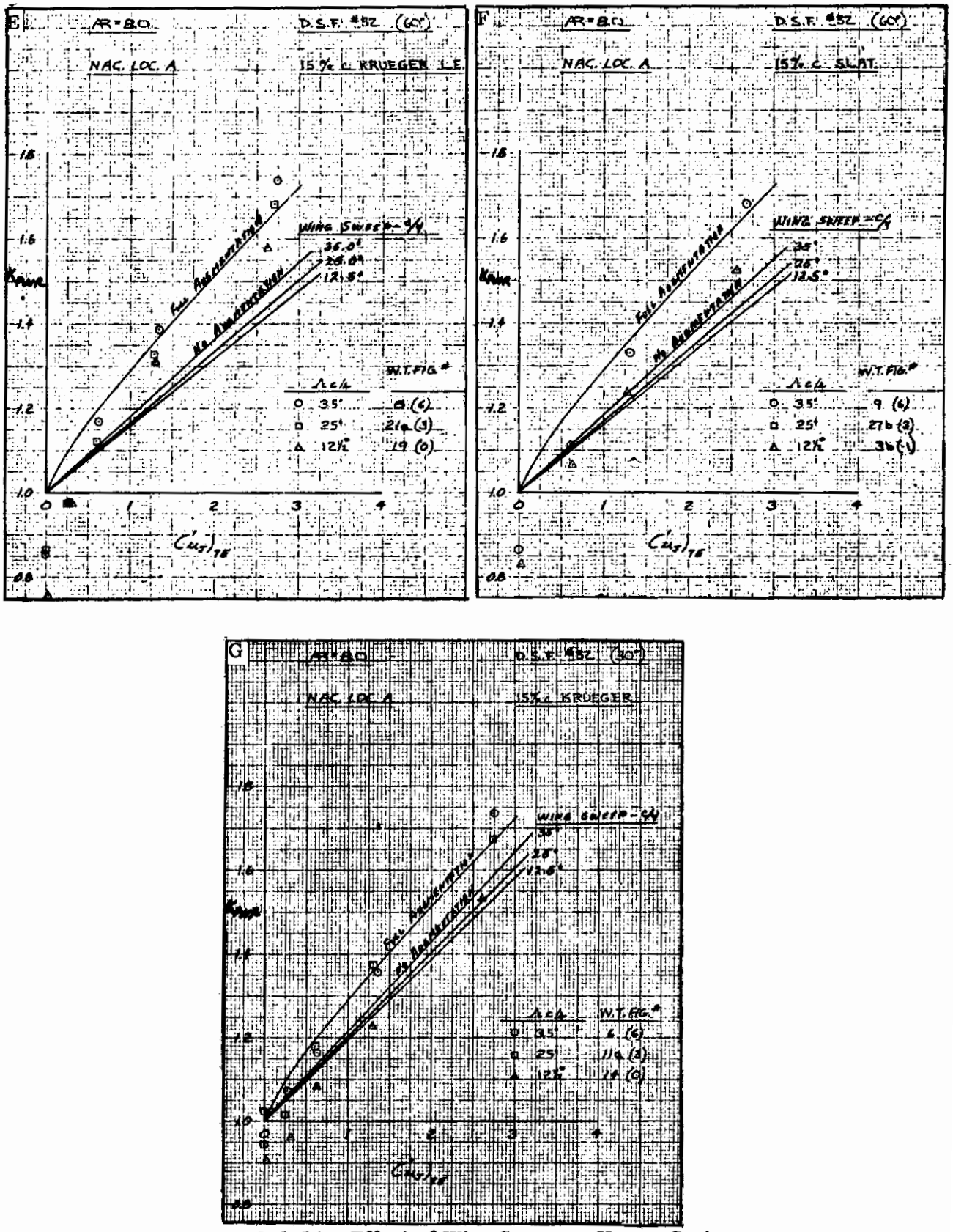

Figure 3.1-14. Effect of Wing Sweep on K_{pwr} Cont

3.2 IBF LIFT CURVE SLOPE ANALYSIS

The analysis of the lift curve slope from wind tunnel test data is also presented for the IBF system as the ratio K_{pwr}, which is the ratio of the power-on lift curve slope to the power-off lift curve slope assuming full potential flow. The lift curve slope ratio is presented versus the momentum coefficient as estimated at the trailing edge of the flap and based on the total extended wing area that is spanned by the blowing nozzle. In general, the lift curve slope ratio measured in the wind tunnel tests are equal to, and somewhat greater than, the ratio predicted using Hartunian, Reference 3-4.

3.2.1 EFFECT OF TRAILING EDGE FLAP CONFIGURATION ON K_{pwr}. The difference in the lift curve slope ratio for a single-slotted IBF system and a plain IBF system is shown in the plots of Figure 3.2-1 for configurations with leading edge Krueger on and off and for engine nacelles on and off. No reasonable difference can be seen between the data for the two systems except that, at a momentum coefficient of zero, the single-slotted flap has less separation and therefore a high lift curve slope ratio. This difference rapidly disappears with increasing momentum coefficient and is known as the BLC effect.

The effect of flap deflection of a plain blown flap is shown in Figure 3.2-2 for leading-edge Krueger on and off and for engine nacelles on and off. The lift curve slope ratio is the greatest for large flap deflections and more nearly equal to the theoretical value for the lowest deflection. This spread in lift curve slope ratio is reduced when the configuration includes engine nacelles and is further reduced with a blown leading edge Krueger.

The effect of flap span is shown in Figure 3.2-3. Except with the nacelles off, a decrease in flap span from 100 to 81.6 percent span reduced the lift curve slope ratio.

3.2.2 EFFECT OF LEADING EDGE KRUEGER FLAP ON K_{pwr}. The extension of the leading edge Krueger flap has only a small effect on the lift curve slope ratio. This is shown in Figure 3.2-4 on configurations with different flap deflections and with engine nacelles on and off. The trend is consistent for all configurations tested.

3.2.3 EFFECT OF ENGINE NACELLES ON K_{pwr}. The effect of cruise engine nacelles located on the wing lower surface is shown in Figure 3.2-5 for the 12.5 and 25 degree swept wings. Unpowered engine nacelles have a small effect on the lift curve slope ratio for both wings and at all flap deflections. This small effect is a tendency to slightly increase the ratio for the 25-degree swept wing (Figures 3.2-5a through 3.2-5d) and decrease the ratio for the limited data available on the 12.5 degree swept wing at a flap deflection of 30 degrees (Figures 3.2-5e and 3.2-5f). At 60 degrees of flap deflection for this wing, there is no effect of the unpowered engine nacelles on K_{pwr} (Figure 3.2-5g).

The effect of powered cruise engine nacelles is also shown on some of the Figure 3.2-5 plots. Test data with the powered engine nacelles has been corrected to exclude the increment in K_{pwr} due to the engine jet thrust. Therefore, the variation in lift curve slope ratio includes only the effect of the IBF system. Test data shows that the engine jet stream increases the lift curve slope ratio and essentially eliminates any effect of the unpowered nacelle on K_{pwr}. It is therefore concluded that the engine nacelles have no effect on the lift curve slope ratio for the IBF systems tested.

3.2.4 EFFECT OF WING SWEEP ON K_{pwr}. The effect of wing sweep shown in Figure 3.2-6 indicates that the higher sweep wing (25 degrees) has a higher lift curve slope ratio than the lower sweep wing. This is similar to the effect of sweep found on the EBF systems.

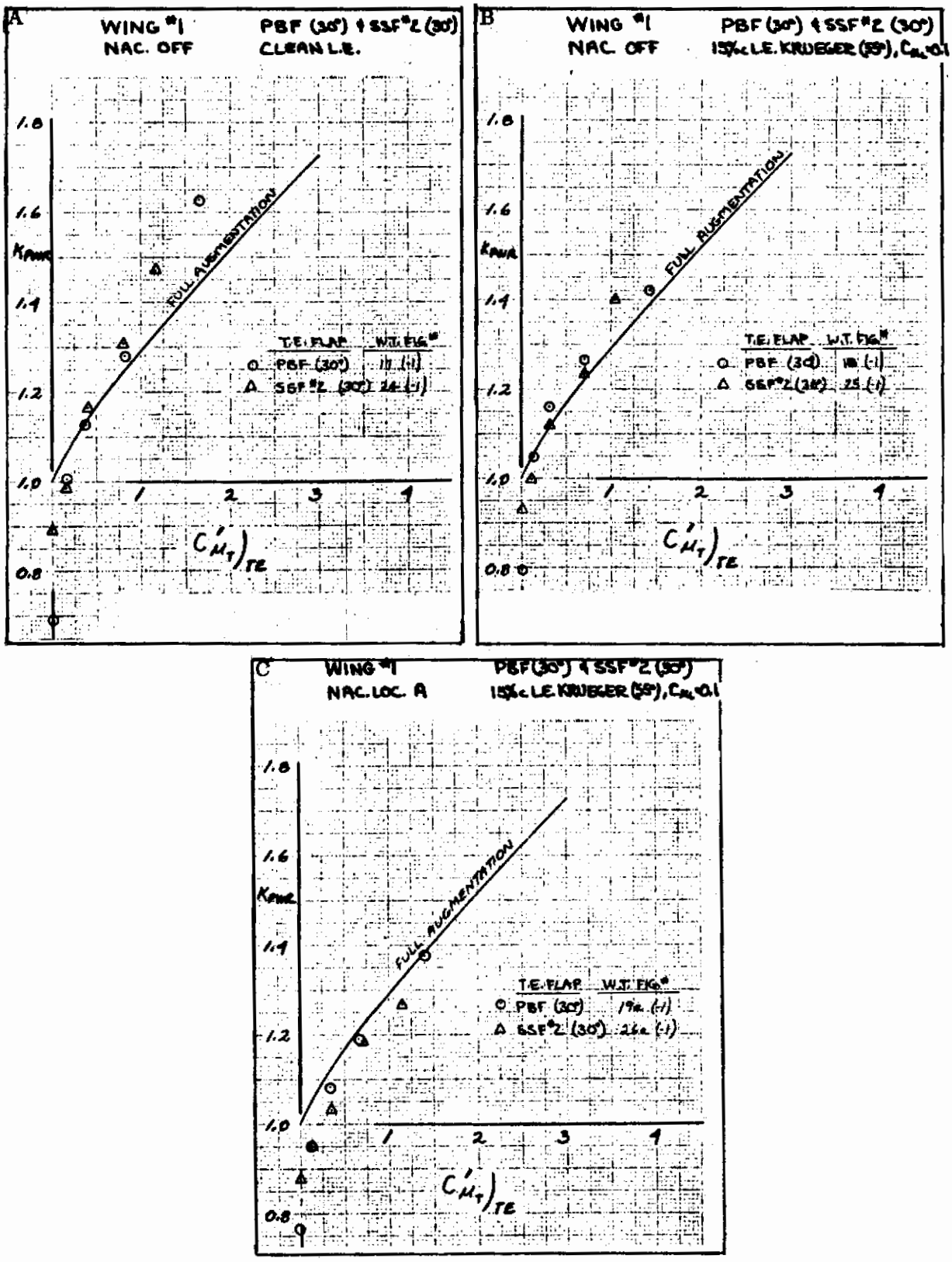

Figure 3.2-1. Effect of Trailing Edge Flap Configuration on K_{pwr}

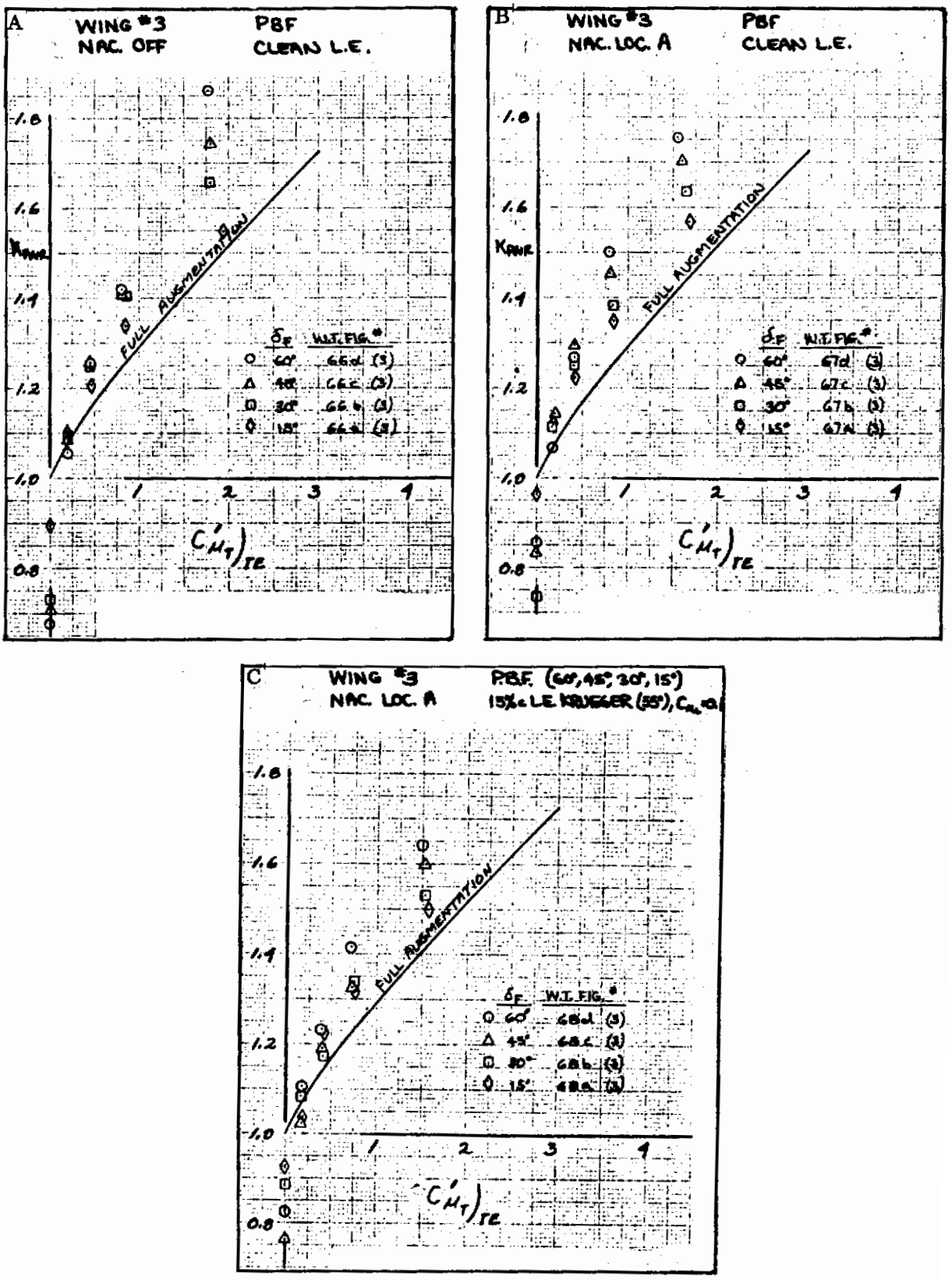

Figure 3.2-2. Effect of Trailing Edge Flap Deflection on K_{pwr}

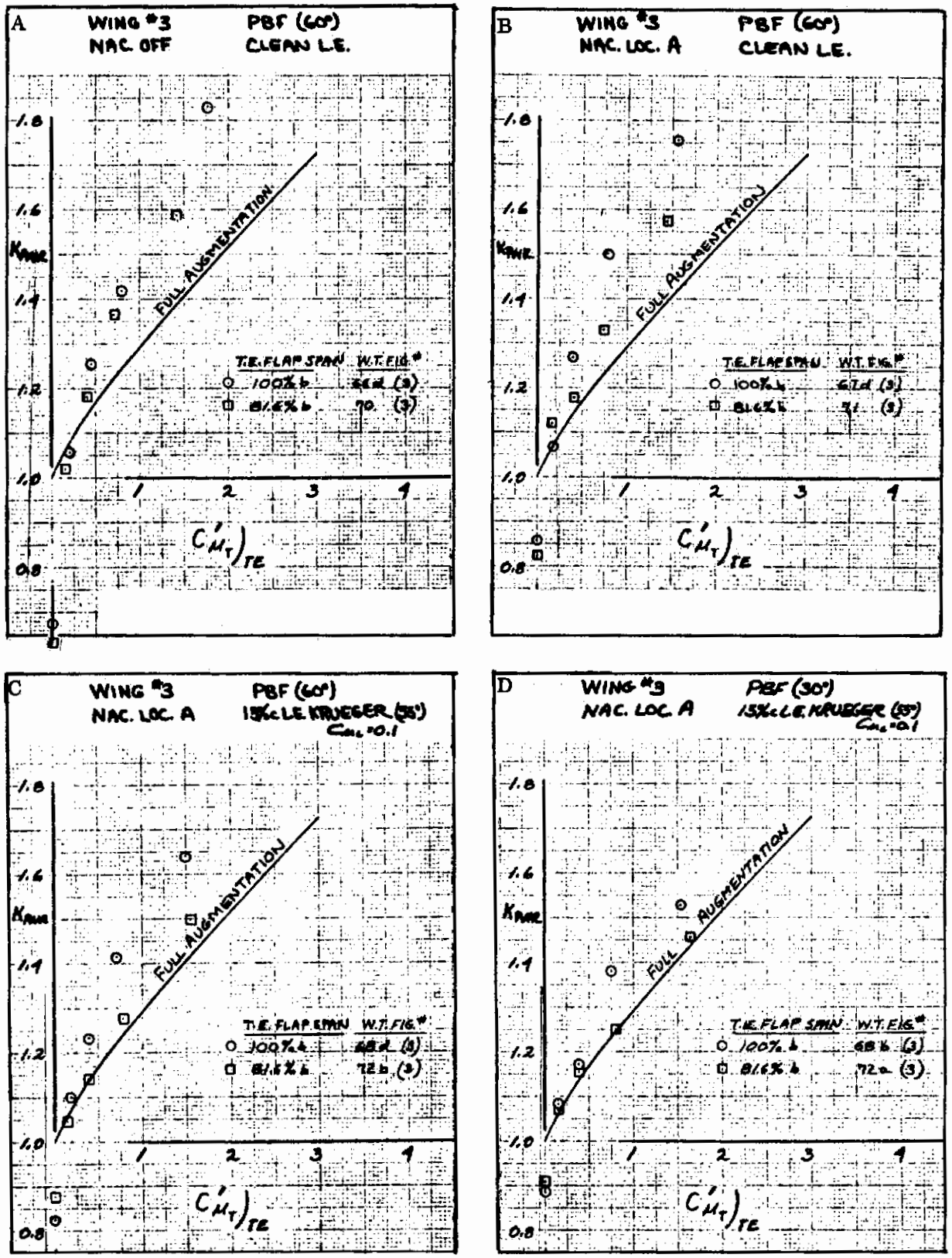

Figure 3.2-3. Effect of Partial Span Trailing Edge Flap on K_{pwr}

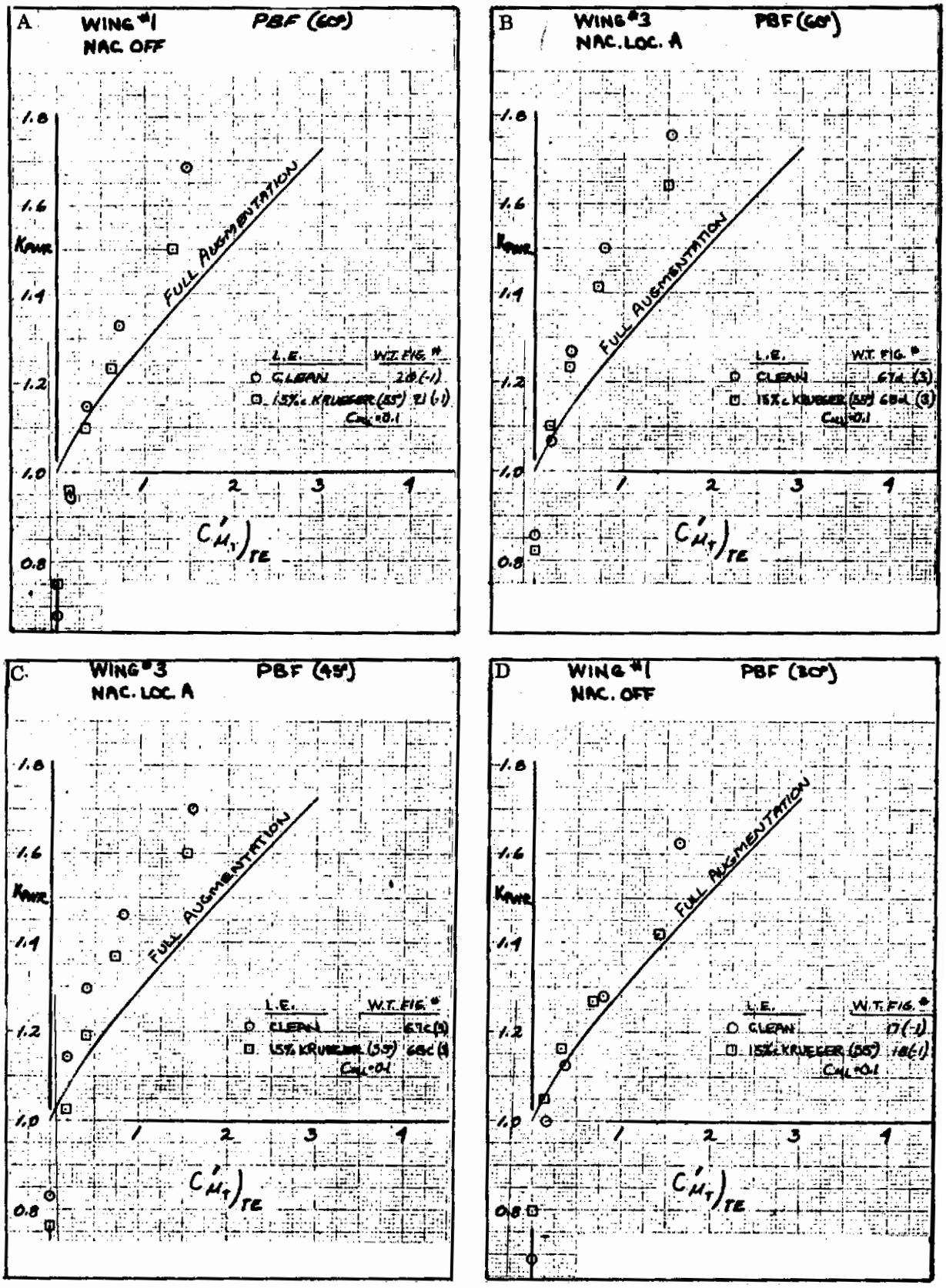

Figure 3.2-4. Effect of Leading Edge Configuration on K_{pwr}

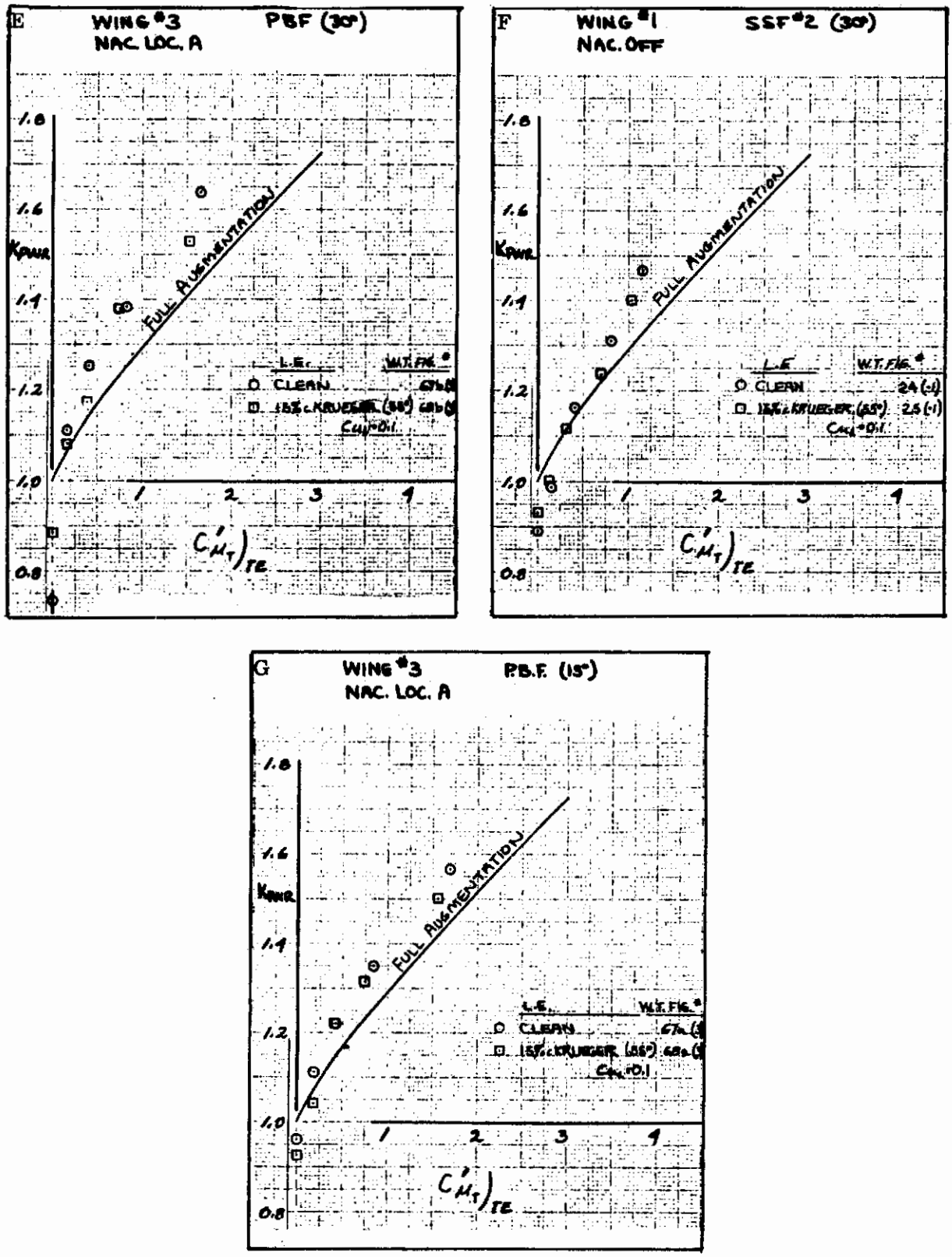

Figure 3.2-4. Effect of Leading Edge Configuration on K_{pwr}, Cont

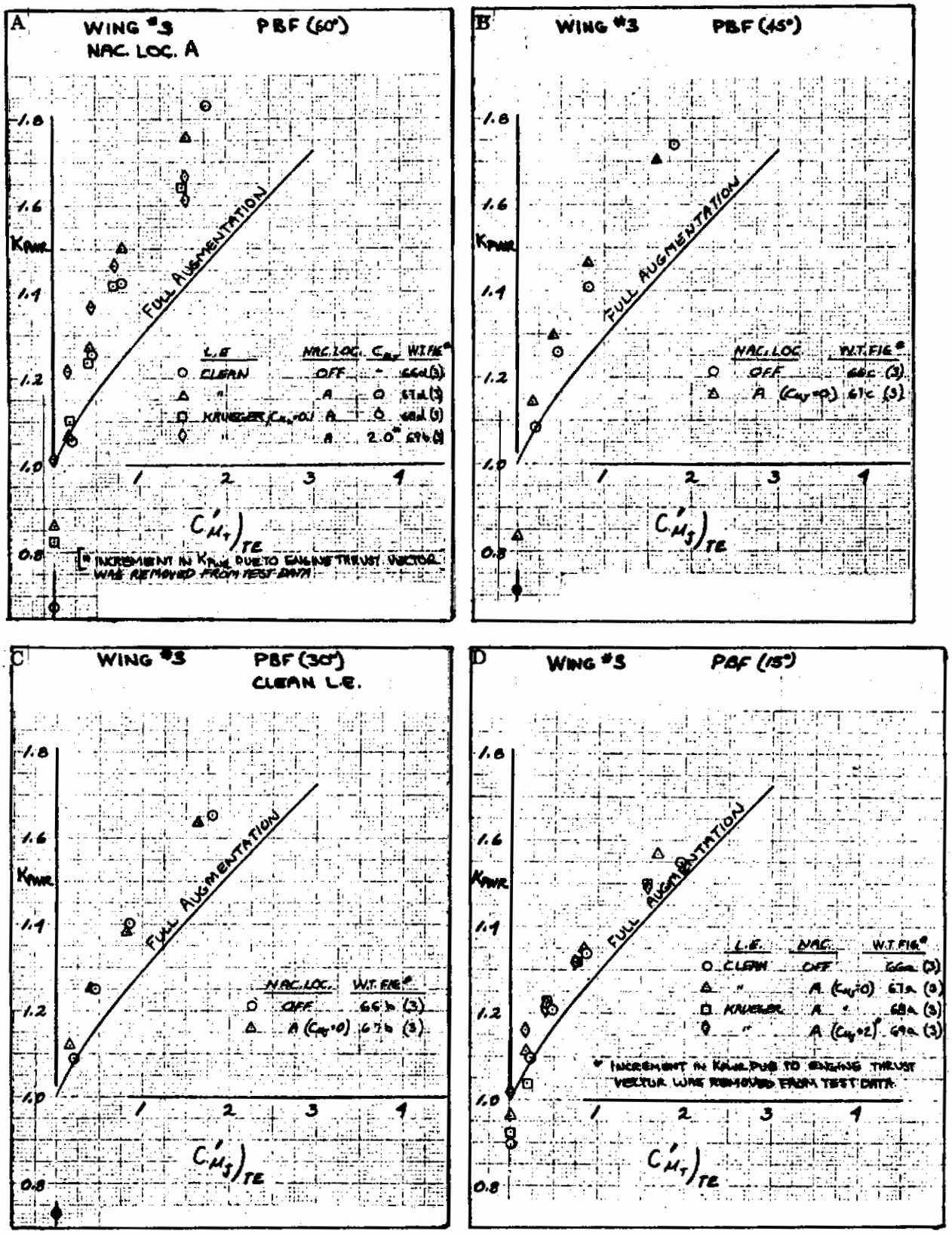

Figure 3.2-5. Effect of Engine Nacelles on K_{pwr}

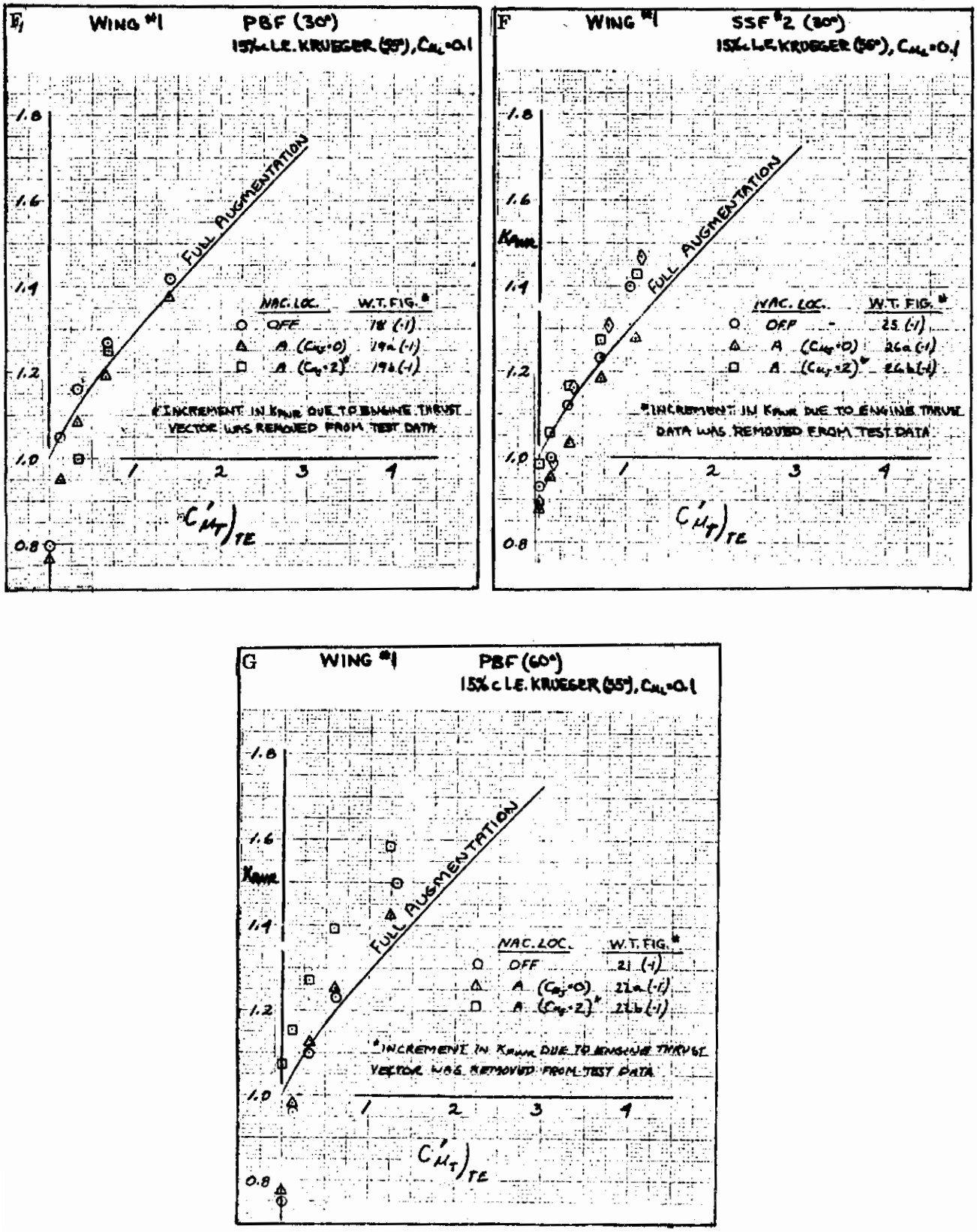

Figure 3.2-5. Effect of Engine Nacelles on K_{pwr}, Cont

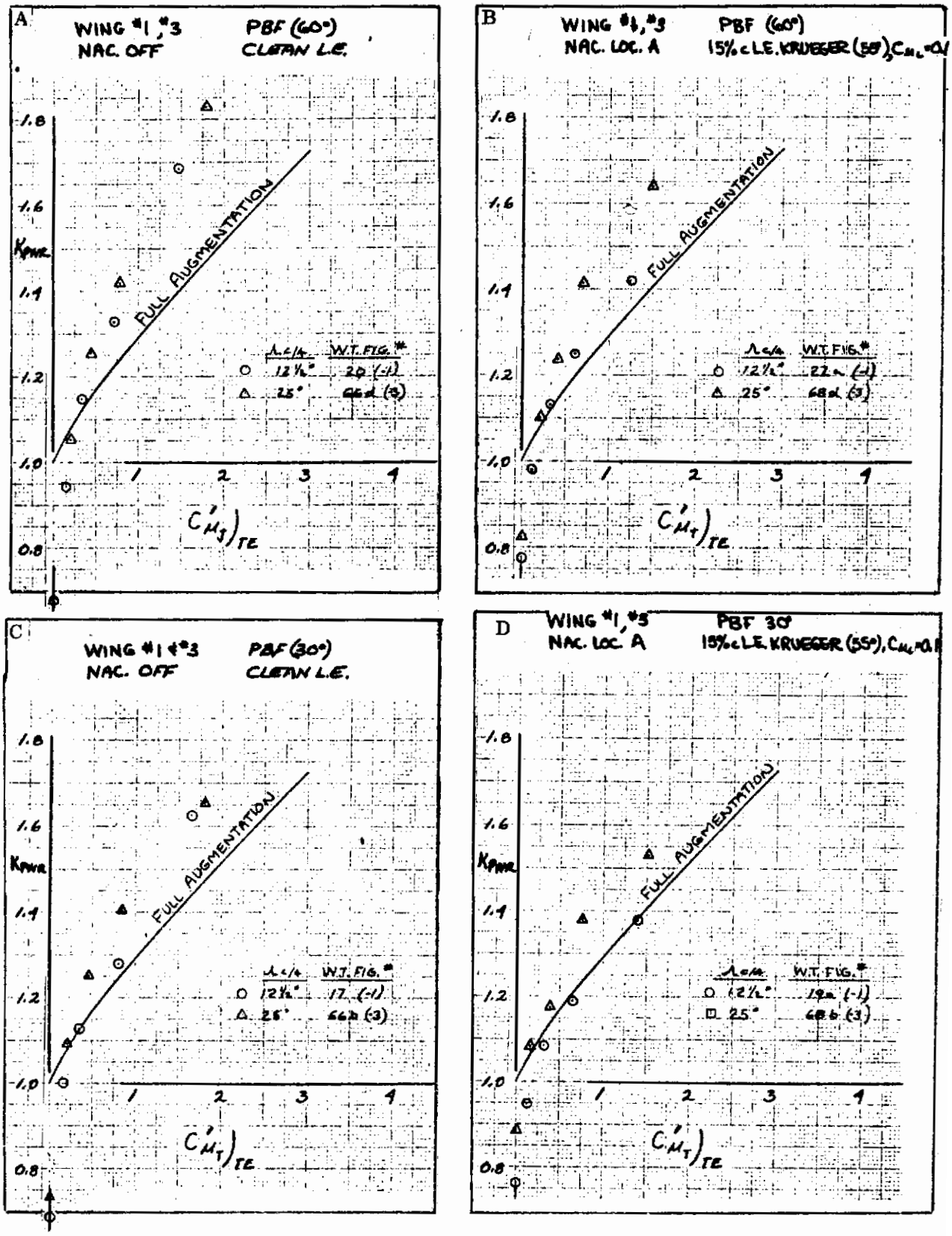

Figure 3.2-6. Effect of Wing Sweep on K_{pwr}

3.3 MF/VT LIFT CURVE SLOPE ANALYSIS

The lift curve slope ratio, K_{pwr}, is also used in the analysis of the wind tunnel test data for the MF/VT system. This term is the ratio of the power-on lift curve slope (including the jet engine thrust vector) to the power-off lift curve slope assuming full potential flow. The lift curve slope ratio is presented versus the momentum coefficient at the jet engine nozzle exit based on the extended wing area, C'_{μ_J}. The data for the MF/VT system is similar to the EBF system, since circulation lift augmentation may develop (depending on the amount of flap that is immersed in the jet stream). This is known as the EBF effect and can be seen throughout the MF/VT data in this section and following sections. The test data is compared to the no-augmentation theory, which assumes that the power-on lift curve slope is equal to the full potential flow power-off lift curve slope plus the lift curve slope due to the lift vector from the jet engine thrust.

3.3.1 EFFECT OF THRUST VECTORING ON K_{pwr}. The effect of jet engine thrust vectoring is shown in Figure 3.3-1. The data shown in these plots indicates trends similar to those for the EBF systems, Paragraph 3.1. The variation with thrust deflection is generally as expected using the unagumented theory except where the system has a change in flap effectiveness with angle of attack, resulting in a high lift curve slope. This trend was noted in the single-slotted EBF system, Paragraph 3.2, and is seen here in Figure 3.3-1c for the double-slotted flap with -3.5 degrees of thrust deflections. A cross-plot of K_{pwr} versus jet deflection angle is presented in Figure 3.3-1e for the double-slotted flap at a deflection of 30 degrees.

3.3.2 EFFECT OF TRAILING EDGE FLAP DEFLECTION ON K_{pwr}. The variation of the lift curve slope with flap deflection is shown in Figure 3.3-2. This is the same data plotted in Figure 3.3-1 except it is plotted to show the effect of flap deflection. Although the scatter is great in this data, it follows the general trend of the unaugmented theory.

3.3.3 EFFECT OF ENGINE NACELLES ON K_{pwr}. A small effect of the chordwise location of the engine nacelle on the lift curve slope ratio is seen in Figure 3.3-3. Generally, the forward nacelle position (nacelle location E) shows a slightly higher lift curve slope ratio. The data follows the estimated variation with momentum coefficient very well, although in many configurations there is a displacement in the lift curve slope ratio, indicating that there is no BLC effect from the jet stream as noted for the EBF systems.

3.3.4 EFFECT OF WING SWEEP ON K_{pwr}. The effect of wing sweep on the lift curve slope ratio is shown in Figure 3.3-4. The test data indicates only small variations with sweep, which can be attributed more to data scatter than a sweep effect.

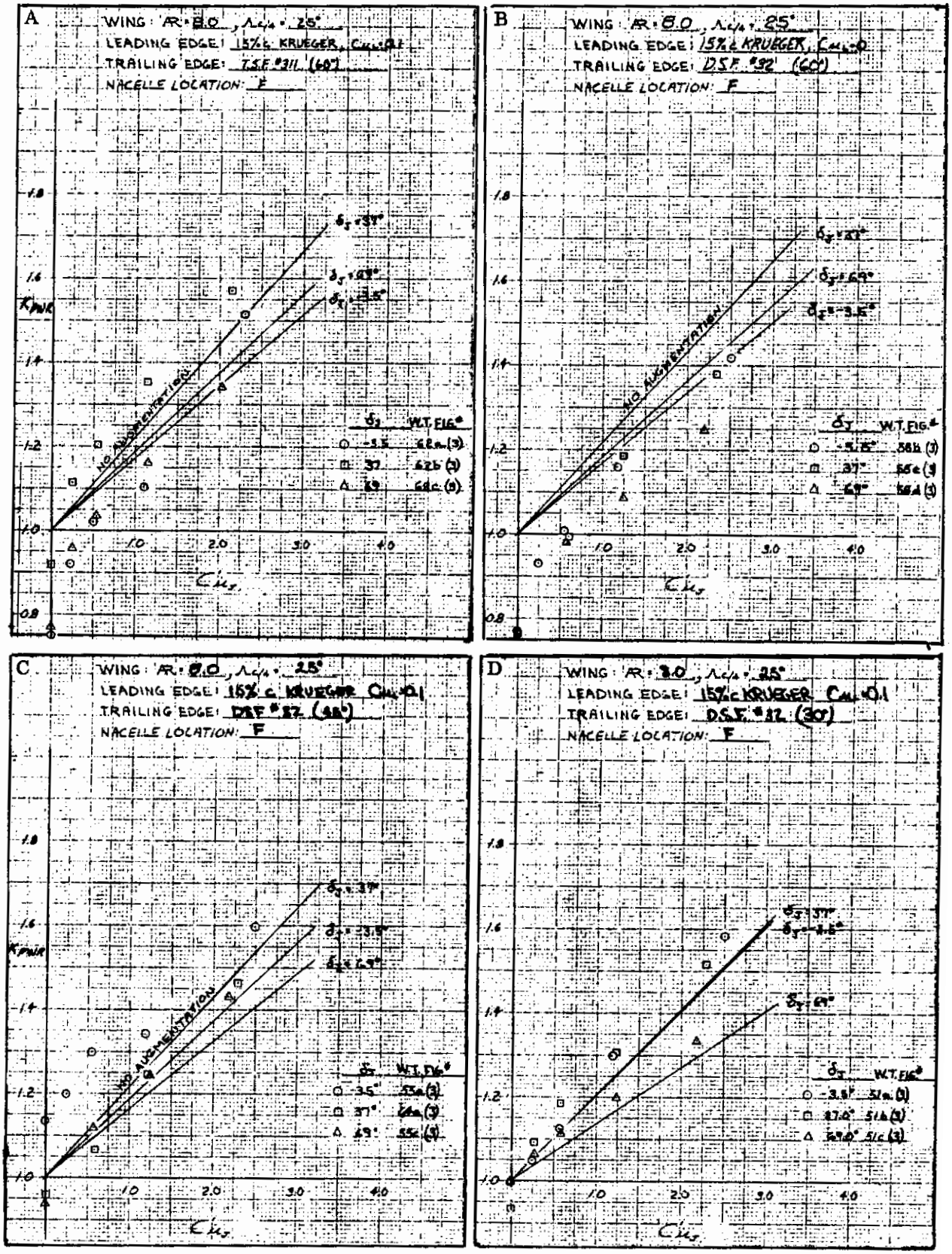

Figure 3.3-1. Effect of Vectored Thrust on K_{pwr}

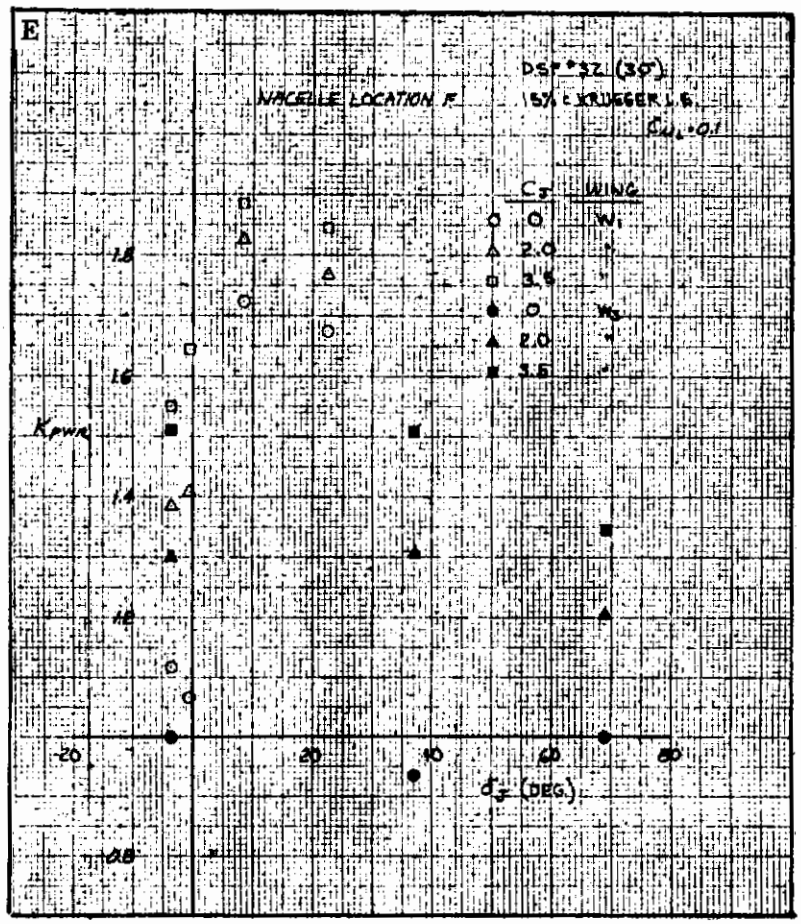

Figure 3.3-1. Effect of Vectored Thrust on K_{pwr}, Cont

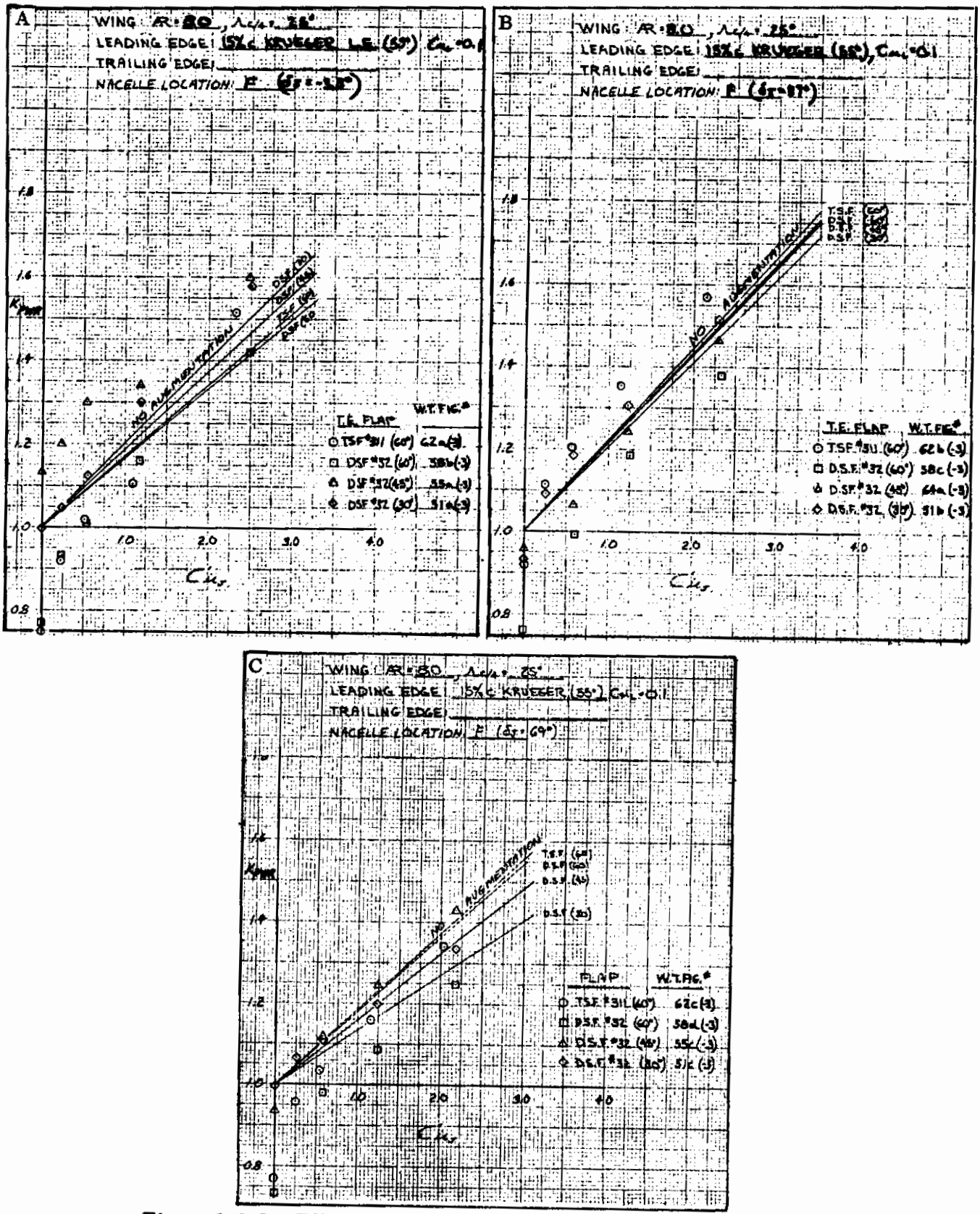

Figure 3.3-2. Effect of Trailing Edge Flap Deflection on K_{pwr}

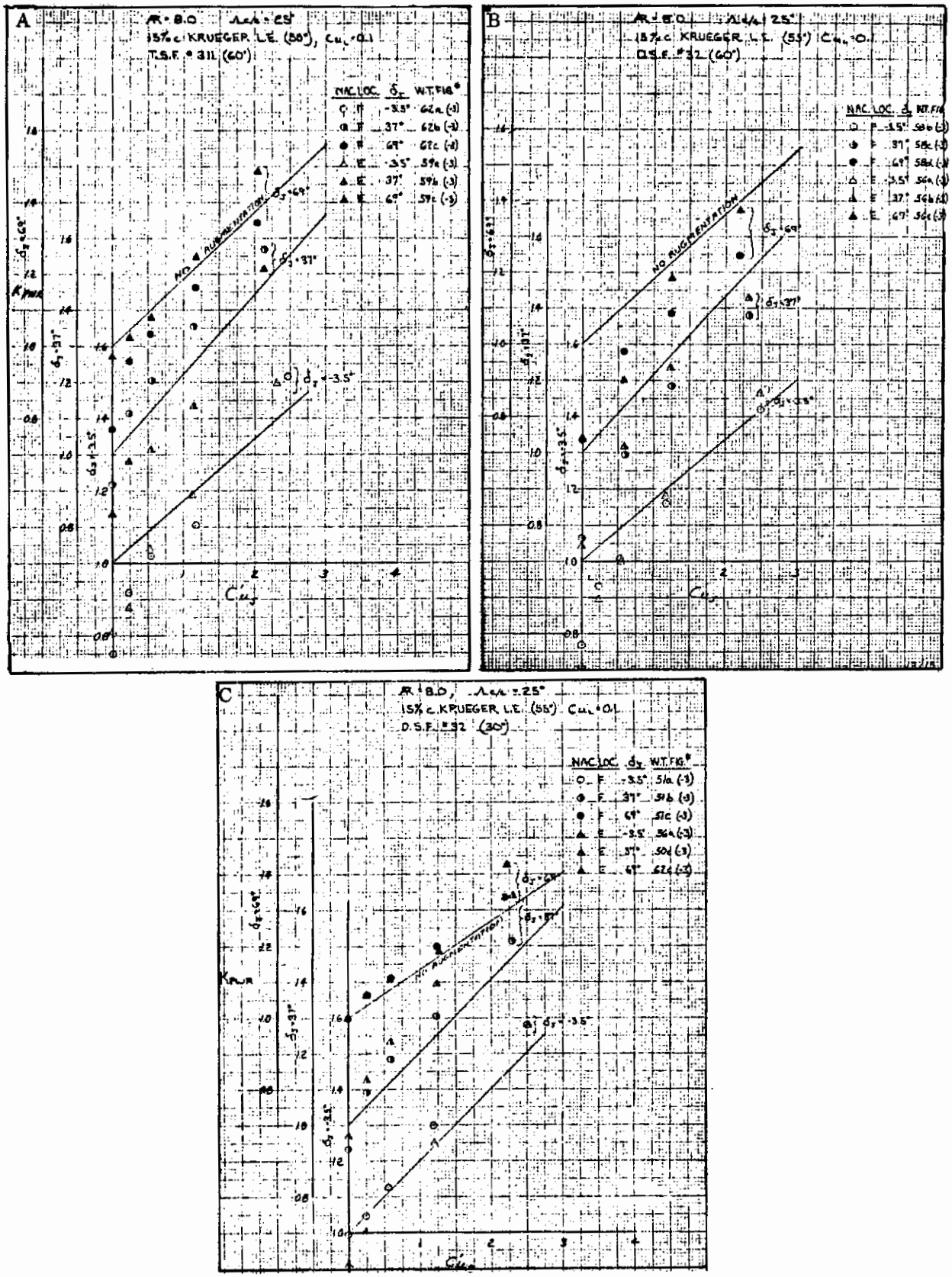

Figure 3.3-3. Effect of Nacelle Chordwise Location on K_{pwr}

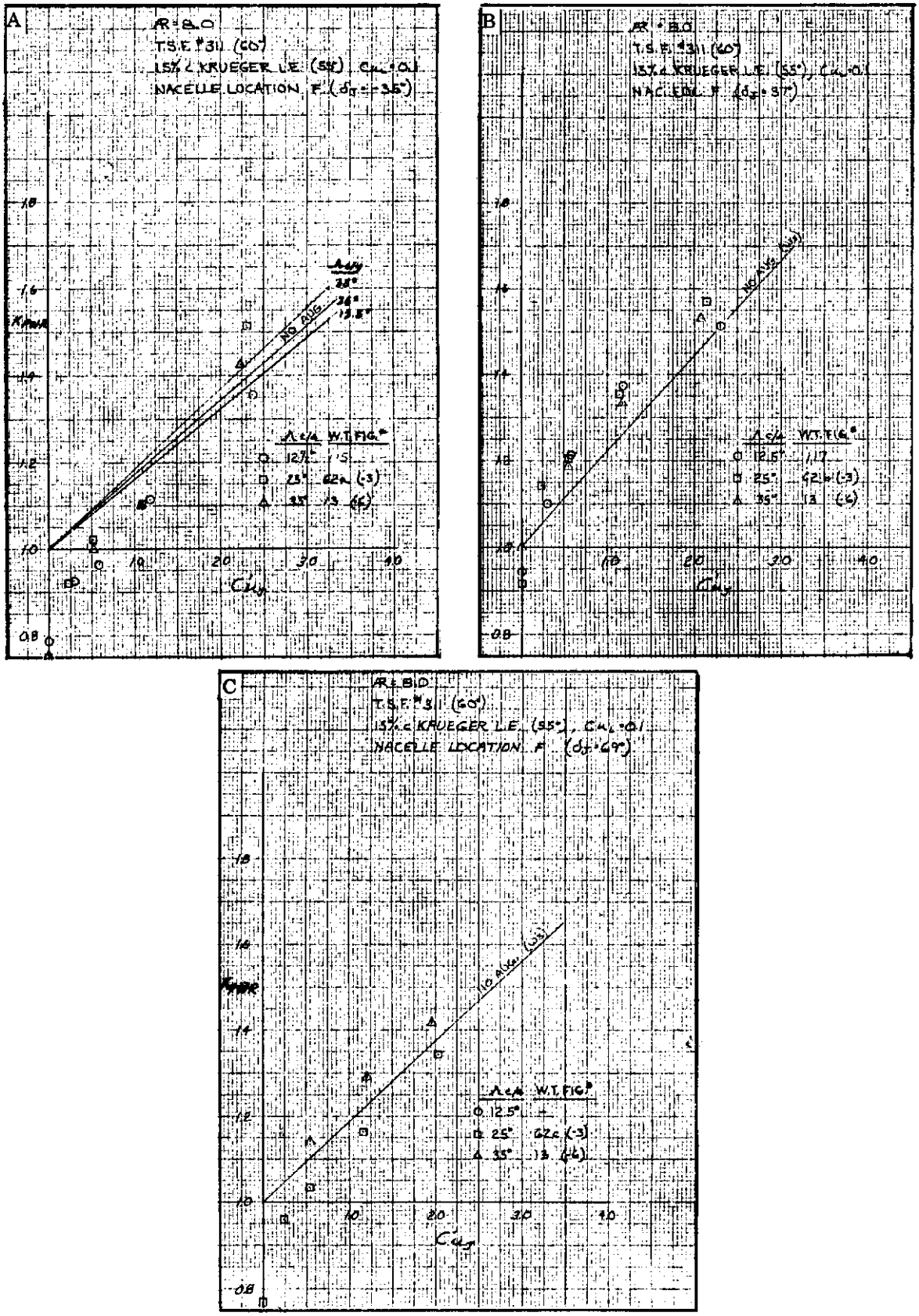

Figure 3.3-4. Effect of Wing Sweep on K_{PWR}

3.4 EBF TRAILING EDGE FLAP LIFT INCREMENT AT α = 0 DEGREES

The trailing edge flap lift effectiveness, $\Delta C'_{L_{TE}}$, as measured from wind tunnel test data, is defined as the increment in lift at zero angle of attack due to the deflection and blowing of a trailing edge flap system. This increment, based on extended wing area, is presented here versus the jet engine momentum coefficient at the trailing edge of the flap, based on extended wing area blown by the jet stream (assumed to be the exposed wing area). This data analysis was made assuming that the EBF system acts aerodynamically similar to an equivalent IBF system. The results of this EBF/IBF analogy, discussed previously in Paragraph 3.1, is also shown in Figure 3.4-1. The flap lift increment for a triple-slotted flap blown with an external jet (EBF) and blown from a nozzle at the knee of the flap (IBF) is shown. The difference between the two theoretical lines shown is in the assumption that jet flow for the IBF system follows the upper surface of the flap to the trailing edge resulting in a total jet deflection angle equal to the flap deflection plus the upper surface angle. For the EBF system, it has been assumed that the jet stream flows through the slots over the upper surface and along the lower surface of the flap, resulting in an average deflection angle approximately equal to the flap deflection. The test data does not show this difference in flap lift effectiveness, indicating that blowing internally over a triple-slotted flap is not an efficient IBF system.

3.4.1 EFFECT OF TRAILING EDGE FLAP CONFIGURATION ON $\Delta C'_{L_{TE}}$. The effect of flap deflection on the flap lift effectiveness term, $\Delta C'_{L_{TE}}$, with power off is shown in Figure 3.4-2 plotted against flap deflection for single, double, and triple slotted flaps on the five wing planforms. The test data shows that the flaps were well designed and performed aerodynamically as well as can be expected from present day state-of-the-art flap design. Correlation with existing empirical theory is excellent for all flaps and deflections.

Variation of flap lift effectiveness with momentum coefficient from the jet engines mounted on the wing is shown in Figure 3.4-3. Each figure shows, for a different wing planform, the effect of the triple- and double-slotted flaps with different deflections. Figure 3.4-3f shows the variation with flap deflection for a single-slotted flap.

Two effects can be noted in these figures regarding flap lift effectiveness. The first one is the BLC effect. With sufficient and proper amounts of blowing over a flapped airfoil at zero angle of attack, the lift of that airfoil will approach full potential flow. This can be seen in these figures for the triple-slotted flap. In Figure 3.4-3a, for example, the test data points at zero momentum coefficient fall well below the full potential estimate (solid line) but with increased blowing the test data becomes coincident with the potential flow line (full augmentation) at higher C'_{μ_J}. This phenomena is especially remarkable since the configuration is a flap extending well in to two jet streams (EBF) and not the normal IBF system, which will be shown later in Paragraph 3.5.

The second effect that can be seen in Figure 3.4-3 is the deterioration in circulation lift (other than reduced effectiveness) that occurs with a reduction in flap deflection and size. Figure 3.4-3b is a good example of this phenomena. This triple-slotted flap, which has the largest chord and the greatest deflection of all of the flaps tested, compares favorably with the Hartunian estimate for jet flap with uniform spreading. This does not say that this flap has uniform spreading across the span; it only means that the effectiveness of the flap is the same as the effectiveness of an IBF system. The reduction in lift effectiveness occurs when the flap is immersed in the jet stream a reduced amount as would occur with the shorter chord, double-slotted flap, especially with less deflection also shown in Figure 3.4-3b. This reduction in lift effectiveness can also be seen dramatically in Figure 3.4-3f, where the very short chord, single-slotted flap is shown deflected at 15 through 60 degrees. At 15 degrees deflection, the jet stream is missing the flap entirely and no augmentation of the circulation lift has developed; at higher deflections, some circulation lift augmentation is obtained. In summary, these figures, and the figures to follow, show that the amount of circulation lift of an EBF system is not only a function of flap chord and flap deflection but is also a function of the amount of flap immersed in the jet stream.

The effect of flap chord on flap lift effectiveness is shown in Figure 3.4-4. Two different flap chords for the triple- and double-slotted flap are shown in these figures, with and without the blowing leading edge Krueger flap. The effect of flap immersion in the jet stream is seen in these figures. The short chord flap is much less effective than the longer chord flap, even less than what Hartunian (jet flap theory) would indicate.

The effect of flap span is shown in Figure 3.4-5. This data shows that when the partial-span flap test data is corrected to full-span flap by the normal power-off flap span effectiveness curve, excellent correlation is obtained with the full-span flap data. Studies with a span load computer program have shown that factors for partial-span blowing are essentially the same factors obtained for power-off, partial-span flaps. These factors were used to obtain this correlation and appear adequate for estimating the lift effectiveness.

3.4.2 EFFECT OF LEADING EDGE CONFIGURATION ON $\Delta C'_{L_{TE}}$. Blowing from the leading-edge Krueger flap has little if any effect on flap lift effectiveness, as shown in Figure 3.4-6. The plots show this for triple- and double-slotted flaps at 60 degrees of deflection.

There is no effect of leading edge devise deflection and chord length on the trailing edge flap lift effectiveness, as shown in Figures 3.4-7 through 3.4-10. The effect of a blowing leading edge Krueger flap and a leading edge slat on other wing planforms is shown in Figure 3.4-11.

3.4.3 EFFECT OF NACELLE LOCATION ON $\Delta C'_{L_{TE}}$. The effect on lift of power-off nacelles mounted on the wing has been shown in Figure 3.1-9. As indicated, the effect on lift at zero angle of attack is small and would be masked by the power effects of the EBF system; therefore, no correction to the power-on data has been made for the presence of the nacelles.

The nacelles had no effect on the flap lift effectiveness when located at different spanwise location. This effect is shown in Figure 3.4-12. Chordwise location also has no effect on flap lift effectiveness. This variation is shown in Figure 3.4-13 for various flap configurations on the different wing planforms.

The effect of jet thrust tilt upward is shown in some of the plots of Figure 3.4-13. For the small additional tilt from -3.5 to -5.5 degrees, no change in effectiveness is seen. For the nacelle in the aft position (location D), more tilt upward should show an increase in effectiveness. This trend can be seen in Figure 3.4-13b, where an upward tilt of -15 degrees resulted in an increase in effectiveness. The most dramatic effect of upward jet tilt is shown in Figure 3.4-14a with the engine nacelle in the lowered position location E) for the wing with the triple-slotted flap. Flap lift effectiveness is shown to be reduced considerably due to lowering the jet stream. In other words, the flap is not immersed into the jet stream as much as in the upper position (Location A) and lift effectiveness is therefore reduced. With the engine nacelle in the lower position and the jet stream deflected upward toward the slots of the flap, flap lift effectiveness is regained.

The effect of engine nacelle height location has a large effect on flap lift effectiveness. As discussed in the previous section on lift curve slope ratio, flap lift effectiveness is a function of the amount of flap immersed in the jet stream. Figure 3.4-14 shows this effect. Flap lift effectiveness for any flap configuration is reduced as the nacelles are lowered away from the wing and trailing edge flap system. The double-slotted flap configuration at 45 and 30 degrees shows no flap lift effectiveness increase with jet blowing. This indicates that the efflux of the jet effectively blows aft beneath the flap trailing edge, showing no circulation lift augmentation and loss in lift due to direct thrust vectoring in the lift direction caused by the -3.5 degree upward tilt of the jet stream. An extreme of this condition is seen in Figure 3.4-14h, where flap lift effectiveness is less than the total of the power-off circulation lift and the thrust/lift vector. This would indicate that the jet stream is destroying the downwash from the flap.

3.4.4 EFFECT OF ASPECT RATIO ON $\Delta C'_{L_{TE}}$. The effects of changing wing aspect ratio on flap lift effectiveness is shown in Figure 3.4-15 for numerous flap configurations and deflections. Test data shown in these figures indicates that there is no variation in flap lift effectiveness within the range of aspect ratios tested, although the theoretical variation shown from Reference 3-4 does show a variation in effectiveness. These estimates have been made by simply correcting the two-dimensional

flap effectiveness estimated by jet flap theory by the ratio of the three-dimensional lift curve slope to the two-dimensional lift curve slope as suggested by lifting line theory. This method does not take into account the spanwise extent of blowing, which has not been changed physically in these tests. Therefore, it is assumed that flap lift effectiveness for EBF systems is not a function of the overall wing aspect ratio but may be a function only of the total spanwise extent of blowing.

3.4.5 EFFECT OF WING SWEEP ON $\Delta C'_{L_{TE}}$. The variation of flap lift effectiveness with changes in wing sweep is shown in Figure 3.4-16 for several leading and trailing edge flap system. Test data shows a reduction in flap lift effectiveness with an increase in wing sweep from 12.5 to 35 degrees, which is the same trend seen in the theoretical variation from Reference 3-4.

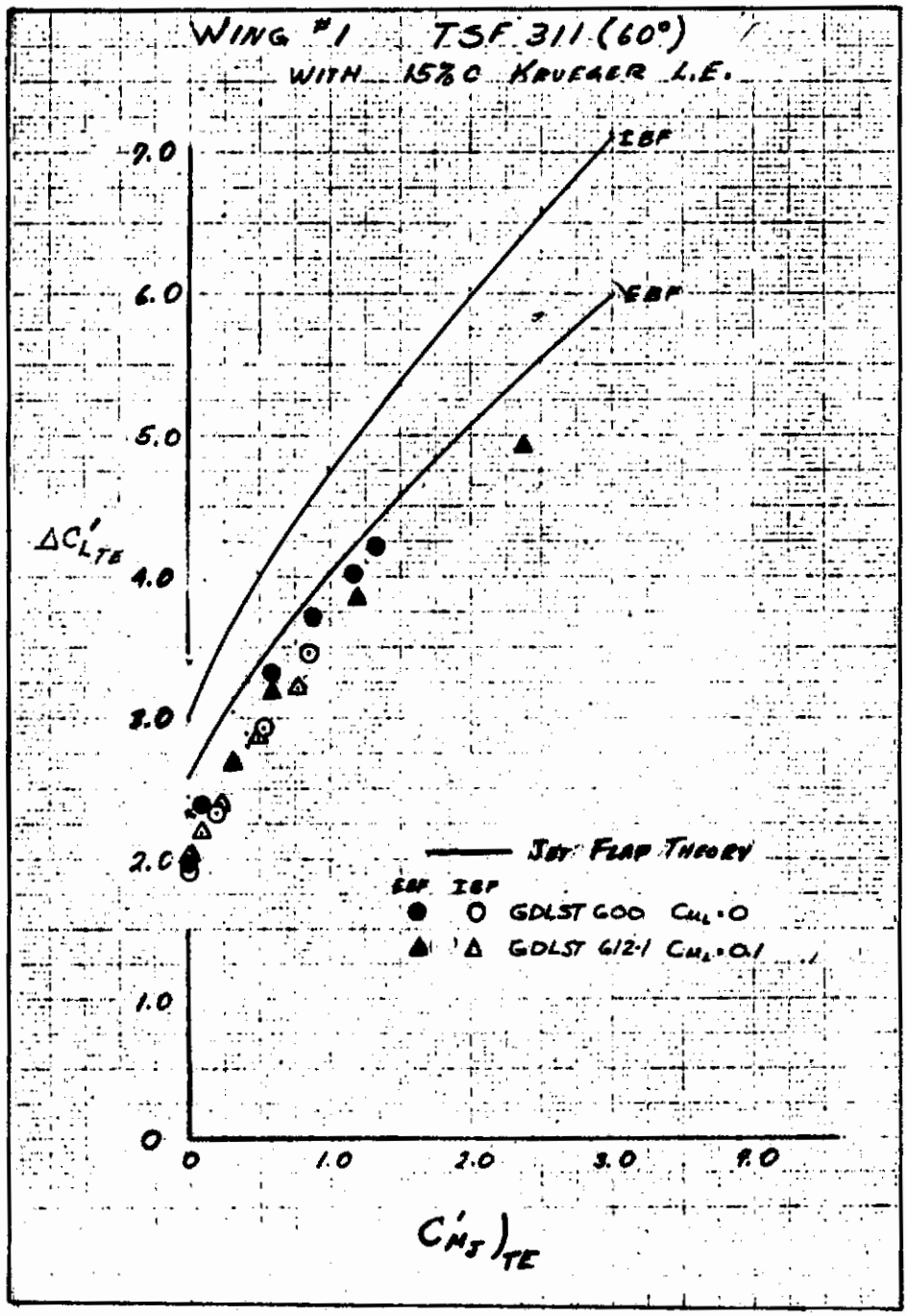

Figure 3.4-1. EBF/IBF Analogy

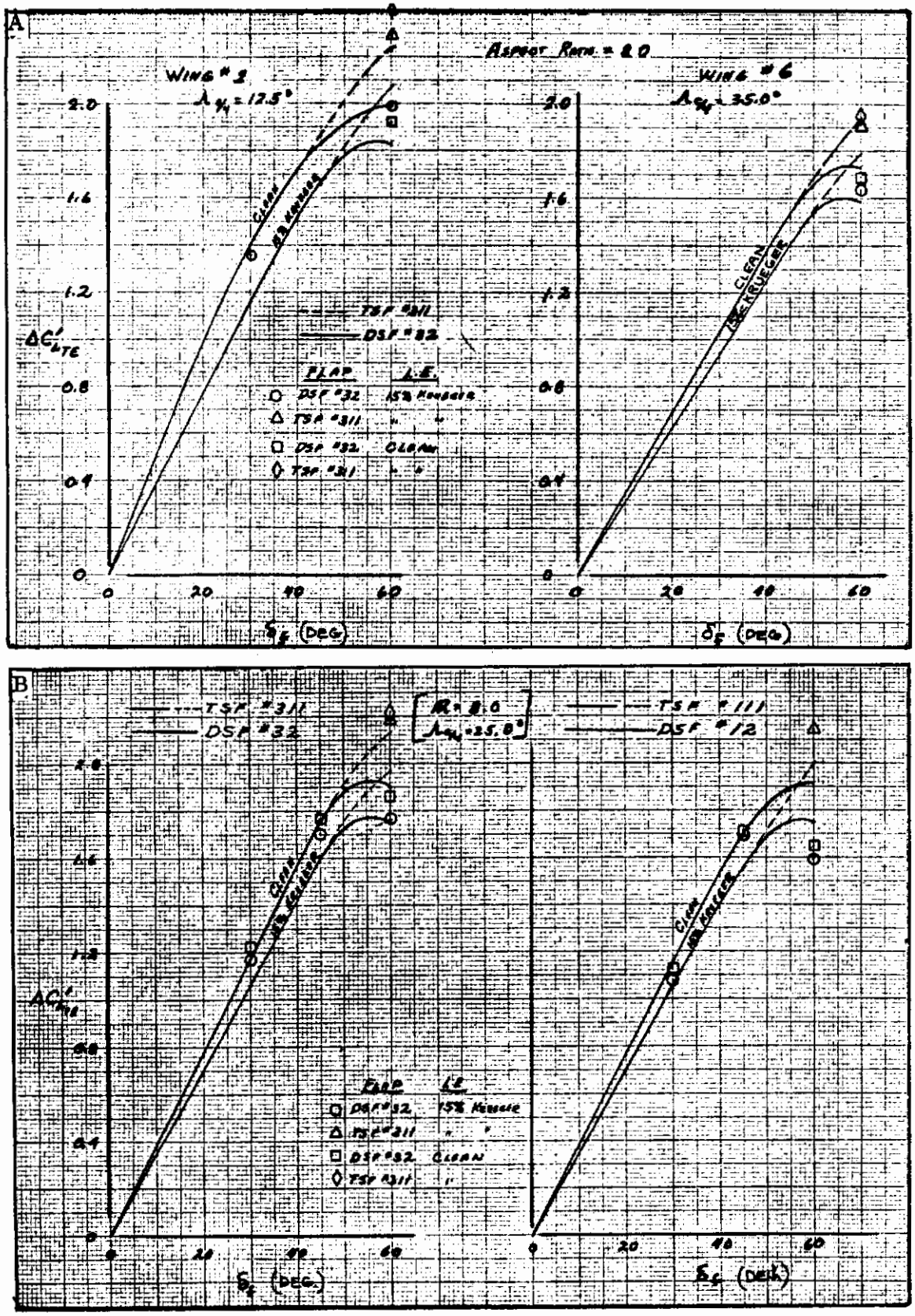

Figure 3.4-2. Effect of Trailing Edge Flap Deflection on $\Delta C'_{L_{TE}}$ -Power Off

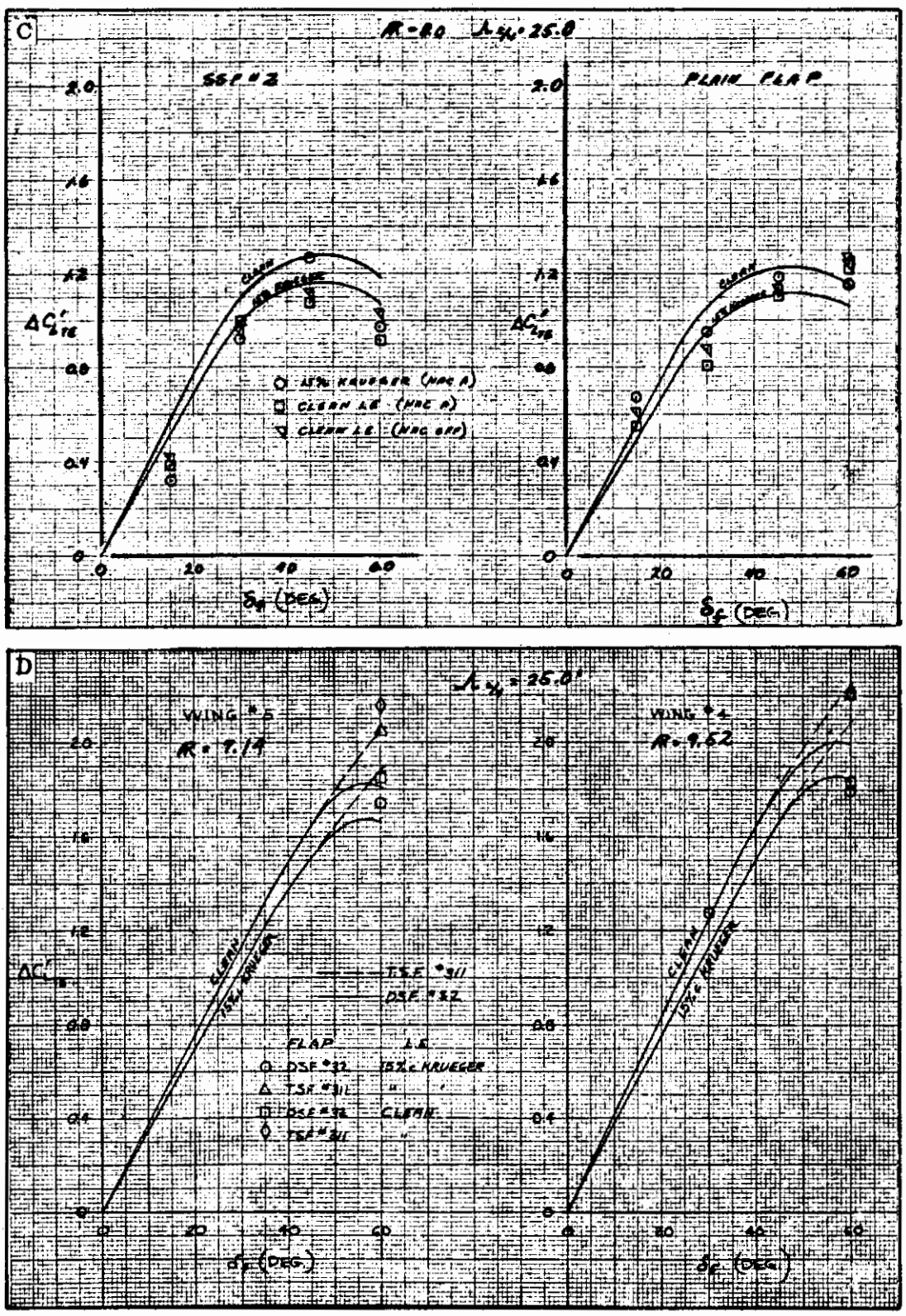

Figure 3.4-2. Effect of Trailing Edge Flap Deflection on $\Delta C'_{L_{TE}}$ -Power Off, Cont

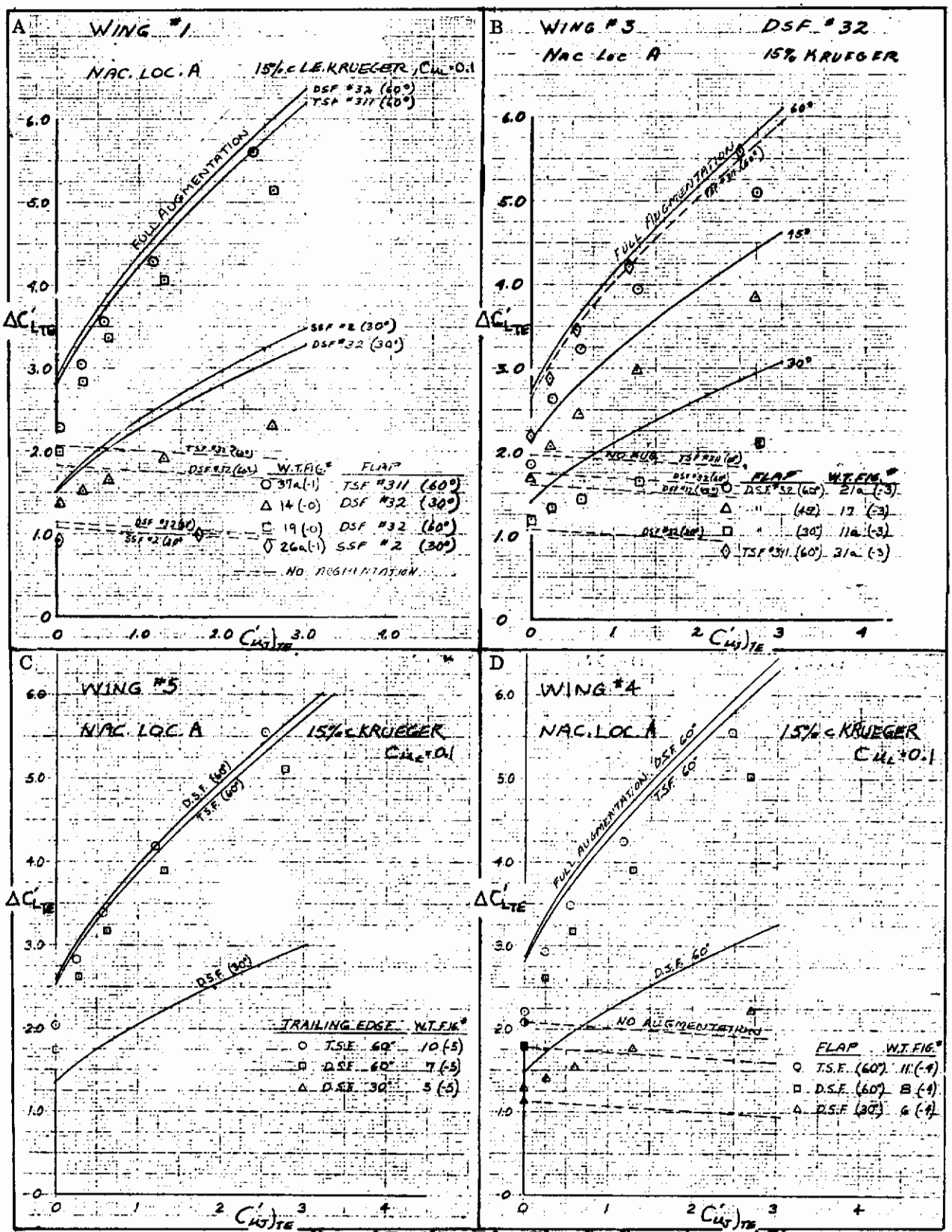

Figure 3.4-3. Effect of Trailing Edge Flap Configuration on $\Delta C'_{L_{TE}}$

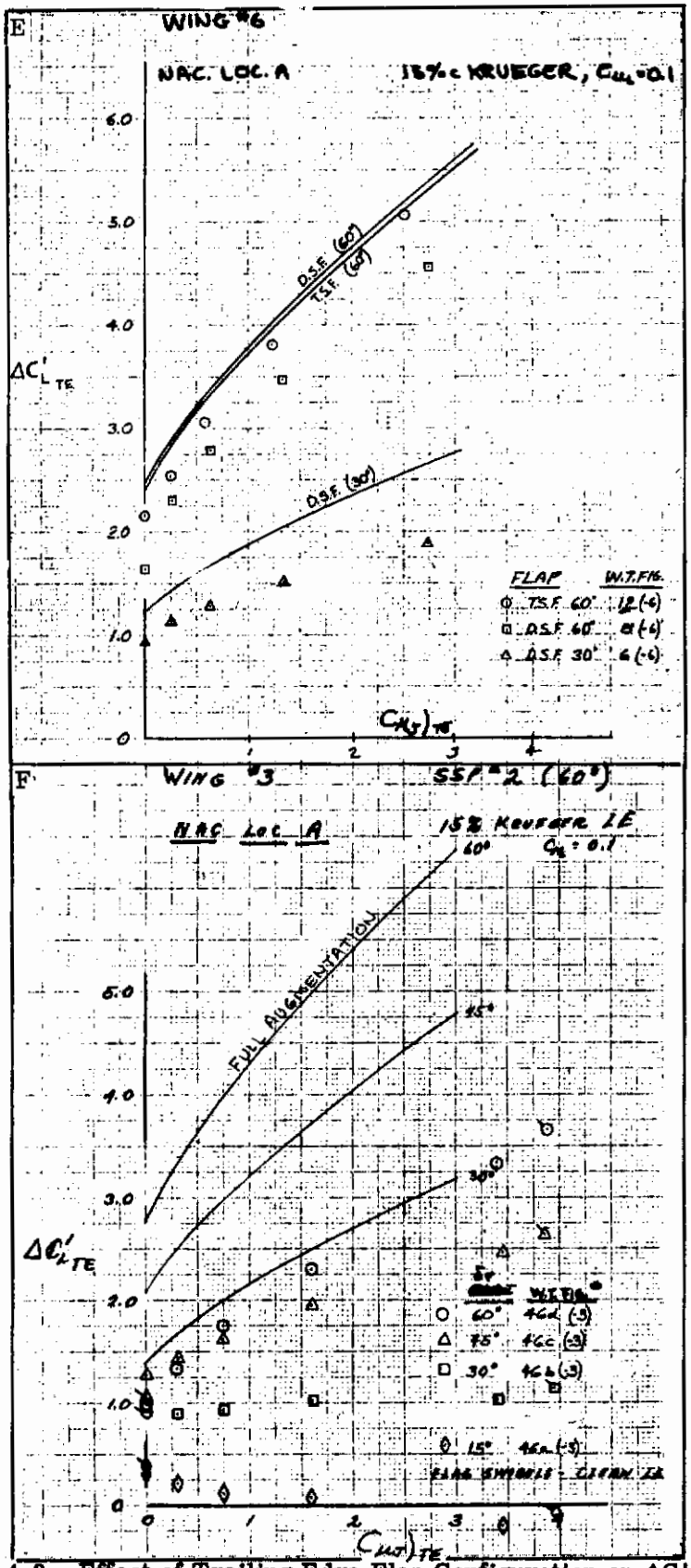

Figure 3.4-3. Effect of Trailing Edge Flap Configuration on $\Delta C'_{L_{TE}}$, Cont

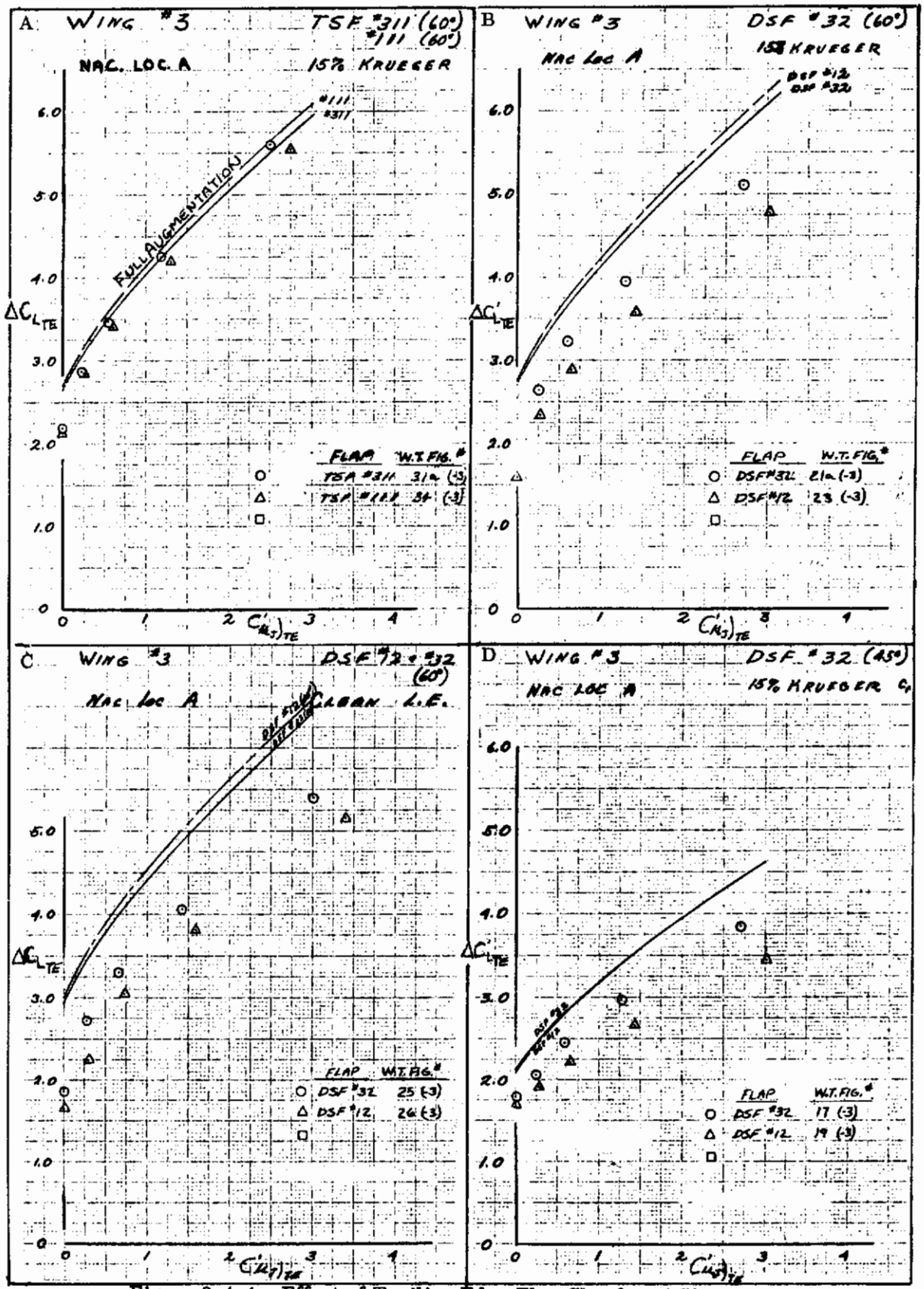

Figure 3.4-4. Effect of Trailing Edge Flap Chord on $\Delta C'_{L_{TE}}$

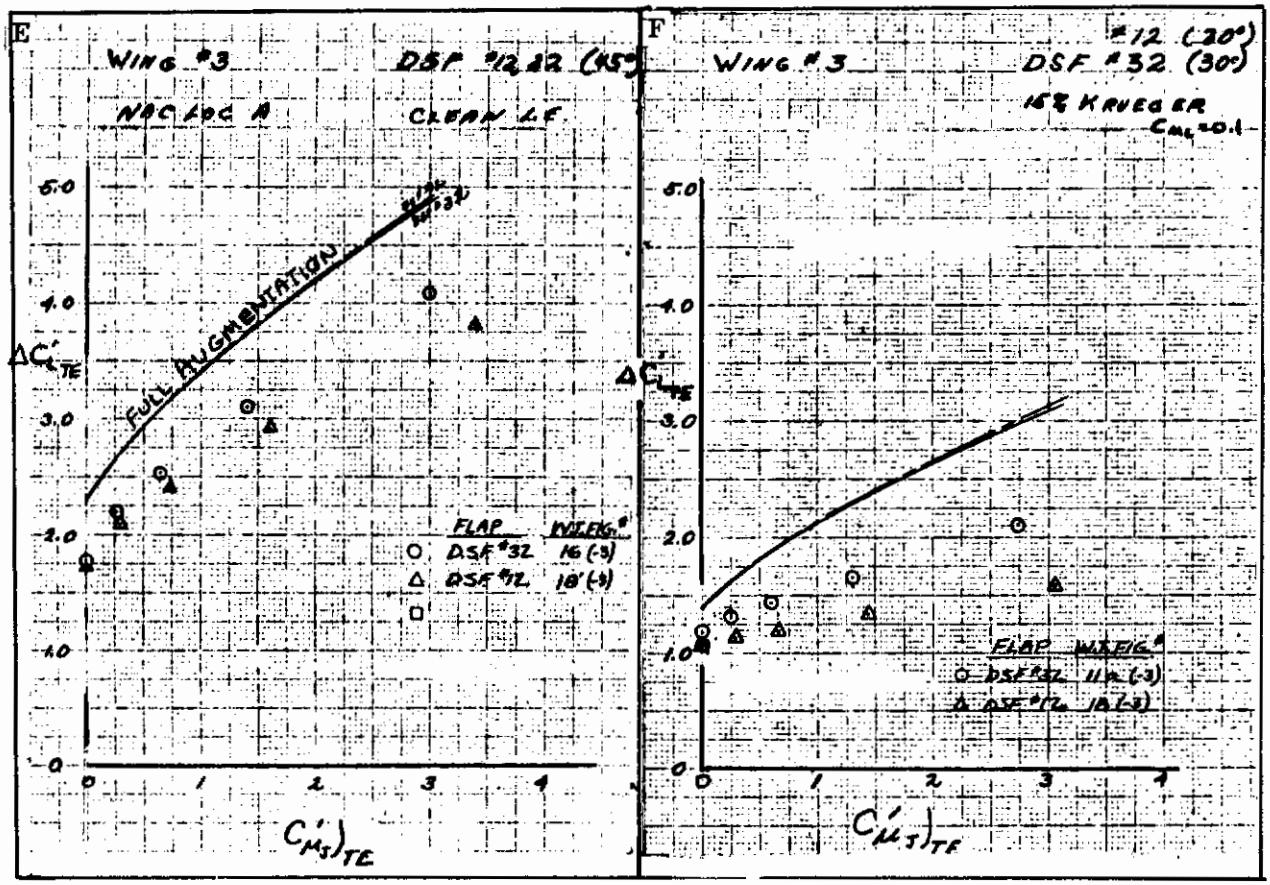

Figure 3.4-4. Effect of Trailing Edge Flap Chord on $\Delta C'_{L_{TE}}$, Cont

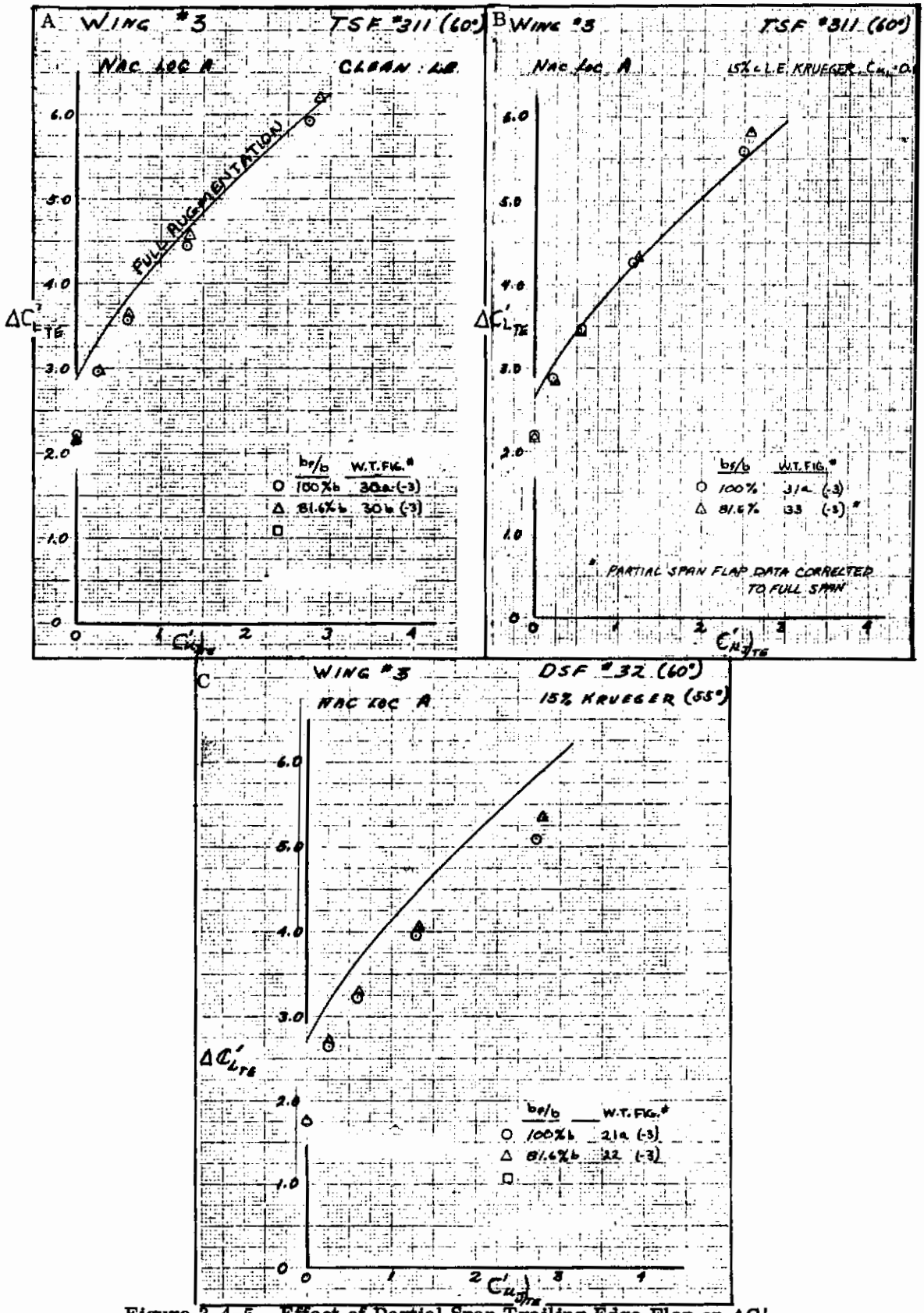

Figure 3.4-5. Effect of Partial Span Trailing Edge Flap on $\Delta C'_{L_{TE}}$

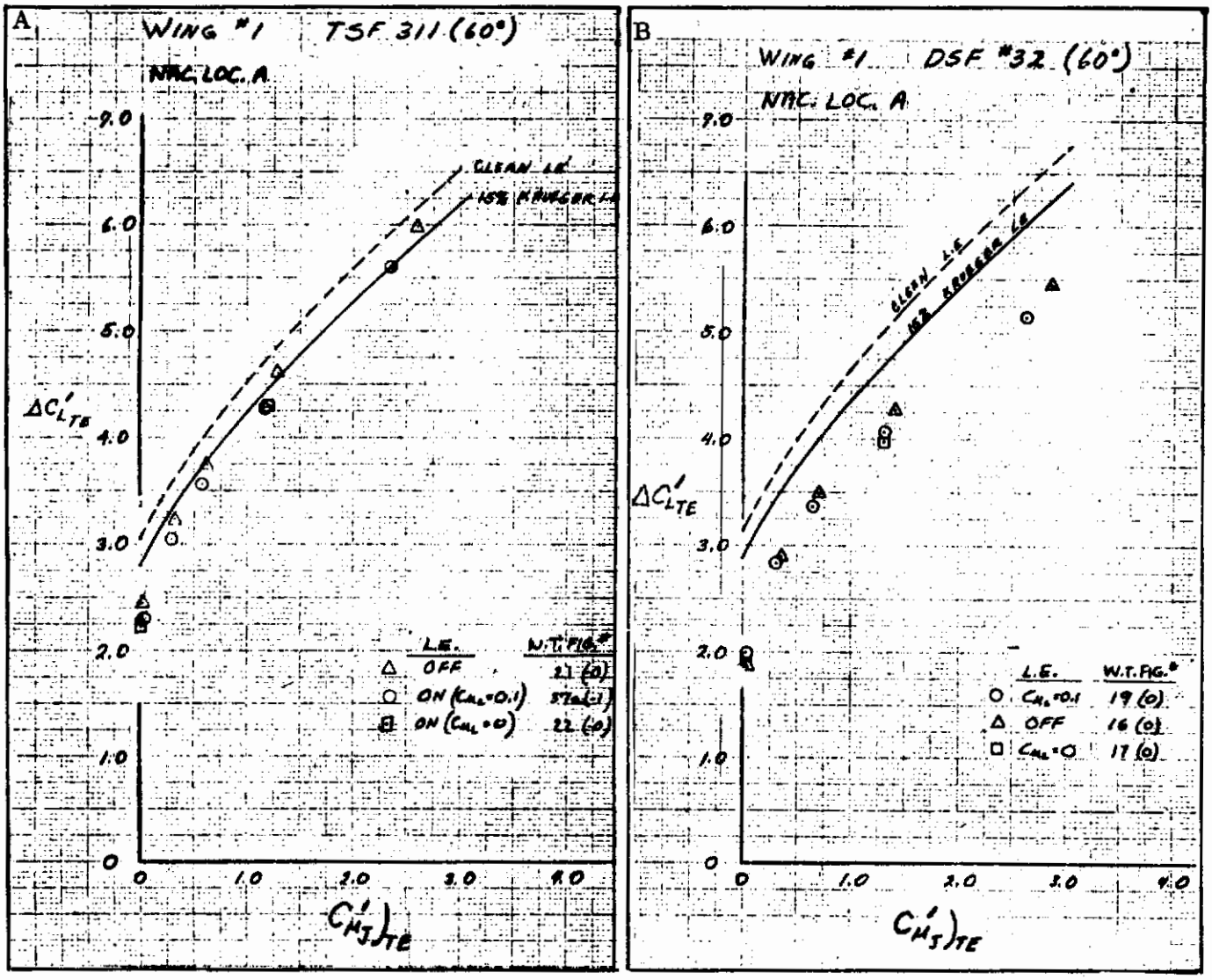

Figure 3.4-6. Effect of Leading Edge Blowing on $\Delta C'_{L_{TE}}$

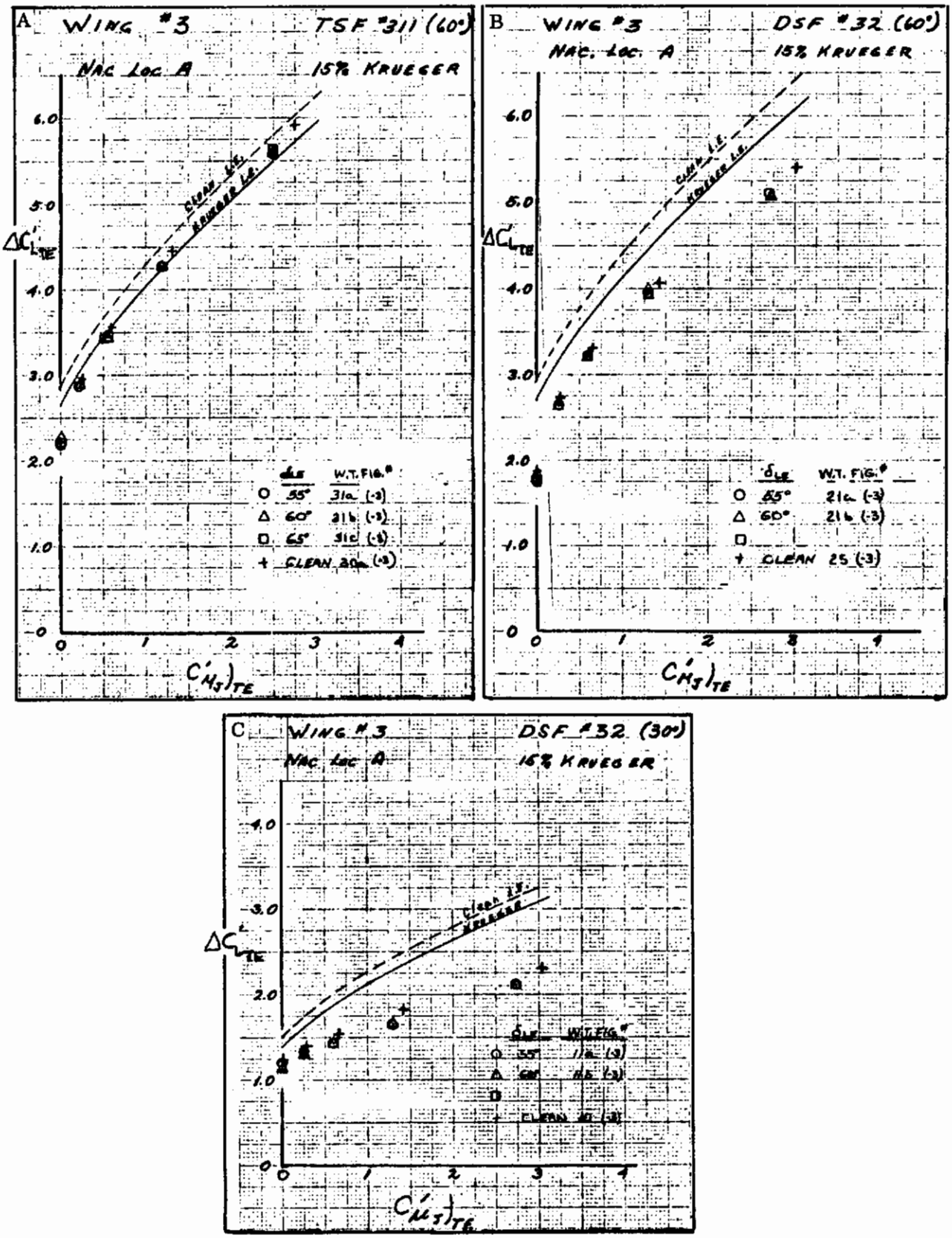

Figure 3.4-7. Effect of Leading Edge Flap Deflection on $\Delta C'_{L_{TE}}$

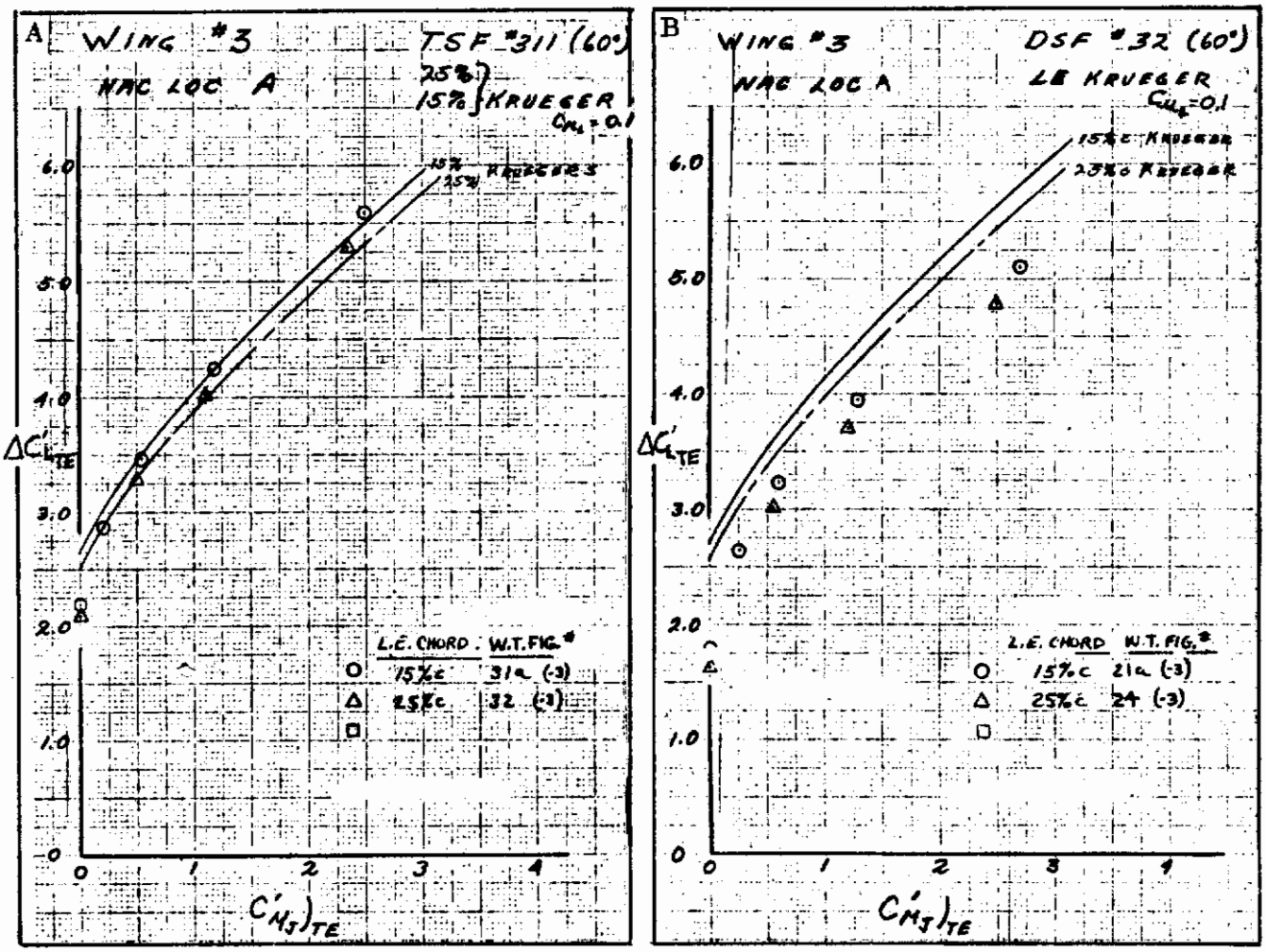

Figure 3.4-8. Effect of Leading Edge Flap Chord on $\Delta C'_{L_{TE}}$

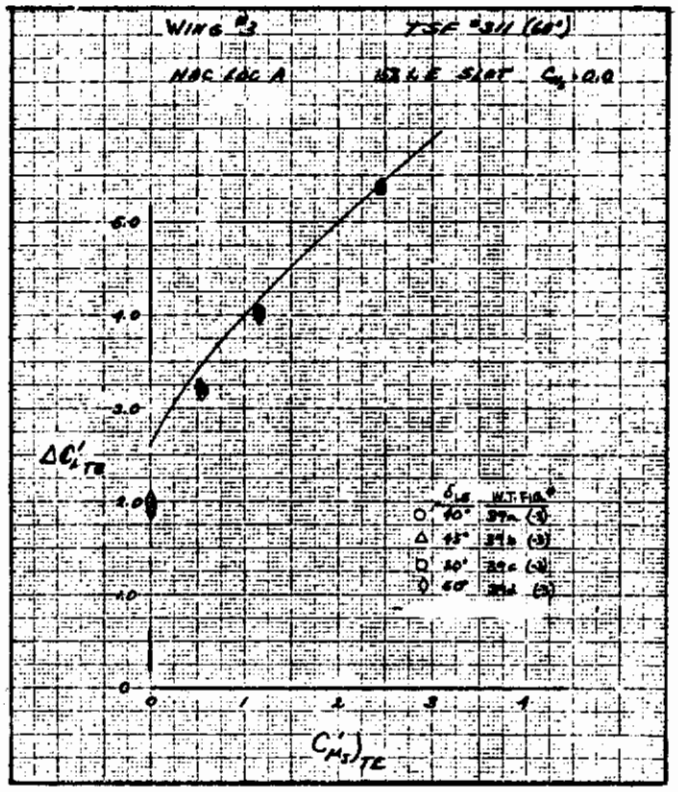

Figure 3.4-9. Effect of Leading Edge Slat Deflection on $\Delta C'_{L_{TE}}$

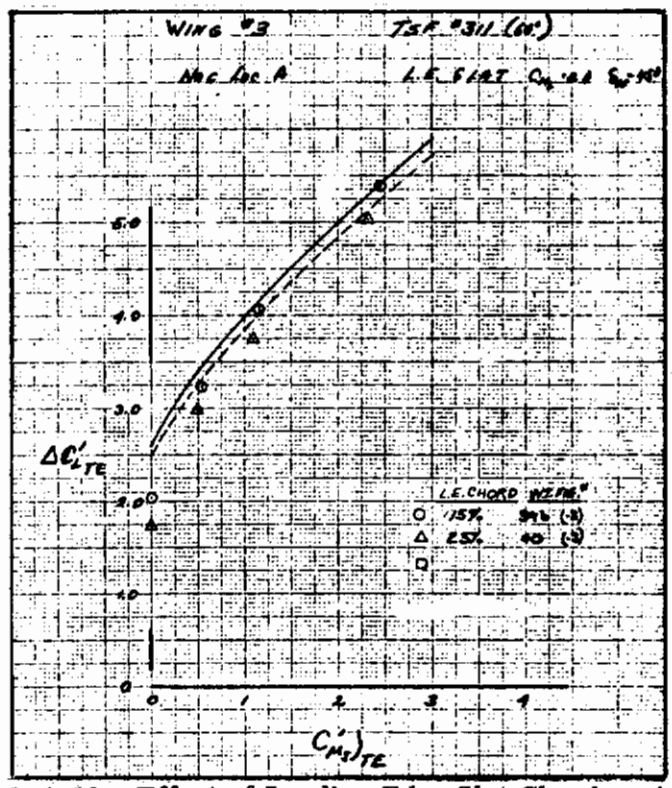

Figure 3.4-10. Effect of Leading Edge Slat Chord on $\Delta C'_{L_{TE}}$

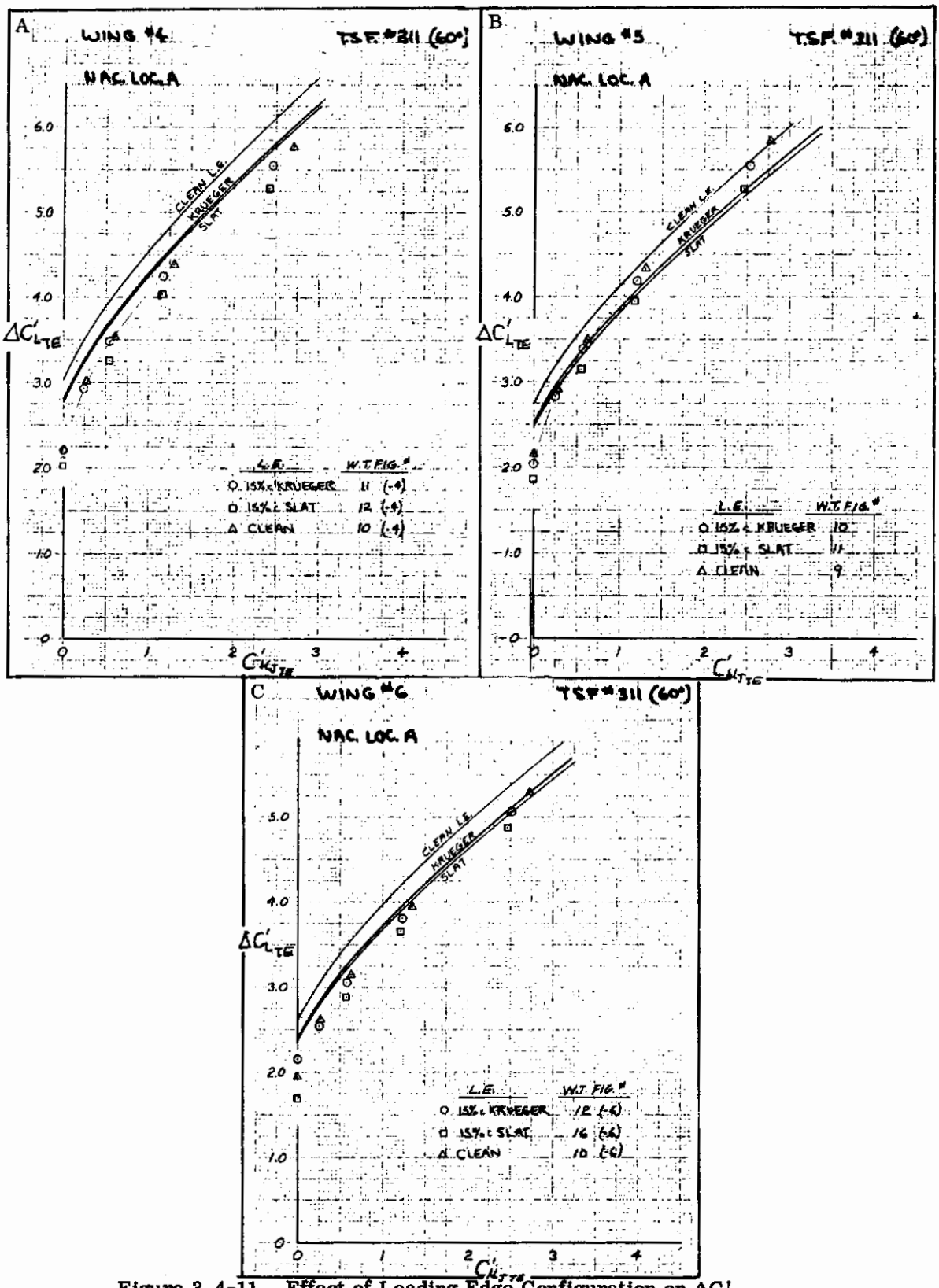

Figure 3.4-11. Effect of Leading Edge Configuration on $\Delta C'_{L_{TE}}$

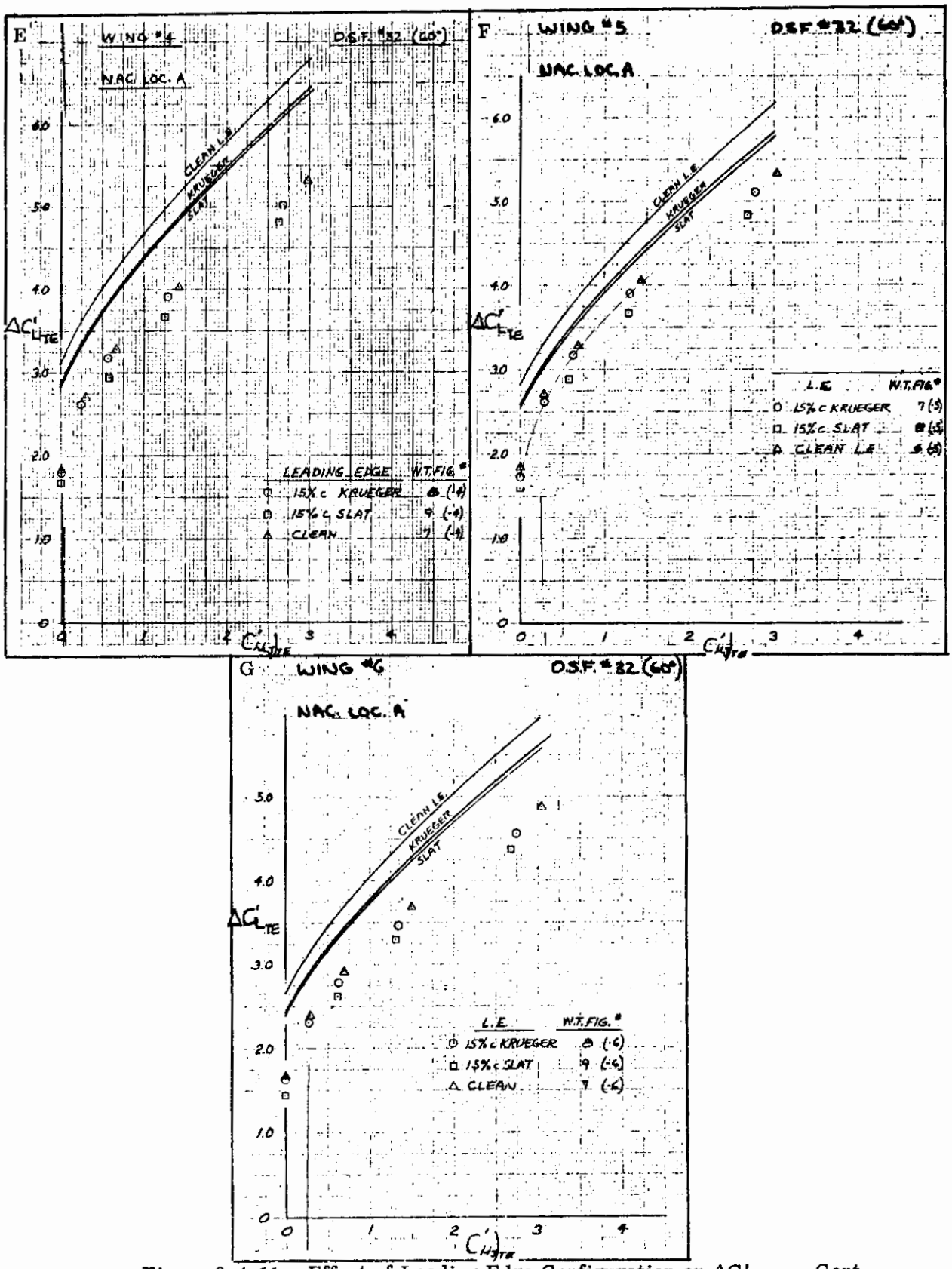

Figure 3.4-11. Effect of Leading Edge Configuration on $\Delta C'_{L_{TE}}$, Cont

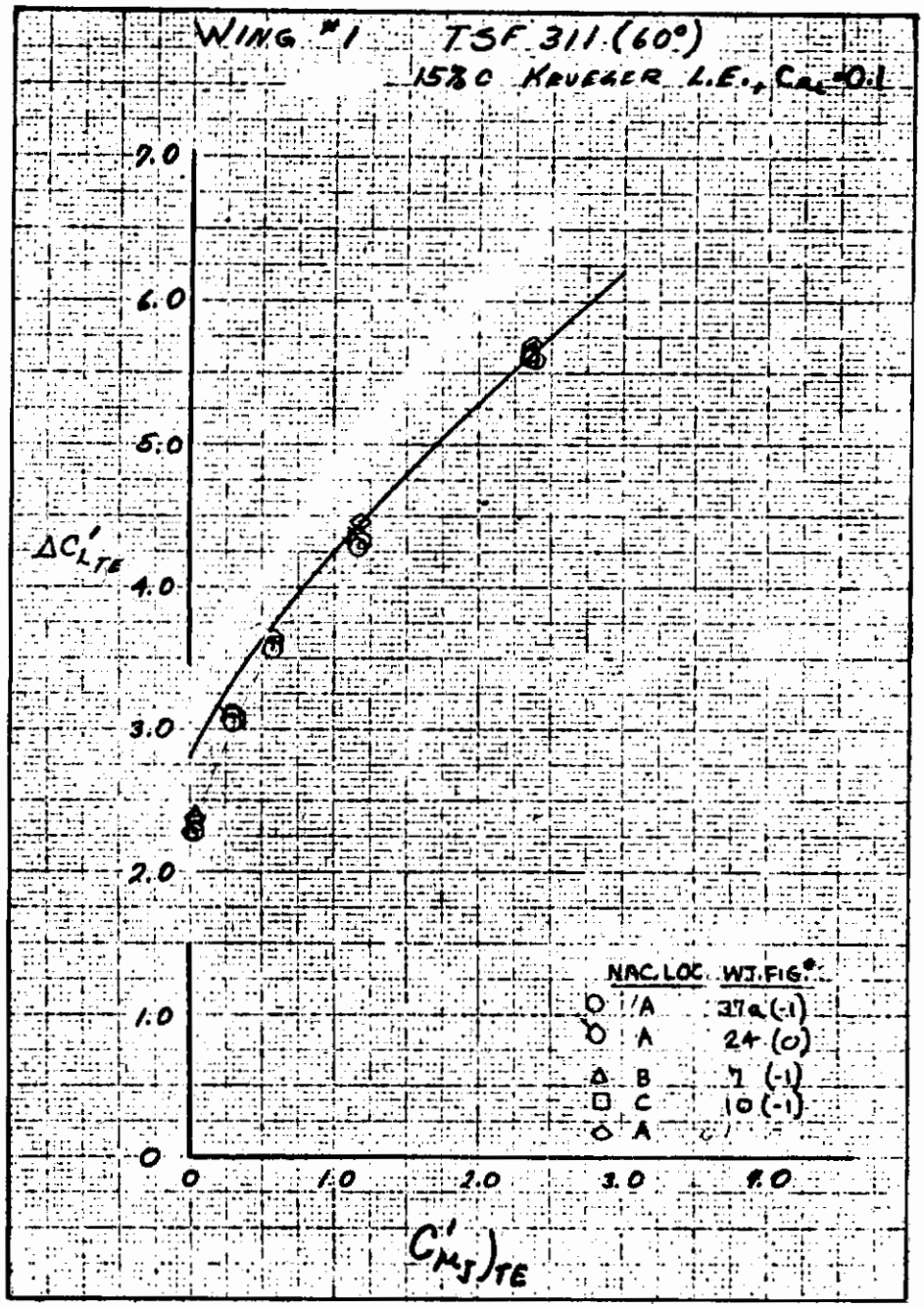

Figure 3.4-12. Effect of Spanwise Nacelle Location on $\Delta C'_{L_{TE}}$

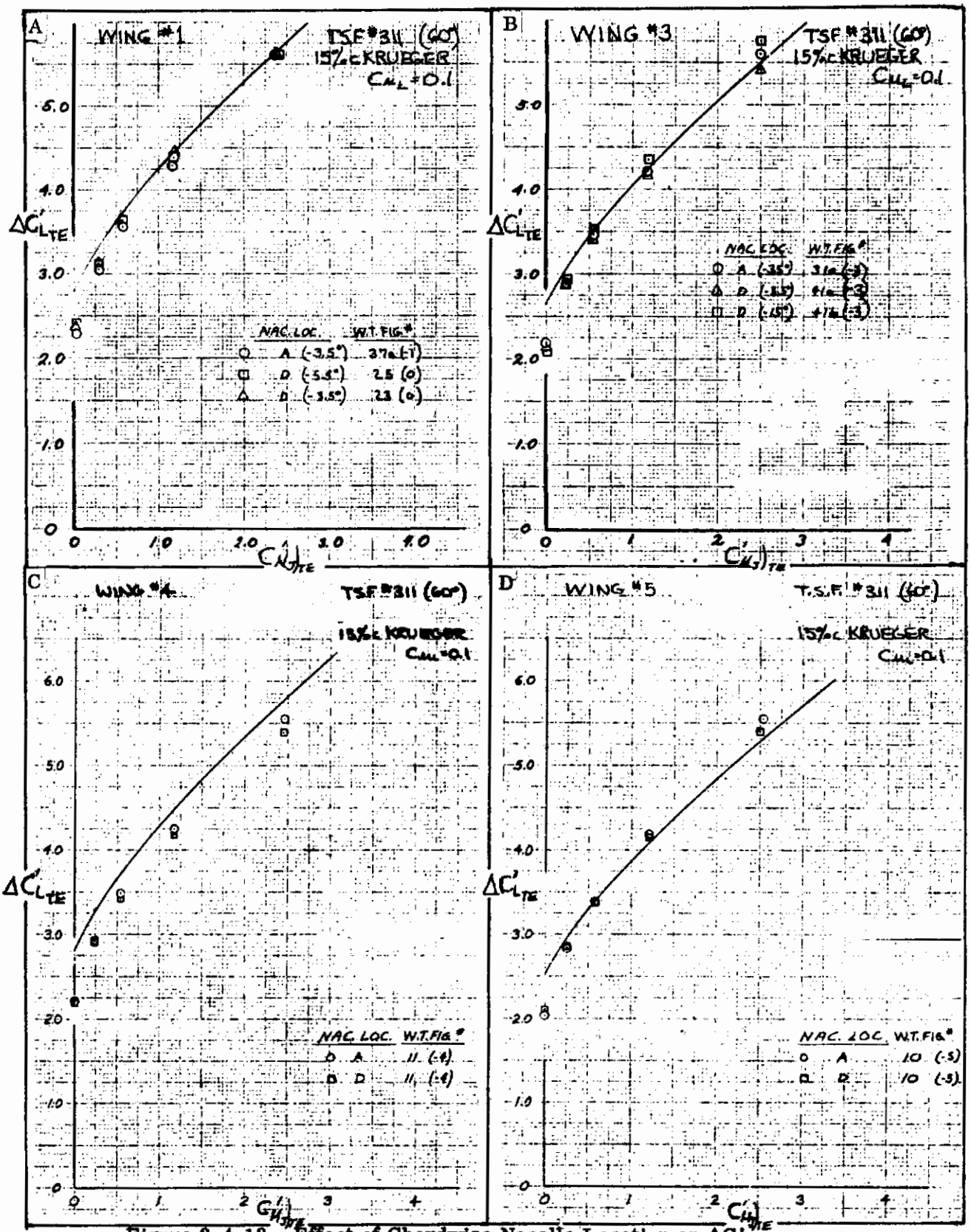

Figure 3.4-13. Effect of Chordwise Nacelle Location on $\Delta C'_{L_{TE}}$

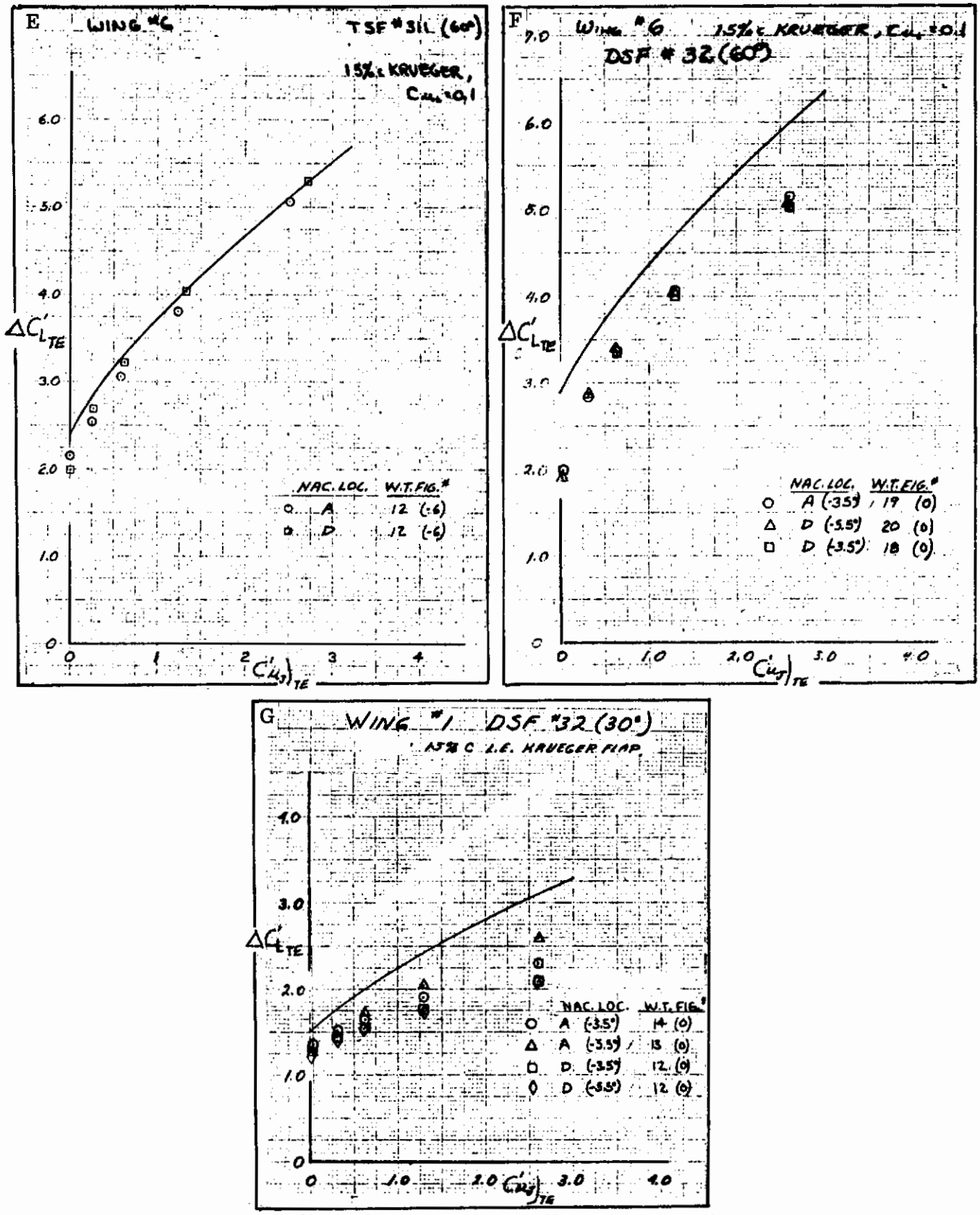

Figure 3.4-13. Effect of Chordwise Nacelle Location on $\Delta C'_{L_{TE}}$, Cont

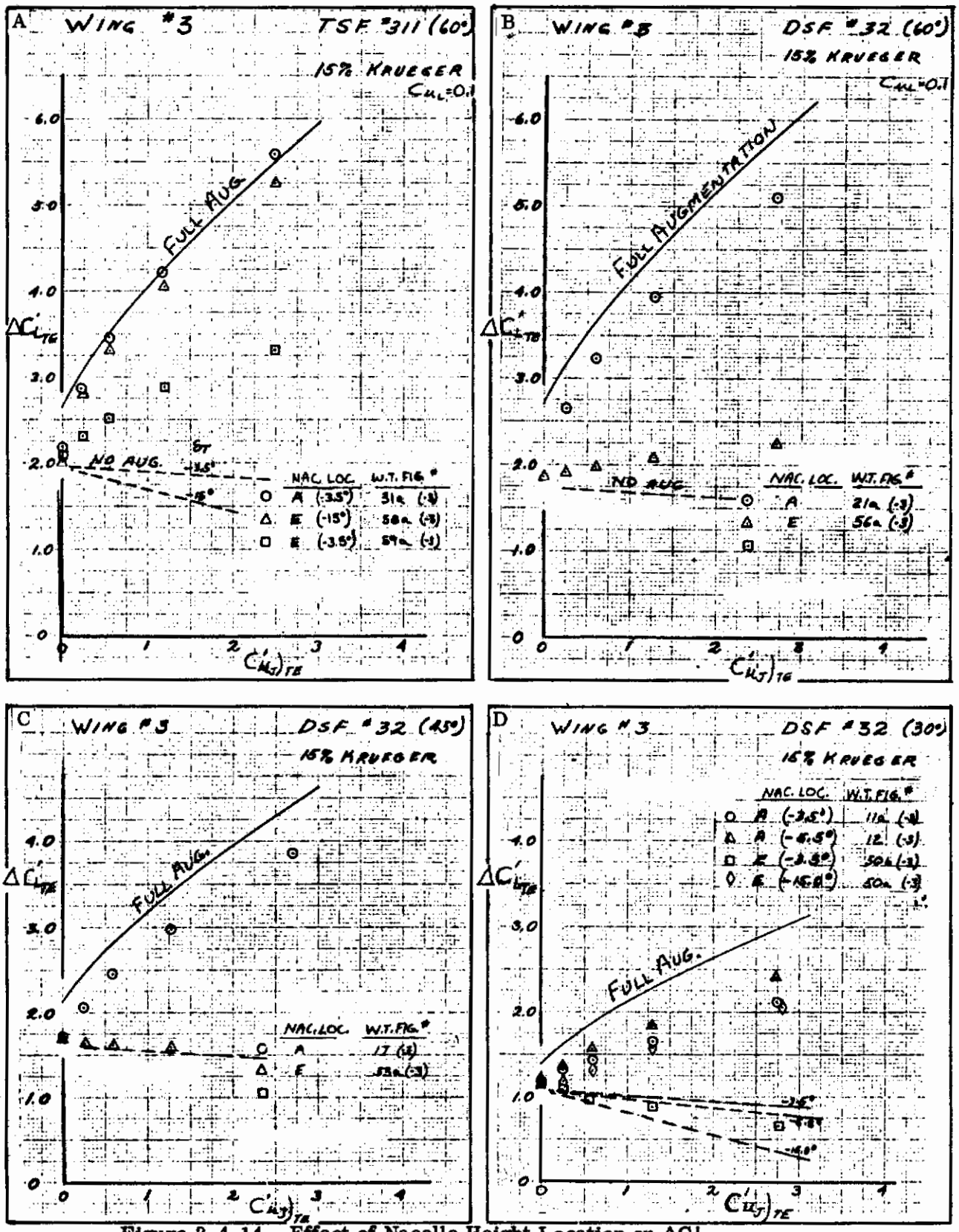

Figure 3.4-14. Effect of Nacelle Height Location on $\Delta C'_{L_{TE}}$

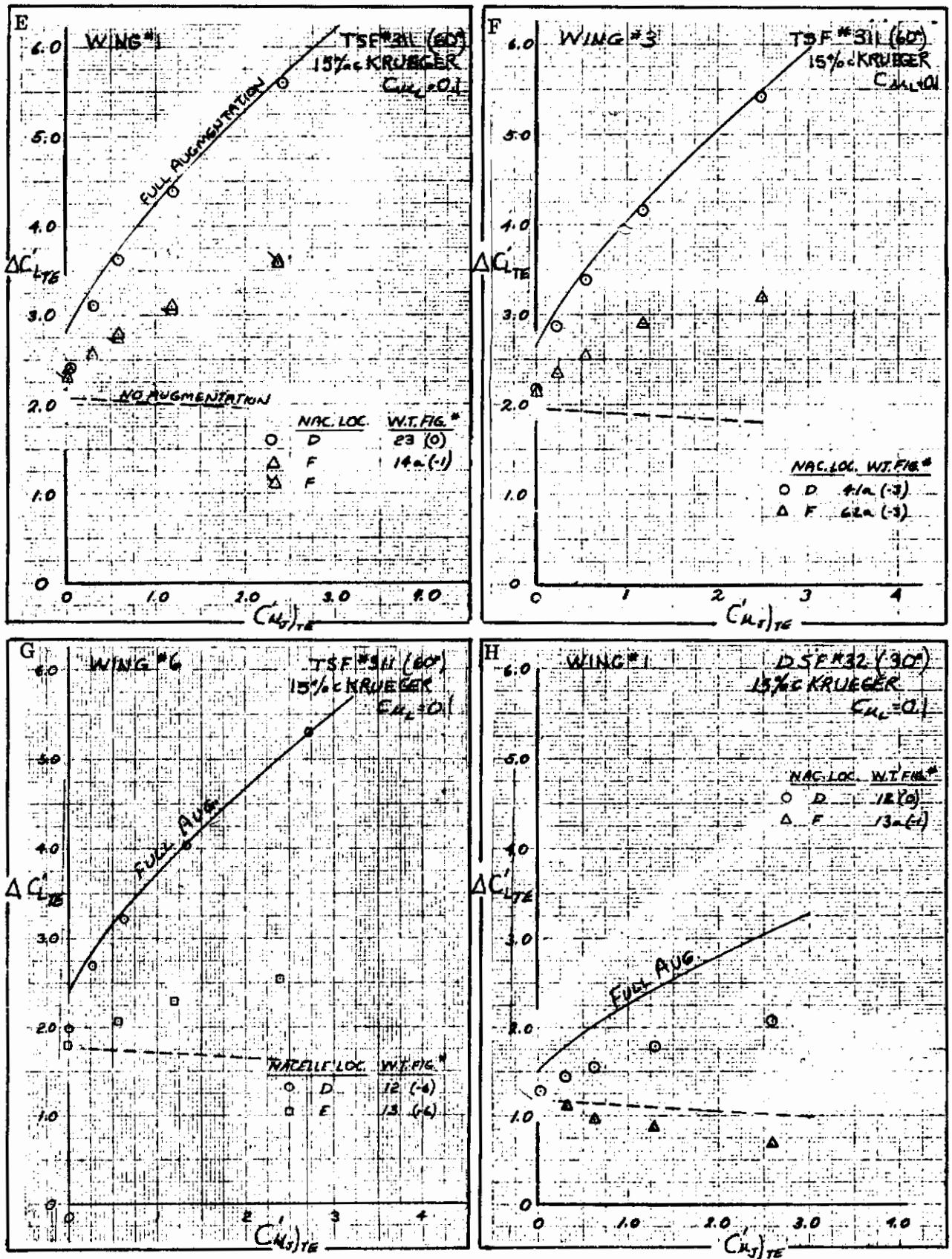

Figure 3.4-14. Effect of Nacelle Height Location on $\Delta C'_{L_{TE}}$, Cont.

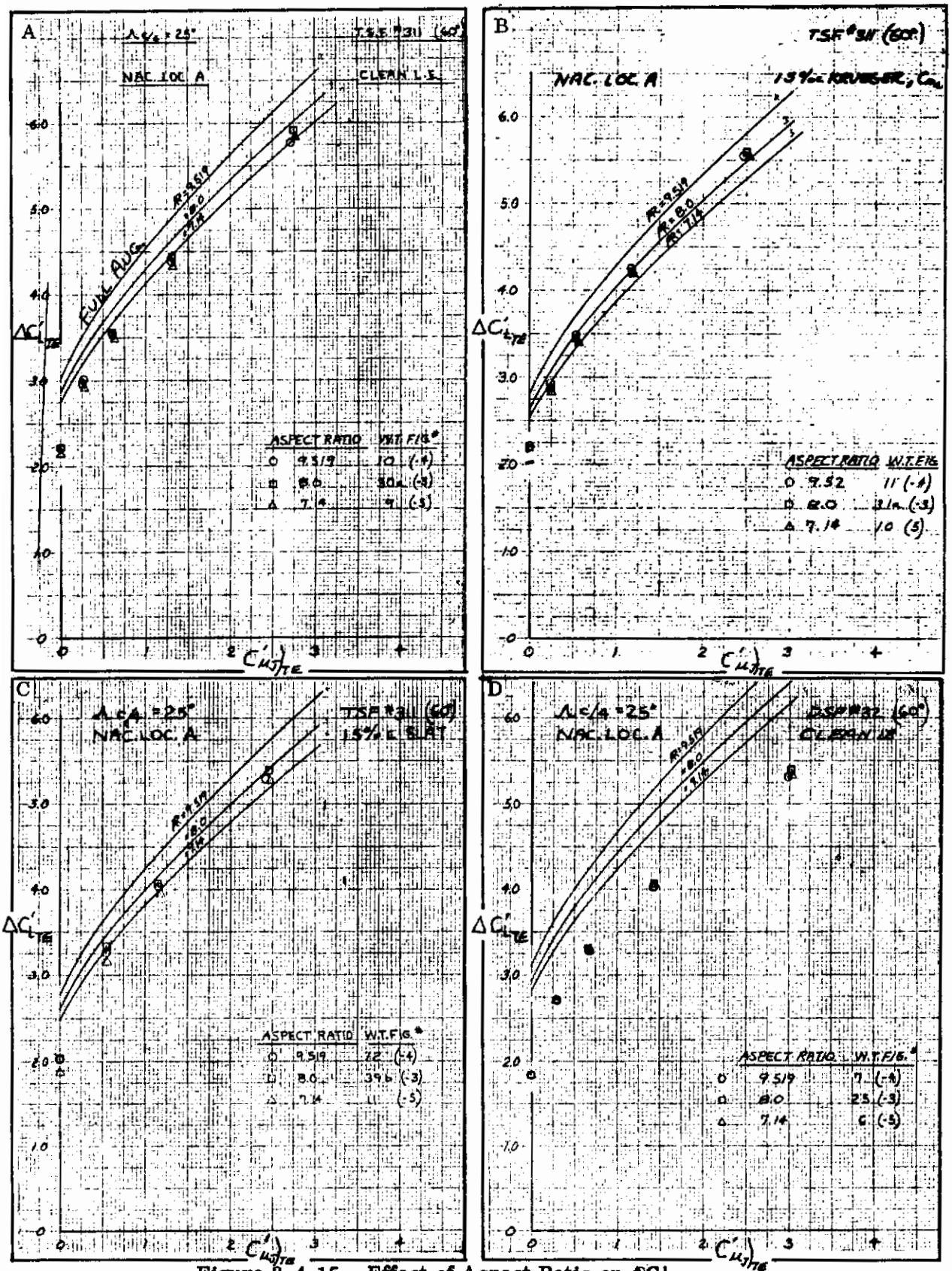

Figure 3.4-15. Effect of Aspect Ratio on $\Delta C'_{L_{TE}}$

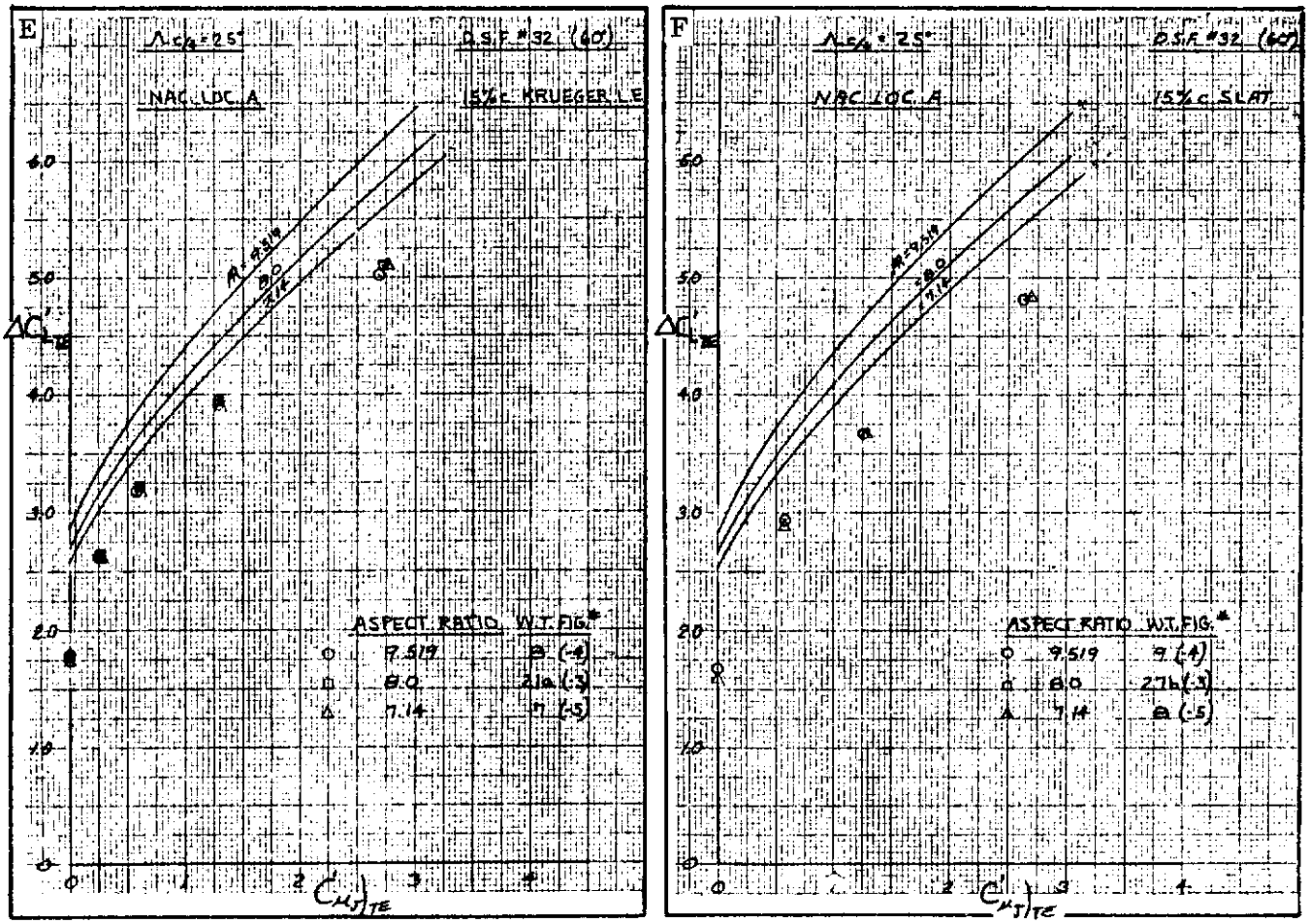

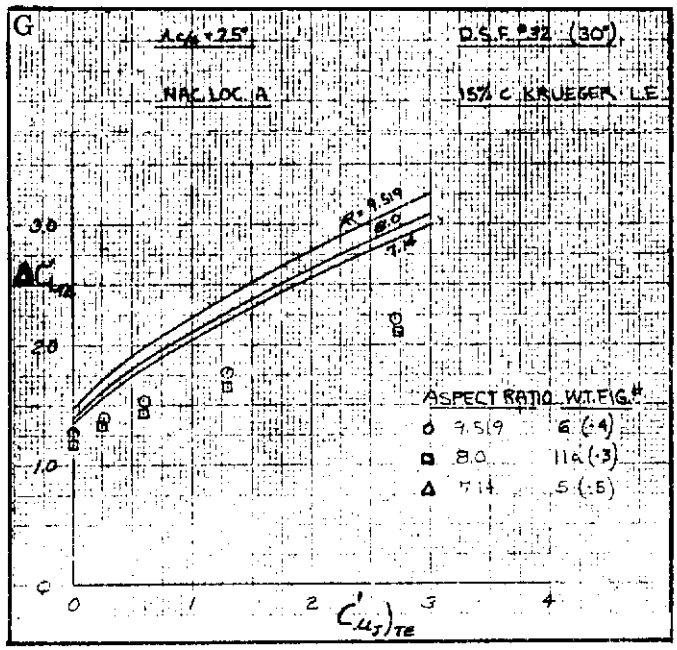

Figure 3.4-15. Effect of Aspect Ratio on $\Delta C'_{L_{TE}}$, Cont

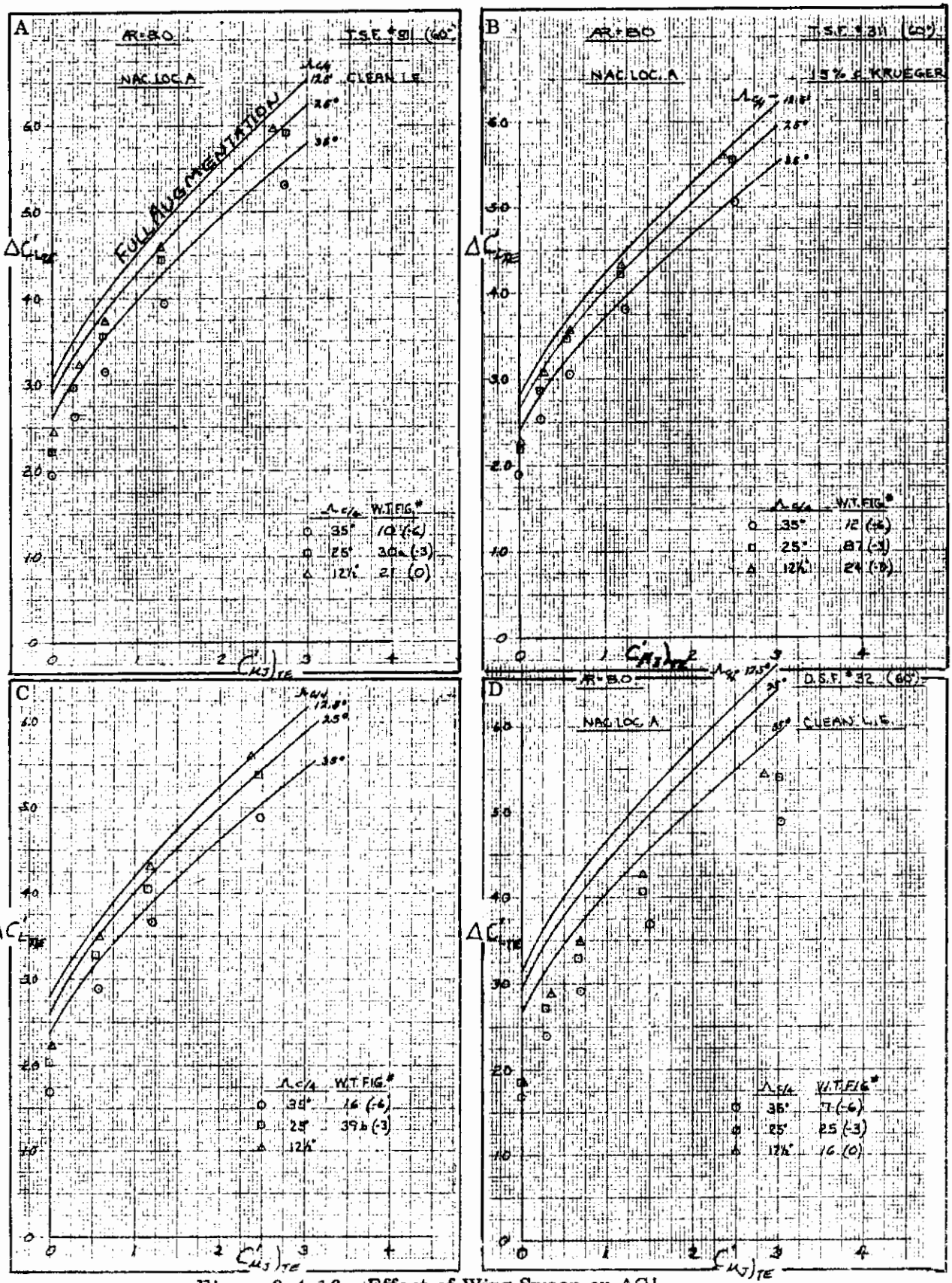

Figure 3.4-16. Effect of Wing Sweep on $\Delta C'_{L_{TE}}$

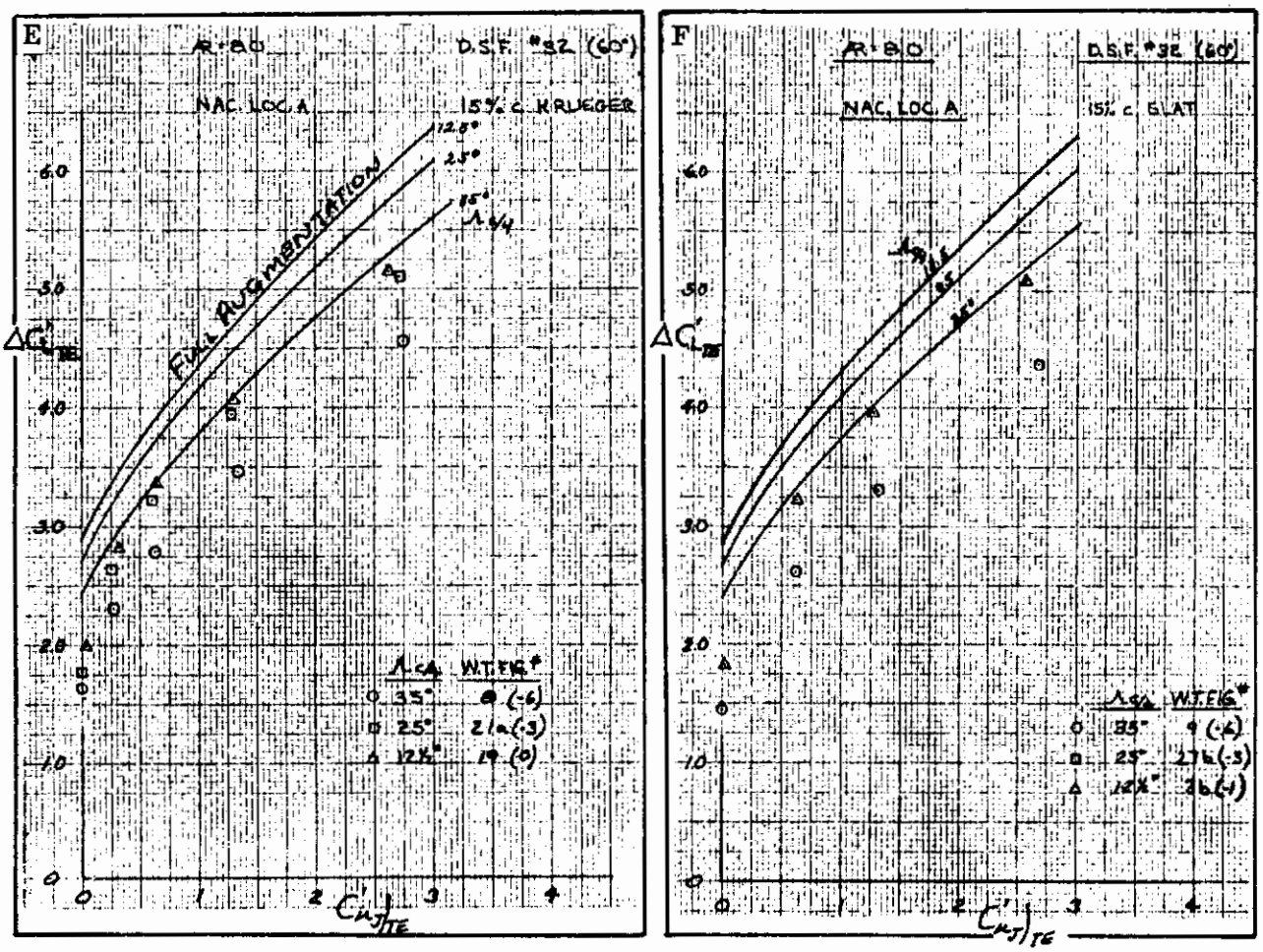

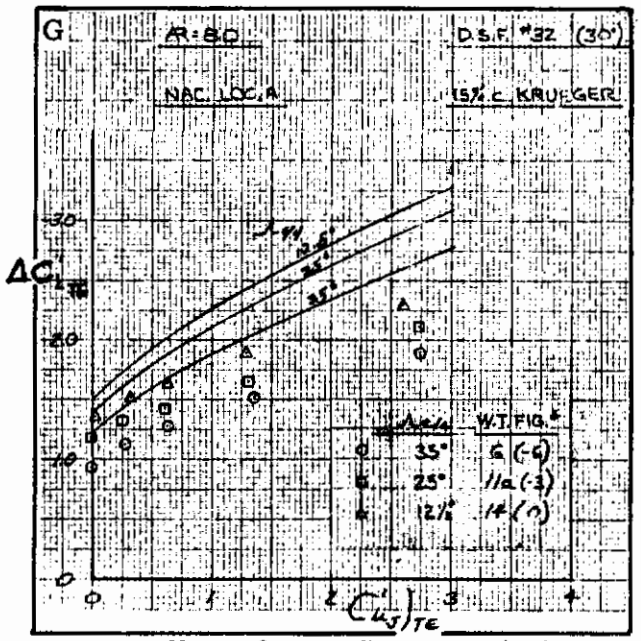

Figure 3.4-16. Effect of Wing Sweep on $\Delta C'_{L_{TE}}$, Cont

3.5 IBF TRAILING EDGE FLAP LIFT INCREMENT AT $\alpha = 0$ DEGREES

The analysis of the flap lift effectiveness data for the IBF system is presented in this section. IBF lift effectiveness, $\Delta C_{L'_{TE}}$, has been defined in the same manner as for the EBF systems (i.e., the increment in lift at zero angle of attack due to deflection and blowing of a trailing edge flap system). This increment is presented in the following analysis as a function of the momentum coefficient estimated at the flap trailing edge, $C'_{\mu_{TE}}$. The momentum coefficient is based on the extended wing area spanned by the blowing slot.

3.5.1 EFFECT OF TRAILING EDGE FLAP CONFIGURATION ON $\Delta C'_{L_{TE}}$. The effect of blowing over a plain flap and a single-slotted flap is shown in Figure 3.5-1. There is no difference between the data except that normally expected for the slight difference in flap chord. Although tests were not run for the single-slotted flap at 60 degrees of deflection, this slotted flap should perform better at the higher deflections and lower blowing rates than the plain flown flap.

The effects of flap deflection on flap lift effectiveness is shown in Figure 3.5-2 for two leading edge configurations and with engine nacelles on and off. The BLC effect discussed in Paragraph 3.4 can also be seen in these figures. For the IBF system, though, less blowing is required to obtain full potential flow, which is represented as the solid line in these figures. Surprisingly, flap lift effectiveness at the higher momentum coefficients is greater than predicted.

The effect of partial-span blown flaps is shown in Figure 3.5-3. For purposes of this comparison between full span and 81.6 percent span flaps, the test data for the partial span flaps have been corrected by the flap span factors developed for unpowered flap systems. Agreement between the test data for the full and corrected partial-span flaps is good at all momentum coefficients, indicating that the normal power-off partial span flap factors are valid for the power-on case tested.

3.5.2 EFFECT OF LEADING EDGE KRUEGER FLAP ON $\Delta C'_{L_{TE}}$. Extension of the leading edge blown Krueger flap has no effect on the trailing edge flap lift effectiveness except as shown in Figure 3.5-4. Differences in the test data are the effects of extending the overall wing airfoil chord by extending the leading edge and effectively reducing the trailing edge flap chord in percent of airfoil chord. This reduced flap chord results in the loss of effectiveness seen in these figures.

3.5.3 EFFECT OF ENGINE NACELLES ON $\Delta C'_{L_{TE}}$. The effect of wing-mounted unpowered jet engine nacelles on flap lift effectiveness is shown in Figure 3.5-5. As shown, unpowered nacelle has only a small effect on the lift at zero angle of attack throughout the range of trailing edge momentum coefficients tested. This small increment is probably due to a lift force on the nacelle and is not an effect of flap lift effectiveness.

A more important effect of the engine nacelle is shown in Figures 3.5-5b through 3.5-5e. These figures include the effect of blowing at a momentum coefficient of two from the engine nacelles. For the 30-degree deflected flap, the engine jet stream produces no EBF effect, as shown in the figures at zero trailing edge nozzle momentum coefficient. For the 60-degree deflection, however, the flap is immersed in the engine jet stream like an EBF system and a small amount of augmentation is produced (Figure 3.4-4e). With trailing edge nozzle momentum coefficient other than zero, flap lift augmentation does not become as large as the effectiveness without jet engine blowing. The engine jet stream cuts the jet sheet being produced by the trailing edge nozzle, thereby reducing the effectiveness of the jet sheet.

3.5.4 EFFECT OF WING SWEEP ON $\Delta C'_{L_{TE}}$. The effect of wing sweep on flap lift effectiveness of IBF systems is shown in Figure 3.5-6. This sweep effect from the test data is less than expected from the theoretical estimate shown on the figures.

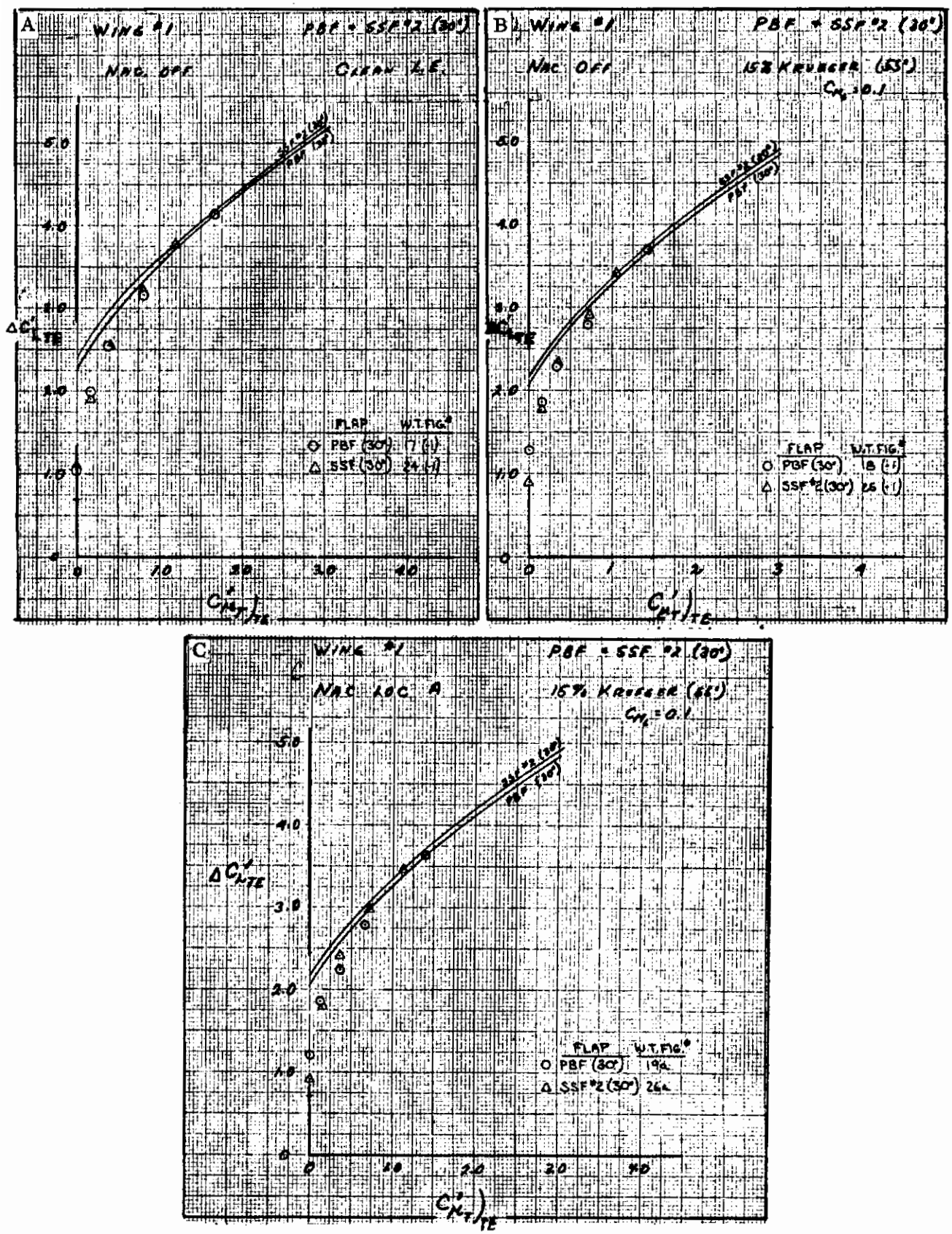

Figure 3.5-1. Effect of Trailing Edge Flap Configuration on $\Delta C'_{L_{TE}}$

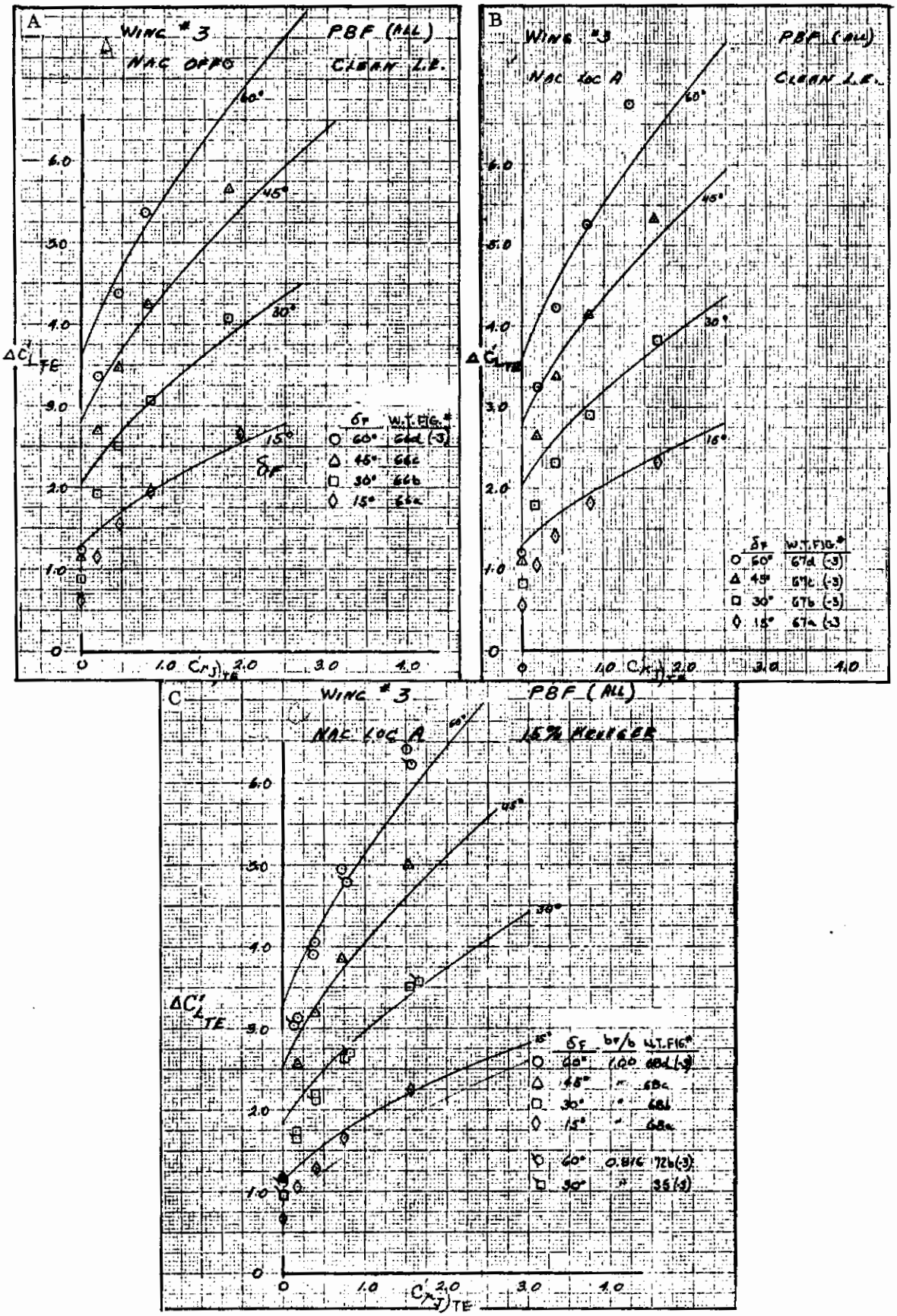

Figure 3.5-2. Effect of Trailing Edge Flap Deflection on $\Delta C'_{L_{TE}}$

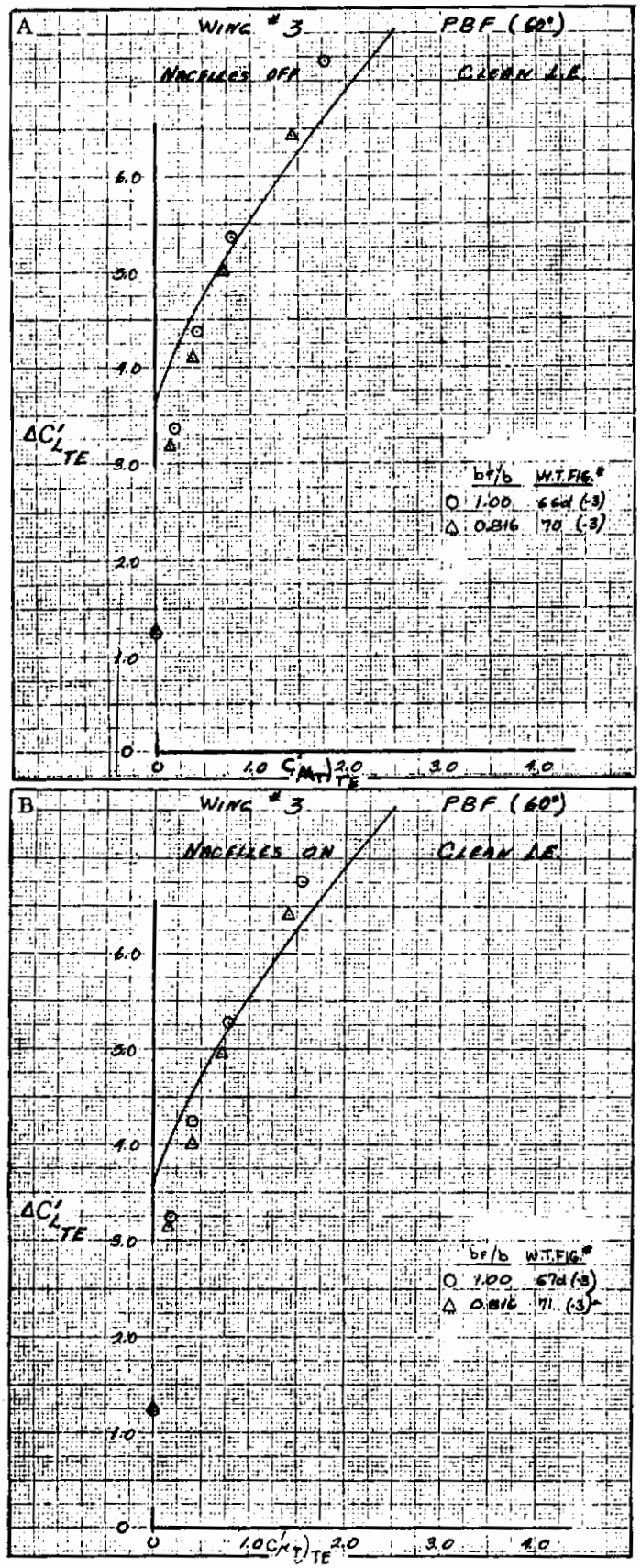

Figure 3.5-3. Effect of Partial Span Trailing Edge Flap on $\Delta C'_{L_{TE}}$

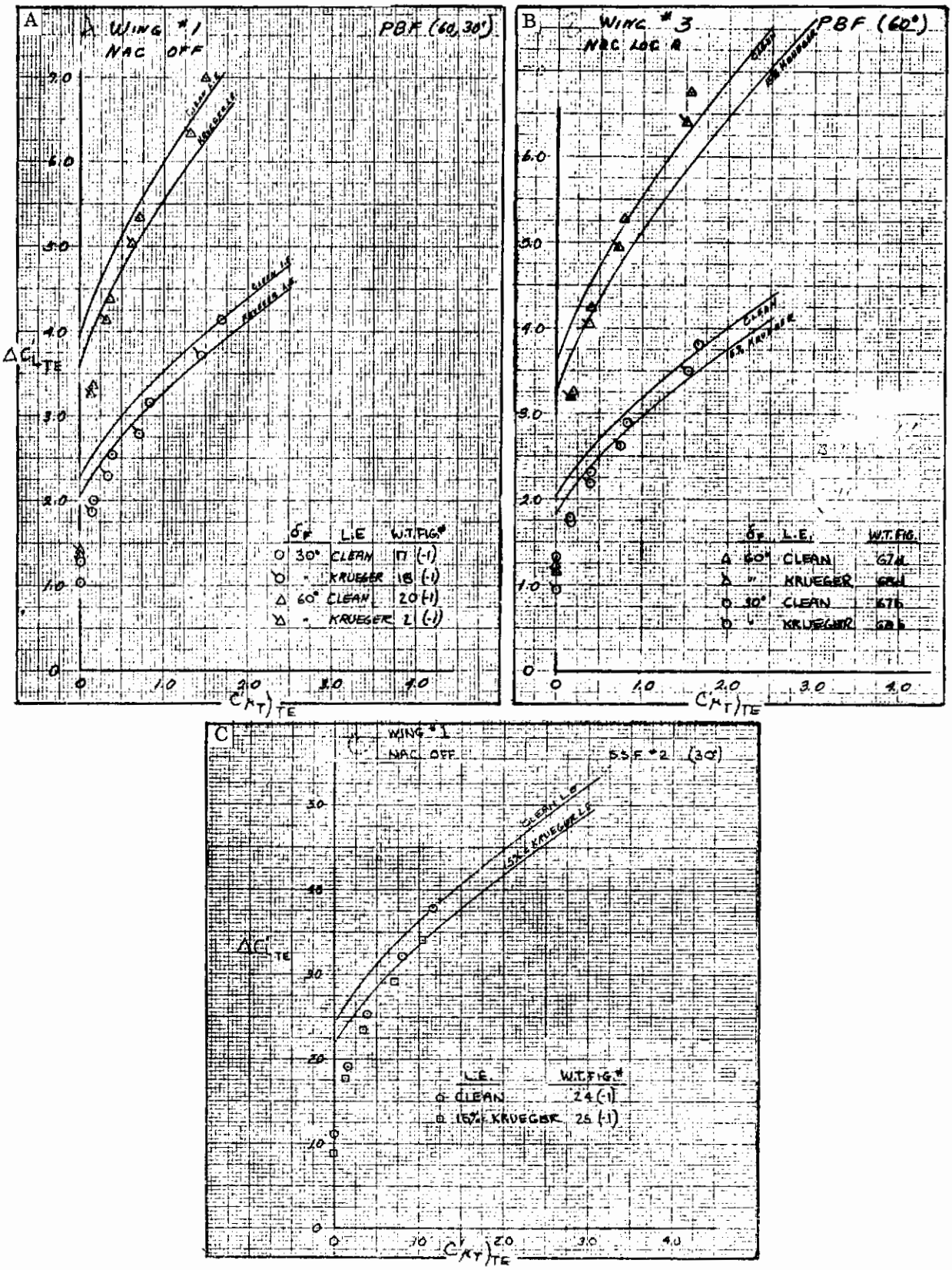

Figure 3.5-4. Effect of Leading Edge Configuration on $\Delta C'_{L_{TE}}$

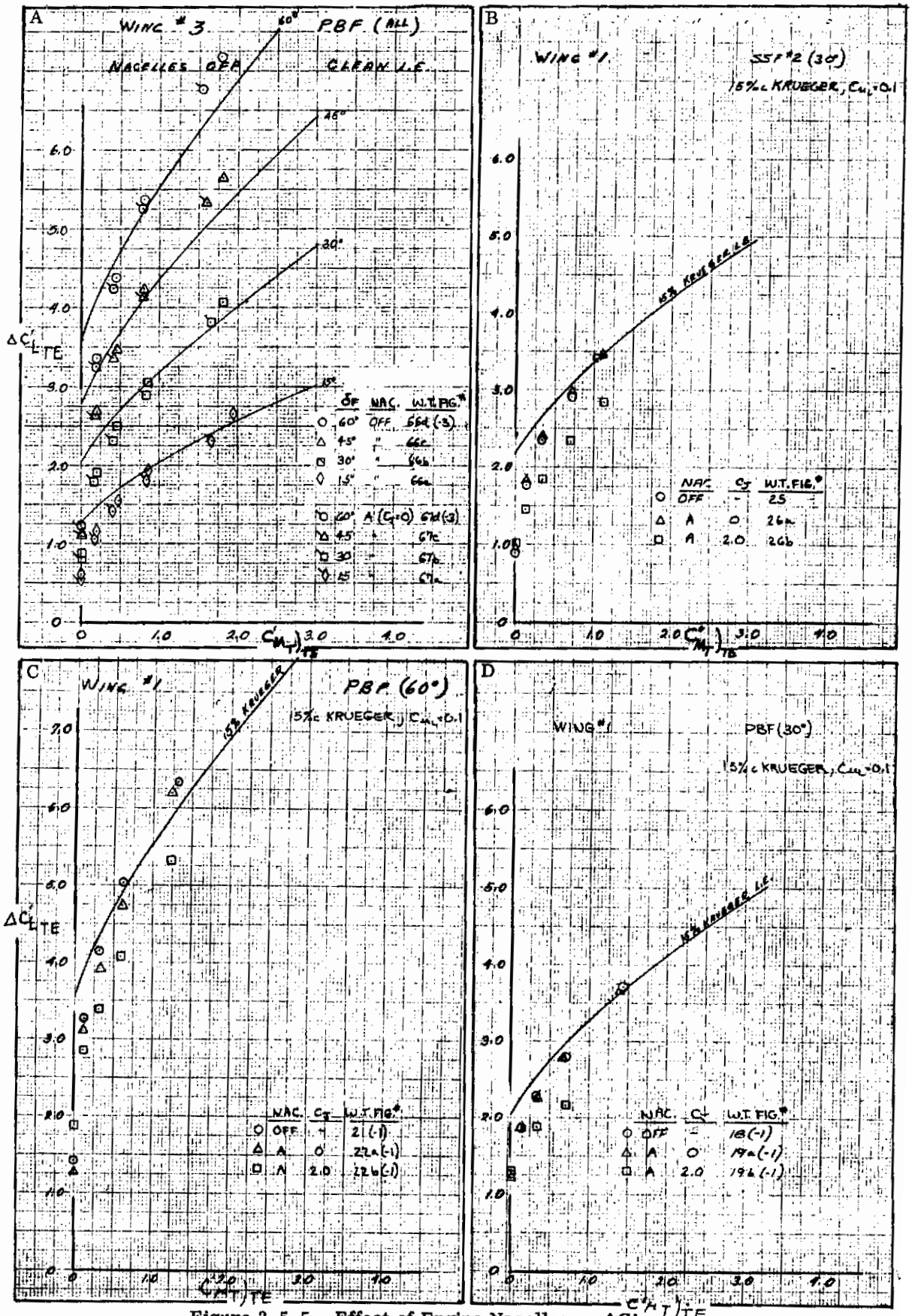

Figure 3.5-5. Effect of Engine Nacelles on $\Delta C'_{L_{TE}}$

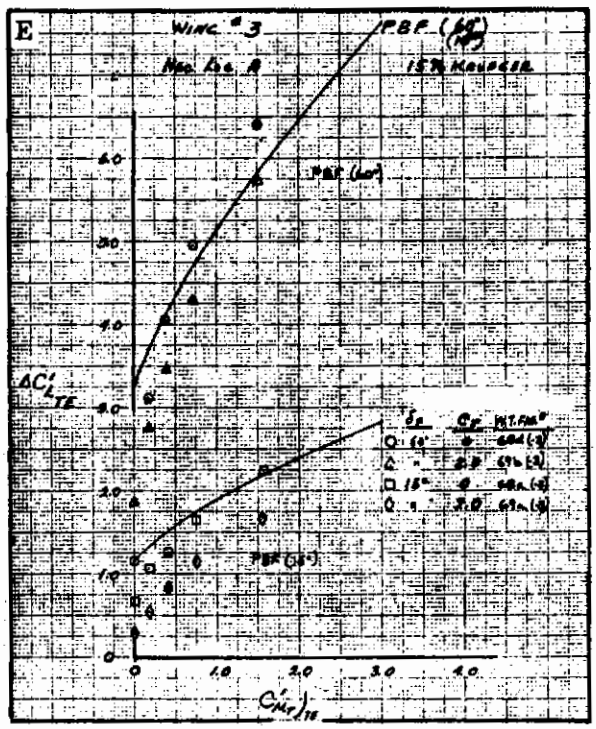

Figure 3.5-5. Effect of Engine Nacelles on $\Delta C'_{L_{TE}}$, Cont

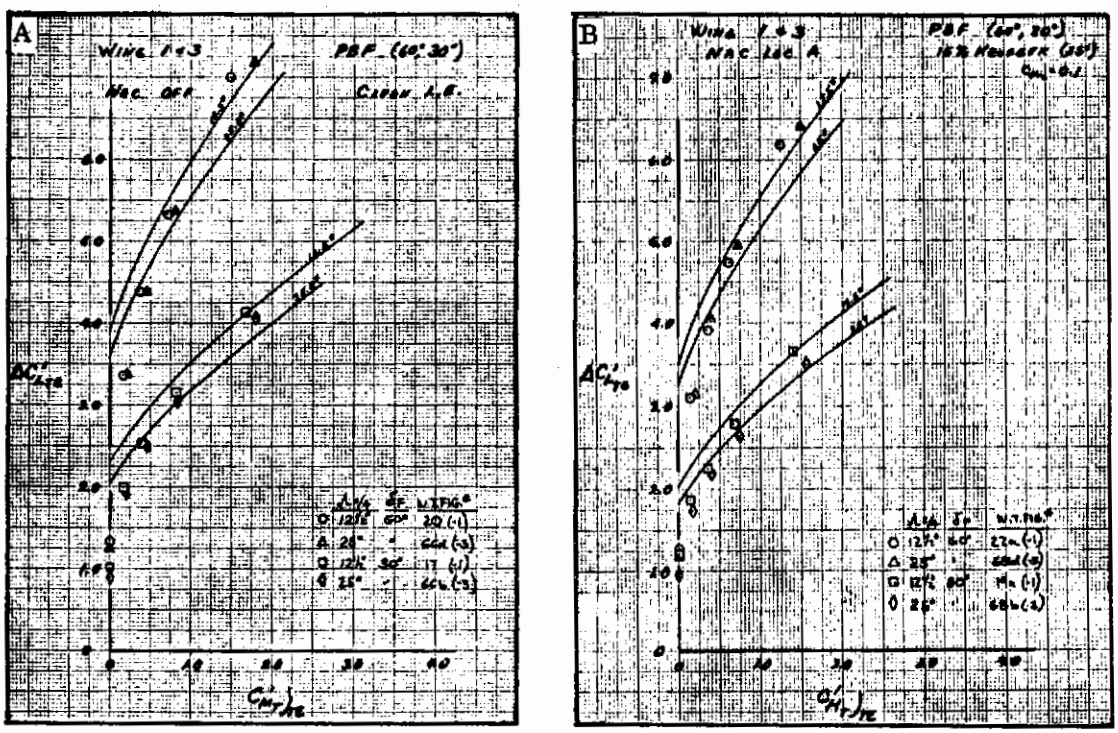

Figure 3.5-6. Effect of Wing Sweep on $\Delta C'_{L_{TE}}$

3.6 MF/VT TRAILING EDGE FLAP LIFT INCREMENT AT α = 0 DEGREES

Trailing edge flap lift effectiveness for a MF/VT system not only includes the increment in lift at zero angle of attack due to deflection of the flap but also the augmentation, both positive and negative, of the circulation lift due to jet engine plus the thrust vector in the lift direction. This total increment, $C'_{L_{TE}}$, based on extended wing area is presented here as a function of momentum coefficient C'_{μ_J}, at the jet engine exit based on the extended wing area.

3.6.1 EFFECT OF THRUST VECTORING ON $\Delta C'_{L_{TE}}$. The effect of deflecting the tail pipe of the jet engines is shown in Figure 3.6-1. Data shown in these figures indicates that at low thrust deflection (-3.5 degrees) and at 60-degree flap deflections, circulation lift is augmented because the flap is immersed in the jet stream like the EBF system. Since the nacelle is located on a long pylon for this data, there is less augmentation than seen in the EBF data of Section 3.4 where the nacelle is located on a short pylon.

Variation of lift effectiveness with thrust deflection is shown in Figure 3.6-1d for the double-slotted flap deflected 30 degrees. This data shows that at the low thrust deflections there is a degradation in lift augmentation due to jet stream interference with the downwash from the wing and flap. At the larger thrust deflections, this loss in augmentation is apparently not recovered, as seen by the difference between the test data and the no augmentation lines shown in the figure.

3.6.2 EFFECT OF TRAILING EDGE FLAP DEFLECTION ON $C'_{L_{TE}}$. The effect of flap deflection on lift increment due to flap and power is shown in Figure 3.6-2. Flap deflection affects lift increment only when the flap is immersed in the jet stream. This effect is seen in Figure 3.6-2a, where the jet stream is not deflected down; at high flap deflections, however, the test data shows greater effectiveness than predicted (assuming no lift augmentation). This is essentially the EBF system. Test data for configurations with thrust deflections equal to 37 and 69 degrees, shown in Figures 3.6-2b and 3.6-2c, indicate that much less augmentation is present and the data is easily represented by the no augmentation theoretical lines shown in the figure.

3.6.3 EFFECT OF ENGINE NACELLE ON $\Delta C'_{L_{TE}}$. The effect of chordwise location of the engine nacelle is shown in Figure 3.6-3 for different flap deflections. Test data indicates a slightly greater lift for the configurations with the engines located aft (nacelle location F). The magnitude of this lift increment increases with increasing momentum coefficient and with increasing thrust deflection. This same effect on lift was seen in NASA test data shown in Reference 3-9.

3.6.4 EFFECT OF WING SWEEP ON $\Delta C'_{L_{TE}}$. The only effect of wing sweep on lift effectiveness of the MF/VT system is the basic reduction in effectiveness that is

present power-off. The effect is shown in Figure 3.6-4 for three thrust deflections. Normal EBF augmentation effects are seen for thrust deflections of near zero (Figure 3.6-4a), but quickly disappear with thrust deflection as seen in (Figures 3.6-4b and 3.6-4c).

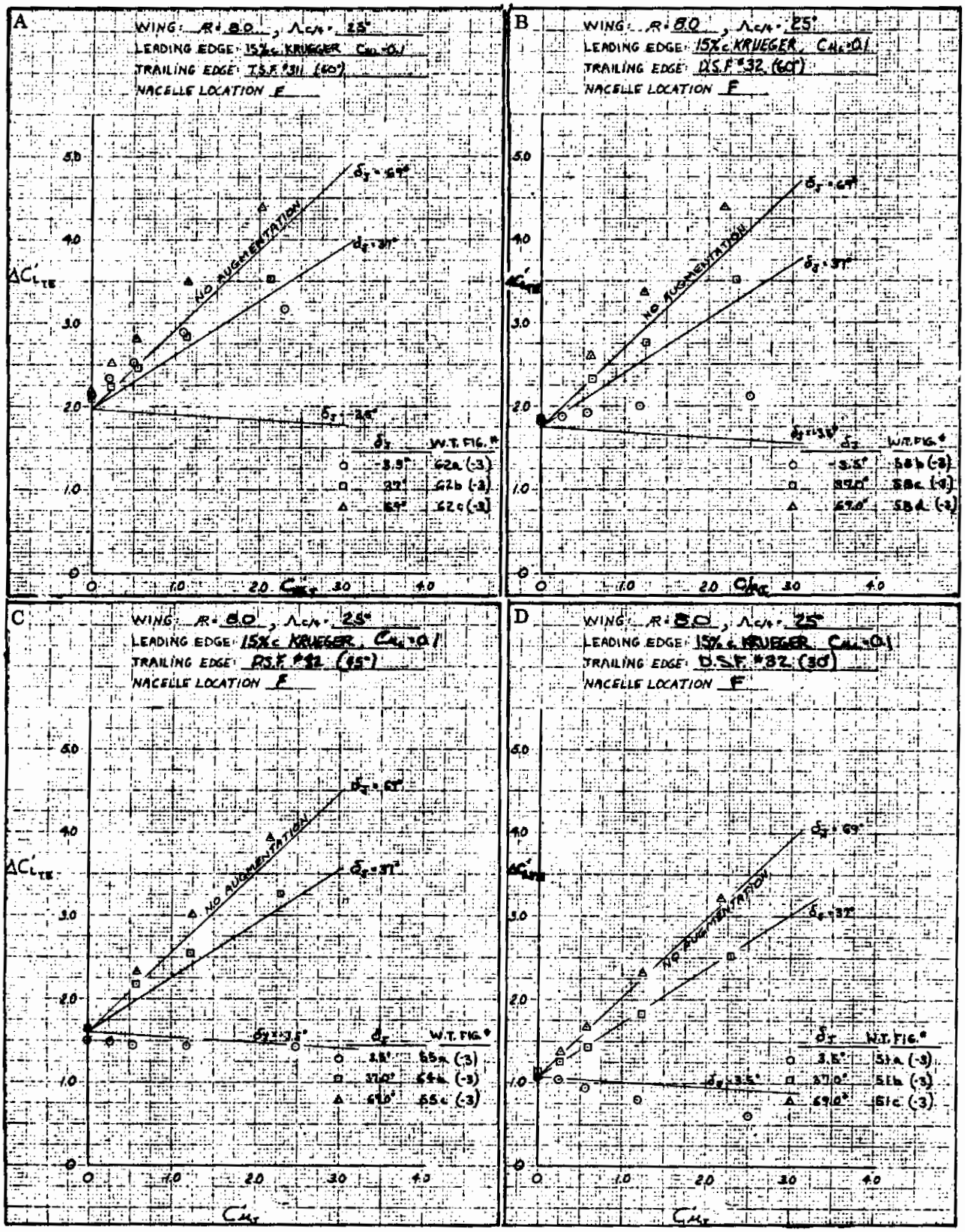

Figure 3.6-1. Effect of Vectored Thrust on $\Delta C'_{L_{TE}}$

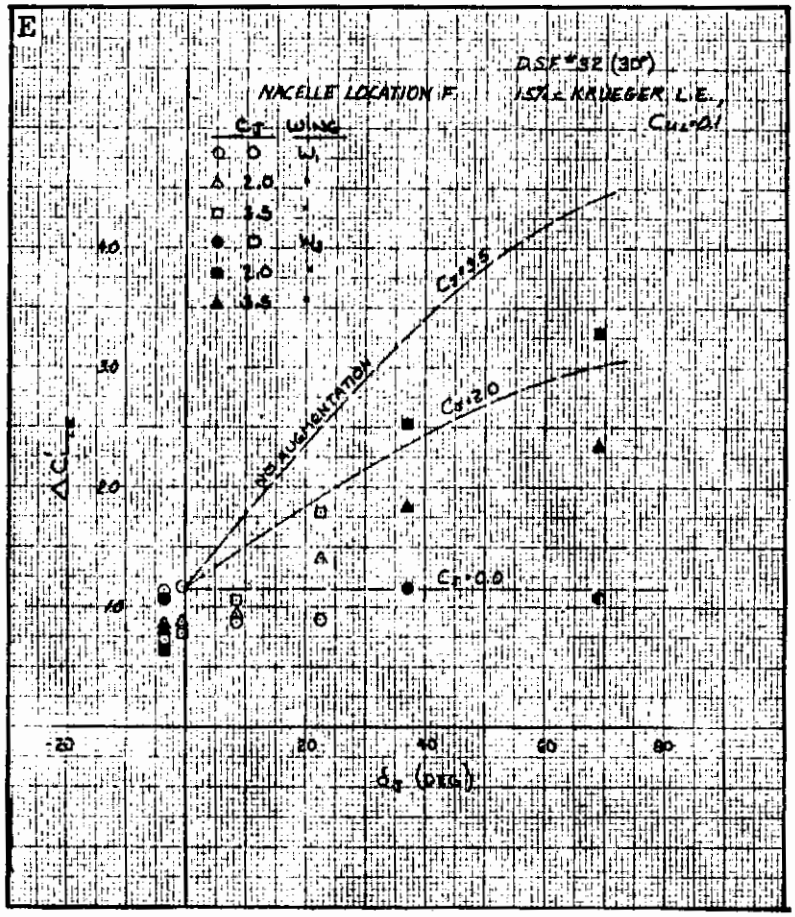

Figure 3.6-1. Effect of Vectored Thrust on $\Delta C'_{L_{TE}}$, Cont

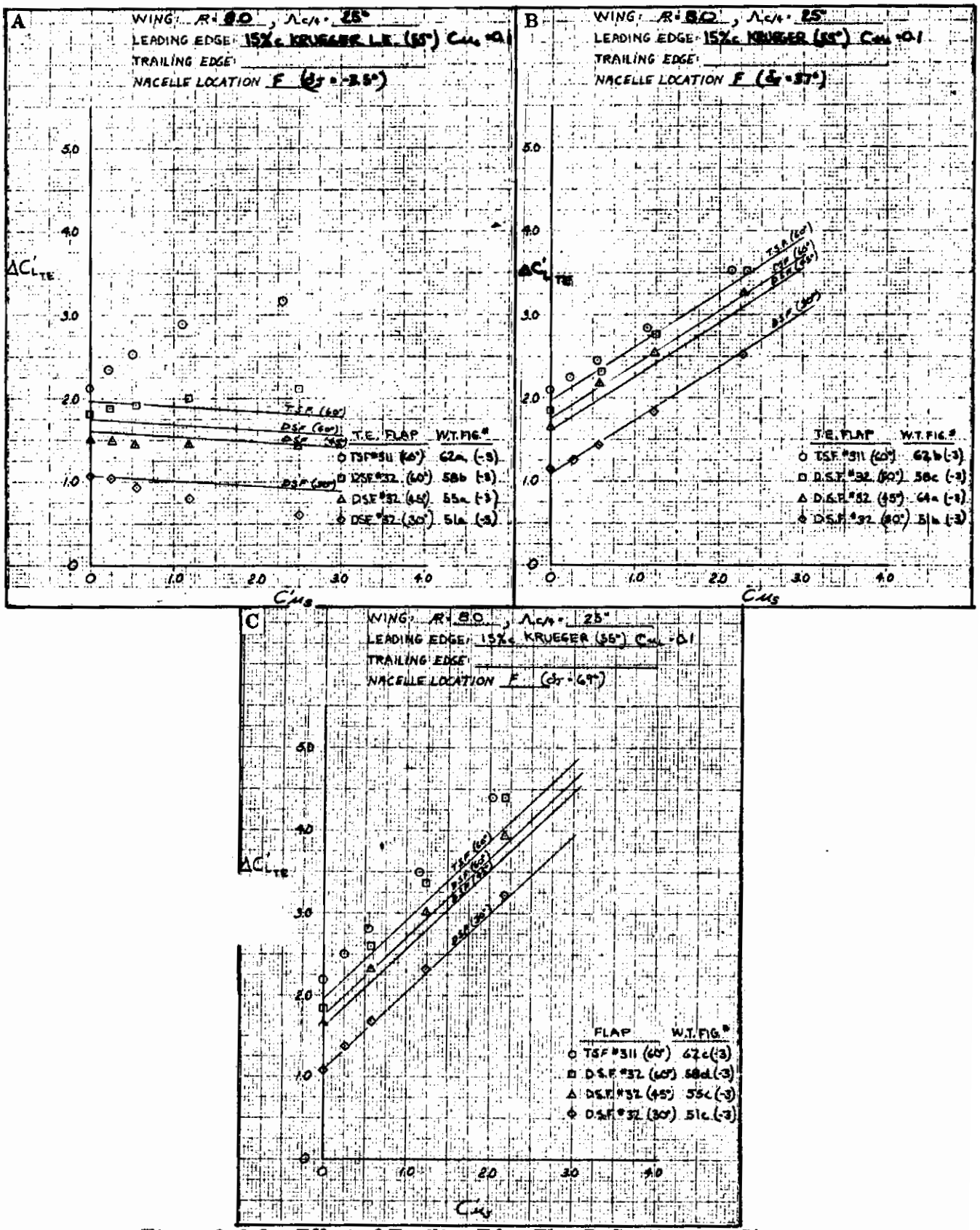

Figure 3.6-2. Effect of Trailing Edge Flap Deflection on $\Delta C'_{L_{TE}}$

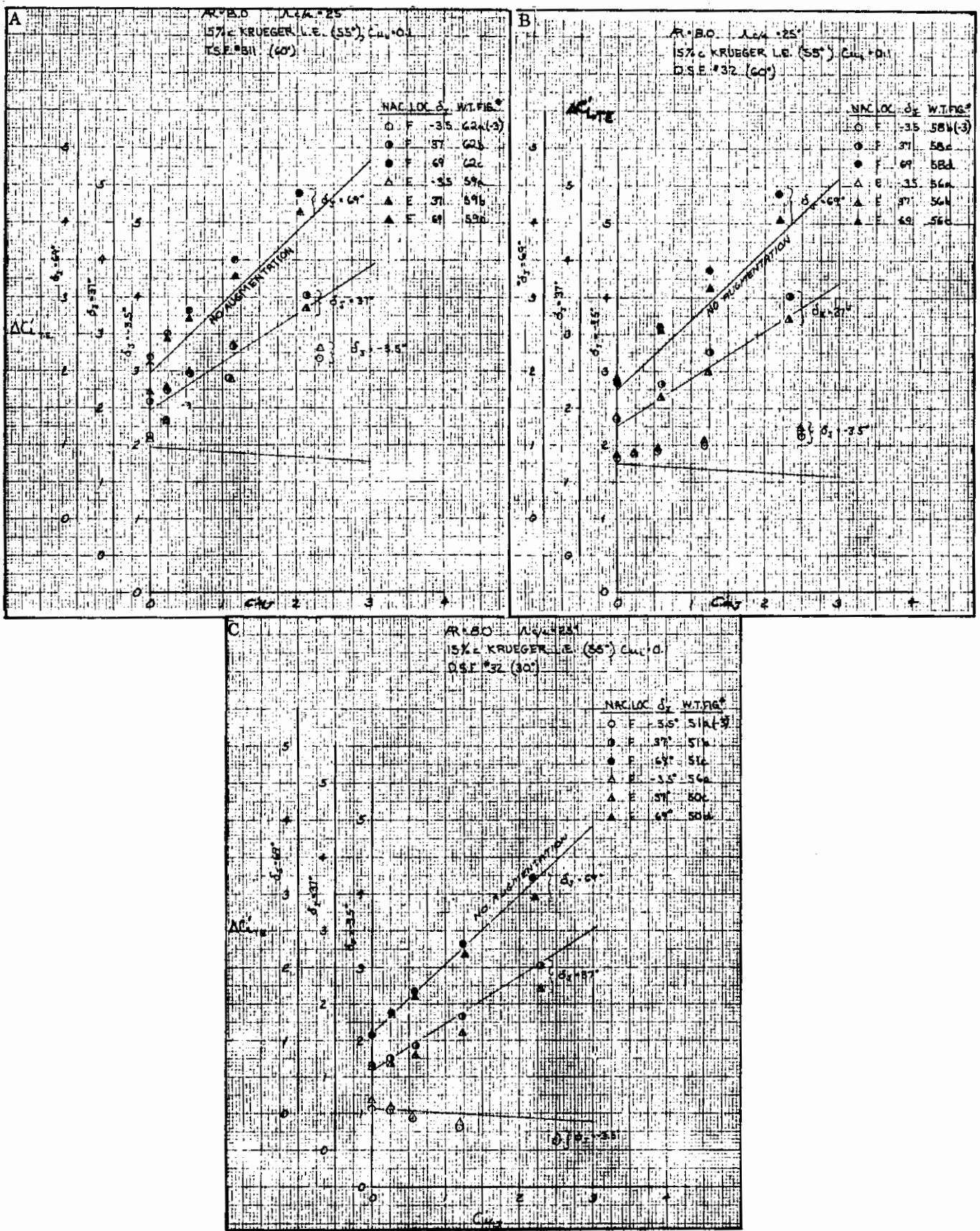

Figure 3.6-3. Effect of Nacelle Chordwise Location on $\Delta C'_{L_{TE}}$

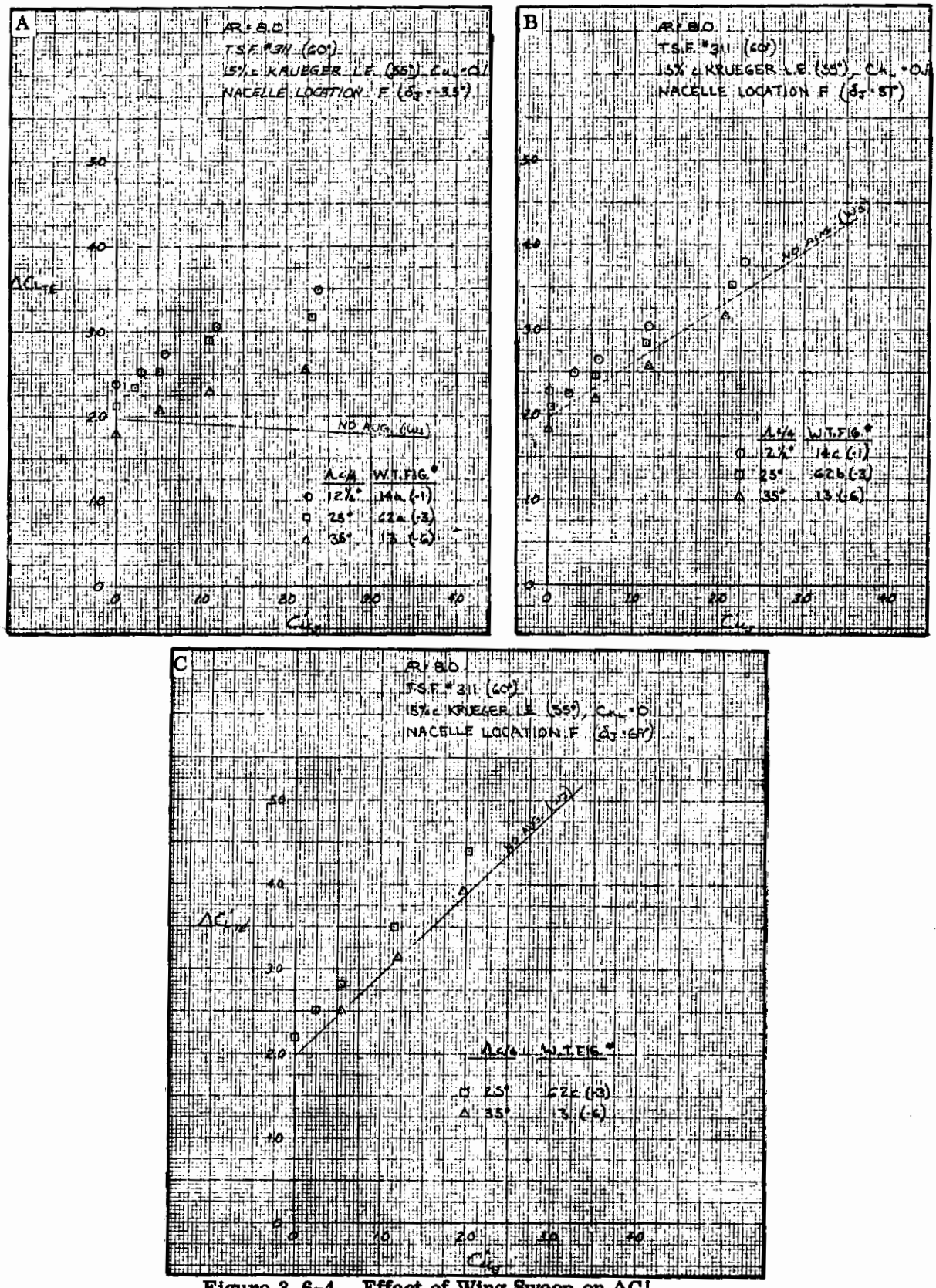

Figure 3.6-4. Effect of Wing Sweep on $\Delta C'_{L_{TE}}$

3.7 POWER OFF INCREMENTAL MAXIMUM LIFT

The increment in maximum lift due to leading and trailing edge flap deflections is discussed here for several configurations of high-lift devices. The term "power-off" used in this discussion refers to blowing on the trailing edge flap system only. Leading edge blowing was tested with a Krueger flap and only at low blowing rates as a BLC device.

3.7.1 EFFECT OF LEADING EDGE CONFIGURATION ON $\Delta C'_{L_{max}})_{LE}$. The increment in maximum lift due to a leading edge device is presented in Figure 3.7-1 as a function of the Krueger flap leading edge blowing momentum coefficient, $C'_{\mu_{LE}}$. As shown, the increment in maximum lift due to leading edge blowing is less for a configuration with flaps extended than for the clean trailing edge configuration. This does not indicate that the leading-edge Krueger maximum lift increment is a function of trailing edge flap configuration, since the overall airfoil chord is extended with trailing edge flap extension, the effective Krueger chord is reduced and therefore the effectiveness of the Krueger is reduced. Since the trend of maximum lift increment with leading edge momentum coefficient is the same with or without trailing edge flaps, the maximum lift increment analyzed here will be for the clean trailing edge configuration.

Blowing from the airfoil leading edge with a Krueger flap increases the maximum lift increment to values greater than the two-dimensional estimate using thin airfoil theory. This indicates that leading-edge blowing acts like trailing-edge blowing in that full potential flow is obtained with proper amounts of blowing but, unlike trailing-edge blowing, supercirculation is not developed at momentum coefficients greater than 0.075. Trailing-edge blowing, as indicated by the triangles in Figure 3.7-1, further increases the supercirculation effect. The momentum coefficient indicated in this figure as Nominal has been used throughout these tests.

The effect of leading-edge flap deflection is shown in Figure 3.7-2. Effective deflection, δ_{eff}, is defined as:

$$\delta_{eff} = C'_{L_{max}})_{LE} \Big/ c'_{\ell_{\delta_{max}}} \cdot K_{b_{LE}} \cdot C_{L\alpha} \Big/ c_{\ell_\alpha}$$

where $c'_{\ell_{\delta_{max}}}$ is the leading-edge flap effectiveness parameter developed from thin airfoil theory in Reference 3-7. Effective deflection has been chosen as the correlation parameter because of the difficulty in defining leading-edge flap deflection.

Test data is shown in Figure 3.7-2 for both a leading edge slat and an unblown and blown Krueger type flap. The blown Krueger type flap test data has been corrected for blowing by removing the effect of blowing shown in Figure 3.7-1. Correlation with thin airfoil theory shown in Reference 3-7 is obtained only when an 0.75 factor is applied to the theoretical results.

3.7.2 EFFECT OF TRAILING EDGE FLAPS ON $\Delta C'_{L_{max}})_{TE}$. The unblown increment is shown in Figure 3.7-3. Data is shown for plain, single-, double-, and triple-slotted flaps on the aspect ratio 8, 25-degree swept wing, and for triple- and double-slotted flaps on the other planforms tested. The data indicated no unusual trends and compared favorably with thin airfoil theory included in the figures. Correlation for the single and plain flaps, Figure 3.7-3c, are not good at deflection angles greater than these where flap stall may occur. The flaps show much better effectiveness when they are blown as shown in the following sections.

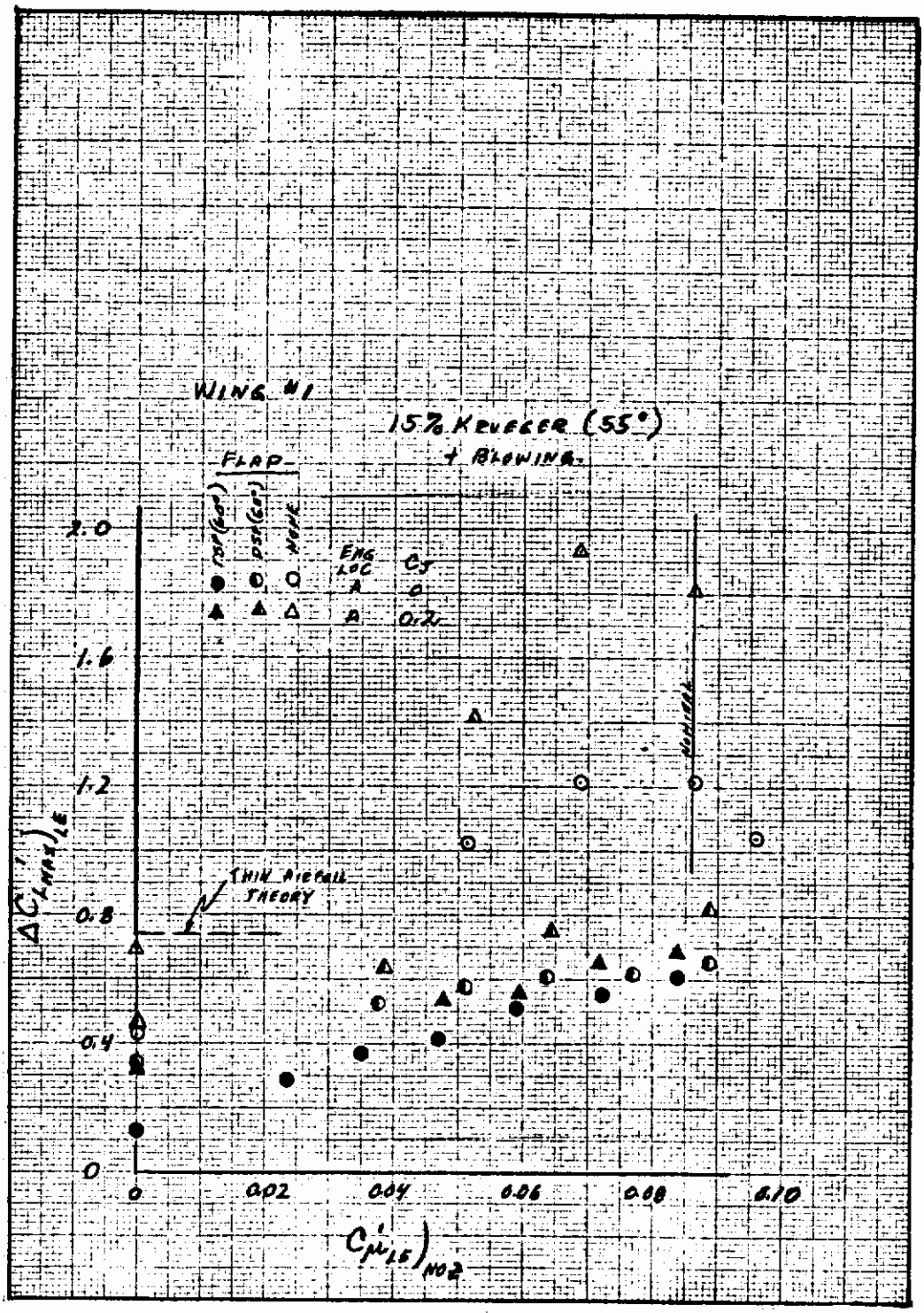

Figure 3.7-1. Effect of Leading Edge Blowing on $\Delta C'_{L_{max}})_{LE}$

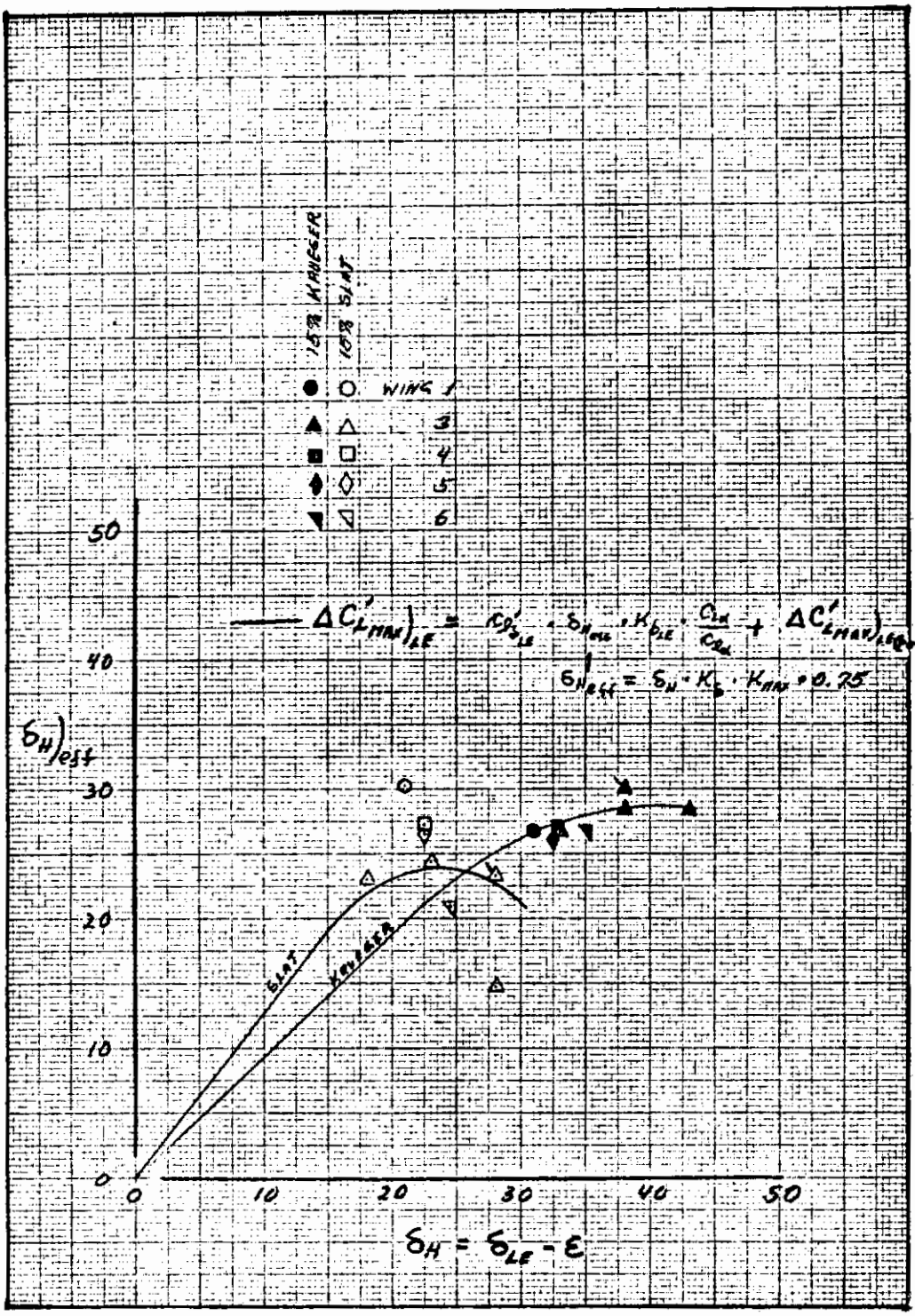

Figure 3.7-2. Effect of Leading Edge Flap Deflection on Leading Edge Effectiveness

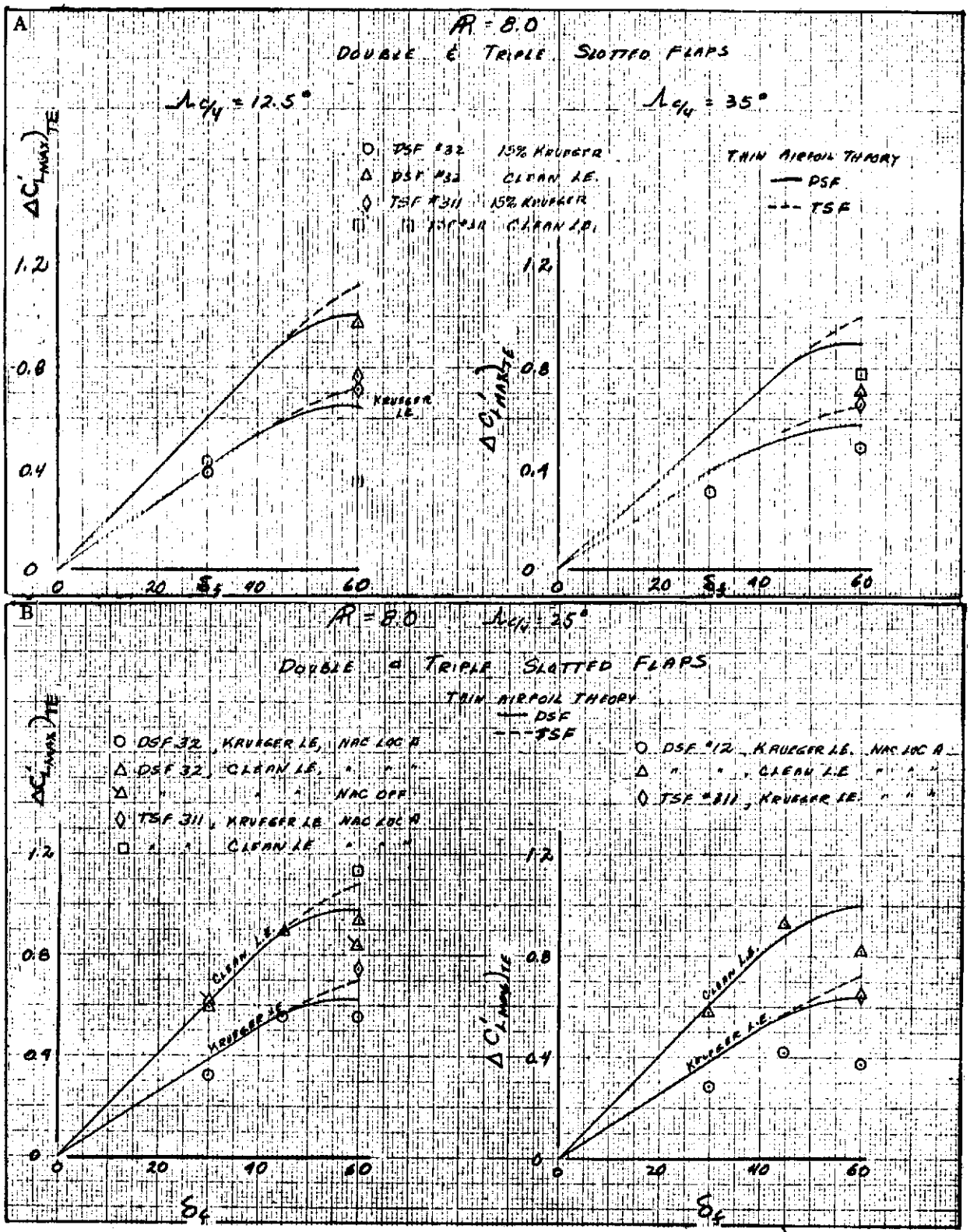

Figure 3.7-3. Effect of Trailing Edge Flap Deflection on $\Delta C'_{L_{max}})_{TE}$

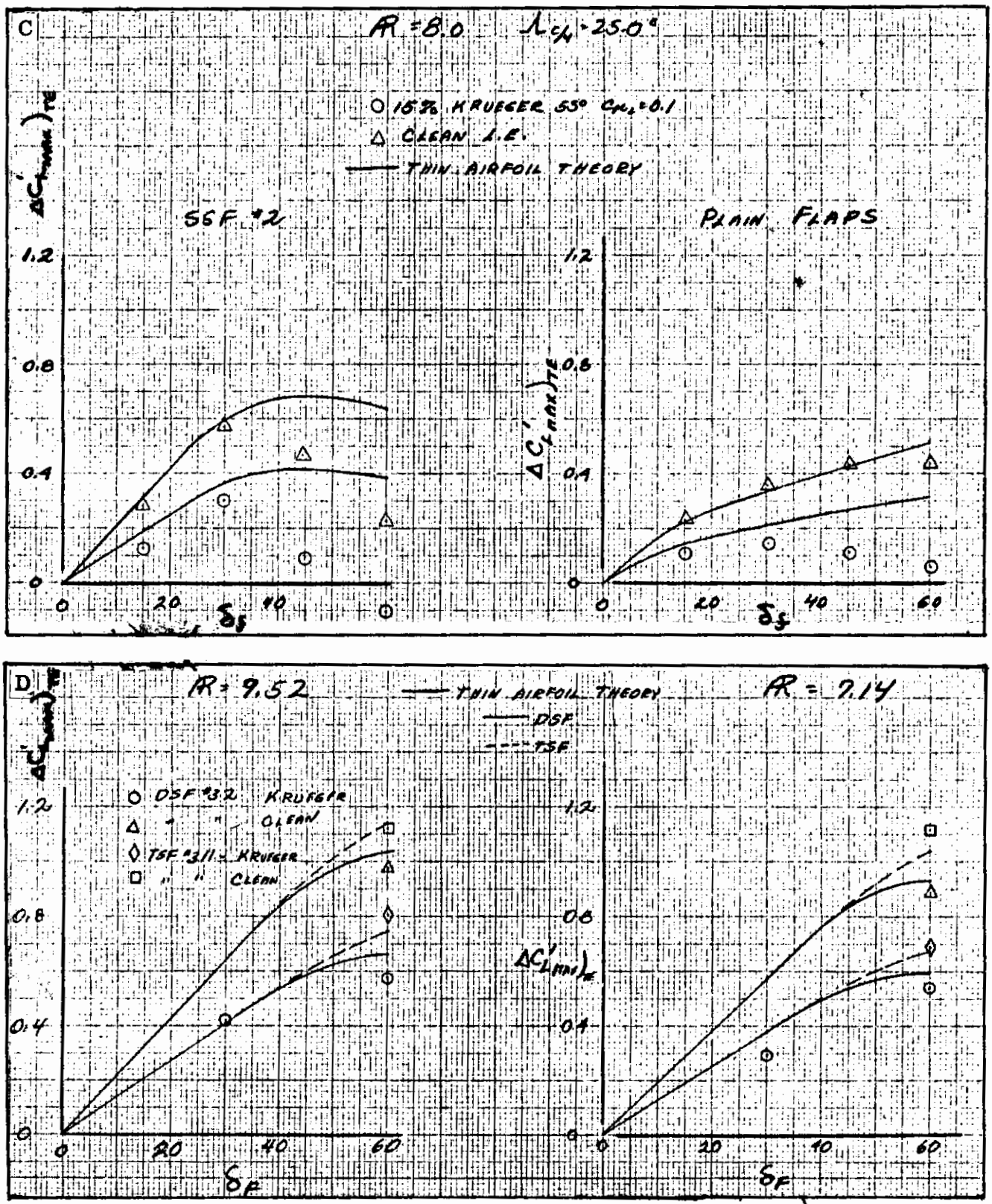

Figure 3.7-3. Effect of Trailing Edge Flap Deflection on $\Delta C'_{L_{max}})_{TE}$, Cont

3.8 EBF INCREMENTAL MAXIMUM LIFT DUE TO POWER

The maximum lift coefficient increment due the application of power from either the jet engines or from a jet nozzle in the wing has been used as the analysis parameter best suited to show the effects of an EBF or IBF system on the maximum lift coefficient of the aircraft. This increment, $\Delta C'_{L_{max}})_{C\mu_J}$, is obtained from test data by taking the difference between the power-on and power-off maximum lift coefficients. Based on the extended wing area and corrected for partial flap span effects, this increment is presented in the following analysis as a function of the momentum coefficient, $C_{\mu_J})_{TE}$, estimated at the flap trailing edge and based on the extended wing span.

A theoretical reference line developed from references 3-5 and 3-6 is shown in the following figures. This estimate uses thin airfoil theory with jet flap theory, which (for maximum lift coefficient) assumes that the airfoil/flap configuration will stall at the same leading edge critical pressure coefficient as the basic airfoil. The theory shows that the increment in maximum lift coefficient due to blowing is three-quarters of the increment in lift coefficient that would be expected at the stall angle of attack. For simplicity, the theoretical reference lines in the figures have not used this three-quarter factor. The test data shows a greater increment than estimated by the theory, indicating that the airfoil/flap stalls at a leading edge critical pressure coefficient greater than the pressure coefficient at which the basic airfoil stalls.

A comparison of this maximum lift increment for EBF and IBF systems with the same triple-slotted flap system is shown in Figure 3.8-1. As discussed in previous sections, this data shows that the two powered lift systems will give about the same maximum lift characteristic.

3.8.1 EFFECT OF FLAP CONFIGURATION ON $\Delta C'_{L_{max}})_{C\mu_J}$. The maximum lift increment for several flap configurations and wing planforms is shown in Figure 3.8-2. The test data does not match the theory, but when the flaps are fully immersed in the jet stream (i.e., TSF 311 and DSF 32 (60 degrees)) the test data is about 1.4 times the theory lines for all momentum coefficients. For flaps that are not fully immersed in the jet stream (i.e., DSF 32 (30 degrees) and SSF 2 all deflections, Figure 3.8-2f), the test data is more like the theoretical data. This indicates that the maximum lift increment due to power is also a function of the amount of flap that is immersed in the jet stream, similar to that discussed in Paragraph 3.4 on flap lift effectiveness at zero angle of attack. This characteristic is seen throughout the following analysis.

The effect of flap chord is shown in Figure 3.8-3. The data shown for both triple- and double-slotted flaps deflected at 60 and 30 degrees indicates only a slight decrease in effectiveness because of reduced chord on the maximum lift increment due to power. This is similar to the effect of chord on flap lift effectiveness discussed in Paragraph 3.4.

The maximum lift increment data for 100 and 81.6 percent span flaps shown in Figure 3.8-4 for several flap configurations indicates that the partial span correction factor used with flap lift effectiveness (see Paragraph 3.4.1) should not be applied to this increment. This is because the cut-off portion of the flap is outside the span affected by the jet stream and apparently $C_{L_{max}}$ is not influenced by power as was $\Delta C'_{L_{TE}}$.

3.8.2 EFFECT OF LEADING EDGE CONFIGURATION ON $\Delta C'_{L_{max}})_{C_{\mu_J}}$. The effects of a leading-edge Krueger flap with and without BLC type blowing on the Krueger is shown in Figure 3.8-5. The leading-edge Krueger, with or without blowing, improves maximum lift effectiveness of engine blowing on the trailing edge flaps, although the simple theory would indicate negligible effect. As expected, blowing from the leading edge has no effect on the trailing edge flap maximum lift increment.

Figures 3.8-6 and 3.8-7 show the effect of varying the leading-edge Krueger and slat deflection and chord, indicating no significant effect on the maximum lift increment due to trailing-edge blowing.

3.8.3 EFFECT OF NACELLE LOCATION ON $\Delta C'_{L_{max}})_{C_{\mu_J}}$. Spanwise location of the engine nacelles has a small effect on the maximum lift increment due to power. As shown in Figure 3.8-8, maximum lift increment is the greatest with the nacelles located inboard on the wing (location B). Even the siamese nacelles (location C) shows a greater lift increment than the basic position (location A). The inboard section of the wing is more heavily loaded with the nacelles located inboard, thereby reducing the load on the tip and allowing the total wing to reach a larger maximum lift coefficient before stall.

Locating the nacelles in the forward rather than the aft position results in a slightly larger increment in maximum lift due to power (Figure 3.8-9). Since this trend was not found on the flap lift effectiveness of $\alpha = 0$ degrees (Paragraph 3.4.3), this effect is attributed to improvements in spanwise loading rather than increased augmentation.

Figure 3.8-9 shows the effect of tilting the jet exhaust upward. This tilt appears to have the same effect on maximum lift as found on the flap lift effectiveness at $\alpha = 0$ degrees (i.e., tilt of the jet stream effectively increases the amount of flap that is immersed in the jet stream and therefore improves augmentation). This is especially true for flap configurations with low deflected flaps, Figure 3.8-9g. The effect of jet tilt is shown even more dramatically in Figure 3.8-10a, where lift augmentation is improved by deflecting the jet up into the flap from a lowered nacelle position where flap immersion (and therefore augmentation) has been reduced.

Locating the nacelle on long pylons beneath the wing (Figure 3.8-10) results in a large effect on the flap maximum lift increment due to power. As discussed in Paragraph 3.4.3 on flap lift effectiveness at zero angle of attack, maximum lift increment is also a function of the amount of flap immersed in the jet stream.

3.8.4 EFFECT OF WING ASPECT RATIO ON $\Delta C'_{L_{max}})_{C_{\mu_J}}$. The effect of wing aspect ratio on the maximum lift increment due to power is presented in Figure 3.8-11. The test data indicates that the increment in maximum lift reduces as the aspect ratio is increased from 7.1 to 9.5. This trend is repeated to various degrees for all flap and leading-edge configurations shown. Since the percent of wing area affected by the jet exhaust is reduced as the aspect ratio is increased, data for different aspect ratios may not be affected if the lift coefficient increment were based only on the wing area affected by the jet exhaust. Since data was not obtained on the amount of spreading of jet exhaust, this assumption cannot be checked.

3.8.5 EFFECT OF WING SWEEP ON $\Delta C'_{L_{max}})_{C_{\mu_J}}$. The effect of wing sweep on the maximum lift increment due to power is presented in Figure 3.8-12. Generally, there appears to be some modest increment to $C'_{L_{max}}$ associated with the wing sweep, but the trend seems to be inconsistent with the predicted trend.

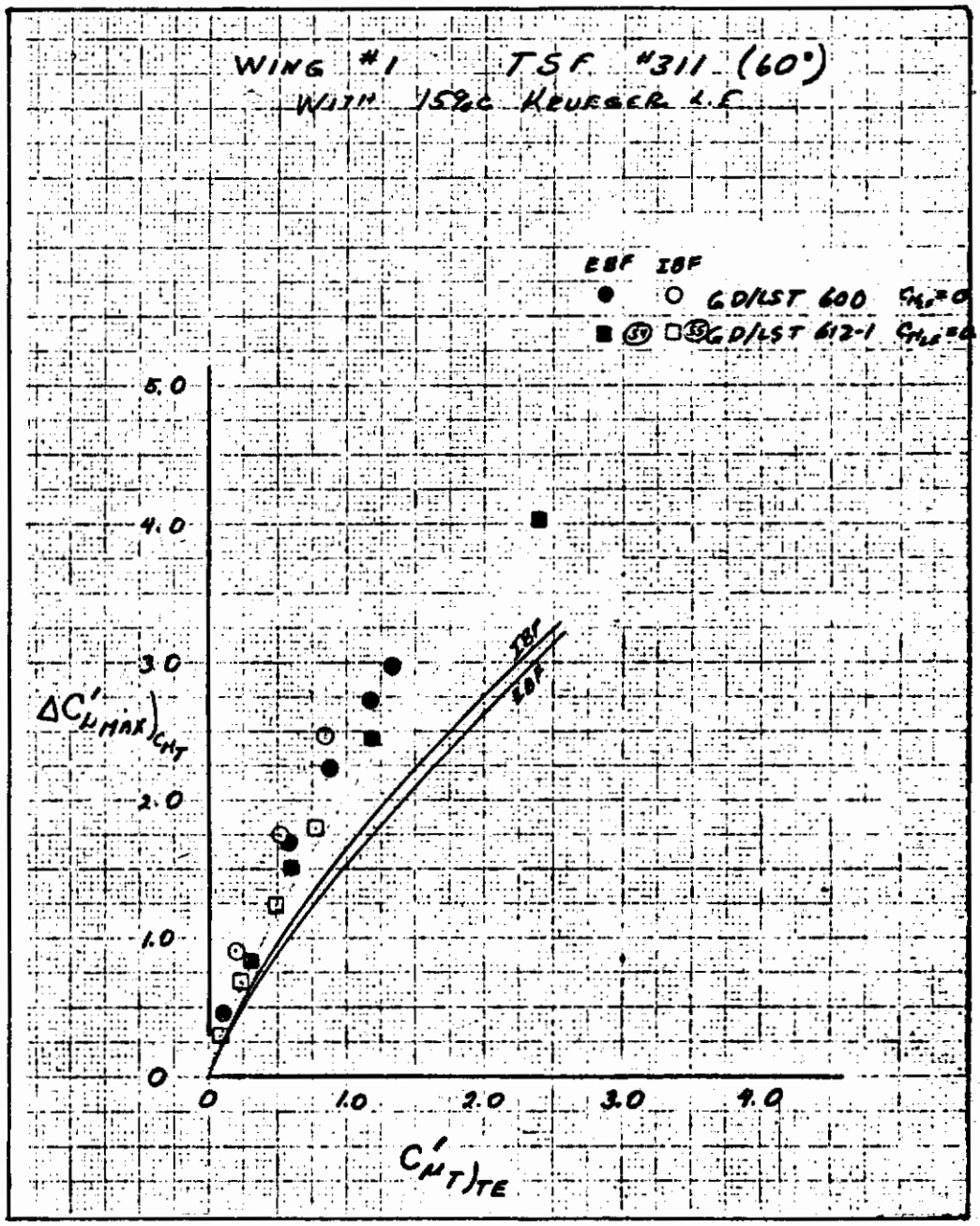

Figure 3.8-1. EBF/IBF Analogy

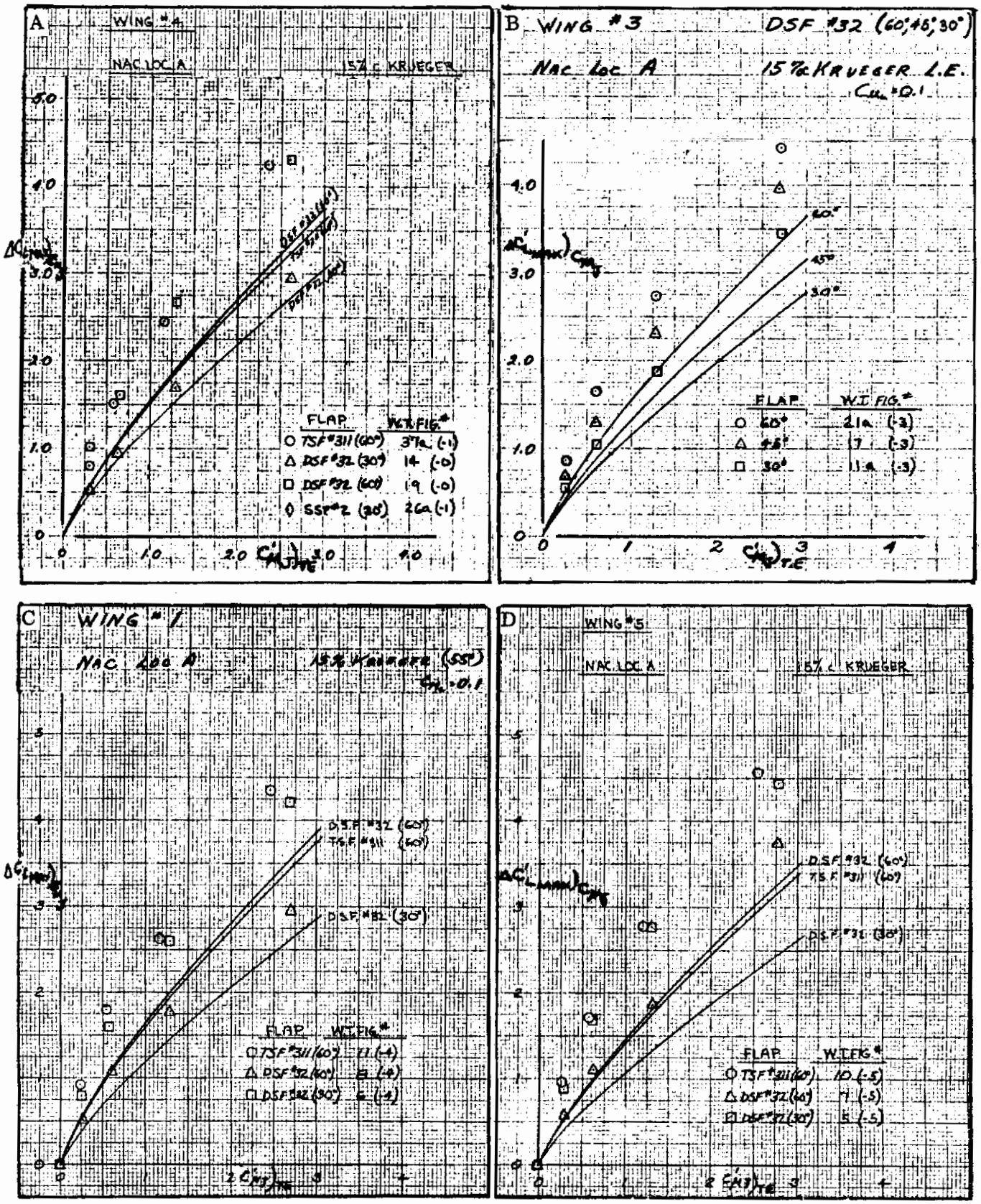

Figure 3.8-2. Effect of Trailing Edge Flap Configuration on $\Delta C'_{L_{max}})_{C_{\mu_J}}$

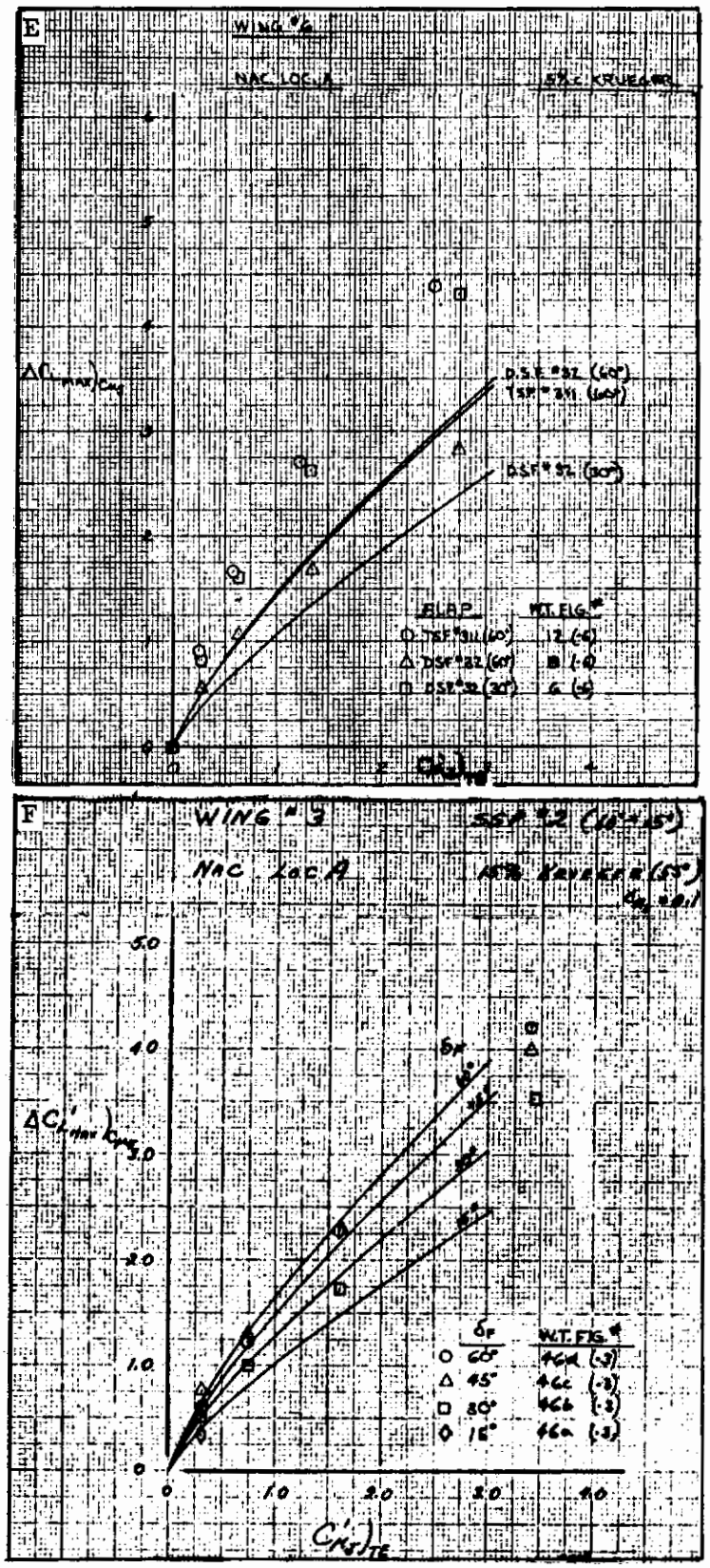

Figure 3.8-2. Effect of Trailing Edge Flap Configuration on $\Delta C'_{L_{max}})_{C_{\mu_J}}$, Cont

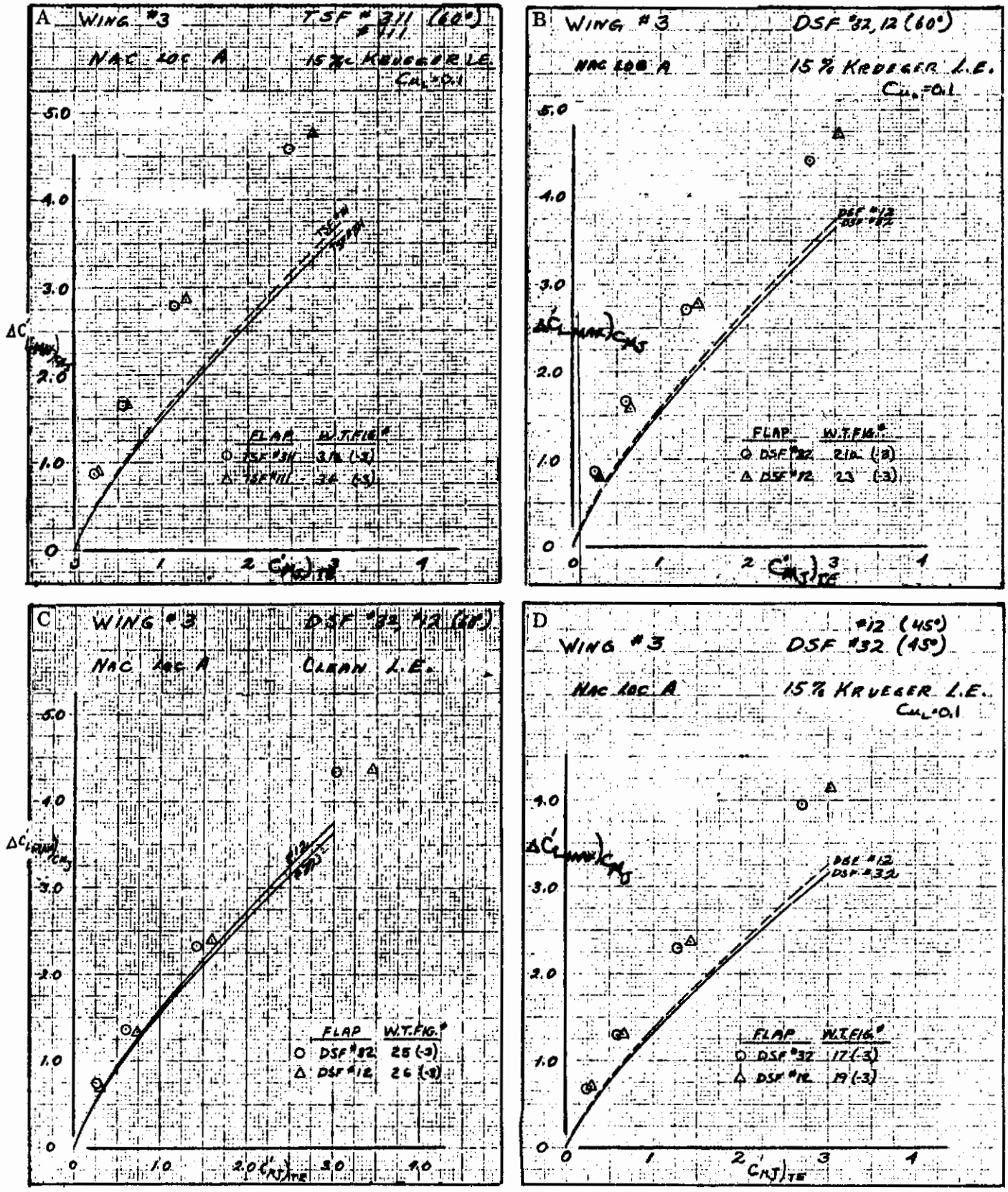

Figure 3.8-3. Effect of Trailing Edge Flap Chord on $\Delta C'_{L_{max}})_{C_{\mu_J}}$

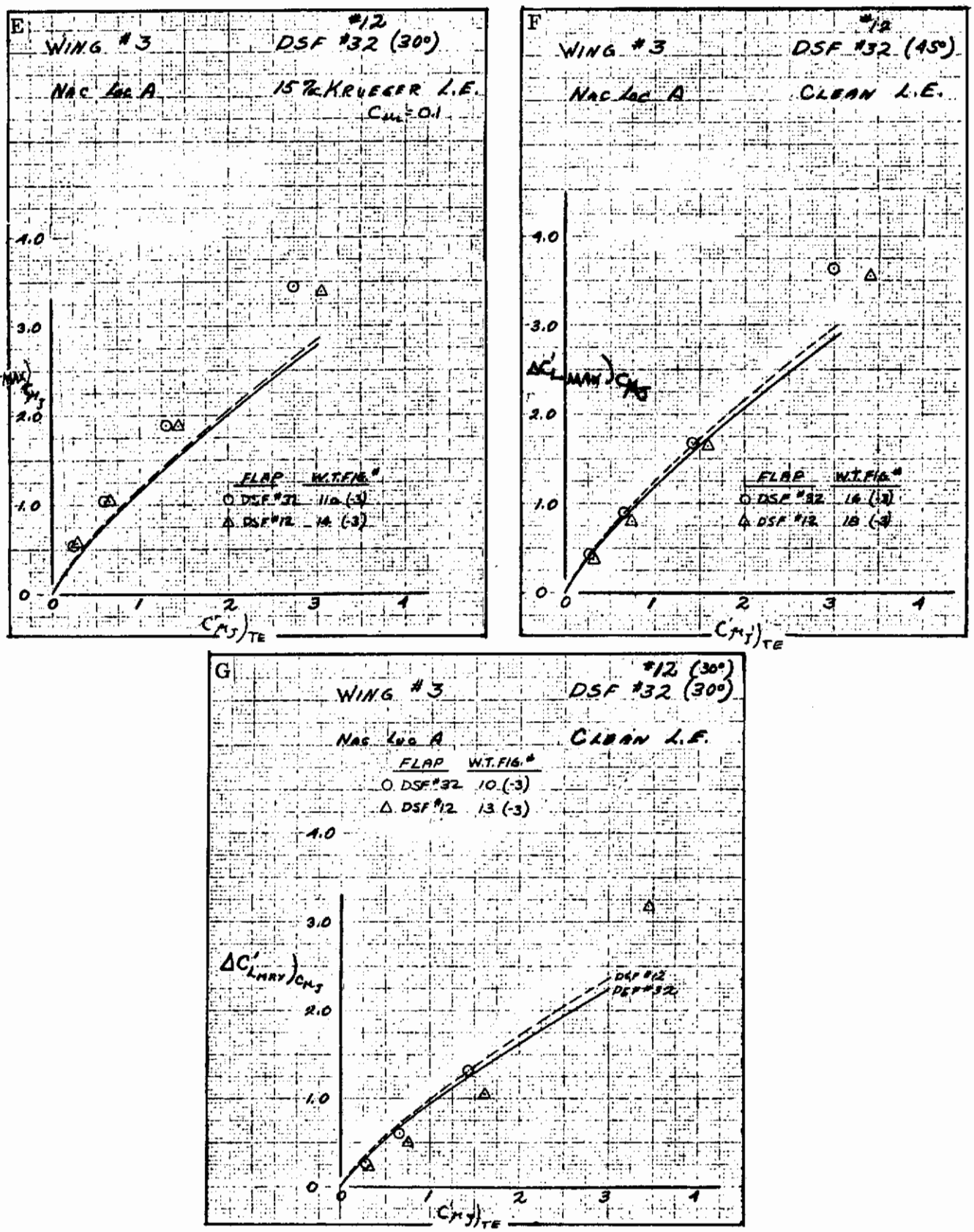

Figure 3.8-3. Effect of Trailing Edge Flap Chord on $\Delta C'_{L_{max}})_{C_{\mu J}}$, Cont

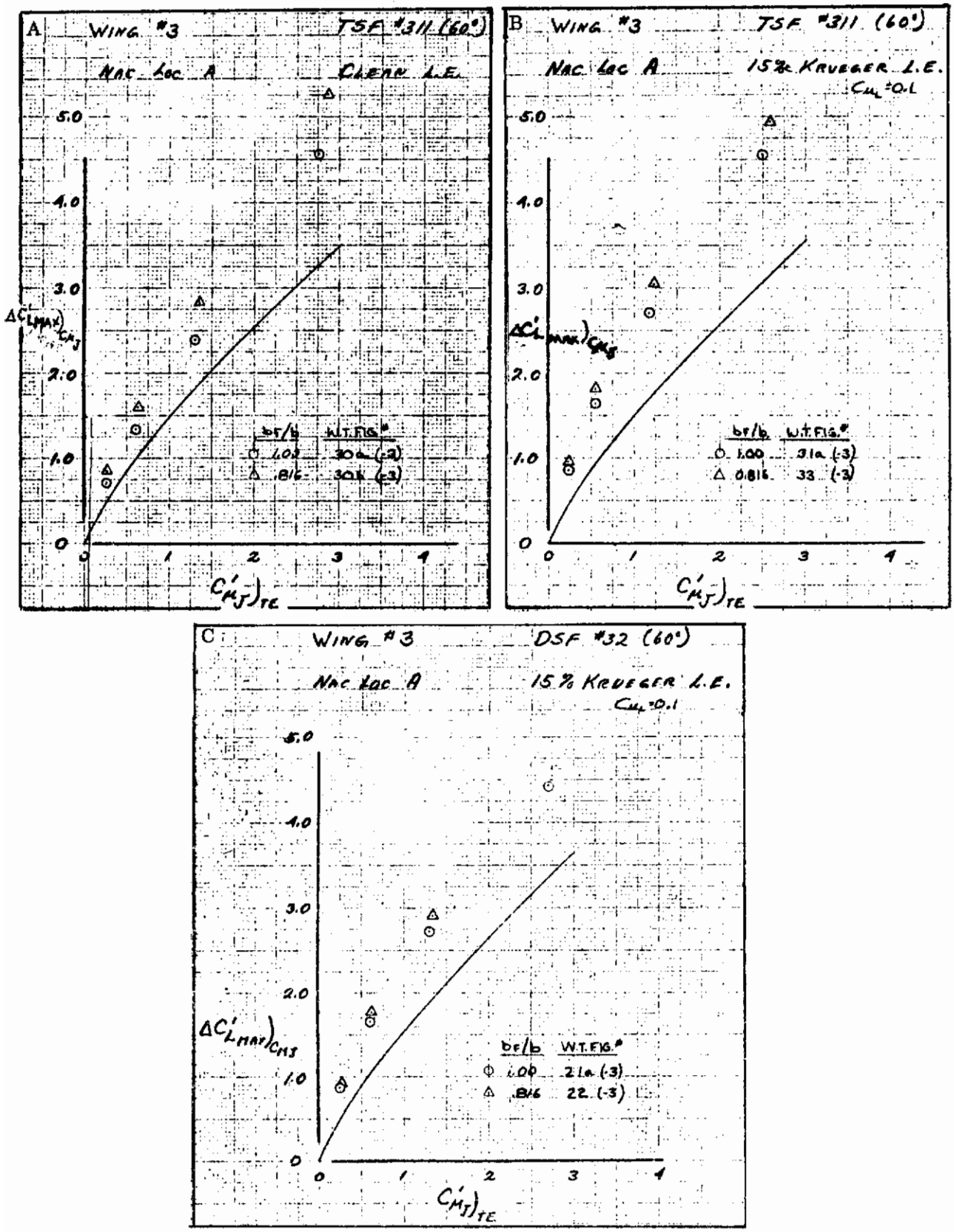

Figure 3.8-4. Effect of Partial Span Trailing Edge Flap on $\Delta C'_{L_{max}})_{C_{\mu_J}}$

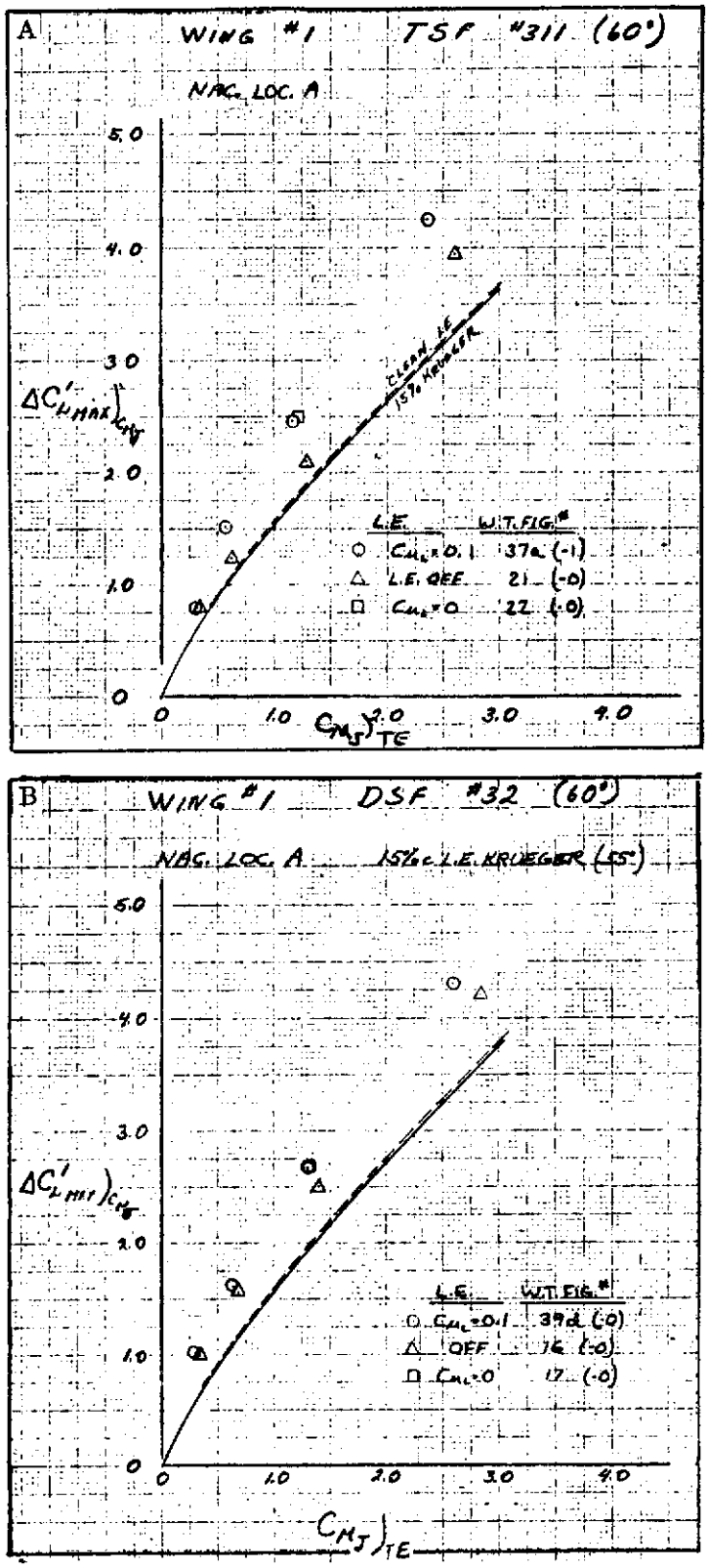

Figure 3.8-5. Effect of Leading Edge Blowing on $\Delta C'_{L_{max}})_{C_{\mu_J}}$

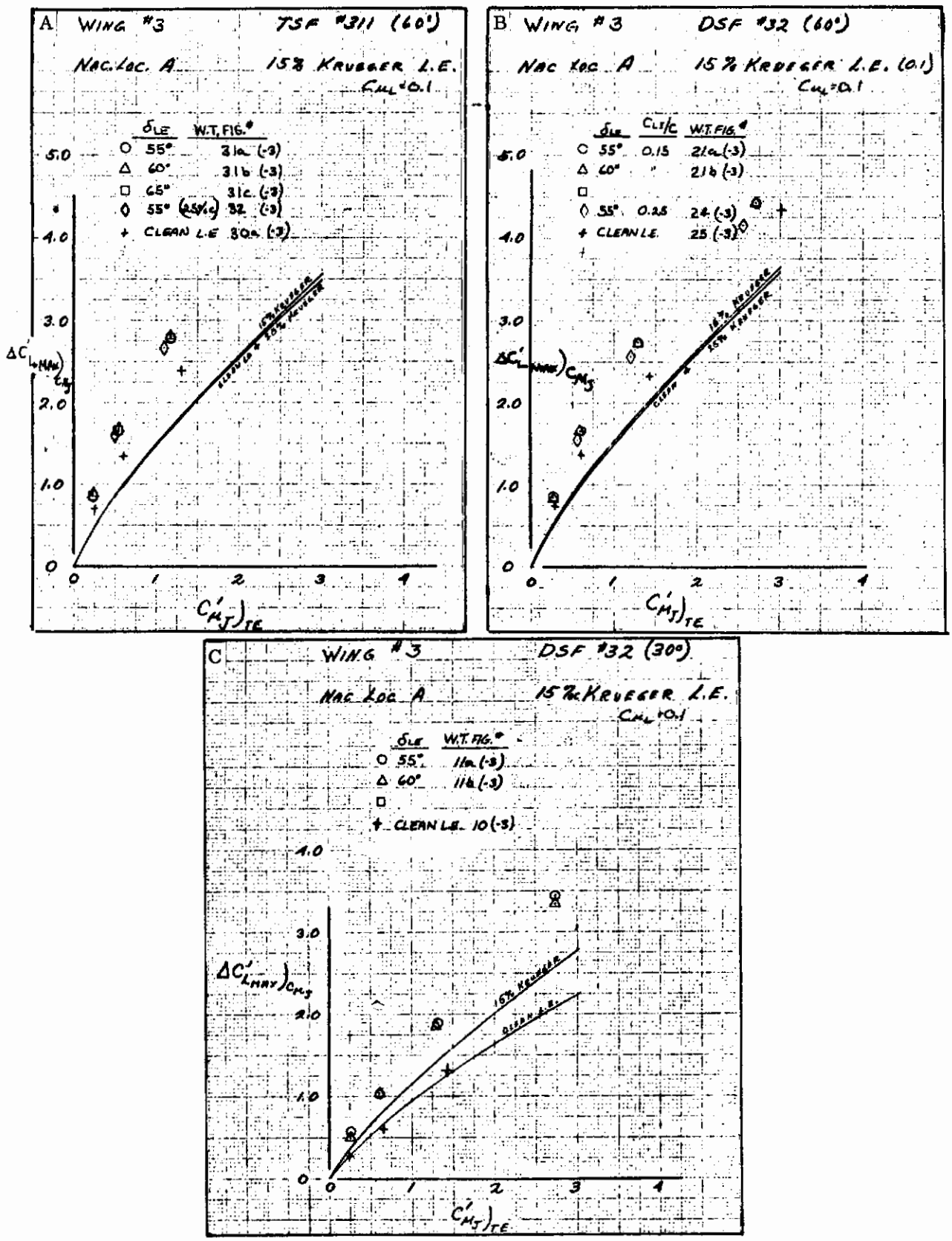

Figure 3.8-6. Effect of Leading Edge Flap Deflection and Chord on $\Delta C'_{L_{max}})_{C_{\mu_J}}$

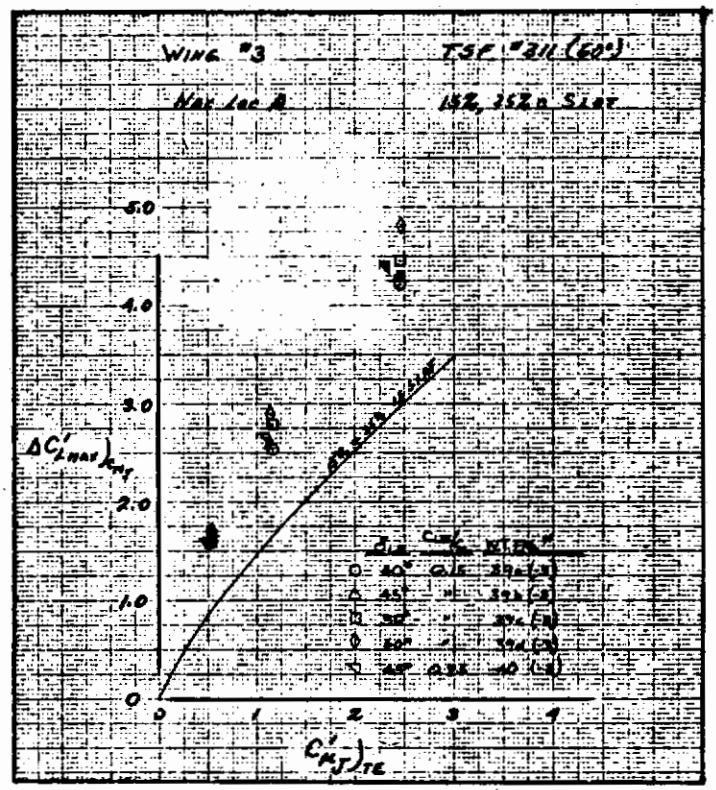

Figure 3.8-7. Effect of Leading Edge Slat Deflection and Chord on $\Delta C'_{L_{max}})_{C_{\mu_J}}$

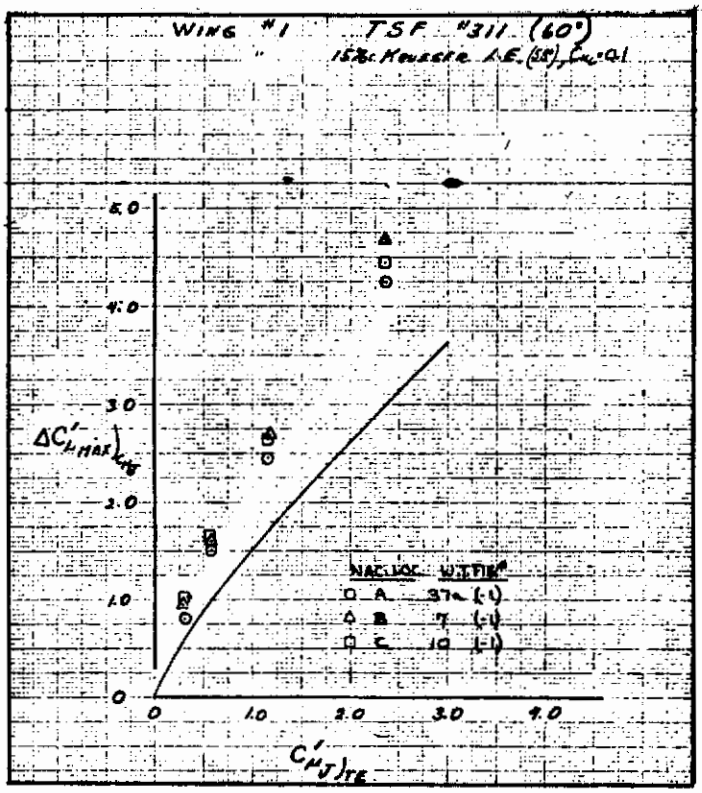

Figure 3.8-8. Effect of Spanwise Nacelle Location on $\Delta C'_{L_{max}})_{C_{\mu_J}}$

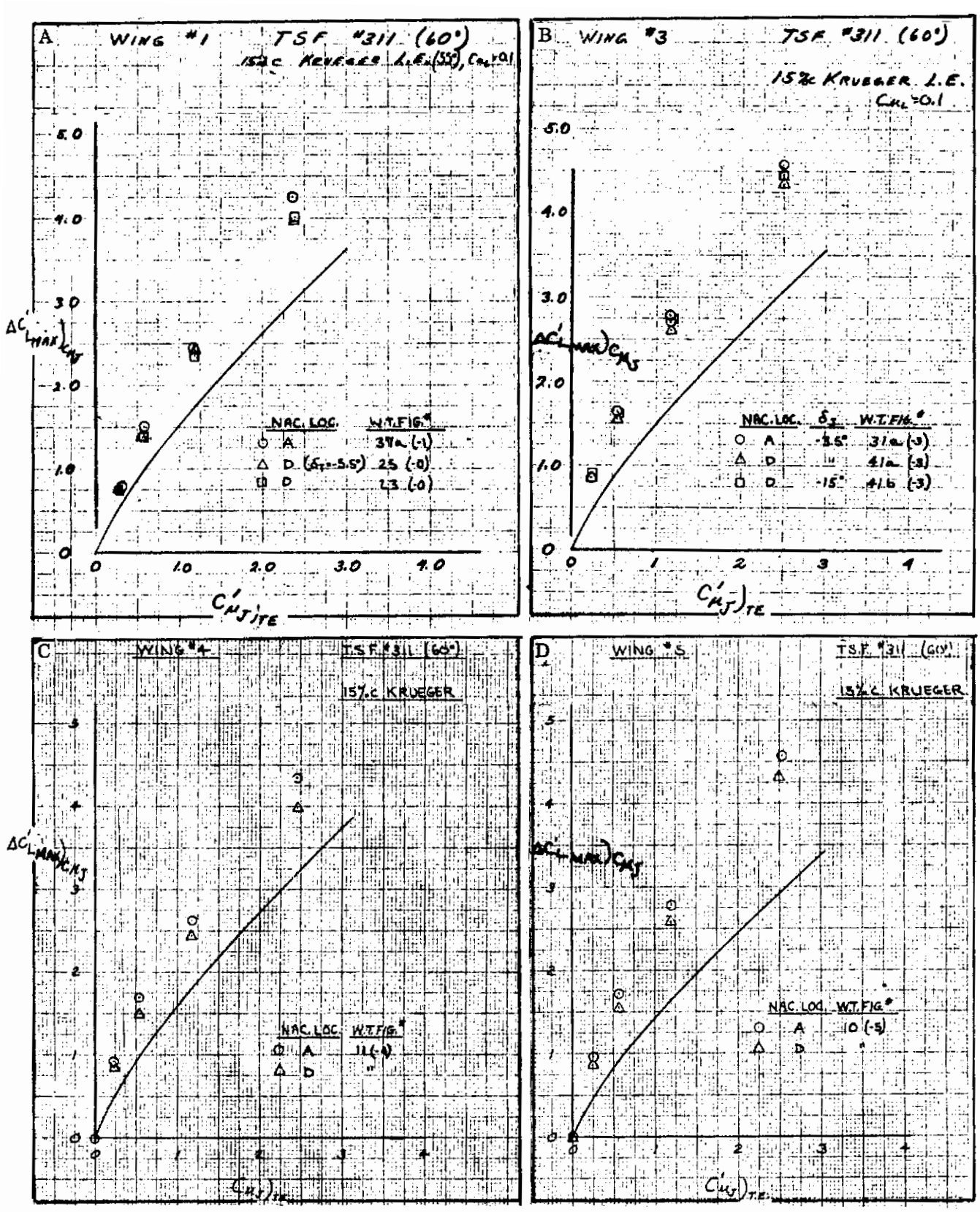

Figure 3.8-9. Effect of Chordwise Nacelle Location on $\Delta C'_{L_{max}})_{C_{\mu_J}}$

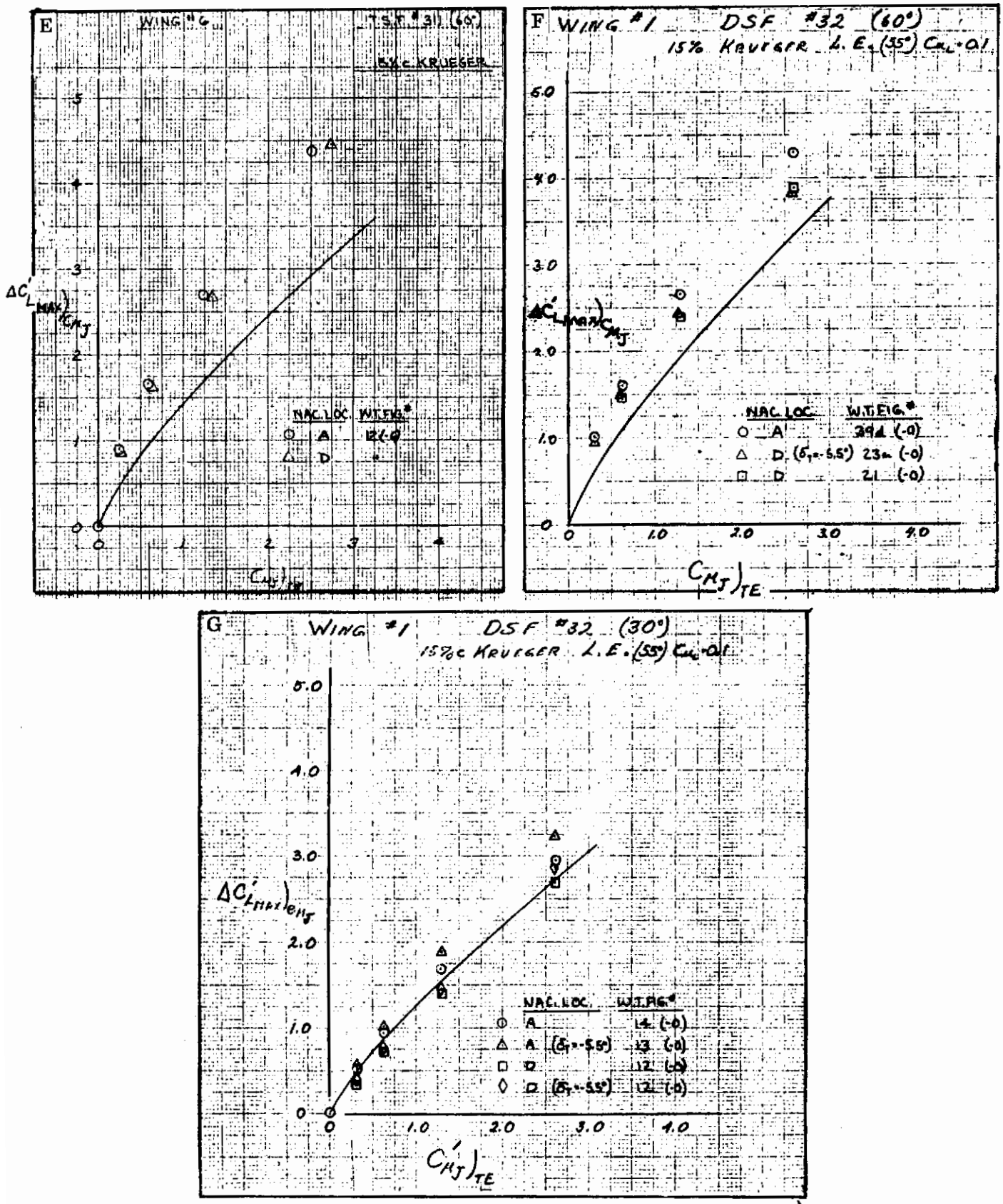

Figure 3.8-9. Effect of Chordwise Nacelle Location on $\Delta C'_{L_{max}})_{C_{\mu_J}}$, Cont

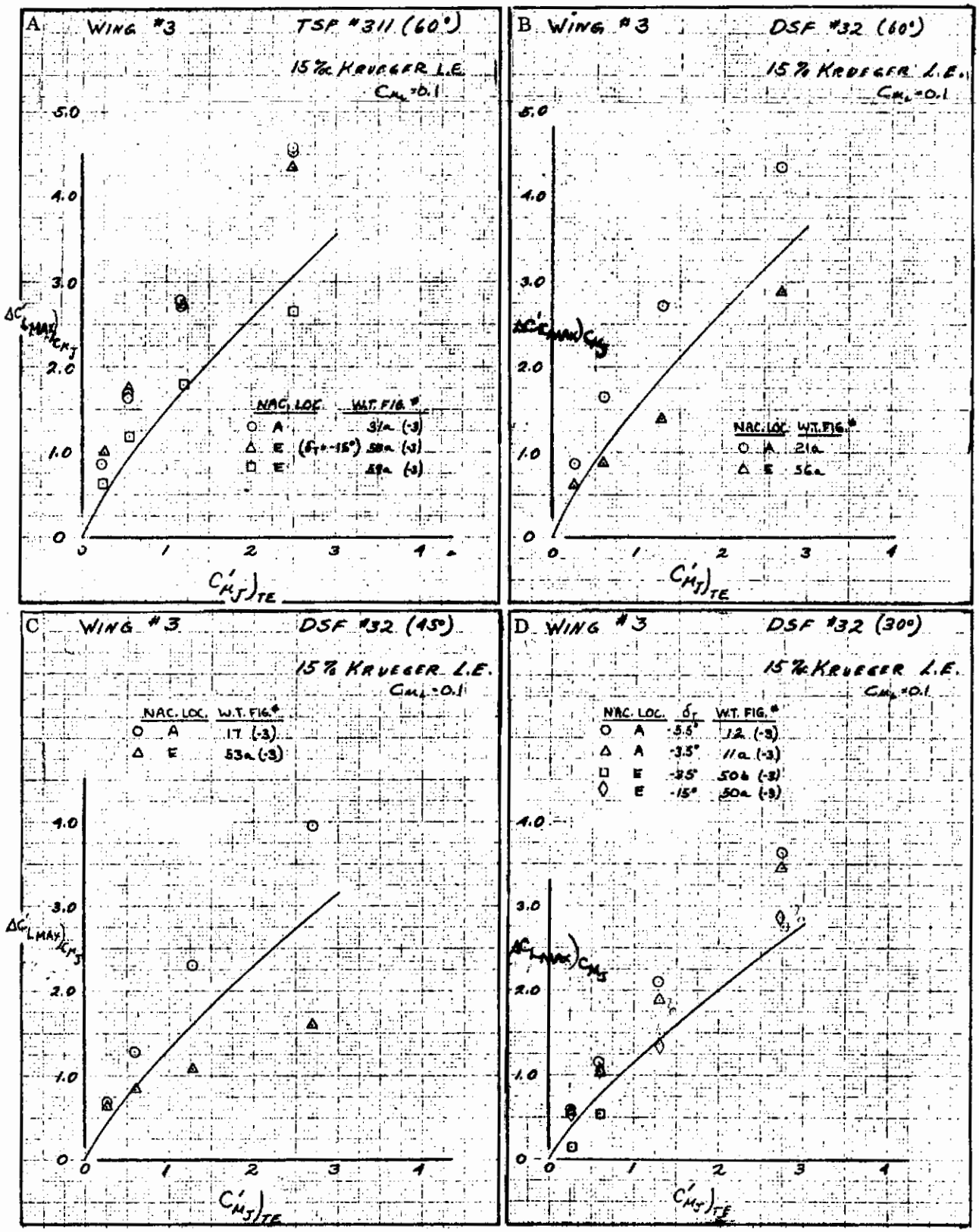

Figure 3.8-10. Effect of Nacelle Height Location on $\Delta C'_{L_{max}})_{C_{\mu_J}}$

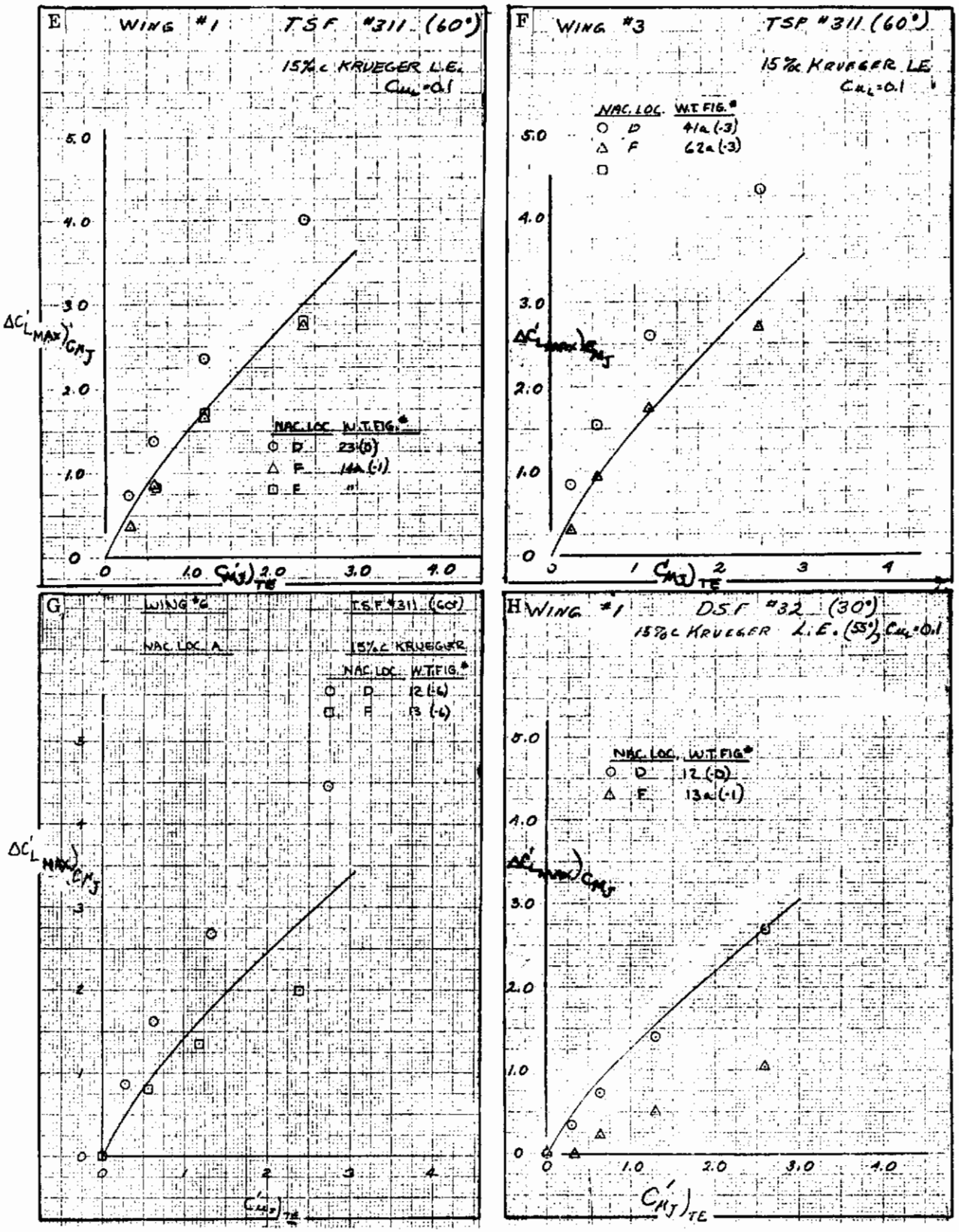

Figure 3.8-10. Effect of Nacelle Height Location on $\Delta C'_{L_{max}})_{C_{\mu_J}}$, Cont

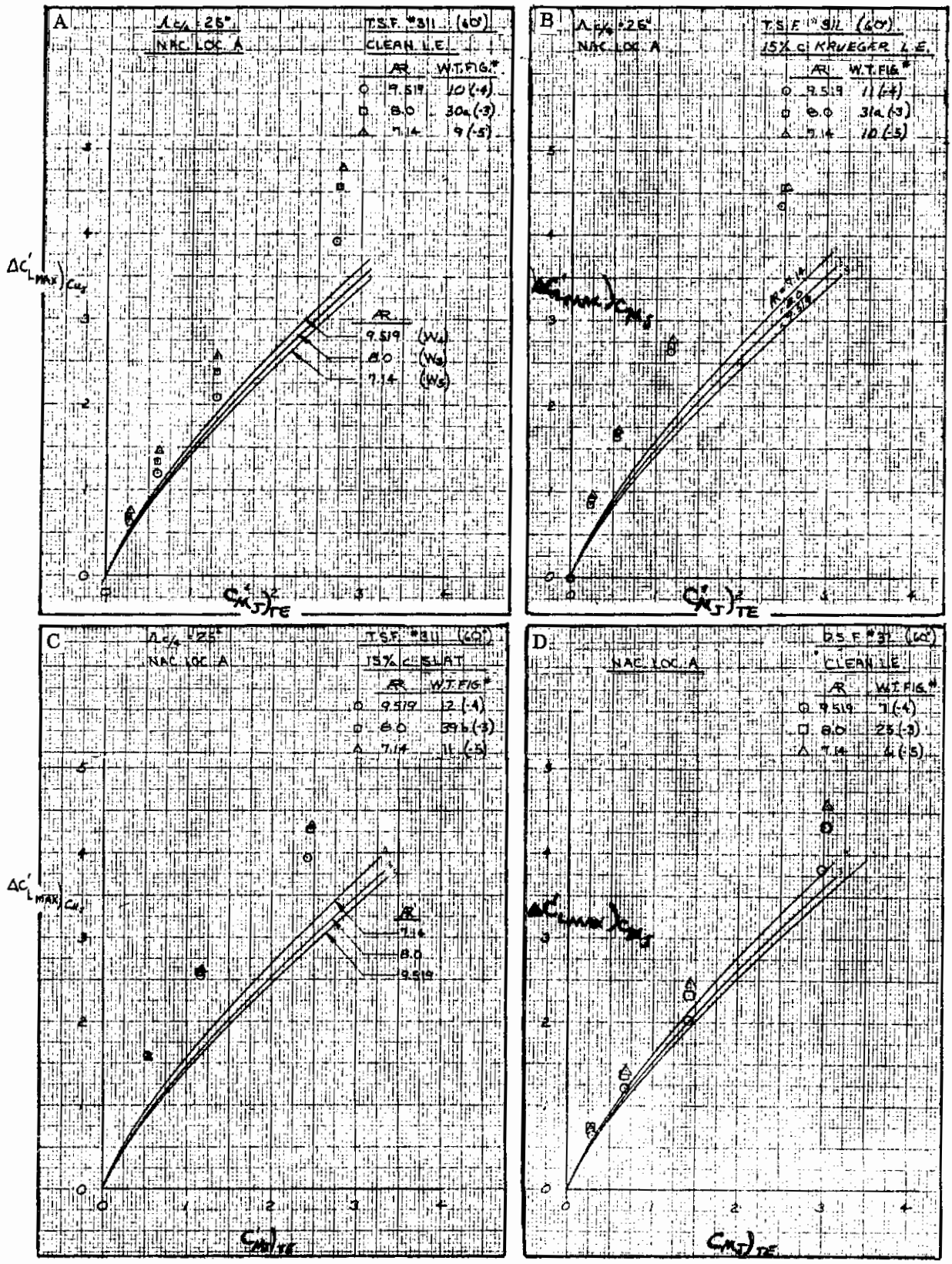

Figure 3.8-11. Effect of Aspect Ratio on $\Delta C'_{L_{max}})_{C_{\mu'_J}}$

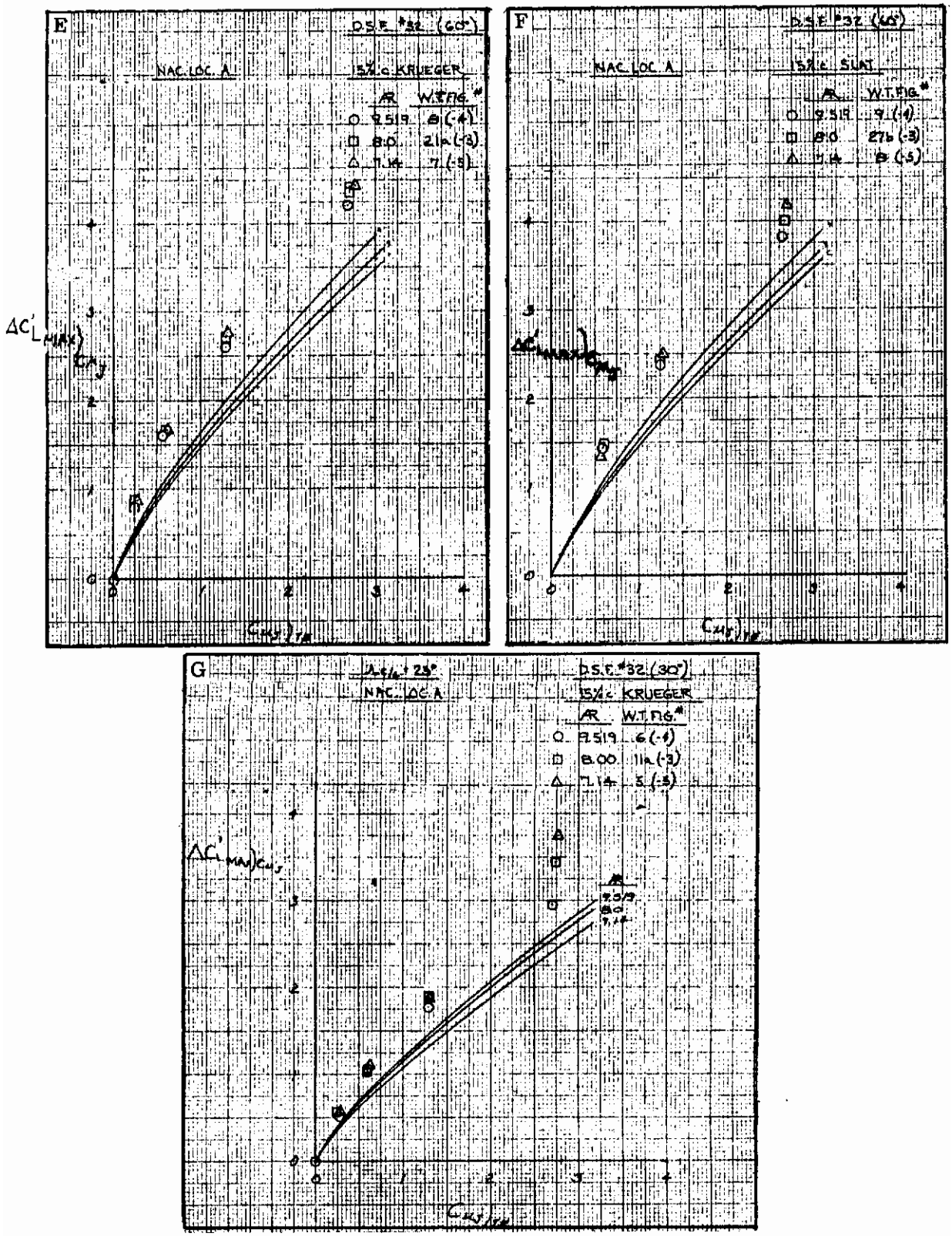

Figure 3.8-11. Effect of Aspect Ratio on $\Delta C'_{L_{max}})_{C_{\mu_J}}$, Cont

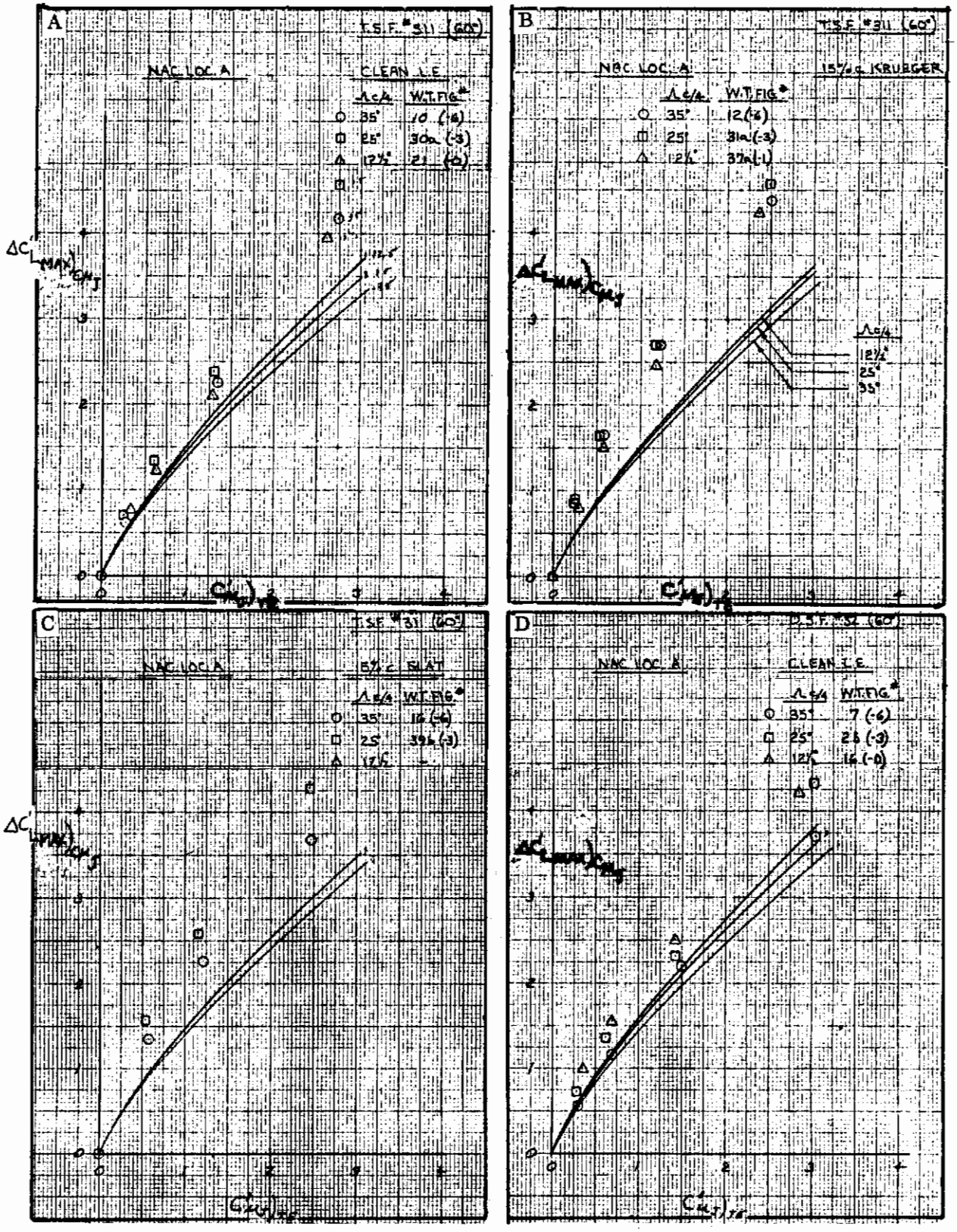

Figure 3.8-12. Effect of Wing Sweep on $\Delta C'_{L_{max}})_{C_{\mu J}}$

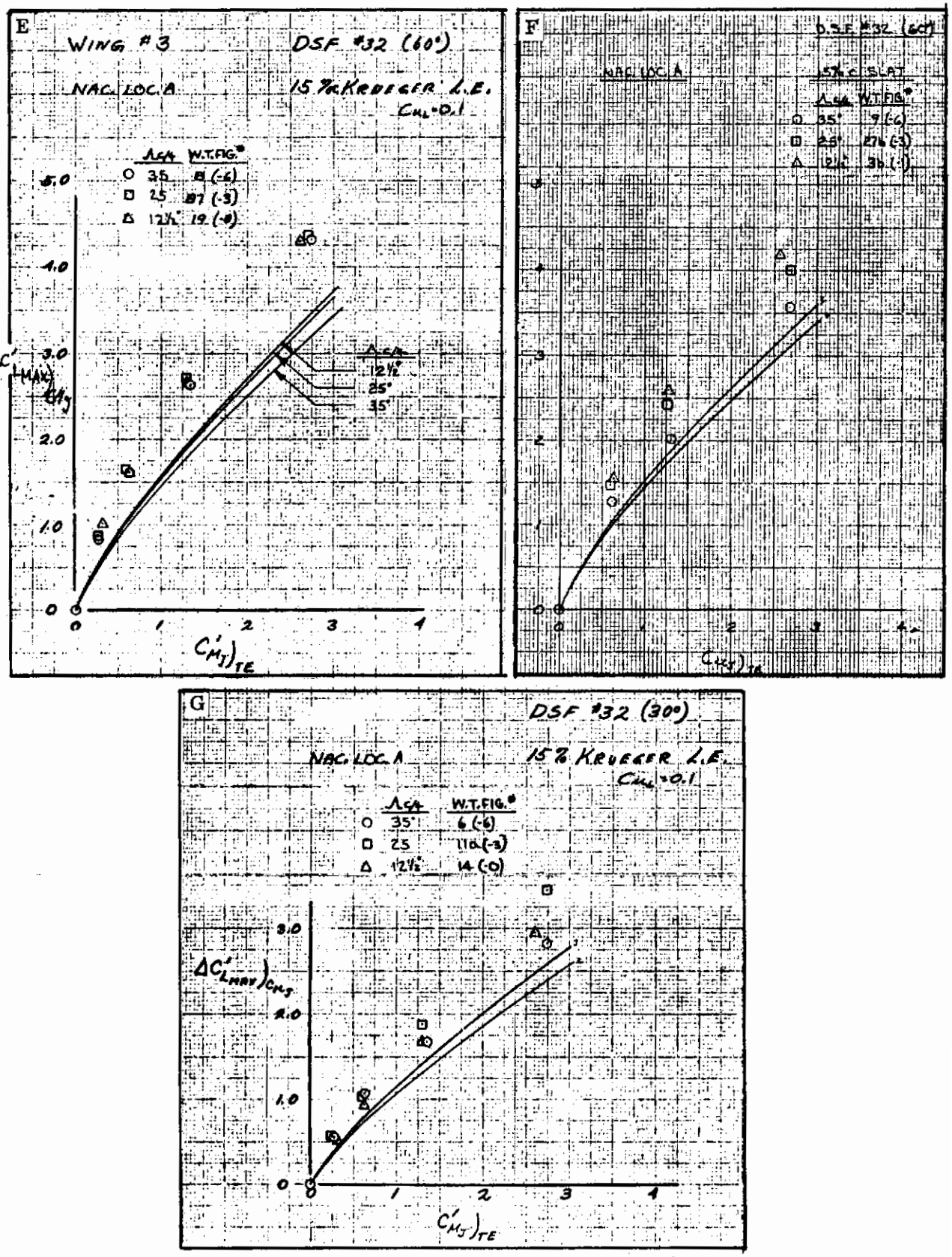

Figure 3.8-12. Effect of Wing Sweep on $\left(\Delta C'_{L_{max}}\right)_{C_{\mu_J}}$, Cont

3.9 IBF INCREMENTAL MAXIMUM LIFT DUE TO POWER

The analysis of maximum lift data due to power for the IBF system is presented as a function of the momentum coefficient estimated at the flap trailing edge and based on the wing area that is spanned by the blowing slot. These relationships are shown in Table 3.0-1.

3.9.1 EFFECT OF FLAP CONFIGURATION ON $\Delta C'_{L_{max}})_{C\mu_T}$. The maximum lift effects of blowing over a plain and single-slotted flap is shown in Figure 3.9-1 for engine nacelles on and off and with and without a blown leading-edge Krueger flap. Since the differences are small and may be attributed to small differences in flap chord and deflection, they are considered negligible. The theoretical estimate shown on these figures and others to follow was taken from References 3-5 and 3-6. The theory estimates maximum lift increment from thin airfoil and jet flap theories, assuming that the airfoil/flap configuration will stall at the same leading edge conditions as the basic airfoil. While this assumption may be reasonably accurate for unpowered airfoils, the assumption is probably not accurate for the power increment. The test data, however, follows closely to twice the theoretical estimate, similar to the EBF system data (Paragraph 3.8.1), and the data with engine nacelles (Figure 3.9-1c) is only about 1.75 greater.

The effect of flap deflection on maximum lift is shown in Figure 3.9-2. The trend with flap deflection is consistently about twice the theoretical estimate.

Partial span flap blowing data has been modified by the span factors used for unaugmented flap systems and presented with full span flap data in Figure 3.9.3. The correction factors seem adequate, since there is little difference between the two sets of data.

3.9.2 EFFECT OF LEADING EDGE KRUEGER ON $\Delta C'_{L_{max}})_{C\mu_T}$. The leading-edge Krueger flap shows only a small effect on the maximum lift increment of the trailing-edge flap, as shown in Figure 3.9-4. The difference in flap maximum lift increment due to airfoil chord extension caused by extending the leading edge is not seen in the test data, but is shown as a difference in the theoretical line. This indicates that for a fixed flap-chord to wing-chord ratio, droop in the leading edge will reduce the maximum lift increment due to trailing edge flaps. No data is available to show this effect.

3.9.3 EFFECT OF ENGINE NACELLE ON $\Delta C'_{L_{max}})_{C\mu_T}$. Test data shows that unpowered engine nacelles mounted on short pylons under the wing have only a small effect on the trailing-edge flap maximum lift increment. A much larger effect is seen on some of the figures where data is shown with the engine nacelles blowing at a momentum coefficient of 2.0 (Figures 3.9-5a, 3.9-5d, 3.9-5f, and 3.9-5g). Maximum lift increment is reduced as much as 20 to 25 percent due to engine-nacelle blowing.

This includes any increase in lift due to EBF effects (probably none for these short chord flaps) and direct thrust lift due to angle-of-attack changes. As discussed in Paragraph 3.5.3, the engine jet exhaust cuts the jet sheet being produced by the trailing-edge nozzle, thereby reducing the maximum lift increment due to blowing the flaps.

3.9.4 EFFECT OF WING SWEEP ON $\Delta C'_{L_{max}})_{C\mu_T}$. The effect on maximum lift increment of changing wing sweep from 12.5 to 25 degrees is small, as shown in Figure 3.9-6. Differences in these plots are due to slight changes in flap chord and deflection because of the mechanical method of changing sweep on the model. For this small range of sweep changes, therefore, it is assumed that there is no effect on maximum lift increment due to the trailing-edge flap.

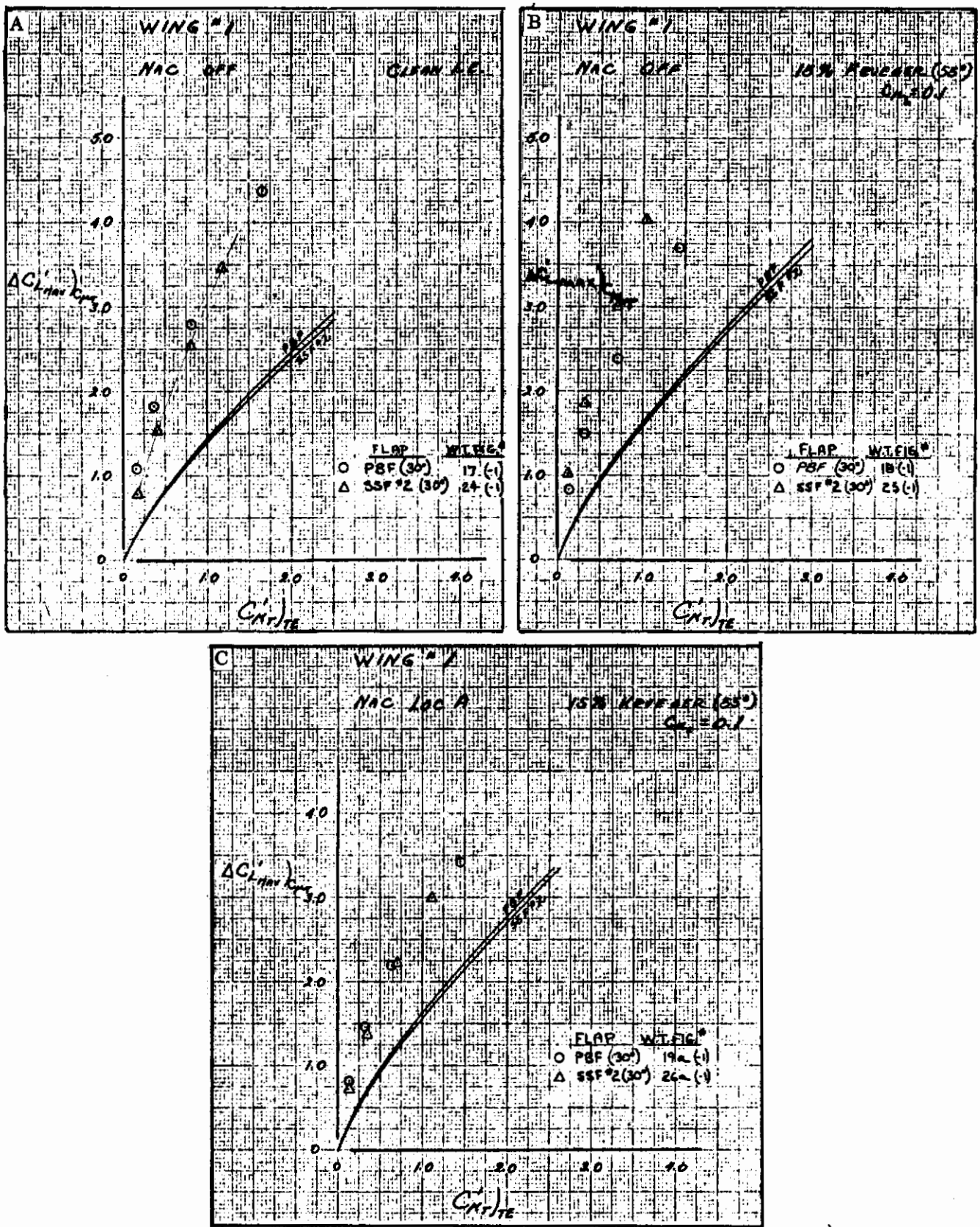

Figure 3.9-1. Effect of Trailing Edge Flap Configuration on $\Delta C'_{L_{max}}$ / C_{μ_T}

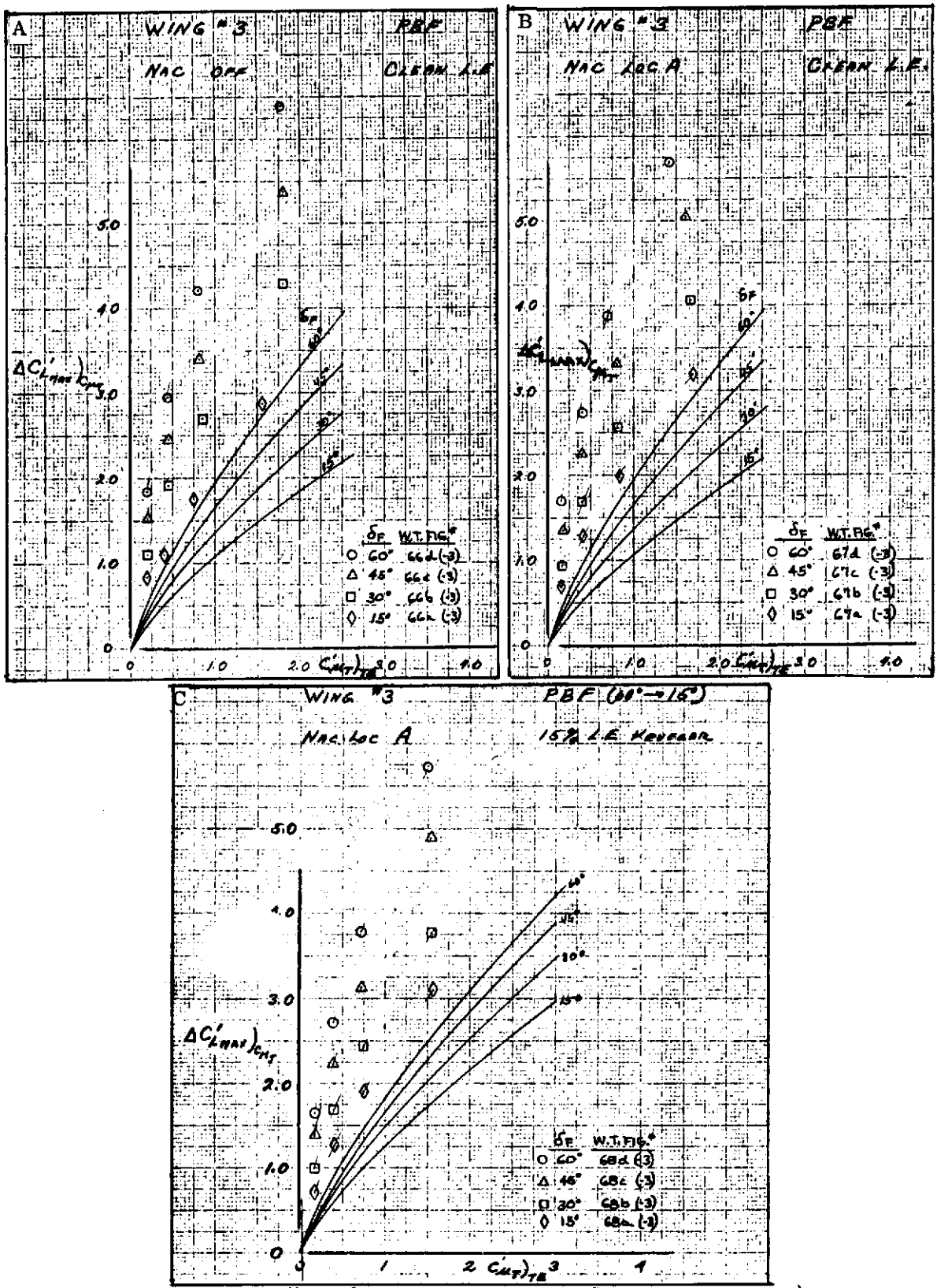

Figure 3.9-2. Effect of Trailing Edge Flap Deflection on $\Delta C'_{L_{max}})_{C_{\mu_T}}$

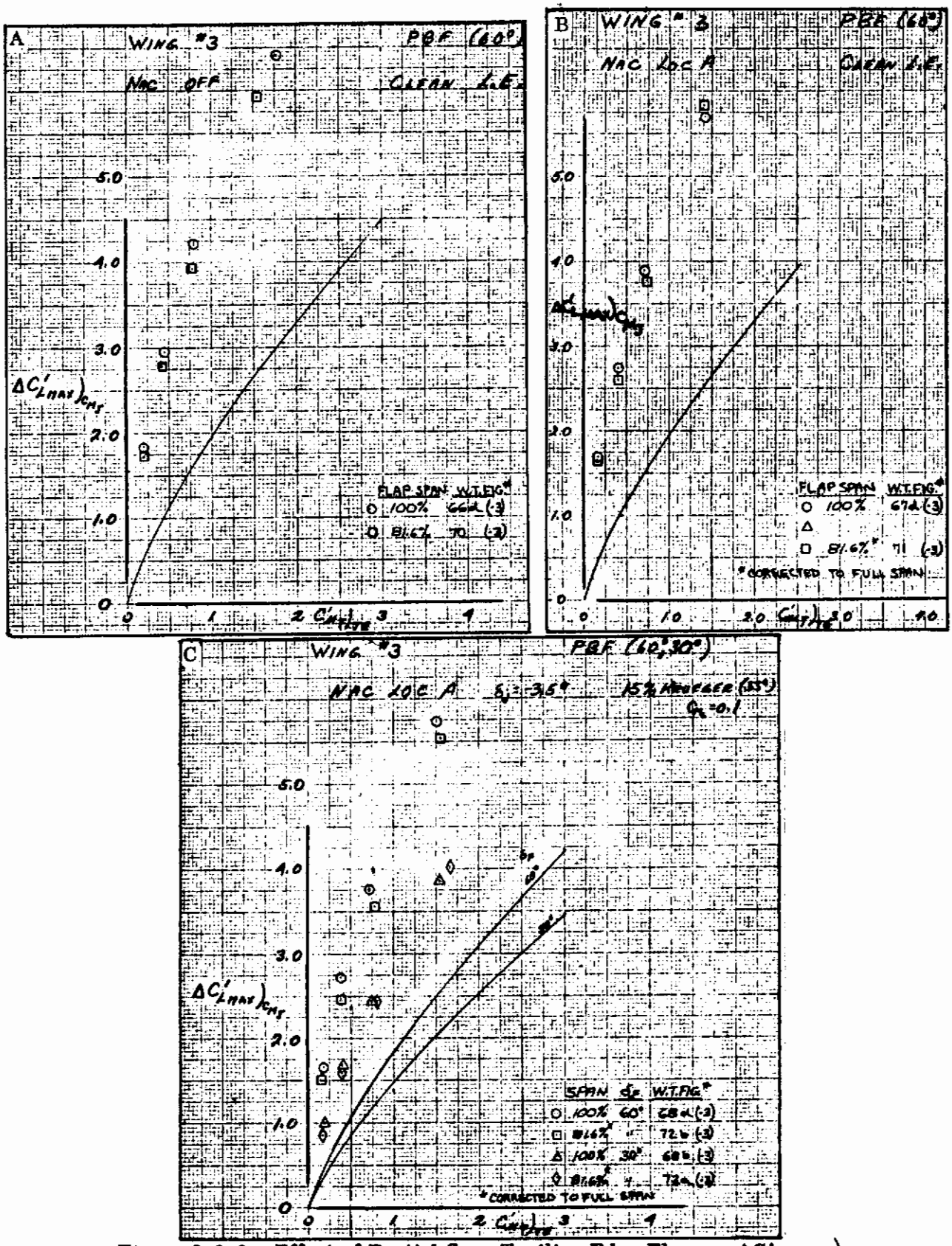

Figure 3.9-3. Effect of Partial Span Trailing Edge Flap on $\Delta C'_{L_{max}})_{C_{\mu_T}}$

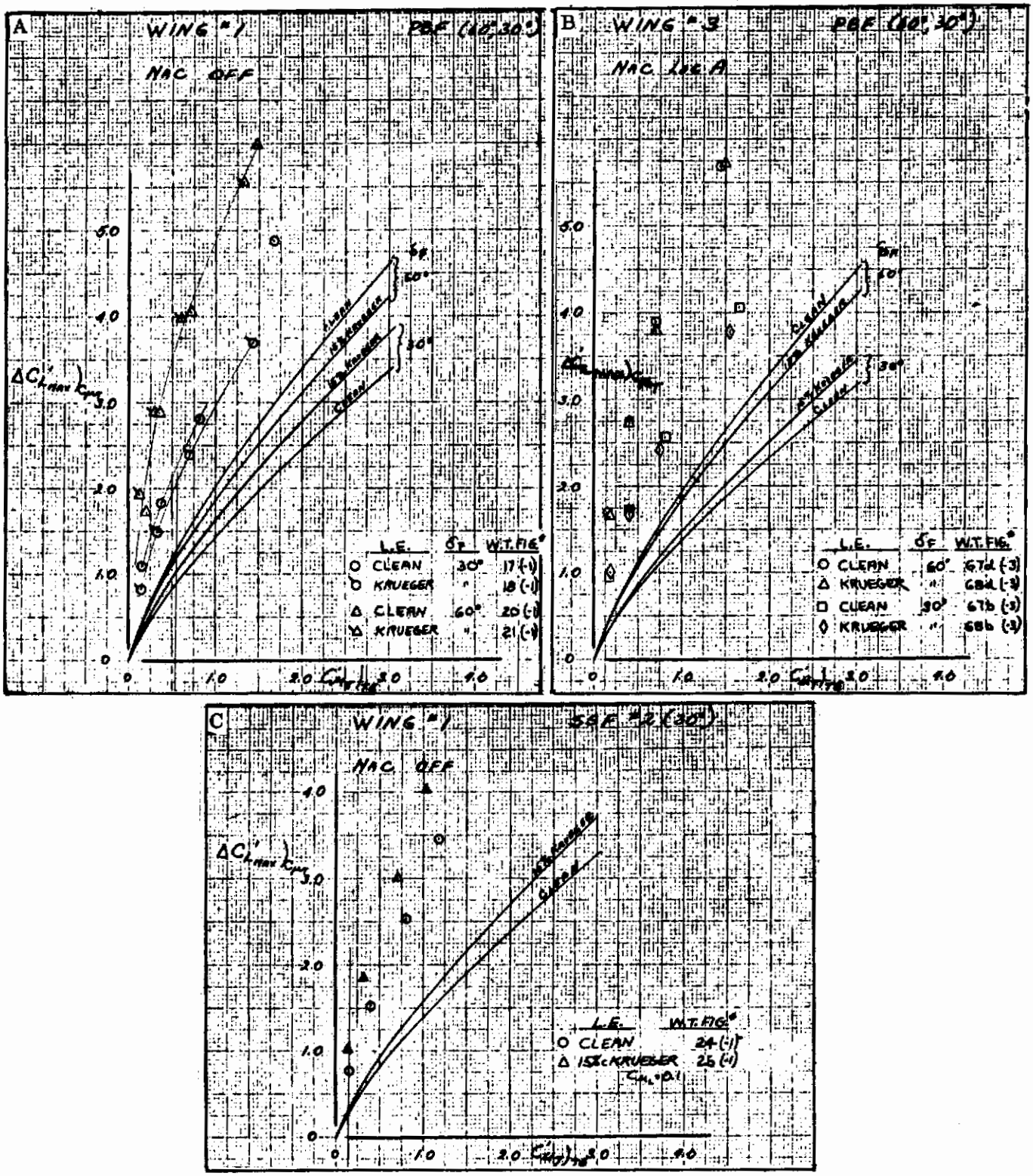

Figure 3.9-4. Effect of Leading Edge Krueger Flap on $\Delta C'_{L_{max}})_{C_{\mu_T}}$

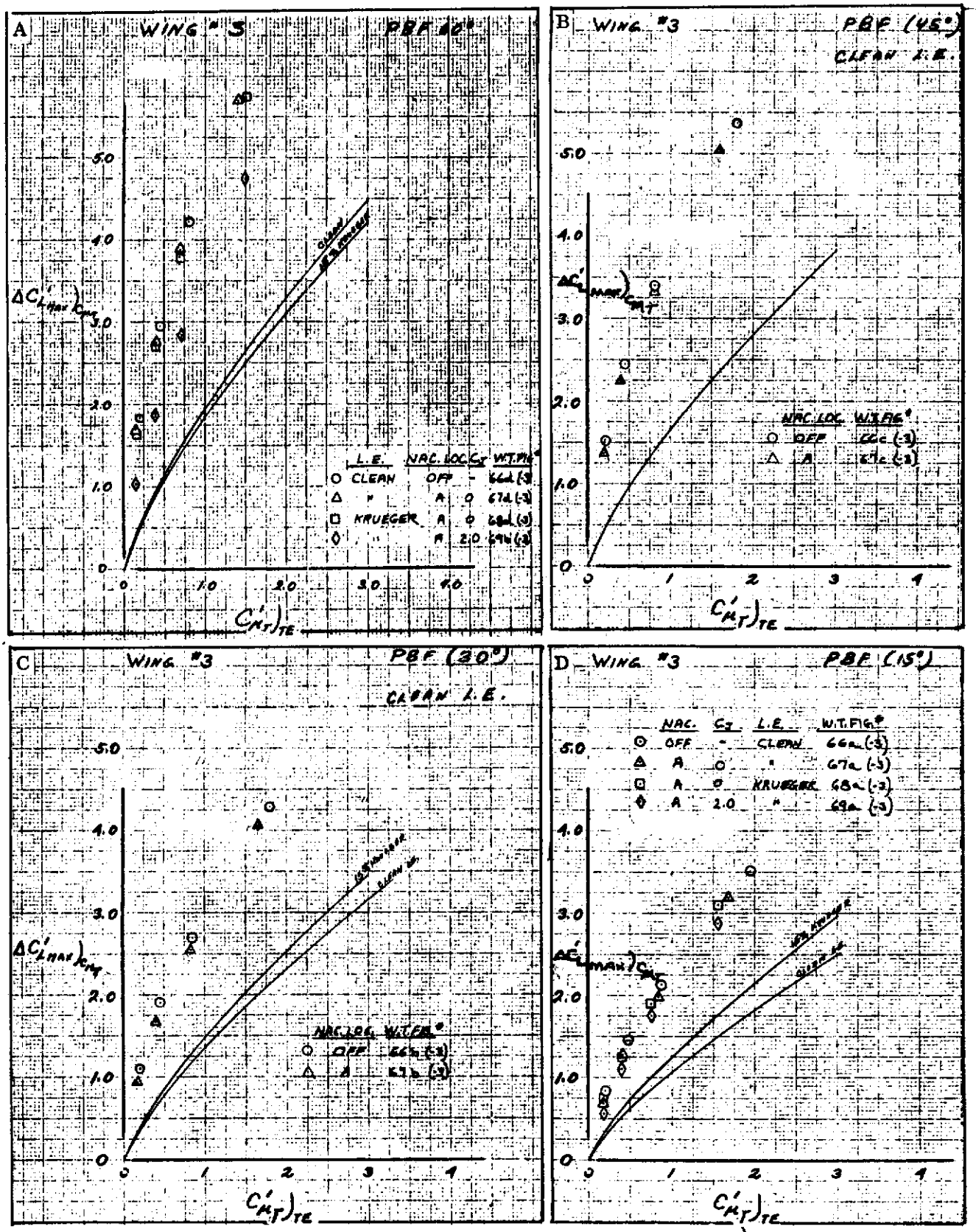

Figure 3.9-5. Effect of Engine Nacelles on $\Delta C'_{L_{max}})_{C_{\mu T}}$

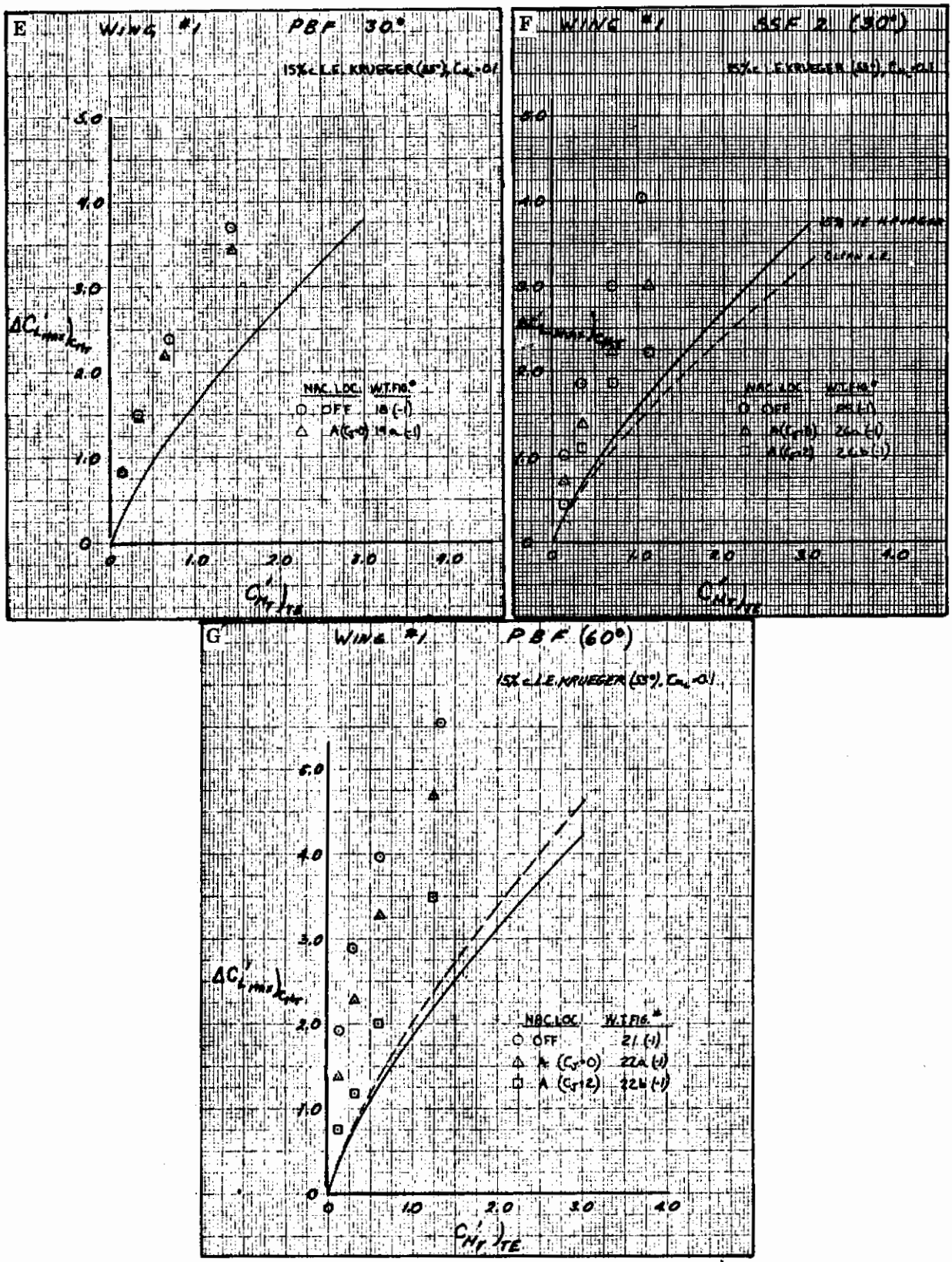

Figure 3.9-5. Effect of Engine Nacelles on $\Delta C'_{L_{max}})_{C_{\mu_T}}$, Cont

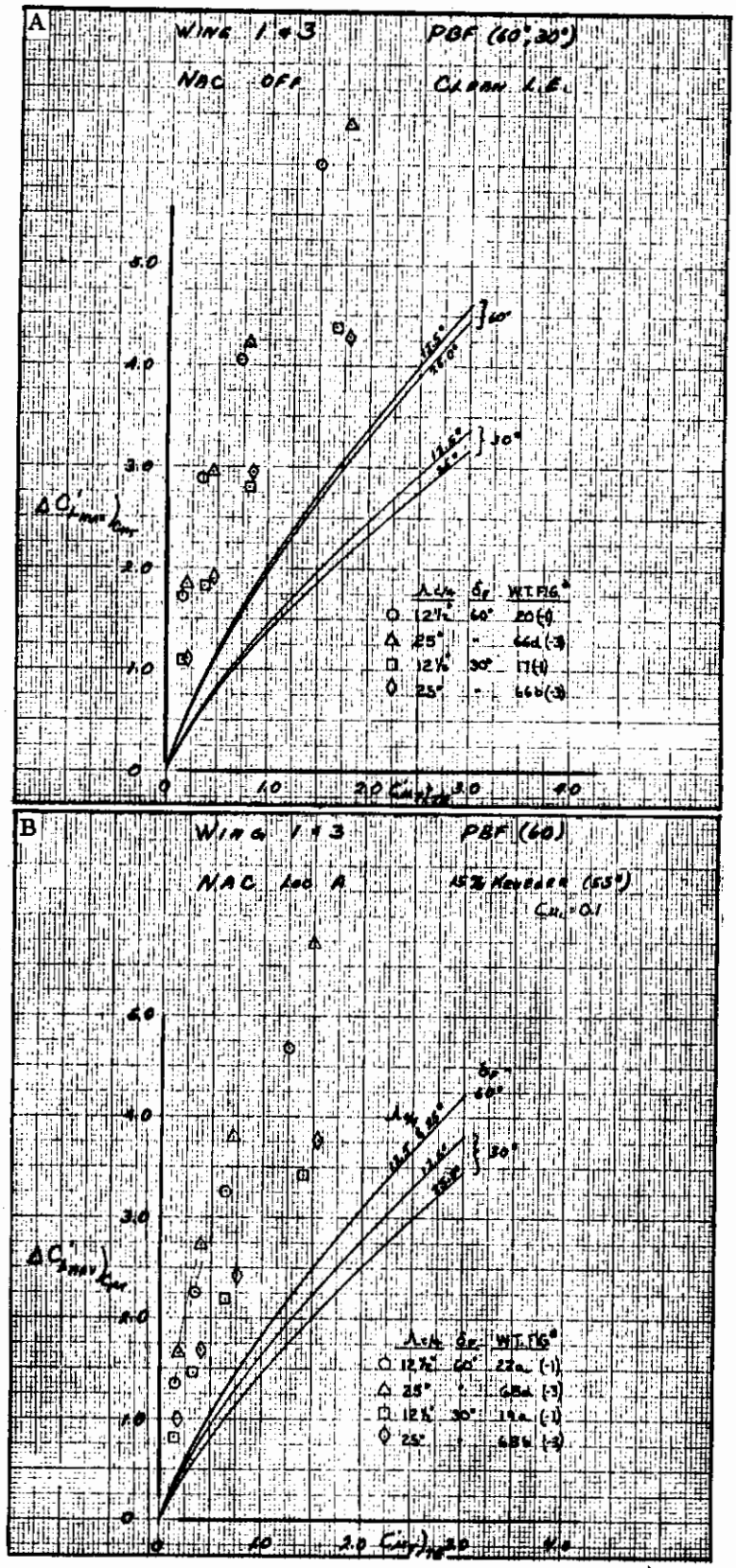

Figure 3.9-6. Effect of Wing Sweep on $\Delta C'_{L_{max}})_{C_{\mu_T}}$

3.10 MF/VT INCREMENTAL MAXIMUM LIFT DUE TO POWER

The analysis of the maximum lift data due to power for the MF/VT system is presented as a function of the momentum coefficient at the jet engine nozzle and based on the extended wing area. Test data generally shows that power has more of an effect on maximum lift than expected from the no-augmentation theory. This is seen throughout the following data.

3.10.1 EFFECT OF THRUST VECTORING ON $\Delta C'_{L_{max}})_{C_{\mu_J}}$. The effect of deflecting the thrust vector on the increment of maximum lift coefficient due to power is shown for several flap configurations in Figure 3.10-1. Like the increment in lift due to flap deflection at zero angle of attack, the data for maximum lift coefficient due to power shows that augmentation of the circulation lift is present at the low thrust deflections. There is still some augmentation at the higher thrust deflections, but the test data more nearly matches the no-augmentation theory. Variation of maximum lift increment with thrust deflection is shown in Figure 3.1-10e for the double-slotted flap deflected 30 degrees.

3.10.2 EFFECT OF TRAILING EDGE FLAP DEFLECTION ON $\Delta C'_{L_{max}})_{C_{\mu_J}}$. The effect of flap deflection on the increment of maximum lift due to power is shown in Figure 3.10-2. At the low deflection (Figure 3.10-2a), where flap circulation lift is still being augmented by immersion into the slipstream (EBF effect), flap deflection shows an effect on maximum lift similar to the effects discussed in Paragraph 3.8. At the large thrust deflections of 37 and 69 degrees (Figures 3.10-2b and c) where there is little augmentation, the effects of flap deflection on the maximum lift increment are minimal.

3.10.3 EFFECT OF ENGINE NACELLE ON $\Delta C'_{L_{max}})_{C_{\mu_J}}$. The chordwise position of the engine nacelle has little effect on maximum lift increment due to power. This comparison is shown in Figure 3.10-3 for three thrust deflections and three flap configurations.

3.10.4 EFFECT OF WING SWEEP ON $\Delta C'_{L_{max}})_{C_{\mu_J}}$. The effect of wing sweep on the increment of maximum lift due to power is shown in Figure 3.10-4. At the low thrust deflection, the system acts very similar to the EBF system discussed in Paragraph 3.8; at high thrust deflections, there is only a small effect of sweep.

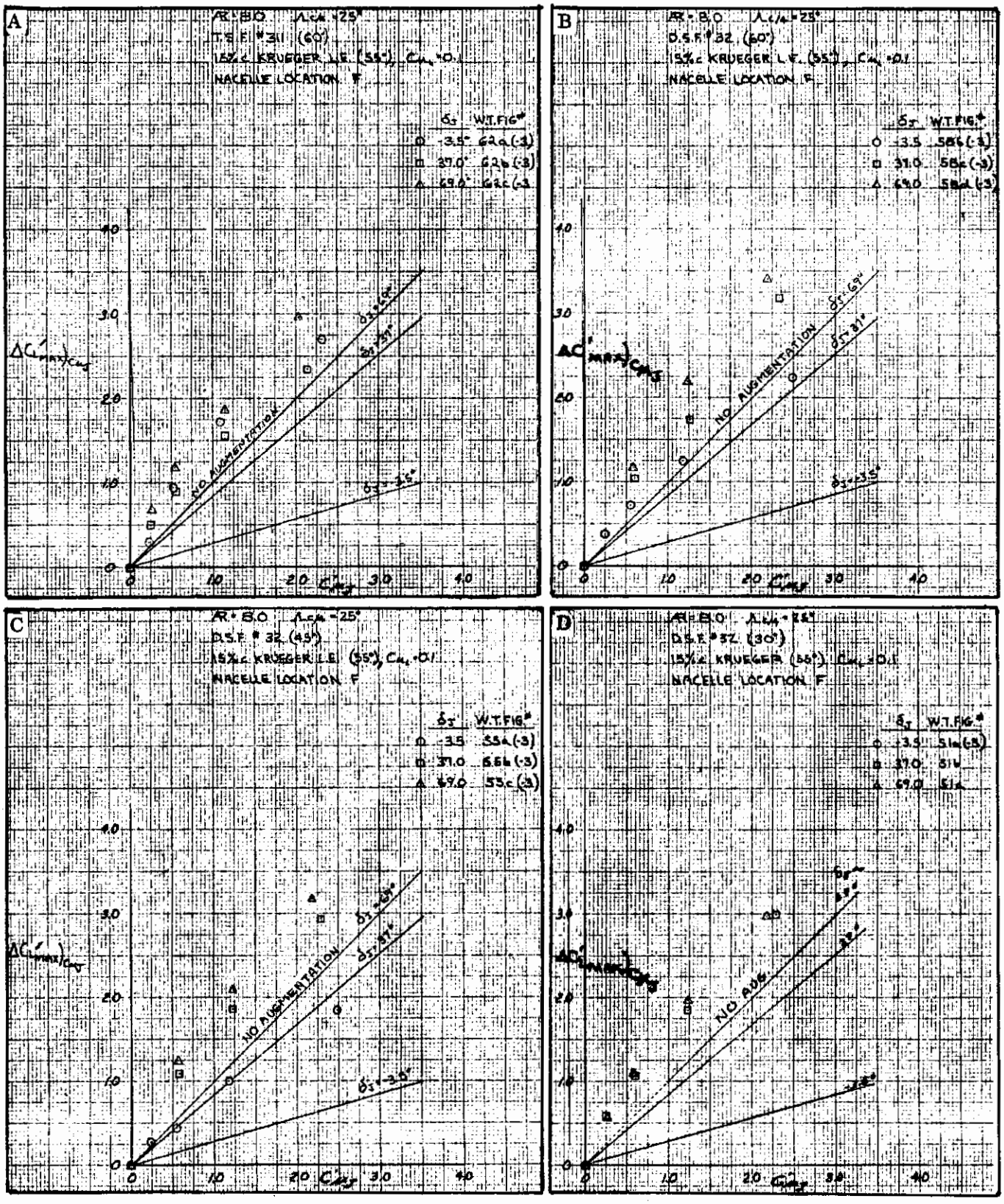

Figure 3.10-1. Effect of Vectored Thrust on $\Delta C'_{L_{max}})_{C_{\mu_J}}$

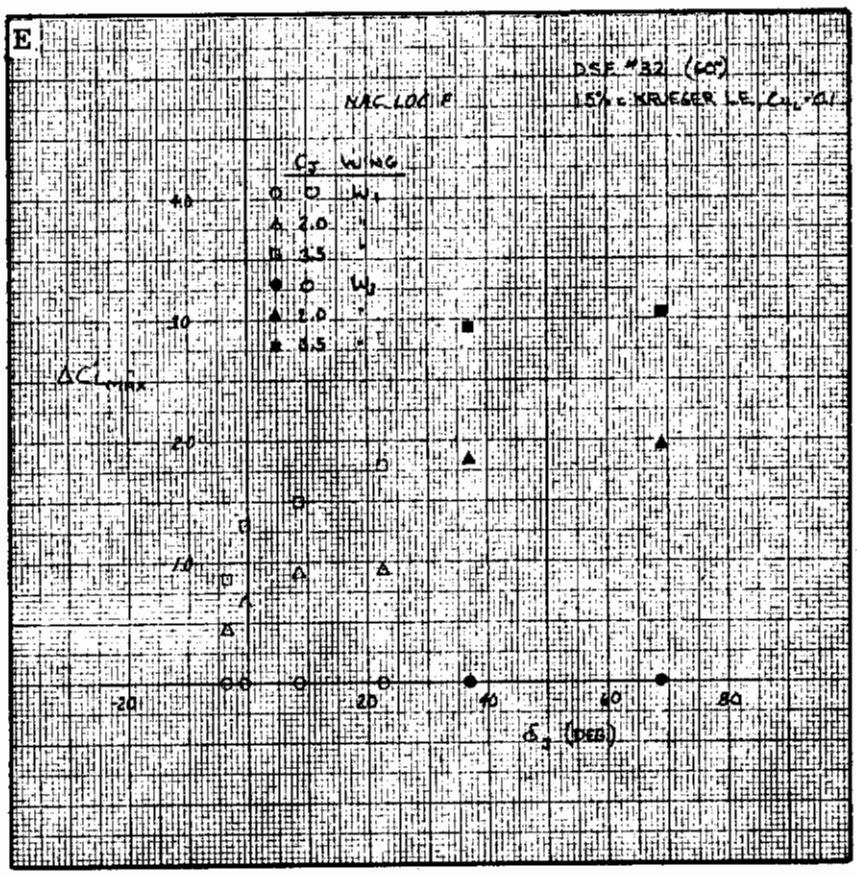

Figure 3.10-1. Effect of Vectored Thrust on $\Delta C'_{L_{max}})_{C_{\mu J}}$, Cont.

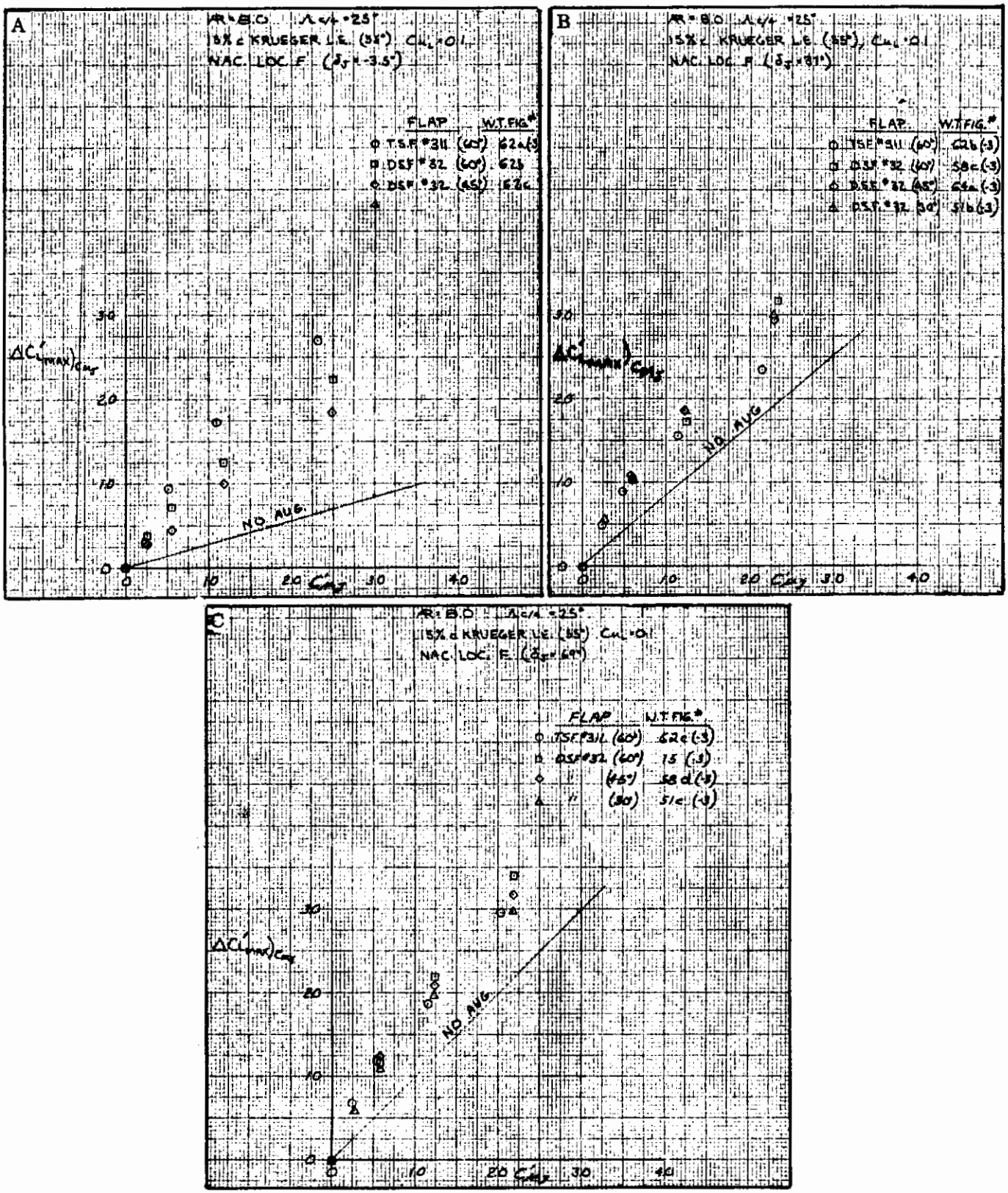

Figure 3.10-2. Effect of Trailing Edge Flap Deflection on $\Delta C'_{L_{max}})_{C_{\mu_J}}$

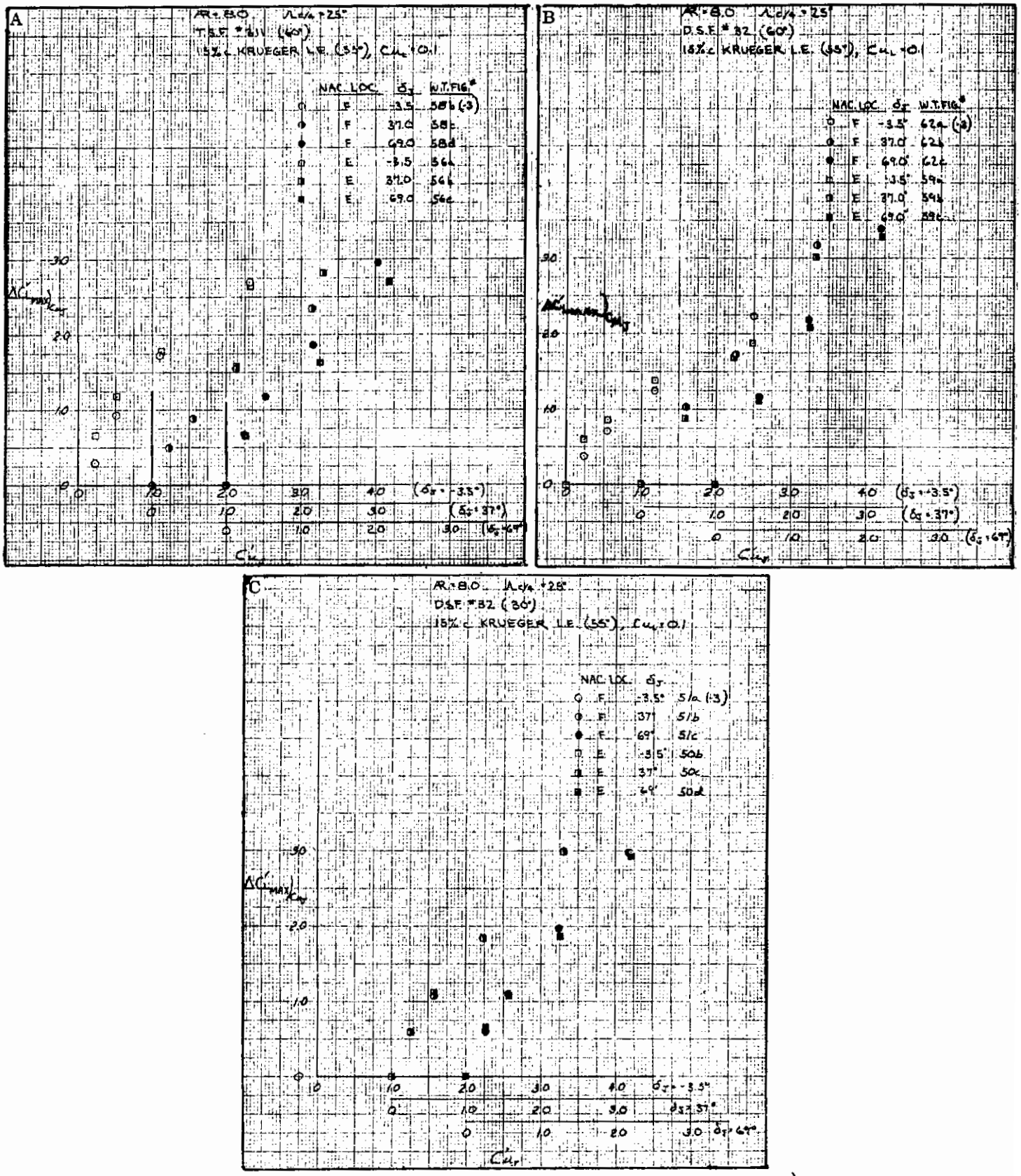

Figure 3.10-3. Effect of Nacelle Chordwise Location on $\Delta C'_{L_{max}})_{C_{\mu_J}}$

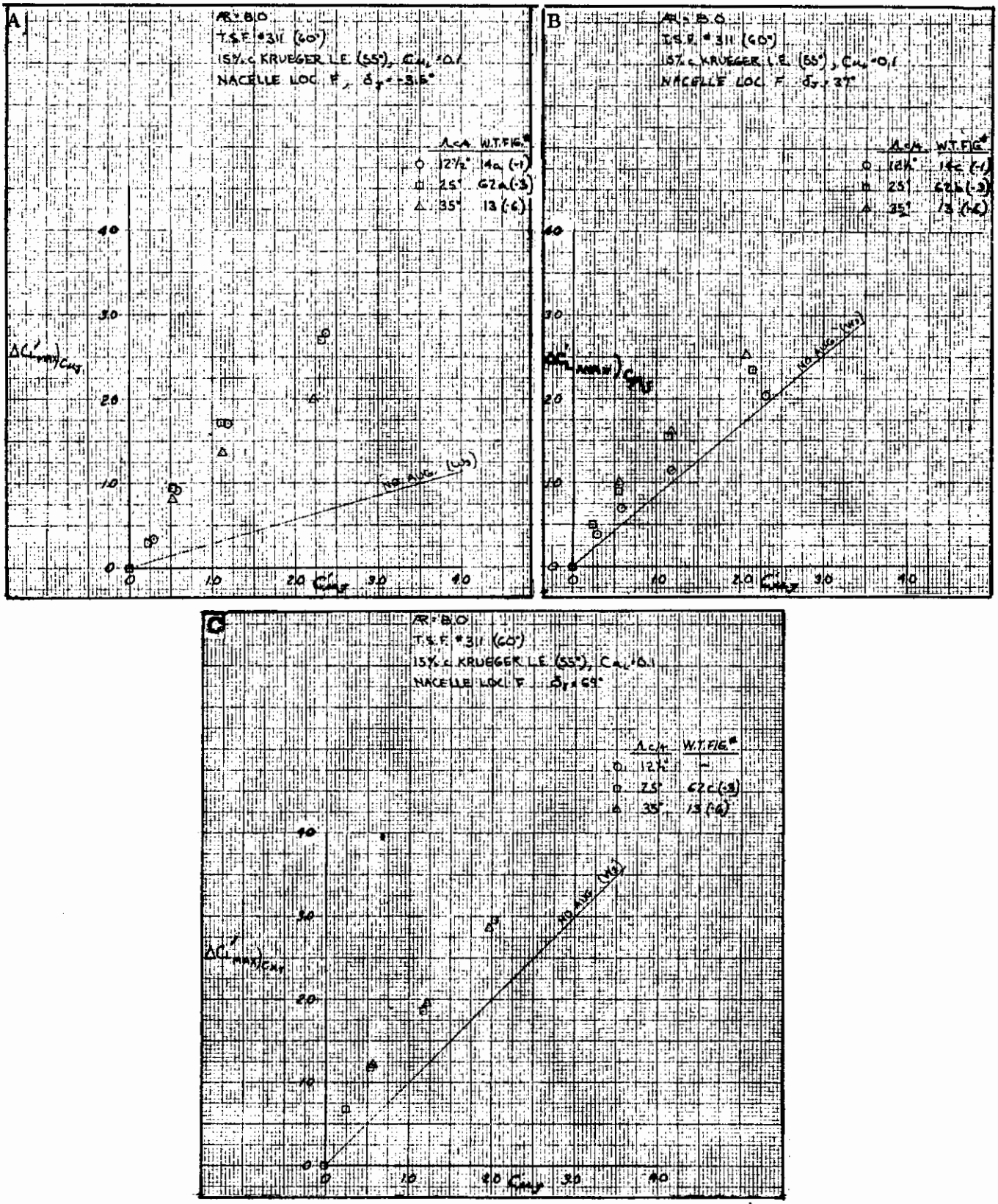

Figure 3.10-4. Effect of Wing Sweep on $\Delta C'_{L_{max}})_{C_{\mu_J}}$

SECTION 4

AXIAL FORCE ANALYSIS

Axial force data based on the wing reference area in the form of aircraft drag coefficient plus the thrust coefficient from engine blowing, leading-edge blowing, and trailing-edge blowing was obtained from GD/LST 612 wind tunnel tests, Reference 1-1. The axial force curve (C_D vs C_L^2) was analyzed using an interactive graphic computer program to measure the following aerodynamic parameters.

$\overline{\text{DCL**2/DCD}}$	Slope of the axial force curve measured in the unseparated lift region of the curve.
$\overline{\text{CD0}}$	The axial force coefficient at zero lift coefficient obtained as a linear extension of the axial force curve slope to $\alpha = 0$ degrees.

These aerodynamic parameters are used to obtain the normal drag terms: induced drag factors, minimum profile drag, and thrust recovery factor. The relationships used to obtain these terms are shown in Table 4.0-1. Thrust recovery of a flap system is obtained as the slope of the variation of $C_{D_{P_{min}}}$ versus C_{μ_T} or C_{μ_J} for IBF or EBF systems, respectively. The reference area used for the drag analysis is the normal basic wing area as defined by the basic planform. These terms are correlated using the momentum coefficient as defined in Table 4.0-1 as the independent variable.

Typical drag durves for two EBF configurations are shown in Figures 4.0-1 and 4.0-2. Each figure shows the test data points from Reference 4-1 for lift-coefficient-squared plotted against drag coefficient at several engine power settings. Data for an externally blown triple-slotted flap at 60 degrees of deflection is shown in Figure 4.0-2. The linear curve fit is shown on the curves covering the estimated linear range of the drag curve. The slope of this line is the term DCL**2/DCD, and the intercept of this line on the $C_L = 0$ axis is the drag term CD0.

Table 4.0-1. Equations Used in Analysis of Axial Force Wind Tunnel Test Data.

Induced Drag Factor

$$e = \frac{\overline{DCL**2/DCD}}{\pi A}$$

Minimum Profile Drag Coefficient

$$C_{D_{P_{min}}} = C_{D_o} - r\,C_\mu = \overline{CD0} - C_{D_R}$$

Thrust Recovery Factor

$$r = \frac{\partial\left(C_{D_{P_{min}}}\right)}{\partial C_\mu}$$

IBF Blowing Momentum Coefficient

$$C_{\mu_T} = \overline{CUT} \cdot \frac{S_T}{S}$$

EBF Blowing Momentum Coefficient

$$C_{\mu_J} = \overline{CJ}$$

Minimum Profile Drag Coefficient - No Augmentation

$$C_{D_{P_{min}}} = C_{\mu_J} \cos\left(-\delta_J\right)$$

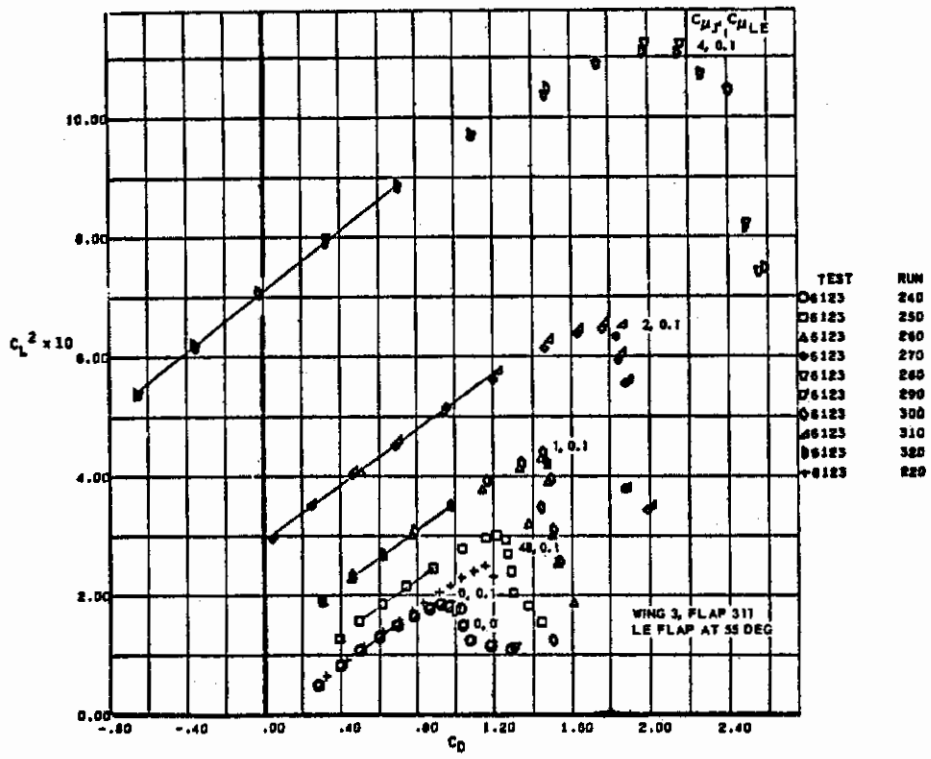

Figure 4.0-1. Typical Drag Curves for EBF Triple-Slotted Flap (60 degrees)

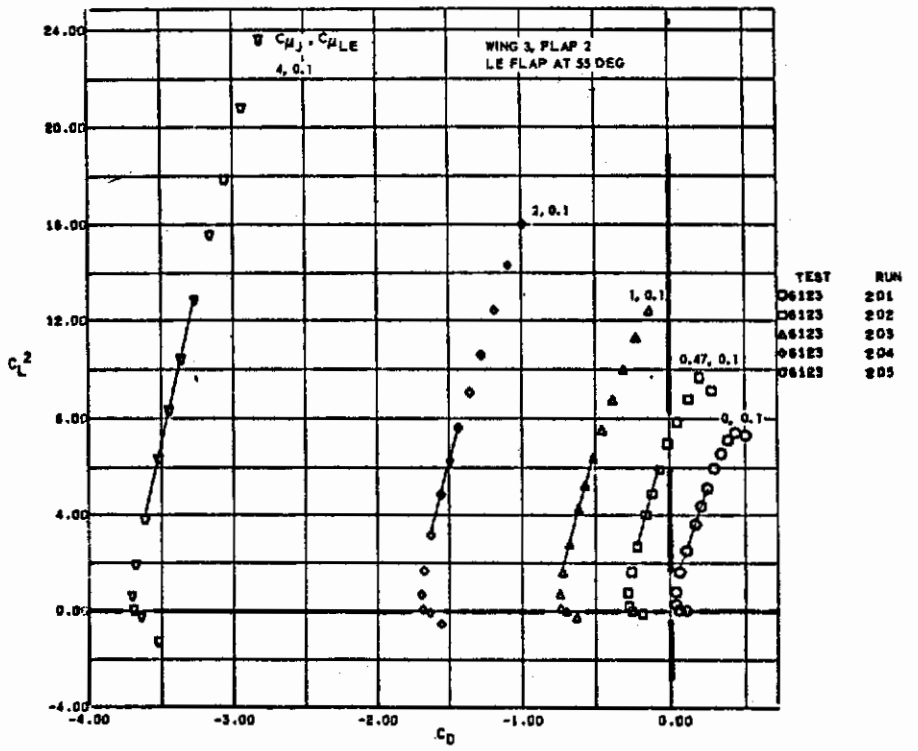

Figure 4.0-2. Typical Drag Curves for EBF Single-Slotted Flap (15 degrees)

4.1 EBF THRUST RECOVERY AND INDUCED DRAG

Analysis of wind tunnel data for the EBF system is shown as the variation of the induced drag factor, e, and the minimum profile drag, $C_{D_{P_{min}}}$, with the jet engine momentum coefficient, C_{μ_J}.

The thrust recovery defined as the change in minimum profile drag with a change in momentum coefficient has been tabulated on the data plots. These values of thrust recovery have been measured using a linear least-squares curve fit of the data points. Comparison values of static turning efficiency are also shown, when available.

The similarity between the thrust recovery data for an EBF system and an IBF system is shown in Figure 4.1-1. Thrust recovery of the IBF system is slightly greater than that for the EBF system. The jet sheet of the IBF system blows only the upper surface of the flap with a high velocity stream, while the jet stream of the EBF system blows both the upper and lower flap surfaces with a lower velocity stream (due to mixing before it hits the flap).

Difficulty in measuring the induced drag factor from test data results in noticable scatter. The major problem is in determining the linear portion, if any, of the $C_L{}^2$ versus C_D curves. But, since a small shift in the measured slope would result in large changes in $C_{D_{P_{min}}}$ and since the thrust recovery data in general is quite acceptable, it seems unlikely that the slope of this drag curve (which is the induced drag factor) would be unreasonable even though large amounts of scatter is apparents in the results.

The only certainty about these results is that the efficiency factor does not generally decrease with momentum coefficient. Basically, the induced drag factor increases slightly with momentum coefficient but not as great as expected from lifting line theory ($e = 1 + 2\ C_{\mu_J}/\pi A$) shown on each of the data curves.

Also presented in this section are static data ($q = 0$) plots for various model configurations from which the static turning efficiency of the jet stream has been measured. As a point of reference, a theoretical estimate of the static data has been made and added to each of these plots. This theory, taken from Reference 4-8, gives the lift and drag relations for jet stream blowing over a planar flap system.

4.1.1 EFFECT OF TRAILING EDGE FLAP CONFIGURATION ON THRUST RECOVERY. Flap deflection has a large effect on the thrust recovery of an EBF system. Data presented in Figures 4.1-2 and 4.1-3 indicates that high flap deflection results in decreased thrust recovery together with increased static turning angle. Figure 4.1-2b shows the static test data for a large series of flap types and deflections. At a constant flap deflection angle (60 degrees), the turning angle decreases along with increases in turning efficiency.

The triple-slotted flap, which penetrates the jet stream the most of any flap configuration, effectively turns the stream 56 degrees. The single-slotted flap, (δ_F = 60 degrees) which is not immersed in the jet stream as much, shows a deflection angle of only 28 degrees. In both of these configurations, the turning efficiency is slightly less than 0.70. However, the double-slotted flap (δ_F = 60 degrees) shows a reduction in efficiency to 0.65. The decrease in turning efficiency is due to an increase of flap immersion into the jet stream. For this same reason, a reduction in flap deflection is accompanied with large increase in turning efficiency. This same trend is seen in Figure 4.1-3b, which shows thrust recovery decreasing with increasing flap deflection.

The comparison of thrust recovery with static turning efficiency shown in Figure 4.1-3b indicates very close simularity for the double-slotted flap deflections but greater thrust recovery than static turning efficiency for the triple-slotted flap. This comparison is shown in Figure 4.1-4 for varied flap configurations and wing planforms. Almost all of the double- and single-slotted flap thrust recovery data, r, is between 1.0 and 1.05 of the static turning efficiency, η_s. While thrust recovery for the triple-slotted flap is usually between 1.05 and 1.15 of the static turning efficiency.

The effects on thrust recovery due to a change in flap chord is small, as shown in Figure 4.1-5. The static turning efficiencies shown in Figure 4.1-2b indicates the same trend, but the static turning angle is reduced as much as eight degrees at a given flap deflection.

Thrust recovery is unchanged with 81.6 percent span flaps, as shown in Figure 4.1-6. Although the slopes of the minimum profile drag curves for the different span flaps are the same, there is a displacement (increase in drag) when going to the partial span flap. This constant amount of drag is the increment in induced drag due to a reduction in span of the flap. This increment is constant with changes in momentum coefficient. Theoretical analysis using the span load calculations (see Section 2) has shown that the increment in drag due to flap cutouts is not a function of momentum coefficient but primarily a function of the amount of flap cutout.

4.1.2 EFFECT OF LEADING EDGE CONFIGURATION ON THRUST RECOVERY. There are no discernable major effects of leading edge configuration, deflection, or chord on the thrust recovery of the EBF configurations tested. Data is shown in Figures 4.1-7 through 4.1-9 for the 15-percent-chord Krueger flap at various deflections and a 25-percent-chord Krueger at 55 degrees of deflection. Also shown is data for a 15-percent-chord leading edge slat at several deflections and a 25-percent-chord slat at 45 degrees of deflection. These configurations are shown in conjunction with numerous trailing-edge flap configurations.

4.1.3 EFFECT OF NACELLE LOCATION ON THRUST RECOVERY. Location of the engine nacelle can have a large effect on the thrust recovery of an EBF system. The effect of the spanwise location of the engine nacelles is shown in Figures 4.1-10 and 4.1-11. Figure 4.1-10 shows the static test data, indicating that dual nacelle location C

(nacelles mounted close together) has a slightly greater turning efficiency than when located apart, while still maintaining the high turning angle of 62 degrees (which is slightly greater than the total flap deflection of 60 degrees). This trend is also seen in the thrust recovery data shown in Figure 4.1-11. Here the thrust recovery increases from 72.5 to 83 percent by changing the location of the outboard engine nacelles to a point beside the inboard nacelle (simulated dual nacelles location C).

Chordwise location of the jet engine exit shows a much less pronounced effect on the thrust recovery and static turning efficiency and deflection. This trend is shown for several flap configurations and wing planforms in Figures 4.1-12 and 4.1-13. A slight decrease in thrust recovery and static turning efficiency is found when the nacelle exit location is moved aft. This decrease in efficiency is also accompanied by a slight reduction in static turning angle (Figure 4.1-12).

Tilting the jet exhaust up toward the flap slots tends to increase the static turning angle but also slightly reduces the static turning efficiency, as shown in Figures 4.1-12 and 4.1-14a. Thrust recovery also reduces slightly when jet exhaust is inclined upward, as seen in some of the plots in Figure 4.1-13.

As seen in the discussion on lift effects, the vertical location of the engine nacelle has an important effect on aerodynamic characteristics. This effect on turning efficiency and deflection (together with thrust recovery) is shown in Figures 4.1-14b and 4.1-15. Figure 4.1-14b shows the large reduction in turning angle accompanied by a small change in turning efficiency (decreased for the triple-slotted flap and increased for the double-slotted flaps) caused by lowering the engine nacelle from near the wing (location A) to a much lower position (location E). This large reduction of turning angle and small increase in turning efficiencies is due to the reduced amount of flap immersed in the jet exhaust.

A similar effect on thrust recovery is seen by lowering the engine nacelles to location E, Figure 4.1-15. The large difference between thrust recovery and static turning efficiency for triple-slotted flaps disappears when the nacelle is lowered to location E, Figure 4.1-15a. This was accompanied by a large loss in flap lift effectiveness, as shown in Figure 4.1-17d. Tilting the thrust line does not increase thrust recovery, even though flap lift effectiveness was improved when the nacelle was in location A as discussed in Paragraph 3.4.3.

4.1.4 EFFECT OF ASPECT RATIO ON THRUST RECOVERY. Changes in wing aspect ratio between 7.1 and 9.5 has little effect on the static turning angle and efficiencies or on thrust recovery. The test data shown in Figures 4.1-16 and 4.1-17 for several flap and leading edge configurations shows this trend throughout.

4.1.5 EFFECT OF WING SWEEP ON THRUST RECOVERY. The static data varies with wing sweep angle as shown in Figure 4.1-18 for various flap configurations

and deflection. Wing sweep is shown to increase spanwise flow of the jet, thereby increasing spreading. This, in turn increases turning efficiency but also reduces the turning angle. This same trend can be seen in the thrust recovery data shown in Figure 4.1-19 for various trailing-edge flap and leading edge configurations.

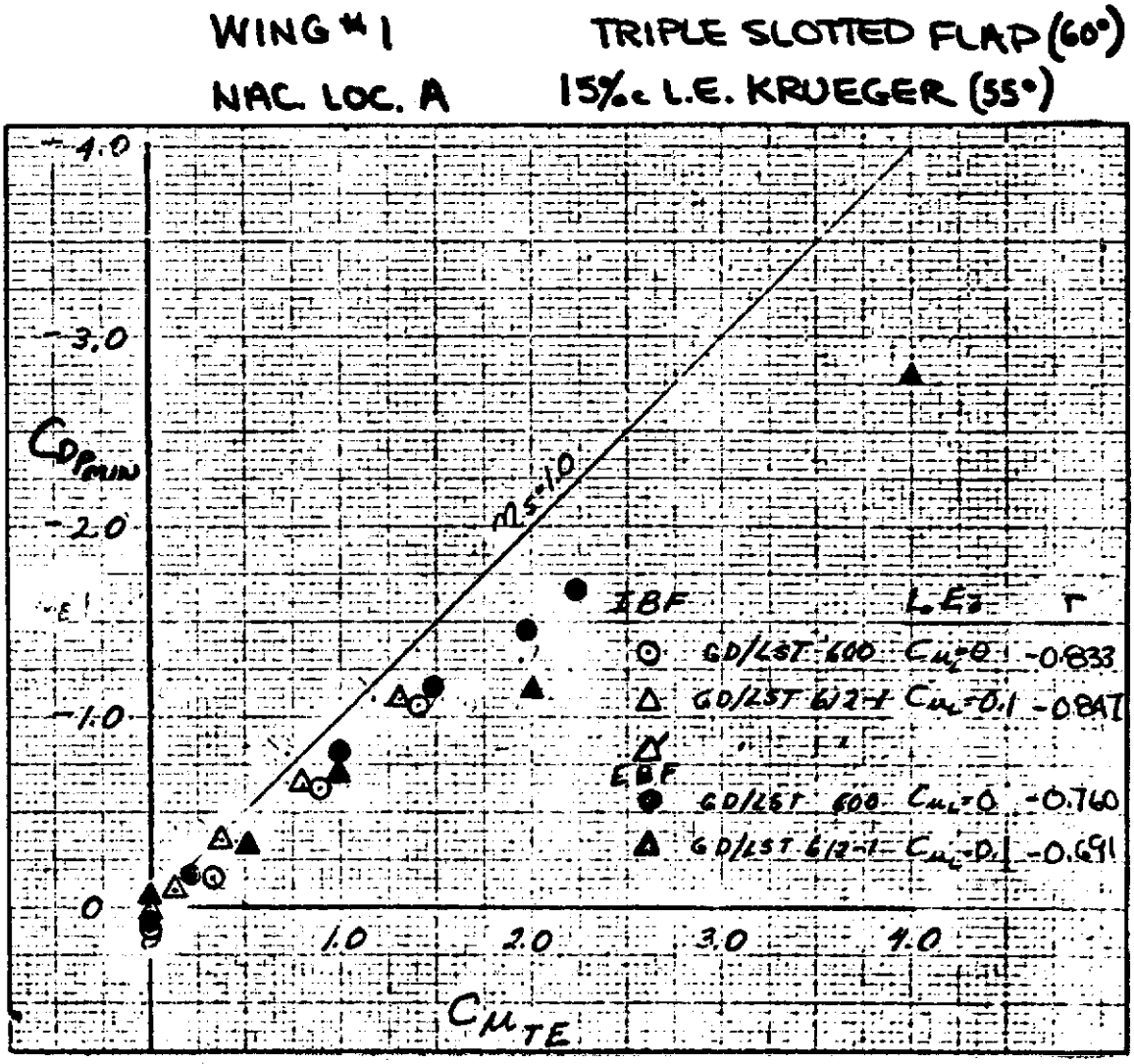

Figure 4.1-1. EBF/IBF Analogy

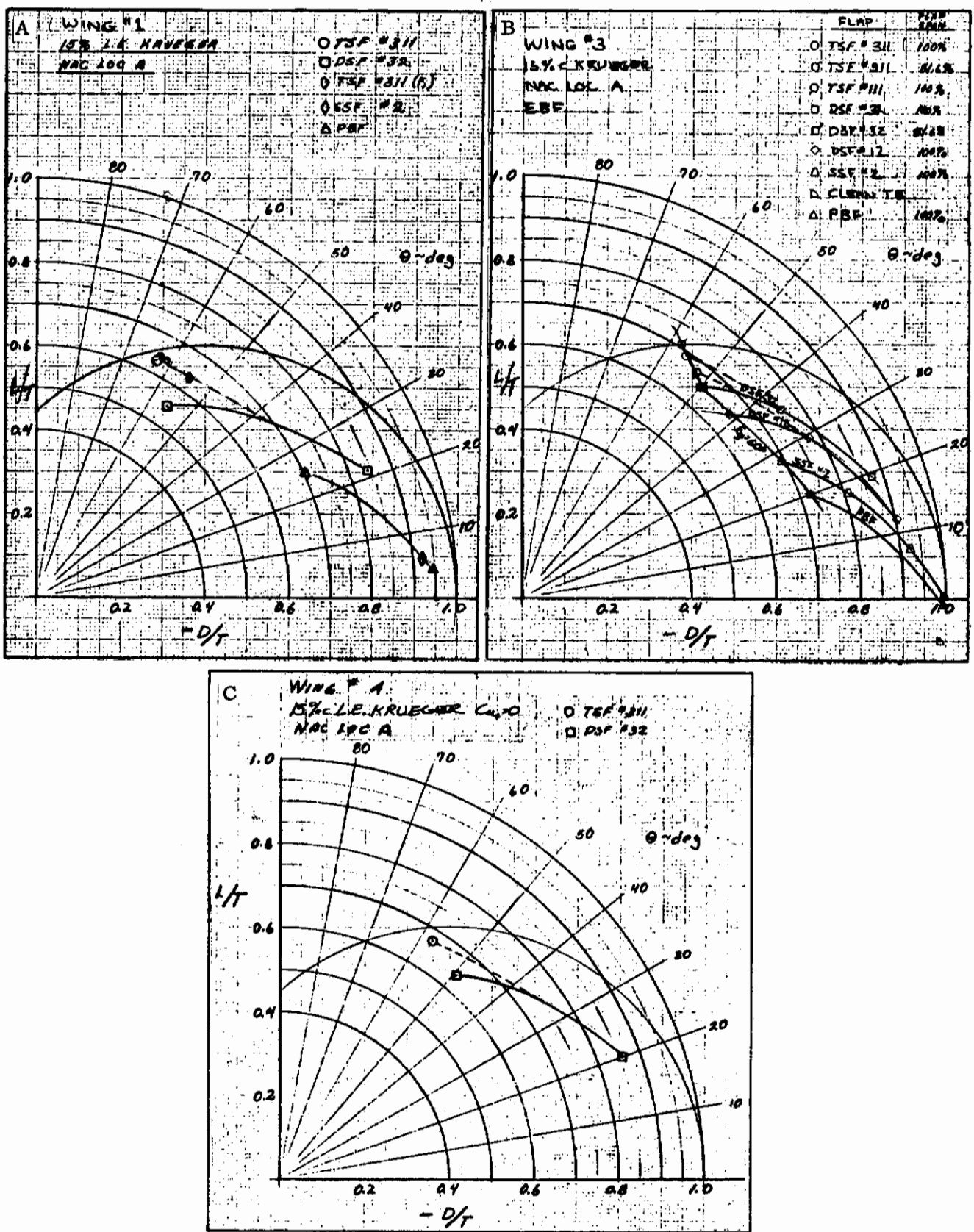

Figure 4.1-2. Effect of Trailing Edge Flap Configuration on Static Turning Efficiency

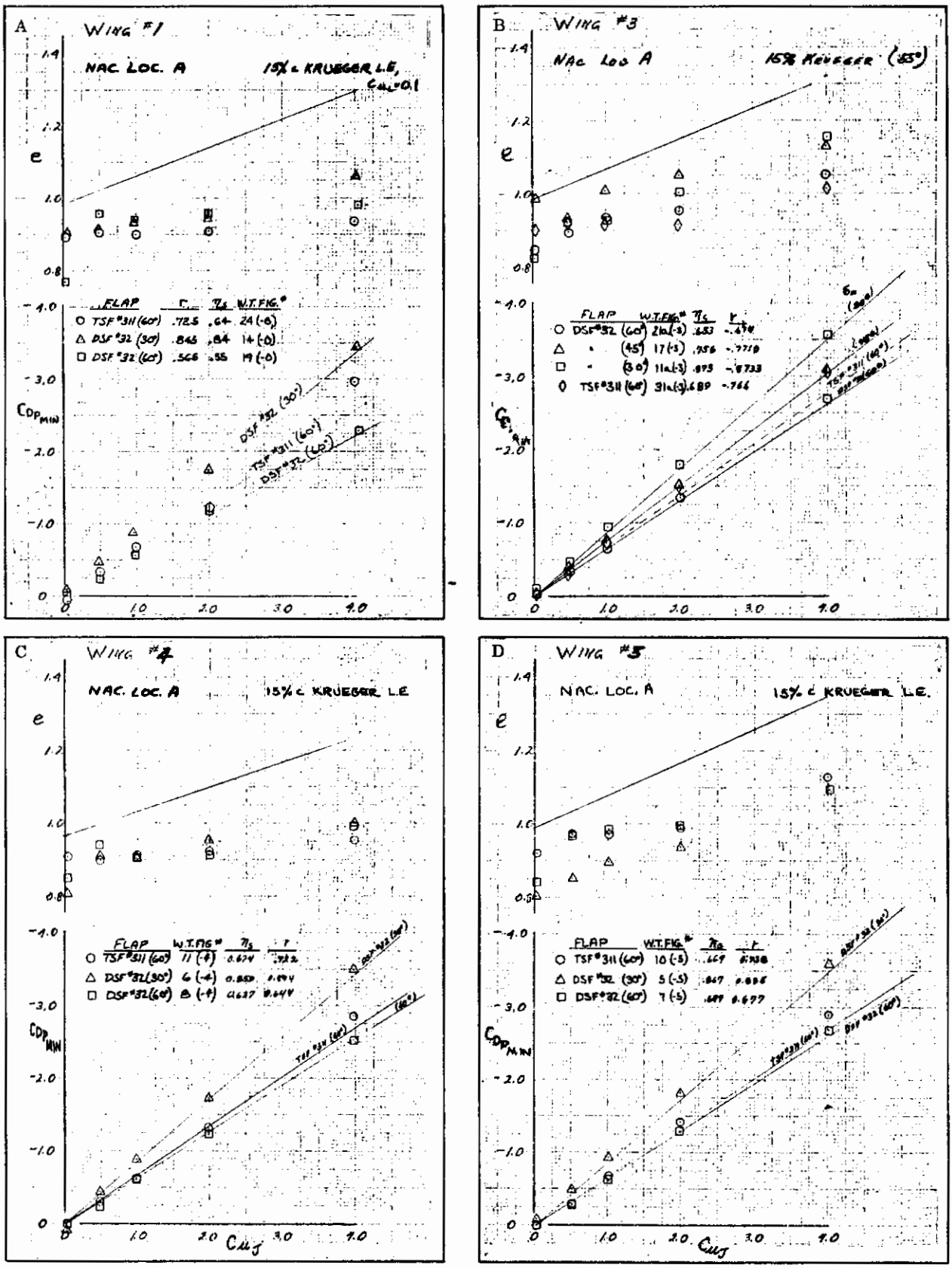

Figure 4.1-3. Effect of Trailing Edge Flap Configuration on Thrust Recovery

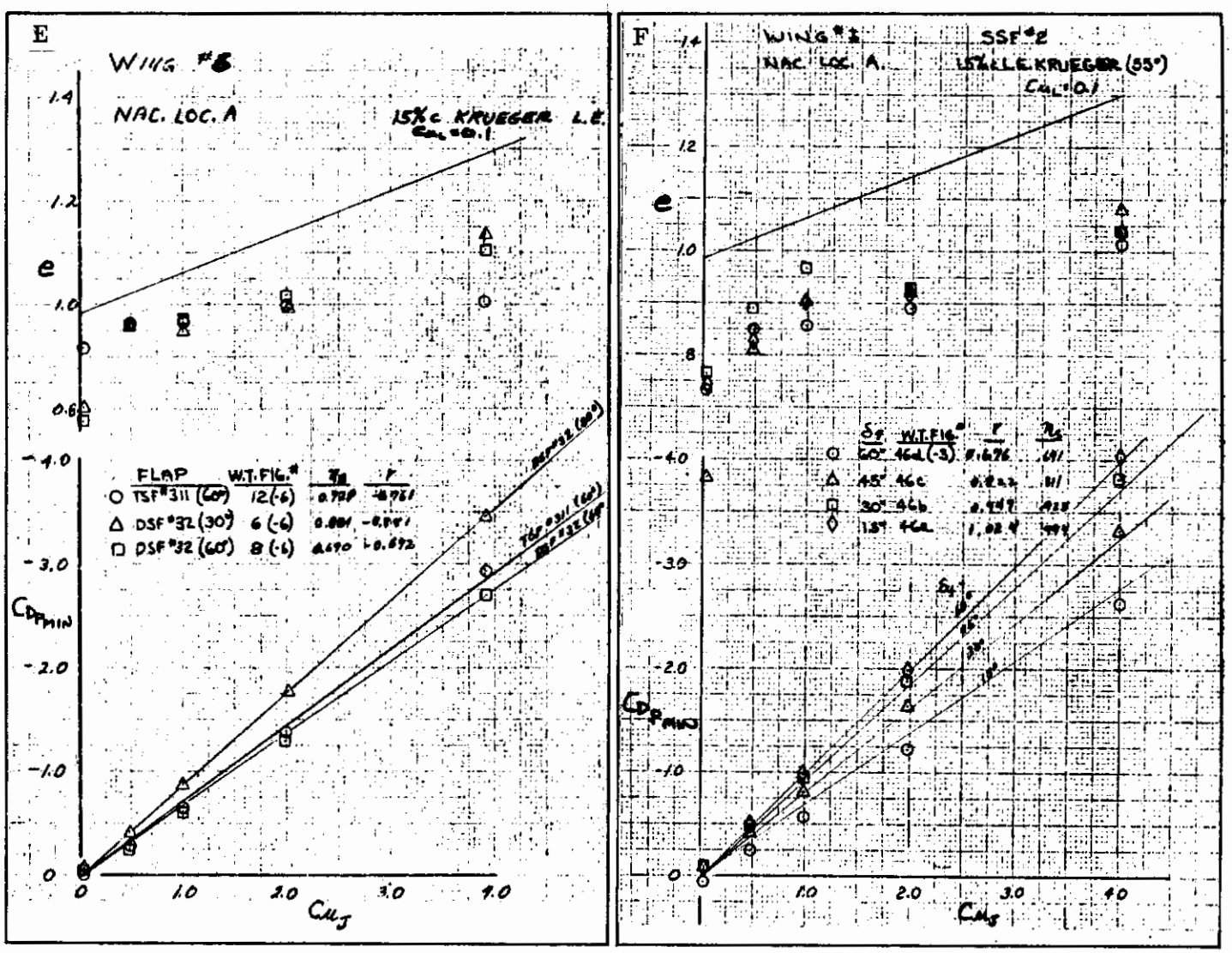

Figure 4.1-3. Effect of Trailing Edge Flap Configuration on Thrust Recovery, Cont

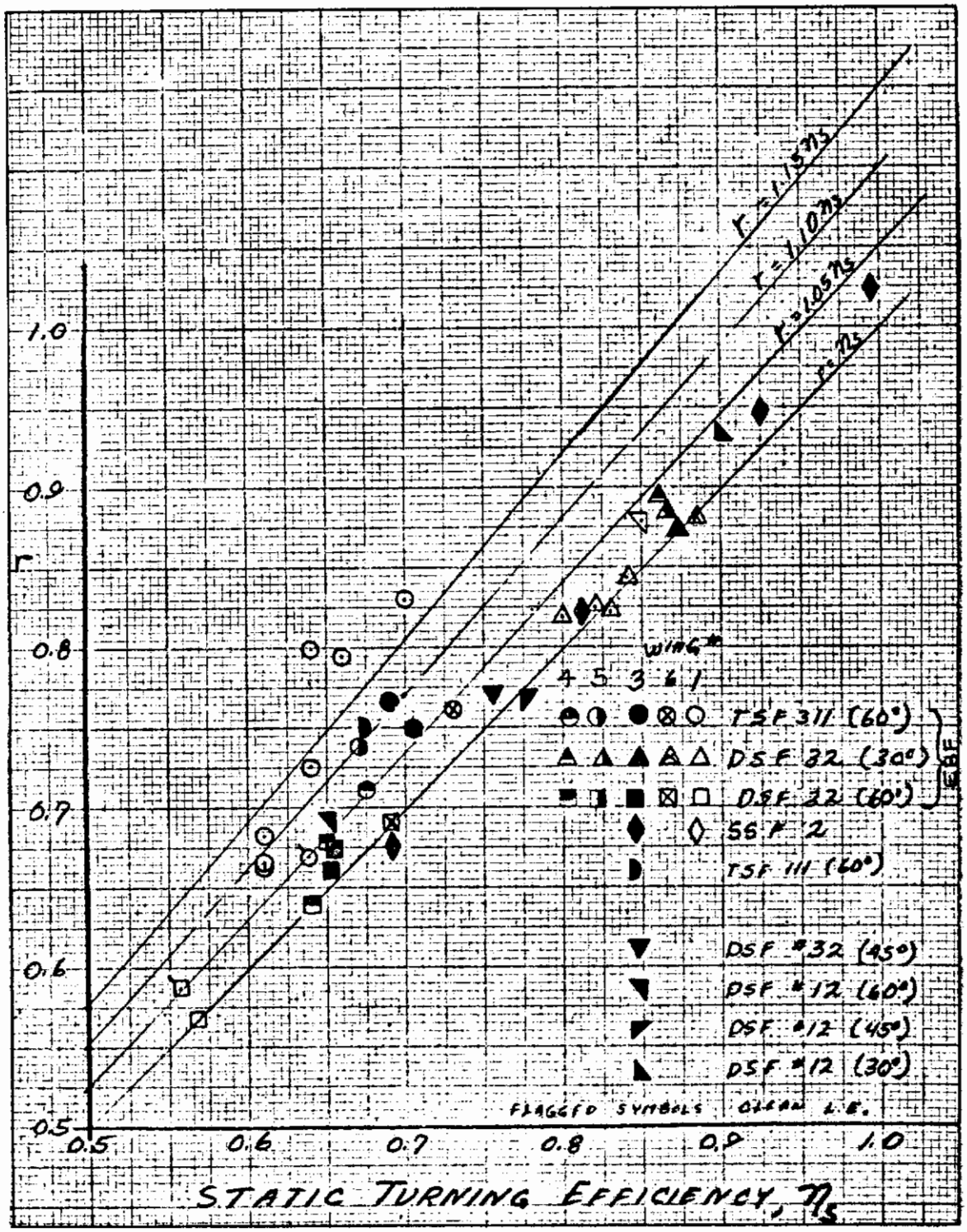

Figure 4.1-4. Correlation of Thrust Recovery with Static Turning Efficiency

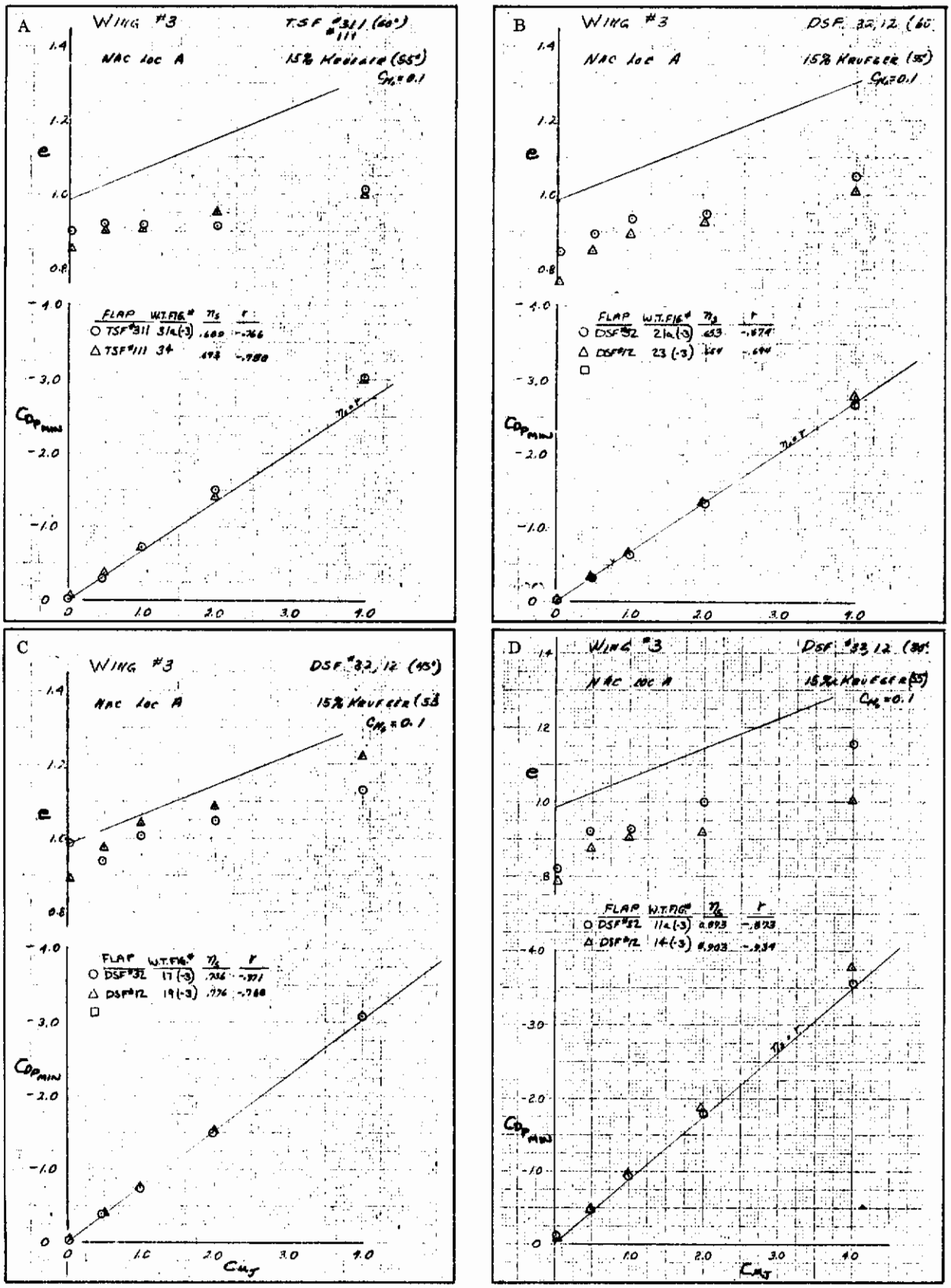

Figure 4.1-5. Effect of Trailing Edge Flap Chord on Thrust Recovery

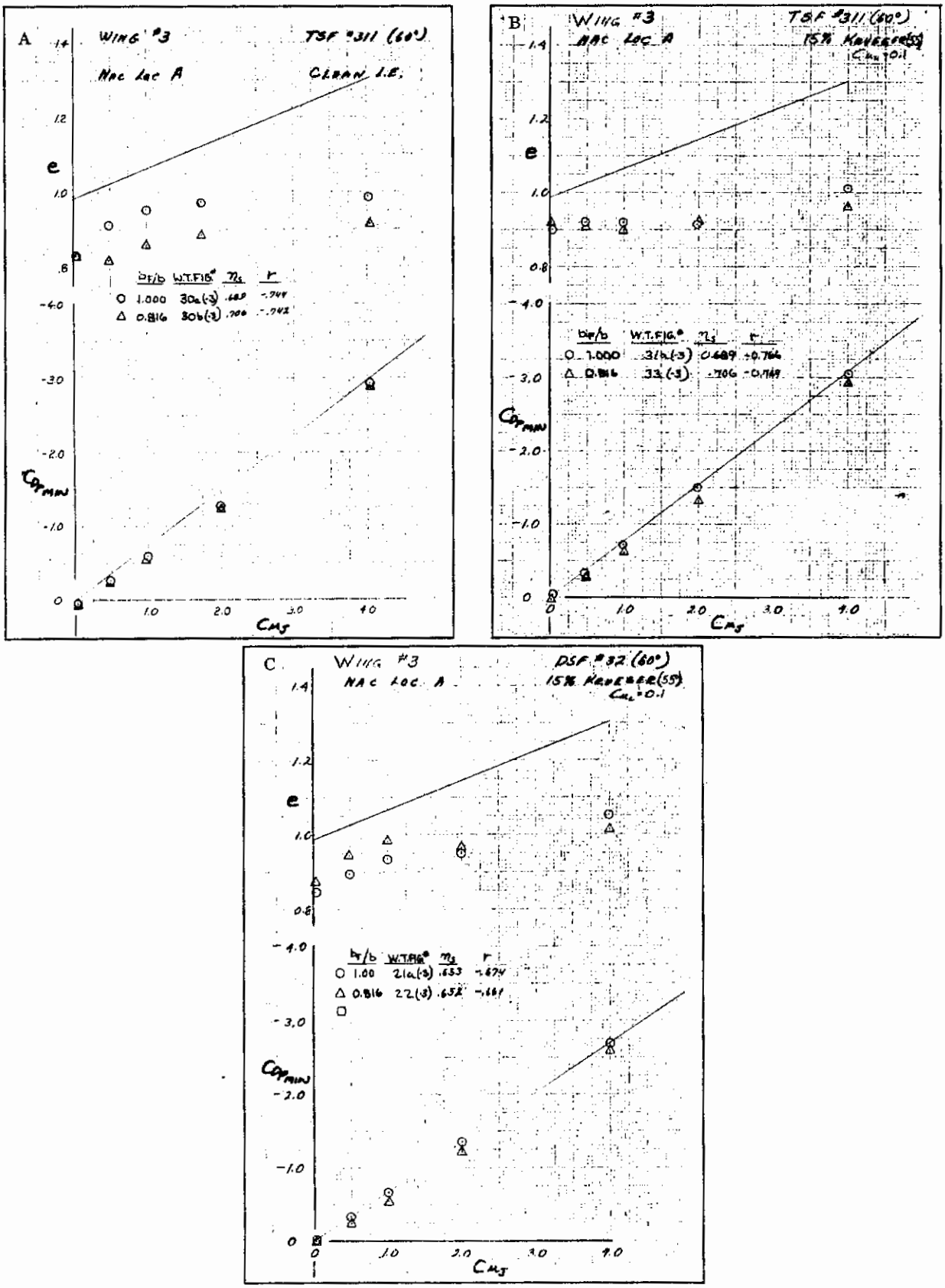

Figure 4.1-6. Effect of Trailing Edge Partial Span Flap on Thrust Recovery

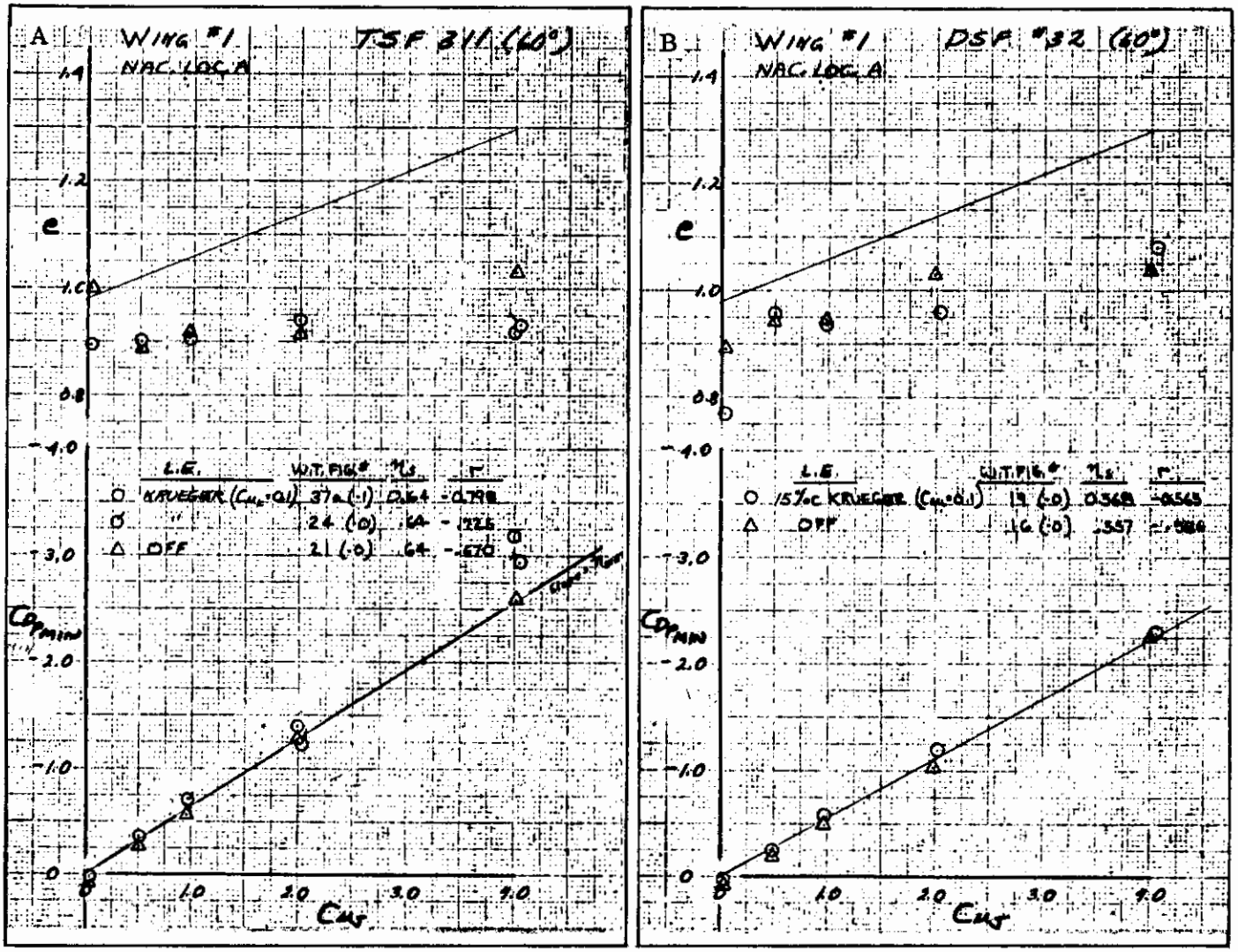

Figure 4.1-7. Effect of Leading Edge Blowing on Thrust Recovery

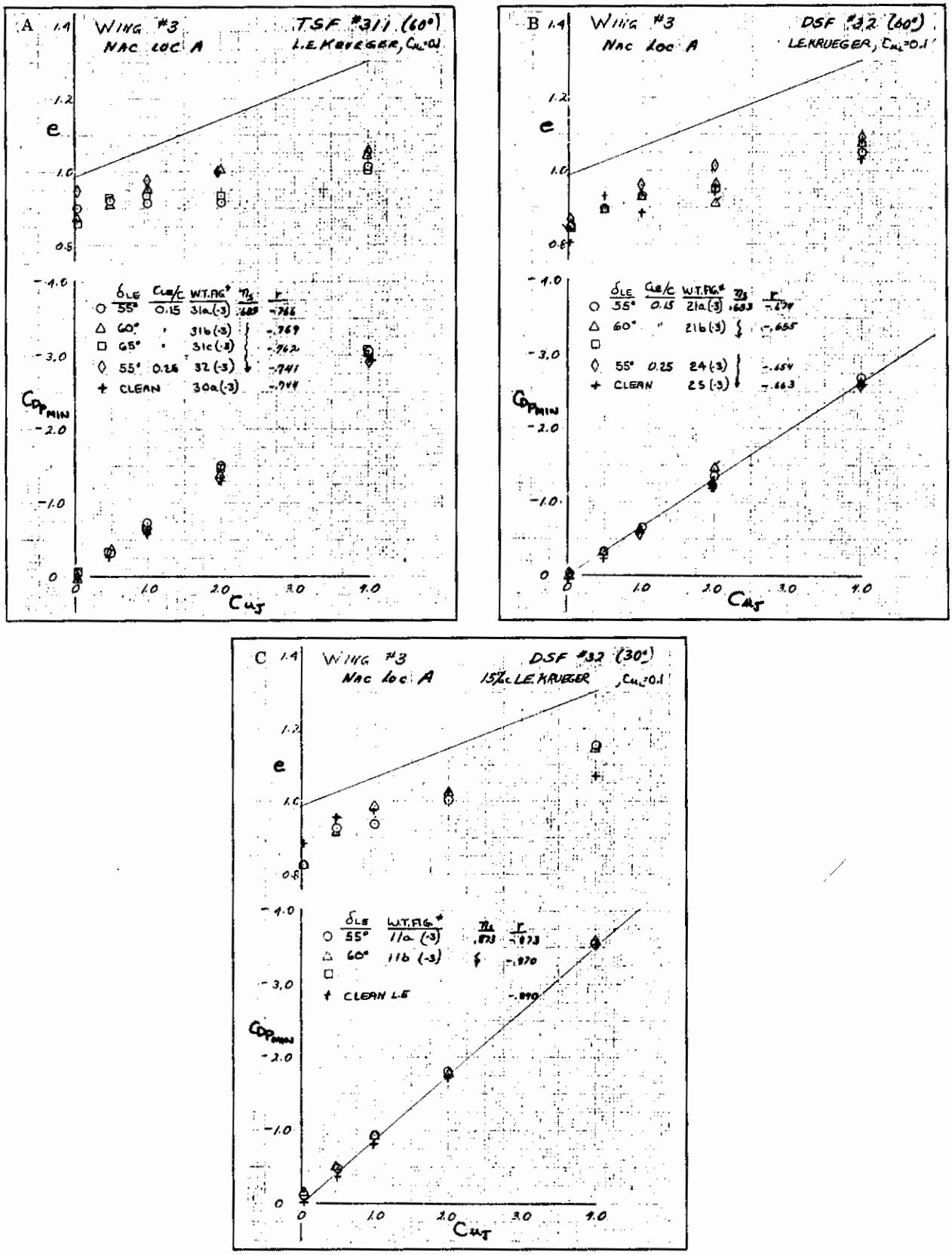

Figure 4.1-8. Effect of Leading Edge Krueger Flap Deflection and Chord on Thrust Recovery

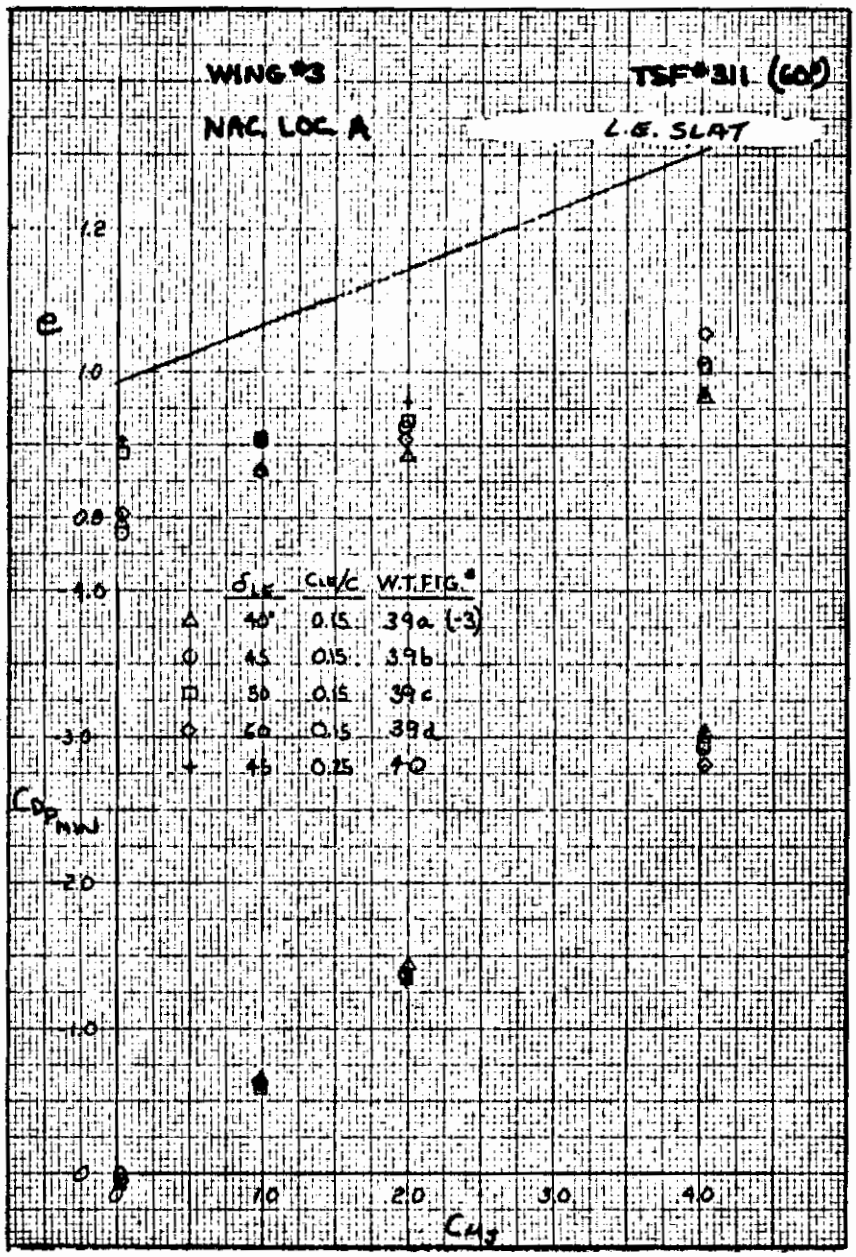

Figure 4.1-9. Effect of Leading Edge Slat Flap Deflection and Chord on Thrust Recovery

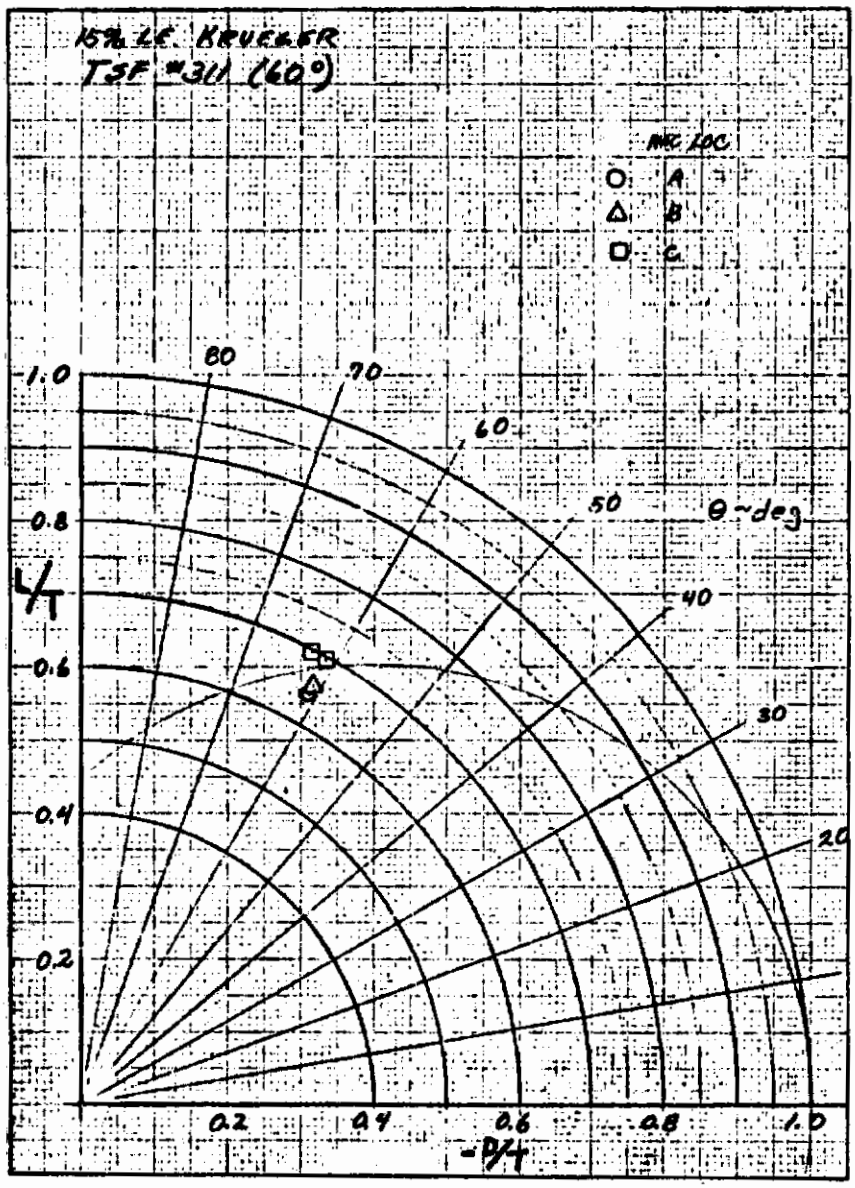

Figure 4.1-10. Effect of Spanwise Nacelle Location on Static Turning Efficiency

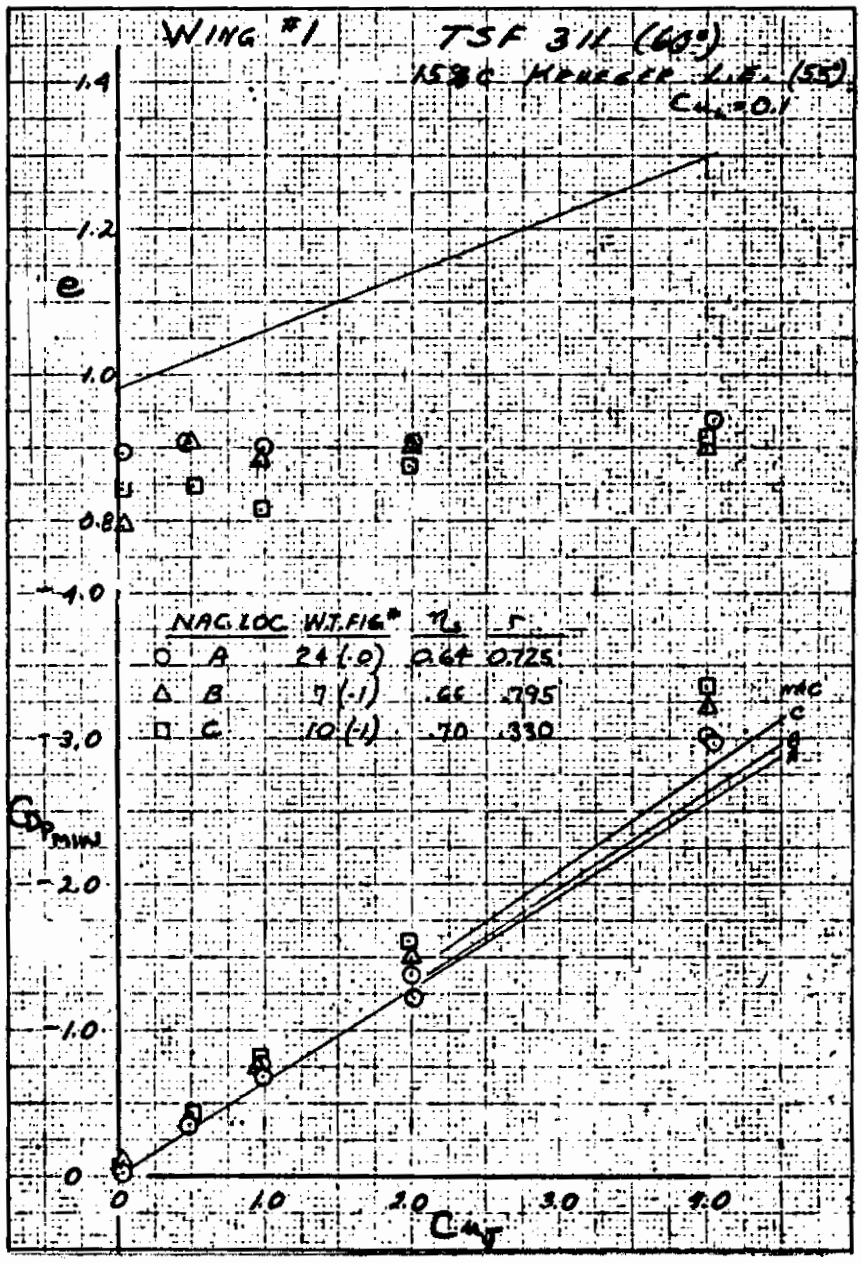

Figure 4.1-11. Effect of Spanwise Nacelle Location on Thrust Recovery

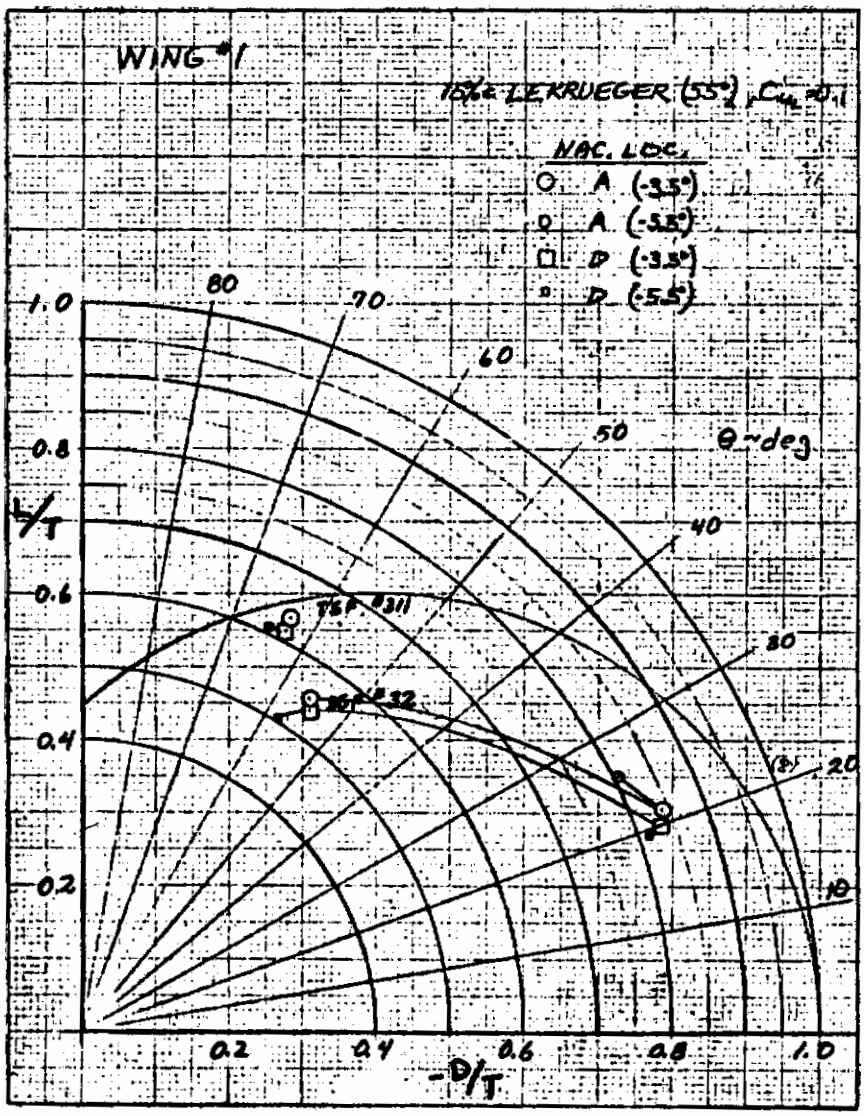

Figure 4.1-12. Effect of Chordwise Nacelle Location on Static Turning Efficiency

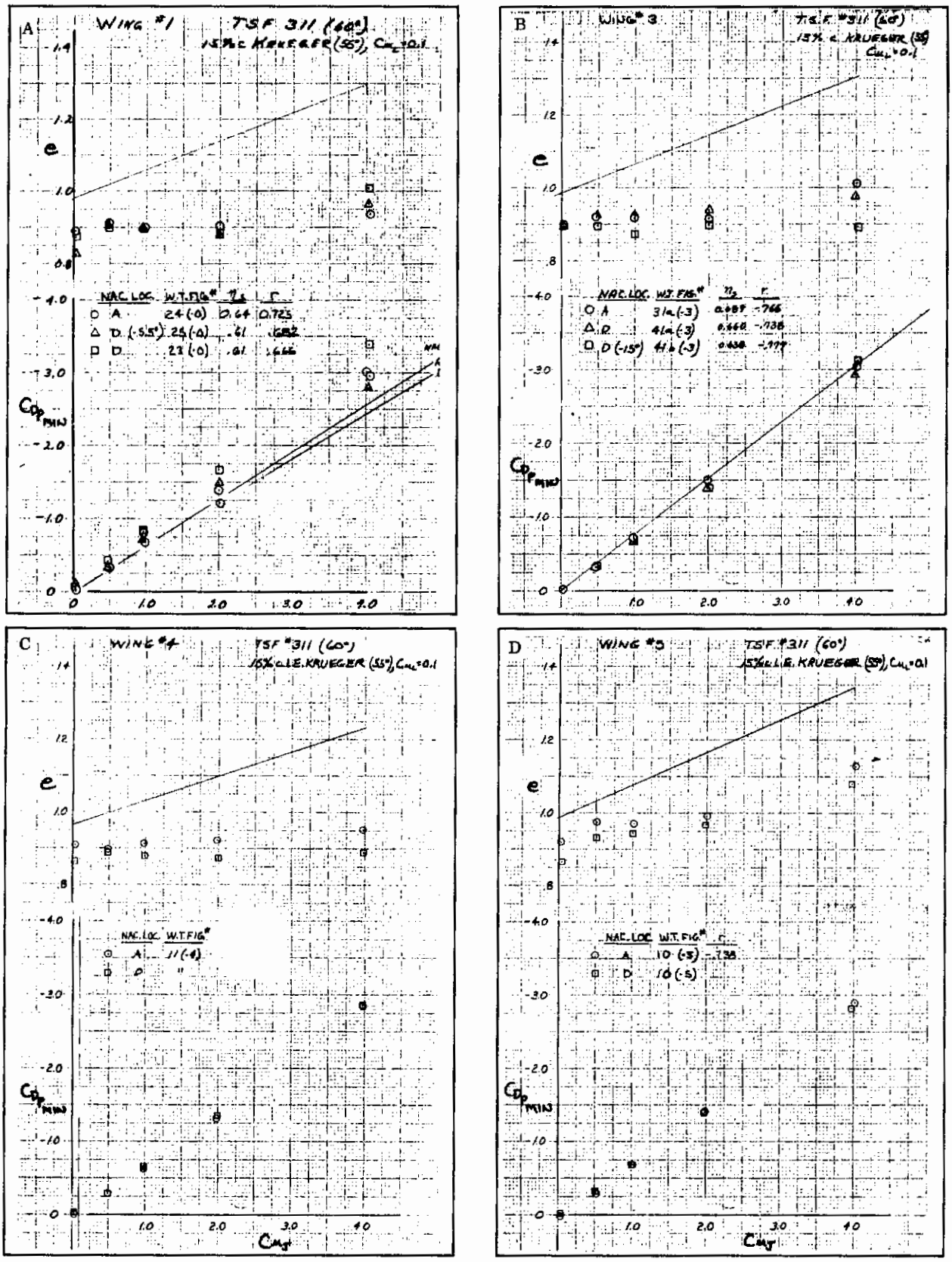

Figure 4.1-13. Effect of Chordwise Nacelle Location on Thrust Recovery

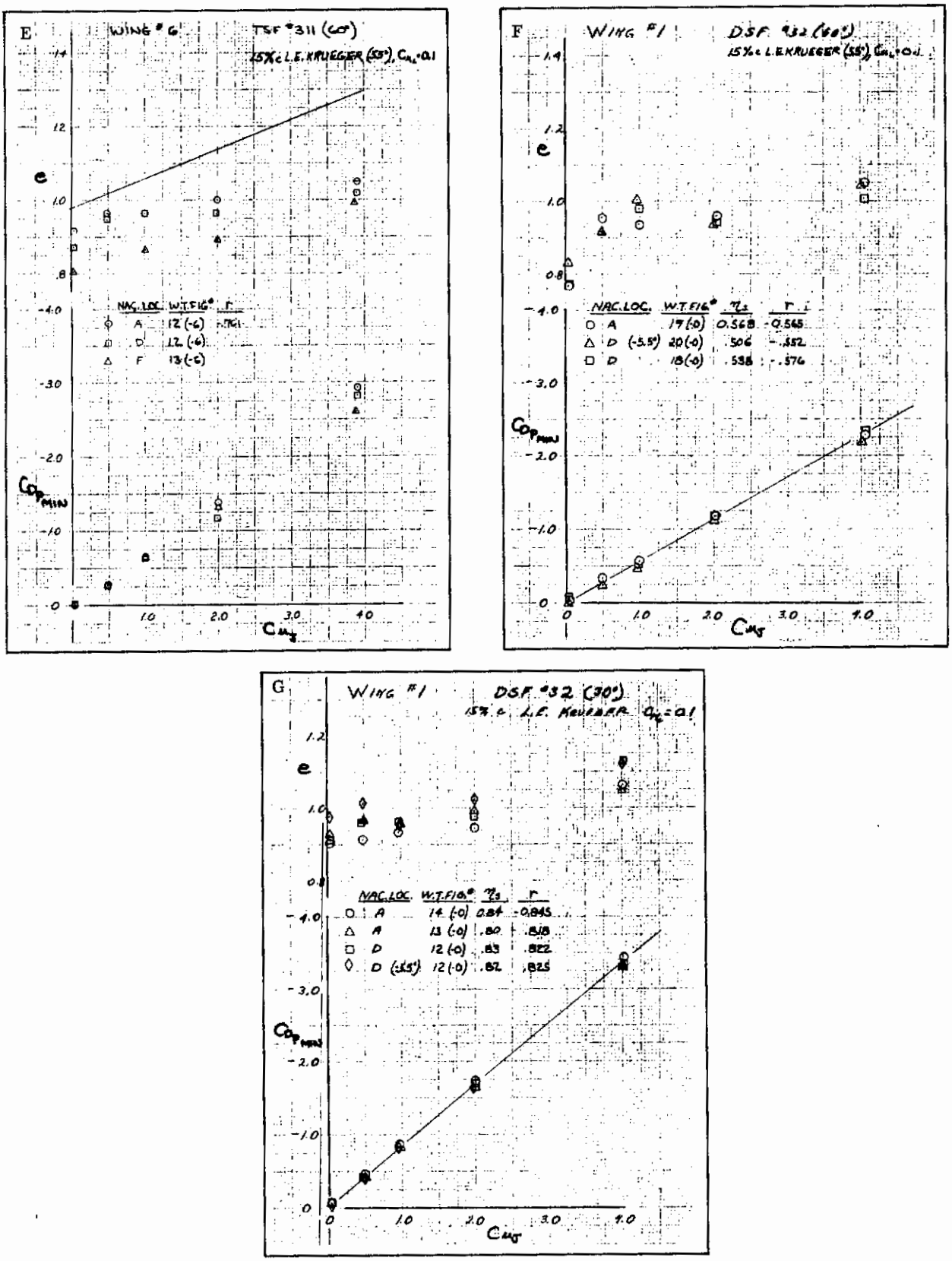

Figure 4.1-13. Effect of Chordwise Nacelle Location on Thrust Recovery, Cont

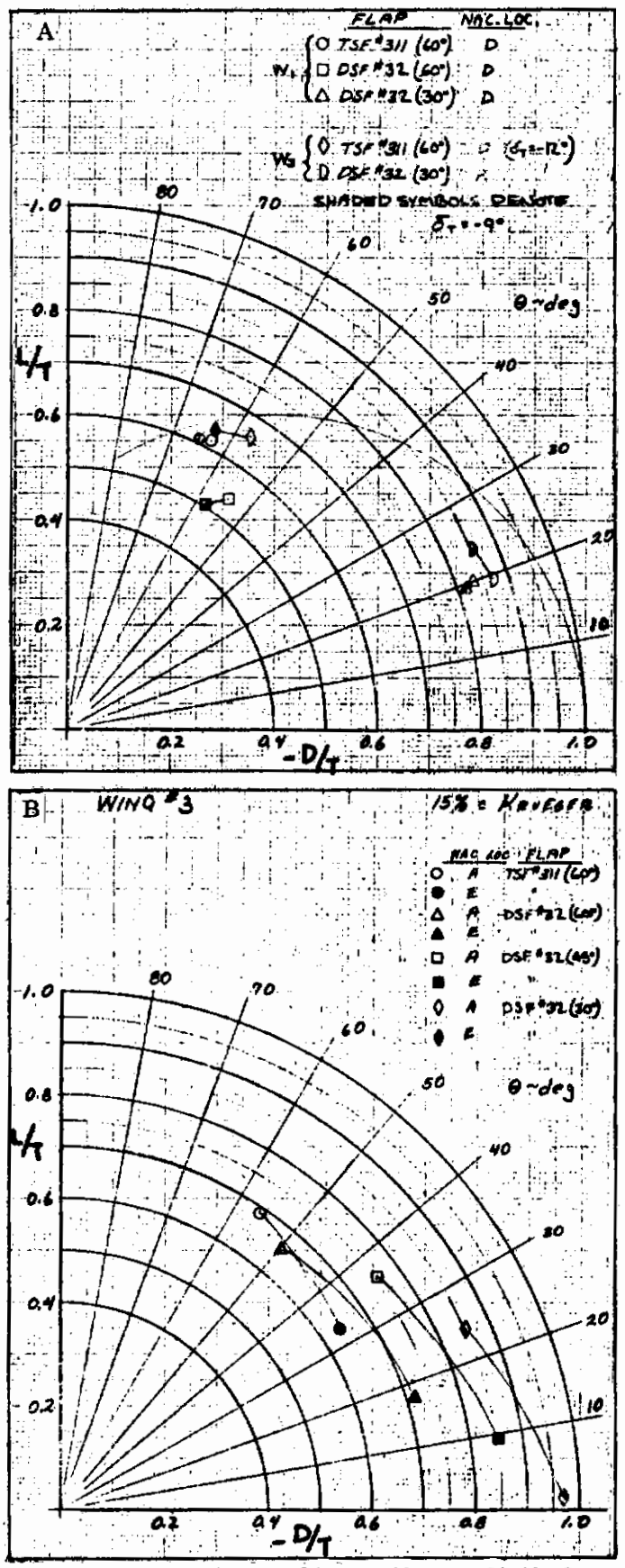

Figure 4.1-14. Effect of Nacelle Height Location on Static Turning Efficiency

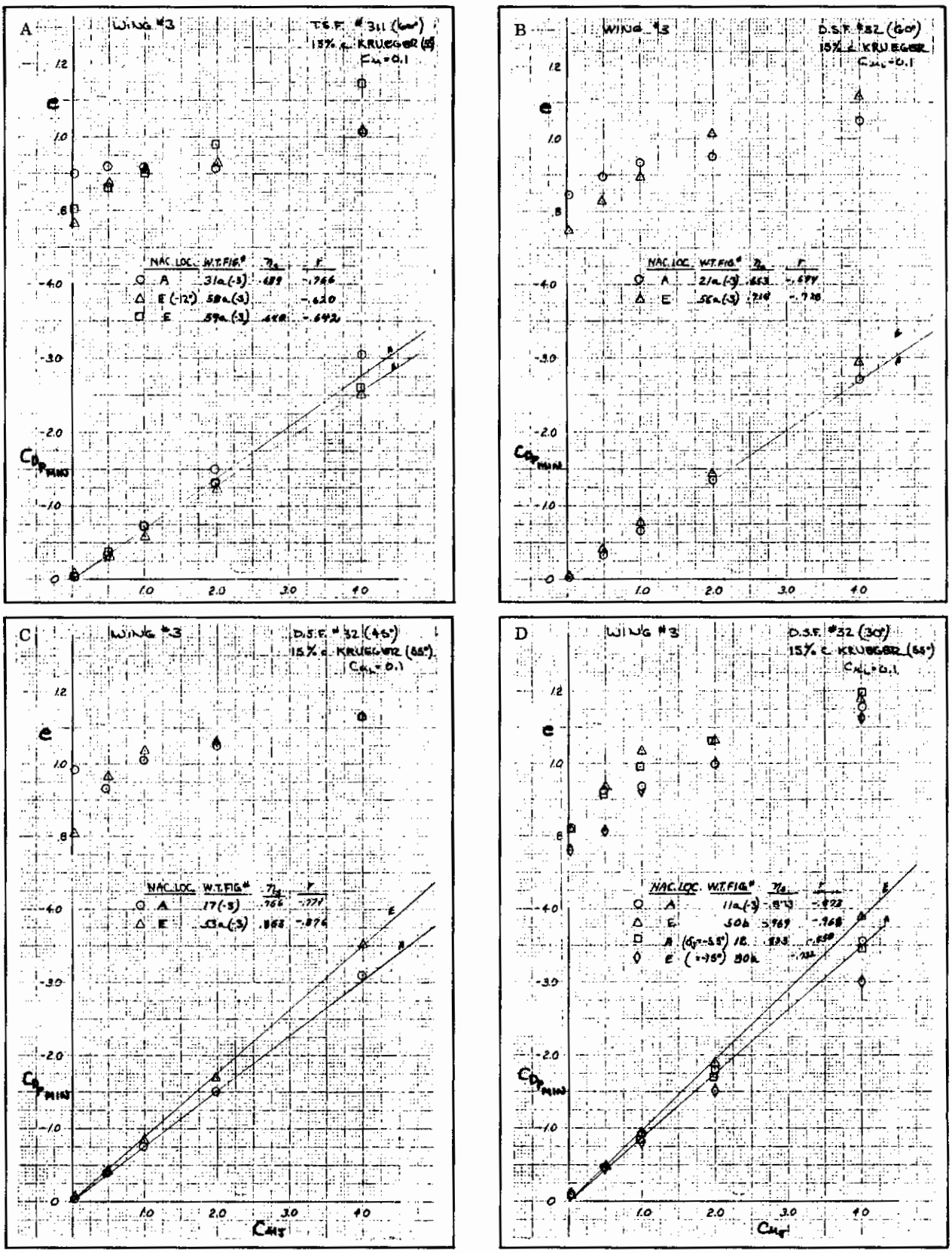

Figure 4.1-15. Effect of Nacelle Height Location on Thrust Recovery

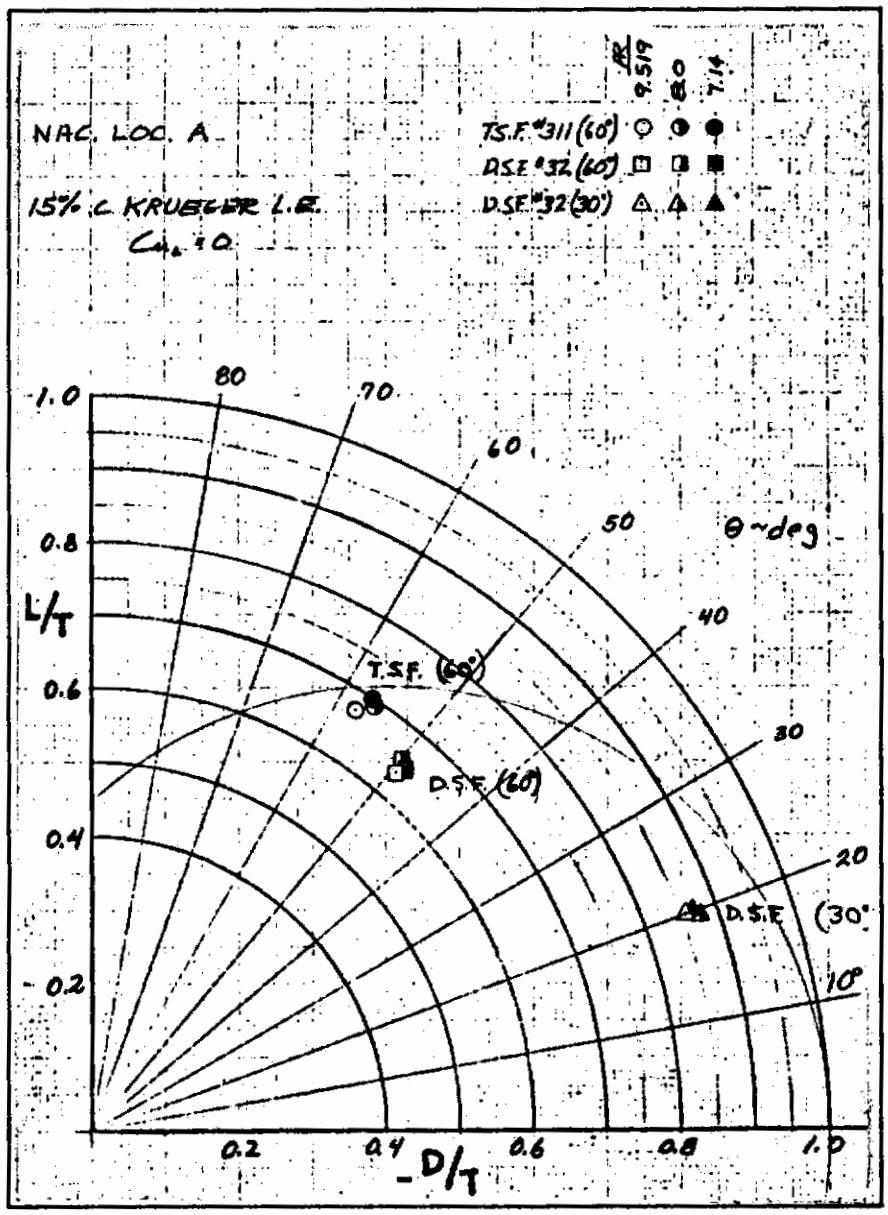

Figure 4.1-16. Effect of Aspect Ratio on Static Turning Efficiency

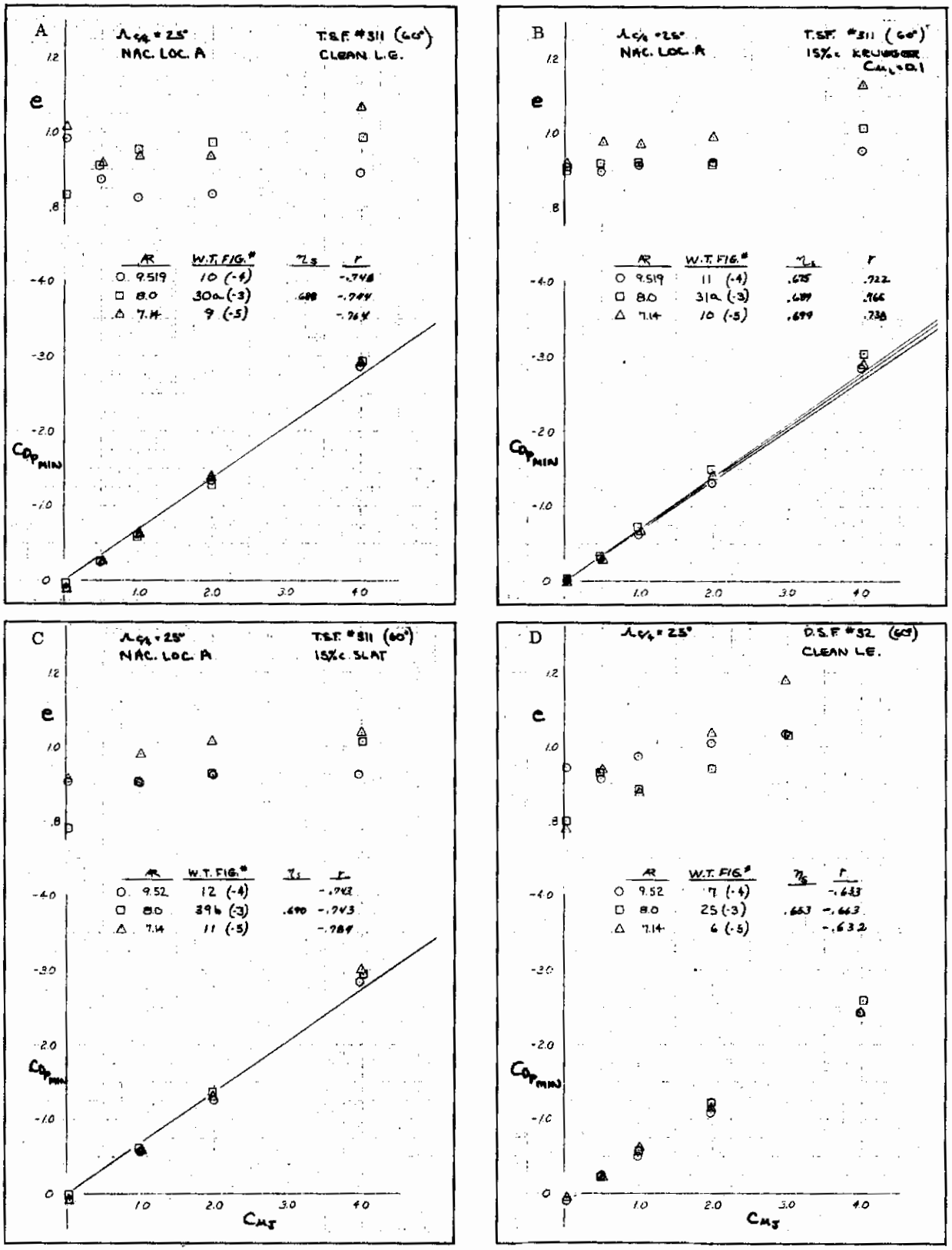

Figure 4.1-17. Effect of Aspect Ratio on Thrust Recovery

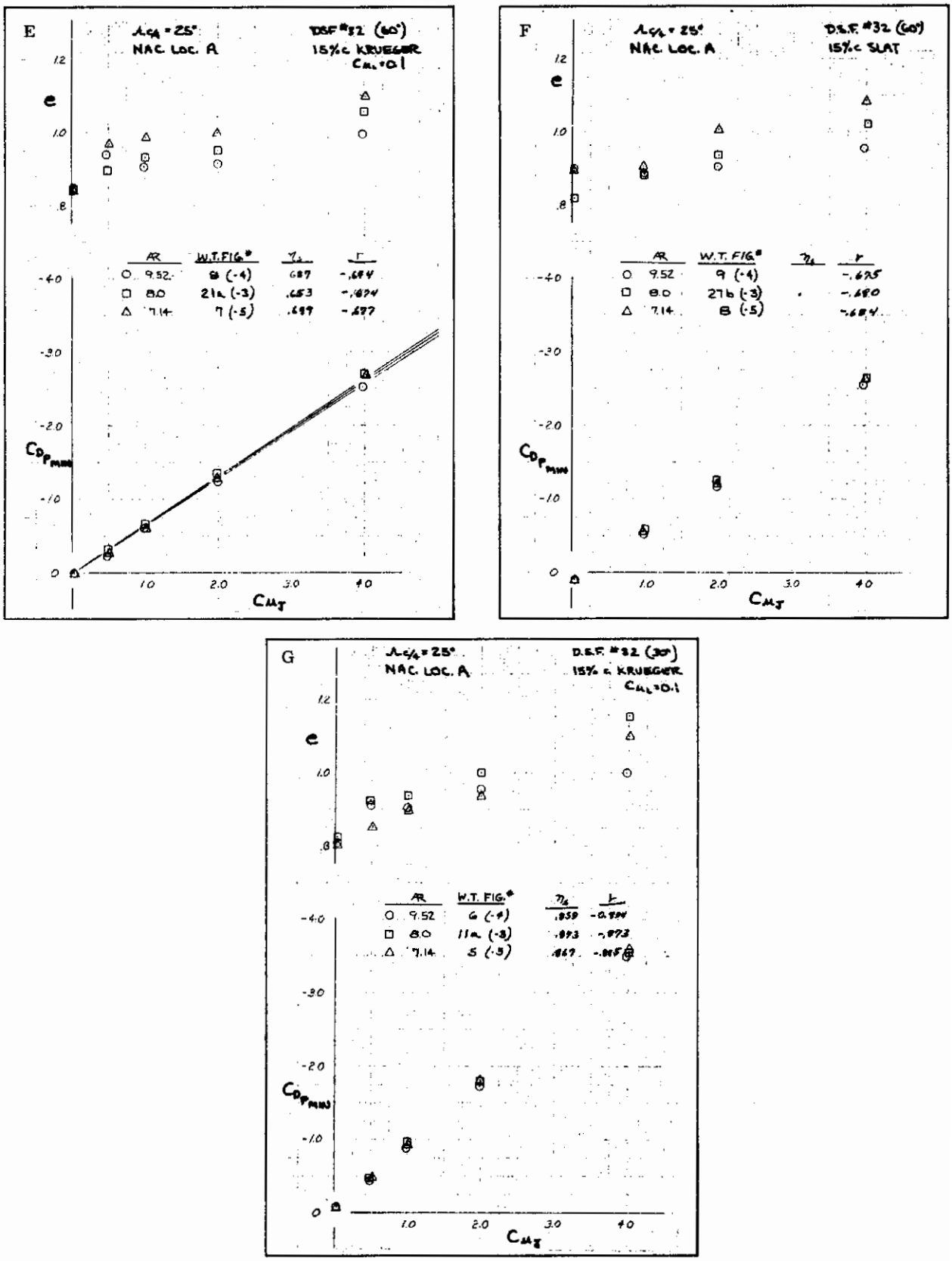

Figure 4.1-17. Effect of Aspect Ratio on Thrust Recovery, Cont

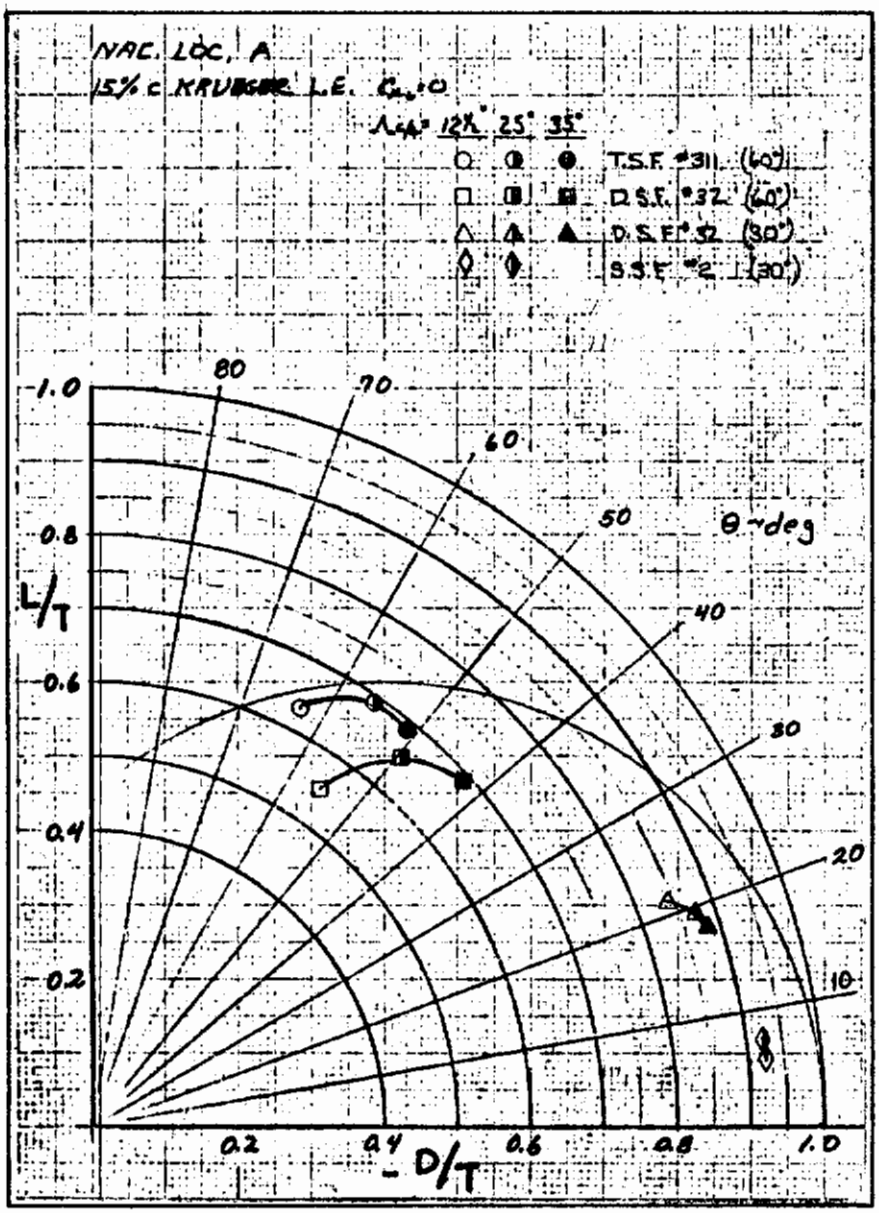

Figure 4.1-18. Effect of Wing Sweep on Static Turning Efficiency

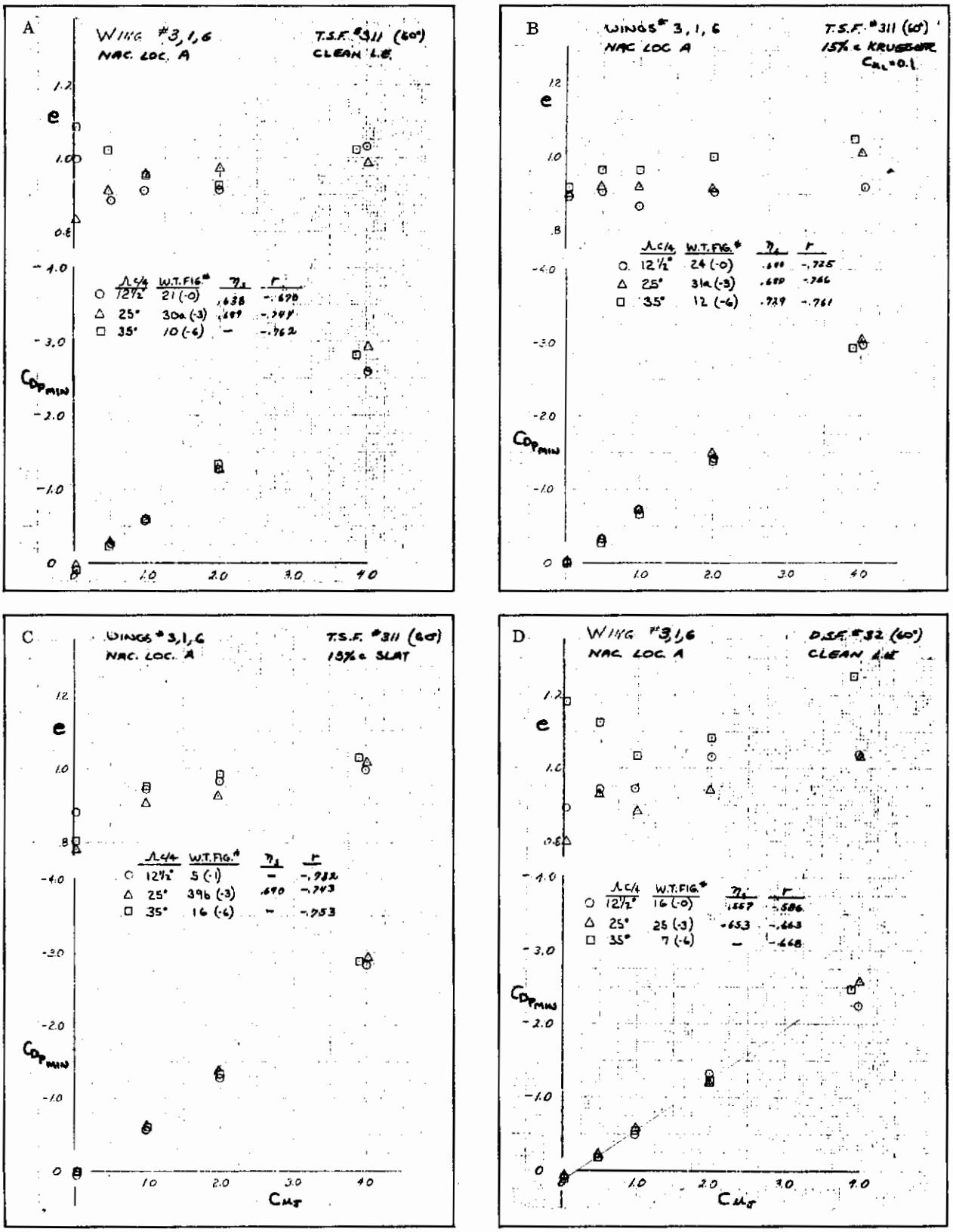

Figure 4.1-19. Effect of Wing Sweep on Thrust Recovery

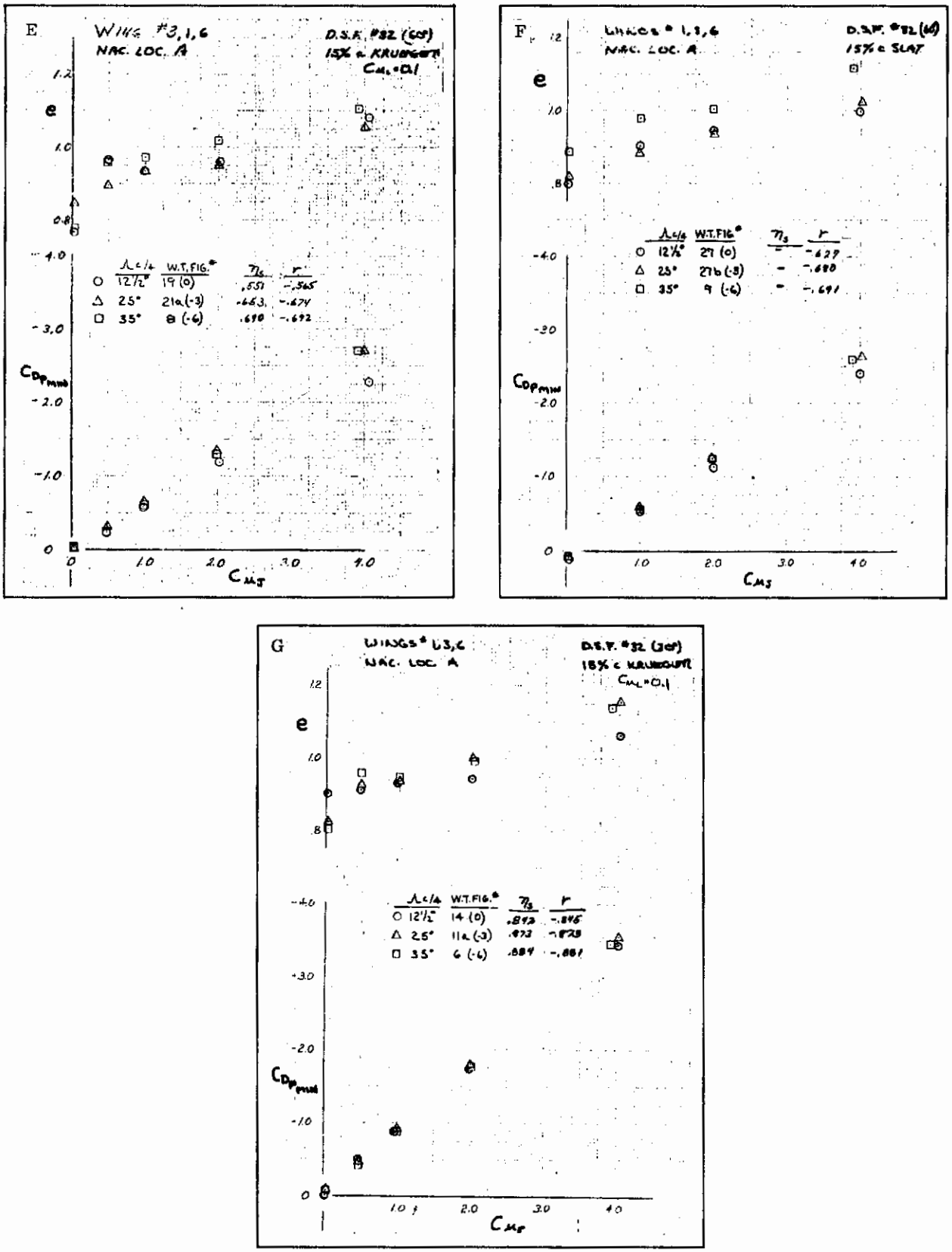

Figure 4.1-19. Effect of Wing Sweep on Thrust Recovery, Cont

4.2 IBF THRUST RECOVERY AND INDUCED DRAG

Results of the wind tunnel test axial force analysis for the IBF systems are shown in this section. The data is presented as the variation of the induced drag factor, e, and the minimum profile drag, $C_{D_{Pmin}}$, with the momentum coefficient $C_{\mu T}$ measured at the nozzle. This momentum coefficient is based on the basic reference wing area not on the area spanned by the blowing slot, as in the discussions on lift. This will make the momentum coefficient and drag coefficient reference to the same area.

Thrust recovery, r, defined as the change in minimum profile drag, $C_{D_{Pmin}}$, with a change in momentum coefficient is tabulated on the data plots along with static turning efficiency. These values of thrust recovery have been measured using a linear least-squares curve fit of the data points.

The effect of momentum coefficient on the induced drag factor is also shown in this analysis. As mentioned in Paragraph 4.1, this parameter is difficult to measure accurately from test data. In general, it can be stated that blowing from the nozzle ahead of the flap increases the induced drag factor but not as much as predicted by lifting line theory. This comparison is seen on some of the figures.

Static test data is seen in Figure 4.2-1 for several IBF configurations. The data shows that turning efficiency is 80 percent for a plain blown flap at 60 degrees of flap deflection, increasing to 84 percent at 30 degrees of flap deflection. Turning angle is greater than the flap deflection angle, but not as great as the deflection angle plus the angle of the upper surface of the flap. The effects of wing sweep, which are also shown, reduce both the turning efficiency and the turning angle, indicating more spanwise flow with the higher swept wing. The single-slotted flap at 30 degrees of flap deflection shows an increase in turning efficiency from 84 to slightly over 90 percent, with only a small reduction in turning angle.

4.2.1 EFFECT OF TRAILING EDGE FLAP CONFIGURATION ON THRUST RECOVERY. The difference in thrust recovery between a single-slotted and a plain IBF is shown in Figure 4.2-2. The single-slotted flap with 30 degrees of deflection shows an increase in thrust recovery over the plain blown flap at the same deflection. This trend is shown for nacelles-off with a clean leading edge and nacelles-on with a Krueger leading edge configuration. This same trend is also shown with static efficiency in Figure 4.2-1.

The effect of flap deflection on thrust recovery is shown in Figure 4.2-3a through 4.2-3c. Thrust recovery is highest with the 60-degree flap deflections and decreases with reductions in flap deflection. This trend is the same for each of the three configurations shown and is readily seen in a crossplot of thrust recovery with flap deflection in Figure 4.2-3d. Here the significant reduction in thrust recovery with flap deflection is seen to approach the static turning efficiency values at the low flap deflection. The large values in thrust recovery at the high flap deflections are due

to a large drag reduction caused by eliminating large areas of non-potential flow on the wing and flap by blowing over the top surface of the flap. These areas of non-potential flow would be less at the lower deflections; therefore, less drag improvement would be available due to flap blowing, resulting in lower thrust recovery.

The effect of flap span, shown in Figure 4.2-4, indicates a large reduction in thrust recovery. This effective difference in thrust recovery can be attributed to an increase in induced drag due to flap cutout and is not a result on change in turning efficiency due to blowing. Large drag changes result from partial span flaps due to a change in effective aspect ratio of the heavily loaded section of the wing that is blown by the jet sheet. This drag is a function of flap lift increment only and does not vary with total lift coefficient. Therefore, it shows an increase in minimum profile drag and not as a change in induced drag factor.

4.2.2 EFFECT OF LEADING EDGE CONFIGURATION ON THRUST RECOVERY. The configuration of the wing leading edge has only a small effect on thrust recovery of the trailing-edge blowing system. This is shown in Figure 4.2-5 where thrust recovery with a blown 15-percent-chord Krueger flap leading edge is slightly improved over the clean leading edge configuration.

4.2.3 EFFECT OF ENGINE NACELLES ON THRUST RECOVERY. The effect of cruise engine nacelles located under the wing is shown in Figure 4.2-6. The data indicates that the power-off nacelles have no effect on thrust recovery of the IBF system. With application of engine power, $C_J = 2.0$, however, thrust recovery of the IBF system is reduced considerably at the large flap deflections (Figure 4.2-6a). At 15 degrees of deflection, there is less reduction in thrust recovery due to cruise engine power.

4.2.4 EFFECT OF WING SWEEP ON THRUST RECOVERY. The effect of wing sweep on thrust recovery is shown in Figure 4.2-7 for two leading-edge configurations, with engine nacelles on and off. The data indicates only a small reduction in thrust recovery with increasing wing sweep from 12.5 to 25 degrees.

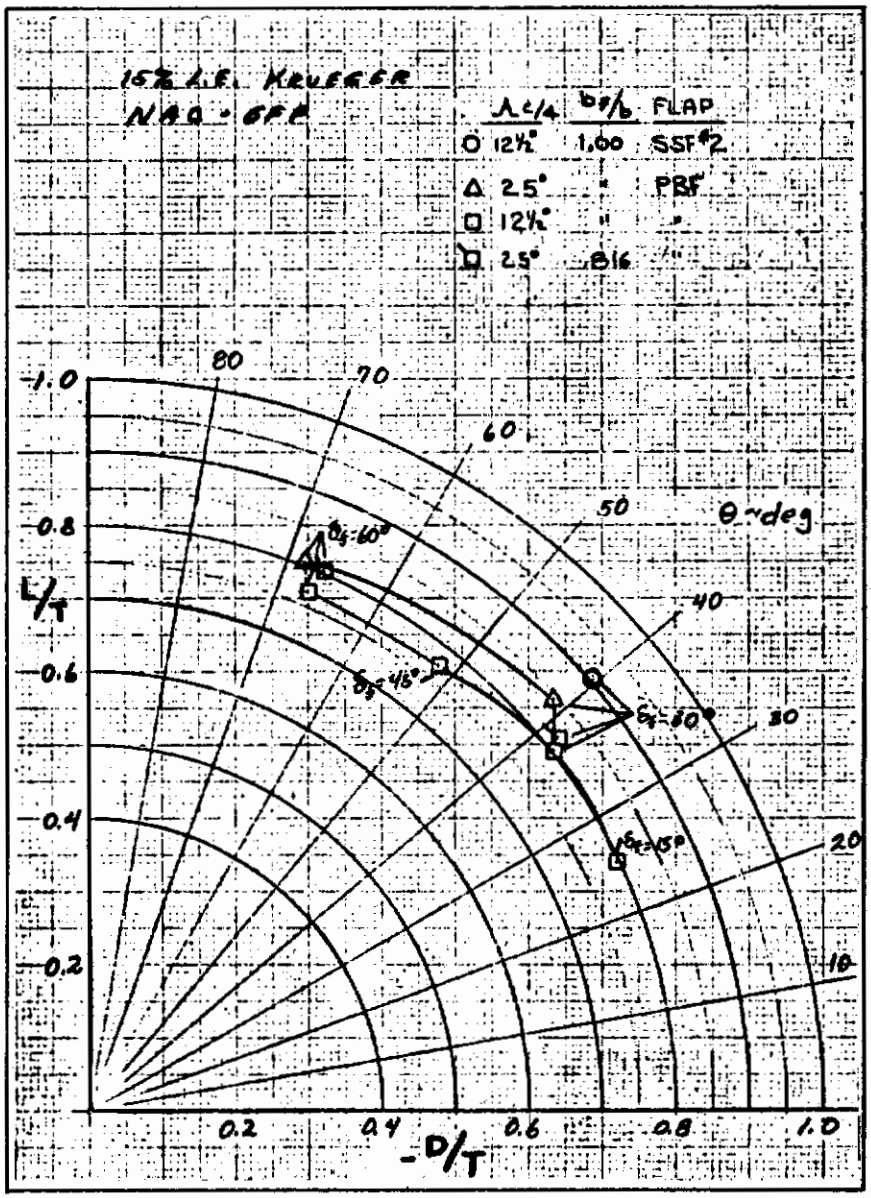

Figure 4.2-1. Effect of Trailing Edge Flap Configuration on Static Turning Efficiency

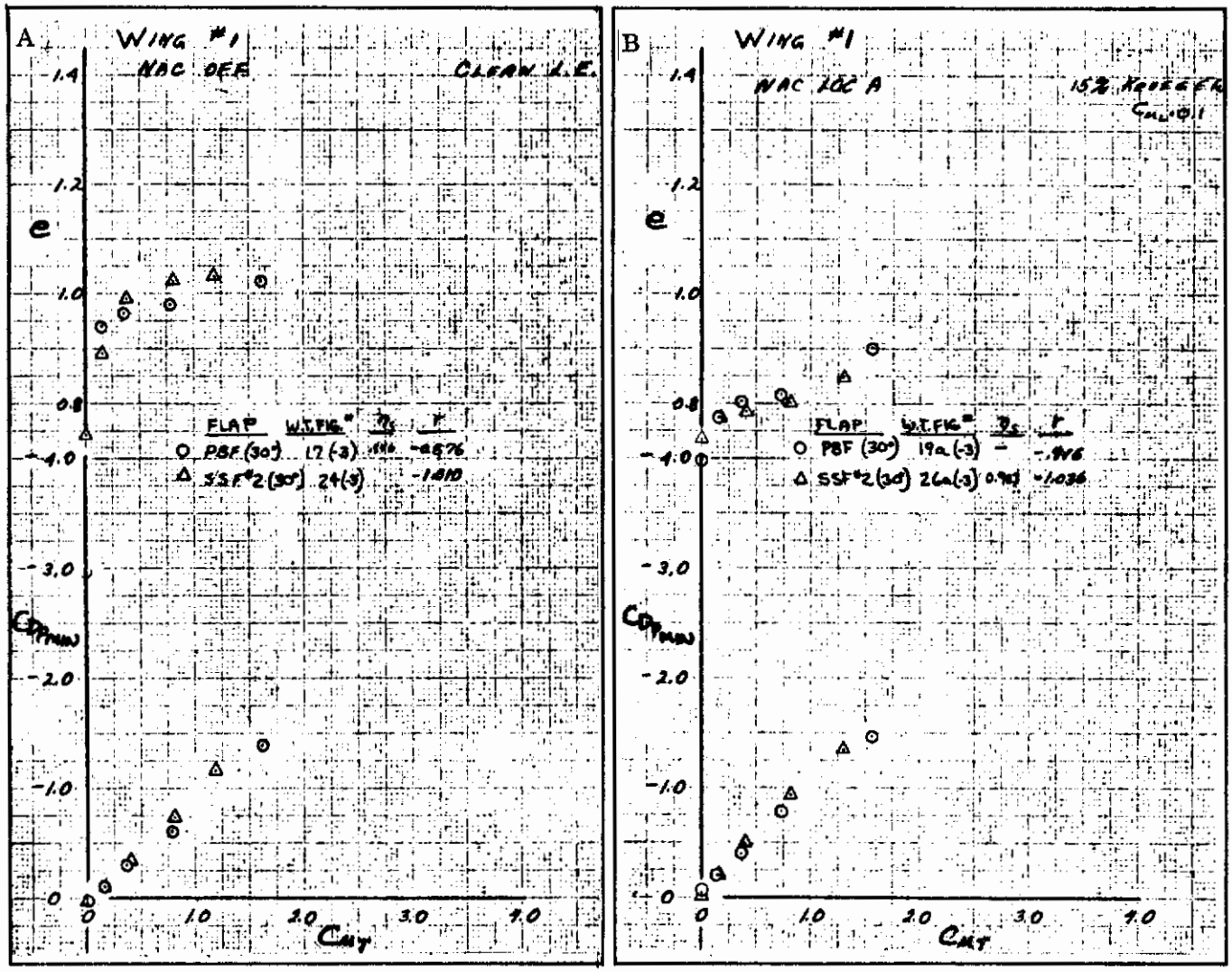

Figure 4.2-2. Effect of Trailing Edge Flap Configuration on Thrust Recovery and Induced Drag

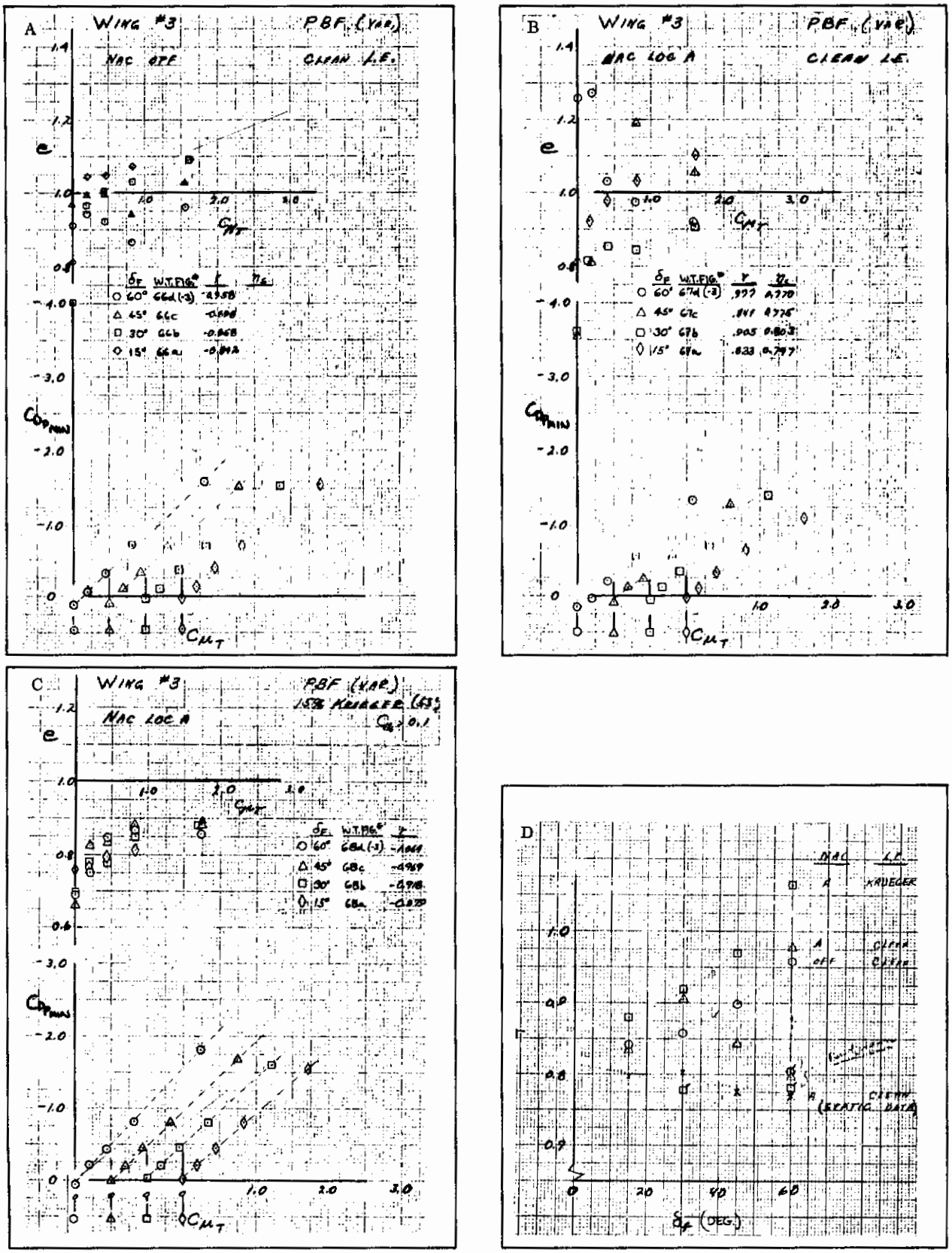

Figure 4.2-3. Effect of Trailing Edge Flap Deflection on Thrust Recovery and Induced Drag

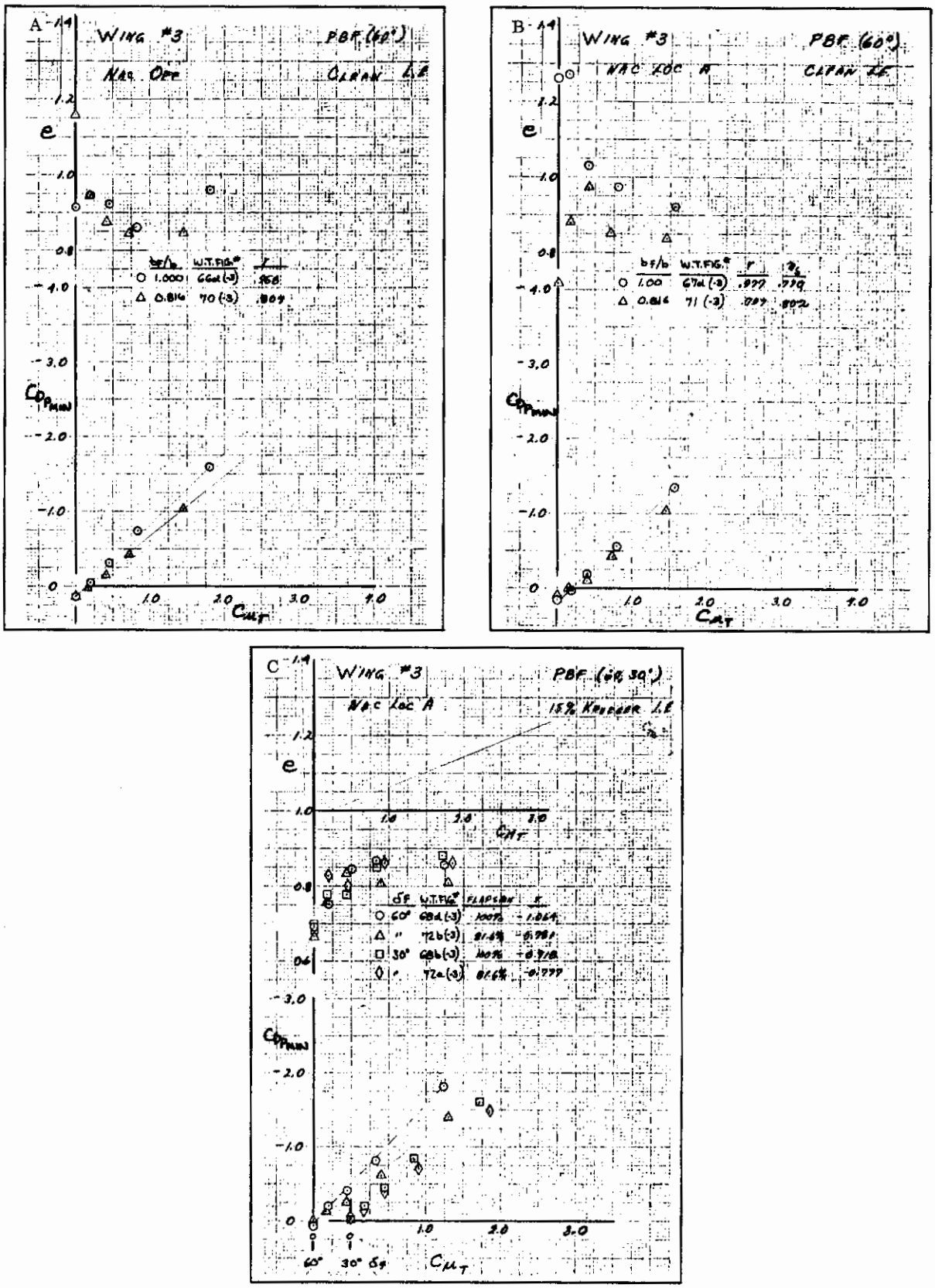

Figure 4.2-4. Effect of Partial Span Trailing Edge Flap on Thrust Recovery and Induced Drag

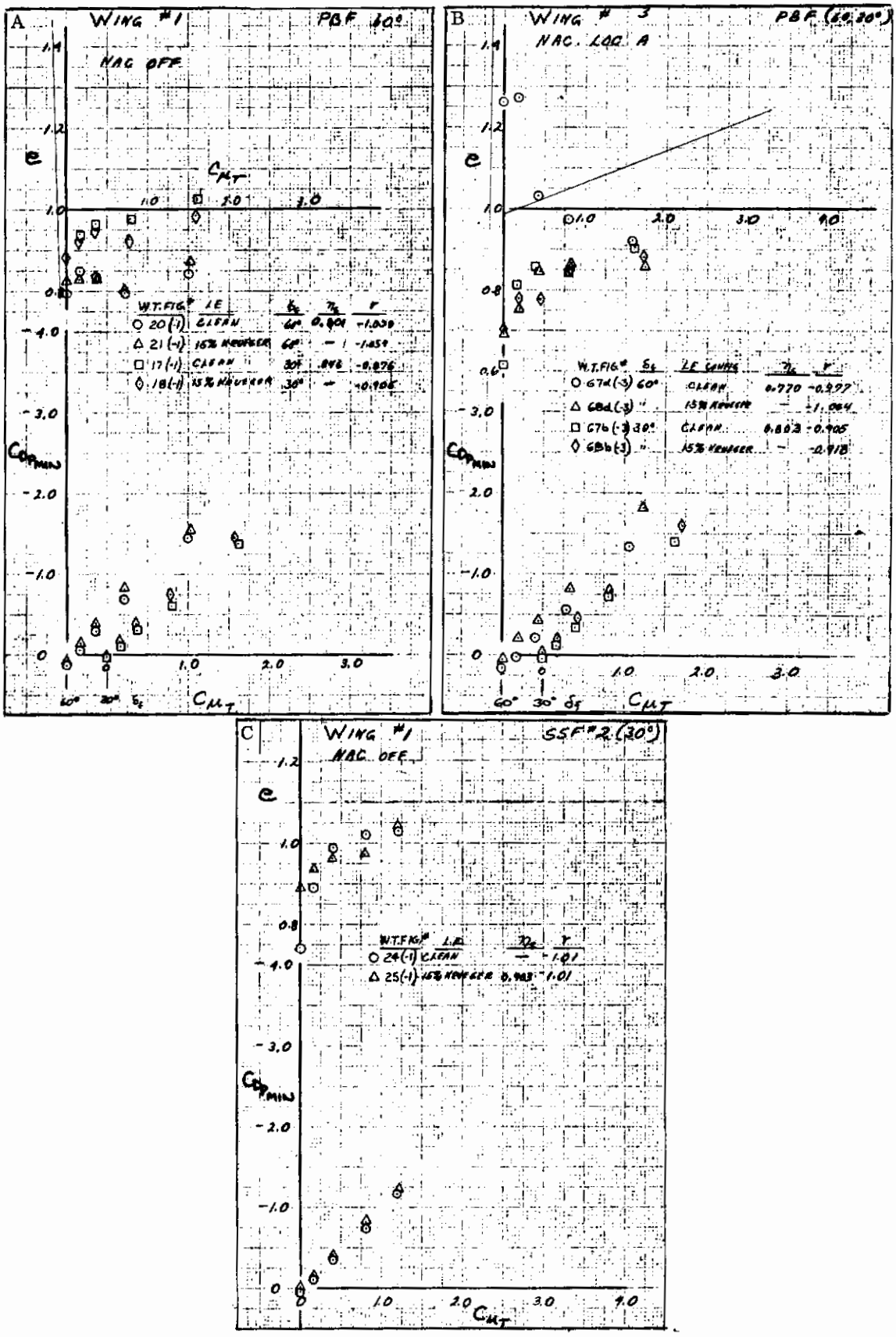

Figure 4.2-5. Effect of Leading Edge Configuration on Thrust Recovery and Induced Drag

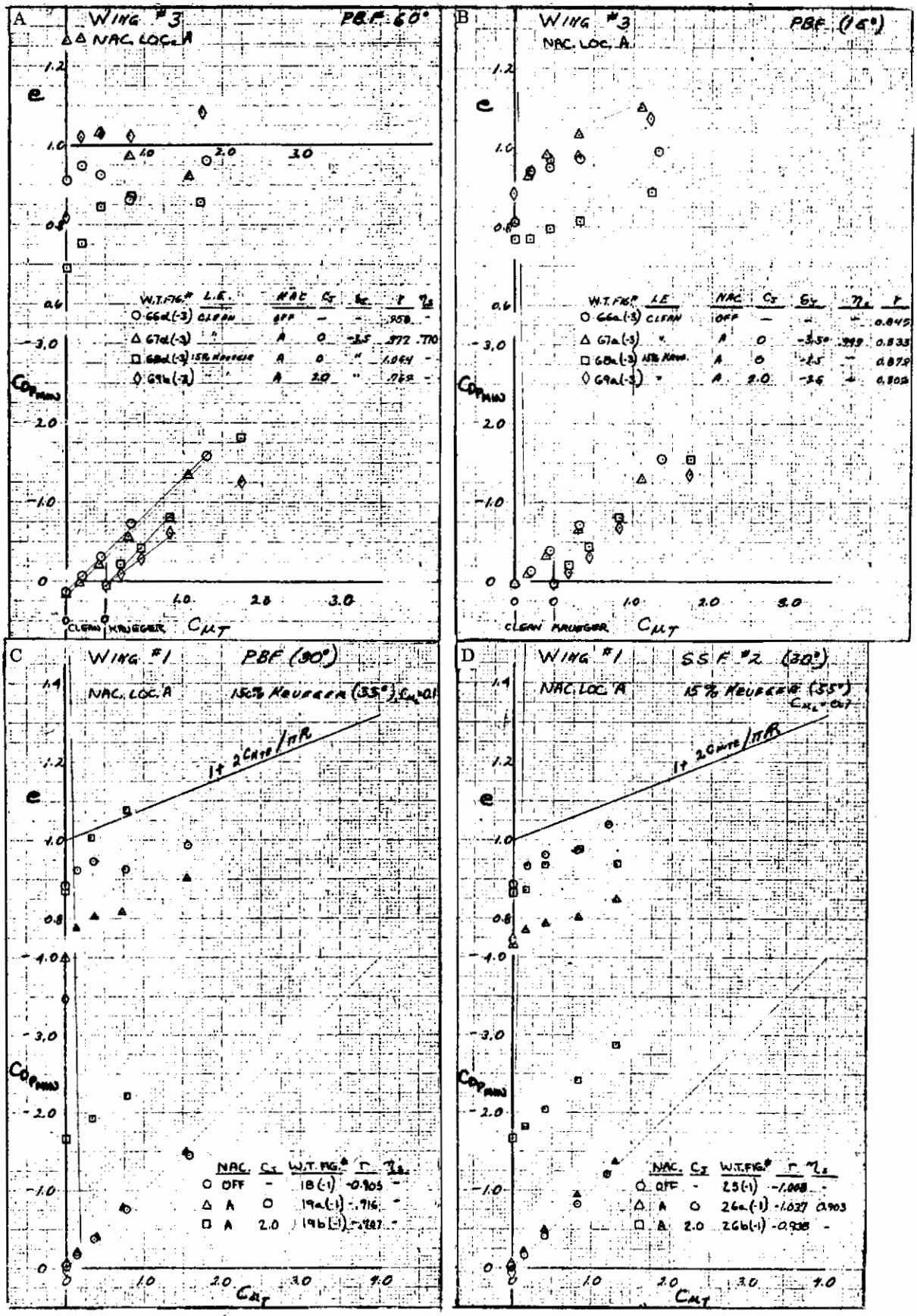

Figure 4.2-6. Effect of Engine Nacelles on Thrust Recovery and Induced Drag

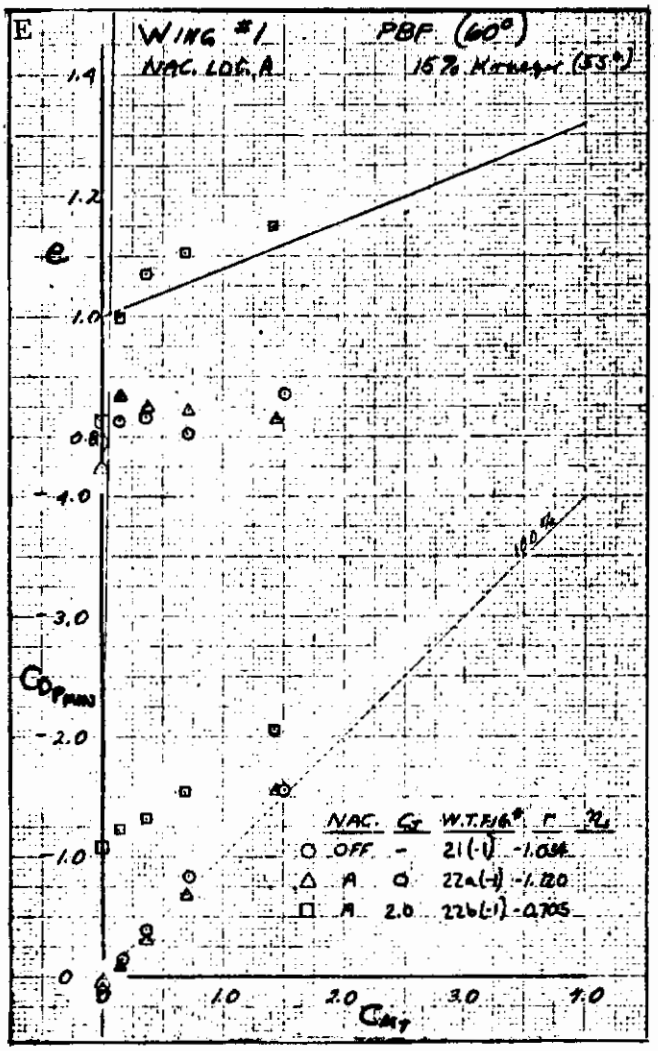

Figure 4.2-6. Effect of Engine Nacelles on Thrust Recovery and Induced Drag, Cont

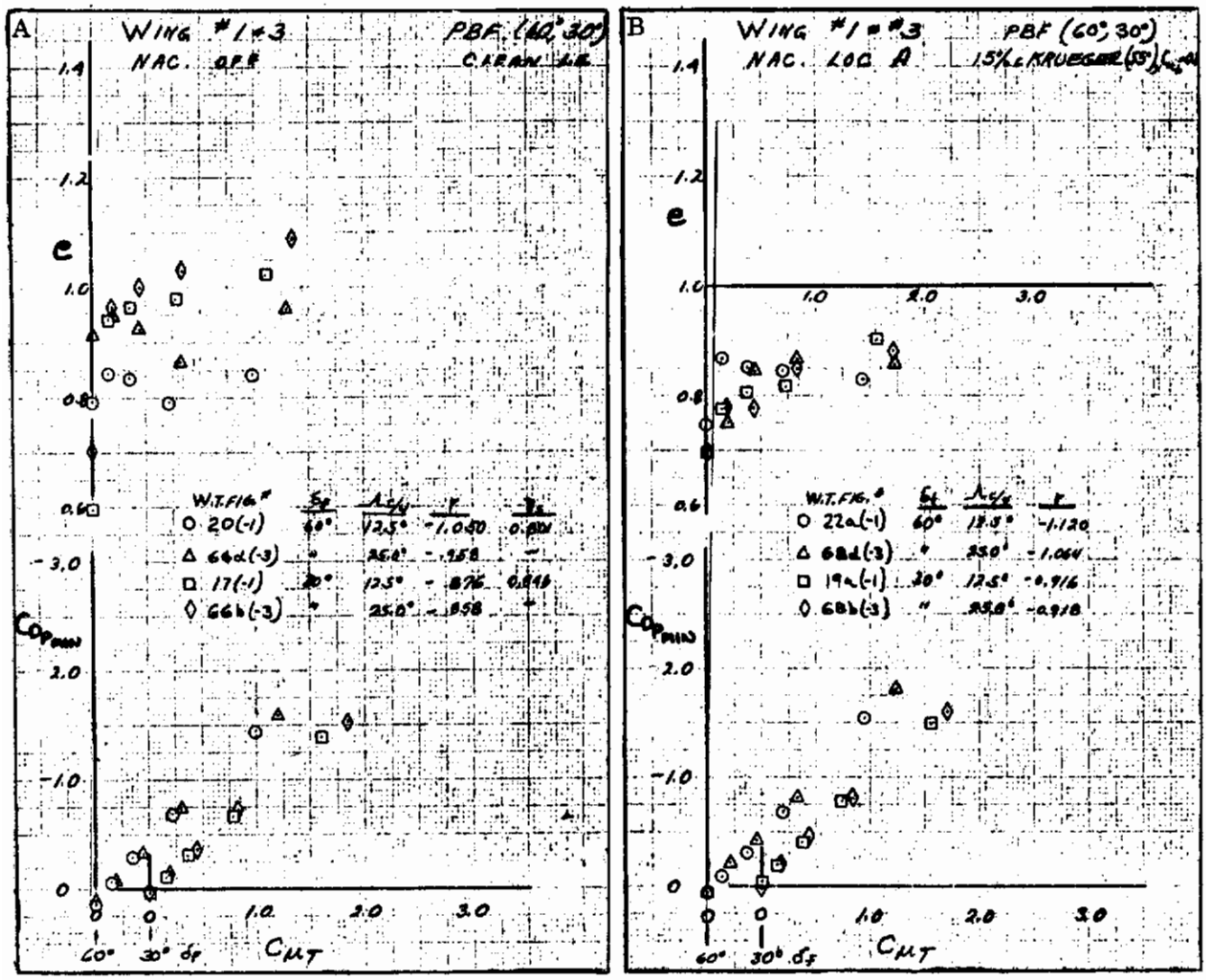

Figure 4.2-7. Effect of Wing Sweep on Thrust Recovery and Induced Drag

4.3 MF/VT THRUST RECOVERY AND INDUCED DRAG

The analysis of the wind tunnel axial force data is presented for the MF/VT system as the variation of the induced drag factor, e, and the minimum profile drag, $C_{DP_{min}}$, with the momentum coefficient of the jet engine, C_{μ_J}. Thrust recovery, r, has been measured for each configuration and tabulated on the plots.

4.3.1 EFFECT OF THRUST VECTORING ON THRUST RECOVERY. The effect of deflecting the thrust vector is shown in Figure 4.3-1 for several trailing edge flap configurations.

4.3.2 EFFECT OF TRAILING EDGE FLAP DEFLECTION ON THRUST RECOVERY. The effect of flap deflection is shown in Figure 4.3-2 for several thrust deflections.

4.3.3 EFFECT OF ENGINE NACELLE ON THRUST RECOVERY. The effect of engine nacelle location is shown in Figure 4.3-3 for several flap configurations and thrust deflections.

4.3.4 EFFECT OF WING SWEEP ON THRUST RECOVERY. The effect of wing sweep is shown in Figure 4.3-4.

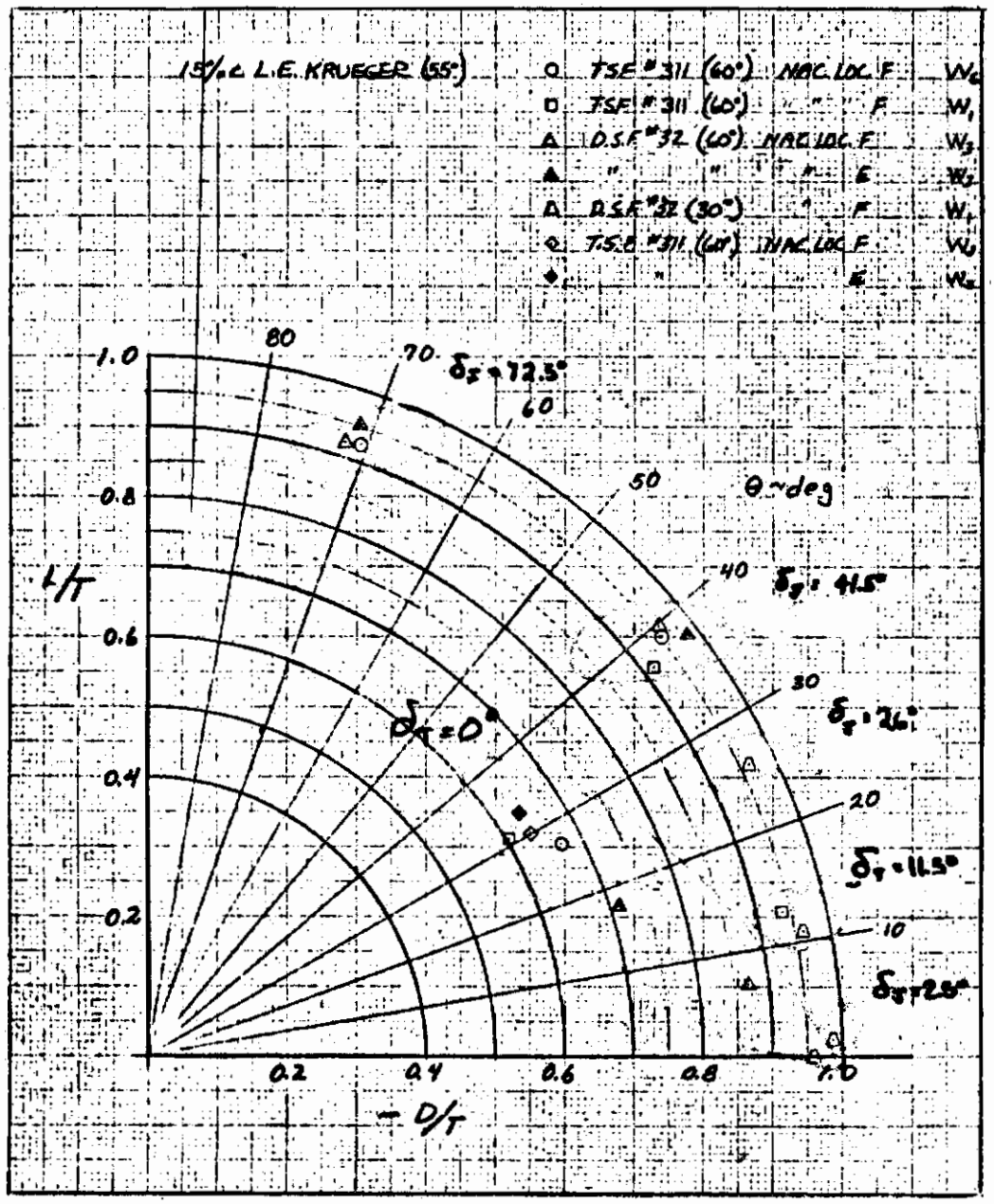

Figure 4.3-1. Effect of Vectored Thrust on Static Turning Efficiency.

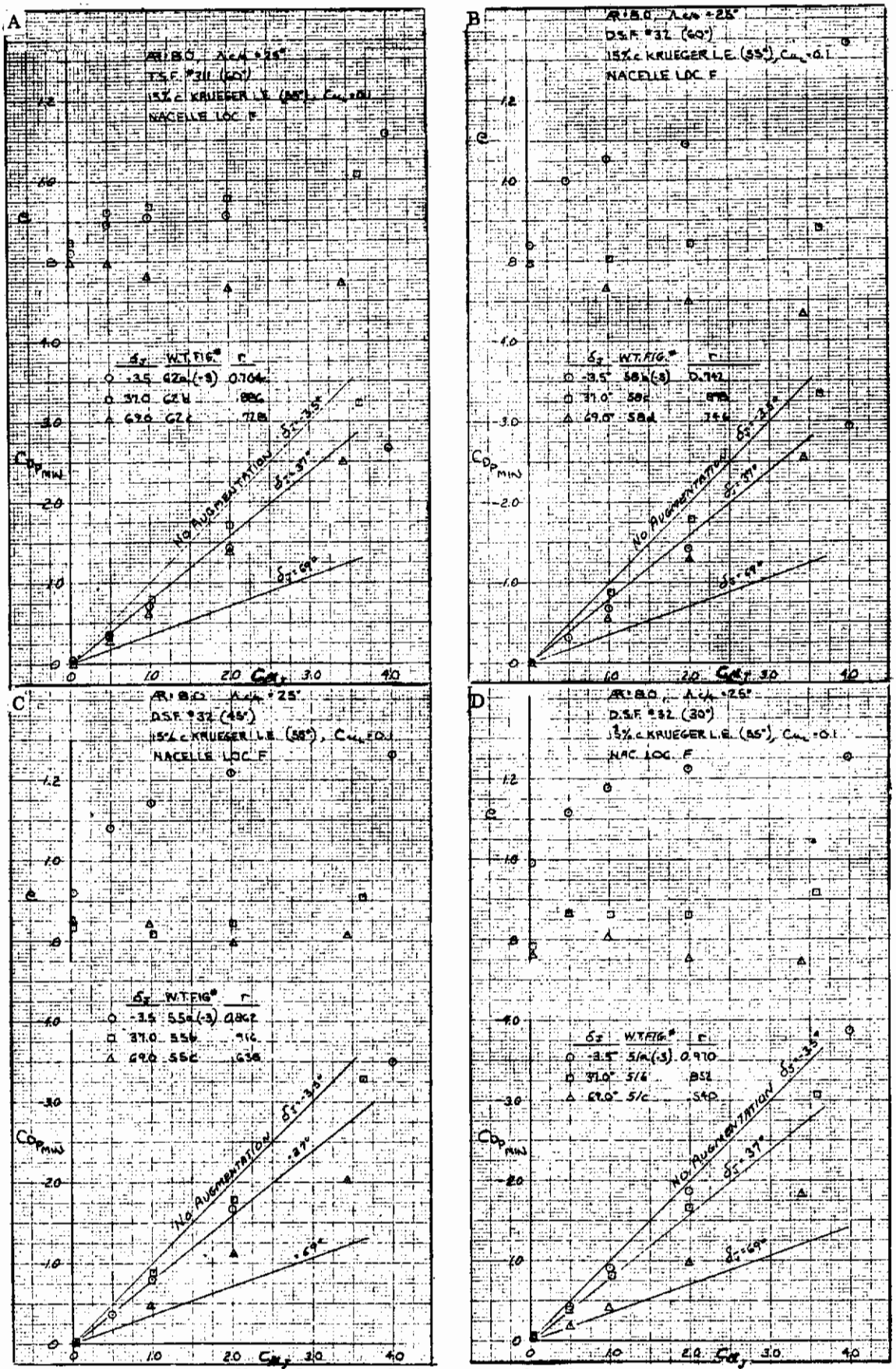

Figure 4.3-2. Effect of Vectored Thrust on Induced Drag and Thrust Recovery.

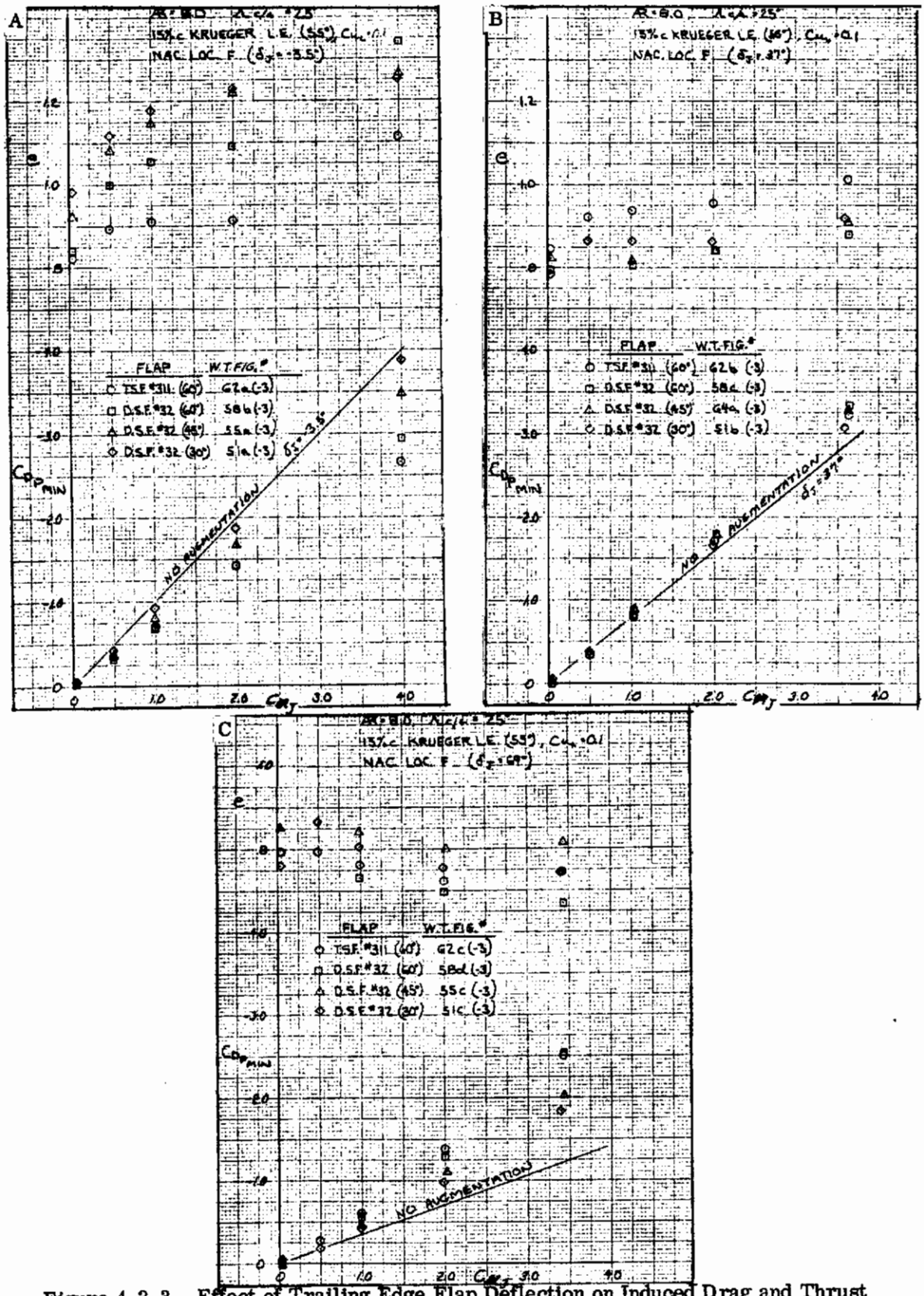

Figure 4.3-3. Effect of Trailing Edge Flap Deflection on Induced Drag and Thrust Recovery.

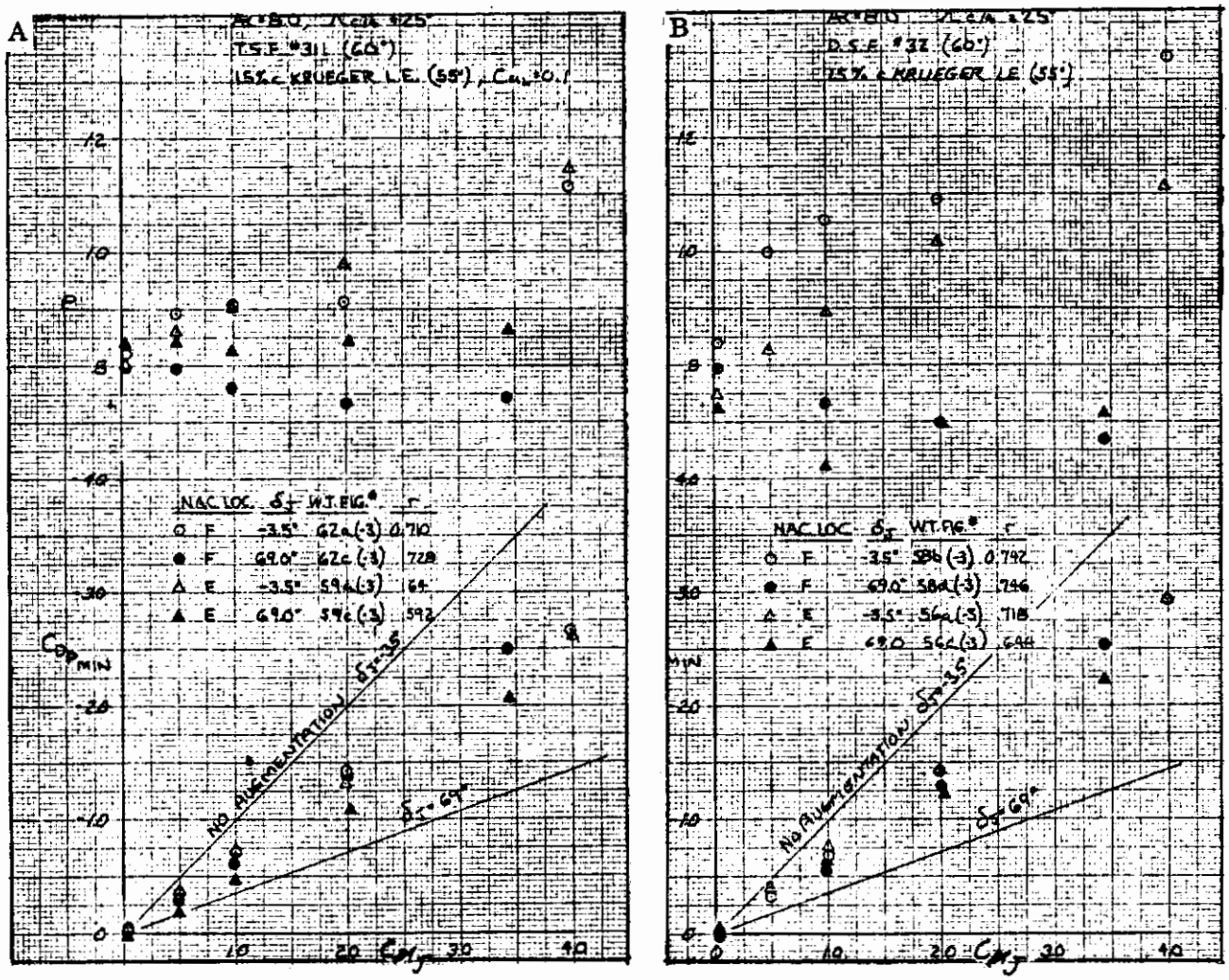

Figure 4.3-4. Effect of Nacelle Chordwise Location on Induced Drag and Thrust Recovery.

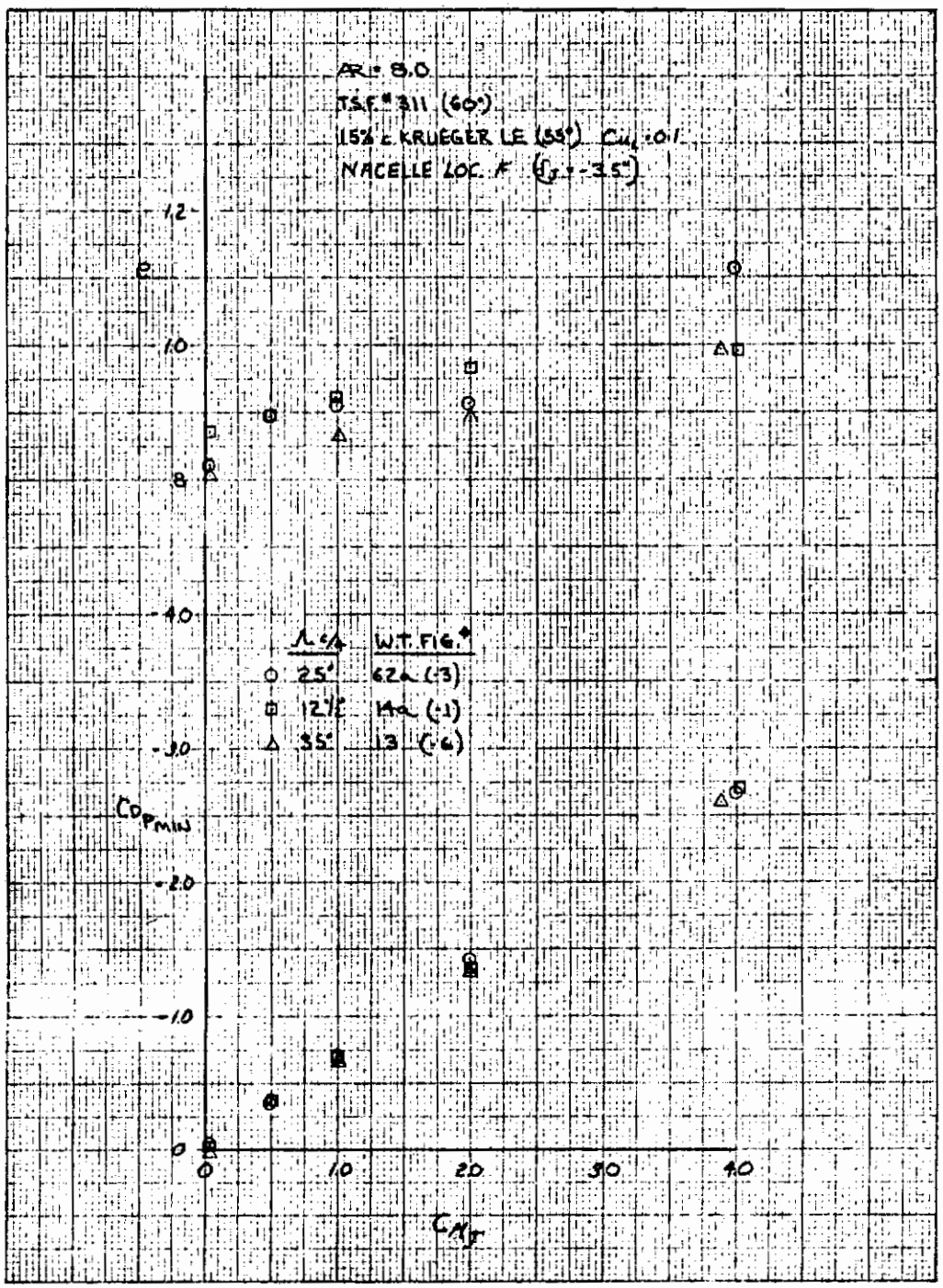

Figure 4.3-5. Effect of Wing Sweep on Induced Drag and Thrust Recovery.

SECTION 5

PITCHING MOMENT ANALYSIS

5.1 TWO DIMENSIONAL DATA

Two-dimensional pitching moment data was obtained from Test GDLST 610. The data analyzed consisted of the test runs of the optimum configurations. The optimum configuration runs (i.e., the combinations of flap and overlap between flaps that provided highest lift) were limited in number.

5.1.1 TWO-DIMENSIONAL MECHANICAL FLAPS. Pitching moment increments are computed using Linear Thin Airfoil Theory. A comparison of test data versus computed values can be seen on Figure 5.1-8 for the case where $C_{\mu_{TE}} = 0$.

5.1.2 TWO-DIMENSIONAL INTERNALLY BLOWN FLAPS. Figure 5.1-1 shows that an angle of attack of zero degrees for blowing coefficients larger than zero is the optimum condition for greatest lift and least relative moment increment for a triple-slotted flap. This condition only shows when the leading edge is not blowing. It also indicates that separation is present. If leading edge blowing is provided, the moment becomes more negative but lift increases considerably. (See Figure 5.1-2.)

A single-slotted flap at a deflection of 30 degrees shows a lessening of moment with angle of attack, indicating that the flow remains attached to the flap and the center of pressure moves slightly forward. (See Figure 5.1-3.) A single-slotted flap at a deflection of 60 degrees shows that the flap starts separating at low blowing rates and tends to keep more of the flow attached to the flap at higher blowing rates, causing the moments to become more negative. (See Figure 5.1-4.)

Increasing leading-edge slat blowing causes the moment to become more negative. (See Figure 5.1-5.) Trailing edge blowing has an effect on the moment produced by the leading-edge flap in that it becomes more negative with increasing blowing rate at the trailing edge. (See Figure 5.1-6.)

A method has been developed using Spence's Jet Flap Theory in conjunction with an efficiency chart based on momentum loss correlations are shown in Figures 5.1-7 and 5.1-8.

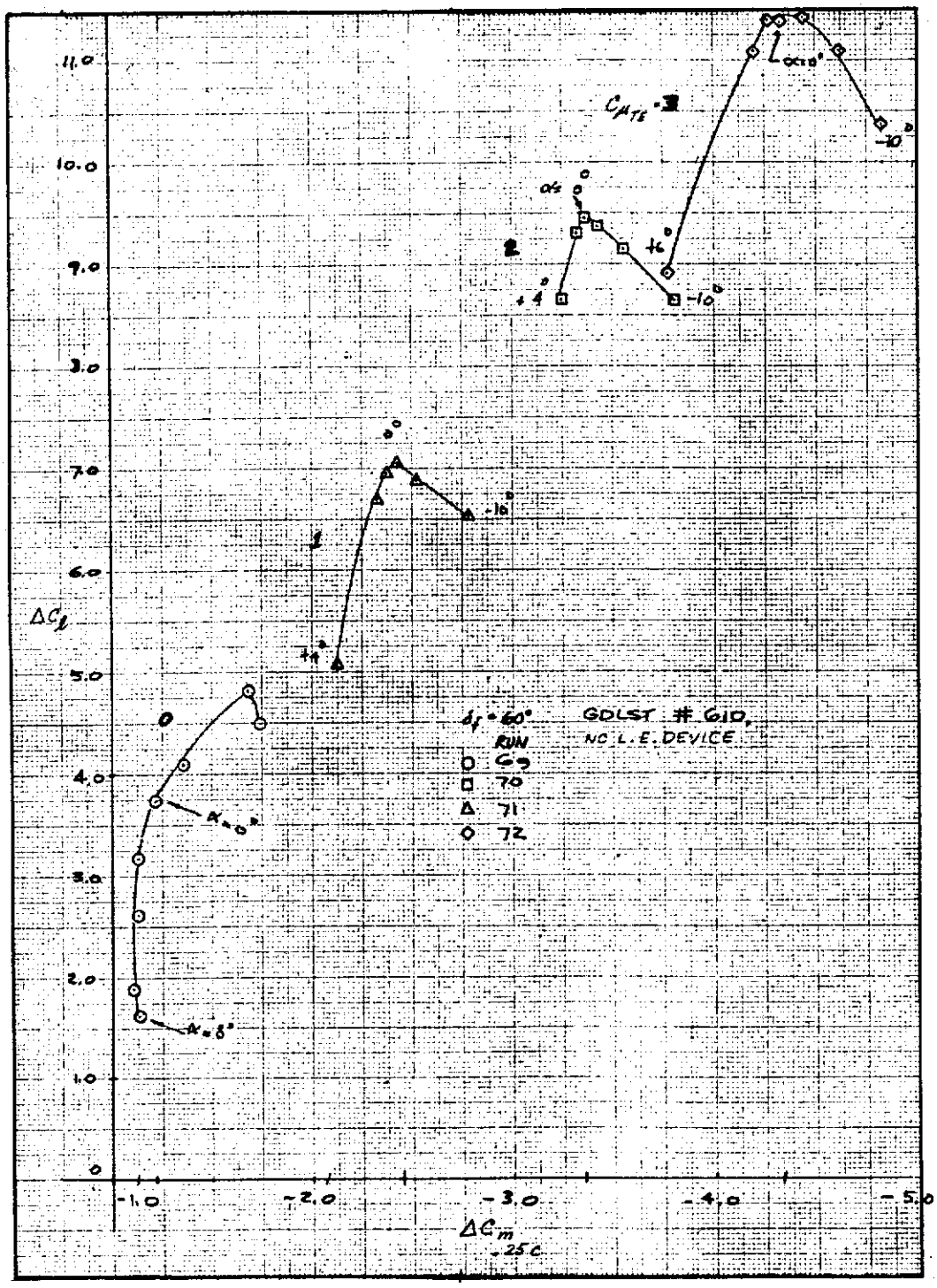

Figure 5.1-1. Effect of Trailing-Edge Blowing on Two-Dimensional Flap Lift and Pitching Moment Increments, Triple-Slotted Flap

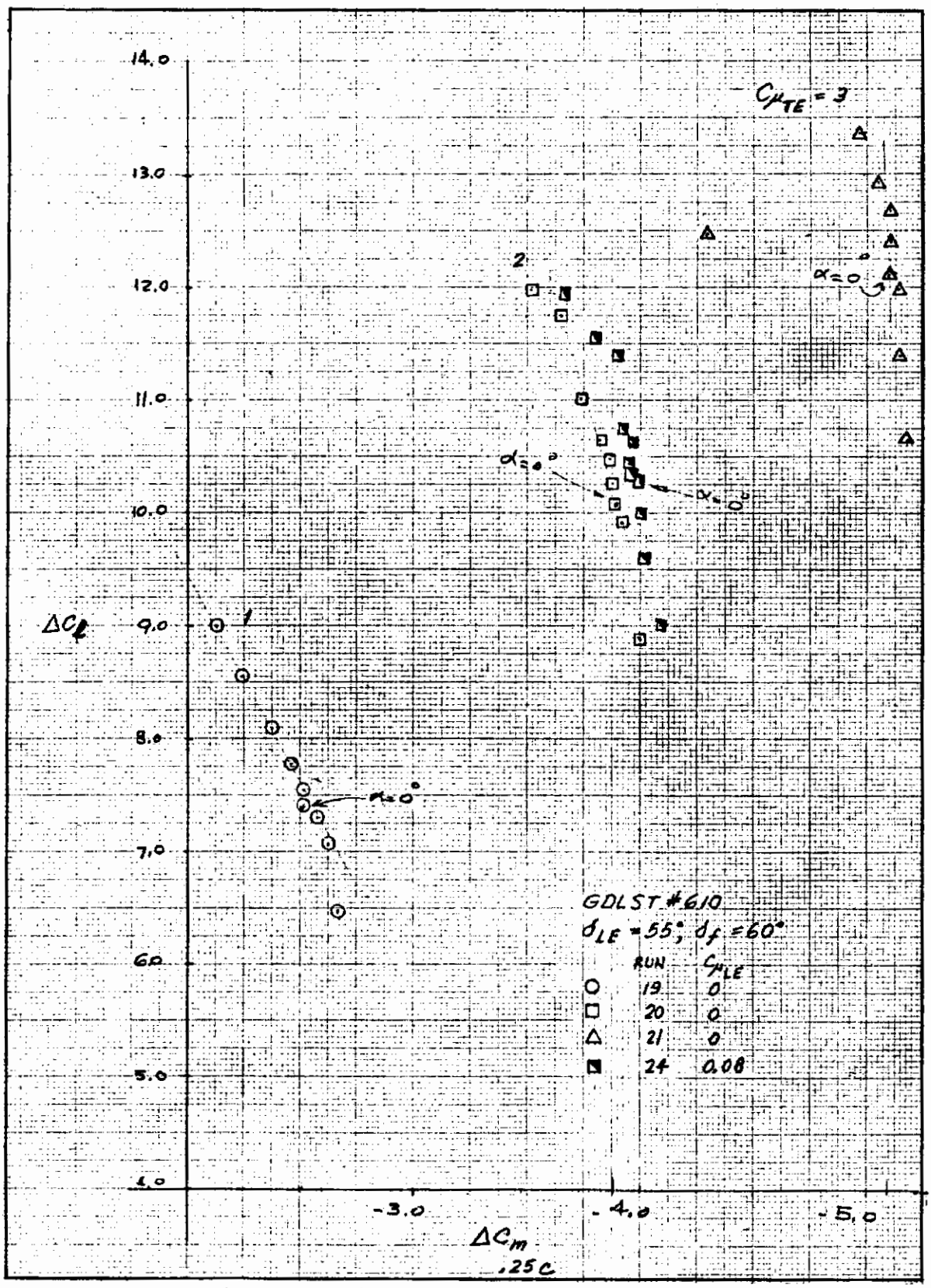

Figure 5.1-2. Effect of Trailing-Edge Blowing on Two-Dimensional Flap Lift and Pitching Moment Increment, Triple-Slotted Flap Plus Leading-Edge Flap.

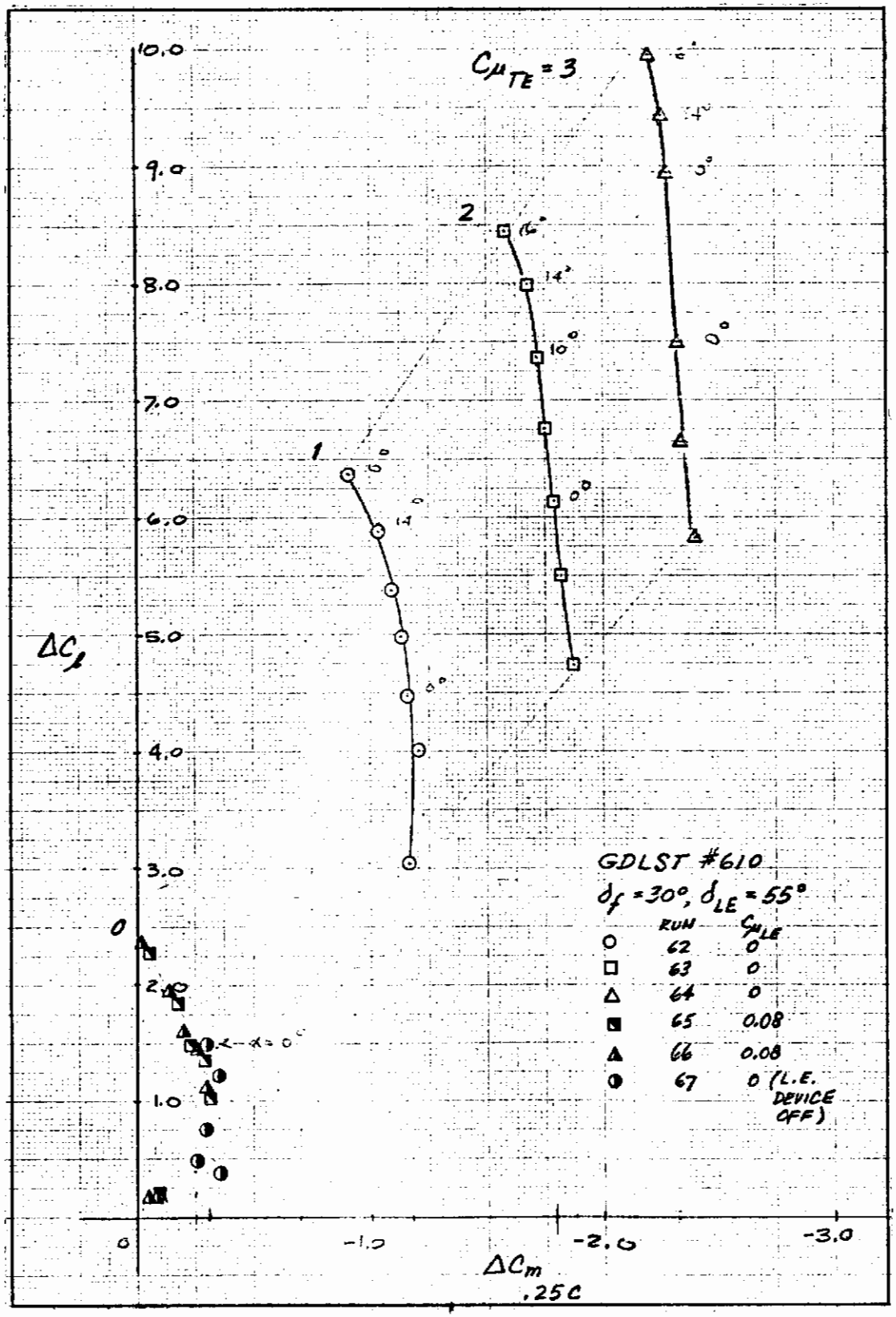

Figure 5.1-3. Effect of Trailing- and Leading-Edge Flap Blowing on Two-Dimensional Flap Lift and Pitching Moment Increments, Single-Slotted Flap at 30 Degrees Plus Leading-Edge Flap

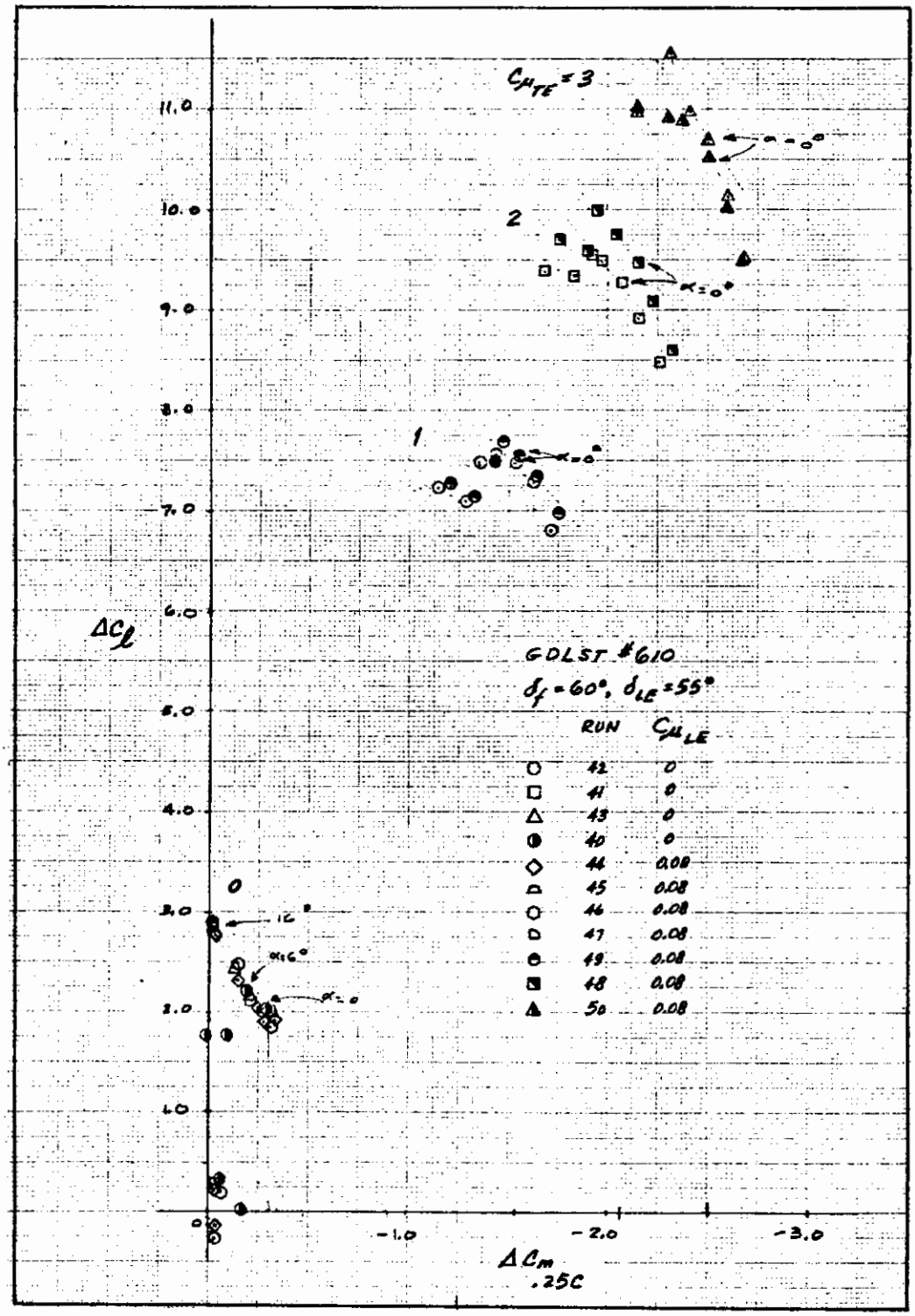

Figure 5.1-4. Effect of Trailing- and Leading-Edge Blowing on Two-Dimensional Flap Lift and Pitching Moment Increments, Single-Slotted Flap at 60 Degrees Plus Leading-Edge Device

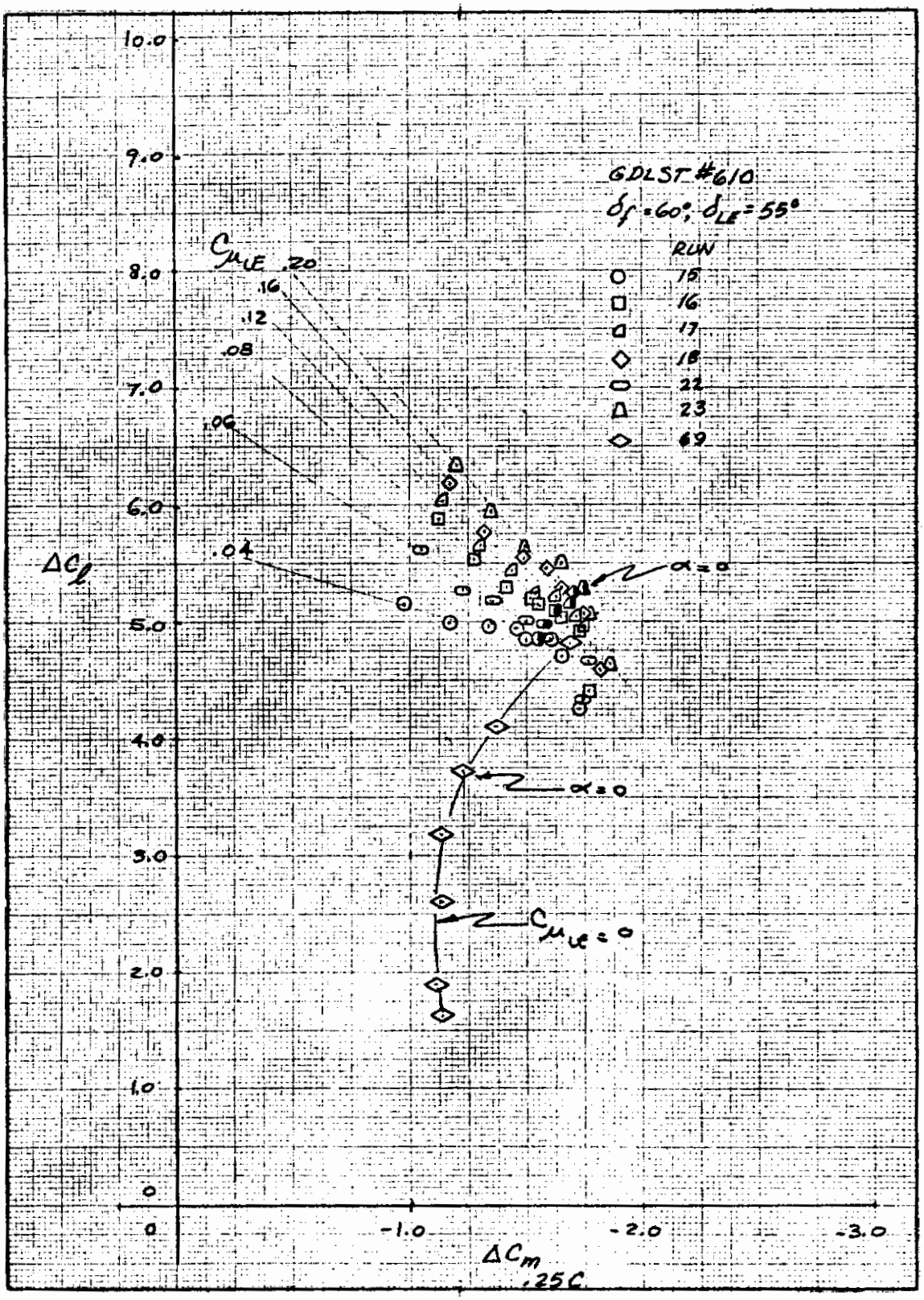

Figure 5.1-5. Effect of Leading-Edge Blowing on Two-Dimensional Flap Lift and Pitching Moment Increments, Triple-Slotted Flap Plus Leading-Edge Flap

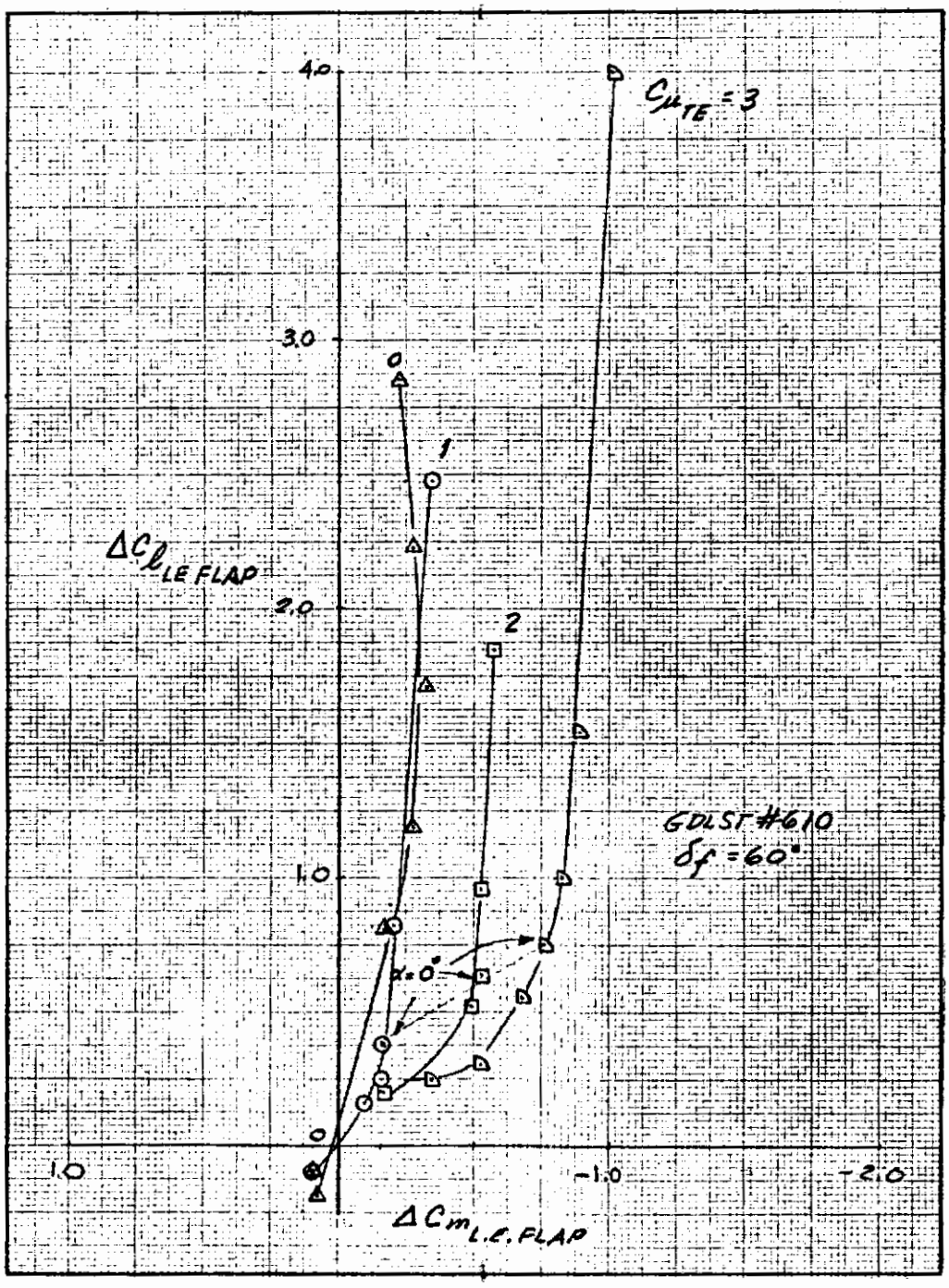

Figure 5.1-6. Effect of the Leading-Edge Device on Two-Dimensional Flap Lift and Pitching Moment Increments, Triple-Slotted Flap

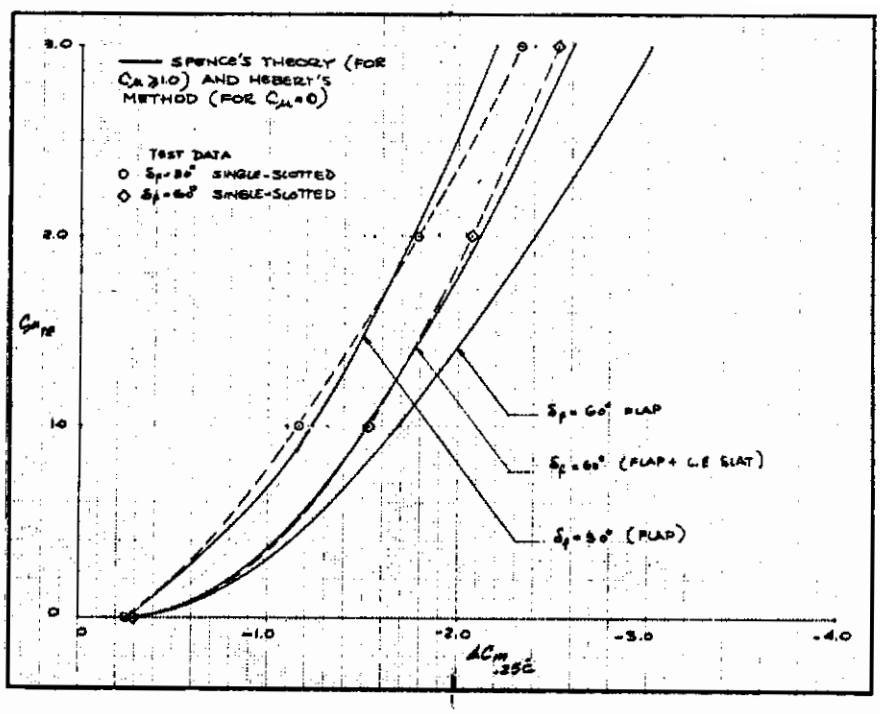

Figure 5.1-7. Correlation of Test Data and Predicted Two-Dimensional Flap Pitching Moment Increments, Single-Slotted Flap

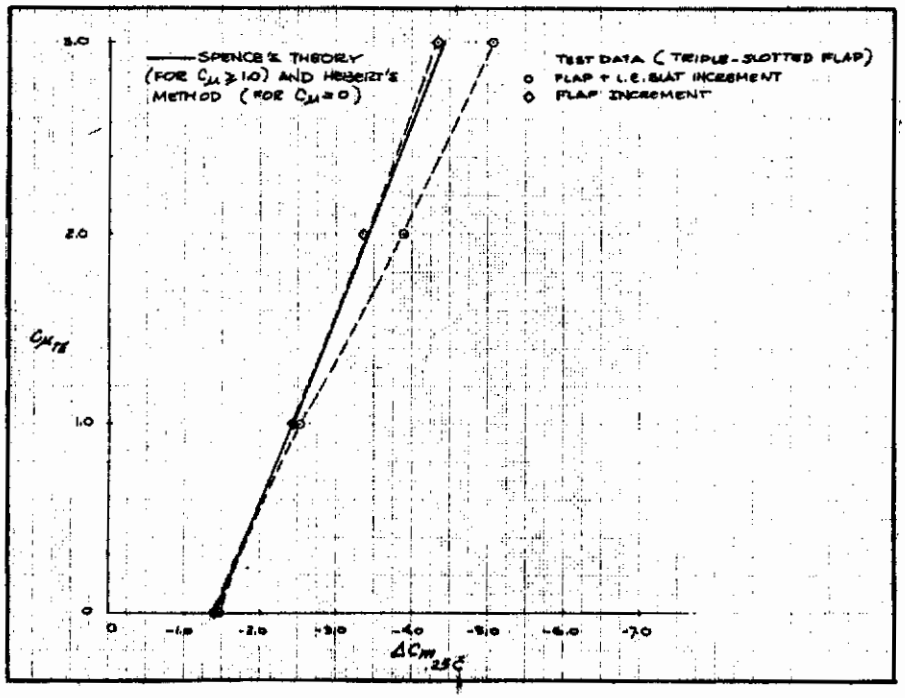

Figure 5.1-8. Correlation of Test Data and Predicted Two-Dimensional Flap Pitching Moment Increments, Triple-Slotted Flap

5.2 THREE DIMENSIONAL DATA

5.2.1 THREE DIMENSIONAL MECHANICAL FLAP. Five wings were tested with various amounts of sweep and different aspect ratios. Two-dimensional theory has been extended to three-dimensional theory by including sweep and aspect ratio. Correlations of test data versus computed values are shown in Table 5.1-1.

5.2.2 THREE-DIMENSIONAL IBF. The effect of a leading-edge slat on the pitching moment increment is negligible compared to the overall effect of the flap. (See Figure 5.2-1.) The IBF method has been extended to include three-dimensional effects. Correlations for Wings 1 and 3 are shown in Figures 5.2-2 and 5.2-3.

5.2.3 THREE-DIMENSIONAL EBF. Extensive tests were performed with the EBF configurations (GDLST 612-1, -3, -4, -5, and -6). Figure 5.2-4 shows the effect of leading-edge blowing on the pitching moment. The increment due to blowing remains constant even though more mass flow is impinging on the trailing-edge flap system. A change in size of the blowing slot results in reduction of the moment, as shown in Figure 5.2-5. Typical data for the different wings and flap systems is shown for various pylon length, engine position, and tail-pipe length. (See Figures 5.2-6 through 5.2-13). The effects of the different leading-edge slats are shown in Figures 5.2-10 through 5.2-13. These figures all indicate that the leading edge slat with the higher deflection, I_{1_u}, produces a larger negative pitching moment increment than the lower deflection (45-degree) leading edge slat, I_{2_u}, where u is the wing number.

The engine positions tested are shown in Figure 5.2-14. Comparing Figure 5.2-15 with the engine positions in Figure 5.2-14 shows that the moment increment is directly related to the amount of the flap system in the jet efflux. If the engine is closer to the flap system, less area is captured and less moment is produced.

An EBF computation scheme was developed to predict moment increments produced by an EBF system. Figures 5.2-16 through 5.3-20 indicate that the relationship between different wings for a set configuration would be a factor combining aspect ratio and sweep.

Figures 5.2-21 through 5.2-25 indicate that the gradient $\Delta C_m/\Delta C_L$ becomes worse with increasing flap size.

Correlations between the test data and the EBF method are shown in Figures 5.2-26 through 5.2-29.

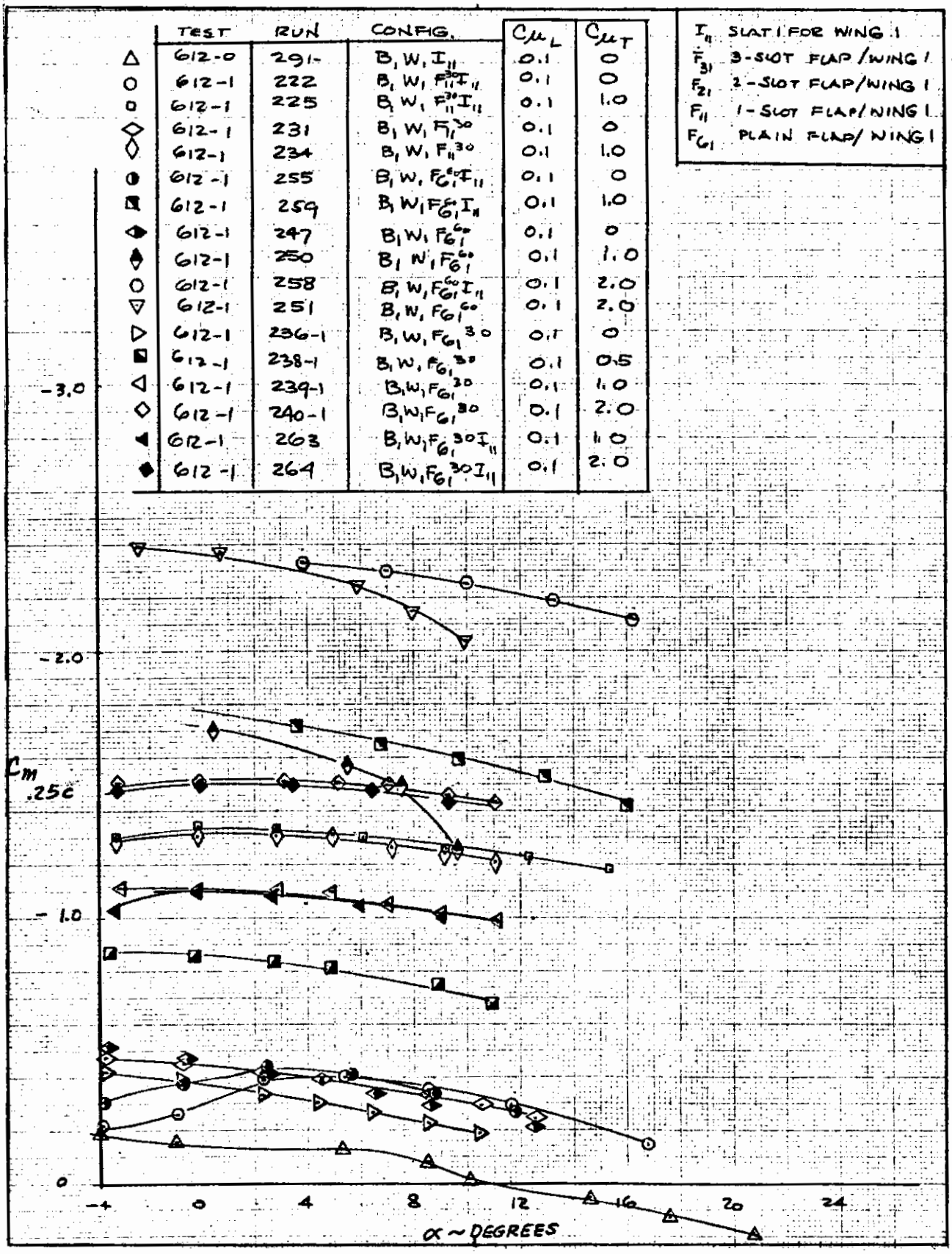

Figure 5.2-1. Three-Dimensional Flap Pitching Moment Increments for IBF

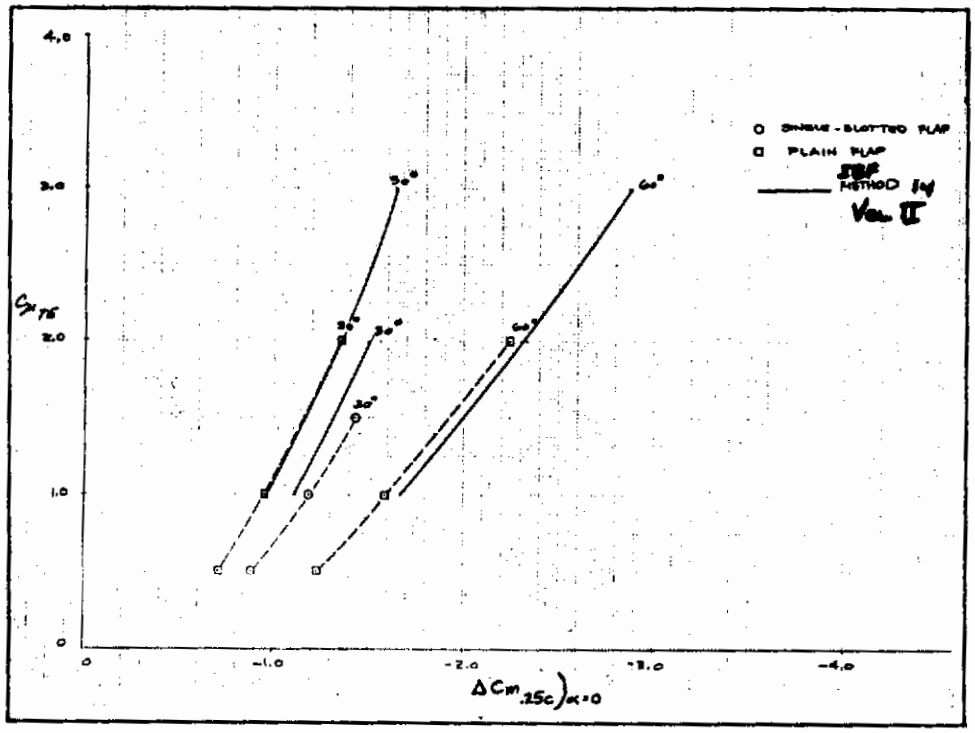

Figure 5.2-2. Correlation of Test Data and Predicted Flap Pitching Moment Increments for IBF, Wing No. 1

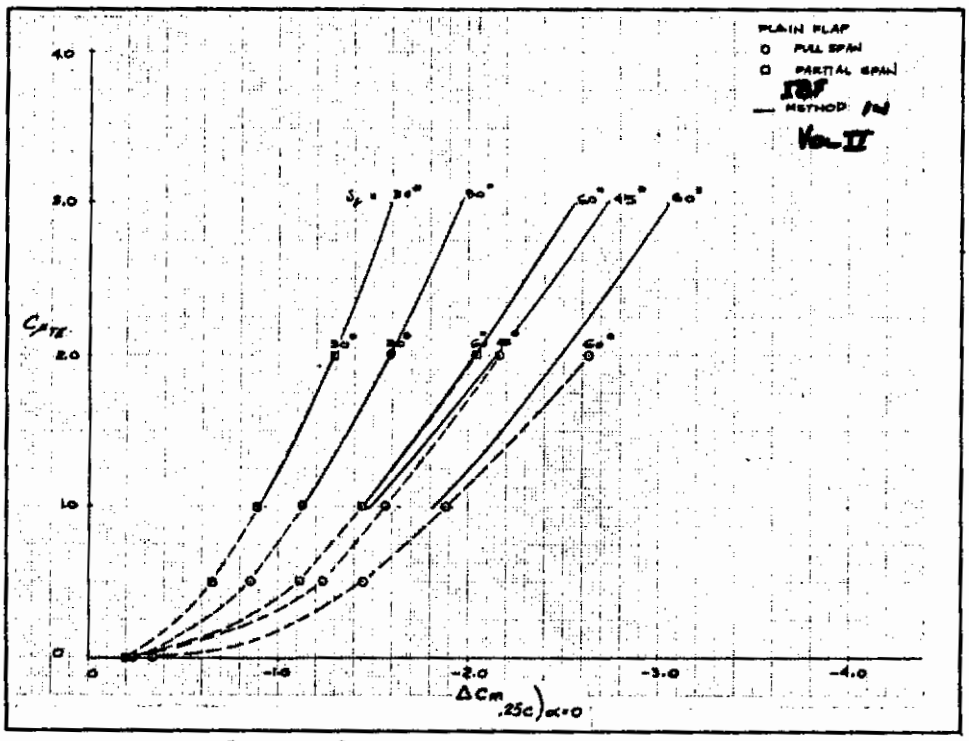

Figure 5.2-3. Correlation of Test Data and Predicted Flap Pitching Moment Increments for IBF, Wing No. 3

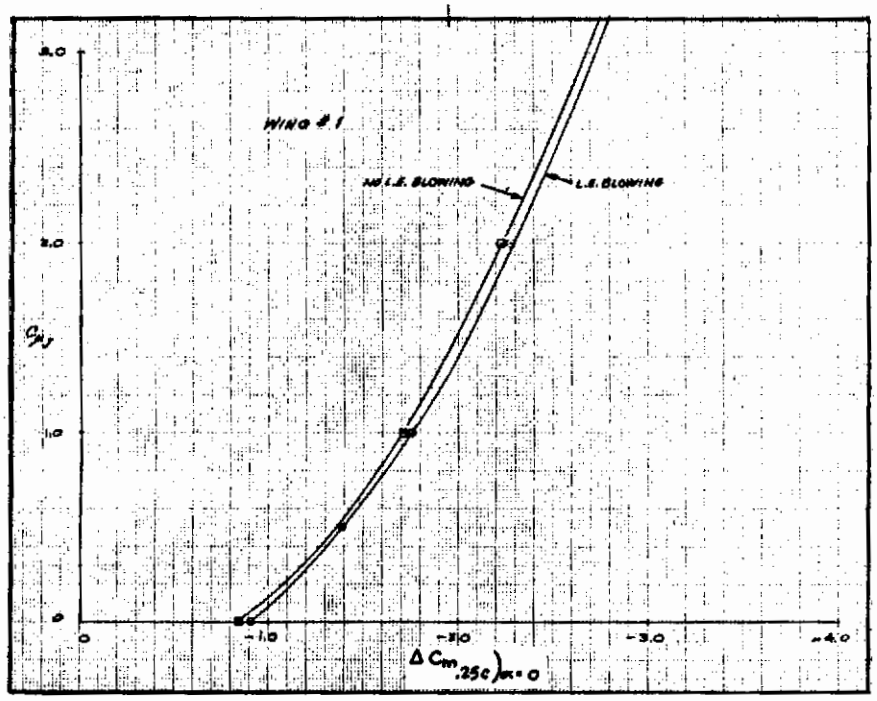

Figure 5.2-4. Effect of Leading-Edge Blowing on Flap Pitching Moment Increments for EBF Double-Slotted Flap at 60 Degrees

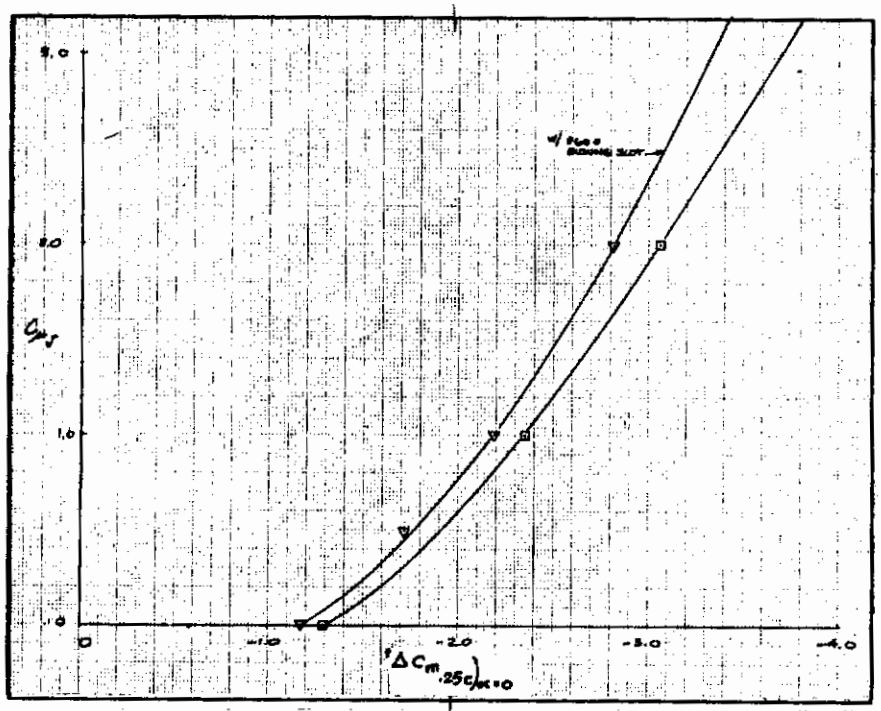

Figure 5.2-5. Effect of Changing Size of Blowing Slot on Flap Pitching Moment Increments for EBF Triple-Slotted Flap at 60 Degrees, Wing No. 1

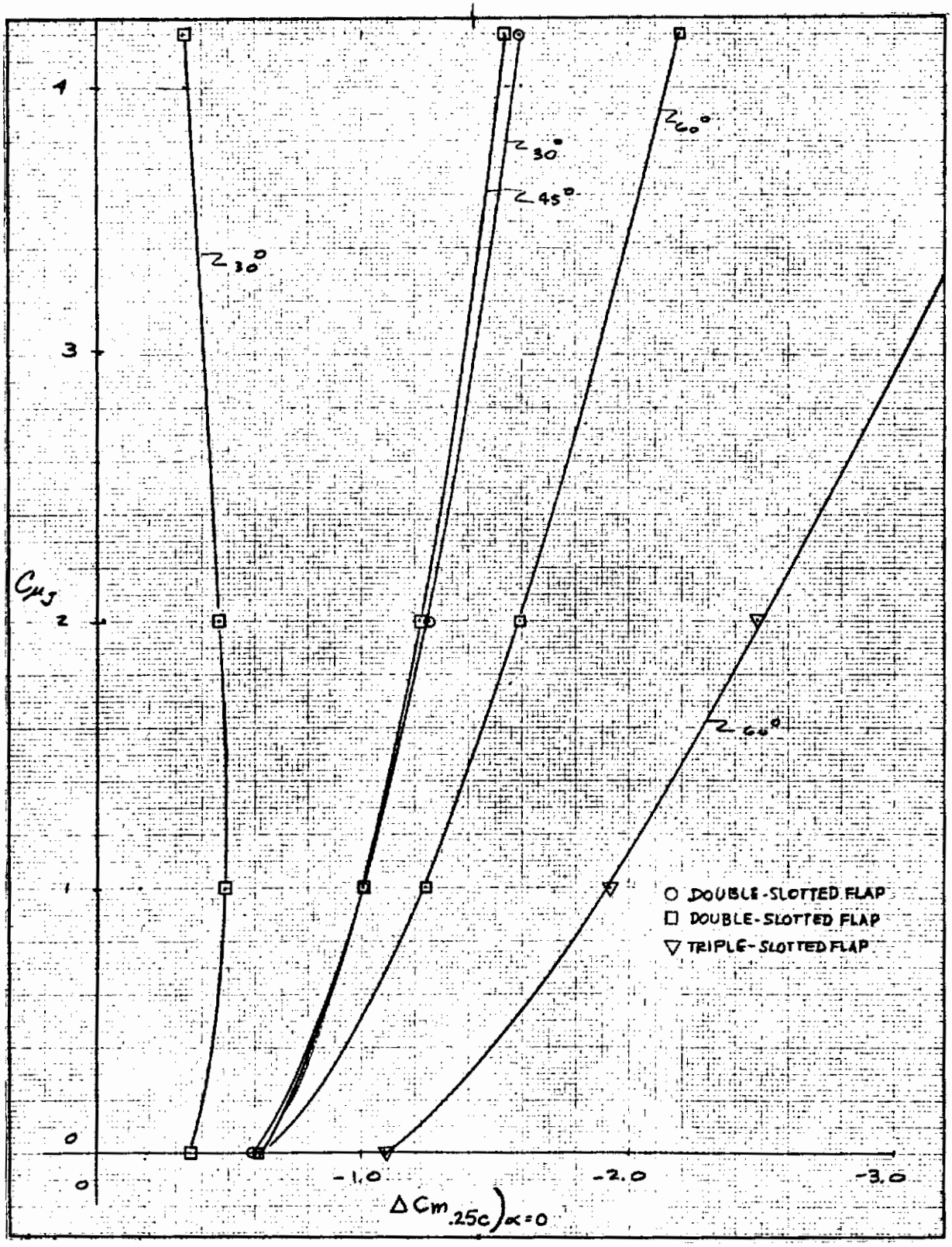

Figure 5.2-6. Effect of Flap Configuration and Deflection on EBF Flap Pitching Moment Increments, Double- and Triple-Slotted Flaps Plus Leading-Edge Flap, Wing No. 3

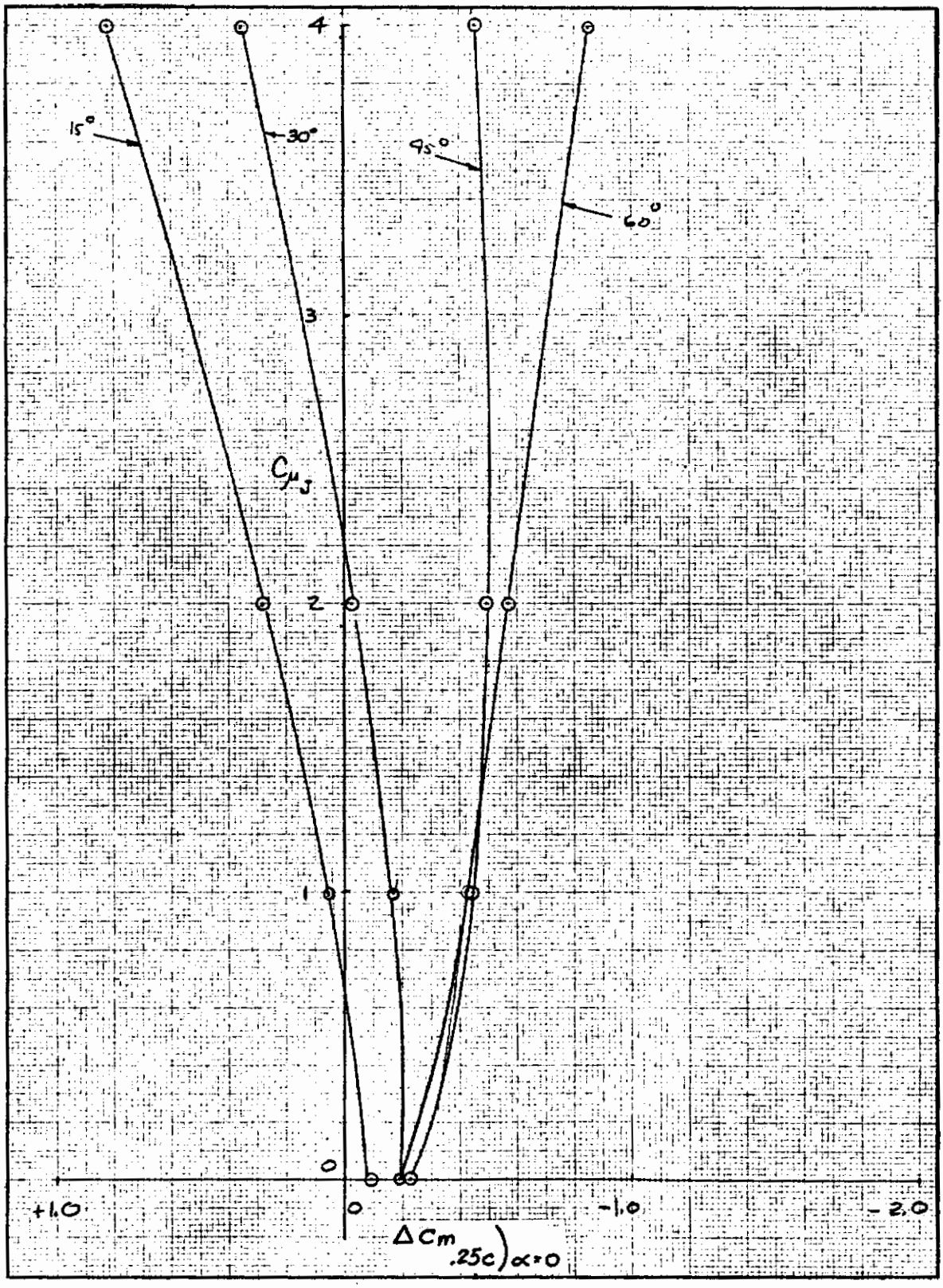

Figure 5.2-7. Effect of Flap Deflection on EBF Flap Pitching Moment Increments, Single-Slotted Flap, Wing No. 3

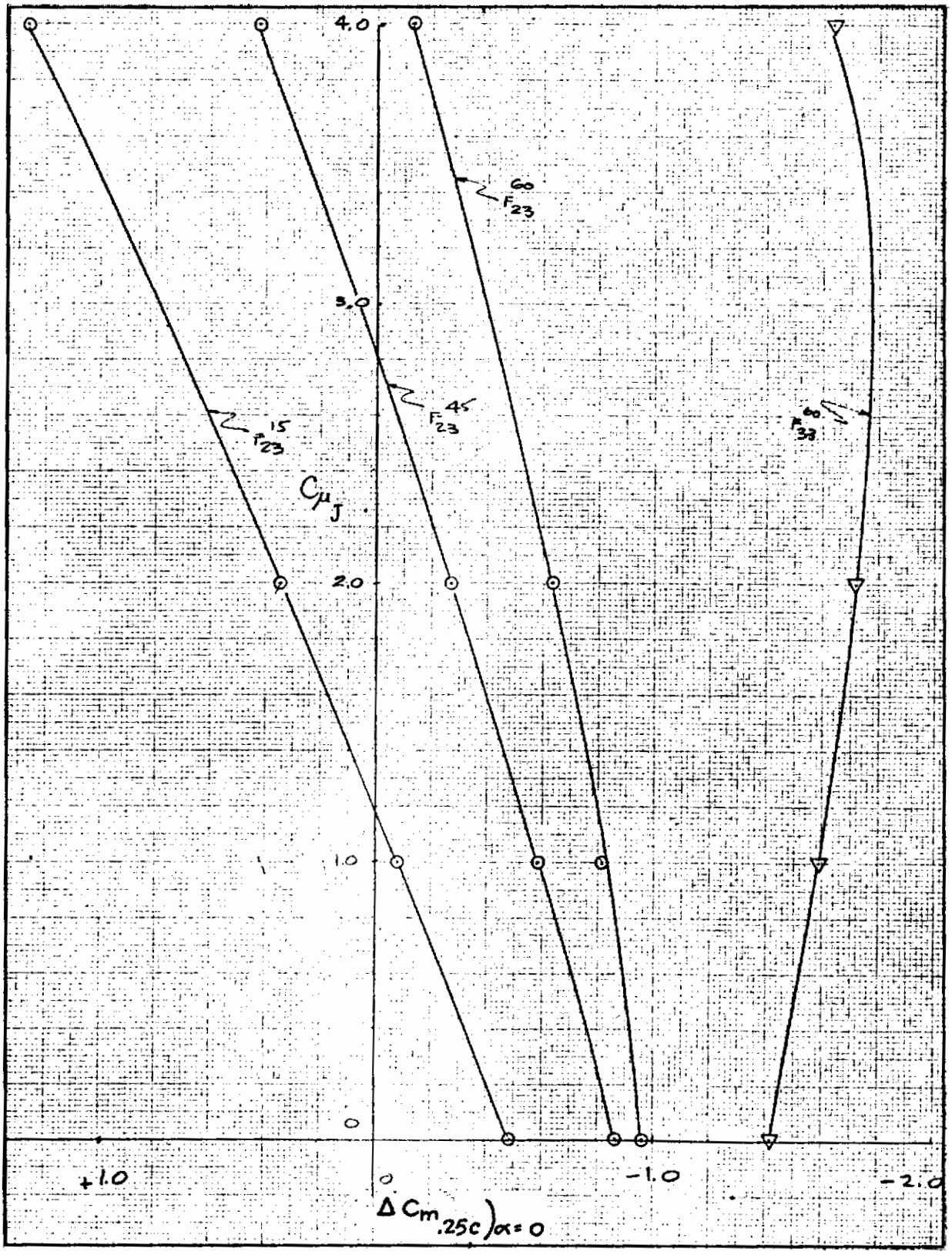

Figure 5.2-8. Effect of Flap Deflection on EBF Flap Pitching Moment Increments, Double- and Triple-Slotted Flaps, Wing No. 3 (Nacelle Position E_7P_5)

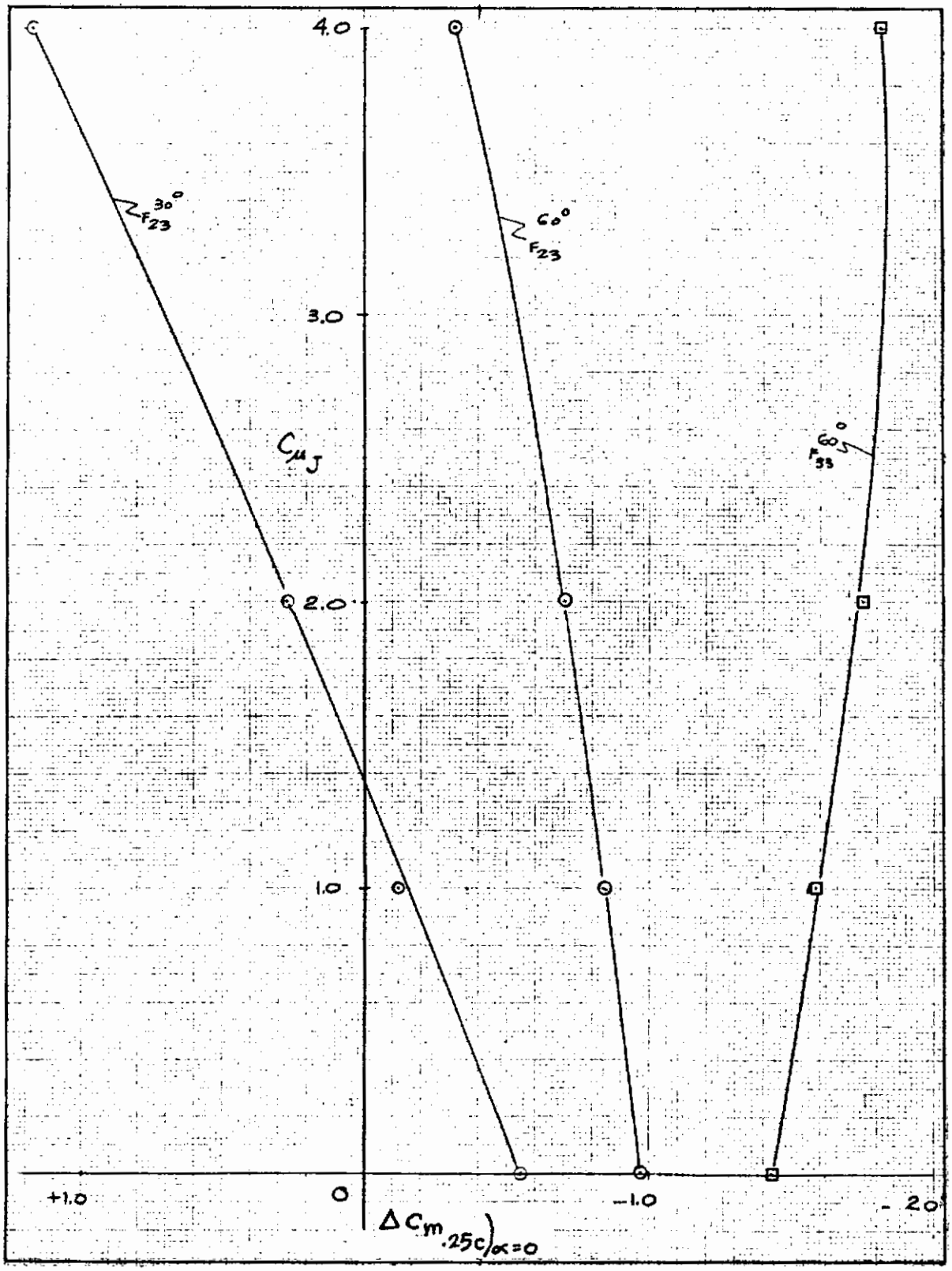

Figure 5.2-9. Effect of Flap Deflection on EBF Flap Pitching Moment Increments, Double- and Triple-Slotted Flaps, Wing No. 3 (Nacelle Position E_3P_5)

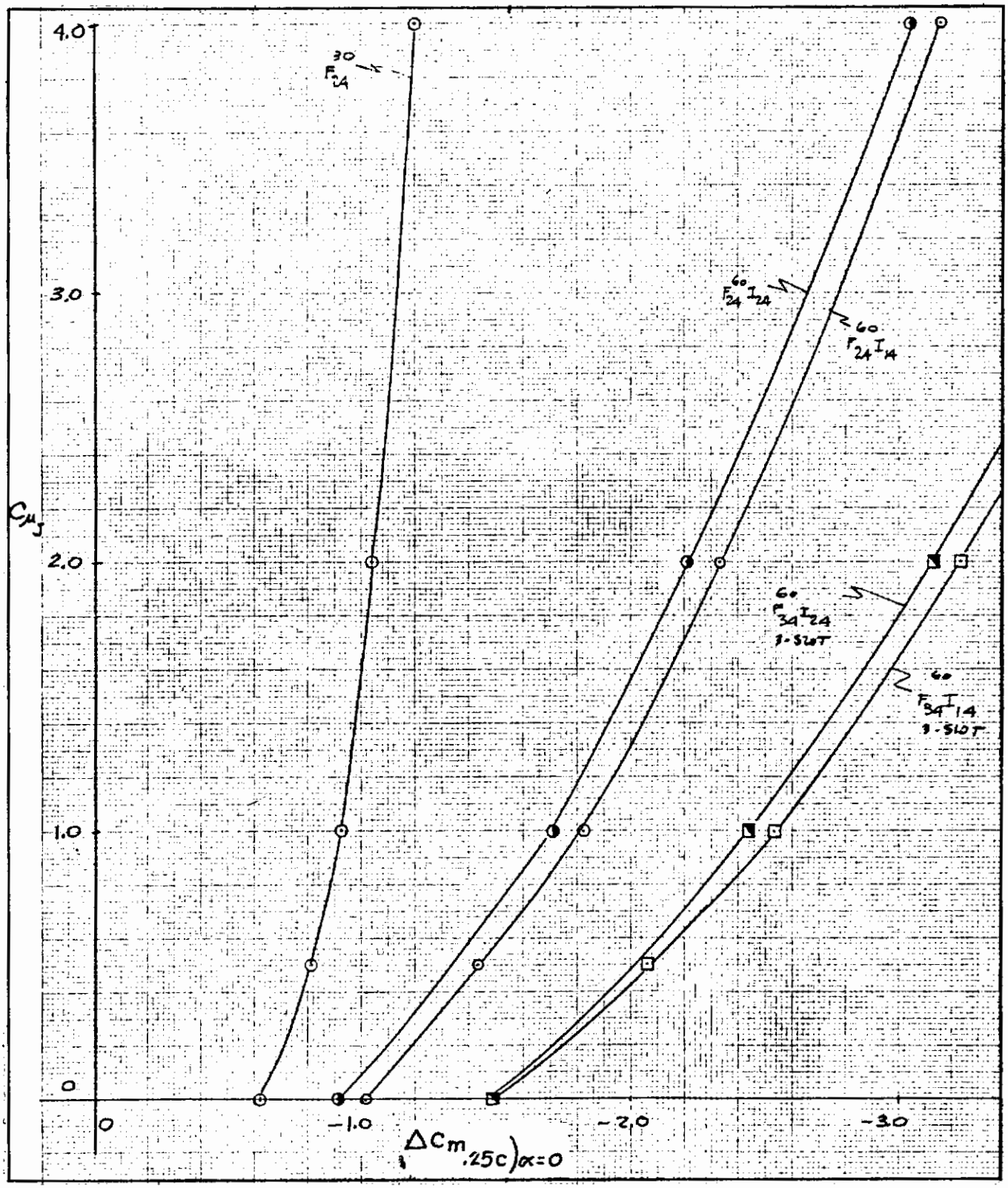

Figure 5.2-10. Effect of Flap Deflection on EBF Flap Pitching Moment Increments, Double- and Triple-Slotted Flaps with and without Leading-Edge Flaps at 55 and 45 Degrees, Wing No. 4

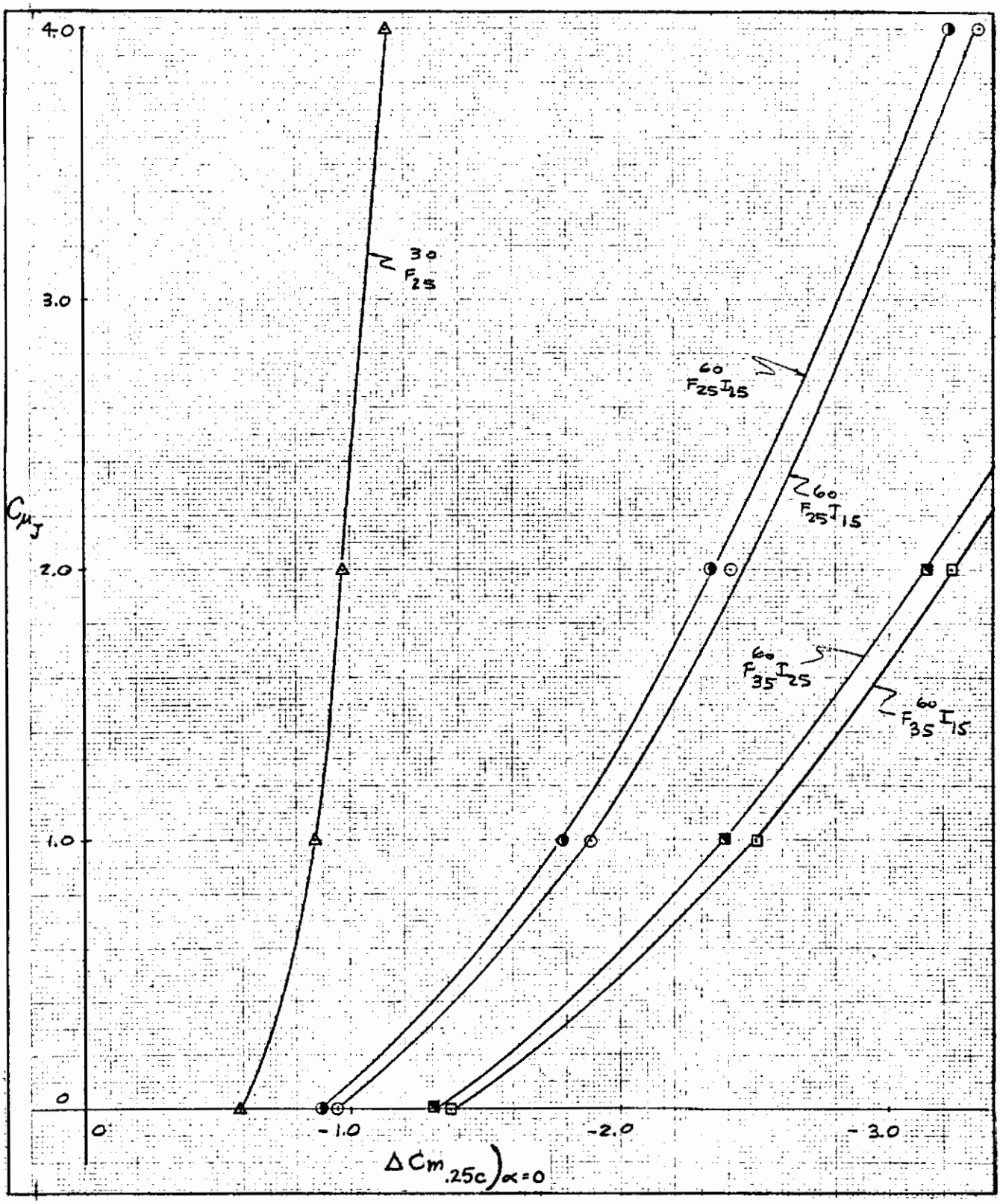

Figure 5.2-11. Effect of Flap Deflection on EBF Flap Pitching Moment Increments, Double- and Triple-Slotted Flaps with and without Leading-Edge Flaps at 55 and 45 Degrees, Wing No. 5

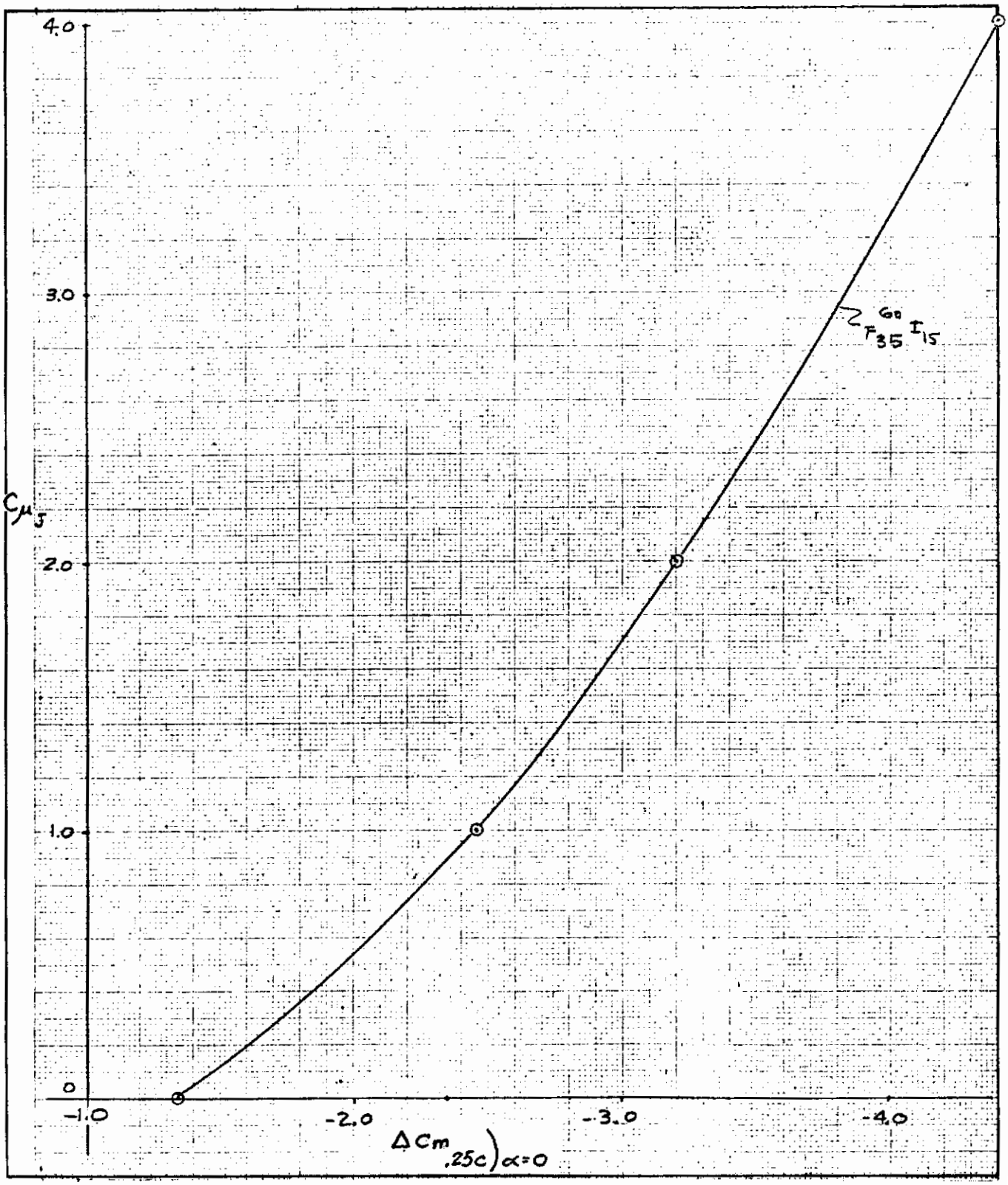

Figure 5.2-12. EBF Flap Pitching Moment Increments for Triple-Slotted Flap Plus Leading-Edge Flaps at 55 Degrees, Wing No. 5

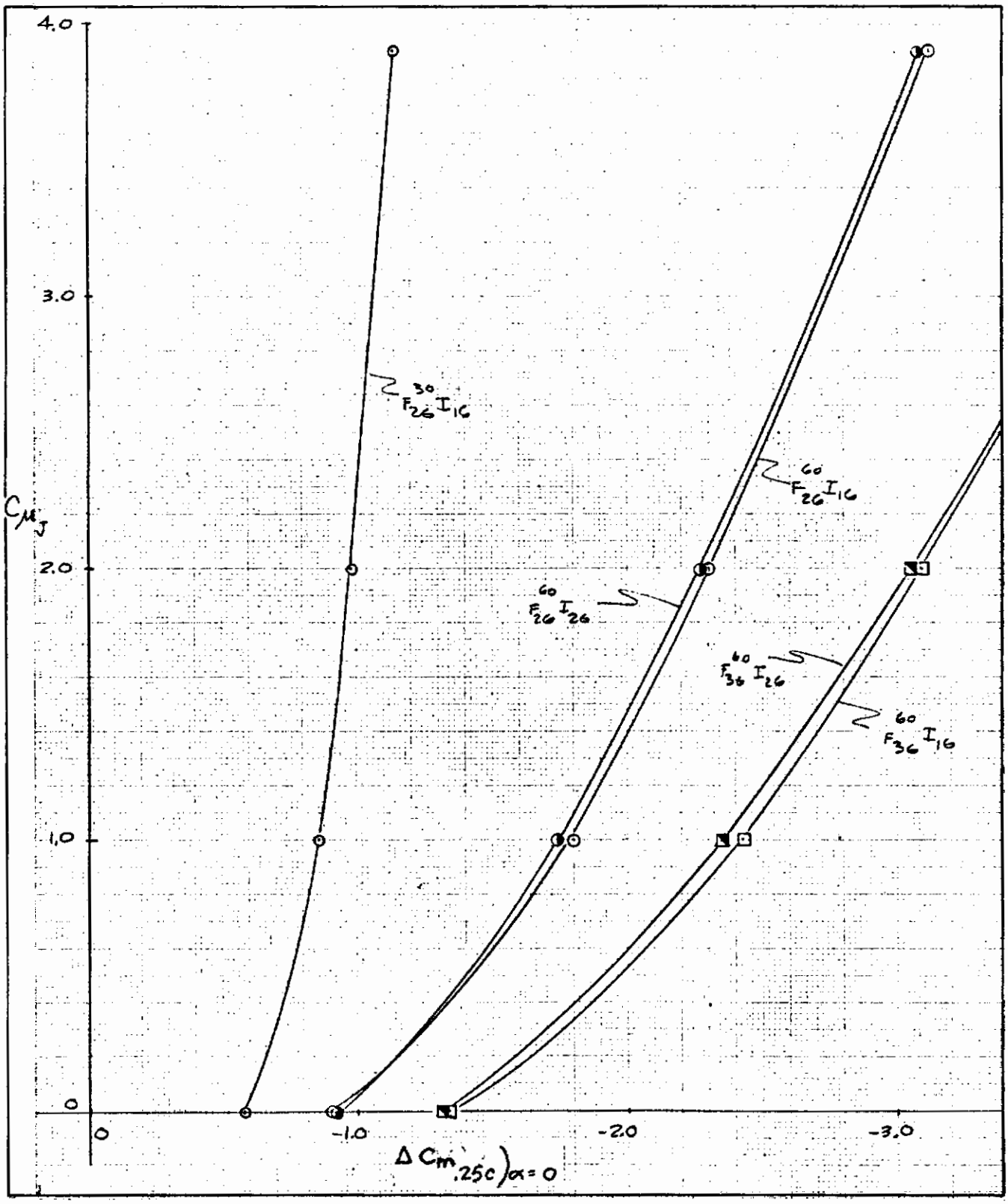

Figure 5.2-13. Effect of Flap Deflection on EBF Flap Pitching Moment Increments, Double- and Triple-Slotted Flaps Plus Leading-Edge Flaps at 55 and 45 Degrees, Wing No. 6

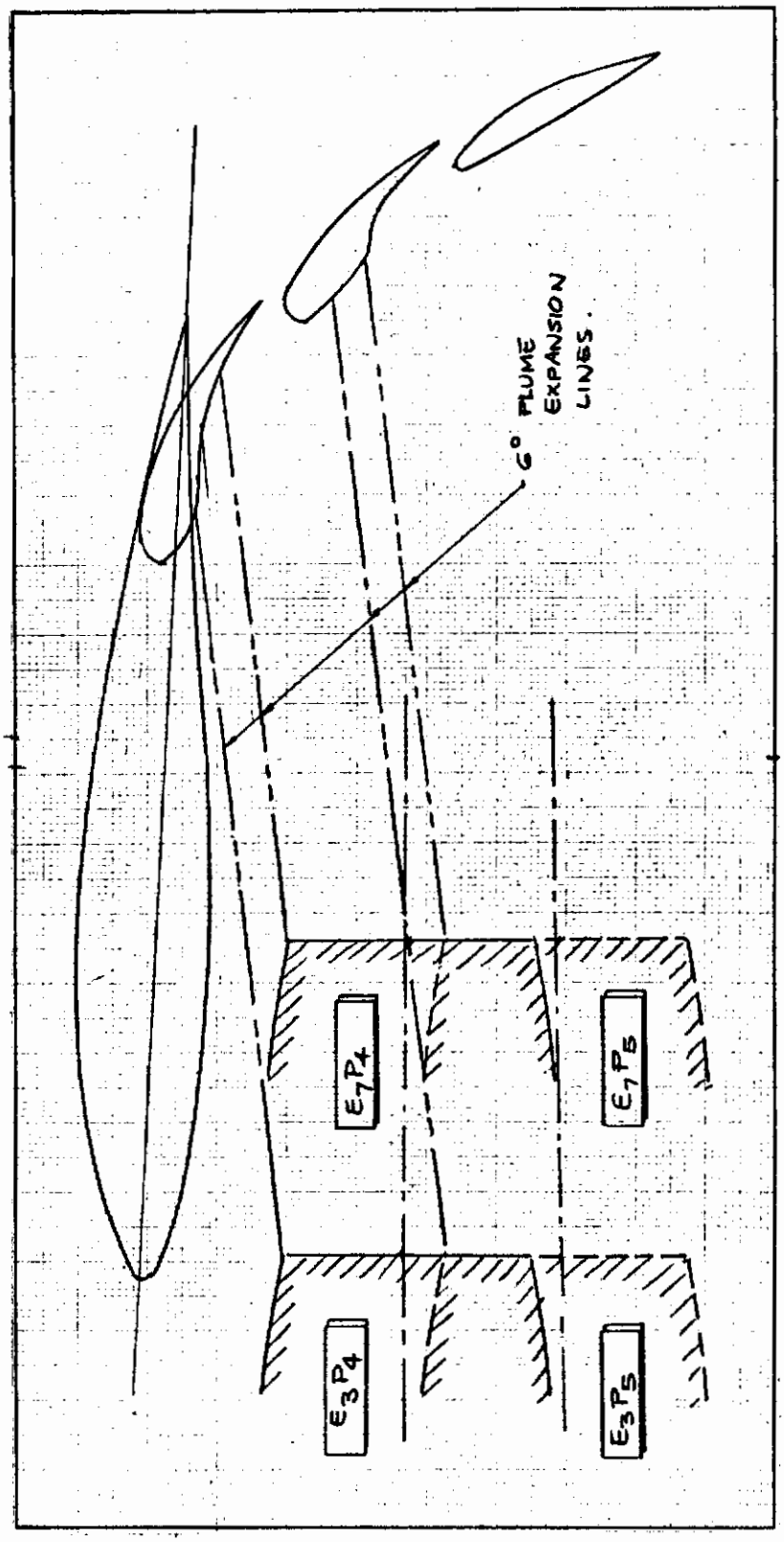

Figure 5.2-14. EBF Engine Locations

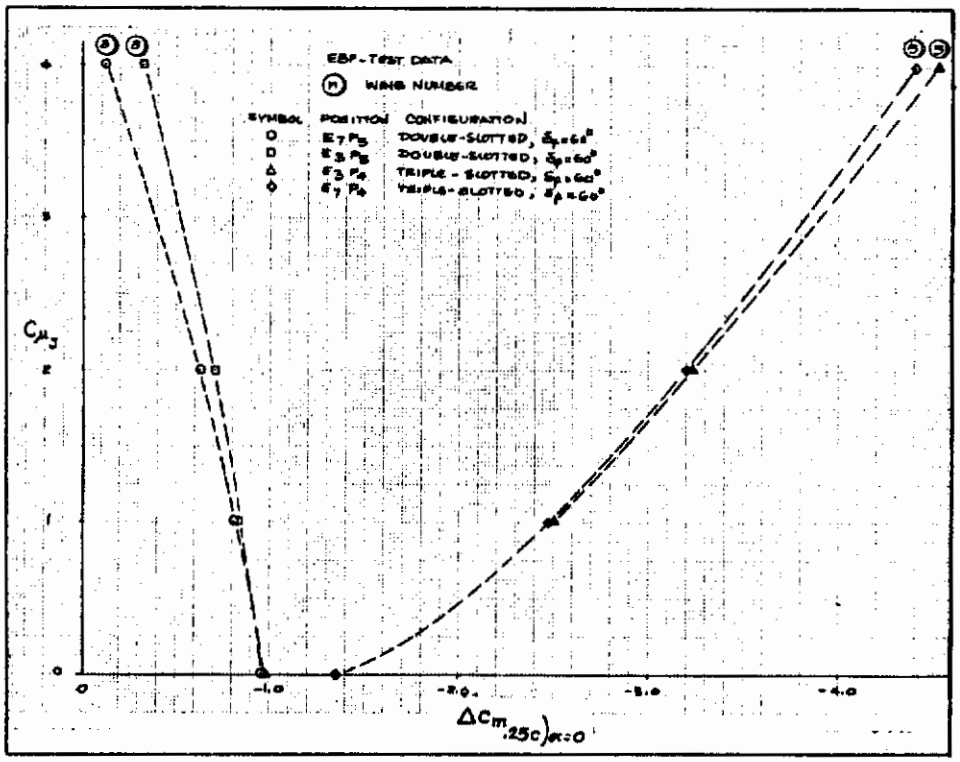

Figure 5.2-15. Effect of Engine Location on EBF Pitching Moment Increments

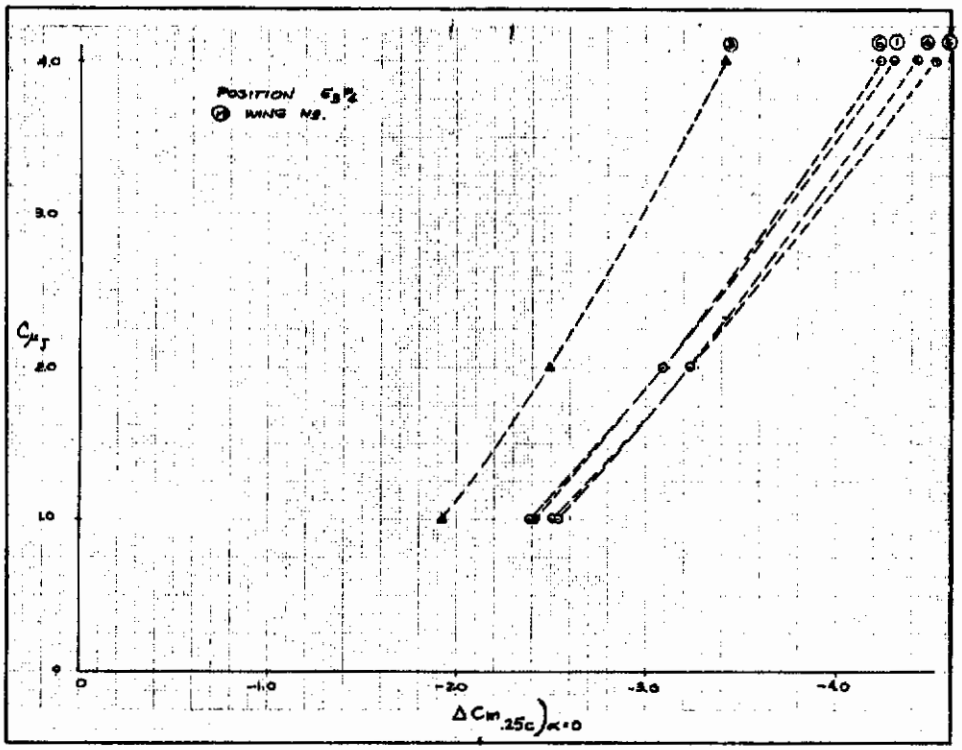

Figure 5.2-16. Effect of Wing Planform on EBF Pitching Moment Increments, Triple-Slotted Flaps at 60 Degrees (Nacelle Position E_3P_4)

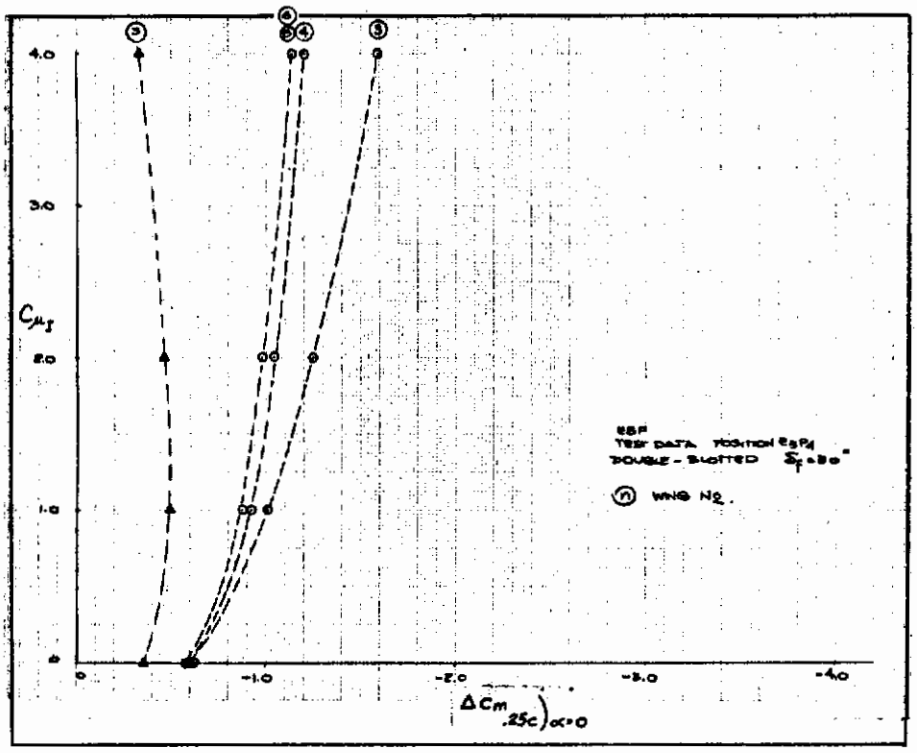

Figure 5.2-17. Effect of Wing Planform on EBF Pitching Moment Increments, Double-Slotted Flaps at 30 Degrees (Nacelle Position E_3P_4)

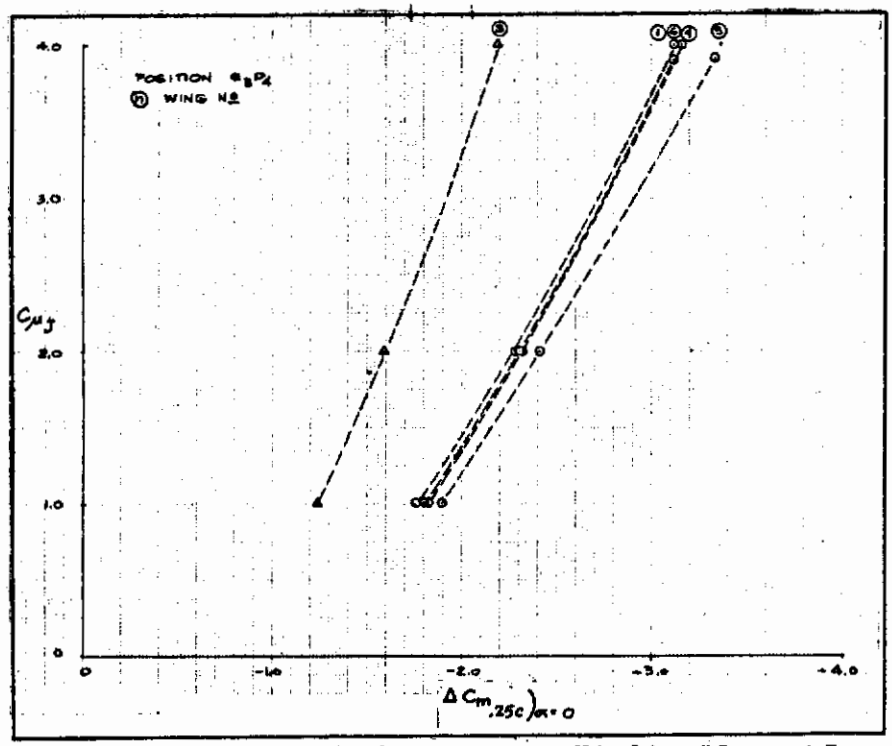

Figure 5.2-18. Effect of Wing Planform on EBF Pitching Moment Increments, Double-Slotted Flaps at 60 Degrees (Nacelle Position E_3P_4)

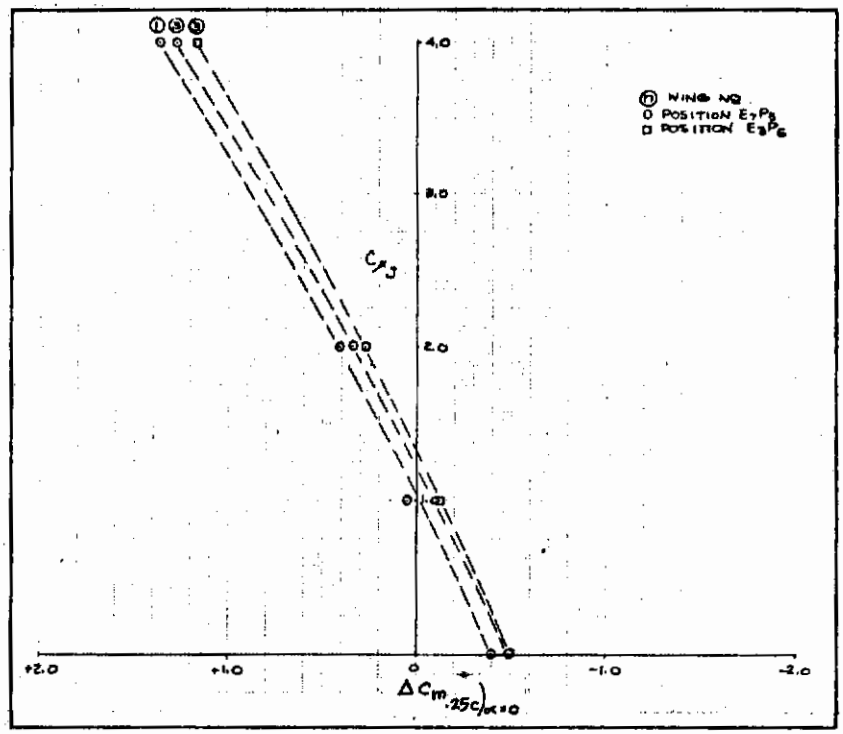

Figure 5.2-19. Effect of Wing Planform on EBF Pitching Moment Increments, Double-Slotted Flaps at 30 Degrees (Nacelle Positions E_7P_5 and E_3P_5)

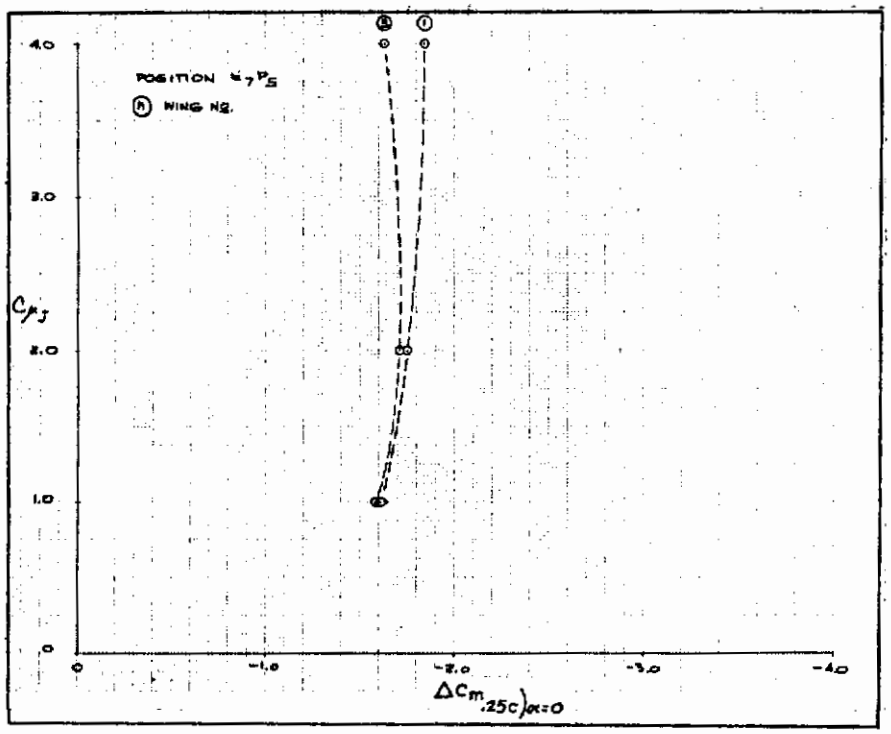

Figure 5.2-20. Effect of Wing Planform on EBF Pitching Moment Increments, Triple-Slotted Flaps at 60 Degrees (Nacelle Position E_7P_5)

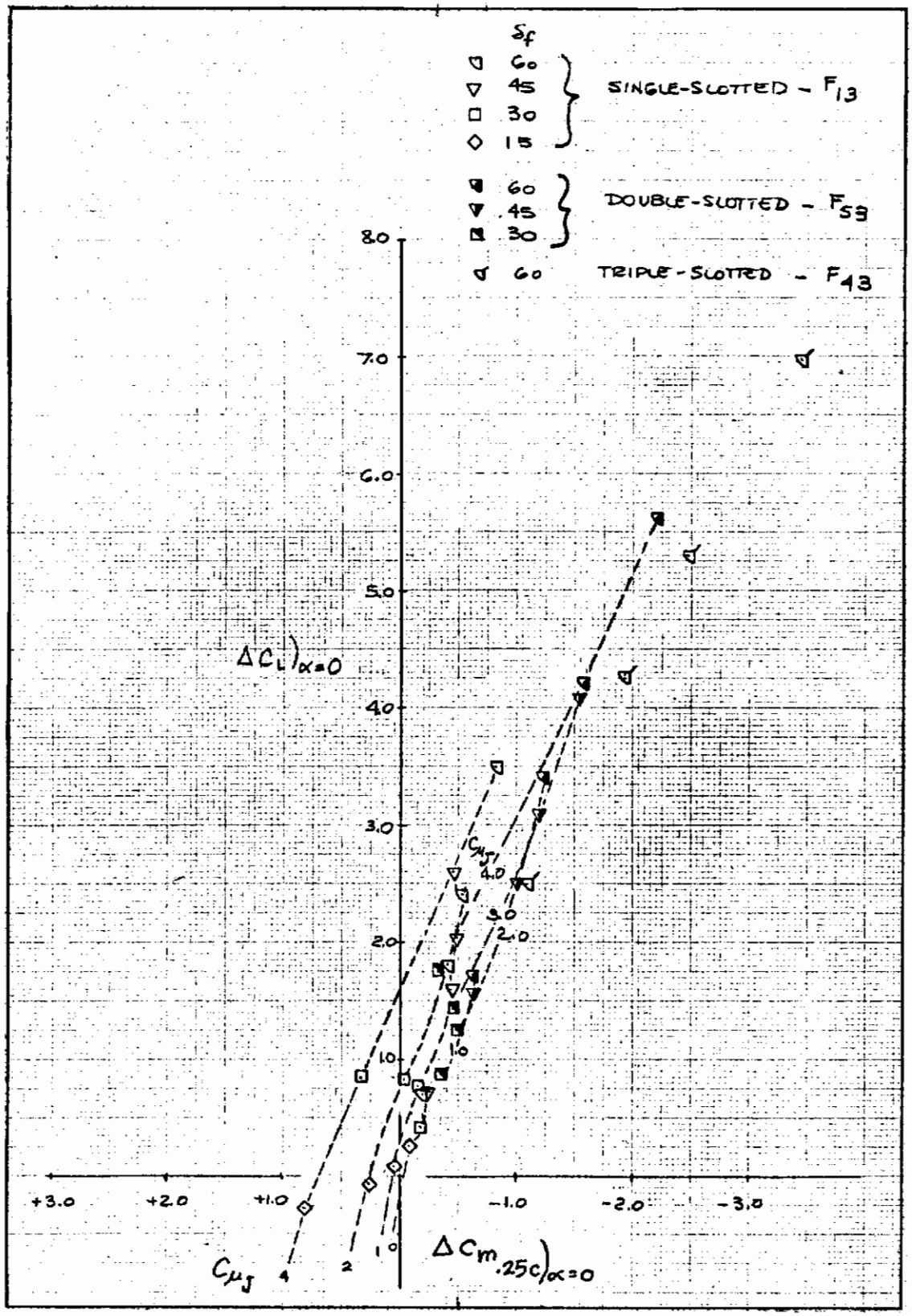

Figure 5.2-21. EBF Lift and Pitching Moment Increments, Wing No. 3 (Nacelle Position E_3P_4)

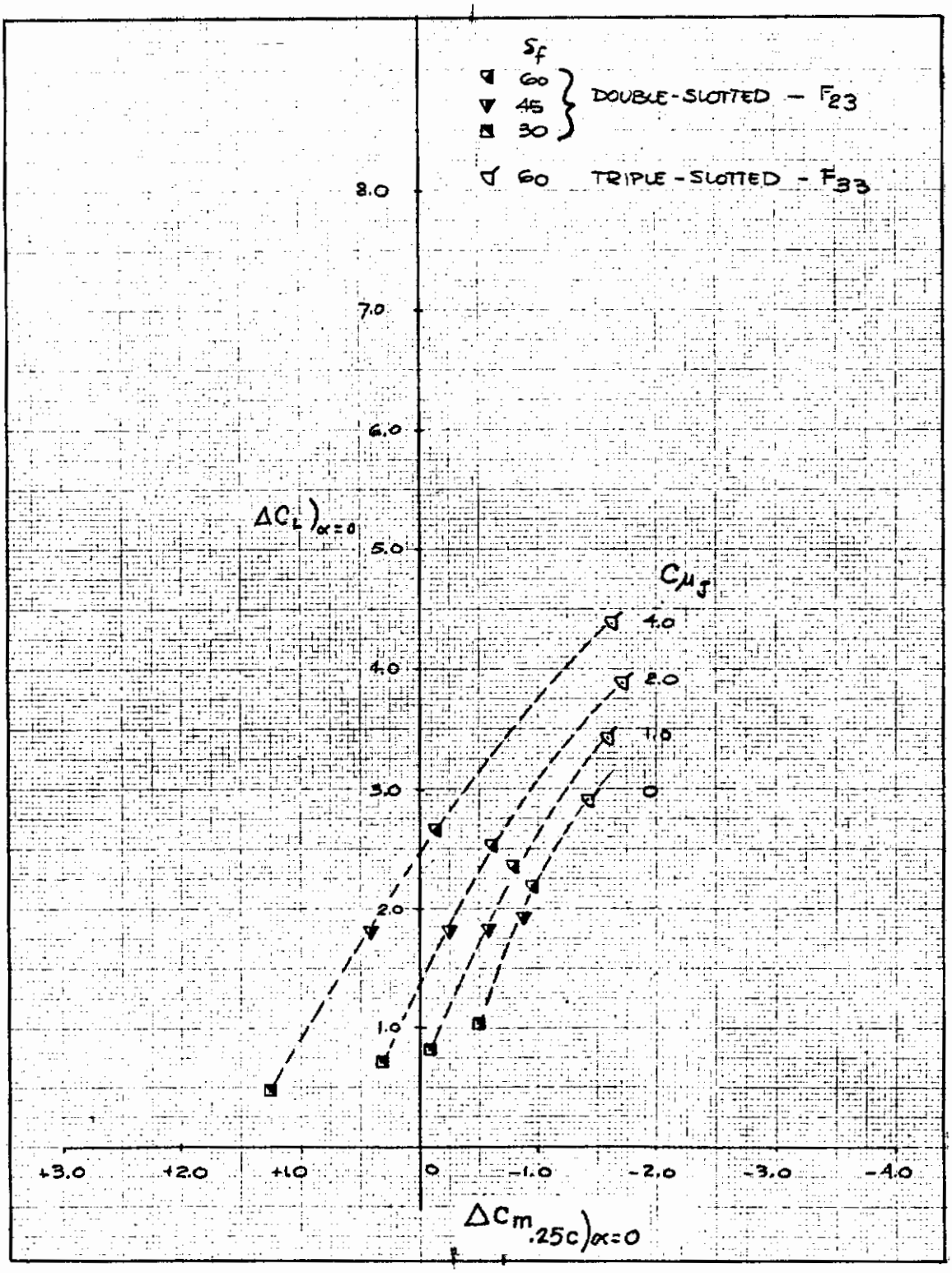

Figure 5.2-22. EBF Lift and Pitching Moment Increments, Wing No. 3 (Nacelle Position E_7P_5)

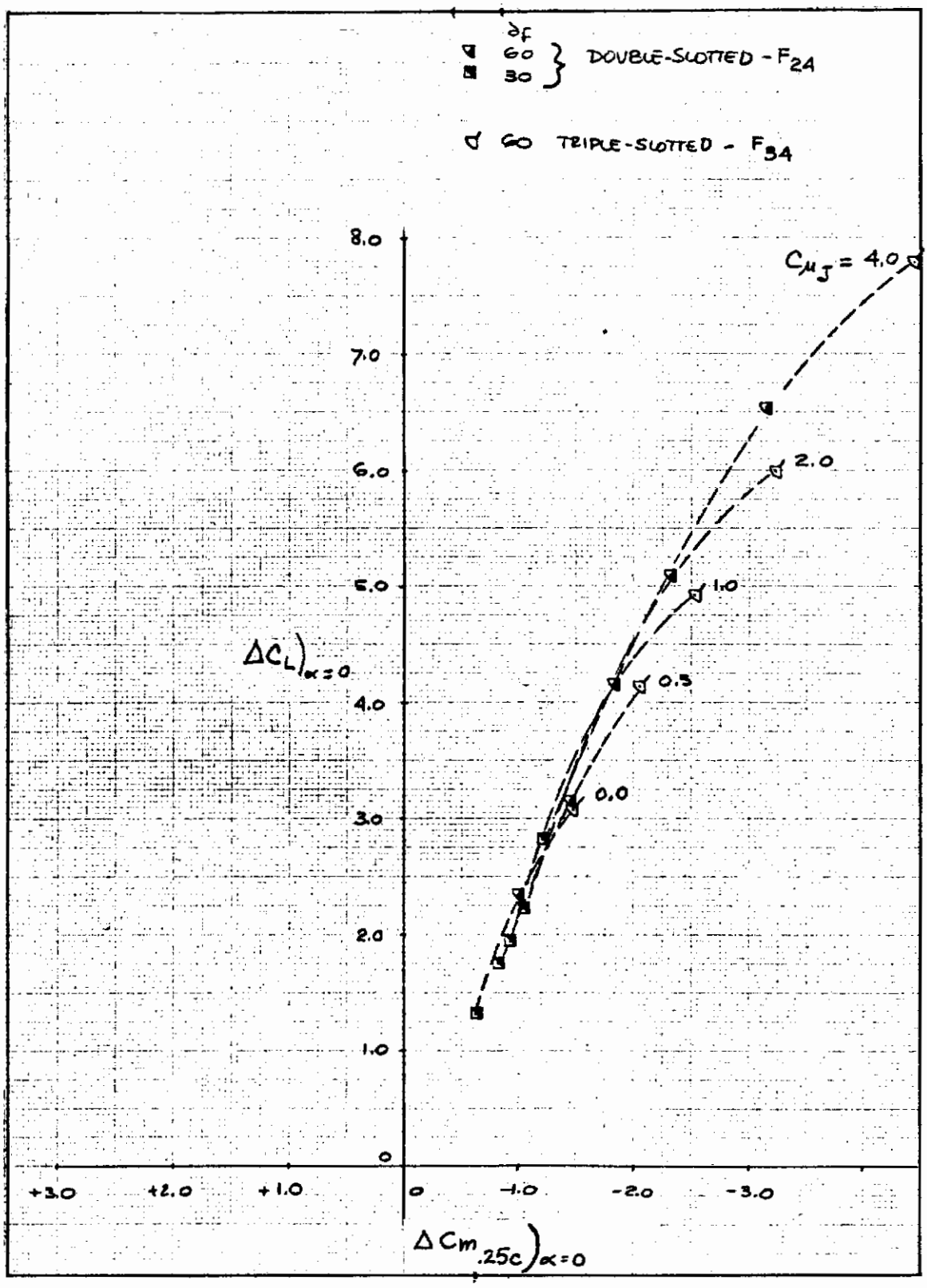

Figure 5.2-23. EBF Lift and Pitching Moment Increments, Wing No. 4 (Nacelle Position E_3P_4)

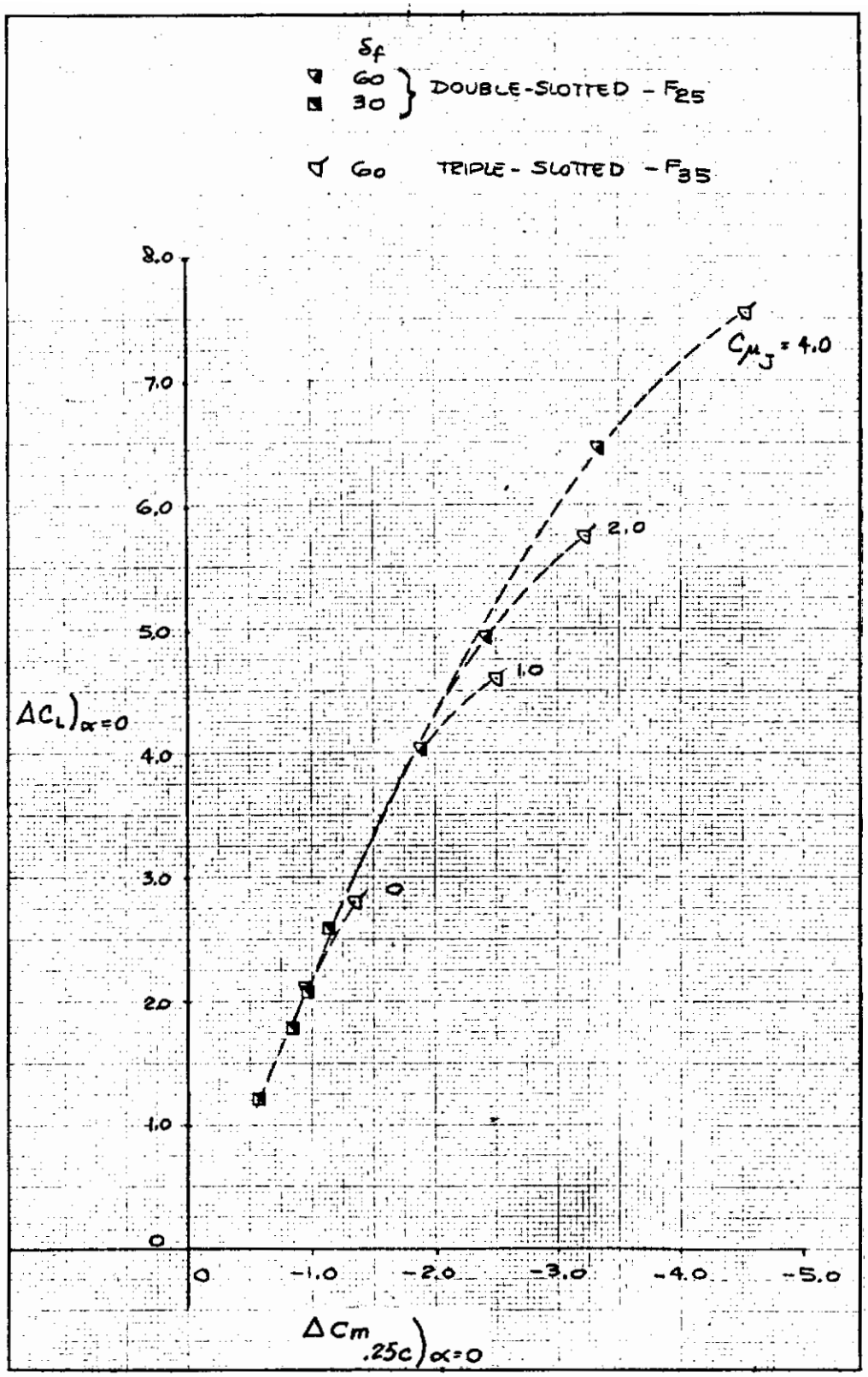

Figure 5.2-24. EBF Lift and Pitching Moment Increments, Wing No. 5 (Nacelle Position E_3P_4)

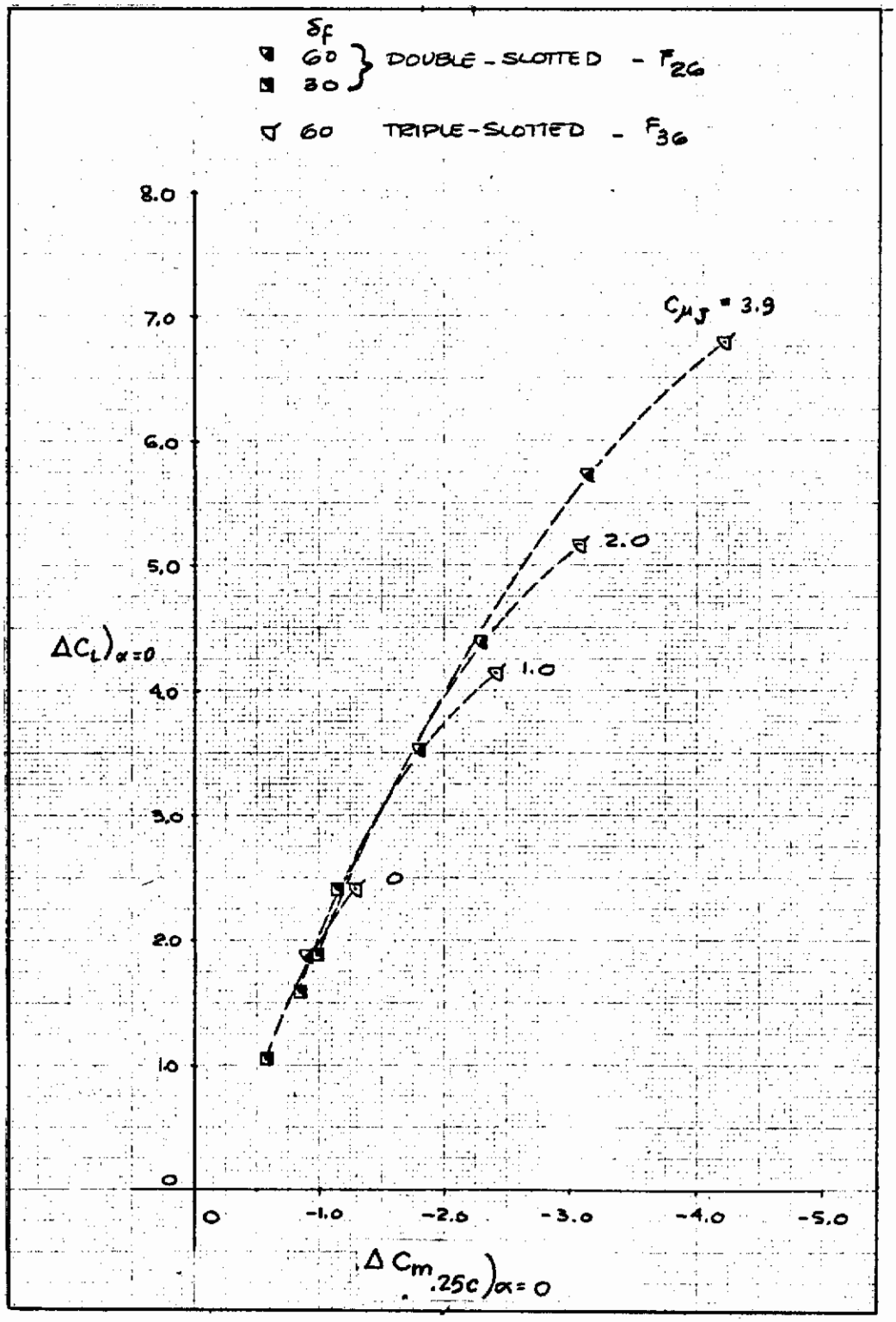

Figure 5.2-25. EBF Lift and Pitching Moment Increments, Wing No. 6 (Nacelle Position E_3P_4)

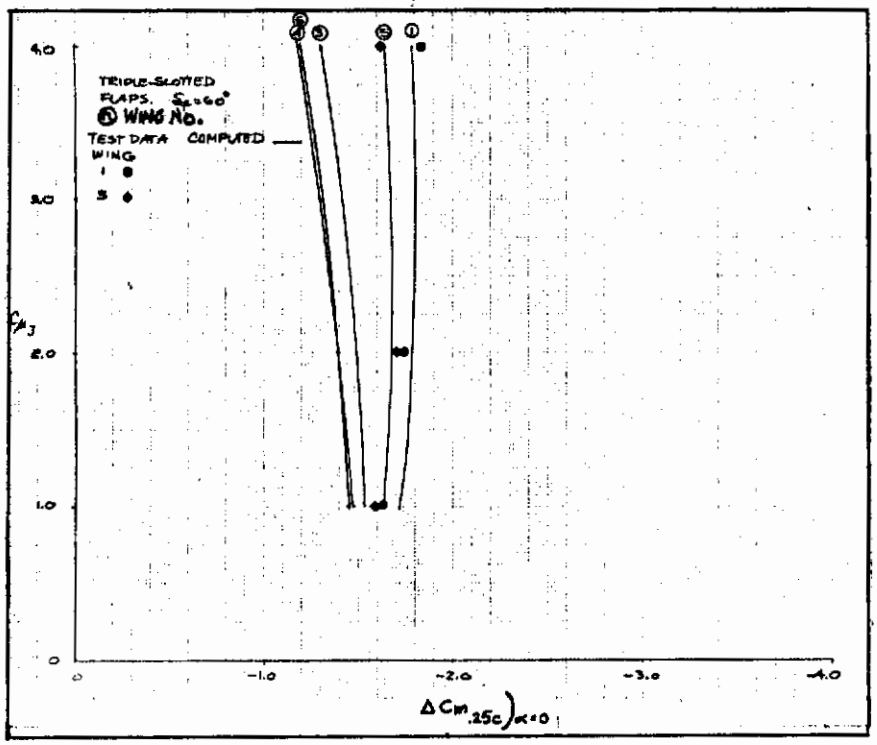

Figure 5.2-26. Correlation of Test Data and Predicted EBF Flap Pitching Moment Increments (Nacelle Position E_7P_5)

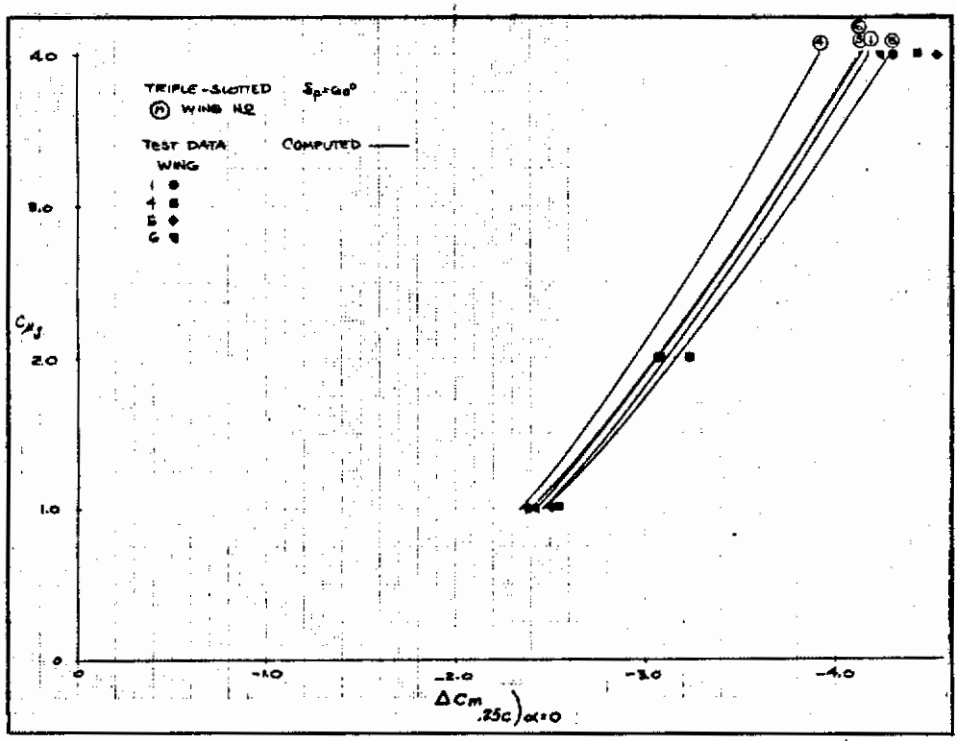

Figure 5.2-27. Correlation of Test Data and Predicted EBF Flap Pitching Moment Increments (Nacelle Position E_3P_4)

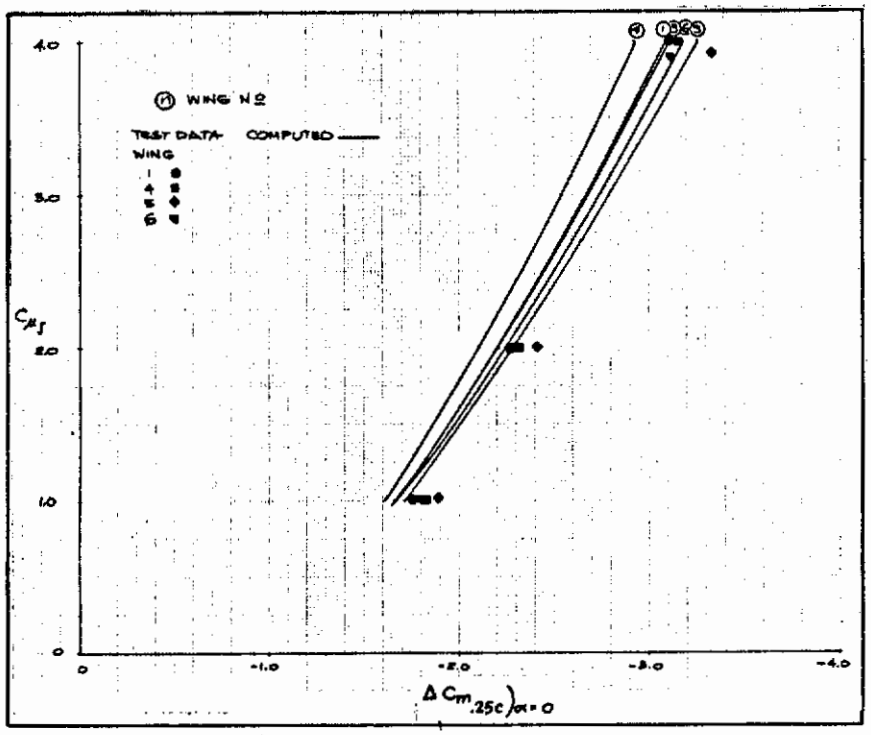

Figure 5.2-28. Correlation of Test Data and Predicted EBF Flap Pitching Moment Increments, Double-Slotted Flaps at 60 Degrees, (Nacelle Position E_3P_4)

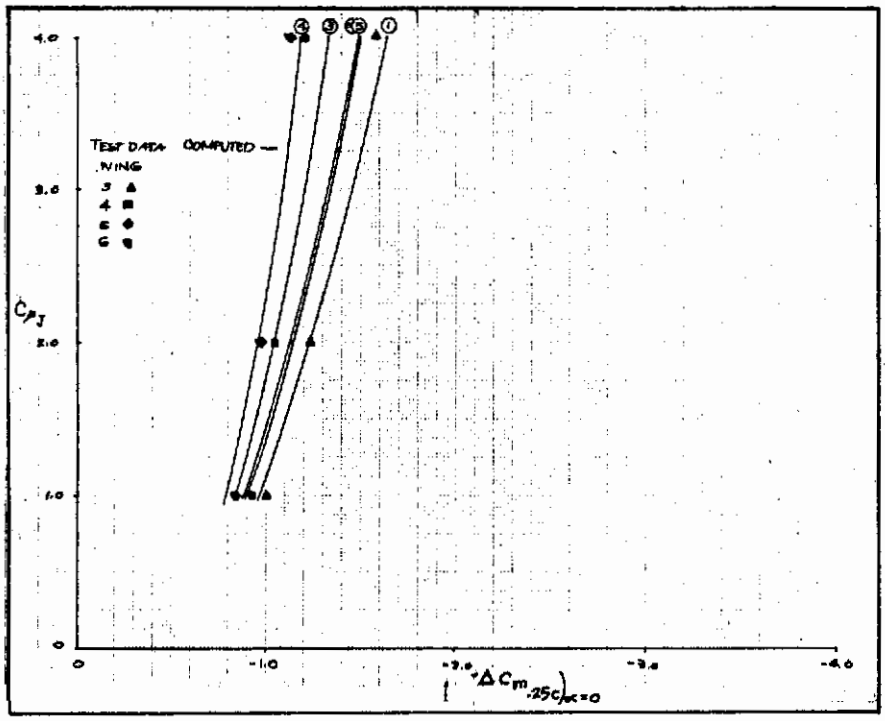

Figure 5.2-29. Correlation of Test Data and Predicted EBF Flap Pitching Moment Increments, Double-Slotted Flaps at 30 Degrees, (Nacelle Position E_3P_4)

SECTION 6

HORIZONTAL TAIL LIFT AND PITCHING MOMENTS

6.1 HORIZONTAL TAIL CHARACTERISTICS

Isolated empennage characteristics were determined on Test GDLST 611. This was accomplished by running a series of body-alone pitch and yaw sweeps at four different tunnel dynamic pressures, which were used as tares for the body-plus-empennage tests. Overall, Test 611 included the effects of Reynolds number on the horizontal and vertical tail, effect of horizontal tail leading edge device, and blowing on the elevator and rudder. In this section, characteristics of the horizontal tail with undeflected elevator are discussed.

6.1.1 EFFECT OF REYNOLDS NUMBER. The State-of-the-Art Design Compendium (Reference 3-7) notes that estimation of the basic horizontal tail lift curve should be amenable to the methodology already existing in the DATCOM. Since the tunnel dynamic pressure (normally q = 15 psf) required to achieve the desired engine thrust coefficients would result in rather low Reynolds number for the empennage, however, tests at four R_N values were included in Test 611 to supplement information in the DATCOM. The conditions investigated were:

Tunnel Dynamic Pressure (psf)	*Horizontal Tail Reynolds No. (X 10^{-6})	Mach No.
15	0.264	0.099
30	0.458	0.140
60	0.654	0.198
110	0.880	0.267

*Based on length of horizontal tail mean aerodynamic chord of 5.753 in.

The effect of these Reynolds number variations on the horizontal tail lift curve is shown in Figure 6.1-1, which indicates that the predominant influence of Reynolds number is on maximum lift coefficient. The significant parameters are:

$R_N \times 10^{-6}$	$*C_{L_{\alpha_H}}$ (deg^{-1})	C_{L_H} max	α_H $C_{L_{max}}$
0.264	0.0647	-0.70	-13.0
0.458	0.0637	-0.740	-13.2
0.654	0.0645	-0.780	-14.6
0.880	0.0615	-0.805	-15.5

*Slopes taken between $\alpha_H = \pm 6$ deg

The effects of R_N on lift curve slope are manifested through the term $C_{\ell_\alpha}/C_{\ell_\alpha}$) theory (DATCOM Section 4.1.1.2, Method 2). The test data does not show a very consistent variation with R_N, but DATCOM procedures were applied to obtain values for $C_{\ell_\alpha}/ C_{\ell_\alpha}$) theory that yield the proper values for $C_{L_{\alpha_H}}$ as reassured from Test 611.

The results are shown in Figure 6.1-2. Using the dashed curve on Figure 6.1-2 to obtain values for $C_{\ell_\alpha}/(C_{\ell_\alpha}$ theory, a horizontal tail lift curve was estimated from DATCOM and compared with measured values. The results are:

$R_N \times 10^{-6}$	$C_{L_{\alpha_H}}$ (deg^{-1})	$C_{L_{\alpha_H}}$ (measured) (deg^{-1})	% Error
0.264	0.0652	0.0647	0.77
0.458	0.0636	0.0637	-0.16
0.654	0.0632	0.0645	-2.02
0.880	0.0640	0.0615	4.07

Average % error = 1.76

The aspect ratio of the horizontal tail used in Test 611 fell in the "high aspect ratio" category as defined in Section 4.1.3.4 of the DATCOM. Consequently, maximum lift is primarily dependent on two-dimensional characteristics, which are obtained from DATCOM Section 4.1.1.4. In the DATCOM methodology, effects of R_N on section characteristics are accounted for in the term $\Delta_3 C_{\ell_{max}}$. (A small Mach number correction was also required for the point at q = 110 psf.) The DATCOM procedures were used to obtain values for $\Delta_3 C_{\ell_{max}}$ that would match the $C_{L_{max}}$ obtained from Test 611, with results as shown in Figure 6.1-3. Since the dashed curve was faired exactly through the four data points, an error summary is inappropriate.

The angle of attack at $C_{L_{max}}$ (DATCOM Section 4.1.3.4) methodology has no terms that are dependent only on Reynolds number. The error summary for DATCOM

estimates of $\alpha_{C_{L_{max}}}$ versus results from Test 611 is:

$R_N \times 10^{-6}$	$\alpha_{C_{L_{max}}}$ (estimate) (deg^{-1})	$\alpha_{C_{L_{max}}}$ (measured) (deg^{-1})	% Error
0.264	-14.1	-13.0	8.46
0.458	-14.6	-13.2	10.61
0.654	-15.1	-14.6	3.42
0.880	-16.1	-15.5	3.87

Average % error = 6.59

6.1.2 EFFECT OF LEADING EDGE DEVICE (Krueger Flap). Test 611 included a limited amount of testing with a Krueger type leading edge device on the horizontal tail. Effectiveness of the Krueger is illustrated in Figure 6.1-4. The tunnel dunamic pressure was 15 psf for those runs. This relatively crude leading edge device was capable of increasing horizontal tail maximum lift coefficient from -0.725 to -1.190 and extended the angle of attack for $C_{L_{max}}$ from -11.5 to -22.3 deg. The effect of the Krueger flap on horizontal tail drag is also shown in Figure 6.1-4. All coefficients are based on horizontal tail area.

6.1.3 CENTER OF PRESSURE LOCATION. Position of the horizontal tail center of pressure was determined from Test 611 to establish the validity of using a geometric tail length (distance between 0.25 $\bar{c}_W$ and 0.25 $\bar{c}_H$) for calculating tail pitching moment increments. For comparative purposes, a tail volume coefficient, $\bar{V}_H$, was determined from the test data according to the following relationship.

$$\bar{V}_H = \left(\frac{X_H}{\bar{c}_H} - \frac{C_{m_H}}{C_{L_H}} \right) \frac{\bar{c}_H}{\bar{c}_W} \frac{S_H}{S_W}$$

In this equation, C_{m_H} is the measured pitching moment, referenced to horizontal tail area and mean aerodynamic chord, with moment center at 0.25 $\bar{c}_H$.

The results are shown in Figures 6.1-5 through 6.1-8, where $\bar{V}_H$ from Test 611 is given as a function of angle of attack for the four tunnel dynamic pressures tested. Least-squares linear curve fits were obtained, and the resulting equations are shown on the figures. The data points did not deviate more than ± 3 percent from the linear relationship (except for those points approaching the singularity at $C_{L_H} = 0$), and there was no consistent variation with Reynolds number. Overall, it seems that accounting for variations of horizontal tail center of pressure location is a refinement, but that acceptably accurate tail pitching moment increments can be calculated by using a $\bar{V}_H$ determined from only the configuration geometry.

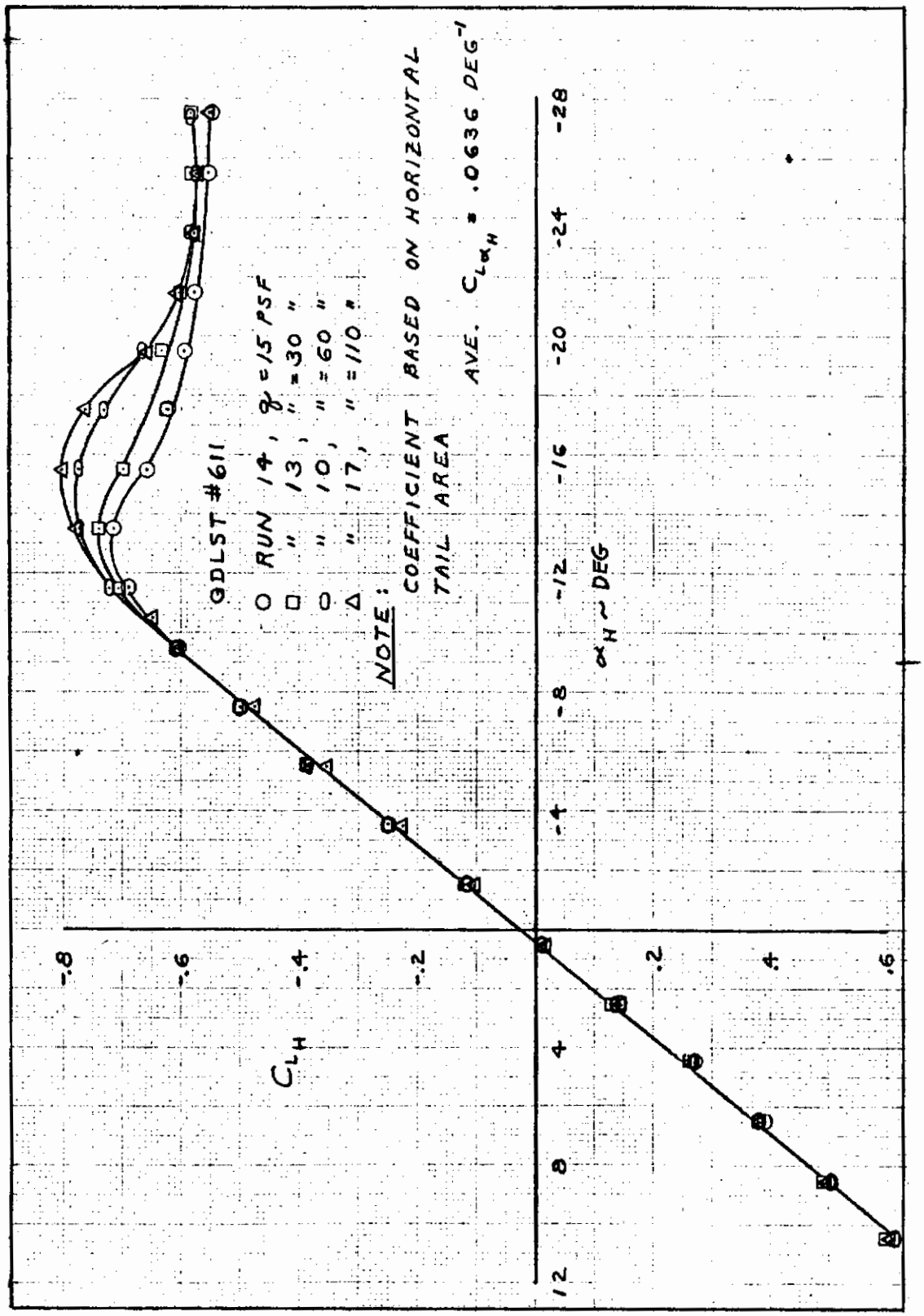

Figure 6.1-1. Horizontal Tail Lift Curve

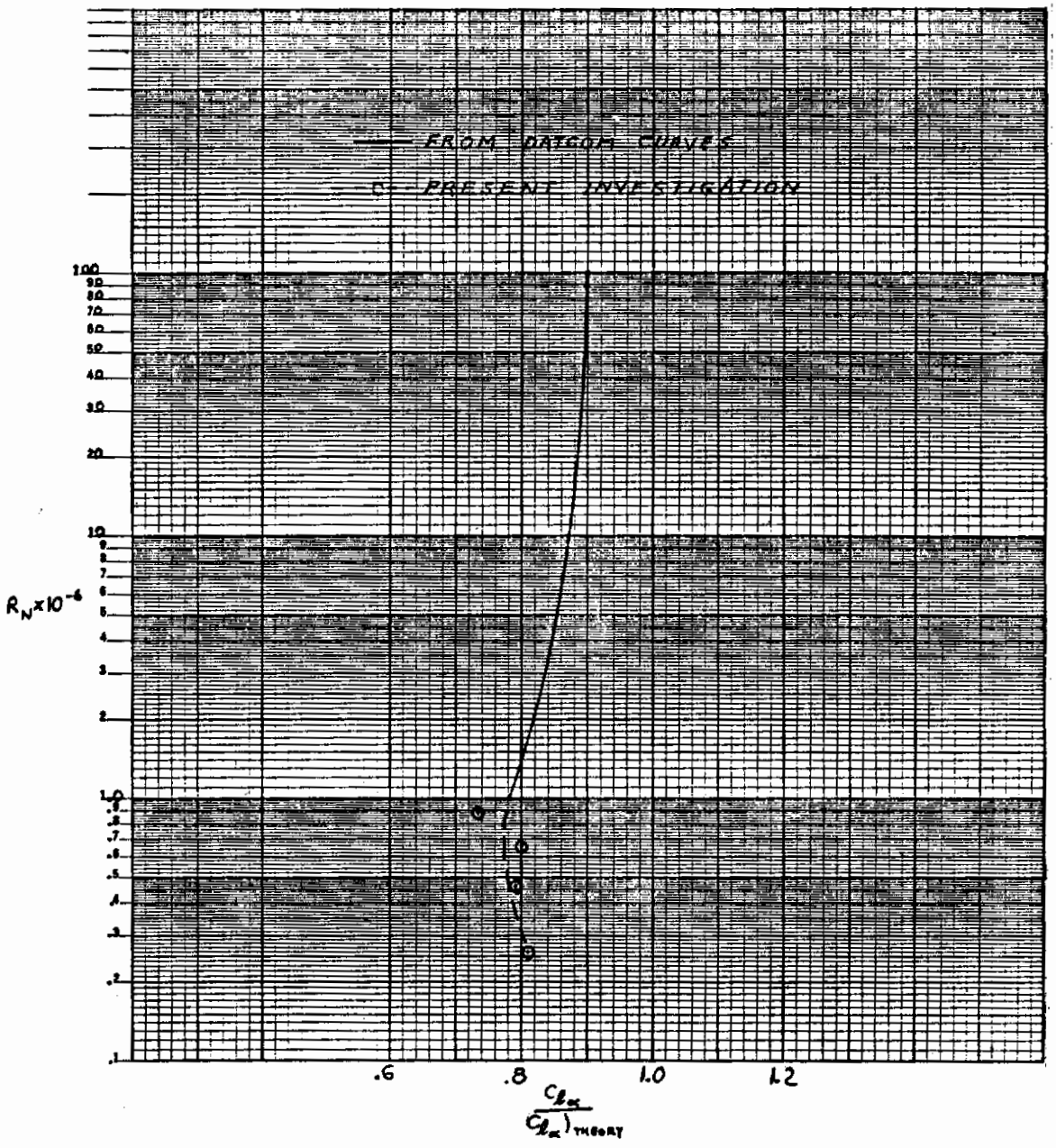

Figure 6.1-2. Effect of Reynolds Number on Section Lift Curve Slope

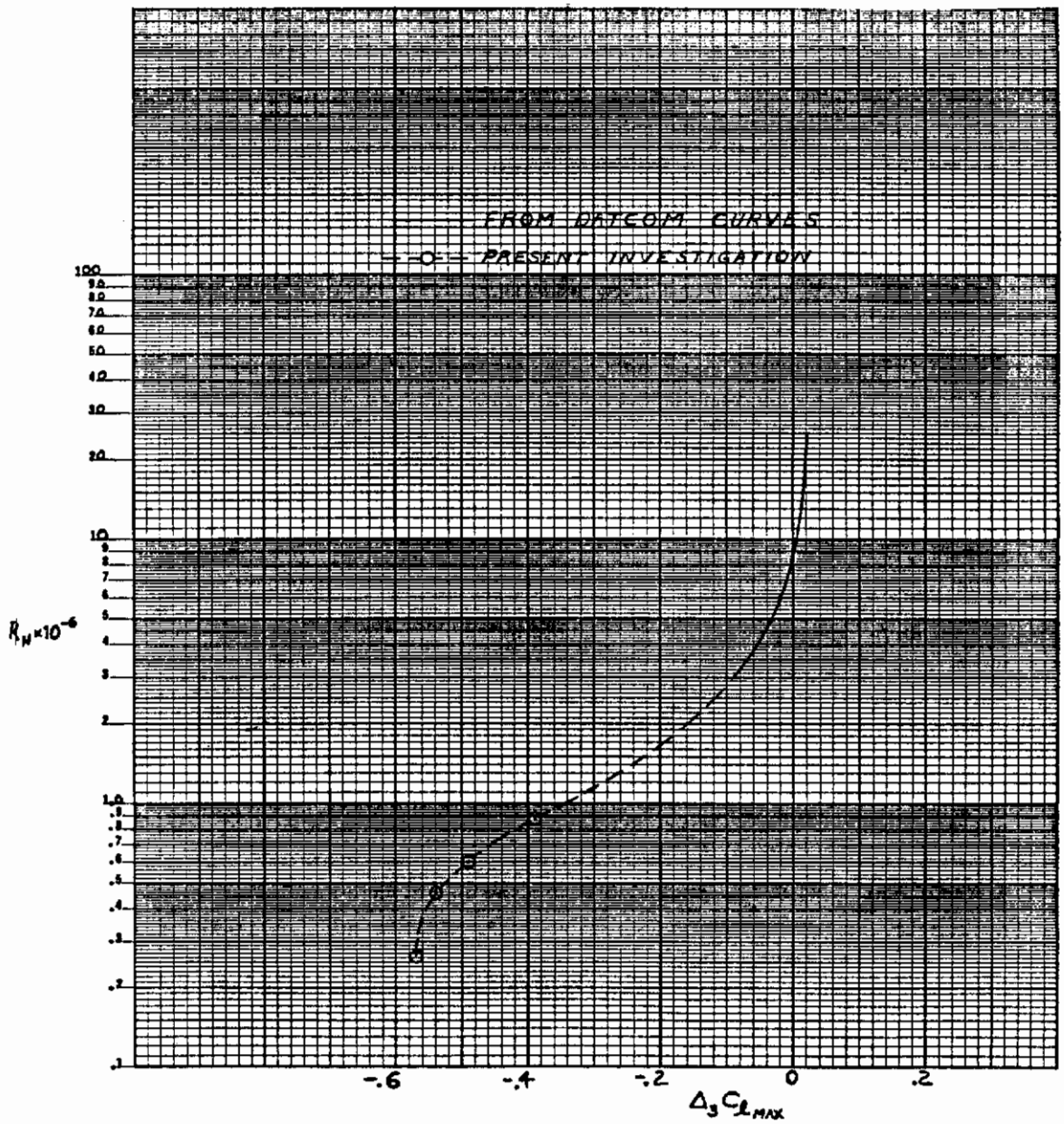

Figure 6.1-3. Effect of Reynolds Number on Section Maximum Lift Coefficient

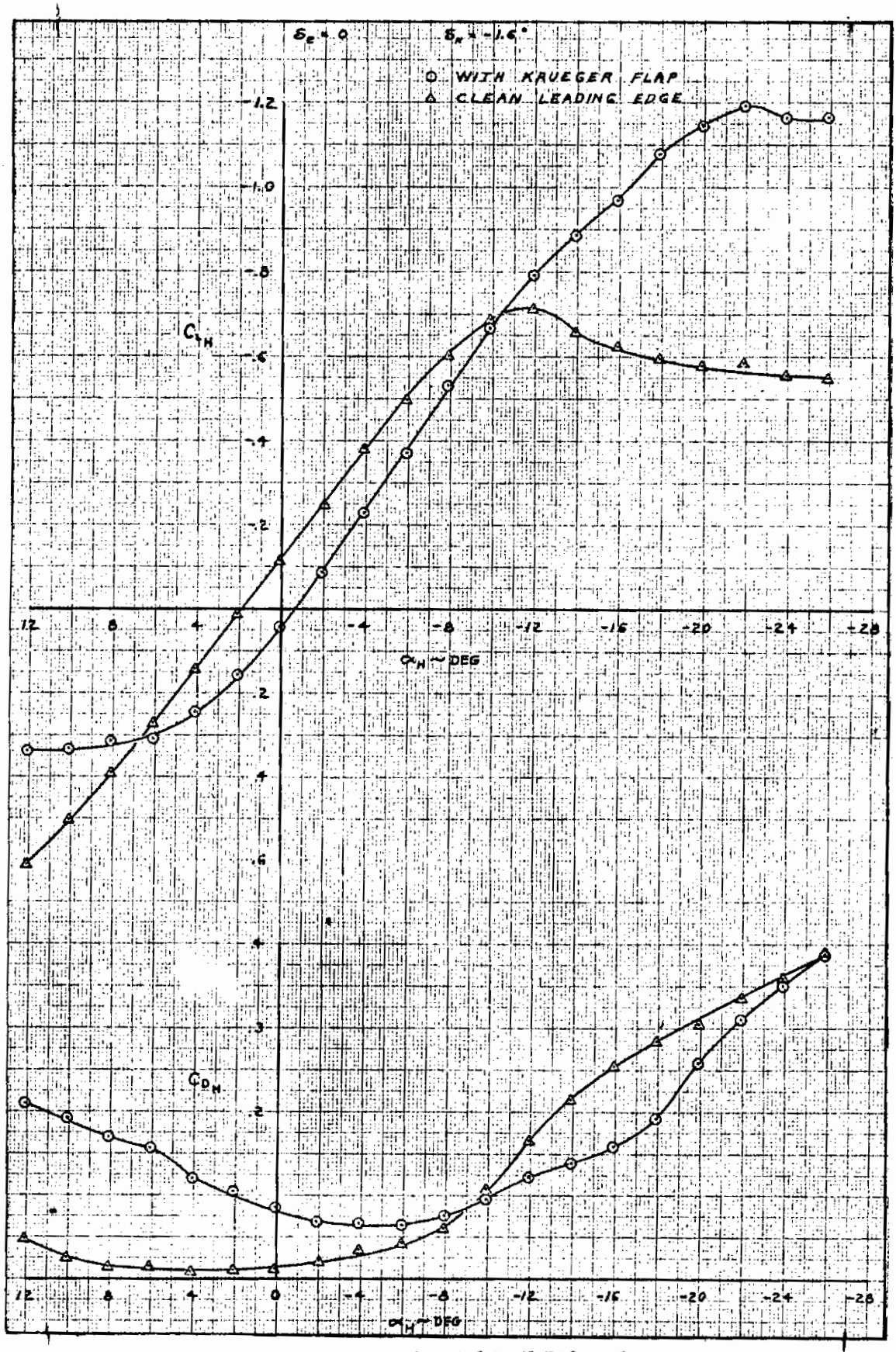

Figure 6.1-4. Horizontal Tail Lift and Drag

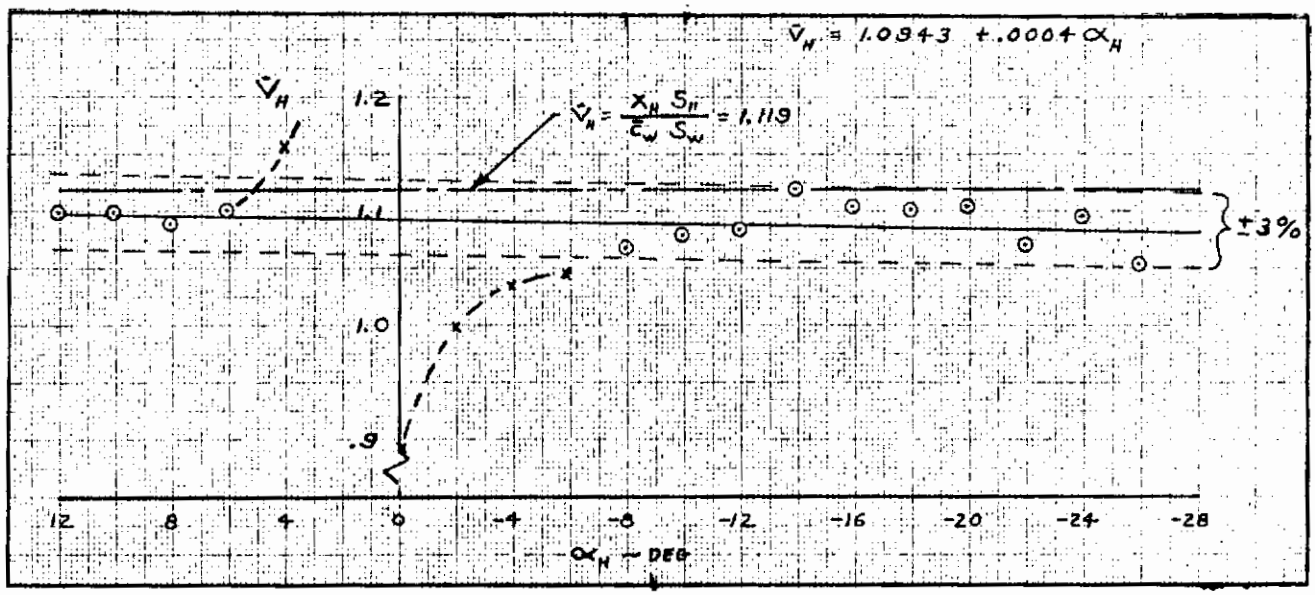

Figure 6.1-5. Effect of Angle of Attack on Horizontal Tail Center of Pressure Location ($q = 15$ lb/ft^2)

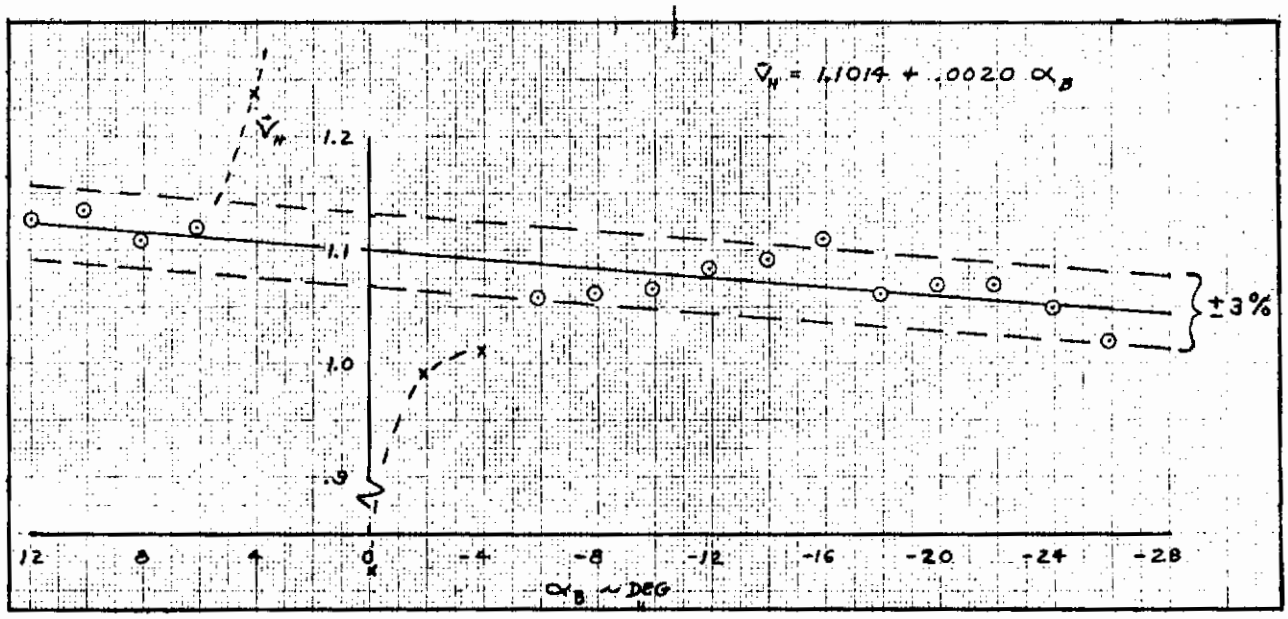

Figure 6.1-6. Effect of Angle of Attack on Horizontal Tail Center of Pressure Location ($q = 30$ lb/ft)

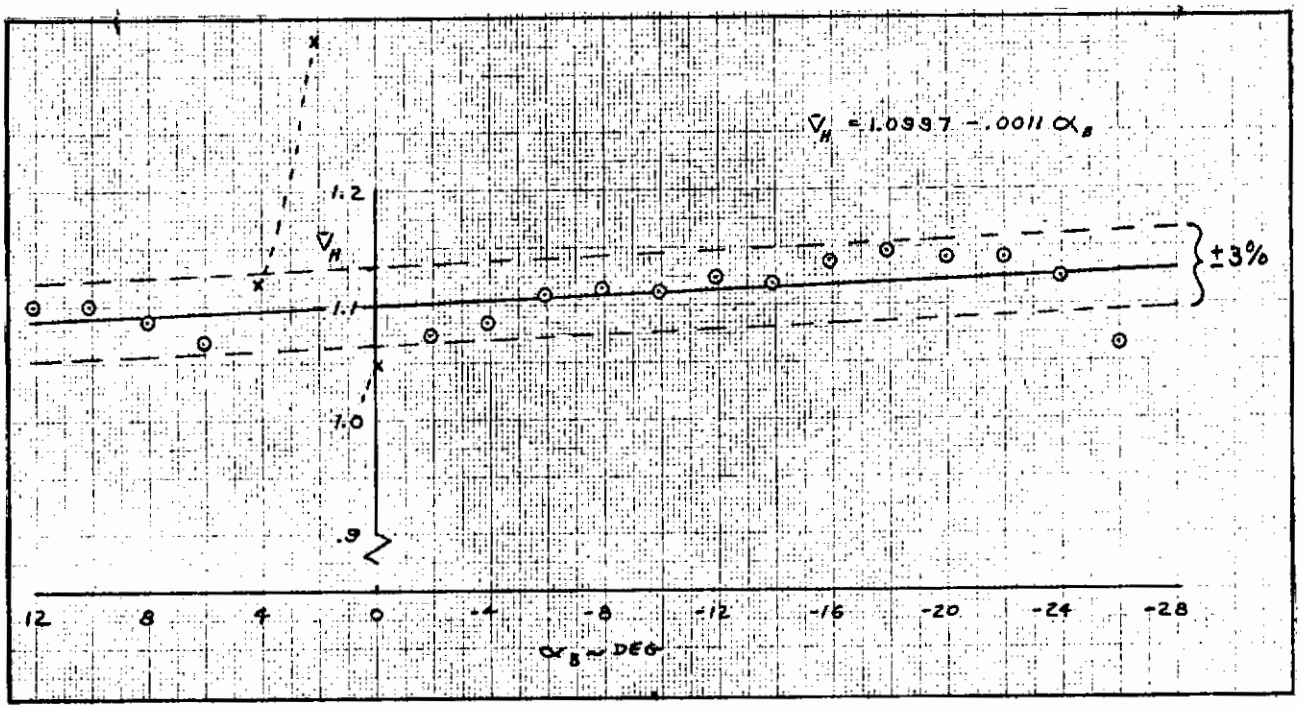

Figure 6.1-7. Effect of Angle of Attack on Horizontal Tail Center of Pressure Location (q = 60 lb/ft)

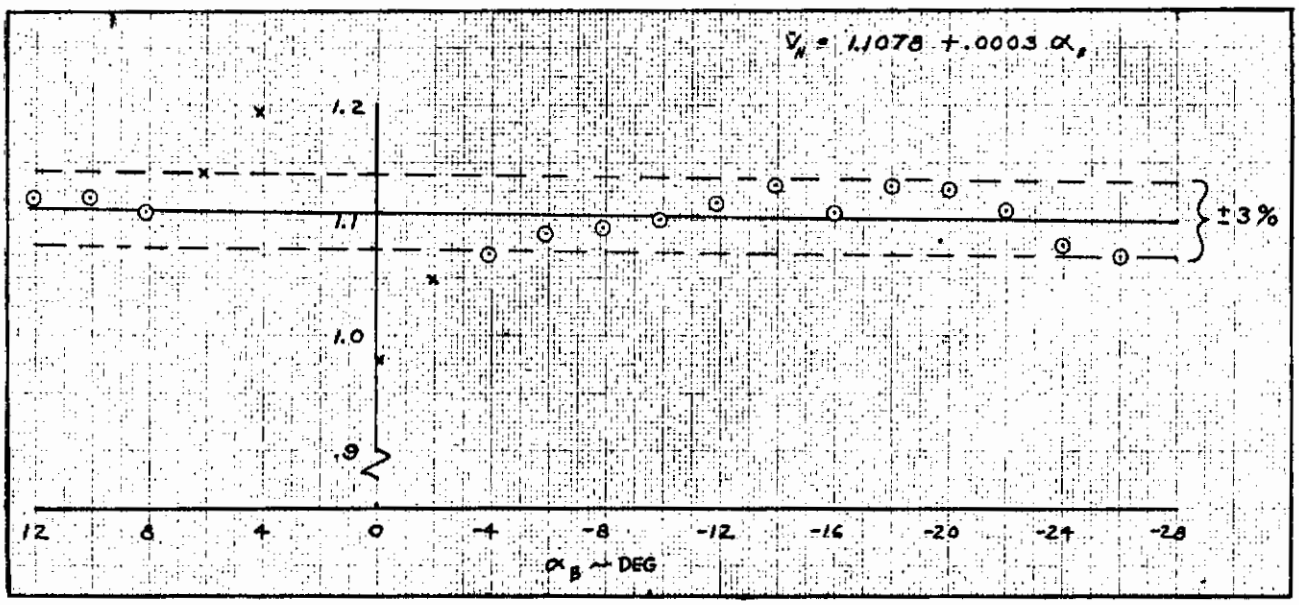

Figure 6.1-8. Effect of Angle of Attack on Horizontal Tail Center of Pressure Location (q = 110 lb/ft)

6.2 TAIL-ON TEST RESULTS

One feature of this test program is that the major portion of testing was accomplished tail-off. Empennage characteristics are determined from isolated tail tests and a wake rake to measure tail flow fields. Since direct measurements of tail flow field characteristics are not usually accomplished in most configuration design studies, one of the test objectives was to verify that horizontal tail characteristics can be determined from a build-up of isolated tail lift and drag, downwash, and tail dynamic pressure ratio. To accomplish this objective, three configurations in Test 612-0 were tested in the usual manner of running a series of stabilizer incidence variations to extract downwash characteristics. The following configurations were tested tail-on:

Clean Wing (δ_f = 0 deg)

Double Slotted Flap (F_{21}) (δ_f = 30 deg)

Triple Slotted Flap (F_{31}) (δ_f = 60 deg)

The incidence variations were made at δ_H = +5, 0, -5, and -10 degrees, and the three configurations were tested at C_J = 0, 1,0, 2.0, and 4.0.

The basic working data used to perform the analyses was obtained from the Convair Aerospace Digigraphics System and is presented in Figures 6.2-1 through 6.2-12. The incremental tail-on, tail-off pitching moments are shown as a function of angle of attack for the three flap configurations and four thrust coefficients tested.

6.2.1 COMPARISON OF MEASURED DOWNWASH WITH THAT OBTAINED FROM STABILIZER INCIDENCE VARIATIONS. The first comparison is between the downwash angles measured with the wake rake and those obtained from the tail-on runs at various stabilizer incidence settings. Examination of Figures 6.2-1 through 6.2-12 show that, for the triple-slotted flap (F_{31}) and 60 degrees of deflection, the array of stabilizer incidence angles used did not produce tail-on, tail-off intersections (C_{m_H} = 0) at the higher thrust coefficients. Consequently, downwash characteristics cannot be extracted from this data without performing extrapolations, with a resulting deterioration in accuracy of the results. The clean-wing and double-slotted-flap (F_{21}) configurations had intersections throughout the range of thrust coefficients tested. Downwash from the clean wing was relatively insensitive to thrust coefficient variations, and the double-slotted-flap configuration was therefore selected as the example for these comparisons.

Figures 6.2-13 through 6.2-16 show the manner in which the plots of C_{m_H} versus δ_H (for each angle of attack at which a data point was obtained) were interpolated or extrapolated to obtain the stabilizer incidence angle at which C_{m_H} = 0. The downwash angle is then obtained from the relationship:

$$\epsilon = \alpha_W - i_W + \delta_H$$

Results of the comparisons are shown in Figure 6.2-17, where excellent correlation is obtained between the downwash angles extracted from tail-on, tail-off data and that measured with the tail wake rake probes.

6.2.2 COMPARISON OF MEASURED AND BUILT-UP PITCHING MOMENTS. For the triple-slotted-flap configuration, where it was difficult to accurately extract downwash data from the tail-on tests, an evaluation can be made from a build-up of tail-off pitching moments, downwash, dynamic pressure ratio, tail lift, and tail drag to enable a direct comparison with measured tail-on data.

To build up tail-on pitching moments from component data, the tail lift, drag, and pitching moment increments are obtained from the following relationships. The lift and drag increments are:

$$C_{L_H} = (C_{L_H} \cos \epsilon - C_{D_H} \sin \epsilon) \frac{S_H}{S_W} \eta_H$$

$$C_{D_H} = (C_{L_H} \sin \epsilon + C_{D_H} \cos \epsilon) \frac{S_H}{S_W} \eta_H$$

In these equations, C_{L_H} and C_{D_H} are obtained from Figure 5.1-4, where the tail angle of attack is given by:

$$\alpha_H = \alpha_W - \epsilon - i_W + \delta_H$$

The tail pitching moment contribution is then obtained from:

$$C_{m_H} = -\Delta C_{L_H} \left(\frac{\ell_H}{\bar{c}_W}\right) + \Delta C_{D_H} \left(\frac{h_H}{\bar{c}_W}\right)$$

The stability axes moment arms in this equation are given by:

$$\ell_H = X_H \cos (\alpha_W - i_W) + Z_H \sin (\alpha_W - i_W)$$

$$h_H = Z_H \cos (\alpha_W - i_W) - X_H \sin (\alpha_W - i_W)$$

The comparisons between measured and built-up pitching moments are shown in Figures 6.2-18 through 6.2-21. Again, excellent correlation is shown.

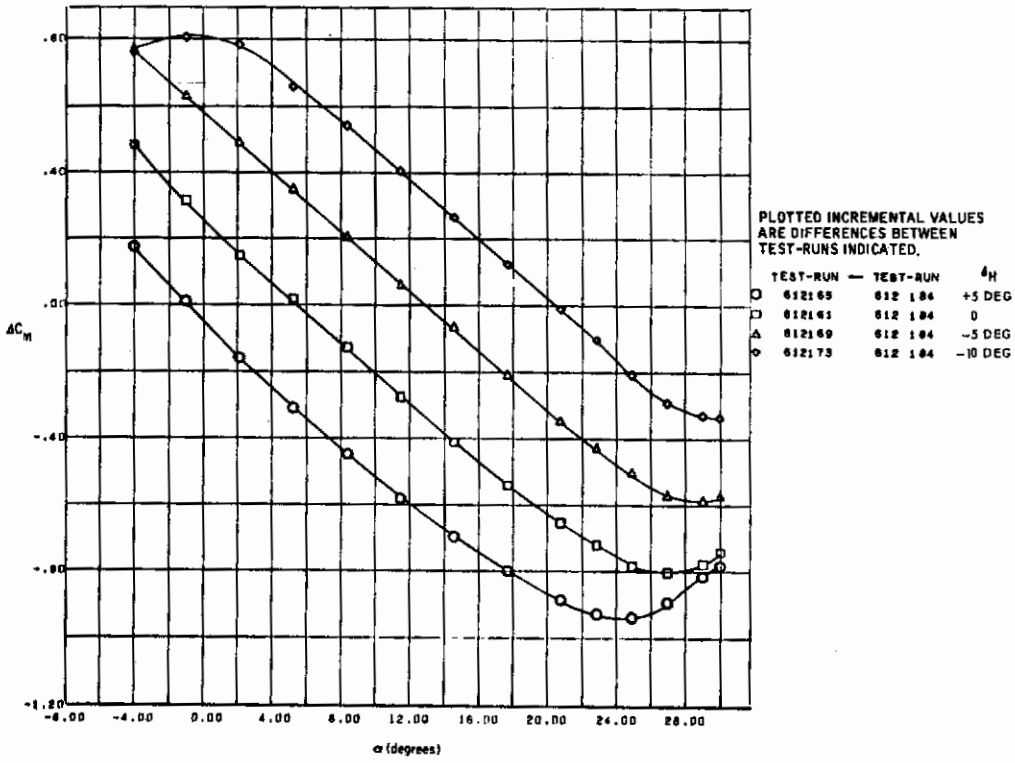

Figure 6.2-1. Tail-On, Tail-Off Pitching Moment Increments, Clean Wing, $C_{\mu_J} = 0$

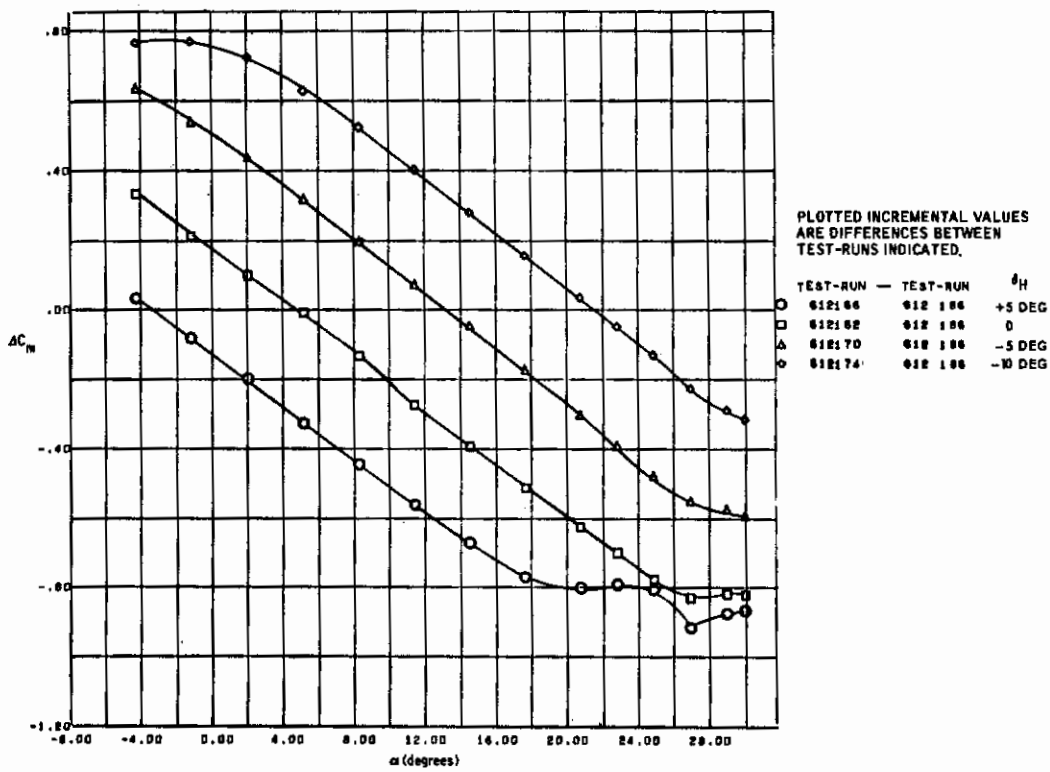

Figure 6.2-2. Tail-On, Tail-Off Pitching Moment Increments, Clean Wing, $C_{\mu_J} = 1.0$

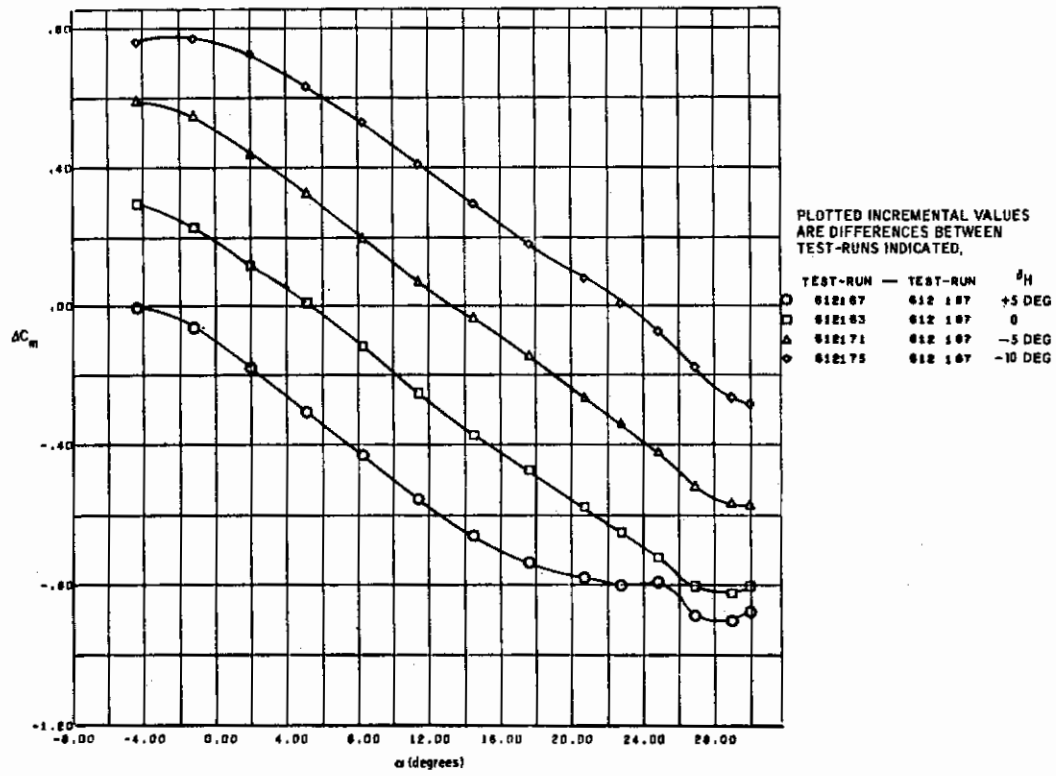

Figure 6.2-3. Tail-On, Tail-Off Pitching Moment Increments, Clean Wing, $C_{\mu_J} = 2.0$

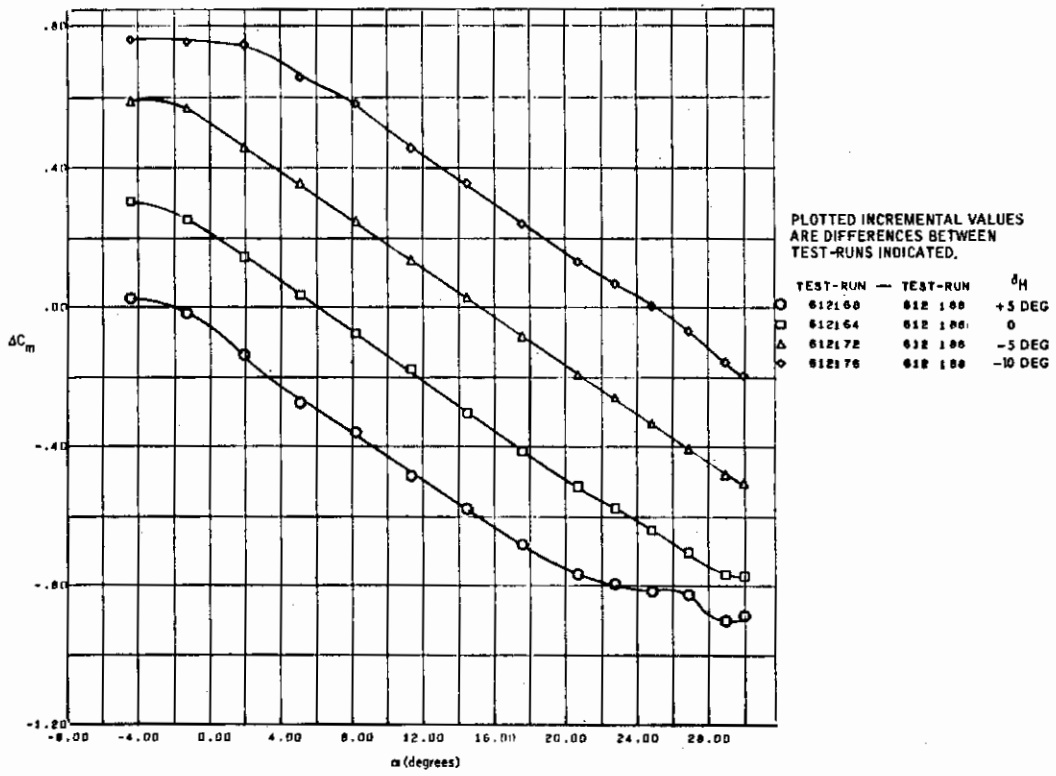

Figure 6.2-4. Tail-On, Tail-Off Pitching Moment Increments, Clean Wing, $C_{\mu_J} = 4.0$

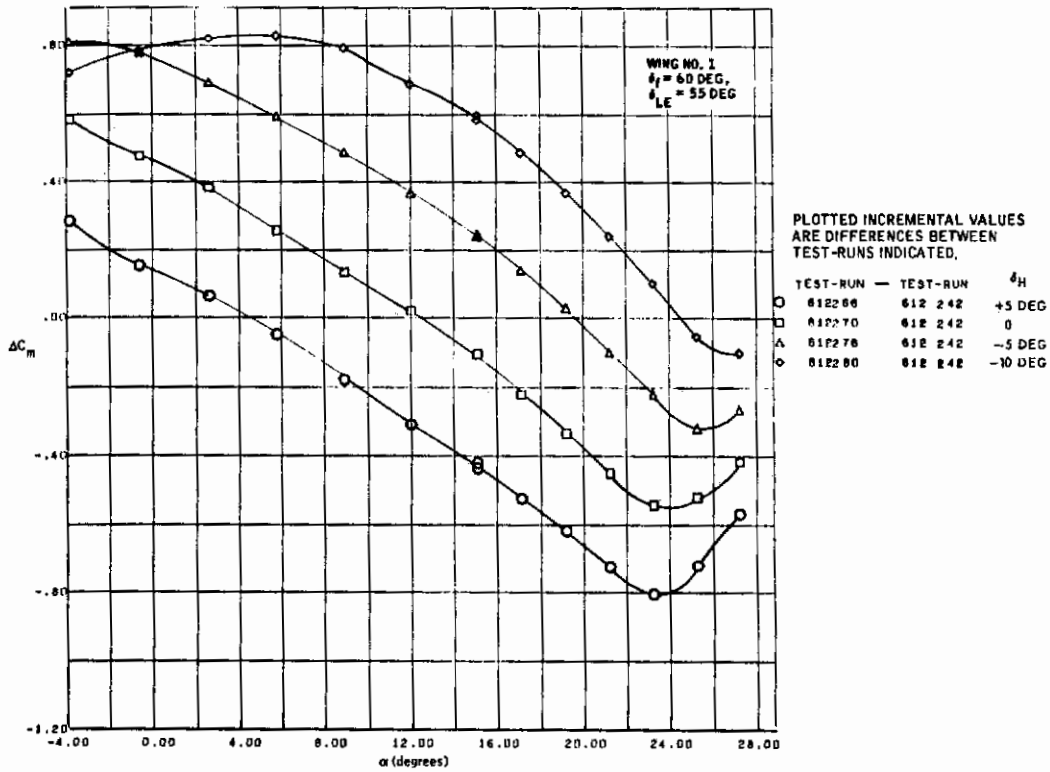

Figure 6.2-5. Tail-On, Tail-Off Pitching Moment Increments, Double-Slotted Flap, $C_{\mu_J} = 0$

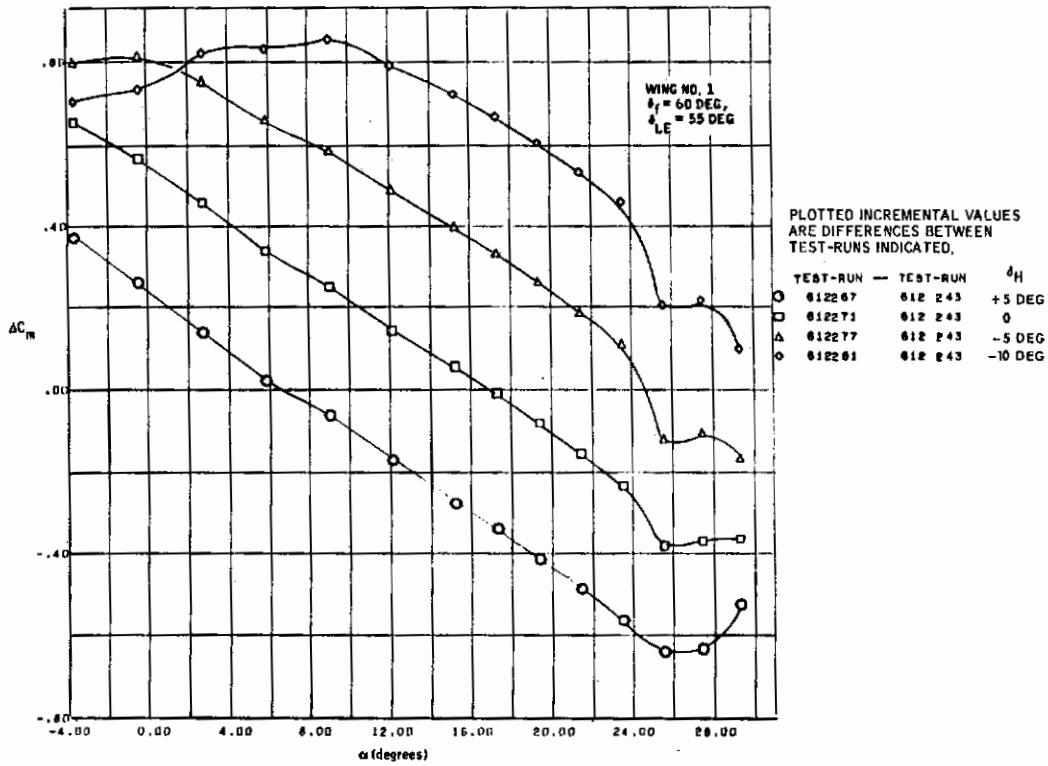

Figure 6.2-6. Tail-On, Tail-Off Pitching Moment Increments, Double-Slotted Flap, $C_{\mu_J} = 1.0$

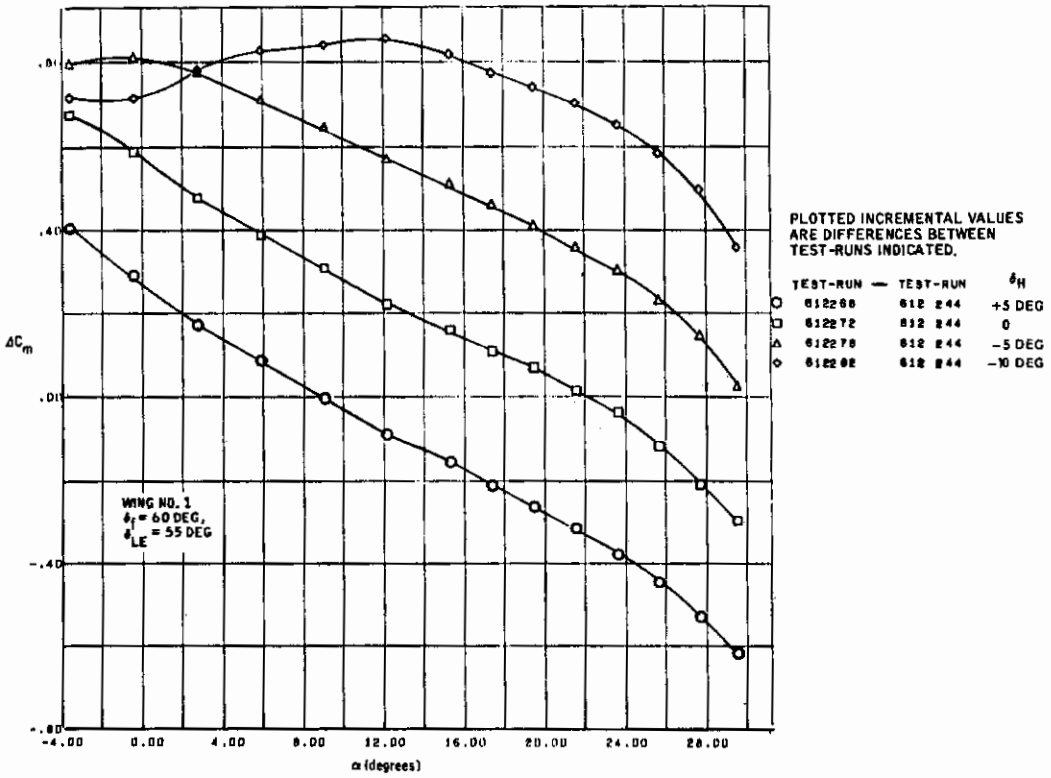

Figure 6.2-7. Tail-On, Tail-Off Pitching Moment Increments, Double-Slotted Flap, $C_{\mu_J} = 2.0$

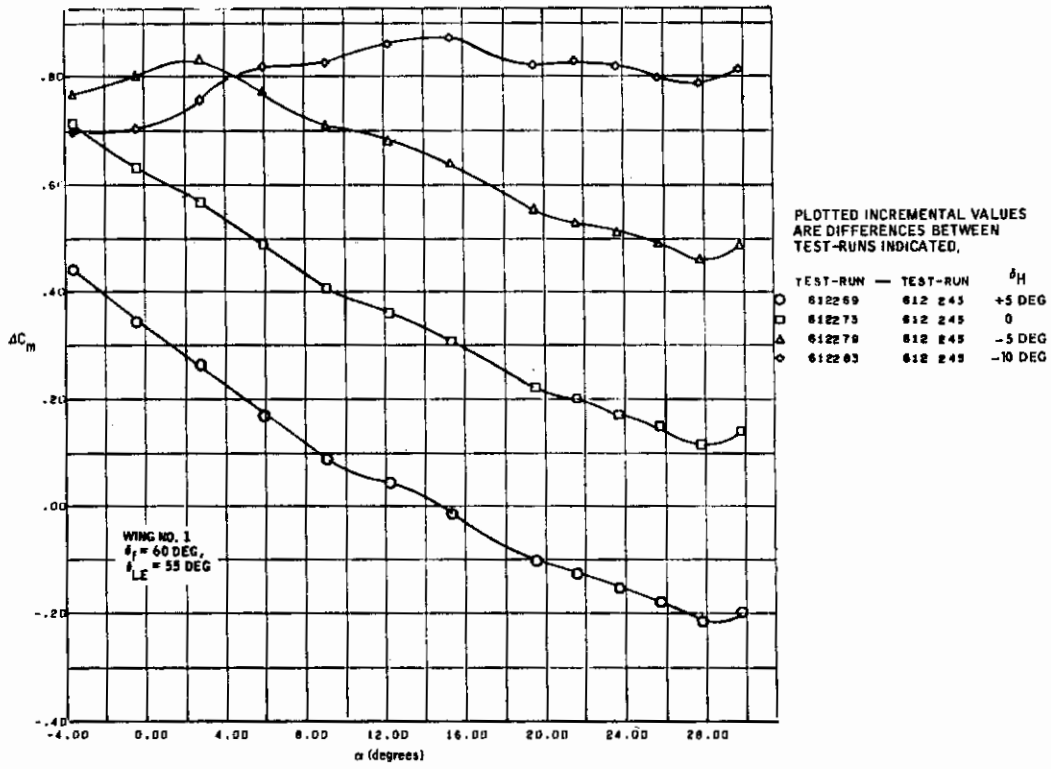

Figure 6.2-8. Tail-On, Tail-Off Pitching Moment Increments, Double-Slotted Flap, $C_{\mu_J} = 4.0$

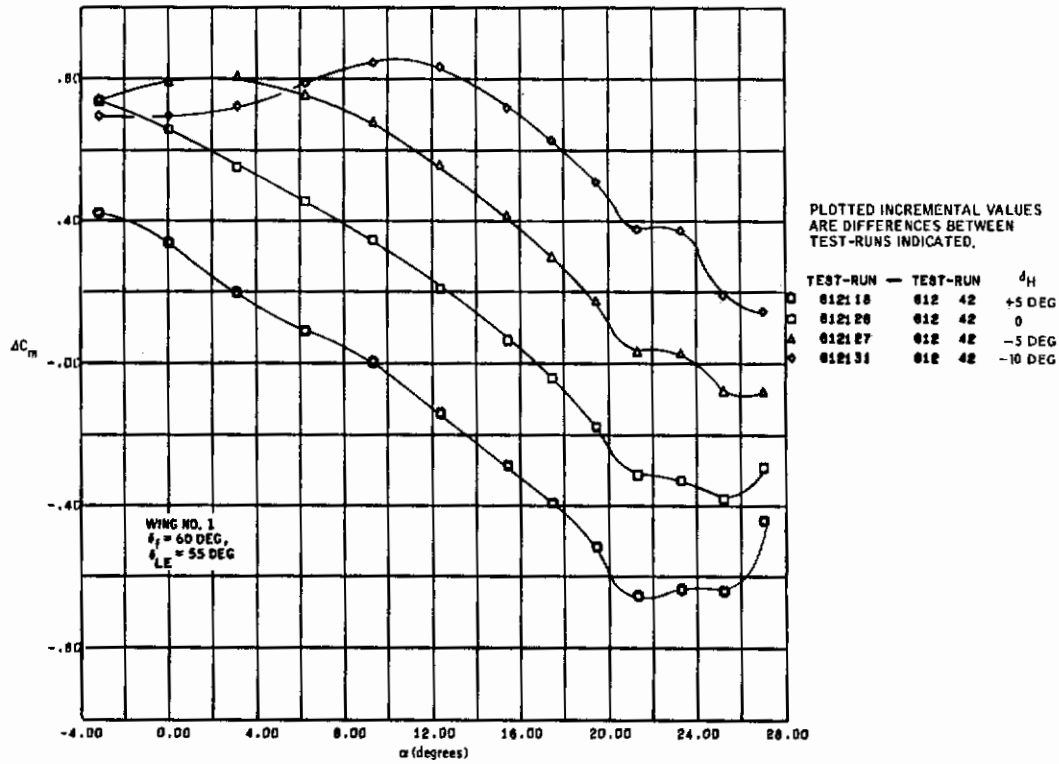

Figure 6.2-9. Tail-On, Tail-Off Pitching Moment Increments, Triple-Slotted Flap, $C_{\mu_J} = 0$

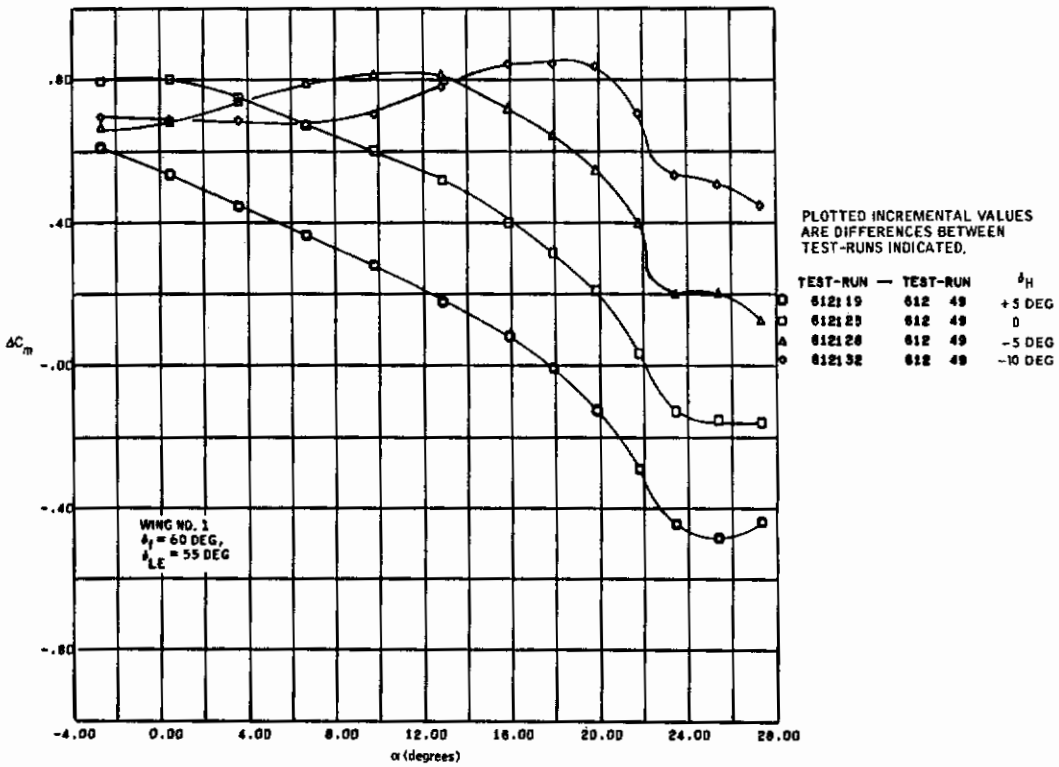

Figure 6.2-10, Tail-On, Tail-Off Pitching Moment Increments, Triple-Slotted Flap, $C_{\mu_J} = 1.0$

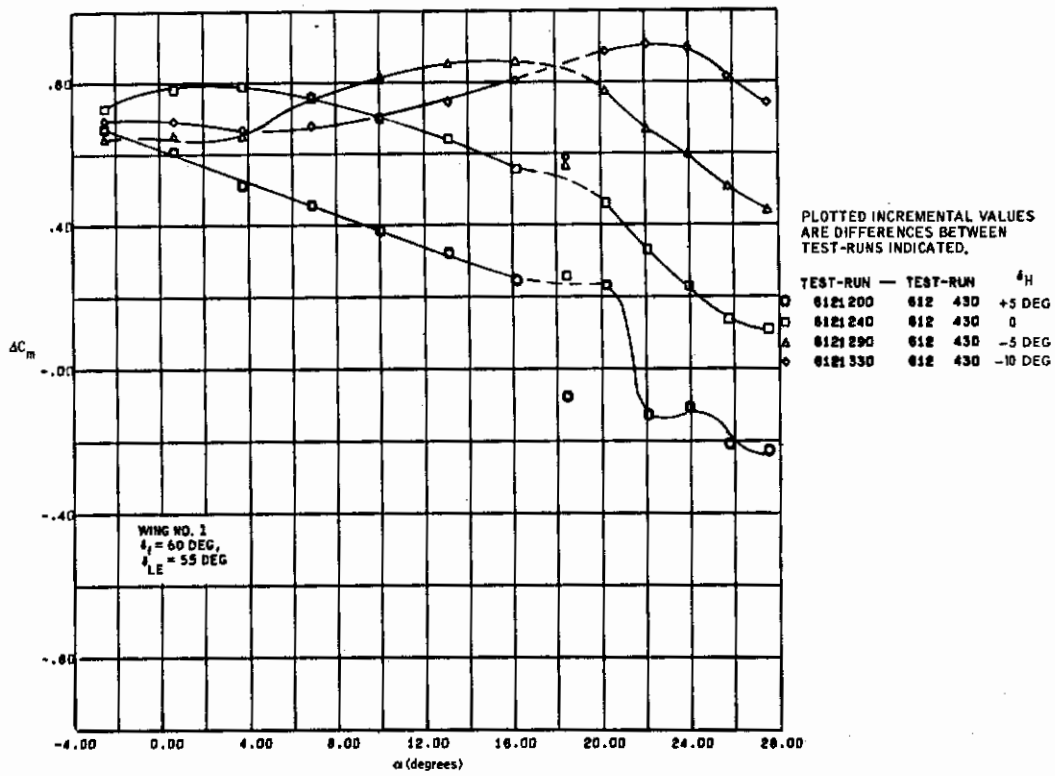

Figure 6.2-11. Tail-On, Tail-Off Pitching Moment Increments, Triple-Slotted Flap, $C_{\mu_J} = 2.0$

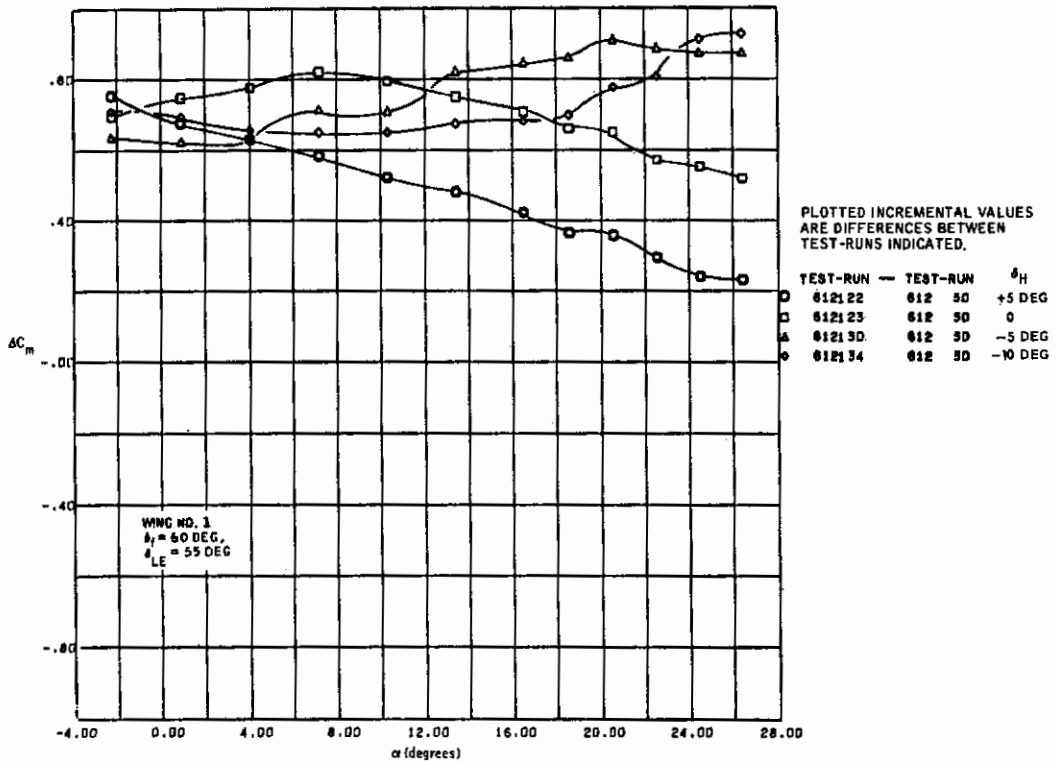

Figure 6.2-12. Tail-On, Tail-Off Pitching Moment Increments, Triple-Slotted Flap, $C_{\mu_J} = 4.0$

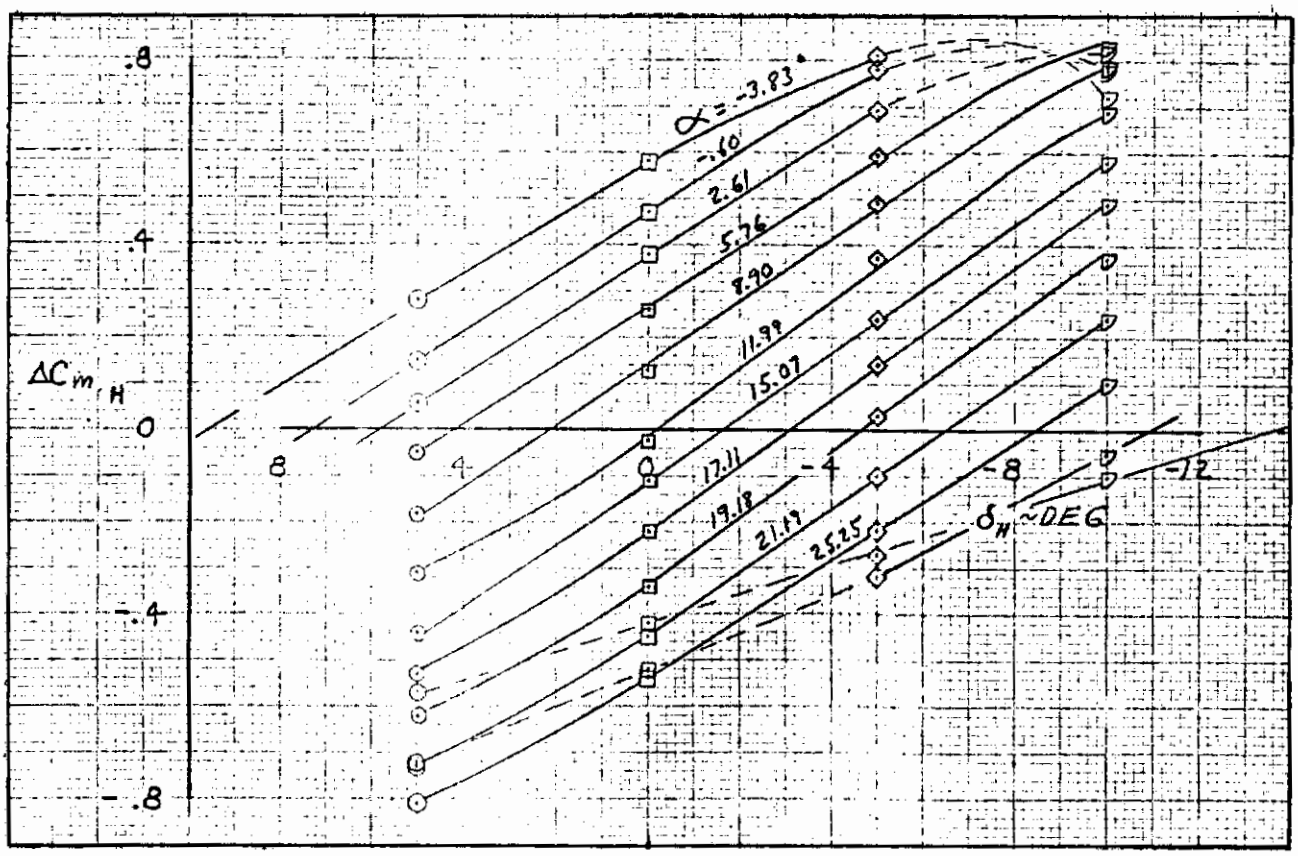

Figure 6.2-13. Stabilizer Incidence Required for Zero Tail Load, Double-Slotted Flap, $C_{\mu_J} = 0$

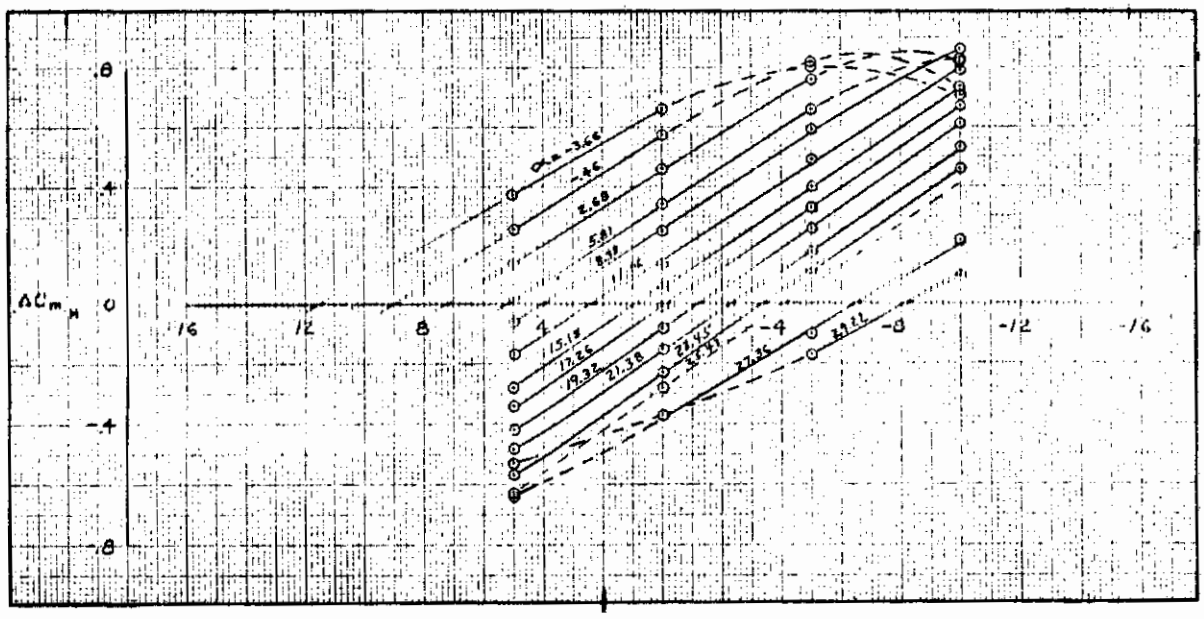

Figure 6.2-14. Stabilizer Incidence Required for Zero Tail Load, Double-Slotted Flap, $C_{\mu_J} = 1.0$

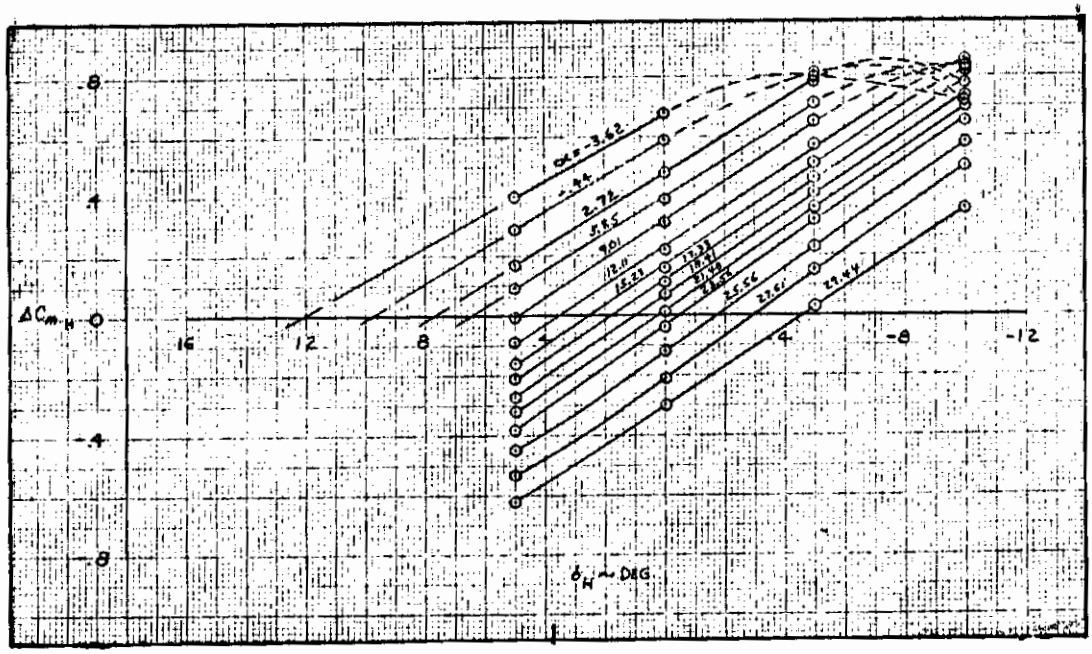

Figure 6.2-15. Stabilizer Incidence Required for Zero Tail Load, Double-Slotted Flap, $C_{\mu_J} = 2.0$

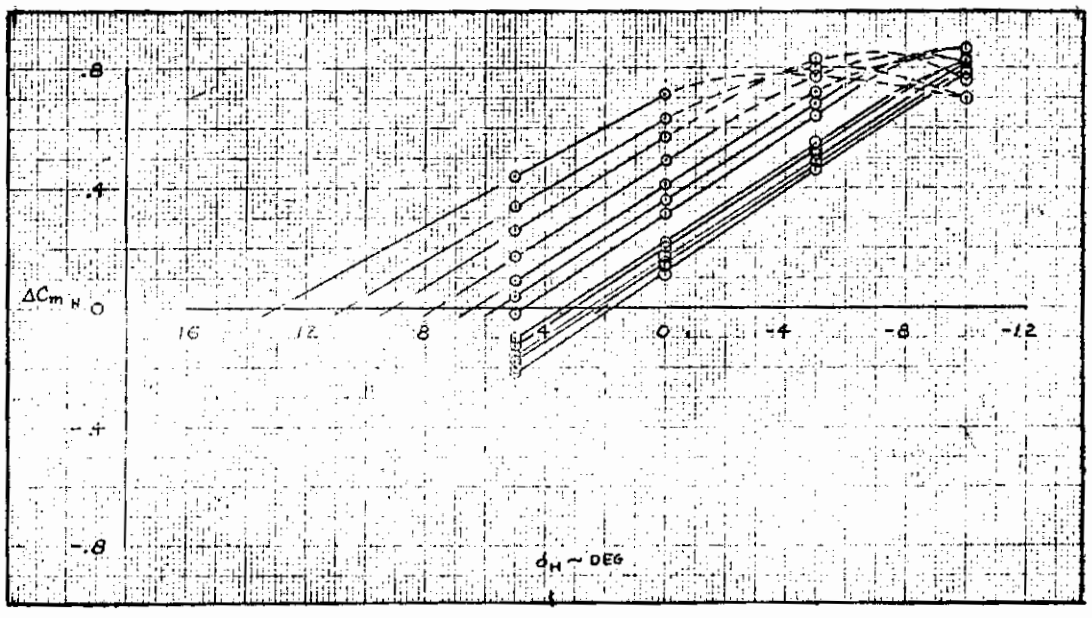

Figure 6.2-16. Stabilizer Incidence Required for Zero Tail Load, Double-Slotted Flap, $C_{\mu_J} = 4.0$

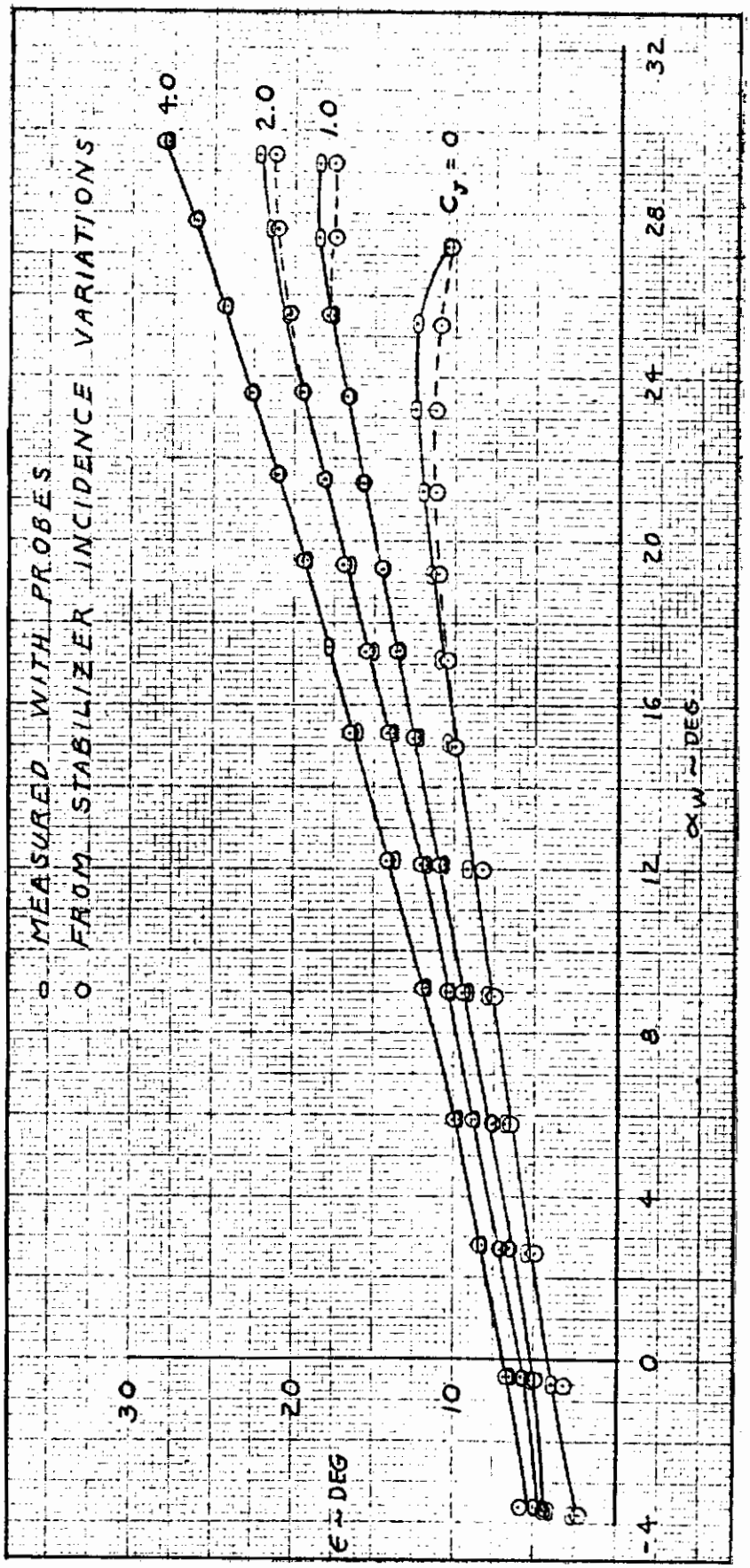

Figure 6.2-17. Comparison of Downwash Extracted from Tail-On Data with Probe Measurements, Double-Slotted Flap

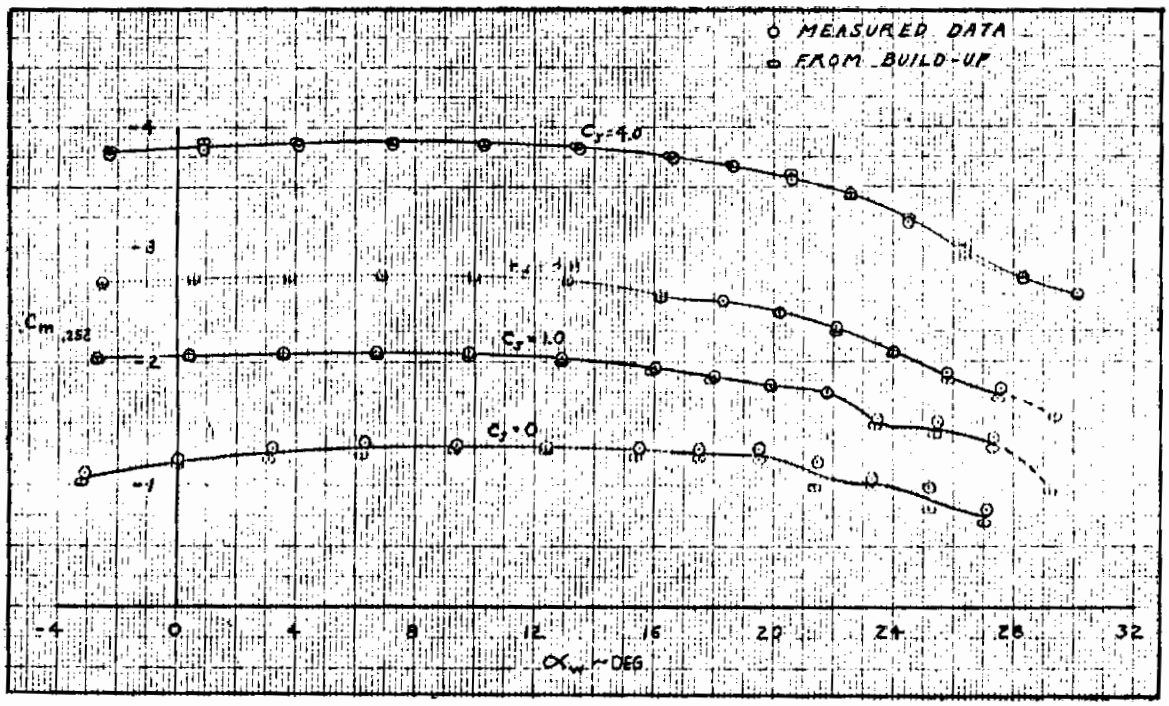

Figure 6.2-18. Comparison of Measured and Built-Up Tail-On Pitching Moments, Triple-Slotted Flap, δ_H = +5 Degrees

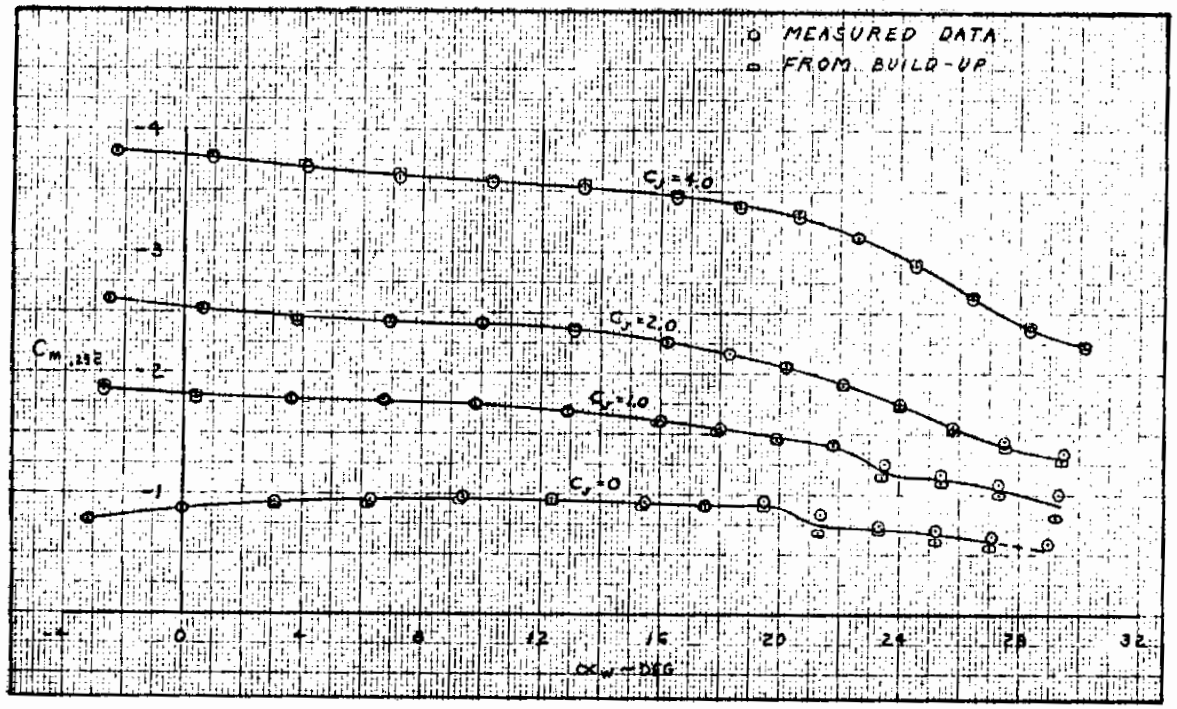

Figure 6.2-19. Comparison of Measured and Built-Up Tail-On Pitching Moments, Triple-Slotted Flap, δ_H = 0 Degrees

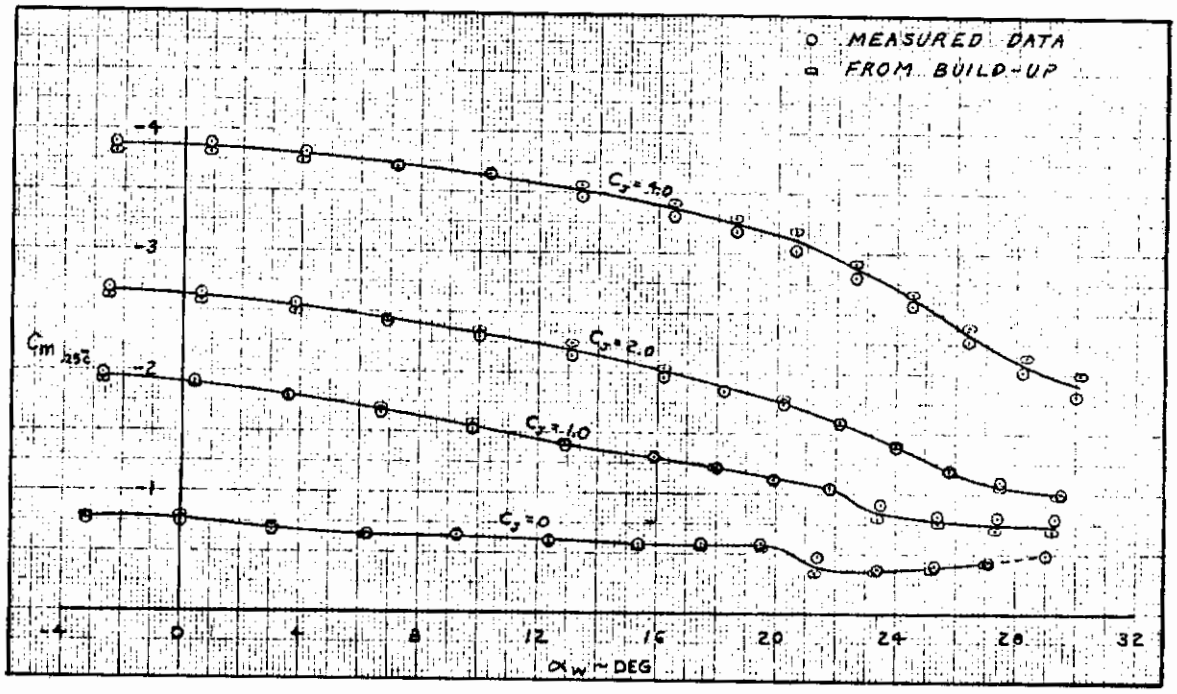

Figure 6.2-20. Comparison of Measured and Built-Up Tail-On Pitching Moments, Triple-Slotted Flap, δ_H = -5 Degrees

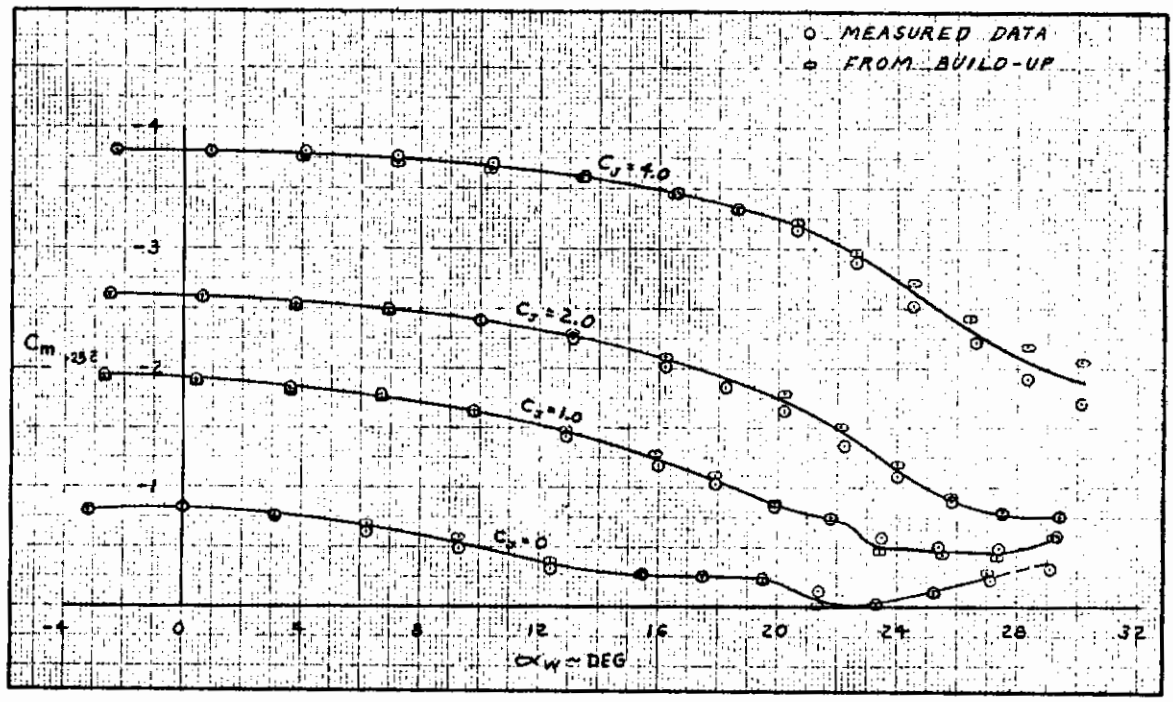

Figure 6.2-21. Comparison of Measured and Built-Up Tail-On Pitching Moments, Triple-Slotted Flap, δ_H = -10 Degrees

6.3 HORIZONTAL TAIL FLOW FIELDS

In the preceding discussions, data was presented to show that tail-on data for a configuration can be obtained from a build-up of isolated tail, tail flow fields, and tail-off characteristics. Tail flow-field characteristics, as measured by the tail wake rake probes, are summarized in this section. The rake consists of twelve probes arranged in two parallel rows, with the capability to take measurements at six water-line locations and two spanwise stations during a single run. Figure 6.3-1 shows the rake installed on the model. The rake was installed for all tail-off runs on which quantitative data was recorded.

Although a detailed rake survey was not always performed, the minimum amount of rake data obtained on each run consisted of reading one probe located at 0.25 $\bar{c}$ of the horizontal tail. Since a considerable amount of tail flow-field data was accumulated during this program, only the more pertinent data is reviewed here. The main objectives of this test program relative to tail flow-field characteristics are to provide data to answer the following questions.

1. How do the three propulsive lift concepts influence tail flow fields?

2. What are the tail flow-field characteristics at potential horizontal tail locations?

In the following paragraphs, data specifically oriented toward these questions will be reviewed.

6.3.1 EFFECT OF POWERED LIFT SYSTEMS ON DOWNWASH AND DYNAMIC PRESSURE RATIO. As a first step in the analysis, data is presented to illustrate overall effects of the three powered lift concepts on tail downwash and dynamic pressure ratio for geometrically similar configurations. This data is shown in Figures 6.3-2 through 6.3-4 for the IBF, EBF, and MF/VT systems, respectively. The wing has an aspect ratio of 8 and the quarter chord line is swept 25 degrees. The downwash and dynamic pressure ratio are averaged values from measurements along four spanwise stations at model fuselage station 78.86 and water line 25.01, which would be typical of a T-tail configuration. All three systems have a blown leading edge slat, and the full-span trailing edge flaps are deflected 60 degrees. The EBF and MF/VT concepts use a triple-slotted arrangement, while the IBF has a plain blown flap. Thrust vectoring angle for the MF/VT is 90 degrees, and $C_{\mu_J} = 0$ on the IBF system.

Effects of the three powered lift systems on the flow-field characteristics manifested in aircraft flying qualities (changes in downwash, downwash gradients, and tail dynamic pressure ratio) are readily apparent from Figures 6.3-2 through 6.3-4. The IBF and EBF configurations produce large changes in both the downwash gradient and

downwash at zero angle of attack. For the IBF, the downwash gradient changes from 0.32 at $C_{\mu_T} = 0$ to 0.62 at $C_{\mu_T} = 2.0$. The EBF produces a change from 0.37 at $C_{\mu_J} = 0$ to 0.67 at $C_{\mu_J} = 4.0$. The magnitude of these changes is generally as expected from results of the Part 1 literature review. (See the Data Basis section in the original Configuration Definition Report, Reference 6-1.) For the MF/VT concept, no information was previously available in the literature, and it was assumed that this system produced no indirect thrust effects on the tail flow fields. However, Figure 6.3-4 shows that this is not the case, since the downwash gradient changes from 0.37 at $C_{\mu_J} = 0$ (same basic flap system as that used with the EBF) to 0.52 at $C_{\mu_J} = 4.0$. The magnitude of this change in downwash gradient indicates that indirect thrust effects are items of concern on the MF/VT concept.

Figures 6.3-2 through 6.3-4 show that the overall effect of increasing thrust or blowing momentum coefficient is to cause the tail dynamic pressure ratio to become independent of angle of attack.

In the preceding paragraphs, test data was selected to illustrate gross effects of the three powered lift concepts on horizontal tail flow fields. The next objective is to understand the mechanism by which these powered lift systems influence the tail flow fields. Since theory for the unpowered case predicts that the downwash angle and downwash gradient are proportional to the lift coefficient and lift curve slope, respectively, the most obvious approach would be to attempt a correlation with lift coefficient. There have been some previous investigations along these lines, but the limited test data available led to inconclusive results. One of the basic questions to be resolved is: should the correlation parameter for a powered lift system be total lift coefficient or only the aerodynamic lift (i.e., direct thrust terms removed)? In this test program, a static calibration run was performed for each configuration to determine the thrust recovery factor, F/T, and the turning angle, θ, so that the direct thrust term can be determined from the following relationship.

$$C_{L_{DT}} = C_{\mu_J} (F/T) \sin (\alpha_W + \theta + i_W)$$

To answer the preceding question, data for the EBF with the triple-slotted flap deflected 60 degrees was used to calculate the ratio of downwash to lift coefficient for two cases: in one, the ratio was based on total lift coefficient and in the other, only aerodynamic lift was used. The results are shown in Figure 6.3-5, where the ratios ϵ/C_L are given as functions of angle of attack. This figure shows that the curves of ϵ/C_L versus angle of attack based on total lift coefficient remain a function of thrust coefficient, but the data essentially collapses into one curve when only the aerodynamic lift is used to define ϵ/C_L. The conclusion, then, is that the correlating parameter is aerodynamic lift.

6.3.2 FLOW-FIELD CHARACTERISTICS AT POTENTIAL HORIZONTAL TAIL LOCATIONS. The previous discussions dealt with flow-field characteristics for tail locations that would be typical of a T-tail arrangement. The objective was to highlight the primary influences of powered lift systems on the tail flow fields. In this discussion, data for configurations on which detailed rake surveys were performed will be presented to define flow field characteristics at various locations behind the wing. In general, a detailed wake survey consisted of measurements at six water-line locations, four spanwise stations, and three fuselage stations.

The first detailed wake surveys were accomplished during Test 612-0 on the EBF configuration with the triple-slotted flap at 60 degrees of deflection. Wing planform had an aspect ratio of 8, with 12.5 degrees of sweep at the quarter chord. Figures 6.3-6 through 6.3-13 identify the overall effect of changes in tail location. At a single spanwise station (model buttock line 5.23, which corresponds to the spanwise location of the mean aerodynamic chord of the horizontal stabilizer used for the tail-on tests), downwash angles at the six water-line locations and two fuselage stations are presented. Model fuselage station (MFS) 62.86 was the most forward location tested and MFS 78.86 the most aft. Model water line (MWL) 25.01 and MFS 78.86 are the water-line and fuselage station locations of the horizontal stabilizer used for the tail-on tests.

For first-order effects, Figures 6.3-6 through 6.3-13 indicate that variations in waterline location produce the largest changes in downwash, and the changes are accentuated as thrust coefficient is increased. Downwash angles increase somewhat at the forward fuselage station, particularly for the lower tail locations. These qualitative observations are in accordance with the trends predicted from classical lifting line theory. The general trends for spanwise variations of downwash were a fairly uniform distribution across the tail span at low angles of attack and the higher tail locations. Increasing thrust coefficient tends to delay the occurrence of spanwise gradients to higher angles of attack. The above trends are illustrated in Figure 6.3-14 for data taken at MWL 25.01 and MFS 78.86.

For a low tail location, there is a non-uniform spanwise distribution of downwash at all angles of attack and thrust coefficients. This is shown in Figure 6.3-15 for probes located at MWL 17.01. No definite pattern was observed for the spanwise variations of downwash, so the average value from the four stations at which measurements were taken was used for quantitative work.

The data from Figures 6.3-6 through 6.3-15 gives a qualitative assessment of downwash characteristics at various distances from the wing. The next step in the analysis will be to present the data in a form more suitable for detailed quantitative analysis. It was previously indicated that aerodynamic lift is a correlating parameter and that the most significant geometric variable is vertical location. For the analysis, vertical location of each probe was related to the moment reference center ($0.25\ \bar{c}_w$) with the following equation:

$$h_H = \left[Z_H \cos (\alpha_w - i_w) - X_H \sin (\alpha_w - i_w) \right] / \bar{c}_w$$

In the preceding equation, reference length is wing mean aerodynamic chord and X_H and Z_H are the body axes longitudinal and vertical distances from the moment reference center to the probe under consideration.

Results of a complete rake survey are presented in Figures 6.3-16 through 6.3-57. The ratio $\epsilon_{ave}/C_{L_{aero}}$ and the downwash angle, ϵ_{ave}, are given as functions of h_H for the three longitudinal stations at which measurements were taken. The value for ϵ_{ave} is obtained from the unweighted average values at four spanwise stations, and $C_{L_{aero}}$ is the lift coefficient with the direct-thrust term removed. The lift curve is shown in Figure 6.3-58. It was previously indicated that the effect of thrust coefficient on downwash could be normalized using $C_{L_{aero}}$ as the correlating parameter. For this stage of the analysis, however, plots have been made for each individual thrust coefficient to provide unbiased fairings for each basic set of data. The data is also shown for a fixed angle of attack, so variations of the parameters with vertical height are with respect to a unique position of the wing wake.

The first point to be considered is an evaluation of how well the data follows relationships predicted by simple lifting line theory. Of the types of span-load distributions for which simple solutions can be obtained, elliptical and uniform loadings would represent the extremes. For elliptical loading, the ratio of downwash at an arbitrary vertical location to the downwash in the plane of the vortex sheet is given by:

$$\epsilon/\epsilon_o = 1 - \frac{\left(\frac{2z}{b}\right)}{\sqrt{\left(\frac{2z}{b}\right)^2 + 1}}$$

The corresponding relationship for uniform loading is:

$$\epsilon/\epsilon_o = \frac{1}{\left[1 + \left(\frac{2z}{b}\right)^2\right]}$$

The preceding equations supply to a vortex model with vortex span equal to the wing span, with z as the vertical distance. Figure 6.3-59 compares the decay in downwash intensity with distance from the vortex sheet as given by the two theoretical relationships. Vertical distance has been non-dimensionalized using wing mean aerodynamic chord as the reference length. The vertical distance in the theoretical relationship is measured with respect to the vortex sheet and the wake does not remain

fixed during a test run, but is displaced downward as angle of attack is increased. Using the curve of h_H versus $\epsilon_{ave}/C_{L_{aero}}$ at α_G = -4 degrees and C_{μ_J} = 0 degrees as a reference, the data points at each succeeding angle of attack were shifted by an increment Δ_h, as shown in the following sketch. This allowed a quantitative comparison of theory with the test data.

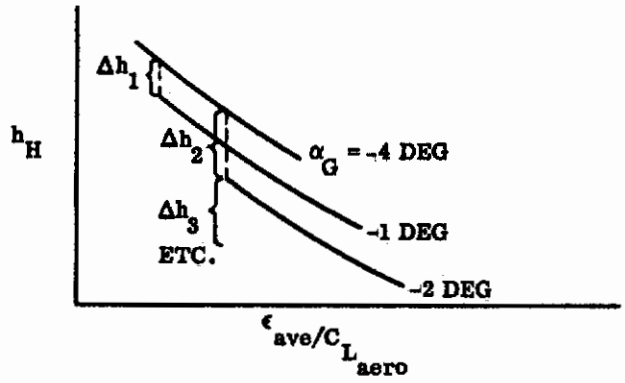

The test data tended to converge at the highest values for h_H (Figures 6.3-16 through 6.3-19). This is also in accordance with the theory, which predicts that downwash becomes independent of span loading at great distances from the wing. To establish a value for downwash in the plane of the vortex sheet, the final adjustment was to match the theoretical equations with the test data at a point corresponding to the highest value for h_H at which measurements were taken. The comparisons are shown in Figures 6.3-60 through 6.3-63 for C_{μ_J} = 0, 1.0, 2.0, and 4.0, respectively. These figures show that the variation of $\epsilon_{ave}/C_{L_{aero}}$ with h_H closely follows the theoretical curve for elliptical span loading. The agreement is extraordinary, considering that some of the data points at the lower values of h_H are at post-stall angles of attack.

In summary, the wake rake data accumulated during this test program indicates that downwash behind a wing with a powered lift system remains a function of the aerodynamic lift, as predicted by classical lifting line theory. Knowing this, extremely large downwash angles are expected for the lift coefficients at which these powered lift systems operate. For aft-tail configurations, it is therefore imperative that the tail be located high above the wing wake to achieve acceptable levels of stability and trimming capability.

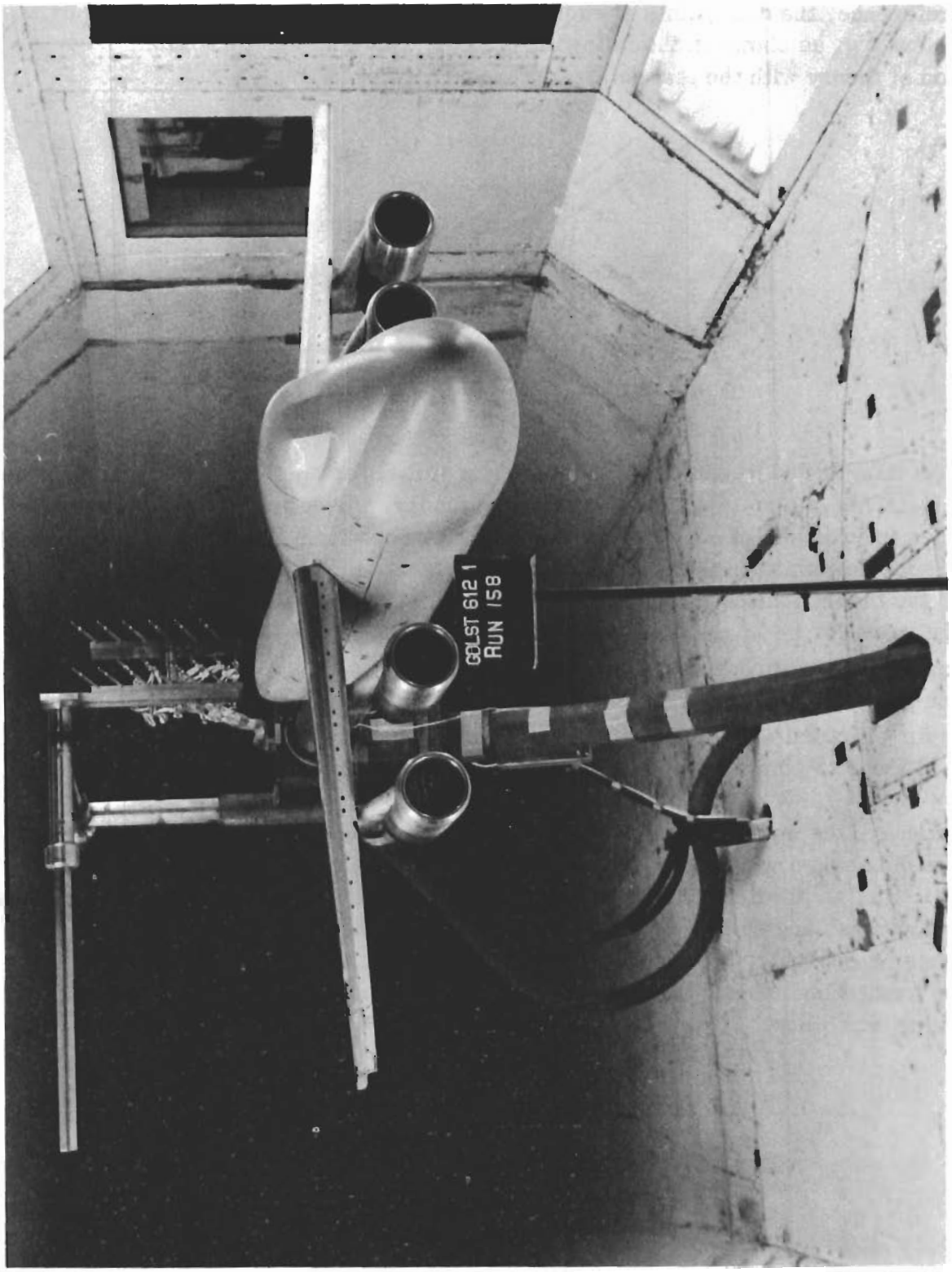

Figure 6.3-1. Tail Wake Rake Installed on Model

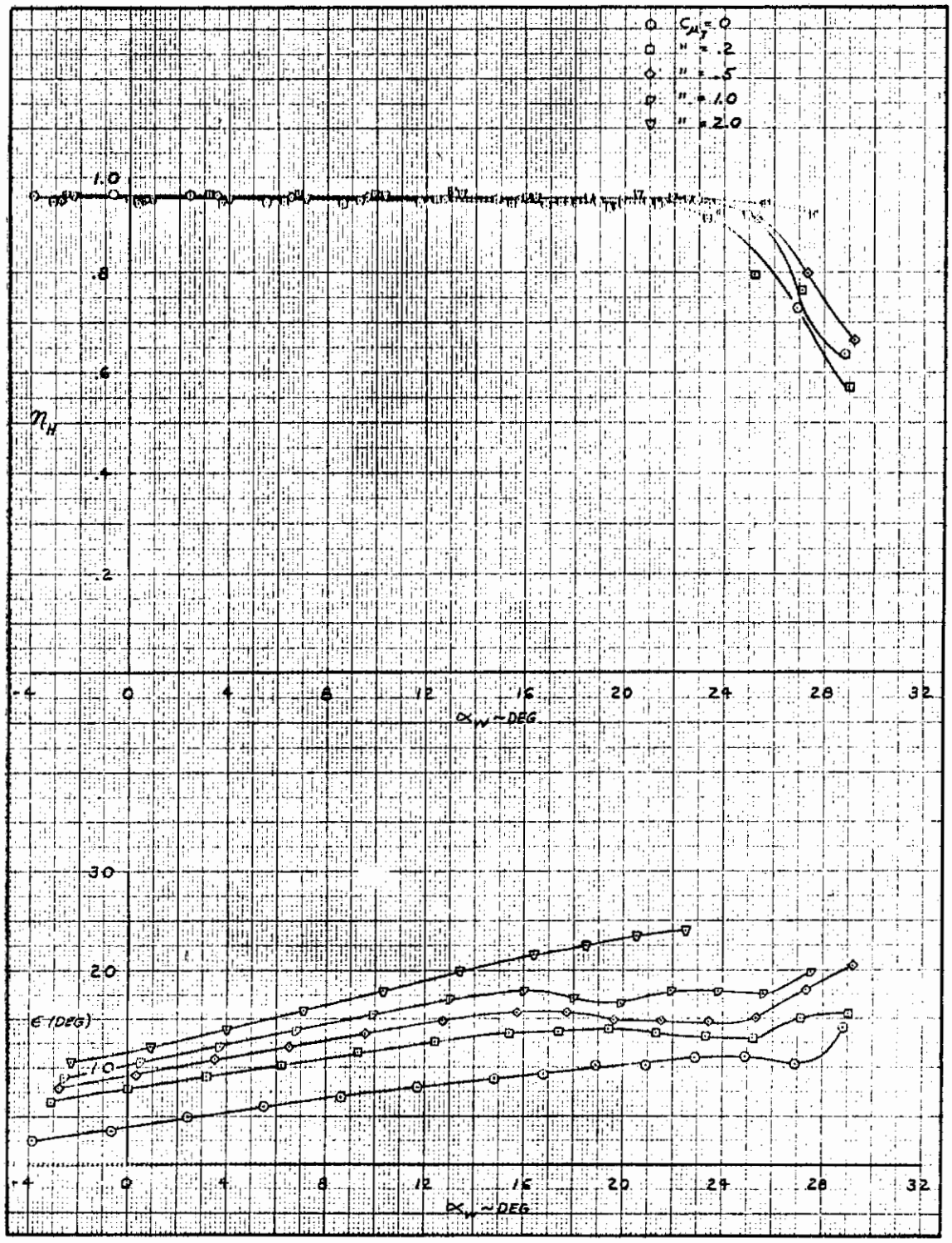

Figure 6.3-2. IBF Downwash and Tail Dynamic Pressure Ratio, Plain Flap at 60 Degrees

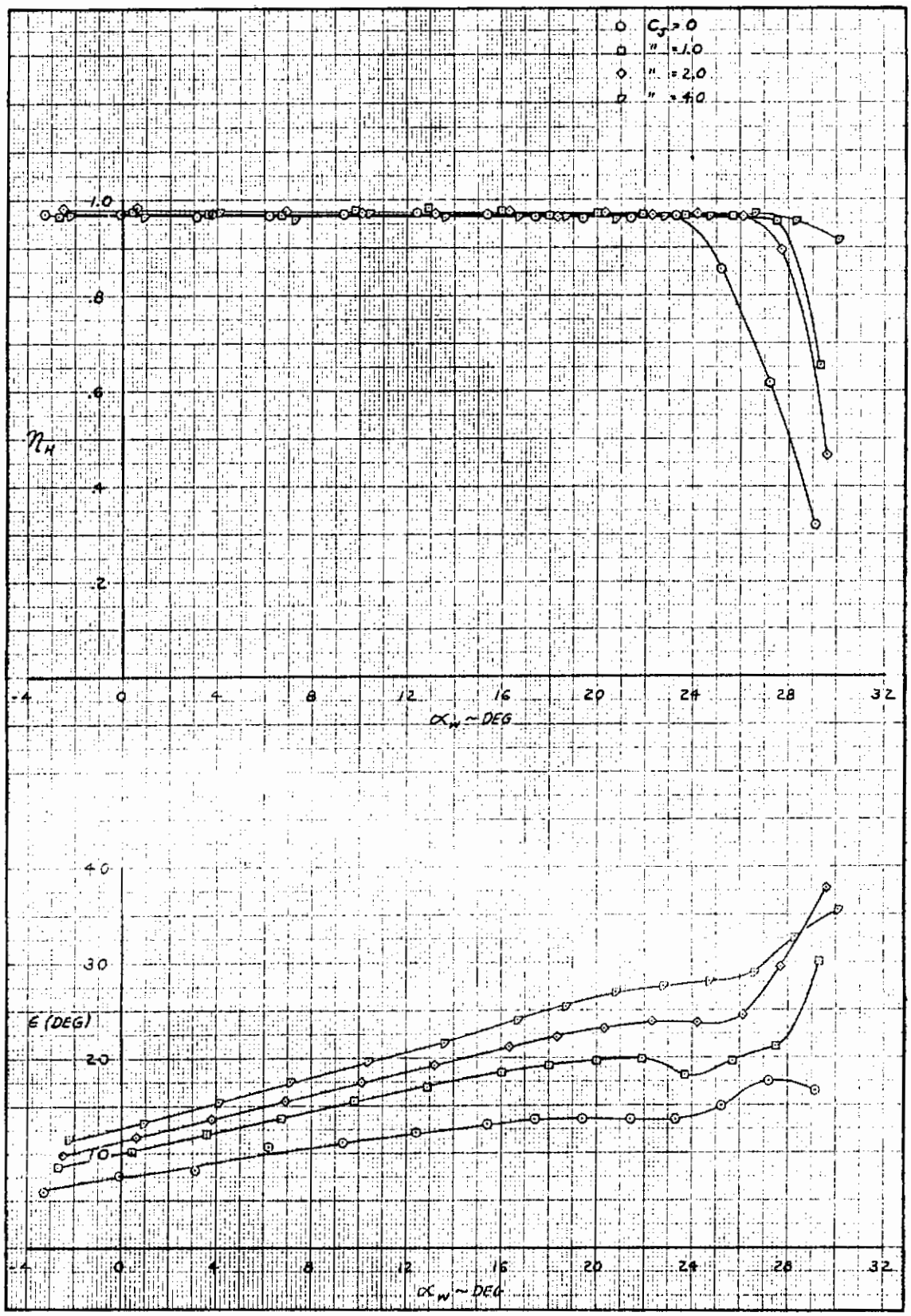

Figure 6.3-3. EBF Downwash and Dynamic Pressure Ratio, Triple-Slotted Flap at 60 Degrees

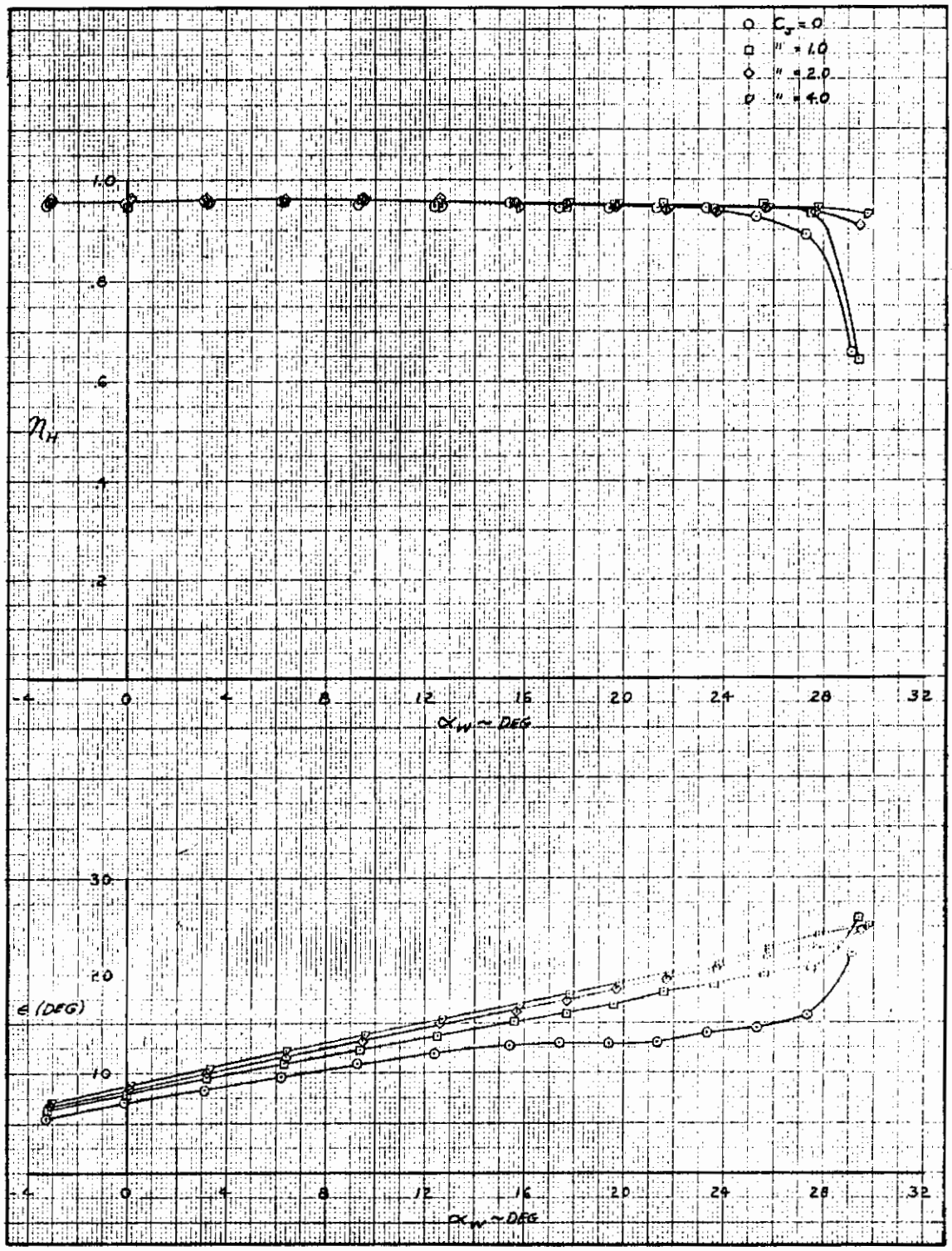

Figure 6.3-4. MF/VT Downwash and Tail Dynamic Pressure Ratio, Triple-Slotted Flap at 60 Degrees (δ_T = 90 deg)

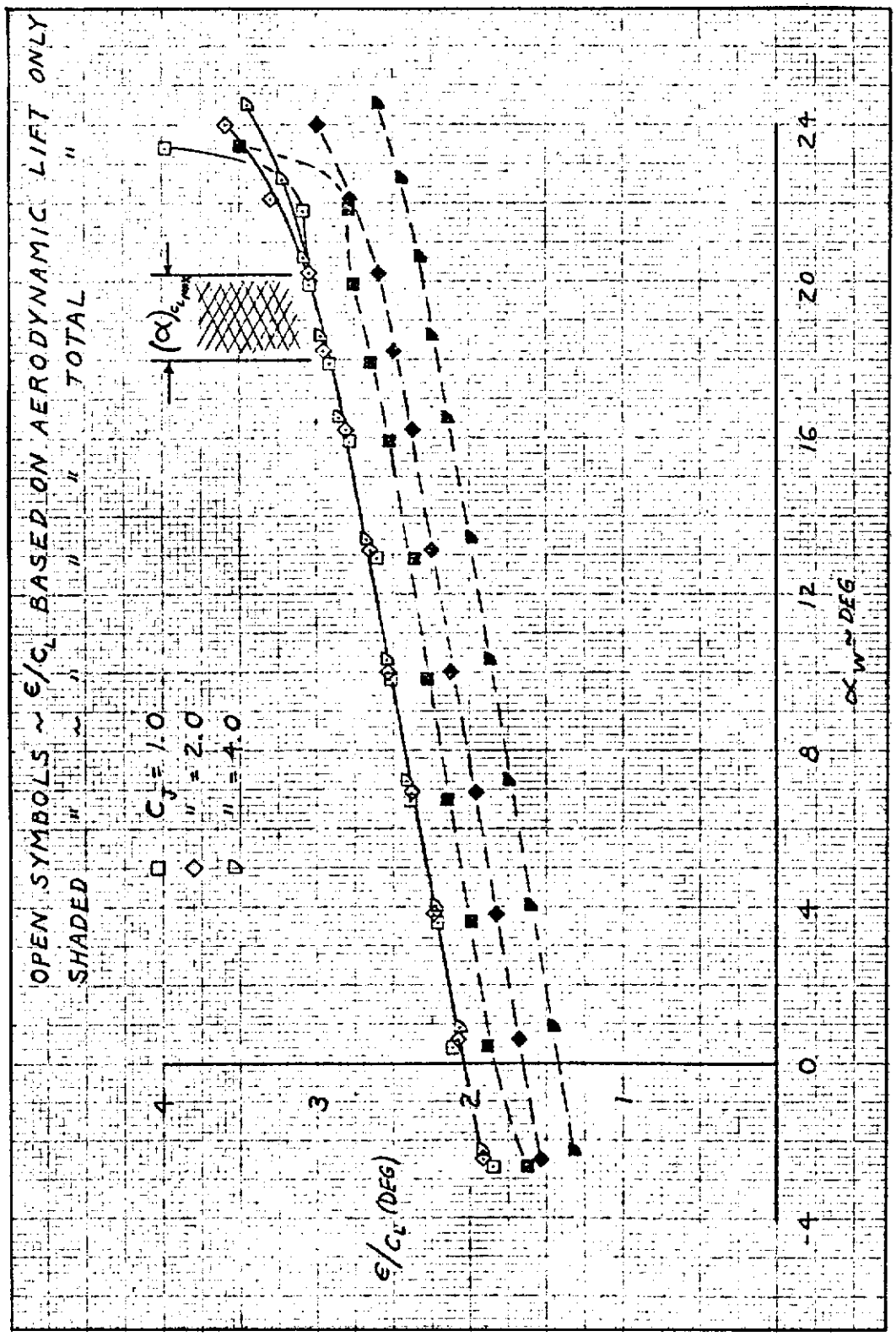

Figure 6.3-5. Effect of Lift Coefficient as a Normalizing Parameter for Downwash Angle

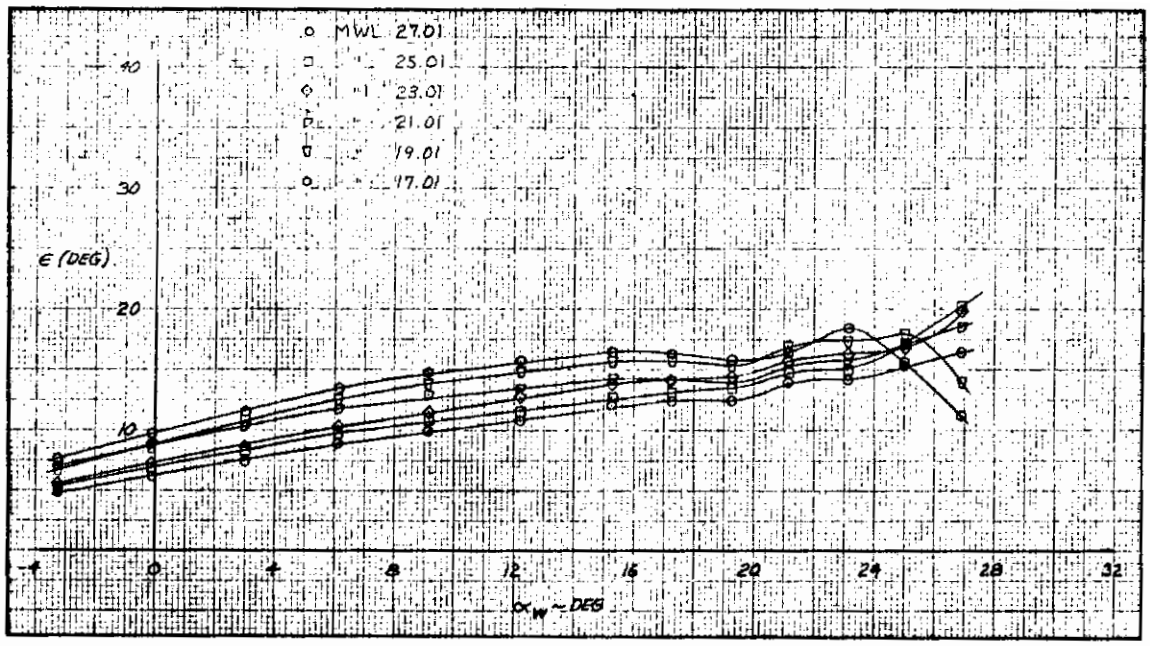

Figure 6.3-6. Effect of Tail Height on Downwash, Triple-Slotted Flap, C_{μ_J} = 0.0, MFS 78.86, MBL 5.23

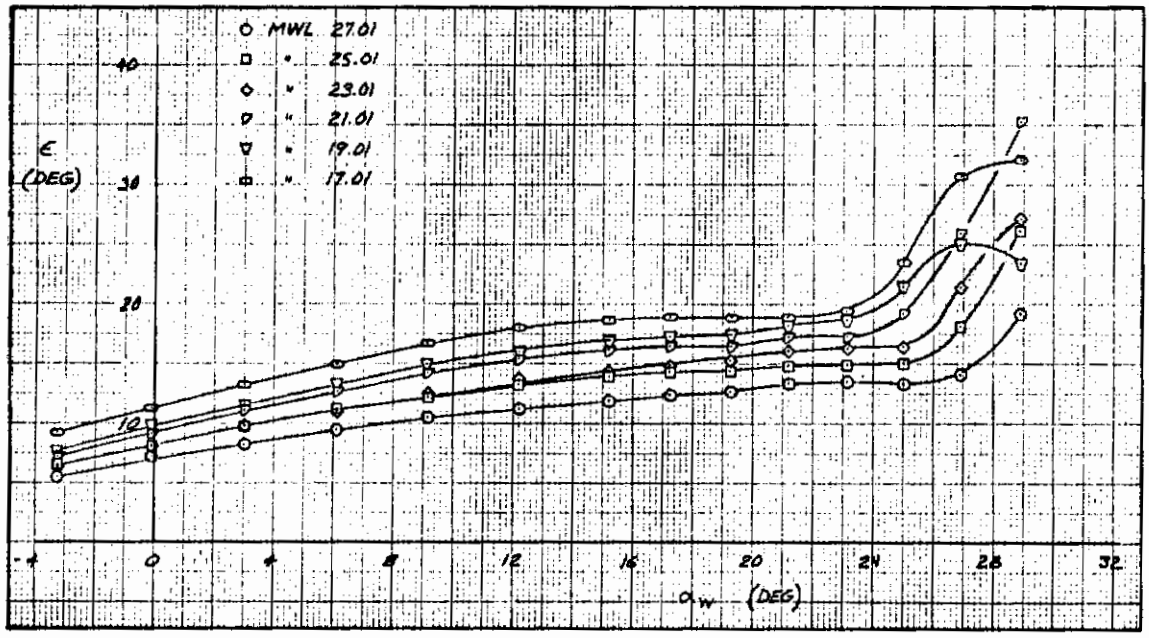

Figure 6.3-7. Effect of Tail Height on Downwash, Triple-Slotted Flap, C_{μ_J} = 0.0, MFS 62.86, MBL 5.23

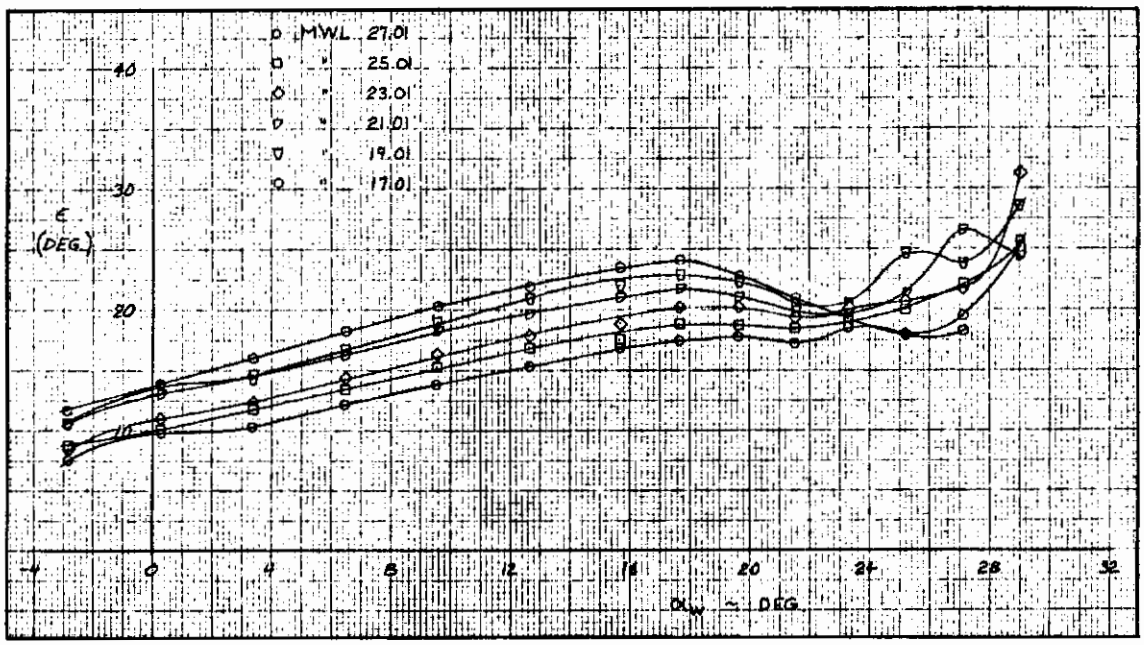

Figure 6.3-8. Effect of Tail Height on Downwash, Triple-Slotted Flap, C_{μ_J} = 1.0, MFS 78.86, MBL 5.23

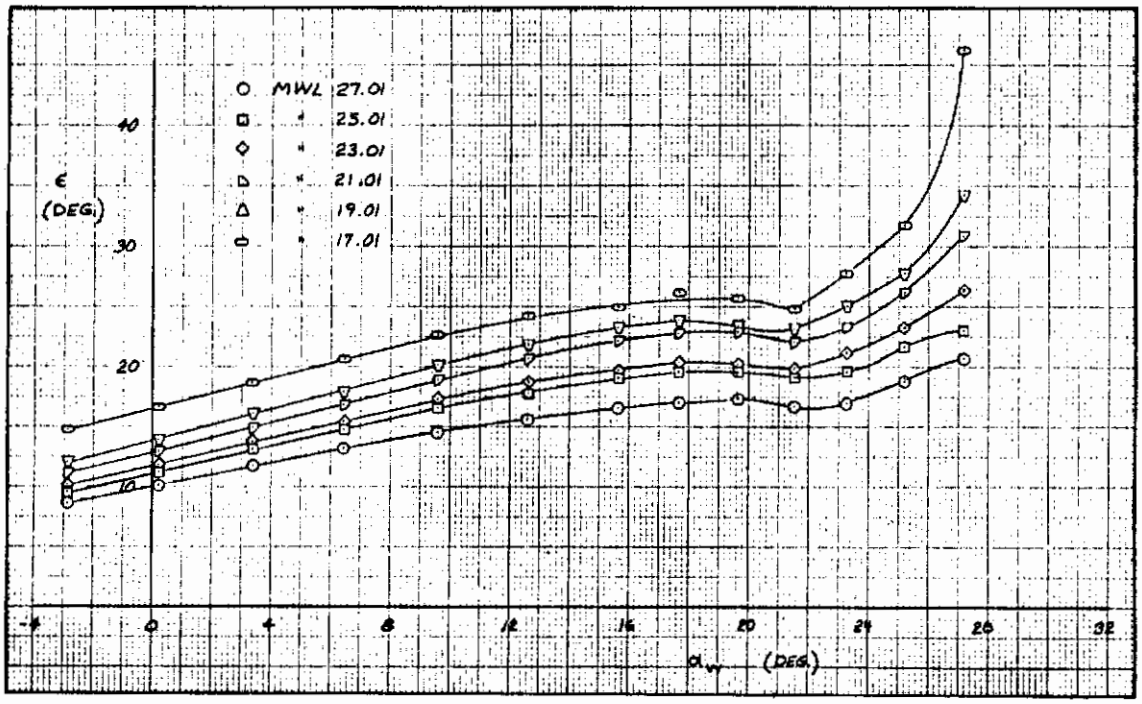

Figure 6.3-9. Effect of Tail Height on Downwash, Triple-Slotted Flap, C_{μ_J} = 1.0, MFS 62.86, MBL 5.23

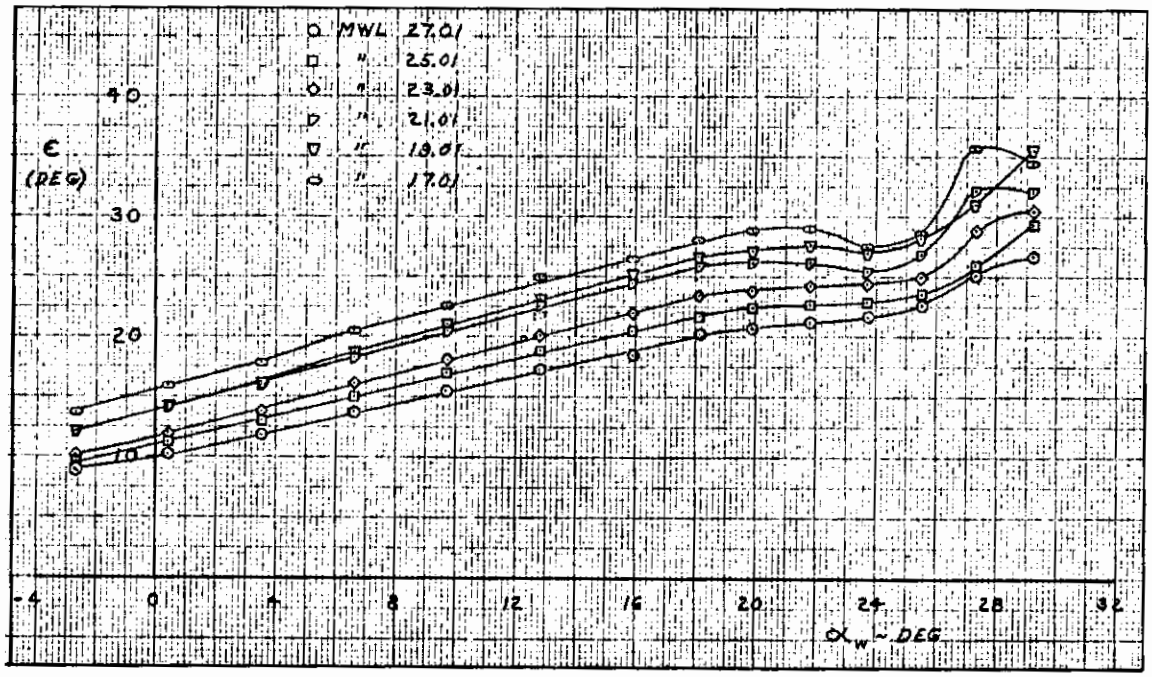

Figure 6.3-10. Effect of Tail Height on Downwash, Triple-Slotted Flap, C_{μ_J} = 2.0, MFS 78.86, MBL 5.23

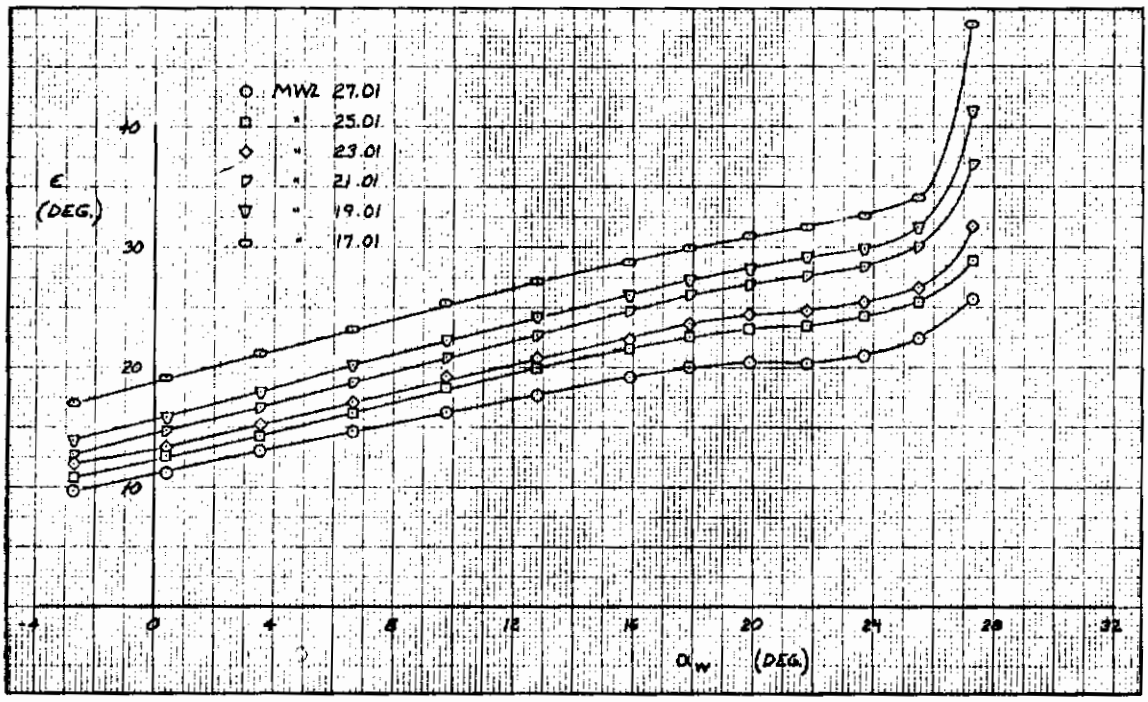

Figure 6.3-11. Effect of Tail Height on Downwash, Triple-Slotted Flap, C_{μ_J} = 2.0, MFS 62.86, MBL 5.23

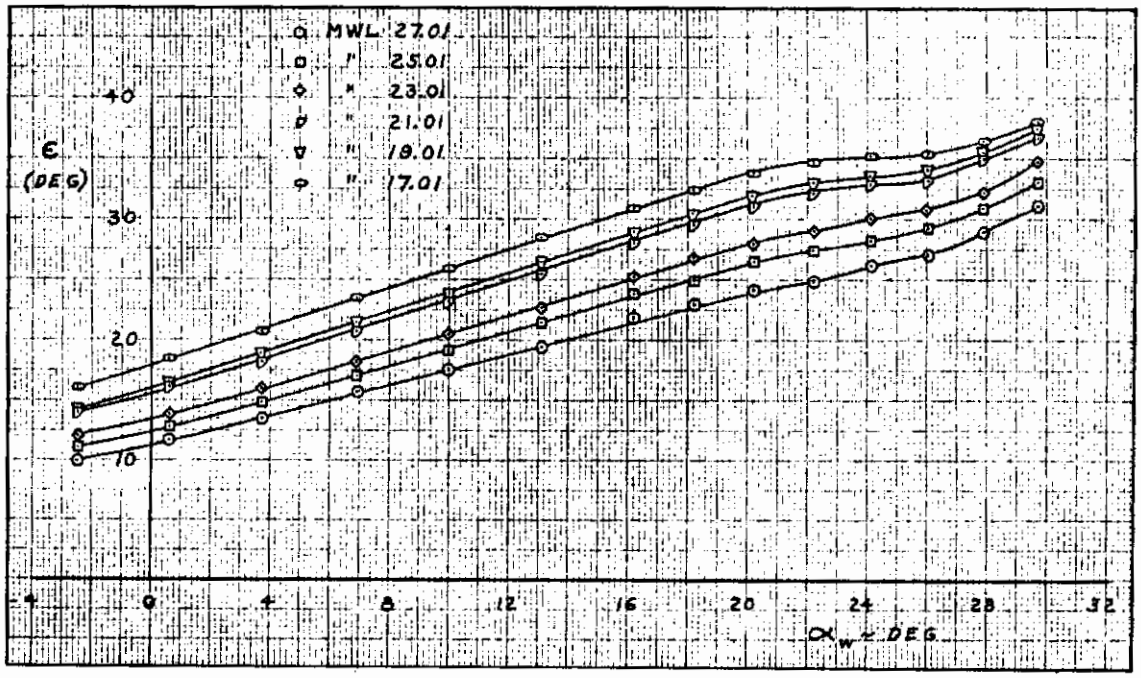

Figure 6.3-12. Effect of Tail Height on Downwash, Triple-Slotted Flap, C_{μ_J} = 4.0, MFS 78.86, MBL 5.23

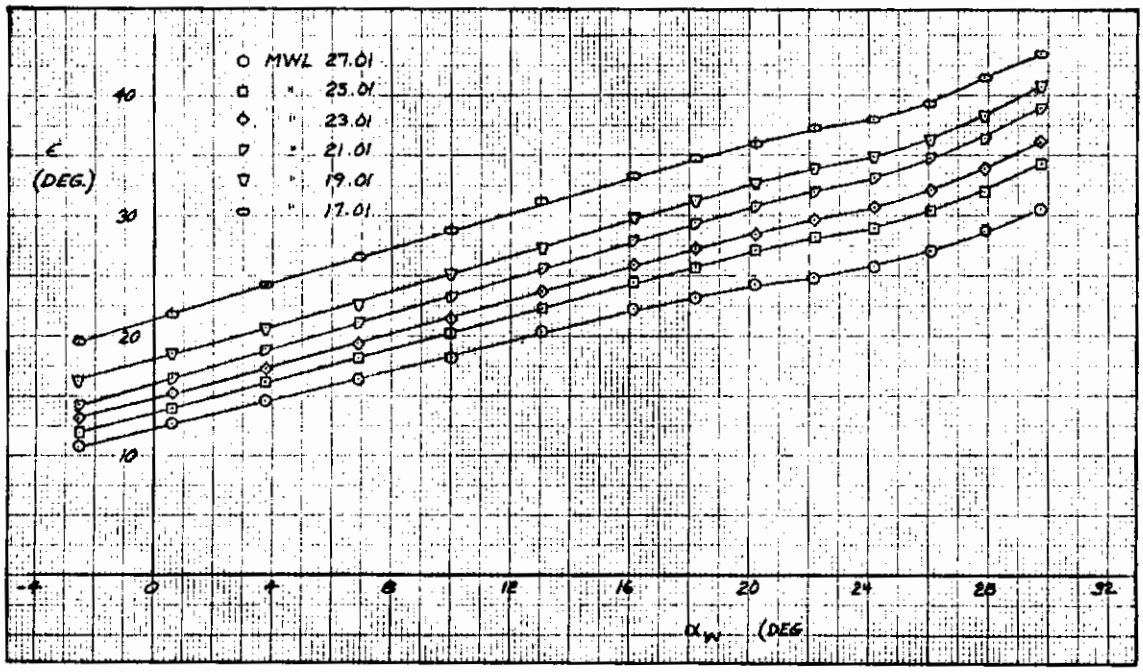

Figure 6.3-13. Effect of Tail Height on Downwash, Triple-Slotted Flap, C_{μ_J} = 4.0, MFS 62.86, MBL 5.23

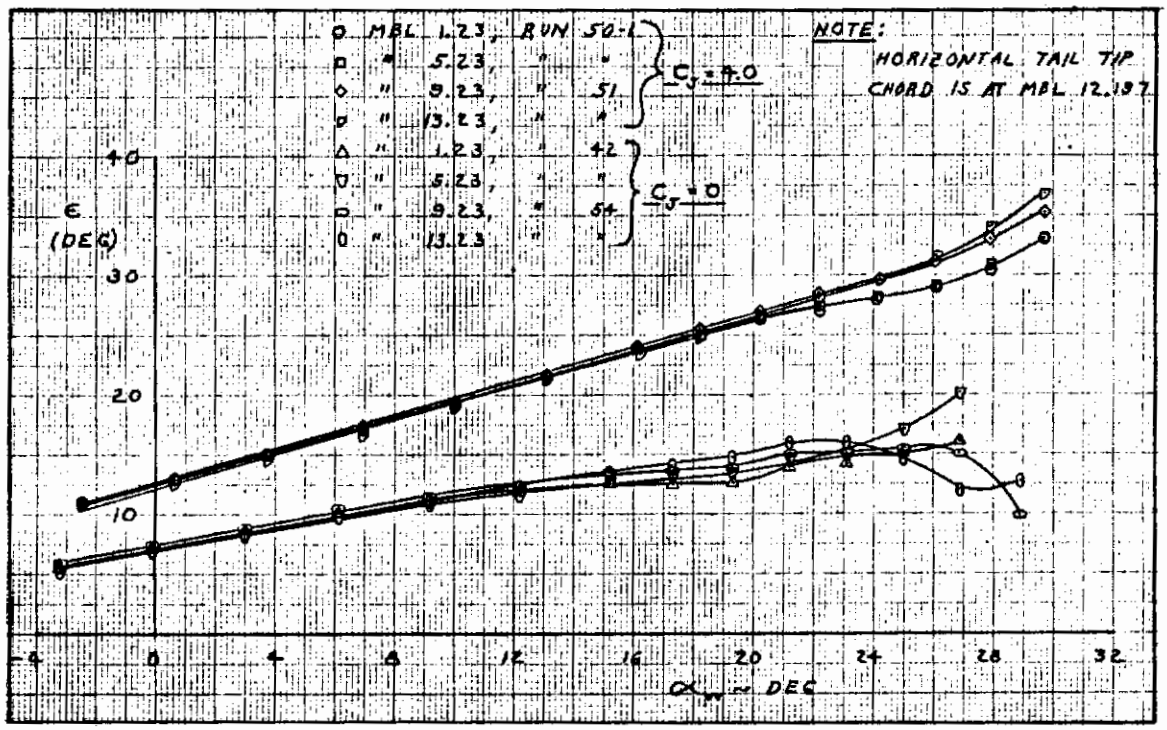

Figure 6.3-14. Spanwise Variation of Downwash, Triple-Slotted Flap, MWL 25.01, MFS 78.86

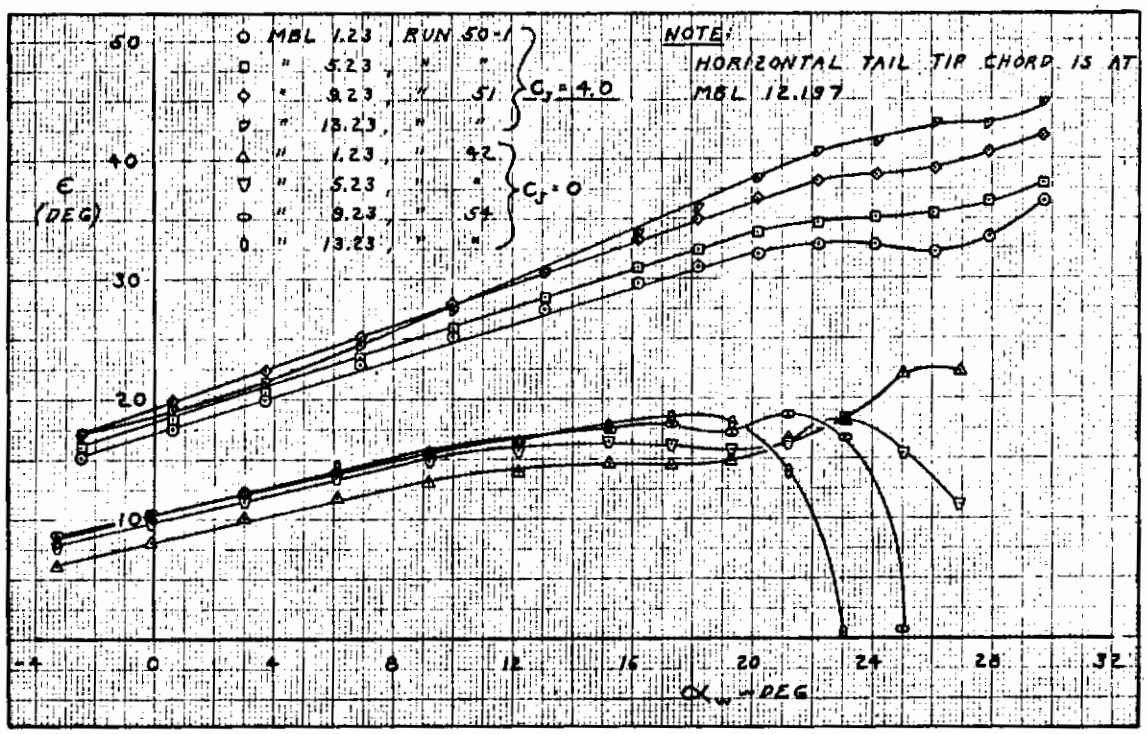

Figure 6.3-15. Spanwise Variation of Downwash, Triple-Slotted Flap, MWL 17.01, MFS 78.86

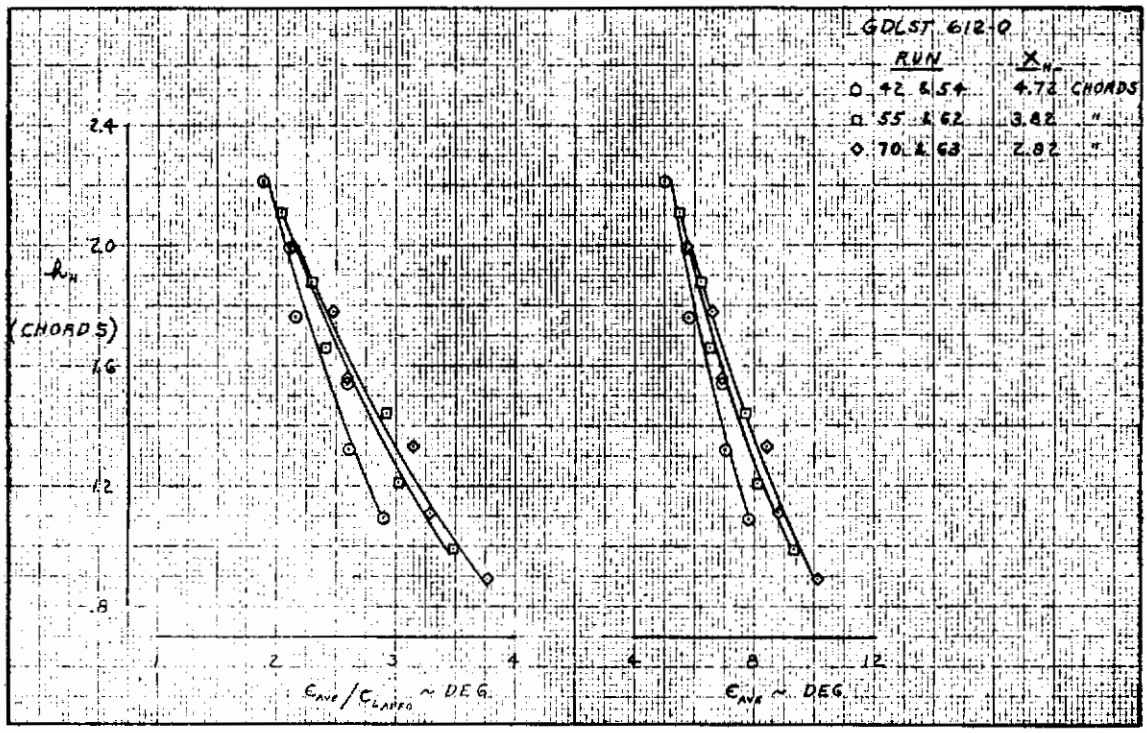

Figure 6.3-16. Effect of Tail Height and Fuselage Station on Downwash, Triple-Slotted Flap, $C_{\mu_J} = 0$, $\alpha_G = -4$ Degrees

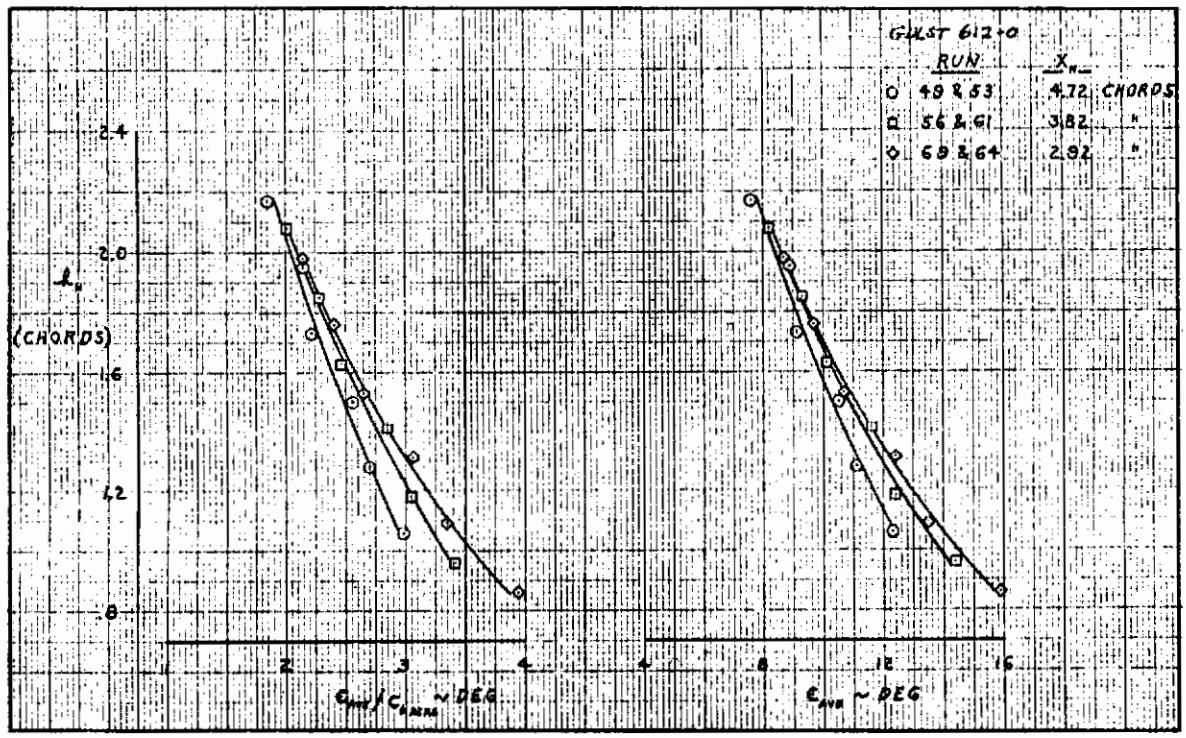

Figure 6.3-17. Effect of Tail Height and Fuselage Station on Downwash, Triple-Slotted Flap, $C_{\mu_J} = 1.0$, $\alpha_G = 4$ Degrees

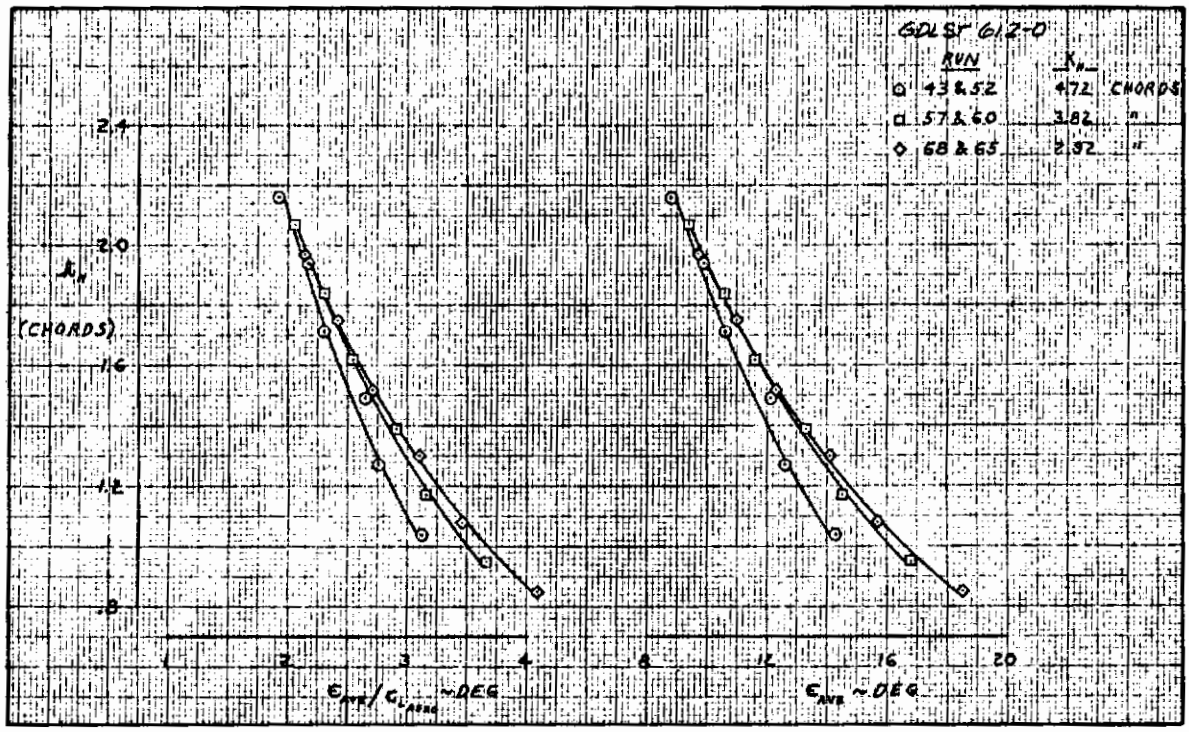

Figure 6.3-18. Effect of Tail Height and Fuselage Station on Downwash, Triple-Slotted Flap, $C_{\mu_J} = 2.0$, $\alpha_G = 4$ Degrees

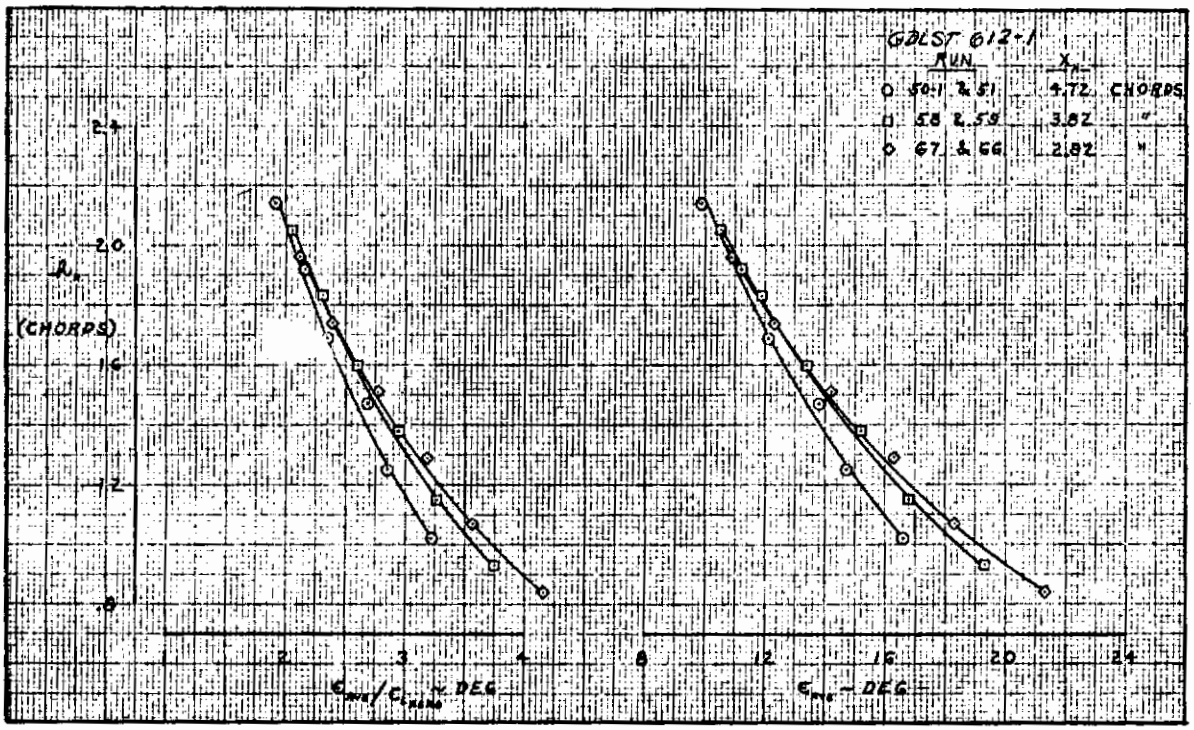

Figure 6.3-19. Effect of Tail Height and Fuselage Station on Downwash, Triple-Slotted Flap, $C_{\mu_J} = 4.0$, $\alpha_G = -4$ Degrees

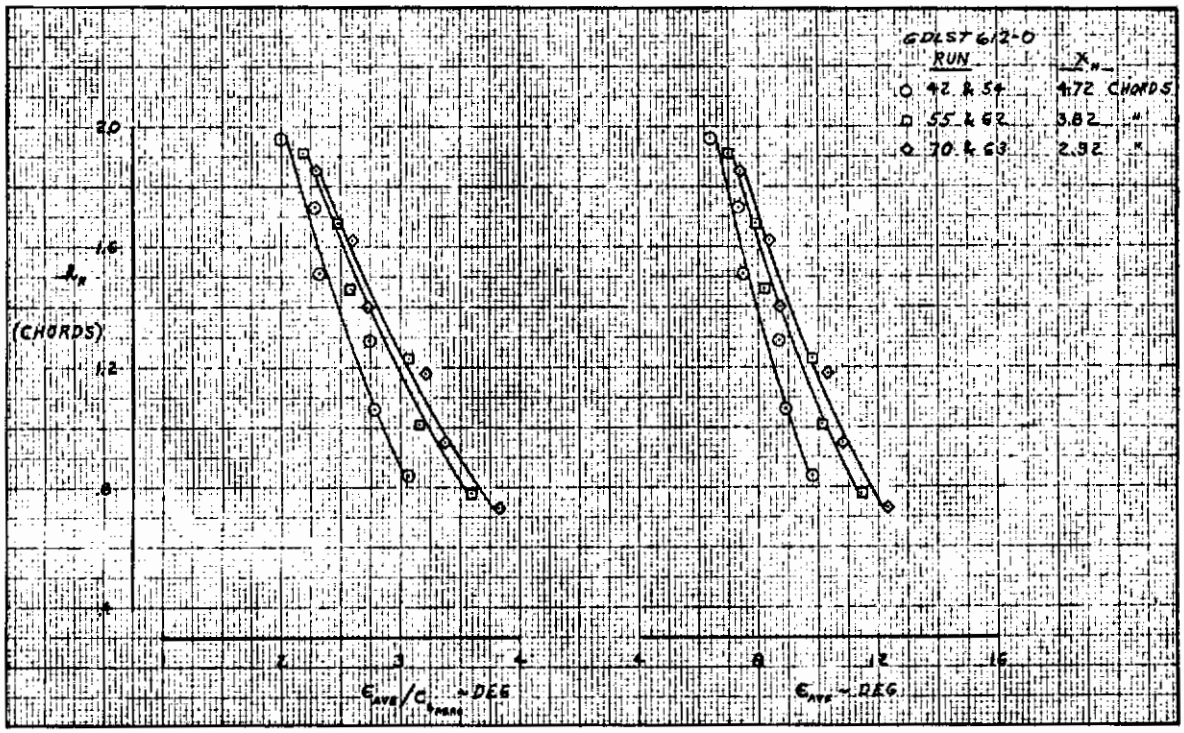

Figure 6.3-20. Effect of Tail Height and Fuselage Station on Downwash, Triple-Slotted Flap, $C_{\mu_J} = 0$, $\alpha_G = -1$ Degree

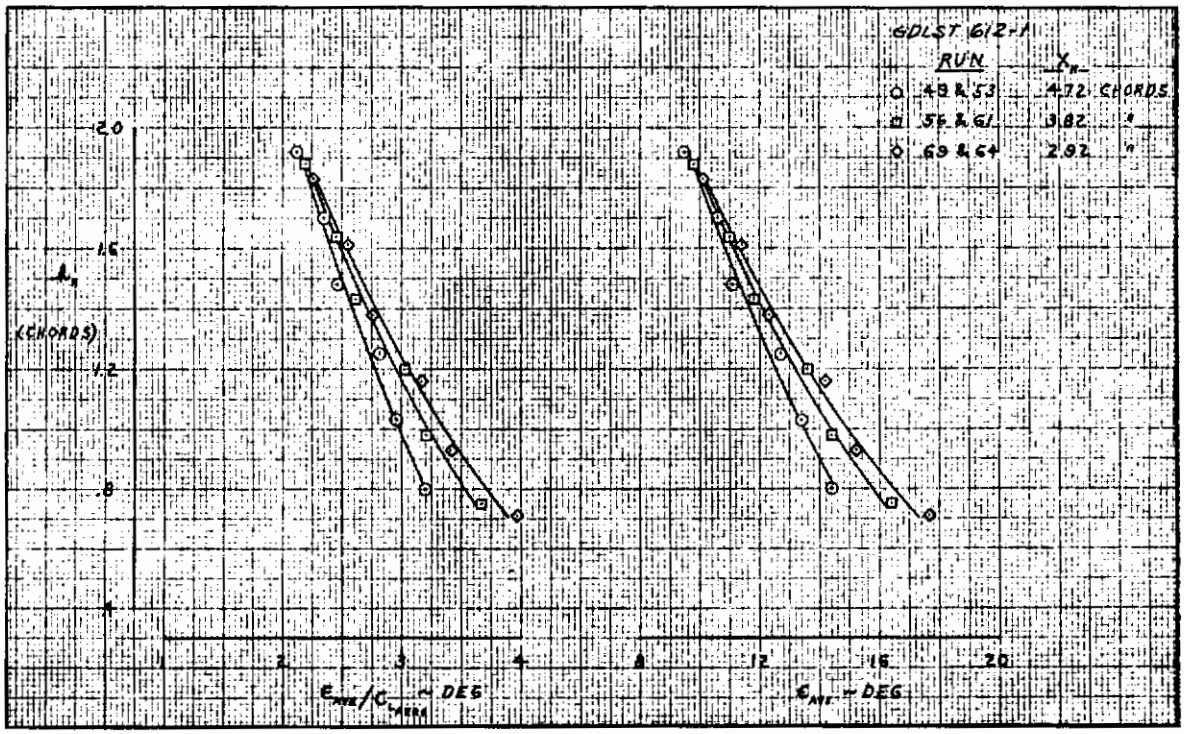

Figure 6.3-21. Effect of Tail Height and Fuselage Station on Downwash, Triple-Slotted Flap, $C_{\mu_J} = 1.0$, $\alpha_G = -1$ Degree

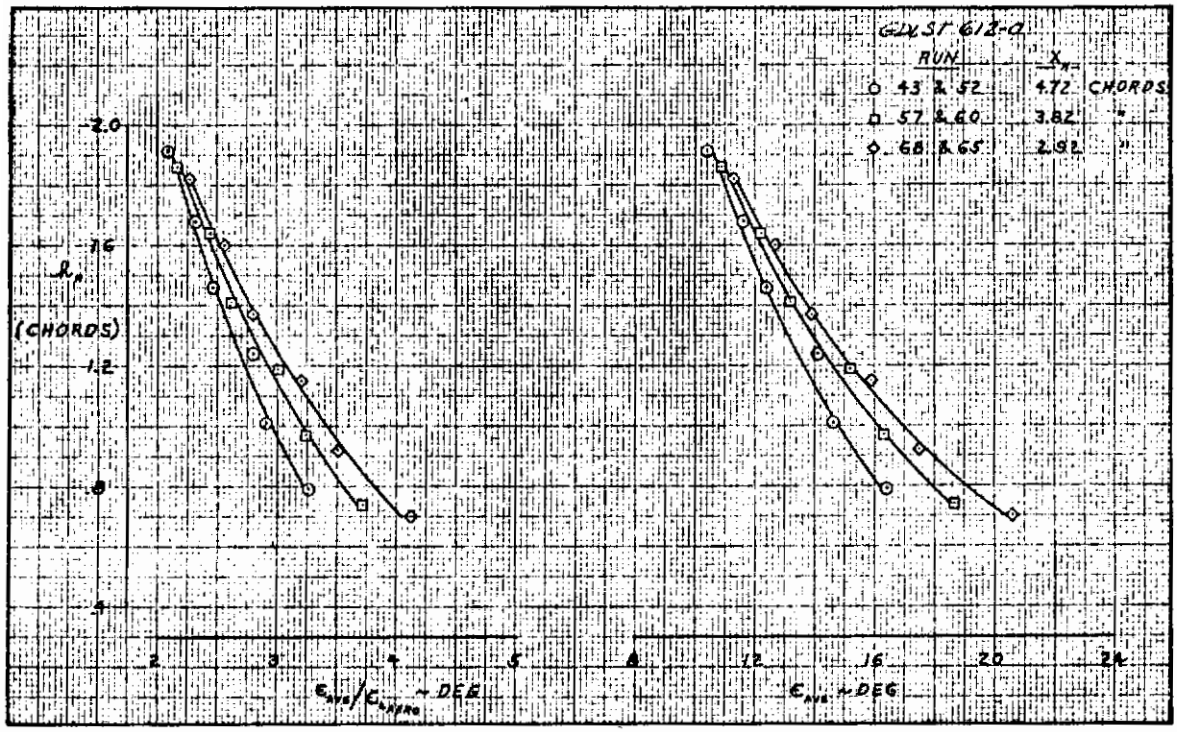

Figure 6.3-22. Effect of Tail Height and Fuselage Station on Downwash, Triple-Slotted Flap, $C_{\mu_J} = 2.0$, $\alpha_G = -1$ Degree

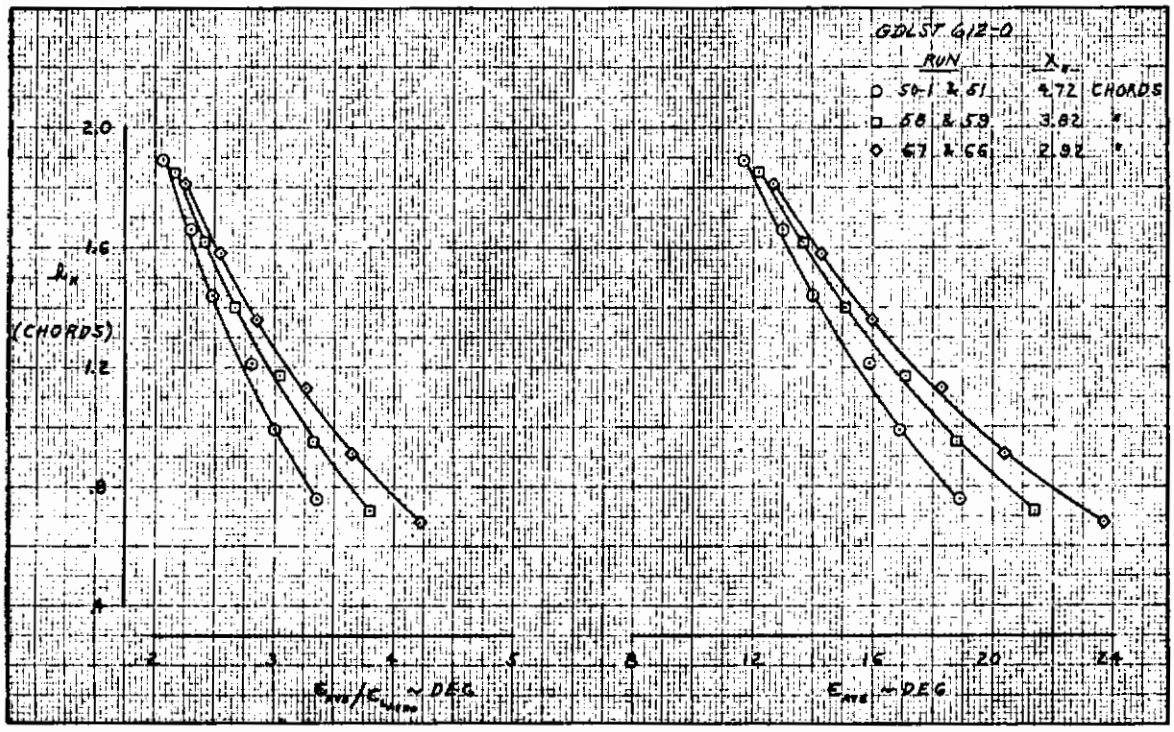

Figure 6.3-23. Effect of Tail Height and Fuselage Station on Downwash, Triple-Slotted Flap, $C_{\mu_J} = 4.0$, $\alpha_G = -1$ Degree

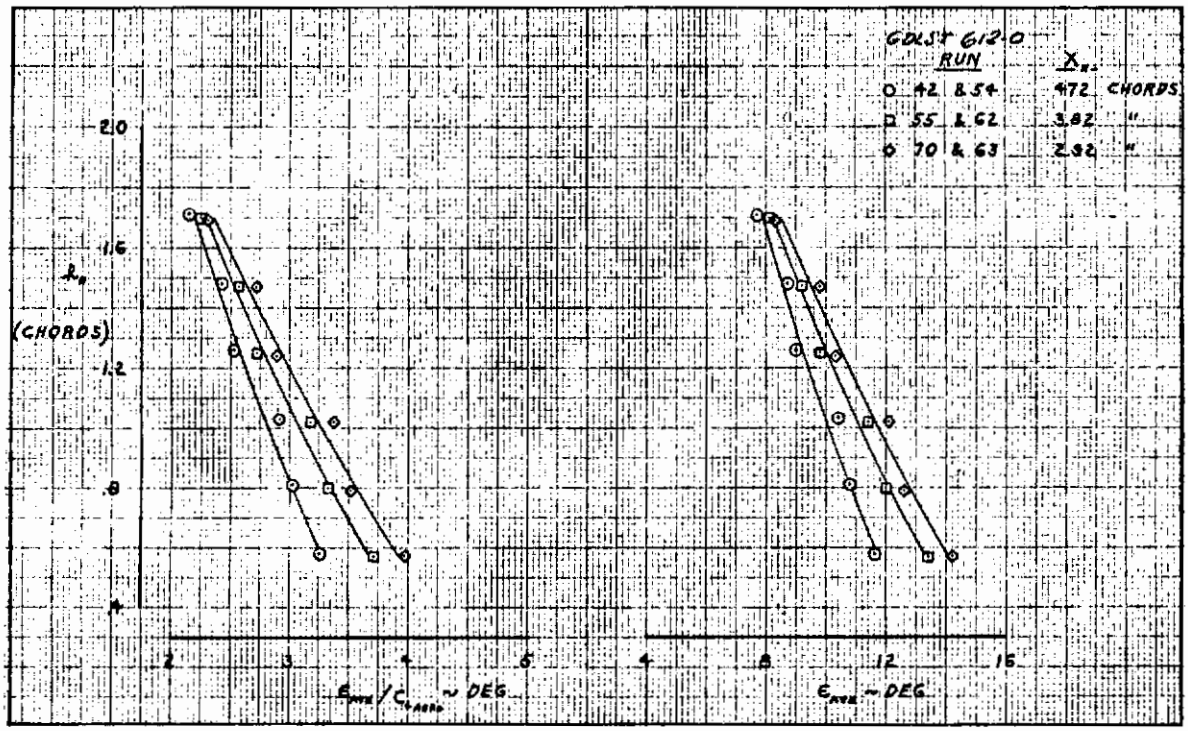

Figure 6.3-24. Effect of Tail Height and Fuselage Station on Downwash, Triple-Slotted Flap, $C_{\mu_J} = 0$, $\alpha_G = 2$ Degrees

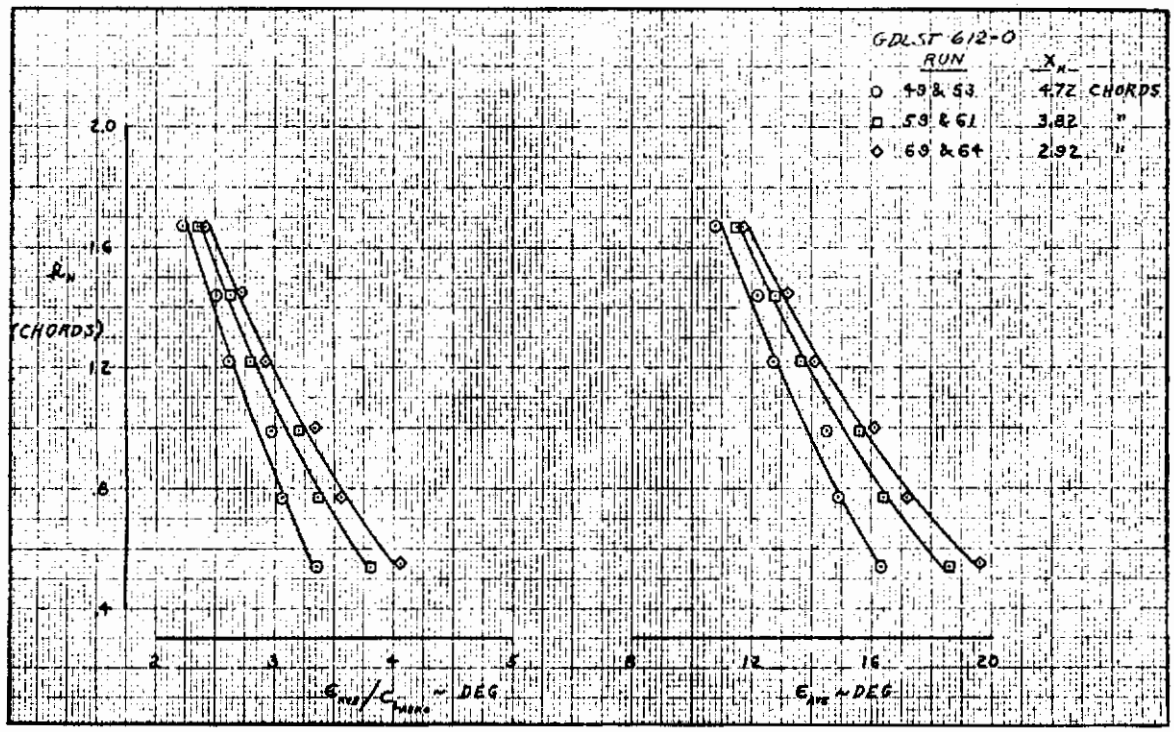

Figure 6.3-25. Effect of Tail Height and Fuselage Station on Downwash, Triple-Slotted Flap, $C_{\mu_J} = 1.0$, $\alpha_G = 2$ Degrees

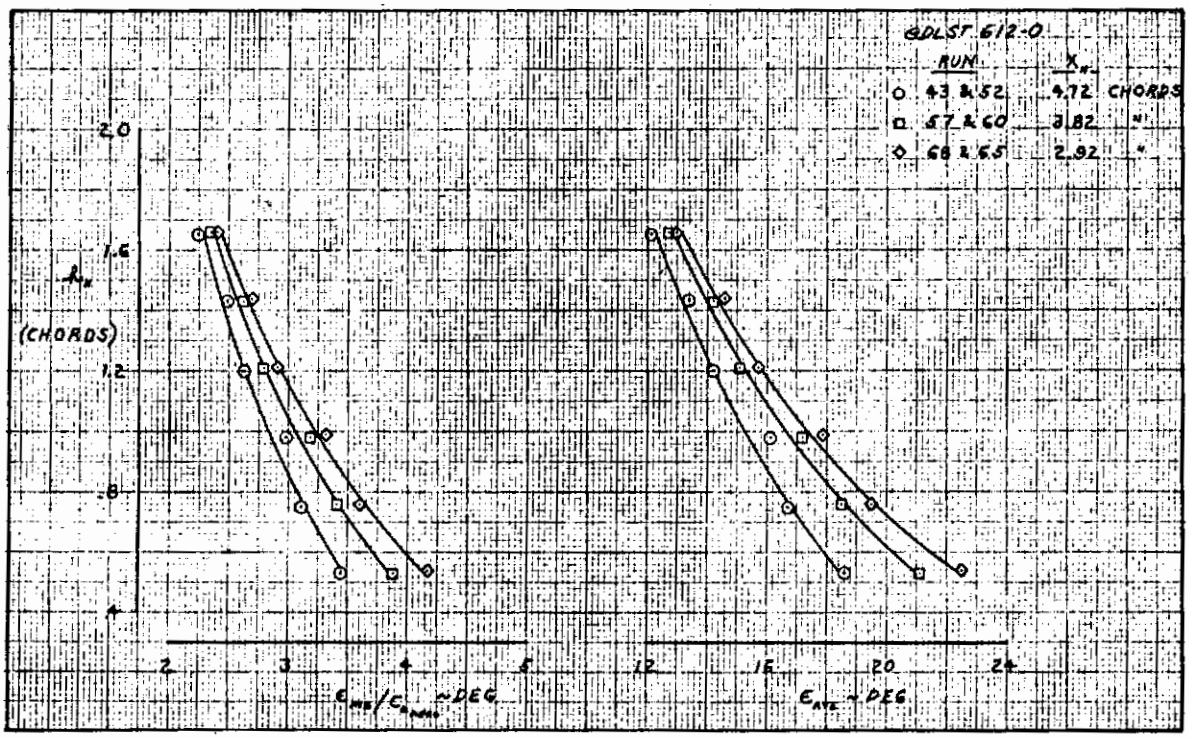

Figure 6.3-26. Effect of Tail Height and Fuselage Station on Downwash, Triple-Slotted Flap, $C_{\mu_J} = 2.0$, $\alpha_G = 2$ Degrees

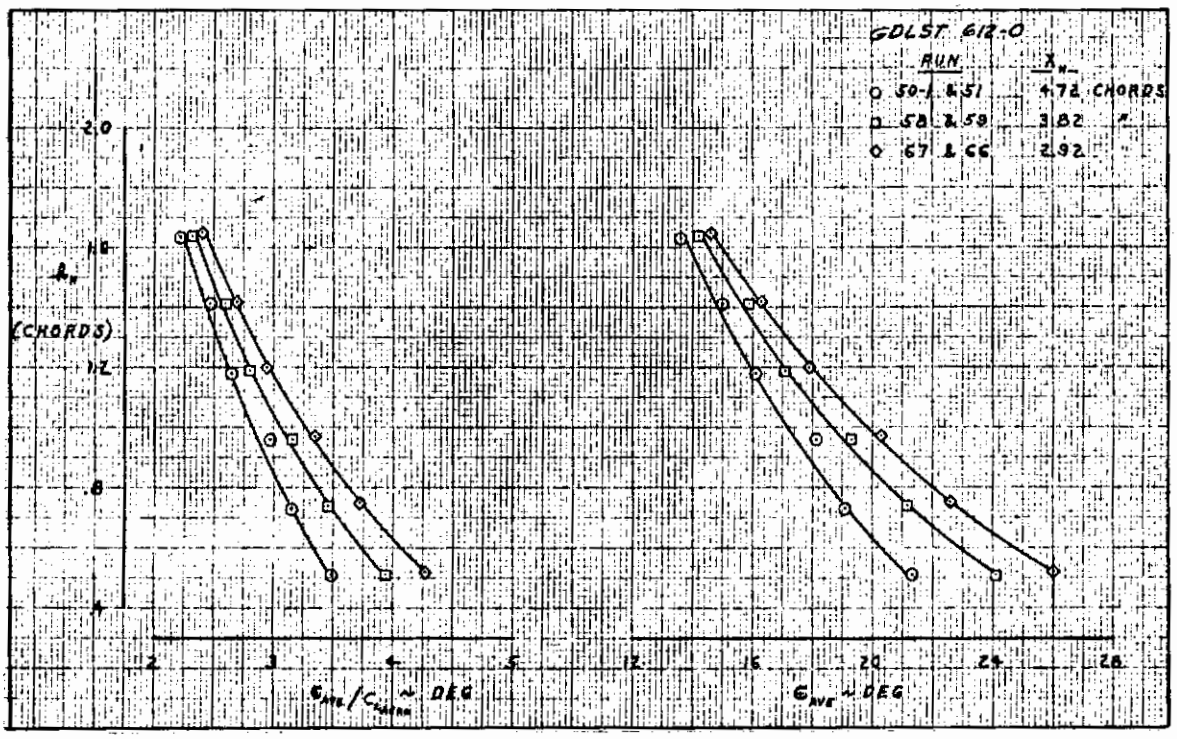

Figure 6.3-27. Effect of Tail Height and Fuselage Station on Downwash, Triple-Slotted Flap, $C_{\mu_J} = 4.0$, $\alpha_G = 2$ Degrees

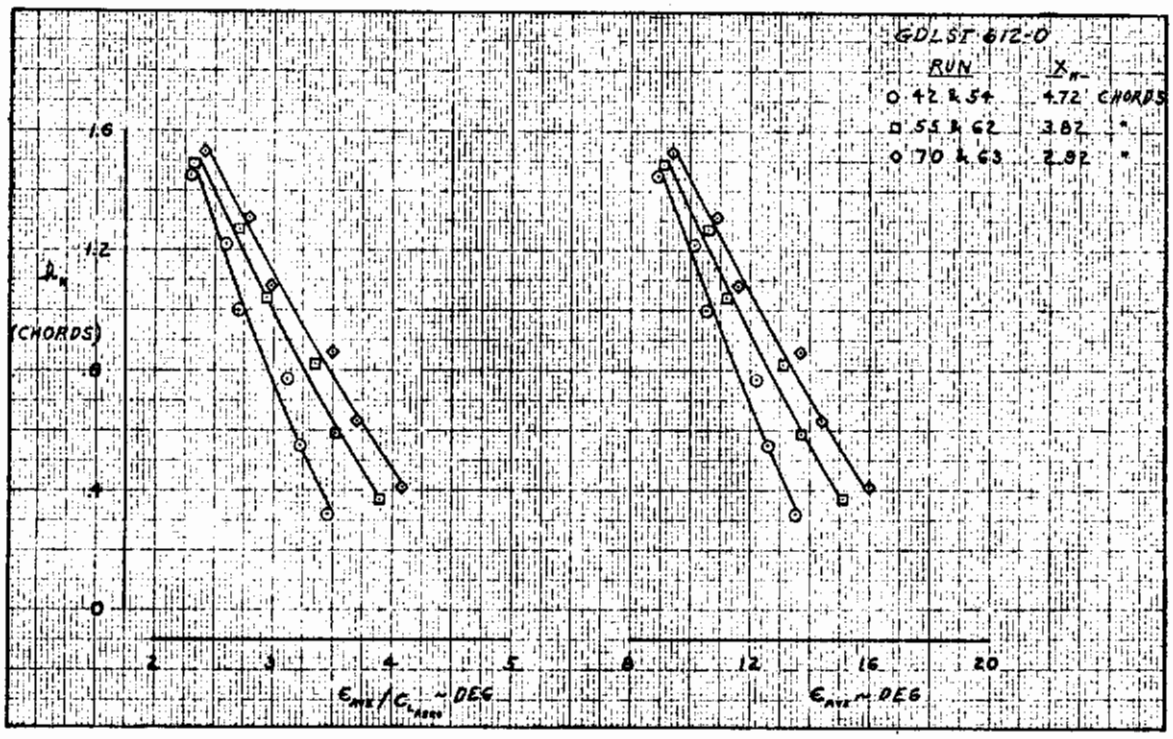

Figure 6.3-28. Effect of Tail Height and Fuselage Station on Downwash, Triple-Slotted Flap, $C_{\mu_J} = 0$, $\alpha_G = 5$ Degrees

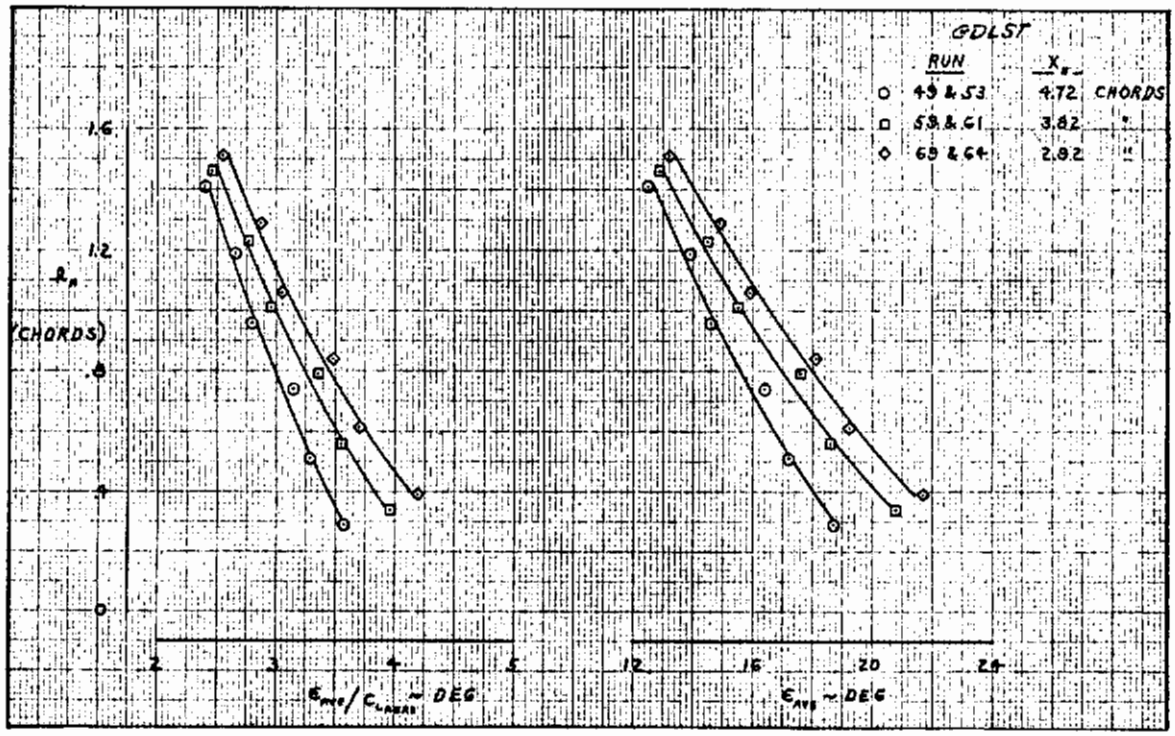

Figure 6.3-29. Effect of Tail Height and Fuselage Station on Downwash, Triple-Slotted Flap, $C_{\mu_J} = 1.0$, $\alpha_G = 5$ Degrees

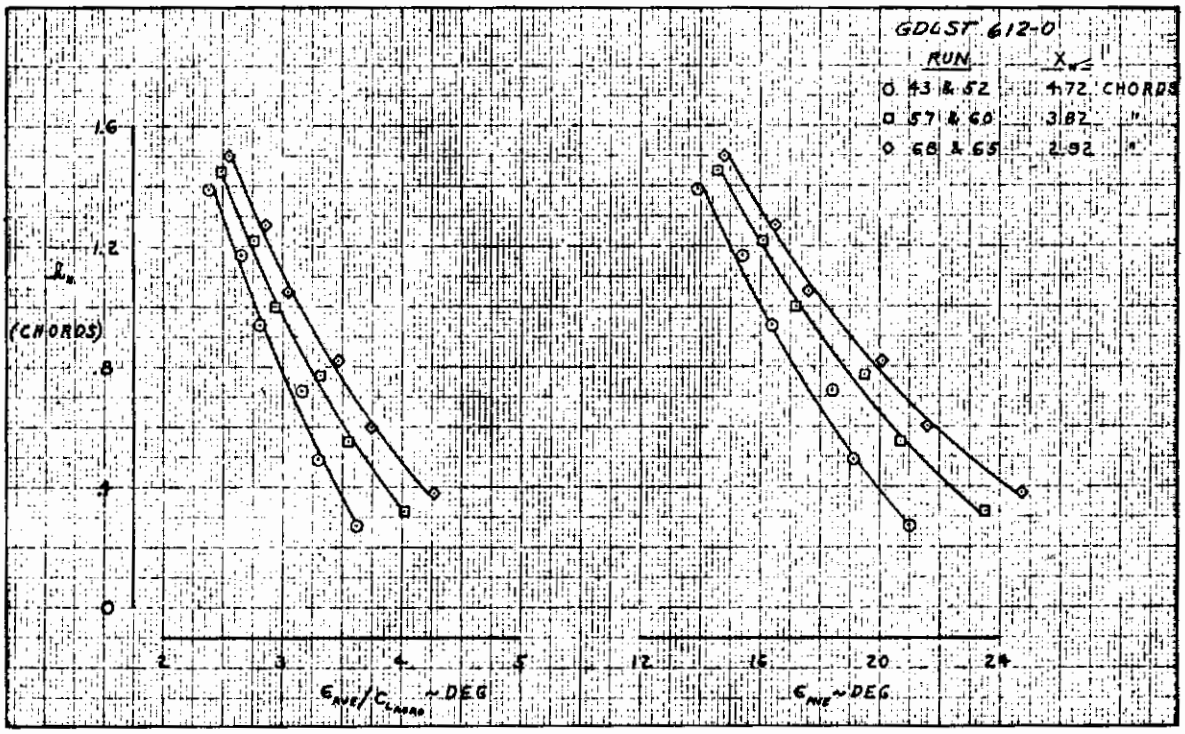

Figure 6.3-30. Effect of Tail Height and Fuselage Station on Downwash, Triple-Slotted Flap, $C_{\mu_J} = 2.0$, $\alpha_G = 5$ Degrees

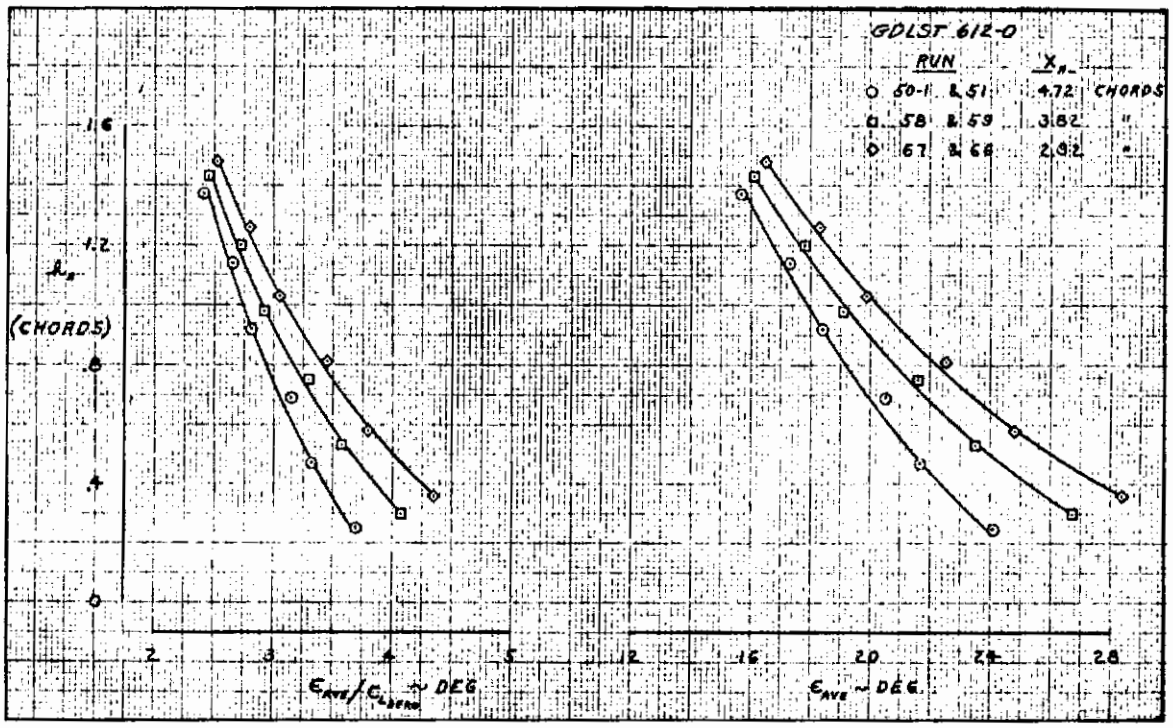

Figure 6.3-31. Effect of Tail Height and Fuselage Station on Downwash, Triple-Slotted Flap, $C_{\mu_J} = 4.0$, $\alpha_G = 5$ Degrees

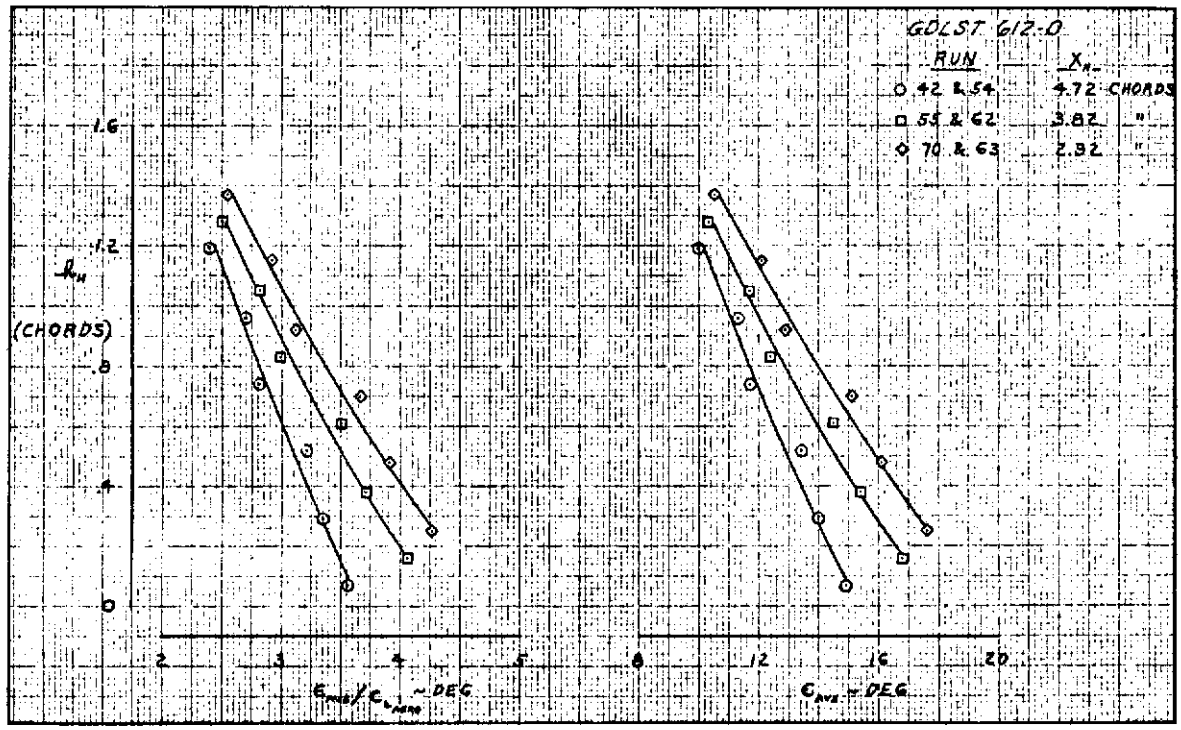

Figure 6.3-32. Effect of Tail Height and Fuselage Station on Downwash, Triple-Slotted Flap, $C_{\mu_J} = 0$, $\alpha_G = 8$ Degrees

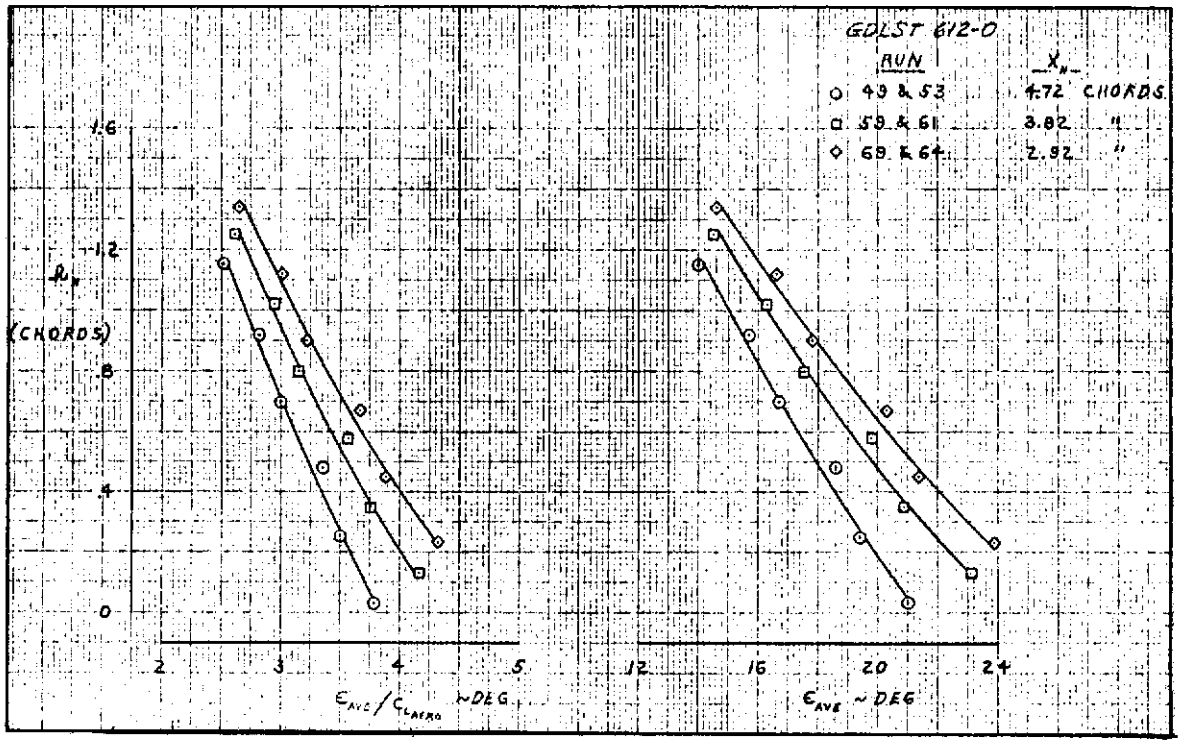

Figure 6.3-33. Effect of Tail Height and Fuselage Station on Downwash, Triple-Slotted Flap, $C_{\mu_J} = 1.0$, $\alpha_G = 8$ Degrees

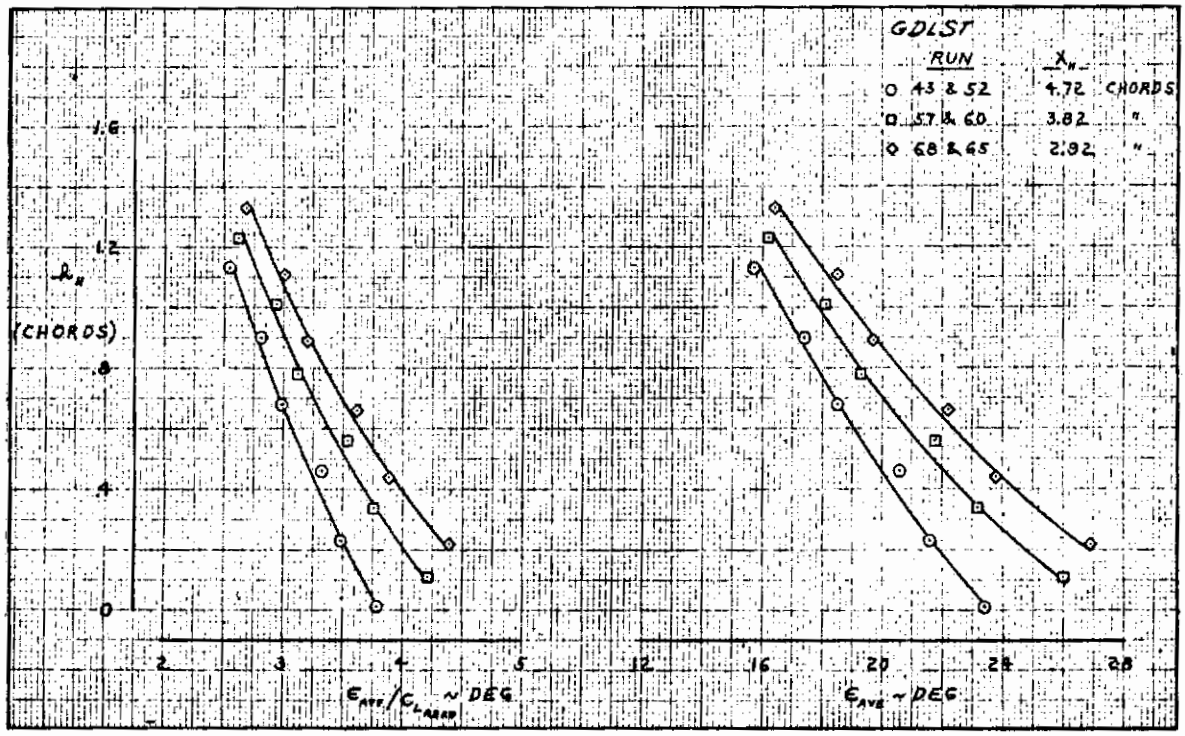

Figure 6.3-34. Effect of Tail Height and Fuselage Station on Downwash, Triple-Slotted Flap, $C_{\mu_J} = 2.0$, $\alpha_G = 8$ Degrees

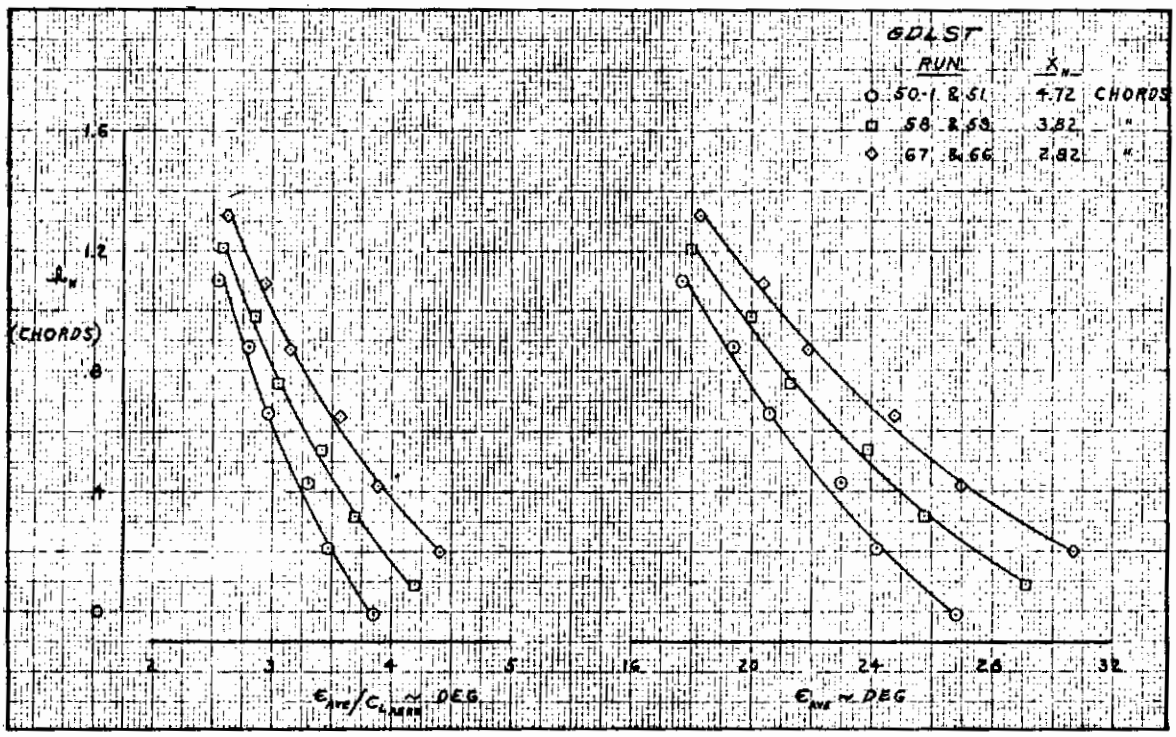

Figure 6.3-35. Effect of Tail Height and Fuselage Station on Downwash, Triple-Slotted Flap, $C_{\mu_J} = 4.0$, $\alpha_G = 8$ Degrees

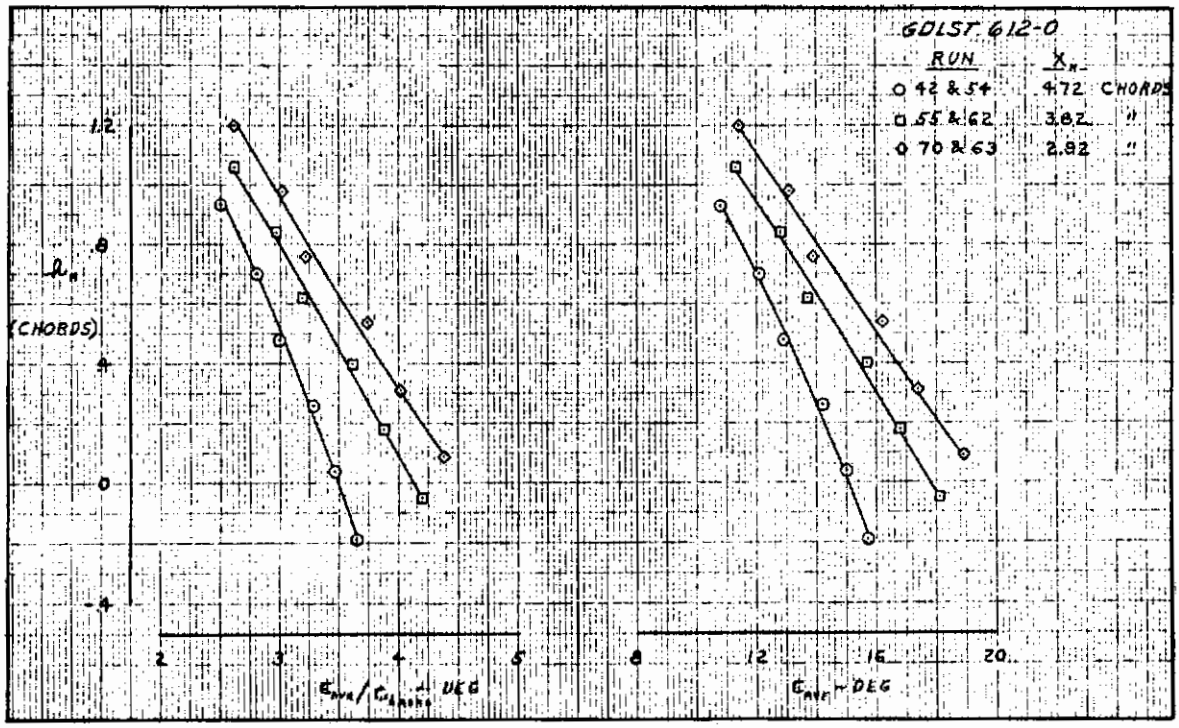

Figure 6.3-36. Effect of Tail Height and Fuselage Station on Downwash, Triple-Slotted Flap, $C_{\mu_J} = 0$, $\alpha_G = 11$ Degrees

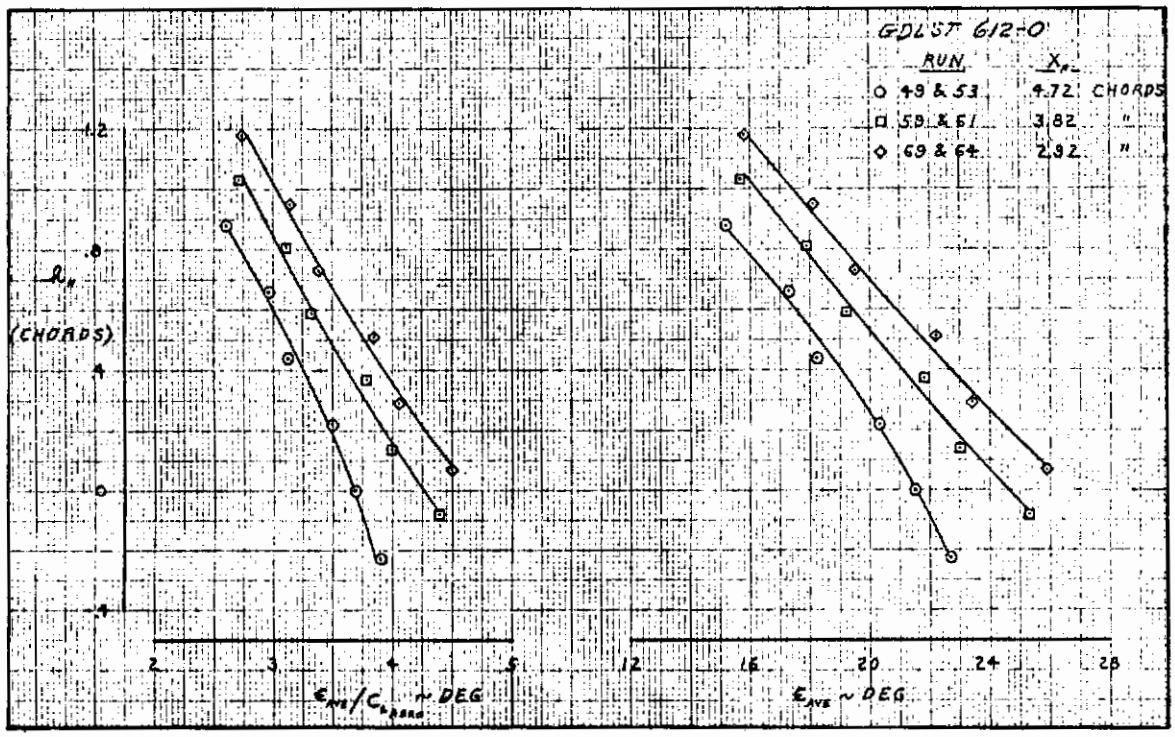

Figure 6.3-37. Effect of Tail Height and Fuselage Station on Downwash, Triple-Slotted Flap, $C_{\mu_J} = 1.0$, $\alpha_G = 11$ Degrees

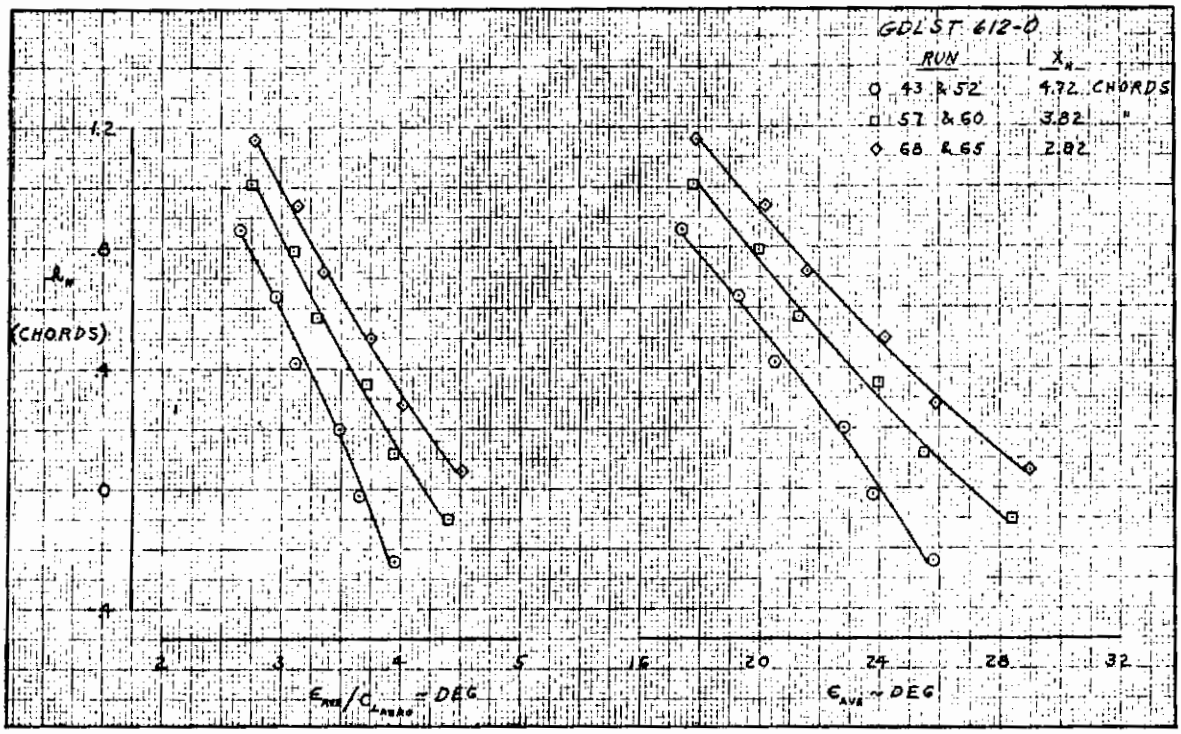

Figure 6.3-38. Effect of Tail Height and Fuselage Station on Downwash, Triple-Slotted Flap, $C_{\mu_J} = 2.0$, $\alpha_G = 11$ Degrees

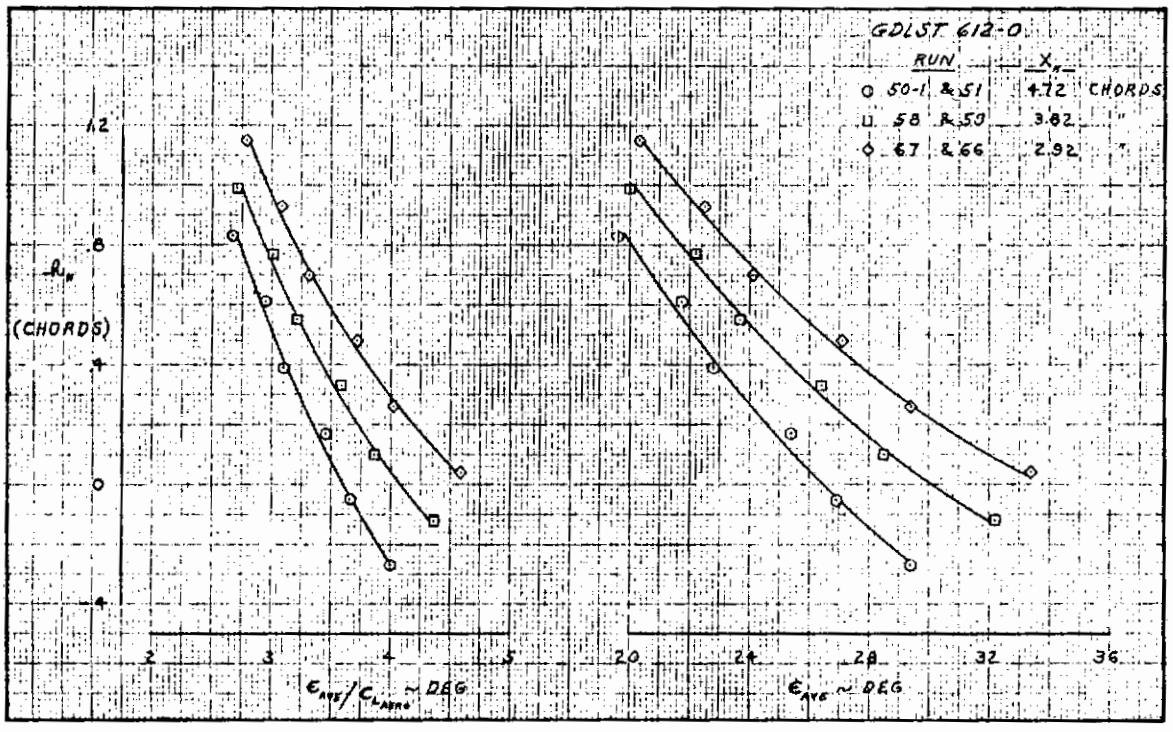

Figure 6.3-39. Effect of Tail Height and Fuselage Station on Downwash, Triple-Slotted Flap, $C_{\mu_J} = 4.0$, $\alpha_G = 11$ Degrees

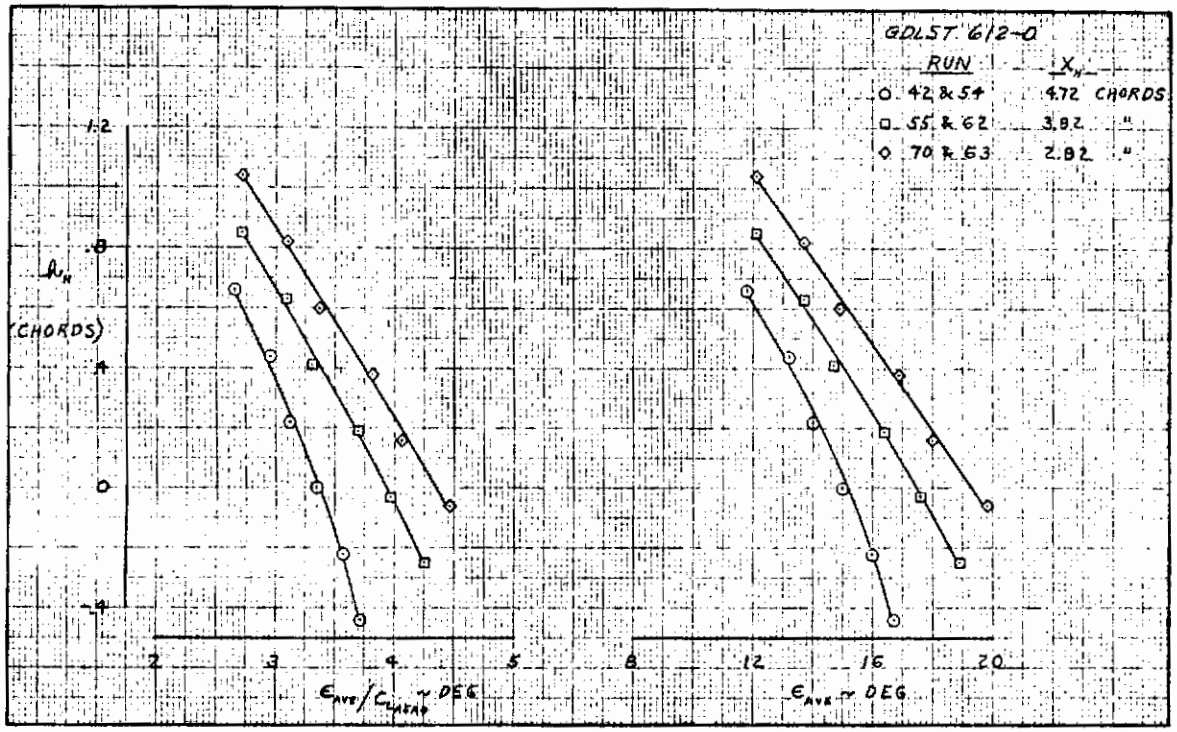

Figure 6.3-40. Effect of Tail Height and Fuselage Station on Downwash, Triple-Slotted Flap, $C_{\mu_J} = 0$, $\alpha_G = 14$ Degrees

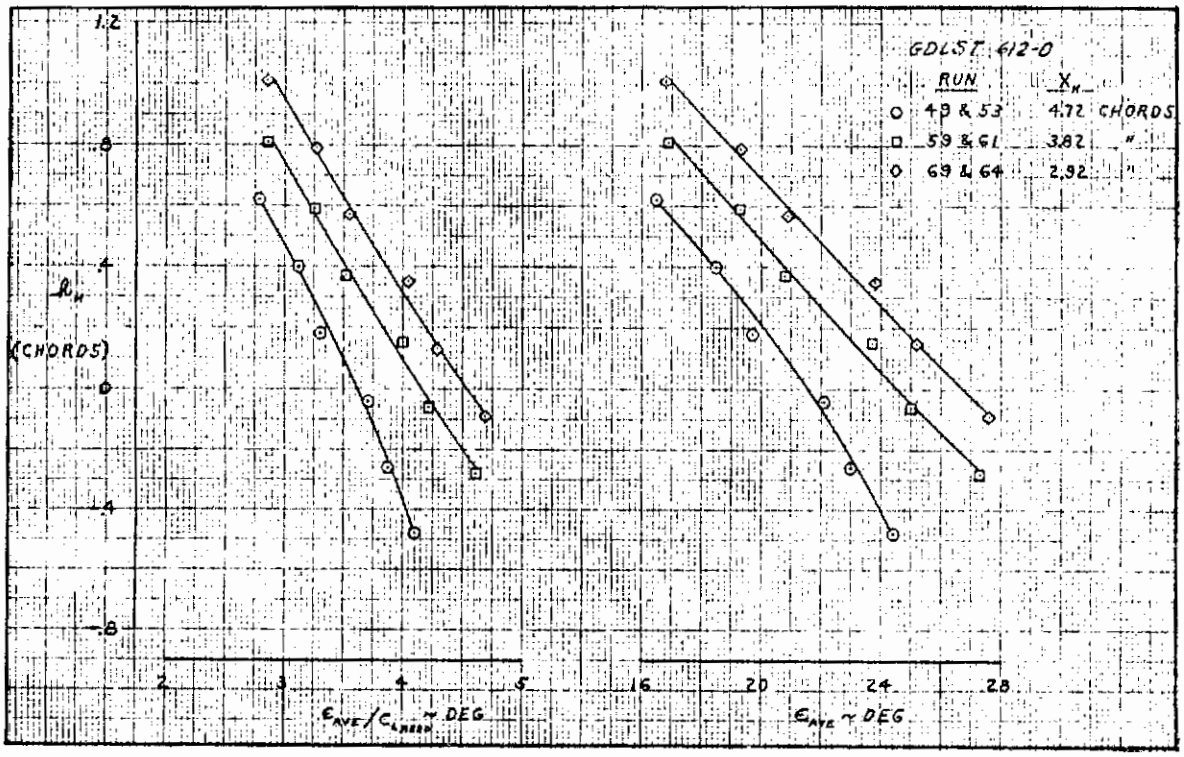

Figure 6.3-41. Effect of Tail Height and Fuselage Station on Downwash, Triple-Slotted Flap, $C_{\mu_J} = 1.0$, $\alpha_G = 14$ Degrees

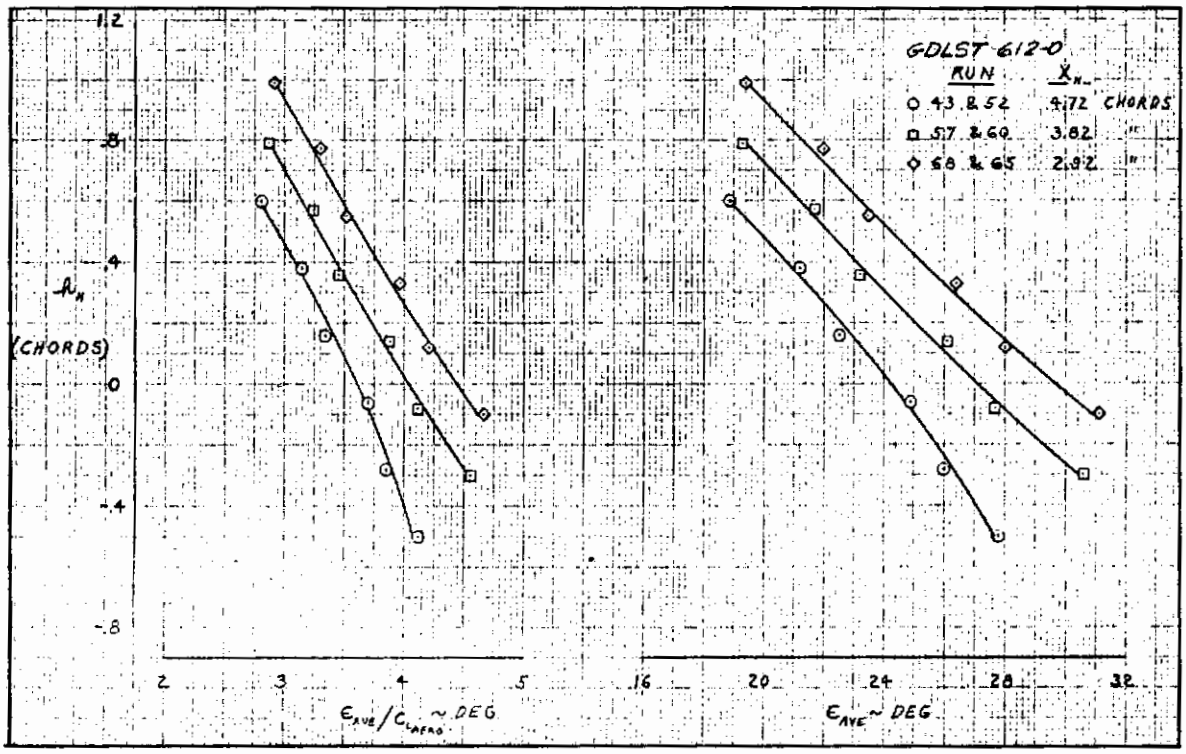

Figure 6.3-42. Effect of Tail Height and Fuselage Station on Downwash, Triple-Slotted Flap, $C_{\mu_J} = 2.0$, $\alpha_G = 14$ Degrees

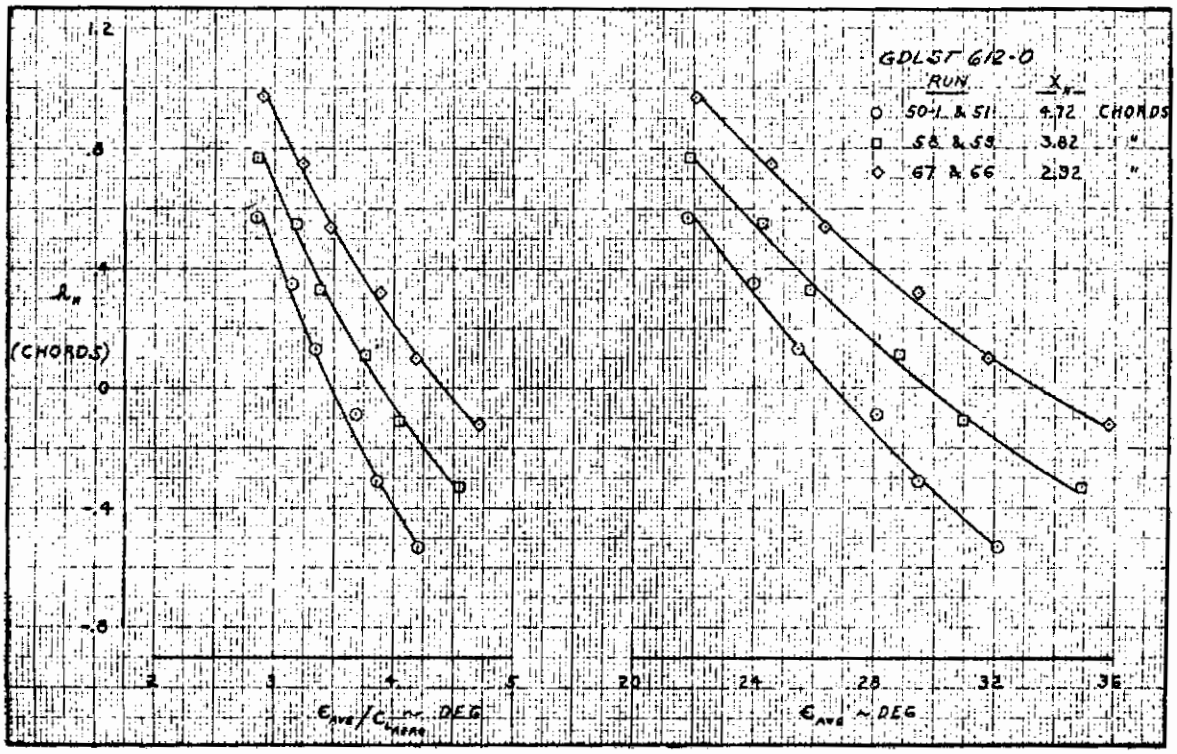

Figure 6.3-43. Effect of Tail Height and Fuselage Station on Downwash, Triple-Slotted Flap, $C_{\mu_J} = 4.0$, $\alpha_G = 14$ Degrees

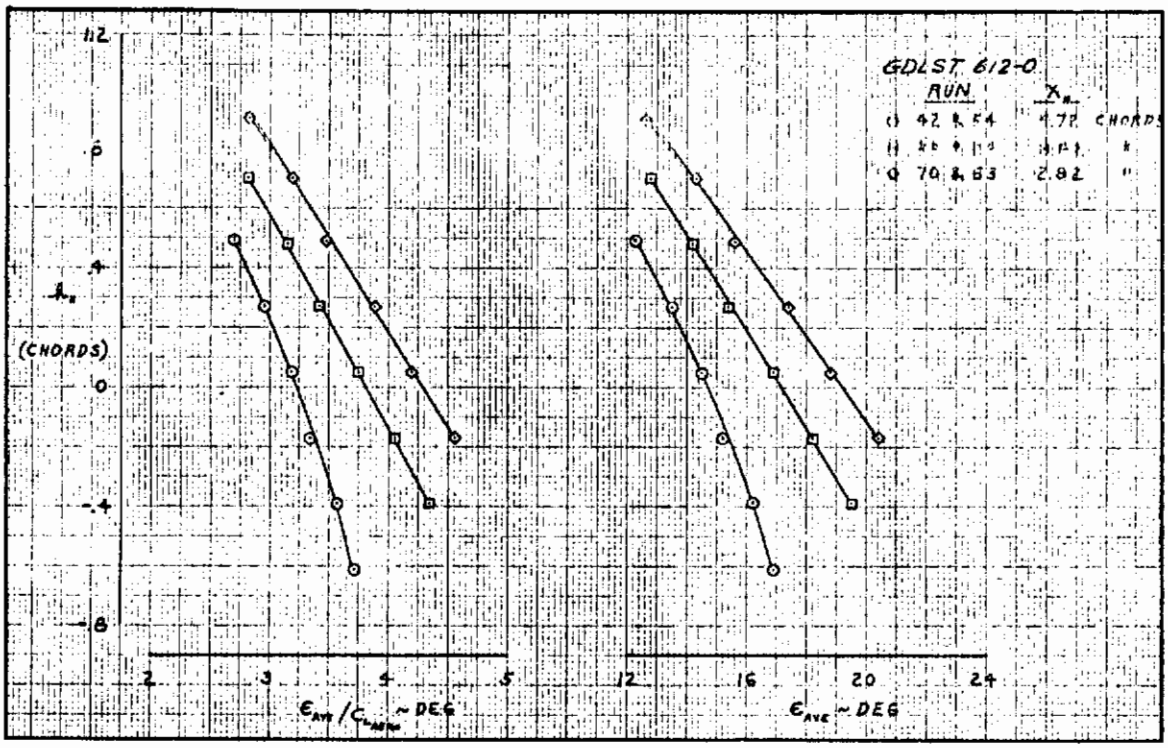

Figure 6.3-44. Effect of Tail Height and Fuselage Station on Downwash, Triple-Slotted Flap, $C_{\mu_J} = 0$, $\alpha_G = 16$ Degrees

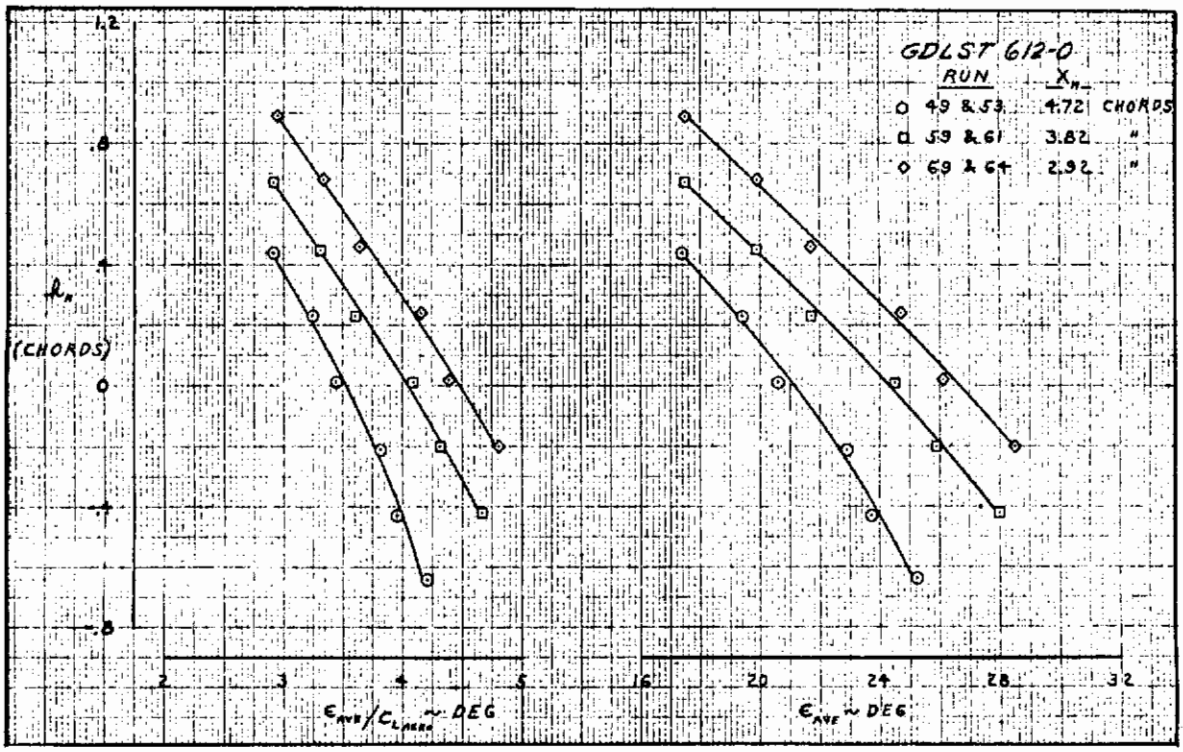

Figure 6.3-45. Effect of Tail Height and Fuselage Station on Downwash, Triple-Slotted Flap, $C_{\mu_J} = 1.0$, $\alpha_G = 16$ Degrees

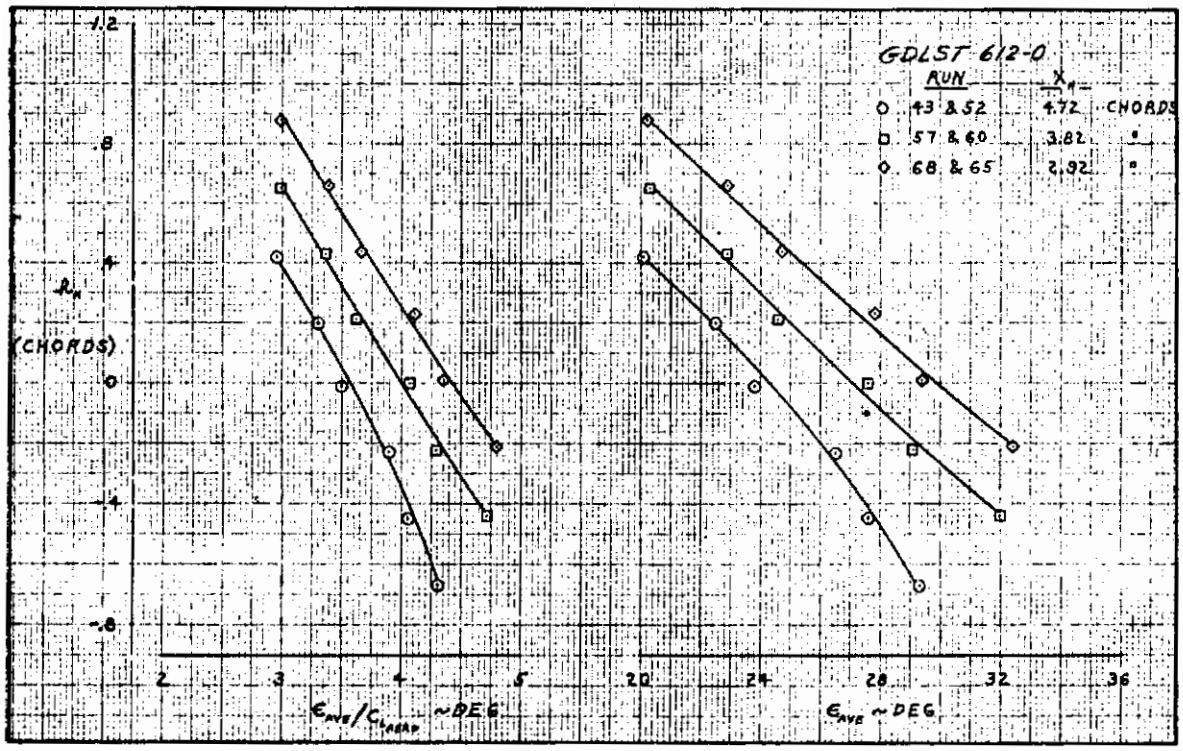

Figure 6.3-46. Effect of Tail Height and Fuselage Station on Downwash, Triple-Slotted Flap, $C_{\mu_J} = 2.0$, $\alpha_G = 16$ Degrees

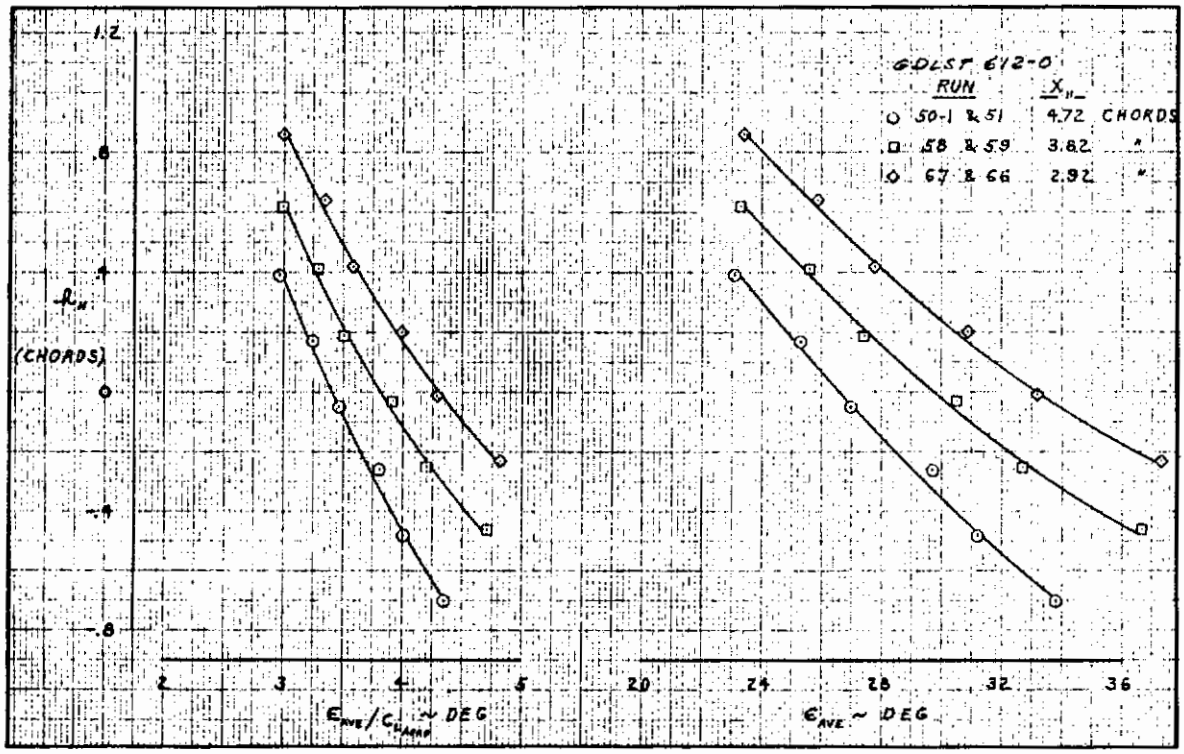

Figure 6.3-47. Effect of Tail Height and Fuselage Station on Downwash, Triple-Slotted Flap, $C_{\mu_J} = 4.0$, $\alpha_G = 16$ Degrees

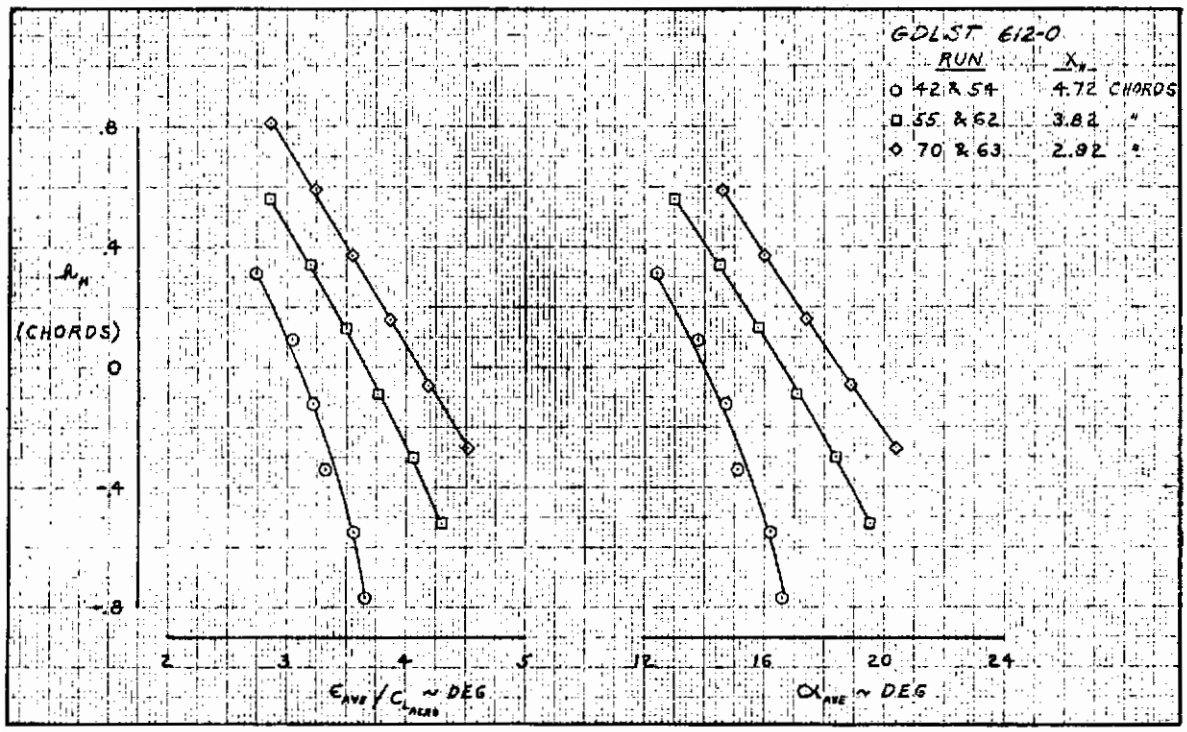

Figure 6.3-48. Effect of Tail Height and Fuselage Station on Downwash, Triple-Slotted Flap, $C_{\mu_J} = 0$, $\alpha_G = 18$ Degrees

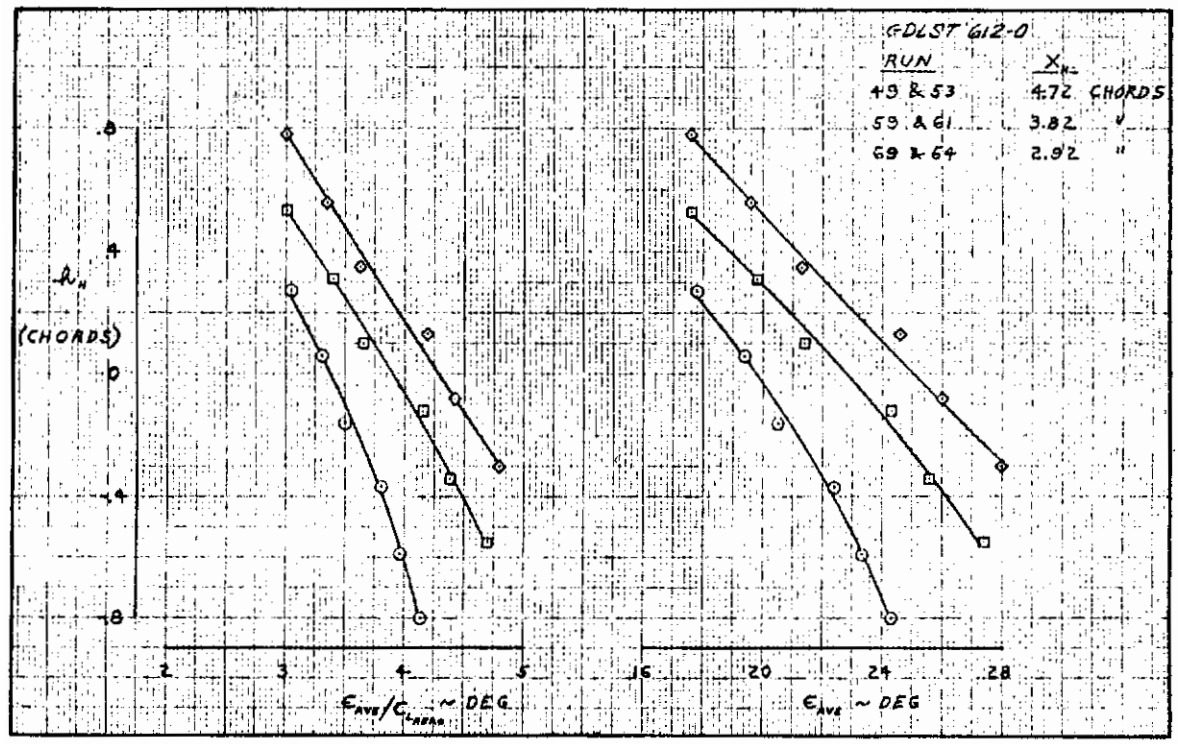

Figure 6.3-49. Effect of Tail Height and Fuselage Station on Downwash, Triple-Slotted Flap, $C_{\mu_J} = 1.0$, $\alpha_G = 18$ Degrees

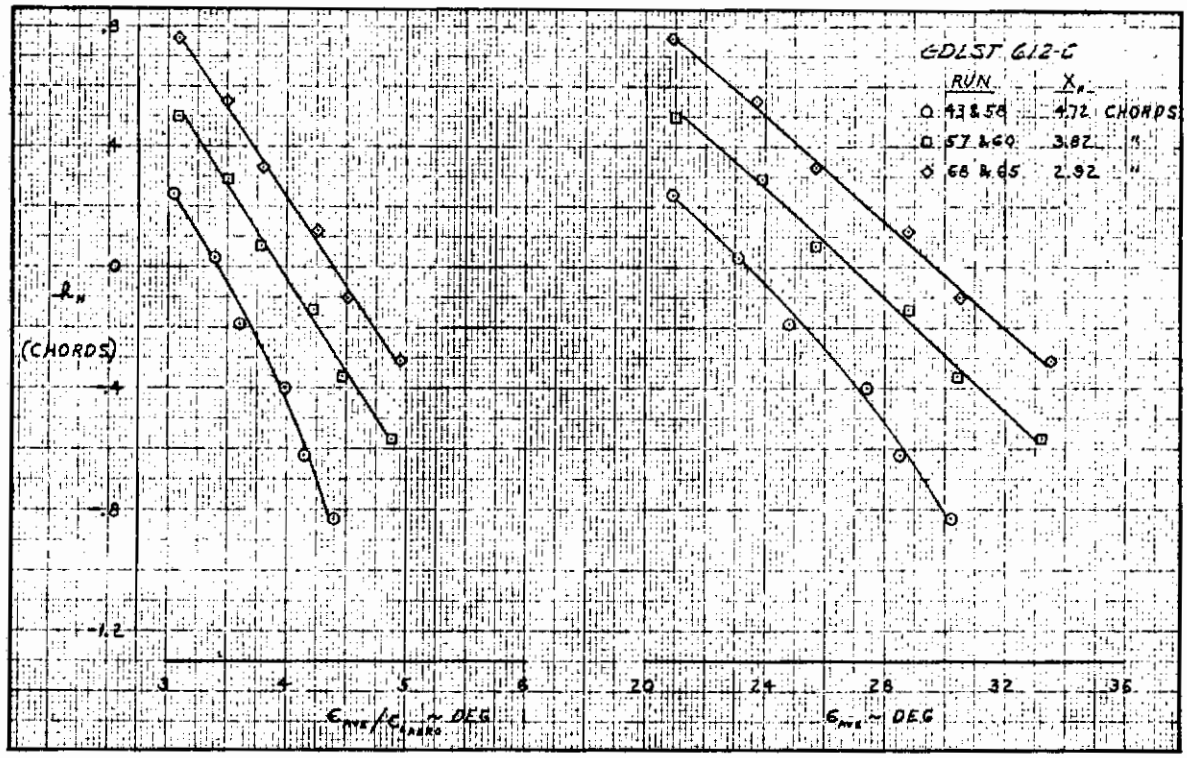

Figure 6.3-50. Effect of Tail Height and Fuselage Station on Downwash, Triple-Slotted Flap, $C_{\mu_J} = 2.0$, $\alpha_G = 18$ Degrees

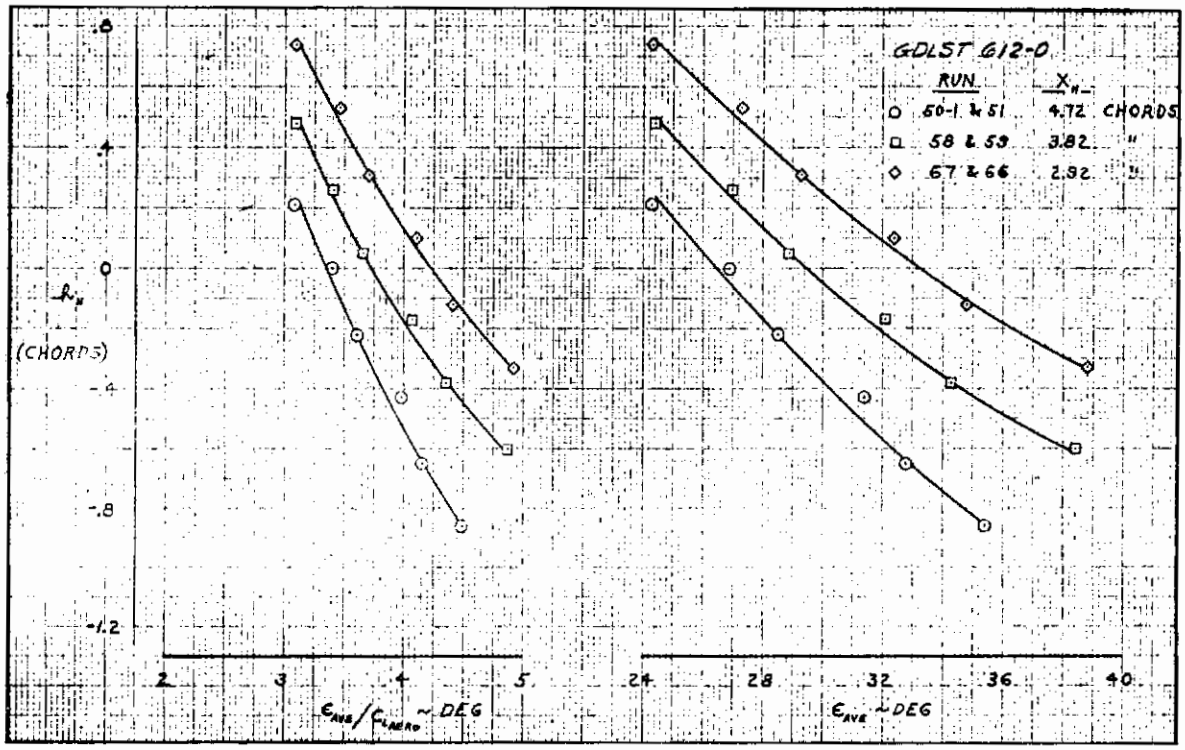

Figure 6.3-51. Effect of Tail Height and Fuselage Station on Downwash, Triple-Slotted Flap, $C_{\mu_J} = 4.0$, $\alpha_G = 18$ Degrees

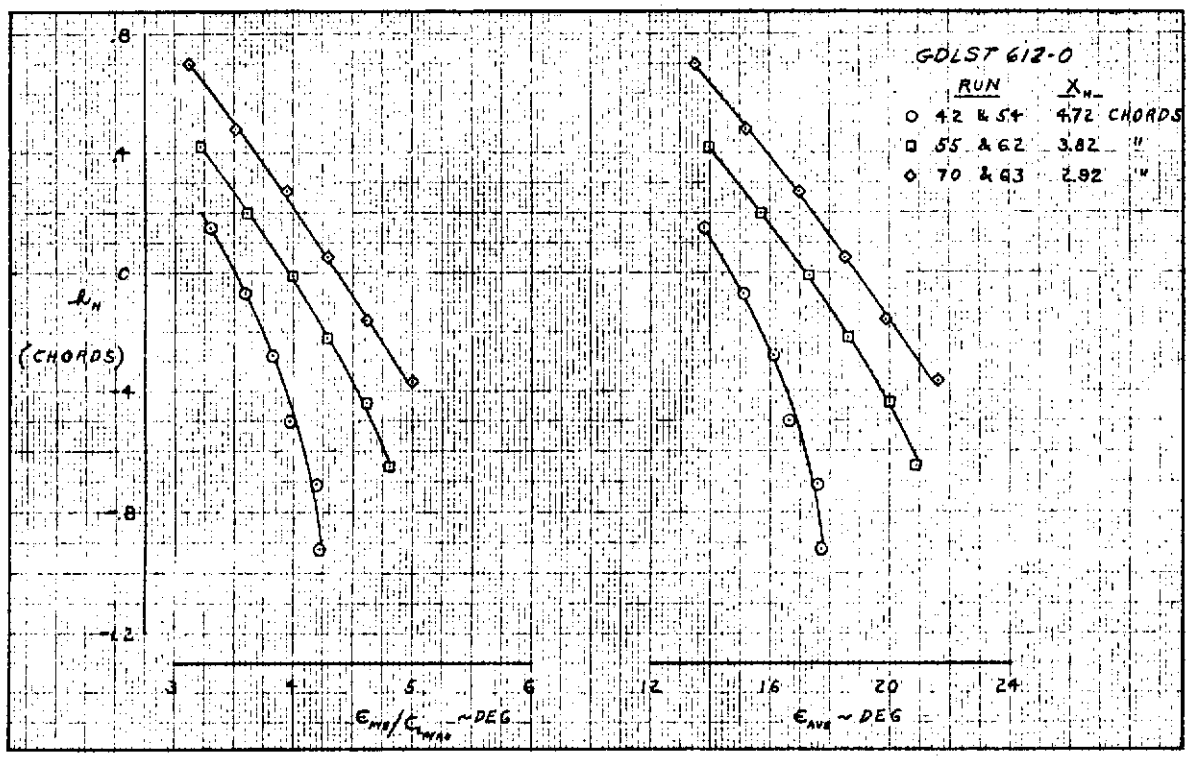

Figure 6.3-52. Effect of Tail Height and Fuselage Station on Downwash, Triple-Slotted Flap, $C_{\mu_J} = 0$, $\alpha_G = 20$ Degrees

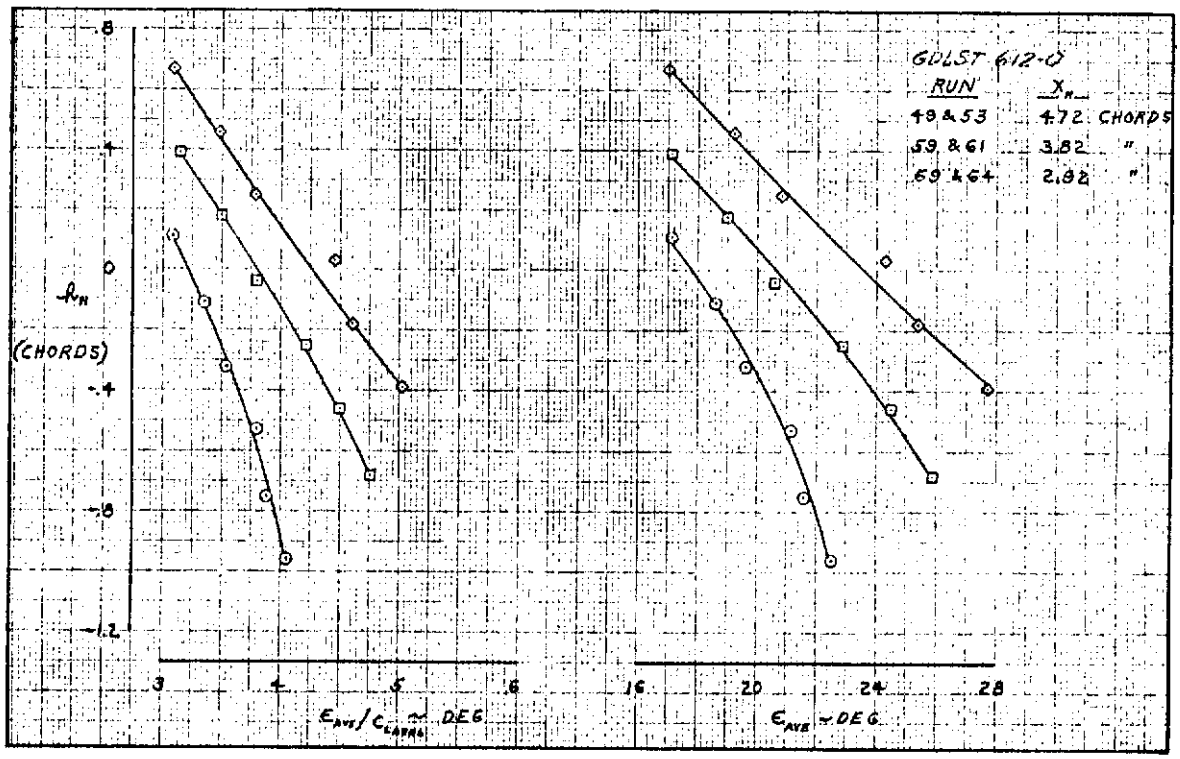

Figure 6.3-53. Effect of Tail Height and Fuselage Station on Downwash, Triple-Slotted Flap, $C_{\mu_J} = 1.0$, $\alpha_G = 20$ Degrees

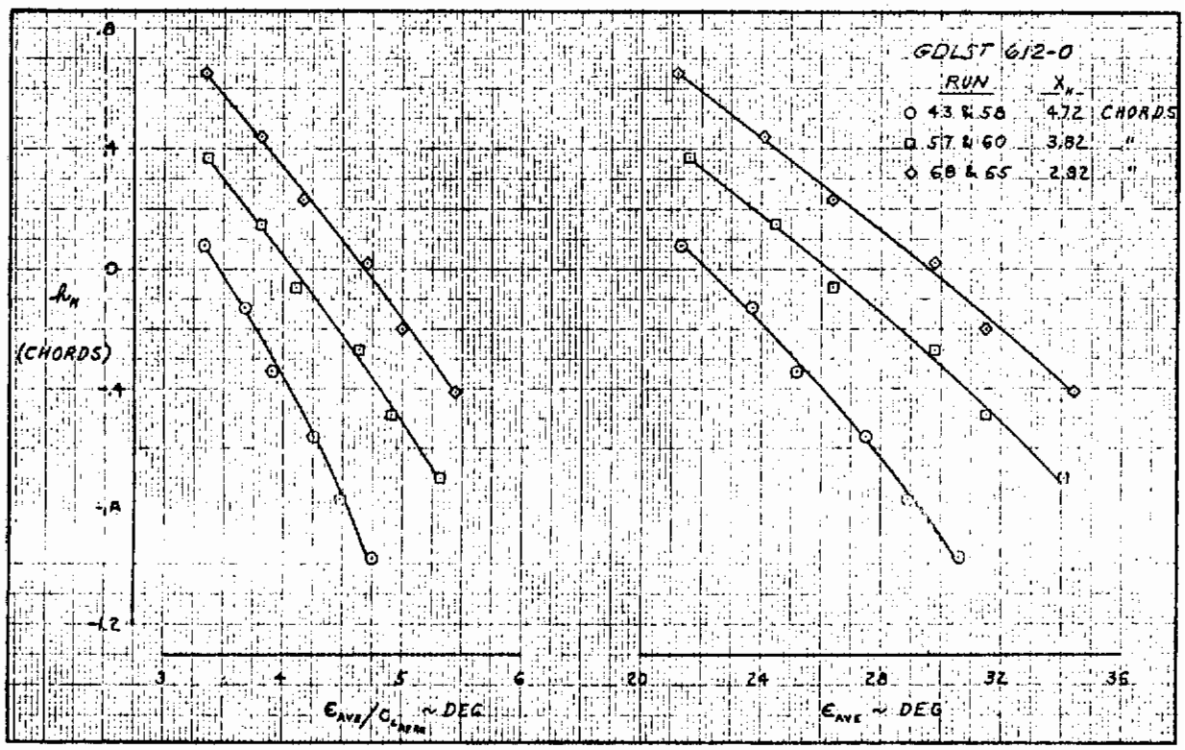

Figure 6.3-54. Effect of Tail Height and Fuselage Station on Downwash, Triple-Slotted Flap, $C_{\mu_J} = 2.0$, $\alpha_G = 20$ Degrees

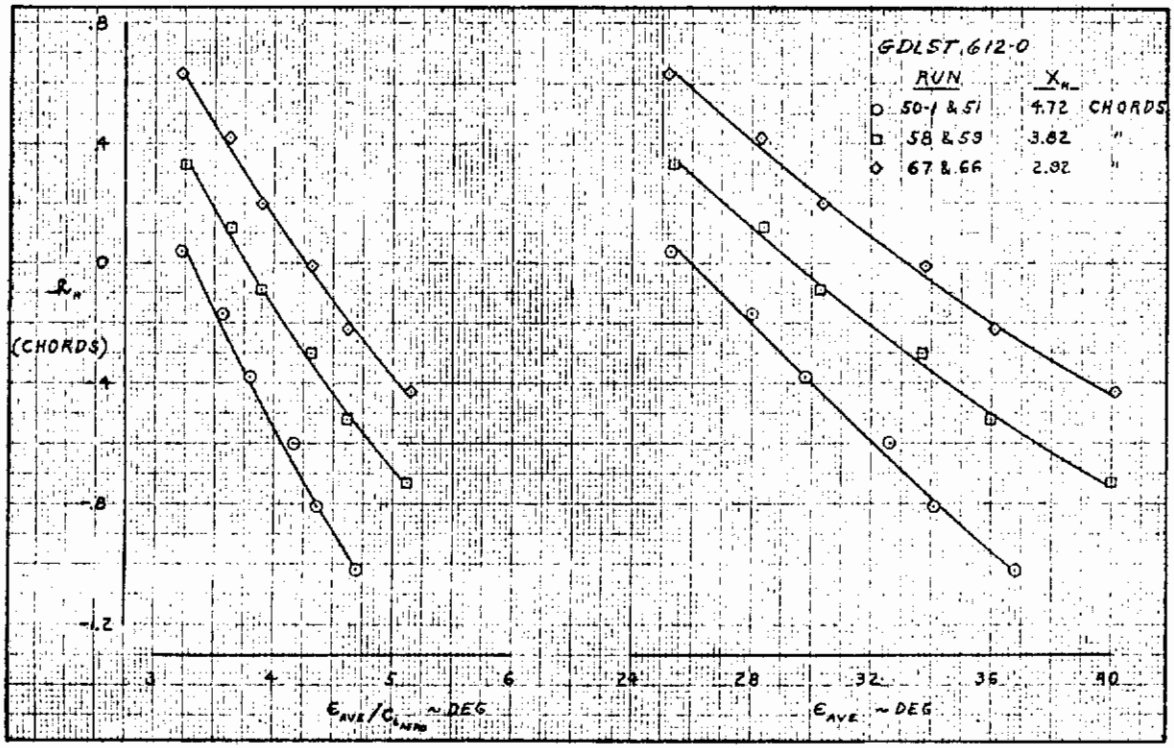

Figure 6.3-55. Effect of Tail Height and Fuselage Station on Downwash, Triple-Slotted Flap, $C_{\mu_J} = 4.0$, $\alpha_G = 20$ Degrees

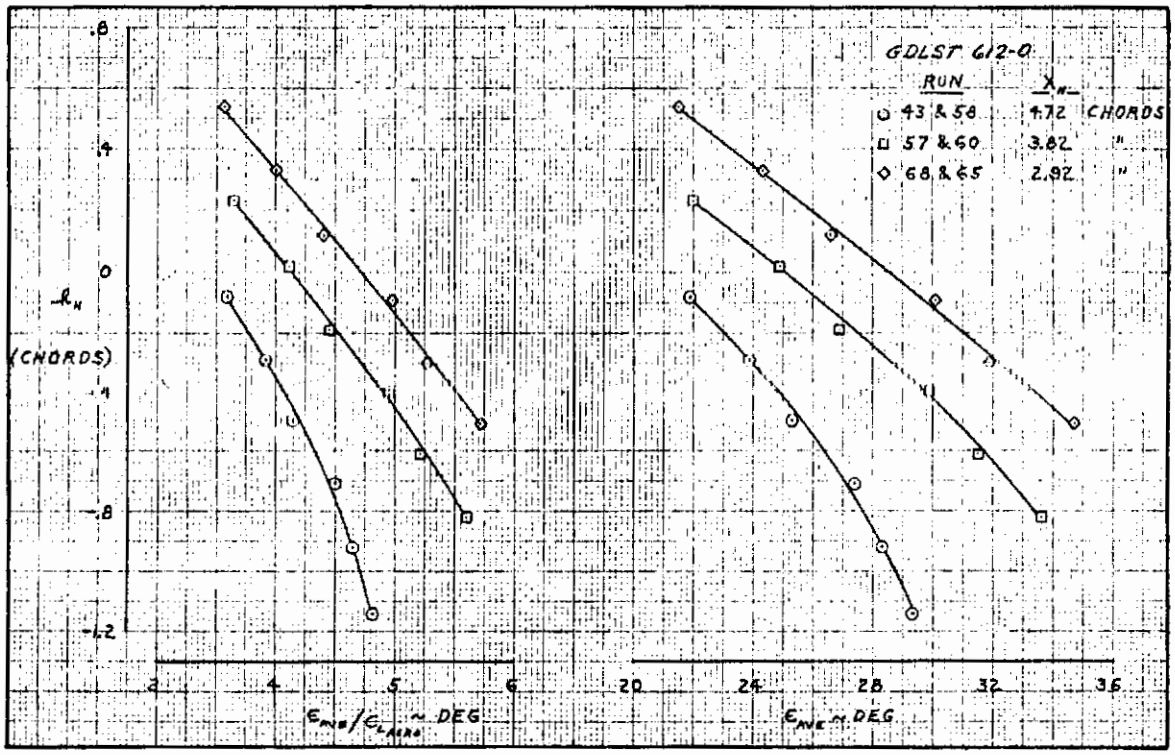

Figure 6.3-56. Effect of Tail Height and Fuselage Station on Downwash, Triple-Slotted Flap, $C_{\mu_J} = 2.0$, $\alpha_G = 22$ Degrees

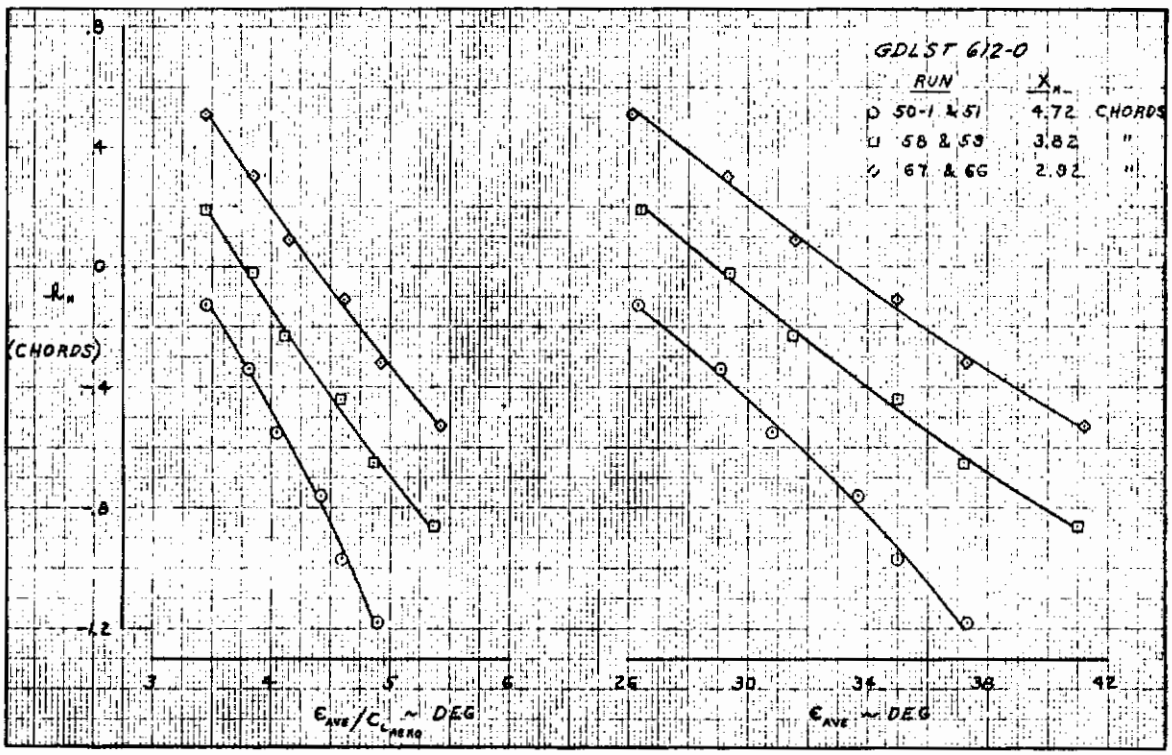

Figure 6.3-57. Effect of Tail Height and Fuselage Station on Downwash, Triple-Slotted Flap, $C_{\mu_J} = 4.0$, $\alpha_G = 22$ Degrees

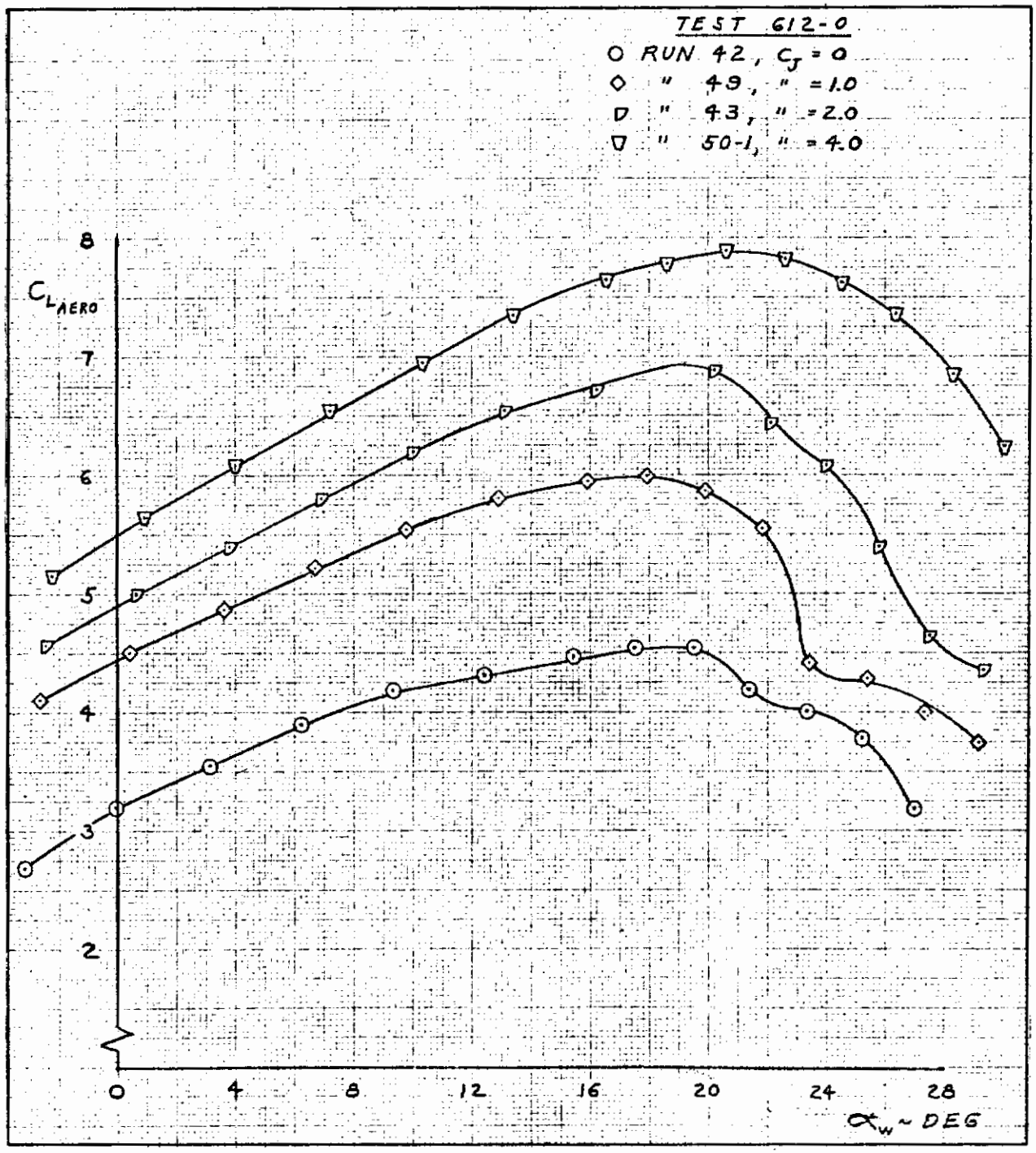

Figure 6.3-58. Aerodynamic and Jet-Induced Circulation Lift, Triple-Slotted Flap

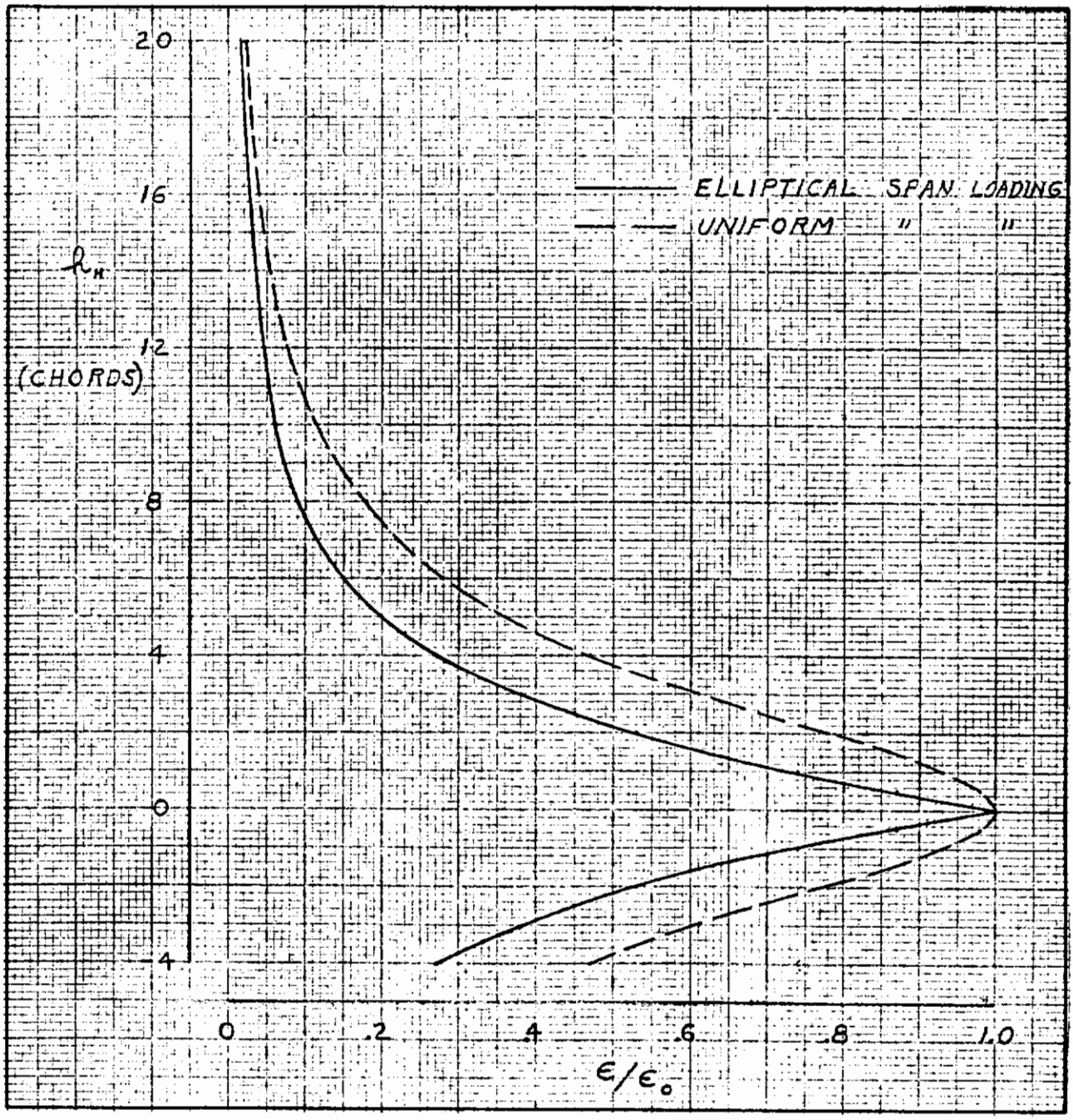

Figure 6.3-59. Theoretical Variation of Downwash with Vertical Distance for Elliptical and Uniform Span Loadings

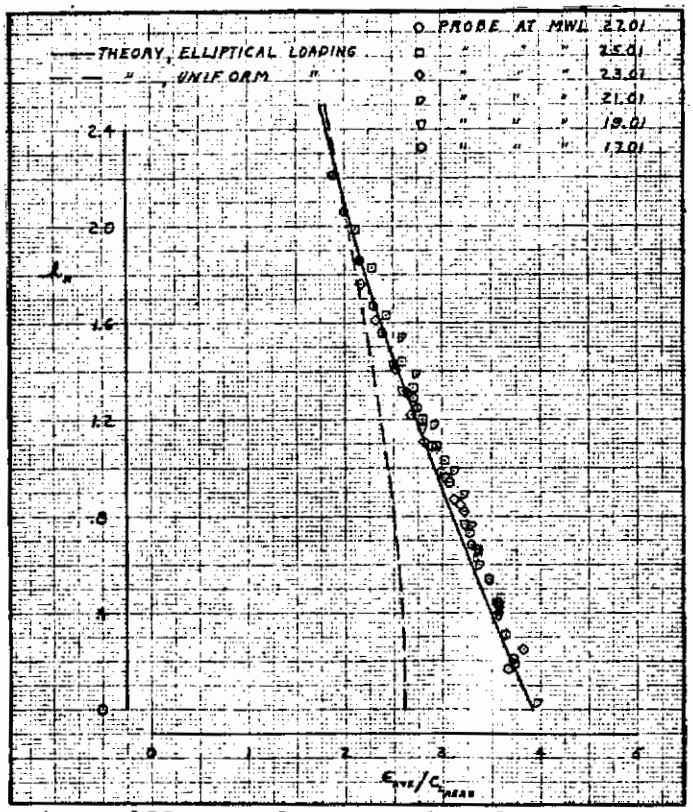

Figure 6.3-60. Comparison of Measured Downwash with Lifting Line Theory, $C_{\mu_J} = 0$

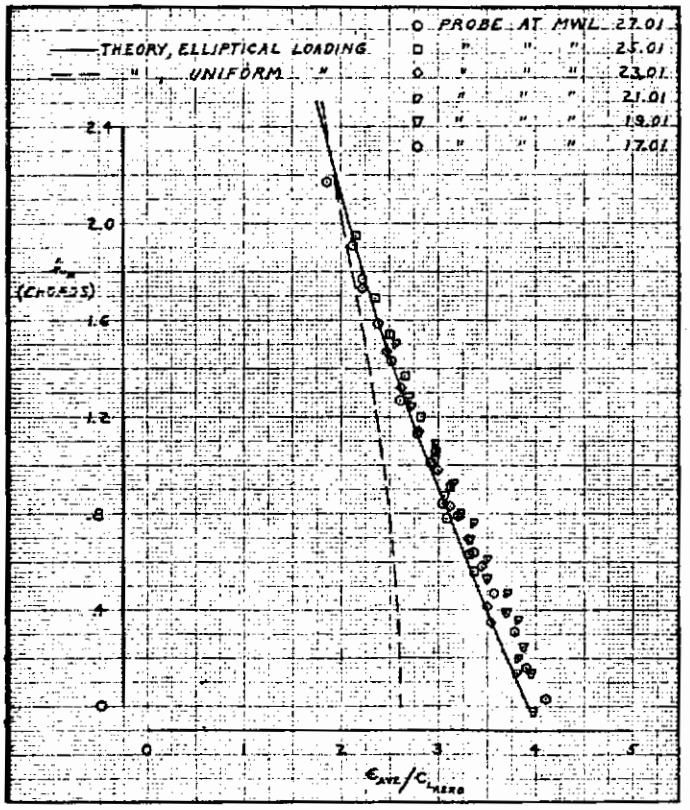

Figure 6.3-61. Comparison of Measured Downwash with Lifting Line Theory, $C_{\mu_J} = 1.0$

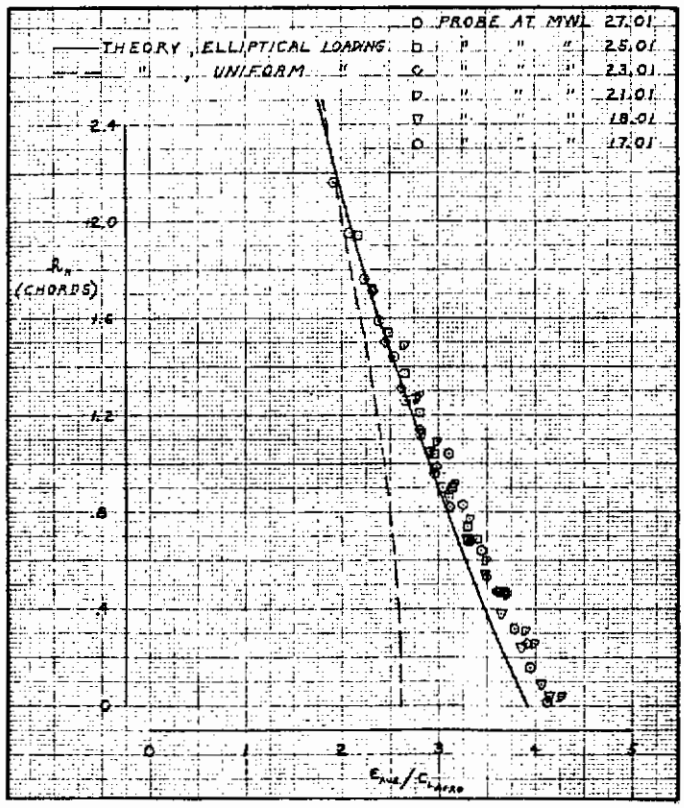

Figure 6.3-62. Comparison of Measured Downwash with Lifting Line Theory, $C_{\mu_J} = 2.0$

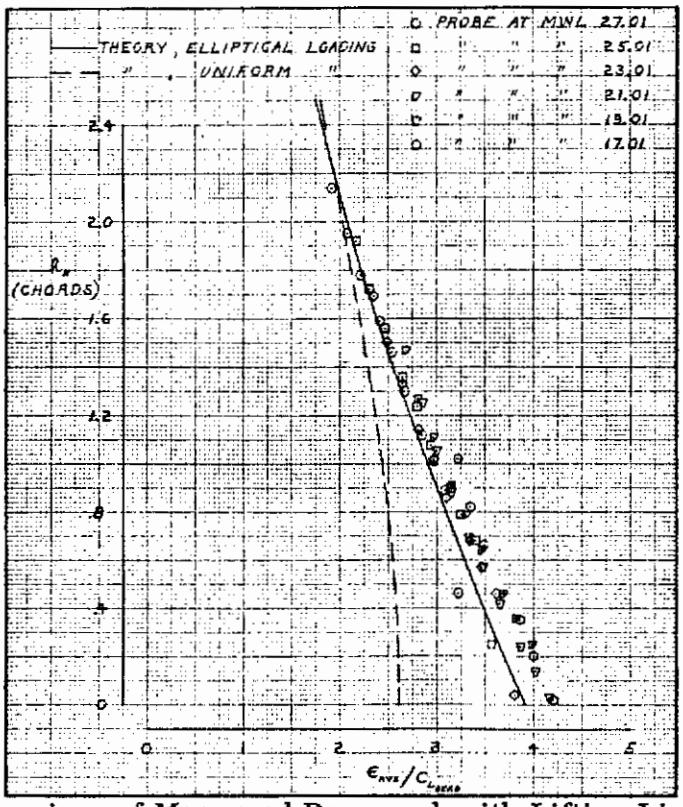

Figure 6.3-63. Comparison of Measured Downwash with Lifting Line Theory, $C_{\mu_J} = 4.0$

SECTION 7

SIDESLIP CHARACTERISTICS

7.1 VERTICAL TAIL CHARACTERISTICS

The vertical tail lift curve was obtained from the isolated empennage tests, GDLST 611, and is presented on Figure 7.1-1. The vertical tail tests were similar to the horizontal tests, in that the effects of Reynolds number was investigated by running yaw sweeps at four different tunnel dynamic pressures. Unlike the horizontal tests, however, Reynolds number effects were not apparent on the vertical tail, since the maximum lift coefficient did not appear to have been exceeded at a 24-degree sideslip angle. The vertical tail lift curve slope was estimated from DATCOM, which gave a value of 0.049 deg^{-1} as compared to 0.053 deg^{-1} measured during the tests. The error was 7.5 percent.

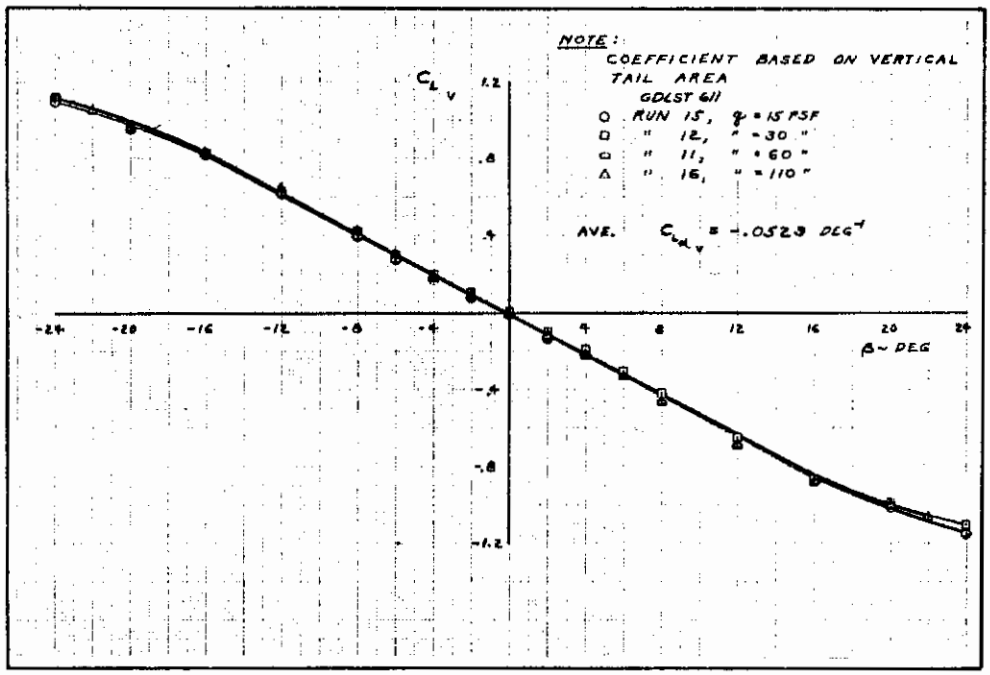

Figure 7.1-1. Vertical Tail Lift Curve

7.2 VERTICAL TAIL FLOW FIELDS AND LATERAL-DIRECTIONAL STABILITY-DERIVATIVES

Most of the lateral-directional data obtained during this test program was obtained with the tail off, with a wake rake installed to measure sidewash and dynamic pressure ratio at the vertical tail. A few check runs were conducted with the tail on.

Flow field characteristics at the vertical tail for the EBF with triple-slotted flaps were determined at three representative angles of attack, as illustrated on Figures 7.2-1 through 7.2-3. These figures show the vertical tail angle of attack, as sensed by the probes, as a function of sideslip angle. The effect of thrust coefficient on sidewash is most pronounced at large sideslip angles and at the higher angles of attack. The vertical tail dynamic pressure ratio was relatively constant with angle of attack and sideslip angle. The sidewash gradient $(1 + \frac{\partial \sigma}{\partial \beta})$ and the average vertical tail dynamic pressure ratio are shown as a function of thrust coefficient in Figure 7.2-4 for the three angles of attack tested.

For the tail-on tests, the Convair Aerospace Digigraphics System was used to determine the increments in C_y, C_n and C_ℓ between the tail-on and tail off configurations for obtaining tail contributions to the lateral-directional stability derivatives C_{y_β}, C_{n_β}, C_{ℓ_β}. The basic working data is shown in Figures 7.2-5 through 7.2-22. A summary plot is presented in Figure 7.2-32, where tail-off C_{y_β}, C_{n_β}, and C_{ℓ_β}, along with the tail contributions, are shown as a function of thrust coefficient. The effect of thrust coefficient is somewhat erratic, but it would appear that the most significant changes occur on tail-off values for C_{y_β} and C_{n_β}. A comparison of the tail contributions to the static lateral-directional stability derivatives obtained from measured test data with that obtained from a build-up of component data is shown in Figure 7.2-24. The comparison is not so precise as that noted in the longitudinal case, but the built-up data is adequate for configuration design studies.

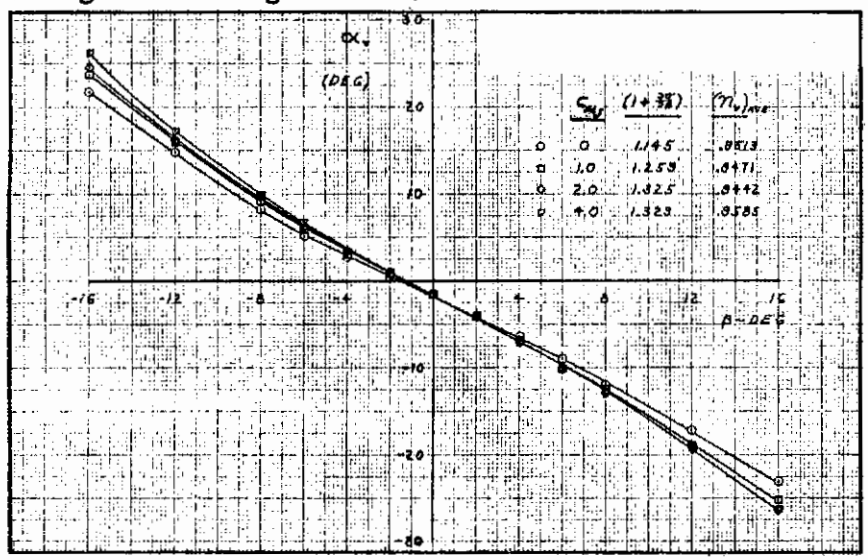

Figure 7.2-1. Effect of Thrust Coefficient on Vertical Tail Flow Field, Triple-Slotted Flap at 60 Degrees, α_G = 0 Degrees

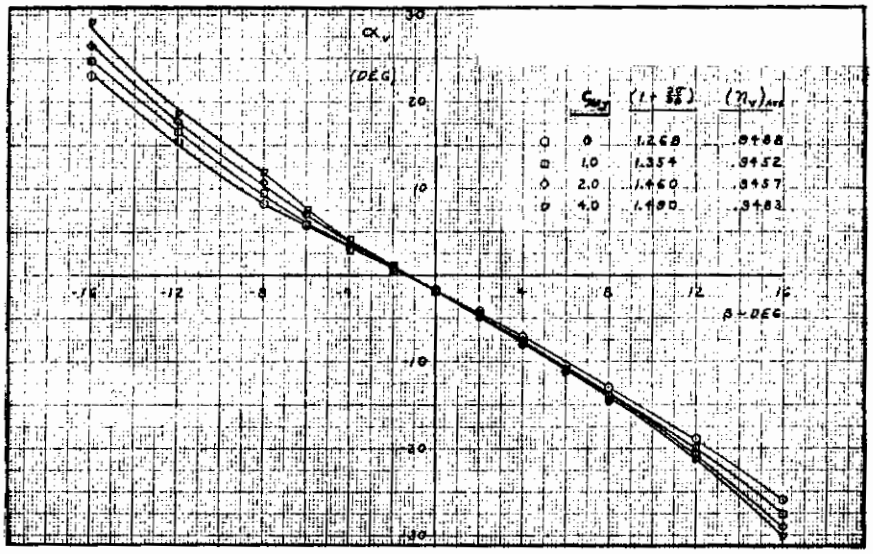

Figure 7.2-2. Effect of Thrust Coefficient on Vertical Tail Flow Field, Triple-Slotted Flat at 60 Degrees, α_G = 10 Degrees

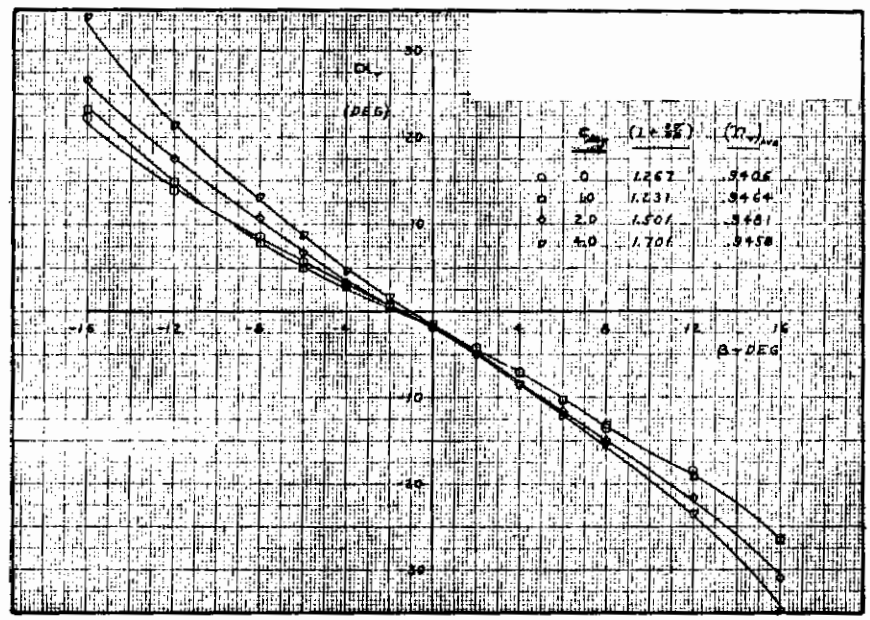

Figure 7.2-3. Effect of Thrust Coefficient on Vertical Tail Flow Field, Triple-Slotted Flap at 60 Degrees, α_G = 17 Degrees

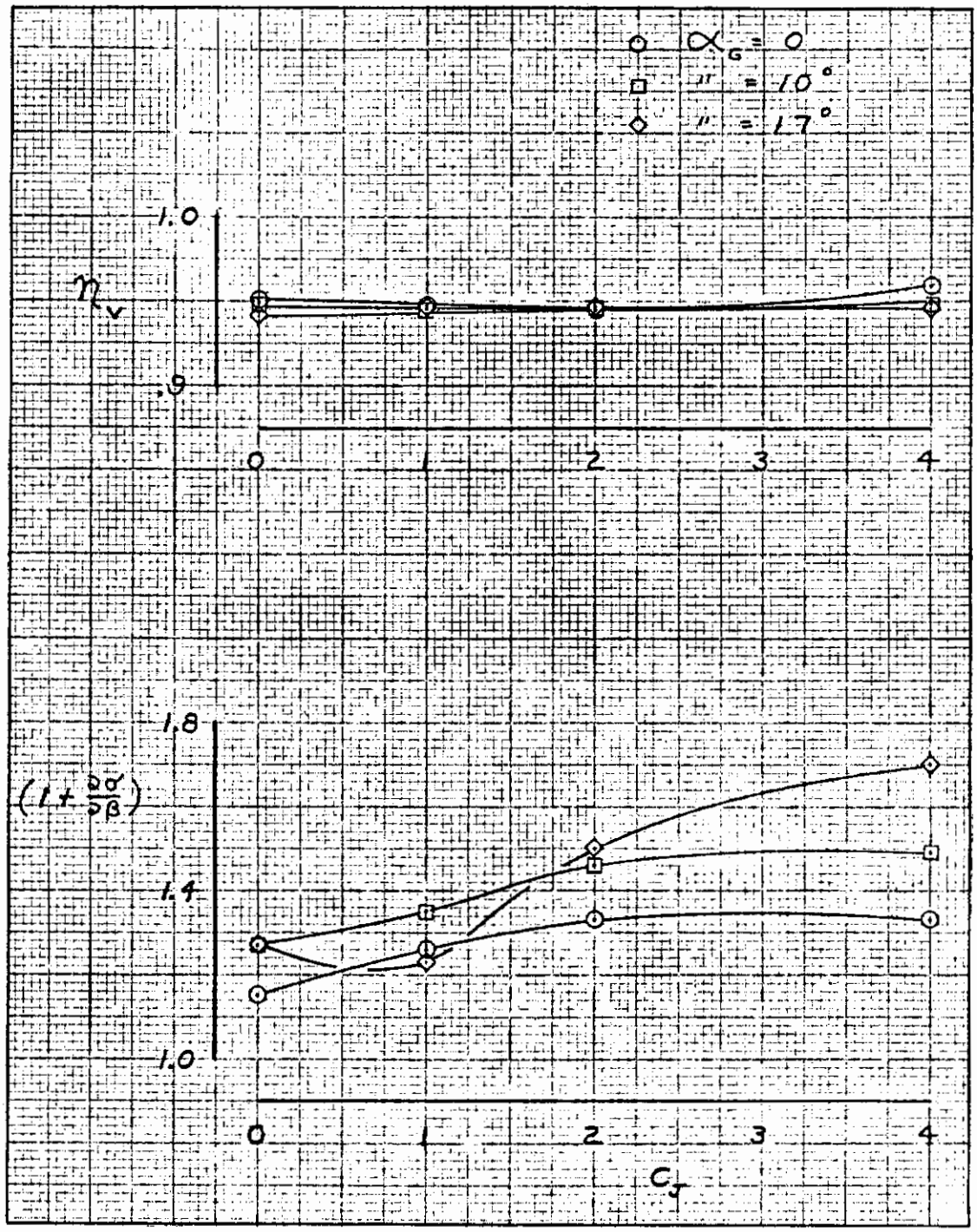

Figure 7.2-4. Effect of Thrust Coefficient and Angle of Attack on Sidewash Gradient and Tail Dynamic Pressure Ratio, Triple-Slotted Flap at 60 Degrees

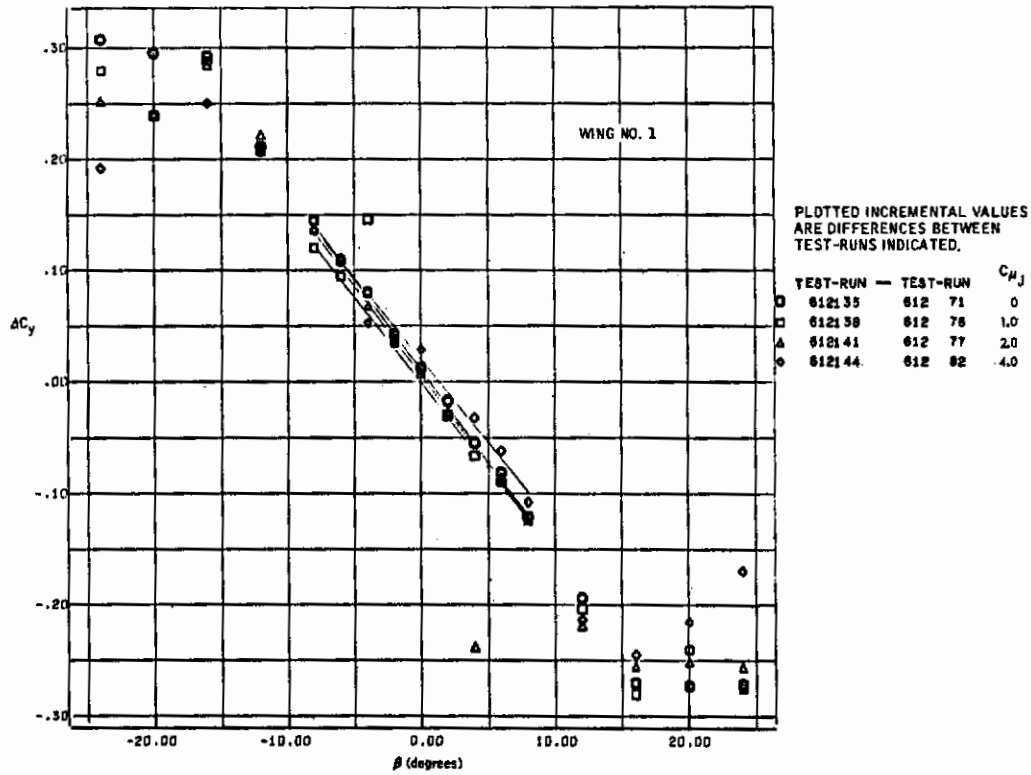

Figure 7.2-5. Vertical Tail Side Force Increments, Triple-Slotted Flap at 60 Degrees, α_G = 0 Degrees

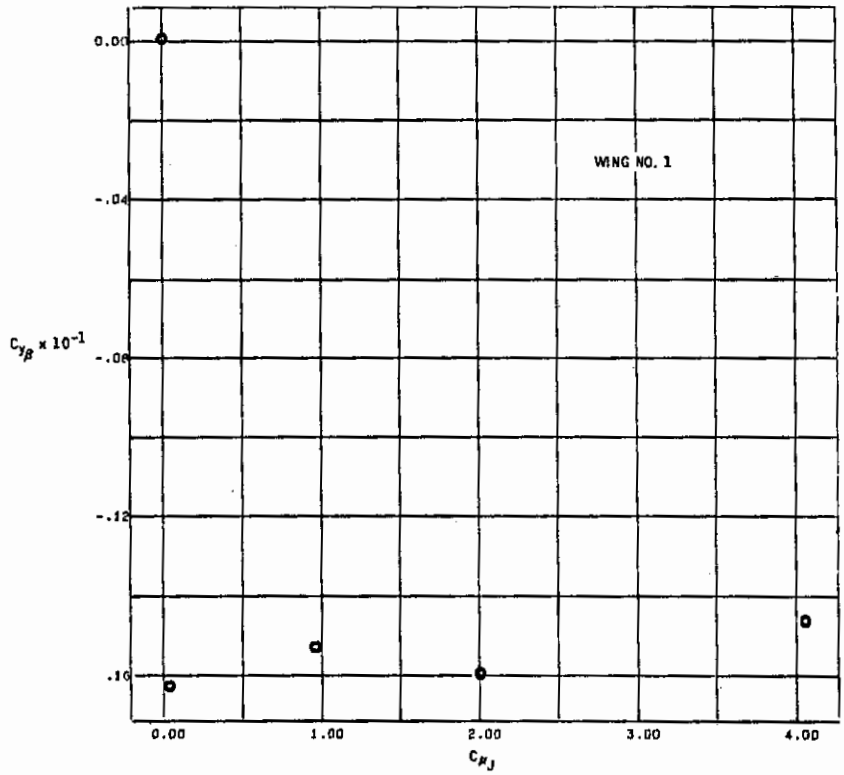

Figure 7.2-6. Effect of Thrust Coefficient on C_{y_β}, Triple-Slotted Flap at 60 Degrees, α_G = 0 Degrees

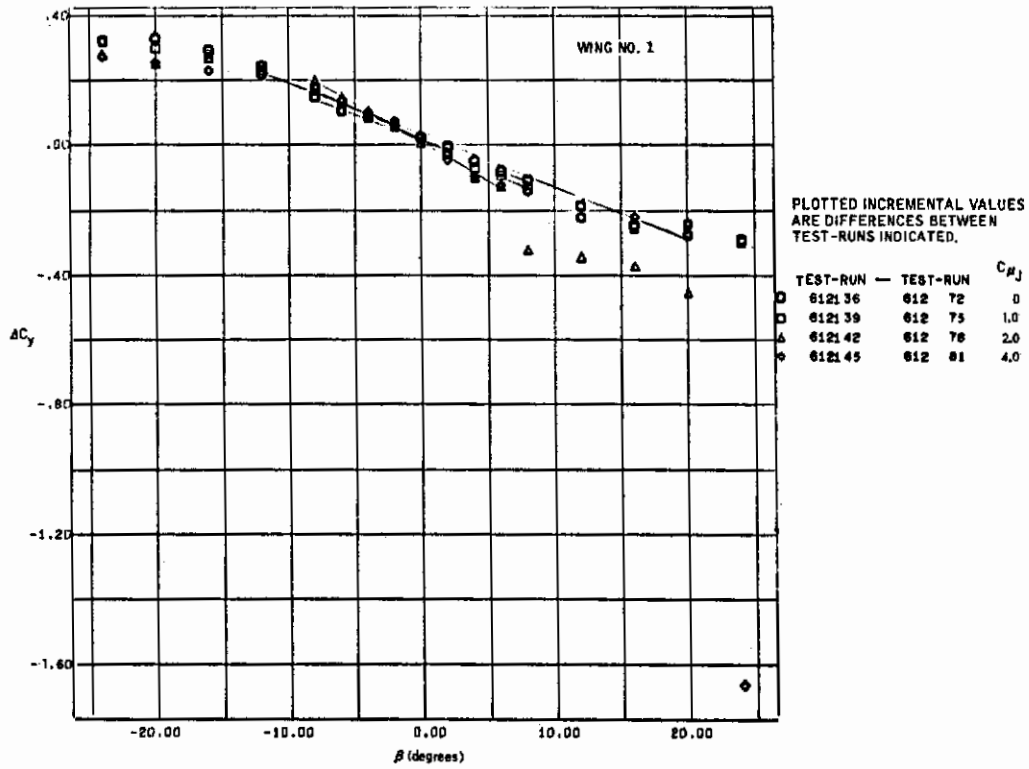

Figure 7.2-7. Vertical Tail Side Force Increments, Triple-Slotted Flap at 60 Degrees, α_G = 10 Degrees

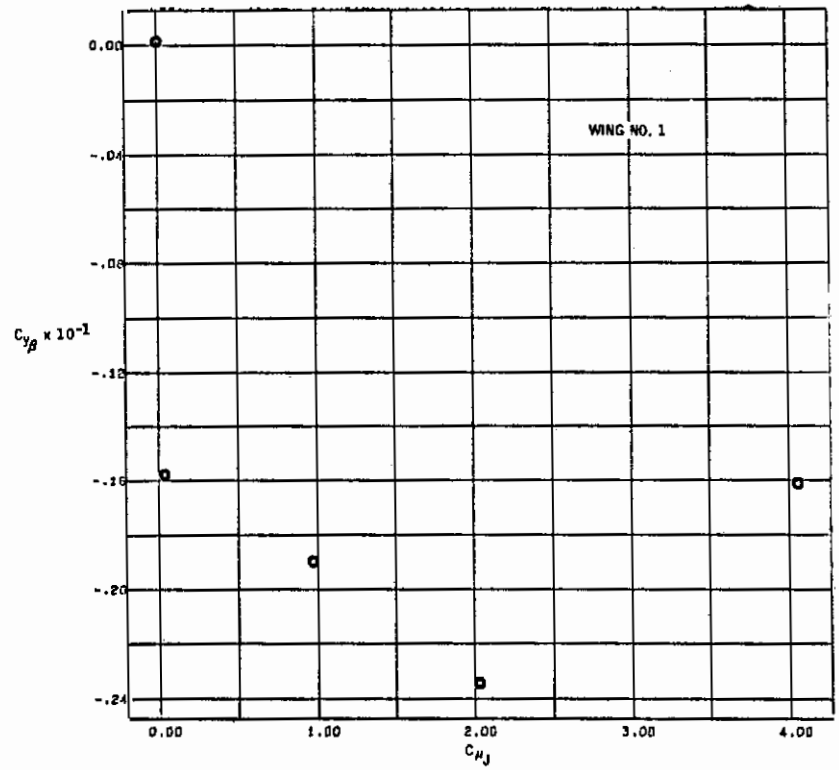

Figure 7.2-8. Effect of Thrust Coefficient on C_{y_β}, Triple-Slotted Flap at 60 Degrees, α_G = 10 Degrees

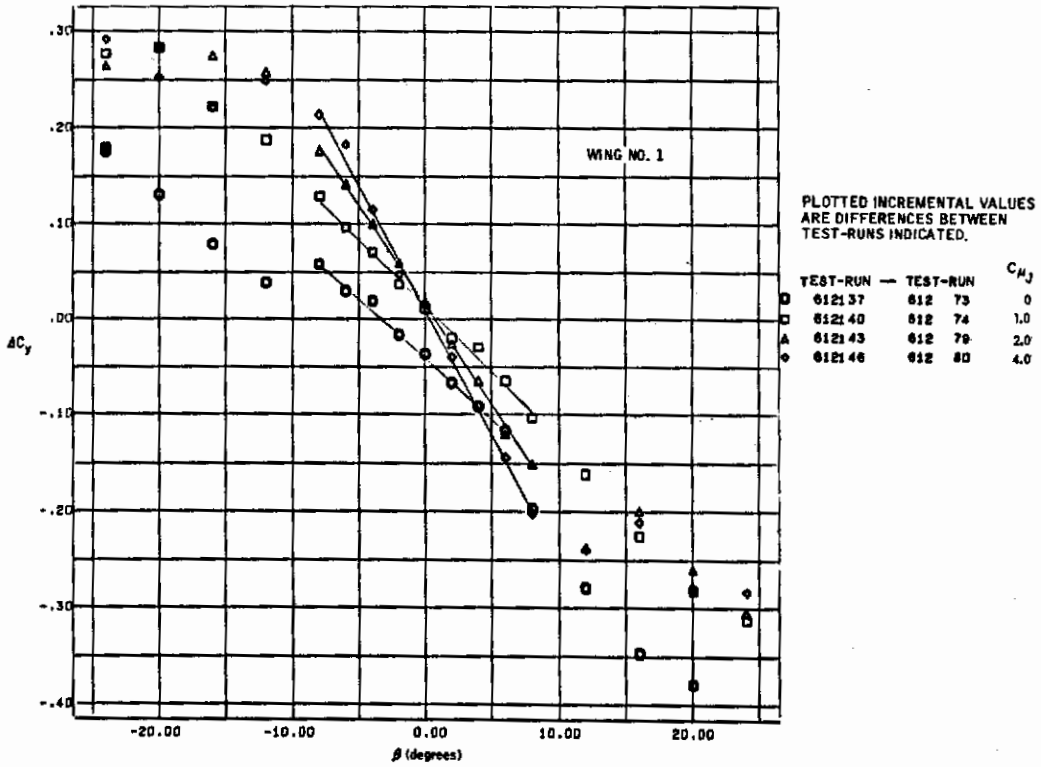

Figure 7.2-9. Vertical Tail Side Force Increments, Triple-Slotted Flap at 60 Degrees, α_G = 17 Degrees

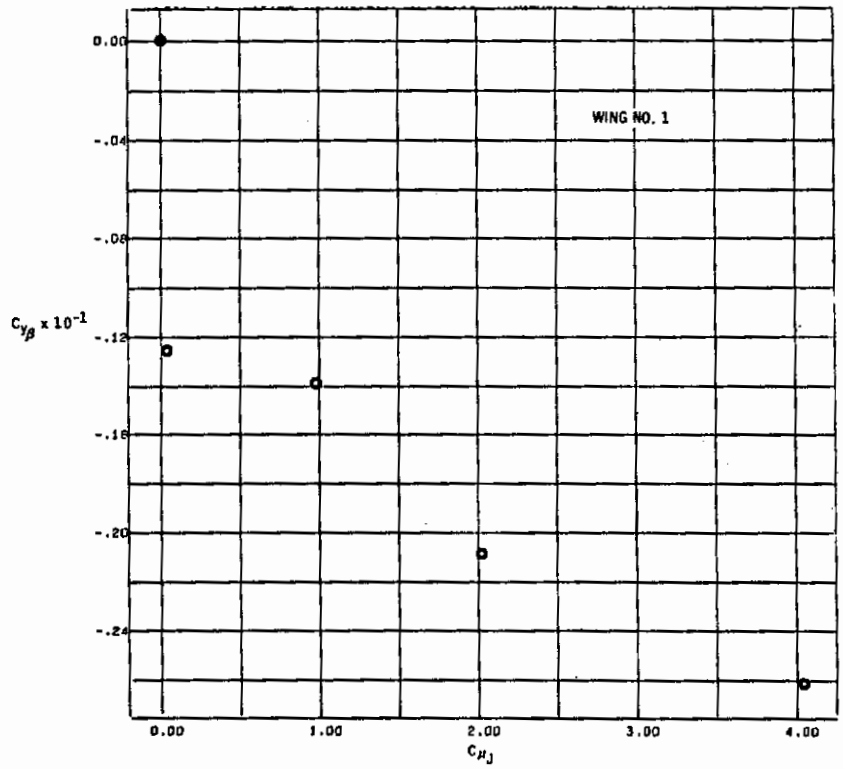

Figure 7.2-10. Effect of Thrust Coefficient on C_{y_β}, Triple-Slotted Flap at 60 Degrees, α_G = 17 Degrees

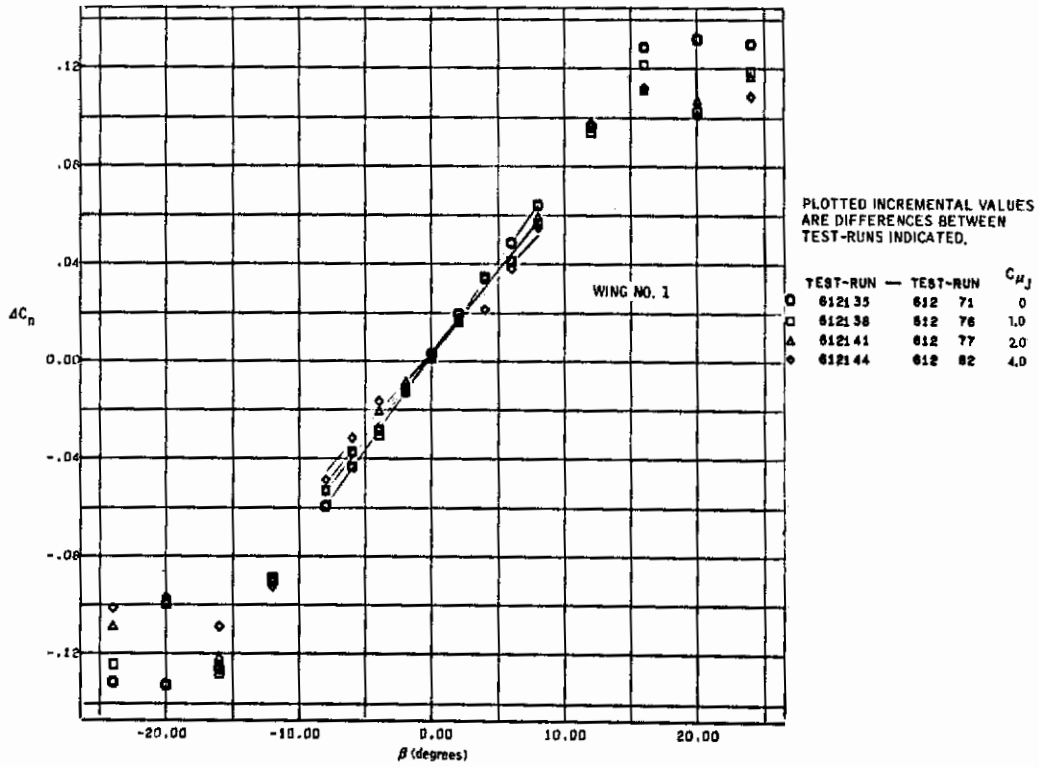

Figure 7.2-11. Vertical Tail Yawing Moment Increments, Triple-Slotted Flap at 60 Degrees, α_G = 0 Degrees

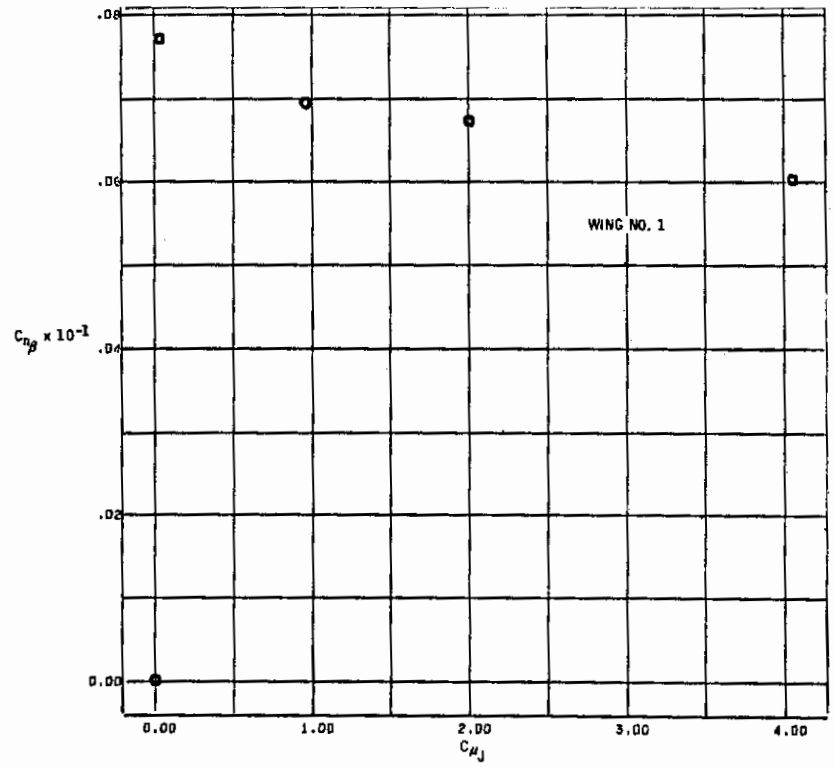

Figure 7.2-12. Effect of Thrust Coefficient on C_{n_β}, Triple-Slotted Flap at 60 Degrees, α_G = 0 Degrees

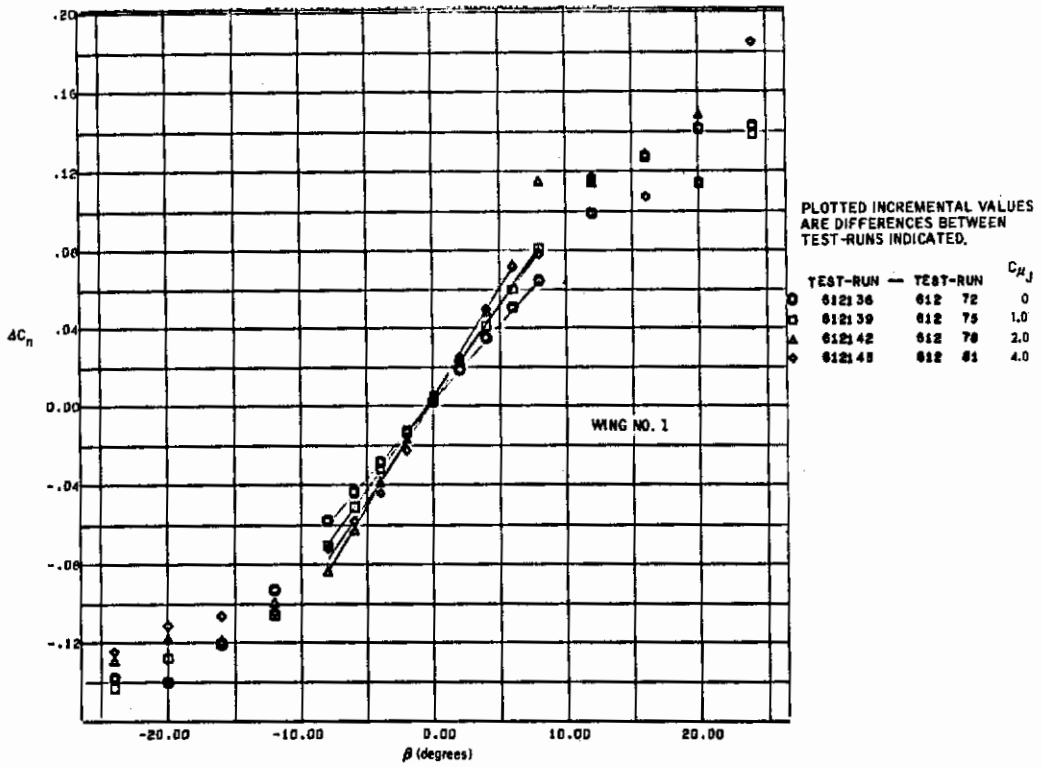

Figure 7.2-13. Vertical Tail Yawing Moment Increments, Triple-Slotted Flap at 60 Degrees, α_G = 10 Degrees

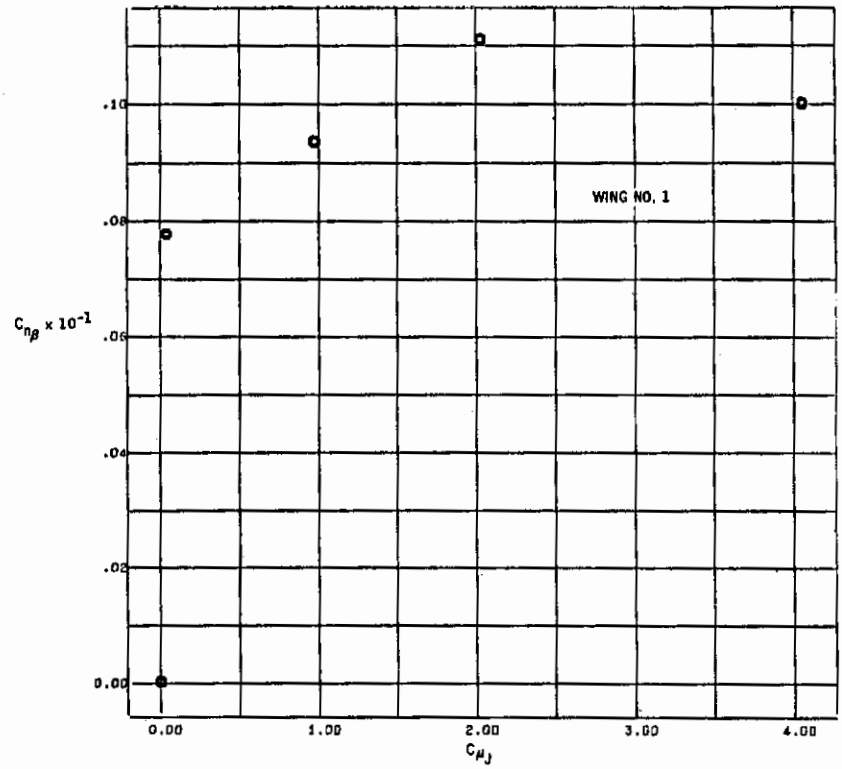

Figure 7.2-14. Effect of Thrust Coefficient on C_{n_β}, Triple-Slotted Flap at 60 Degrees, α_G = 10 Degrees

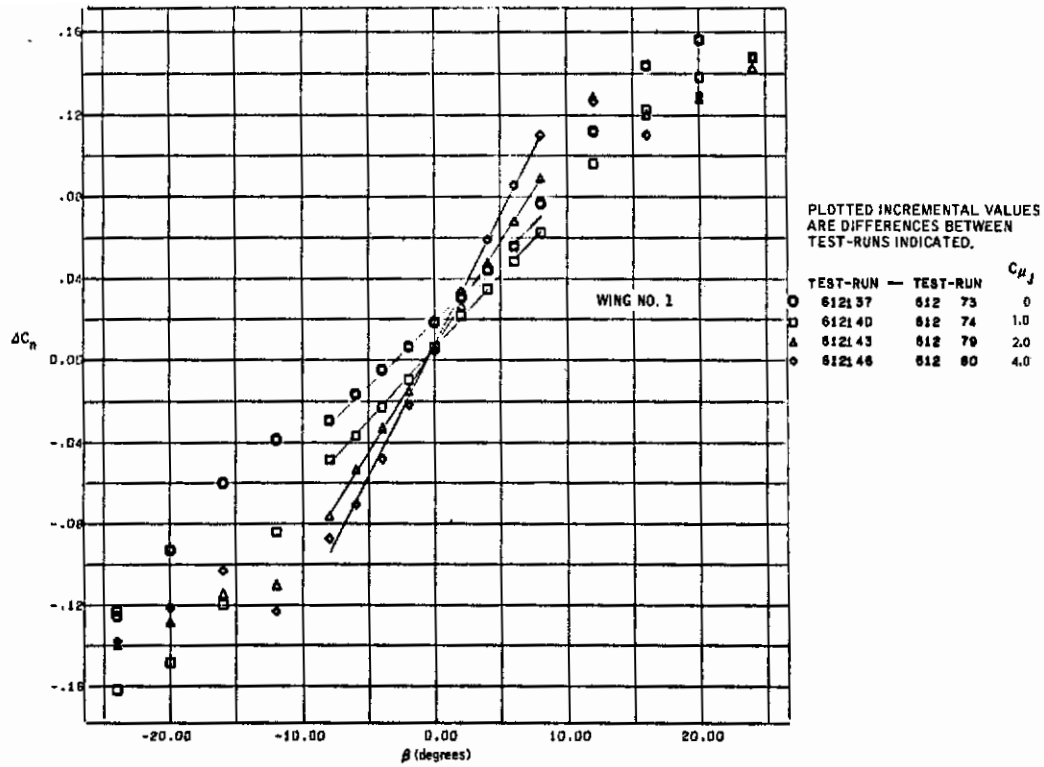

Figure 7.2-15. Vertical Tail Yawing Moment Increments, Triple-Slotted Flap at 60 Degrees, α_G = 17 Degrees

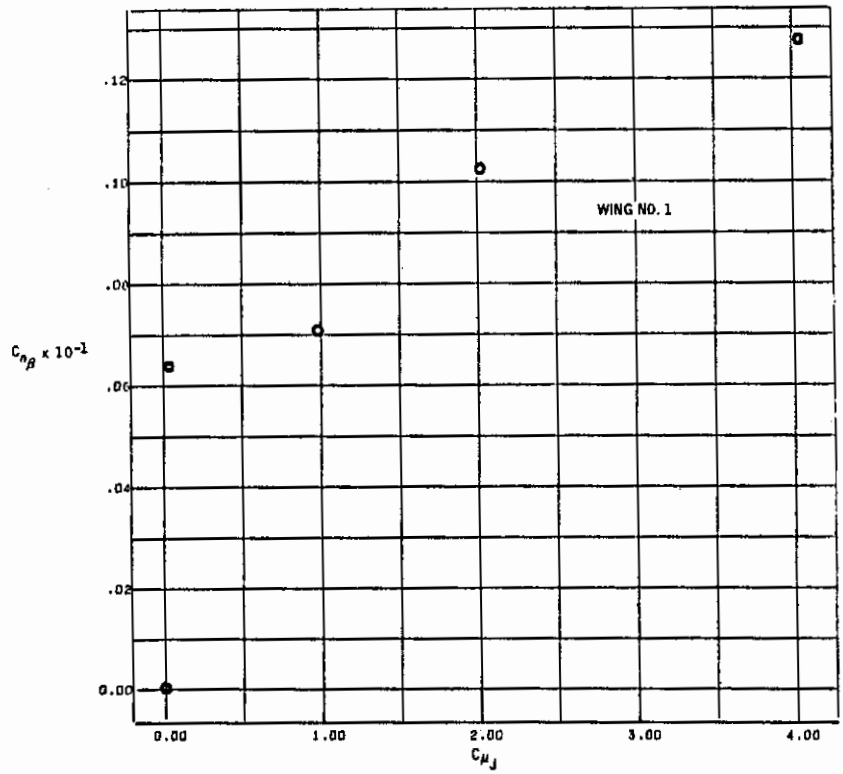

Figure 7.2-16. Effect of Thrust Coefficient on C_{n_β}, Triple-Slotted Flap at 60 Degrees, α_G = 17 Degrees

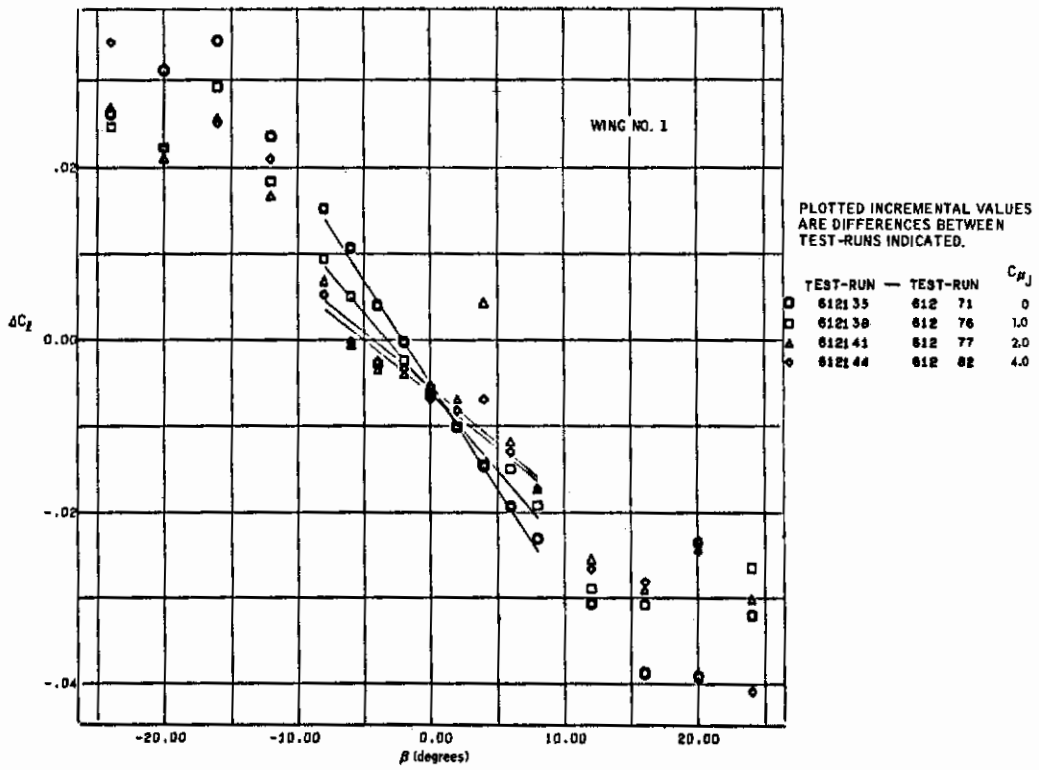

Figure 7.2-17. Vertical Tail Rolling Moment Increments, Triple-Slotted Flap at 60 Degrees, α_G = 0 Degrees

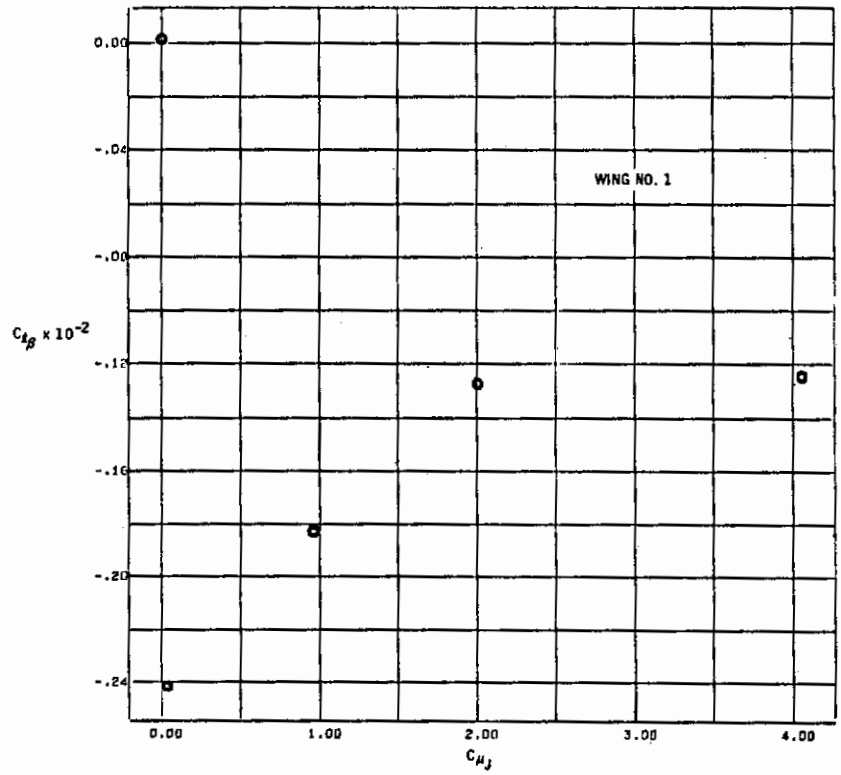

Figure 7.2-18. Effect of Thrust Coefficient on C_{l_β}, Triple-Slotted Flap at 60 Degrees, α_G = 0 Degrees

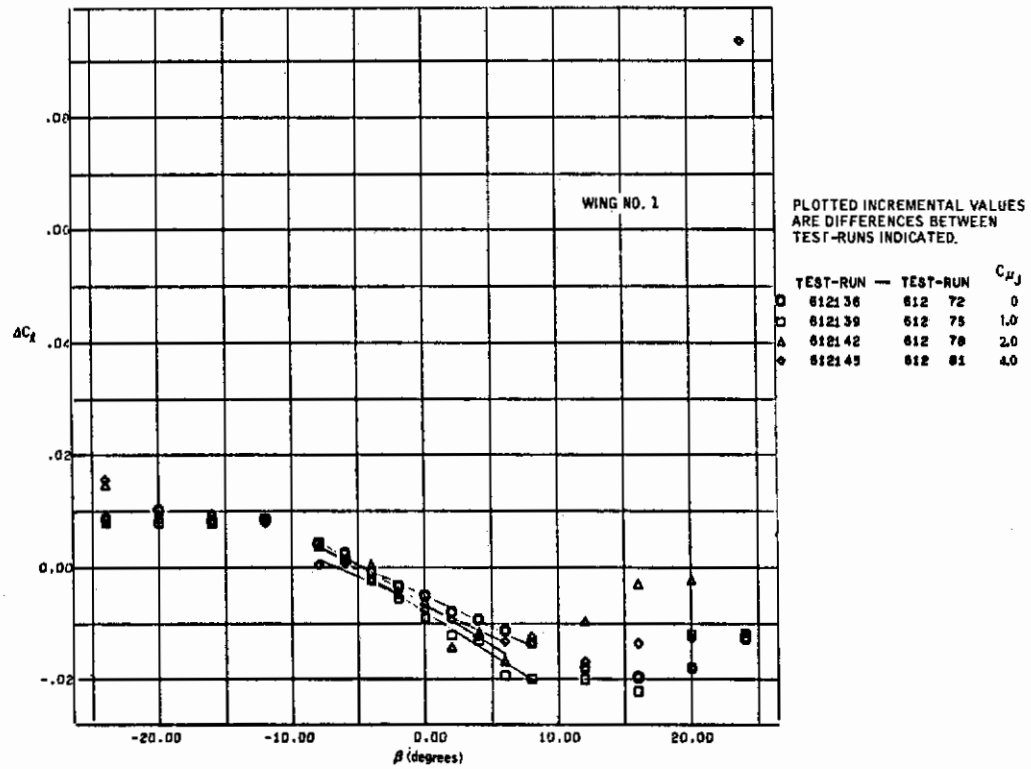

Figure 7.2-19. Vertical Tail Rolling Moment Increments, Triple-Slotted Flaps at 60 Degrees, α_G = 10 Degrees

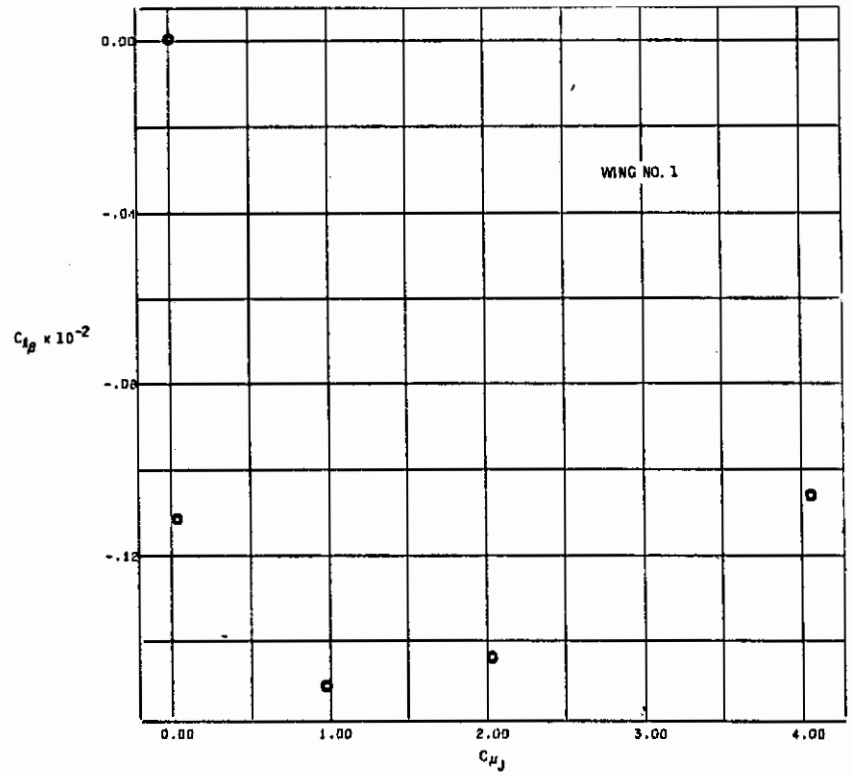

Figure 7.2-20. Effect of Thrust Coefficient on C_{ℓ_β}, Triple-Slotted Flap at 60 Degrees, α_G = 10 Degrees

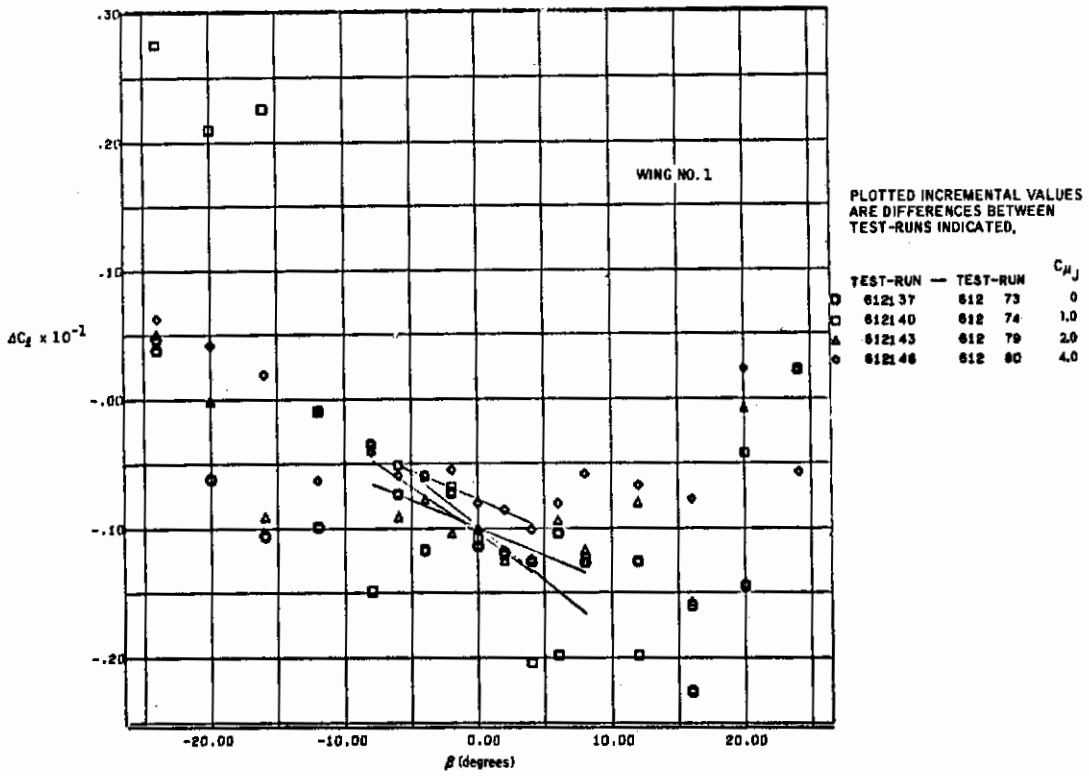

Figure 7.2-21. Vertical Tail Rolling Moment Increments, Triple-Slotted Flap at 60 Degrees, α_G = 17 Degrees

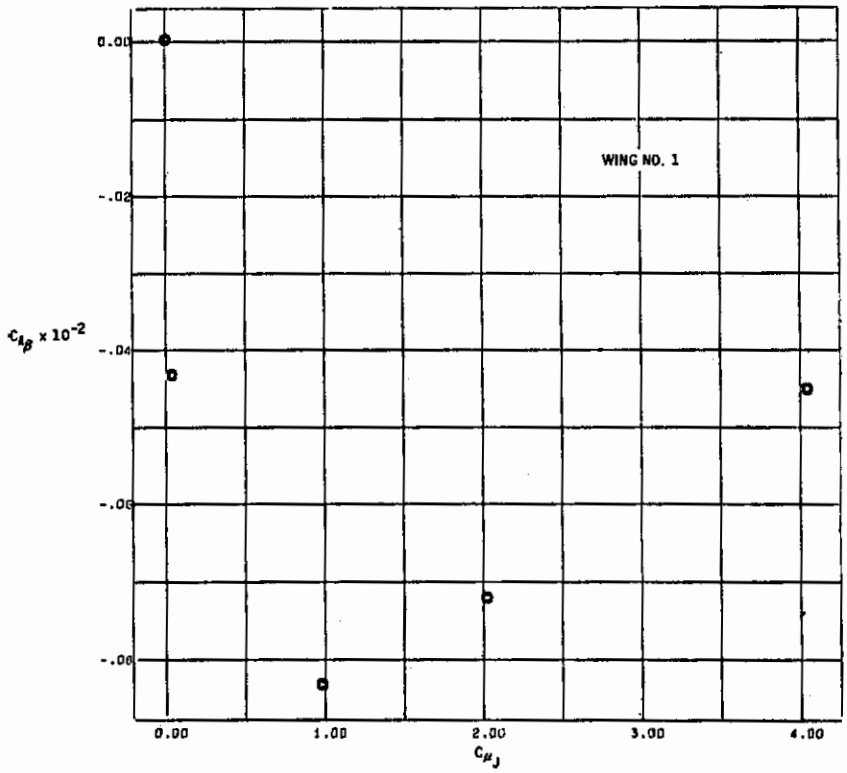

Figure 7.2-22. Effect of Thrust Coefficient on C_{ℓ_β}, Triple-Slotted Flap at 60 Degrees, α_G = 17 Degrees

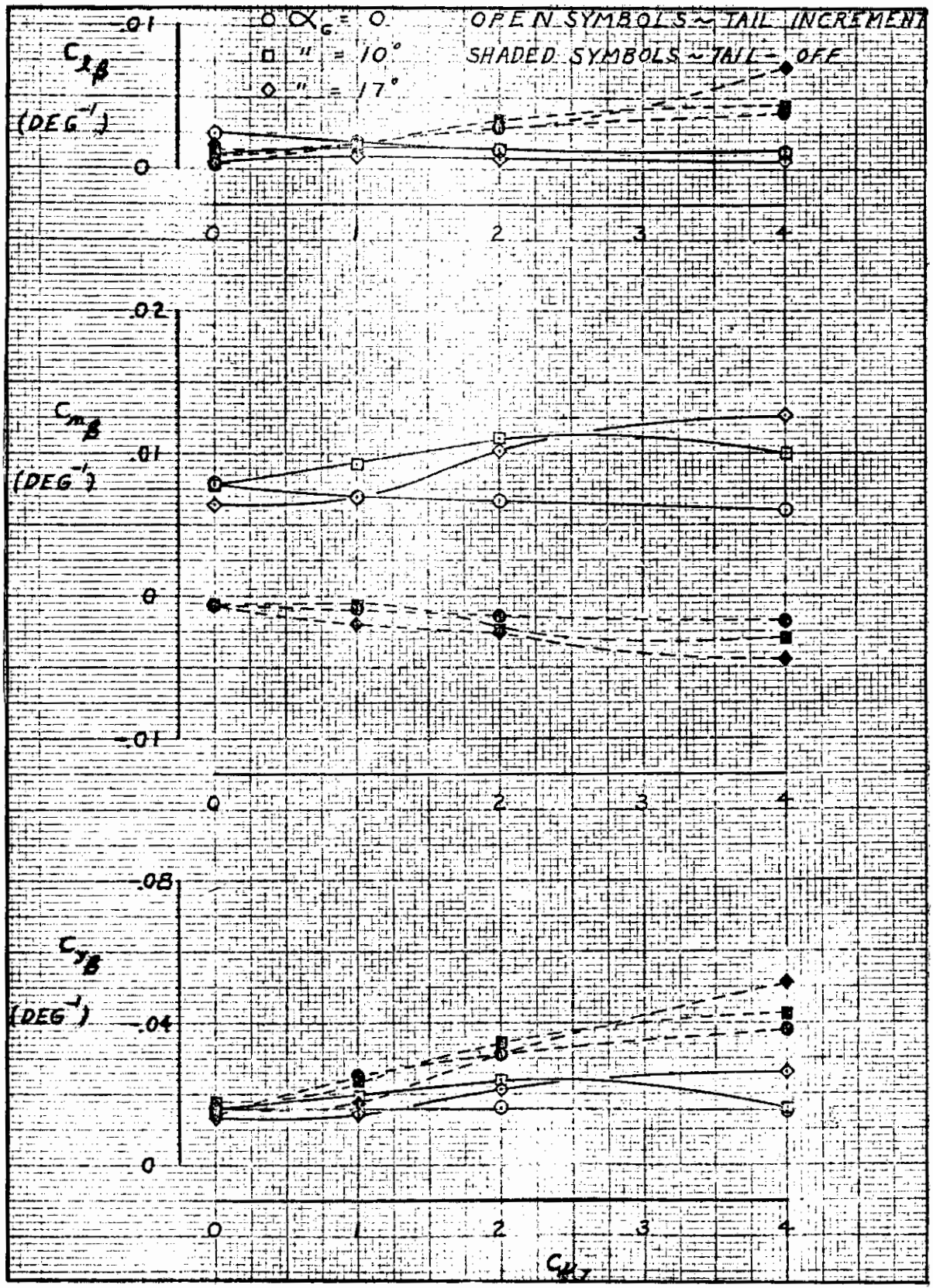

Figure 7.2-23. Effect of Thrust Coefficient and Angle of Attack on Static Lateral-Directional Stability Derivatives

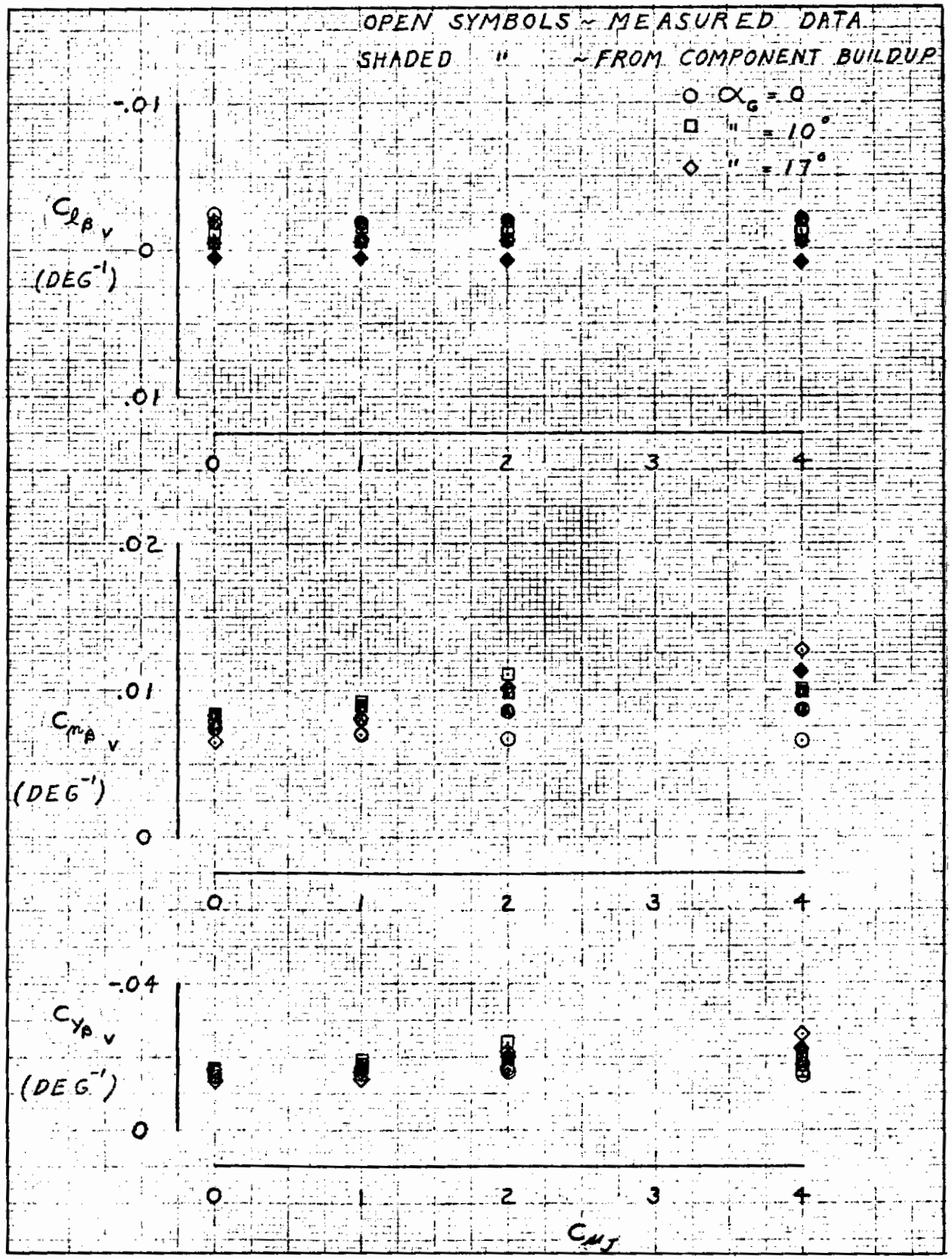

Figure 7.2-24. Comparison of Measured and Built-Up Tail Contributions to the Static Lateral-Directional Stability Derivatives

SECTION 8

CONTROL DEVICES

8.1 WING SURFACE CONTROLS

The wing surface control devices that were tested during this program were conventional ailerons (with and without blowing) and flap-type spoilers. The ailerons covered 18.4 percent of the wing span, with a chord that was 25 percent of the wing chord. A deflection angle of 50 degrees per side was available. The ailerons were tested only on the wing that had a 25-degree sweep angle and an 8.0 aspect ratio, with the triple-slotted, partial-span flaps. The spoilers were 18 percent of the wing chord and either 100 or 81.6 percent of the span, with a maximum deflection of 60 degrees.

Lateral control effectiveness data for these devices is given in Figures 8.1-1 through 8.1-48. These figures were generated with the Convair Digigraphics System, and show the incremental rolling and yawing moments due to deflection of the lateral control as a function of angle of attack.

The ailerons were tested with the EBF powered-lift concept to determine whether aileron effectiveness would be influenced by engine thrust. Results of these tests are shown in Figures 8.1-1 and 8.1-2, where the unblown ailerons were deflected 10 degrees while the engine thrust coefficient was varied. The EBF powered-lift system was found to have a significant influence on aileron effectiveness. At a thrust coefficient of 4.0, the rolling moment produced by the ailerons is only about half of that obtained with power off. Large favorable yawing moments are also indicated as thrust coefficient is increased.

The effect of aileron blowing is illustrated in Figures 8.1-3 through 8.1-8. The blowing rates were chosen to be typical of those used for control surface boundary layer control (BLC), and the momentum coefficients are referenced to that portion of the wing area spanned by an aileron. The most significant point is that rolling moment effectiveness did not increase when aileron deflection was increased from 30 to 60 degrees at a blowing momentum coefficient of 0.15.

Spoiler effectiveness data was obtained for each of the three powered-lift concepts under consideration. Results for the IBF are shown in Figures 8.1-9 through 8.1-16, where spoiler deflections of 20 and 60 degrees were tested for the plain flap at 60 degrees of deflection and the single-slotted flap at 30 degrees of deflection.

One of the major objectives of these tests was to determine if flap blowing would cause flow reattachment behind the spoilers, thereby degrading their effectiveness.

Figure 8.1-9, in which the spoiler is deflected 20 degrees, shows that maximum rolling moment effectiveness is obtained at a momentum coefficient of 0.2 and that spoiler effectiveness is decreased as the momentum coefficient increased beyond that value. However, the effectiveness does not become less than the unblown case at the highest momentum coefficient tested.

When the spoiler is deflected 60 degrees (Figure 8.1-11), spoiler effectiveness increases continuously with momentum coefficient. The same, but accentuated, trends are observed for the single-slotted flap. In Figure 8.1-13, where the spoiler deflection is 20 degrees, maximum effectiveness is again attained at a momentum coefficient of 0.2, but the highest momentum coefficients produced rolling moments that are less than the unblown values. For 60 degrees of spoiler deflection (Figure 8.1-15), approximately the same average rolling moment effectiveness is produced at all momentum coefficients.

Spoiler effectiveness for the EBF is given in Figures 8.1-17 through 8.1-36. Here, too, the objective is to determine if spoiler effectiveness is degraded by flow reattachment. The effects of some configuration variables were also investigated. The following information was obtained for the EBF:

Figures 8.1-17 through 8.1-20:	Baseline configuration
Figures 8.1-21 through 8.1-24:	Effect of moving engines inboard
Figures 8.1-25 through 8.1-28:	Effect of adding engine thrust deflectors, δ_T = -9 degrees
Figures 8.1-29 through 8.1-32:	Effect of changing wing sweep from 12.5 to 25 degrees
Figures 8.1-33 through 8.1-36:	Effect of adding engine thrust deflectors, δ_T = -12 degrees

Examination of this data showed no major changes in lateral control effectiveness resulting from the various configuration changes, although spoiler effectiveness was slightly better for the wing with 12.5 degrees of sweep. The effect of thrust coefficient had generally similar trends to those observed for the IBF, but were accentuated with the EBF concept. For all the EBF configurations tested, rolling moment effectiveness at 20 degrees of spoiler deflection became less than the power-off value at thrust coefficients of 2.0 and 4.0.

Spoiler effectiveness for theMF/VT powered-lift concept is presented in Figures 8.1-37 through 8.1-48, where the thrust deflection angles are 30, 60 and 90 degrees and the high-lift system is the triple-slotted flap at 60 degrees of deflection. For this powered-lift concept, the primary objective of the tests was to determine whether thrust interference terms are present in the spoiler effectiveness data. As expected, the data shows that spoiler effectiveness with the MF/VT concept approached that of the EBF

at the smaller thrust deflection angles, and that power effects became less pronounced as thrust deflection angle increased. The primary effect of thrust at high deflection angles was to prevent fall-off of spoiler effectiveness at high angles of attack.

In summary, the results of these tests indicate that the most desirable lateral control arrangement for use on these powered-lift concepts should be a spoiler-aileron combination. The spoilers are capable of producing large rolling moments at high deflection angles (with further improvements as thrust or flap momentum coefficient increases) but suffer from lack of effectiveness at small deflections. Ailerons, on the other hand, will necessarily be of small span, are adversely affected by the EBF, and are not capable of supplying all of the lateral control capability required, even with blowing. On the positive side, ailerons show no loss of effectiveness near neutral deflection. Consequently, with a properly geared spoiler-aileron combination, the ailerons will provide the lateral control in situations where small, precise bank-angle corrections are required and the spoilers will provide the gross control power required for rapid bank-angle changes and for arresting engine-out rolling moments.

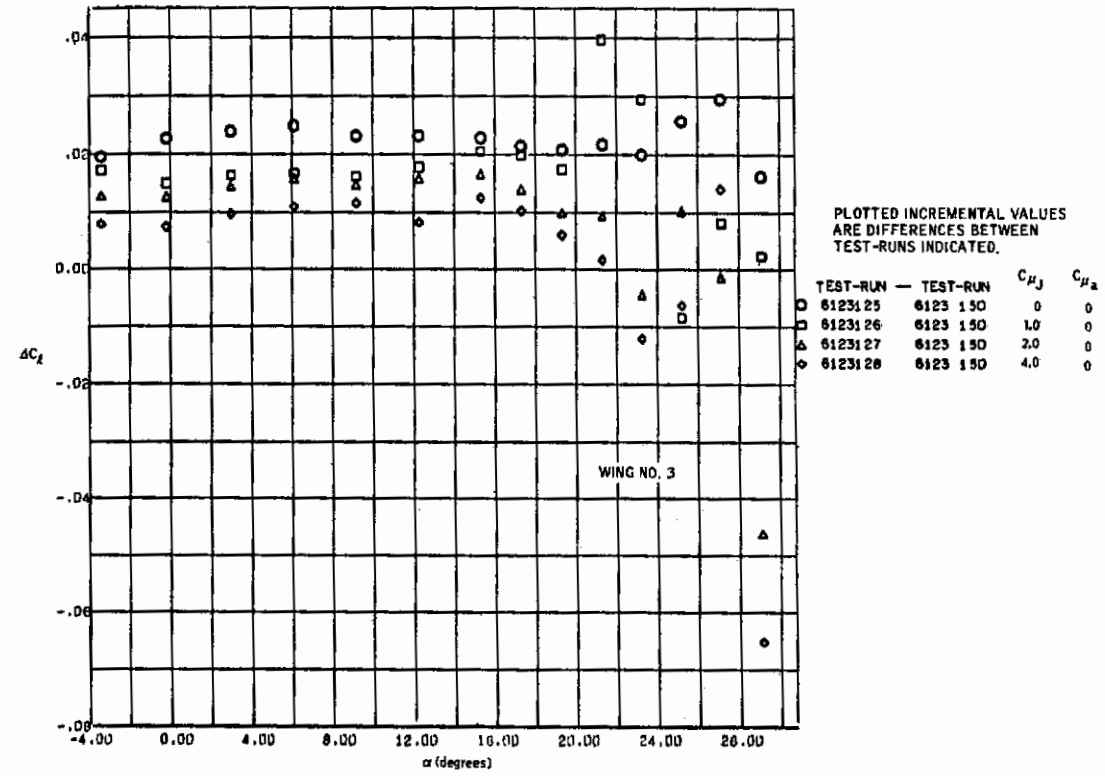

Figure 8.1-1. Effect of Thrust Coefficient on Aileron Effectiveness, Triple-Slotted Flap at 60 Degrees, Rolling Moments, δ_a = ±10 Degrees

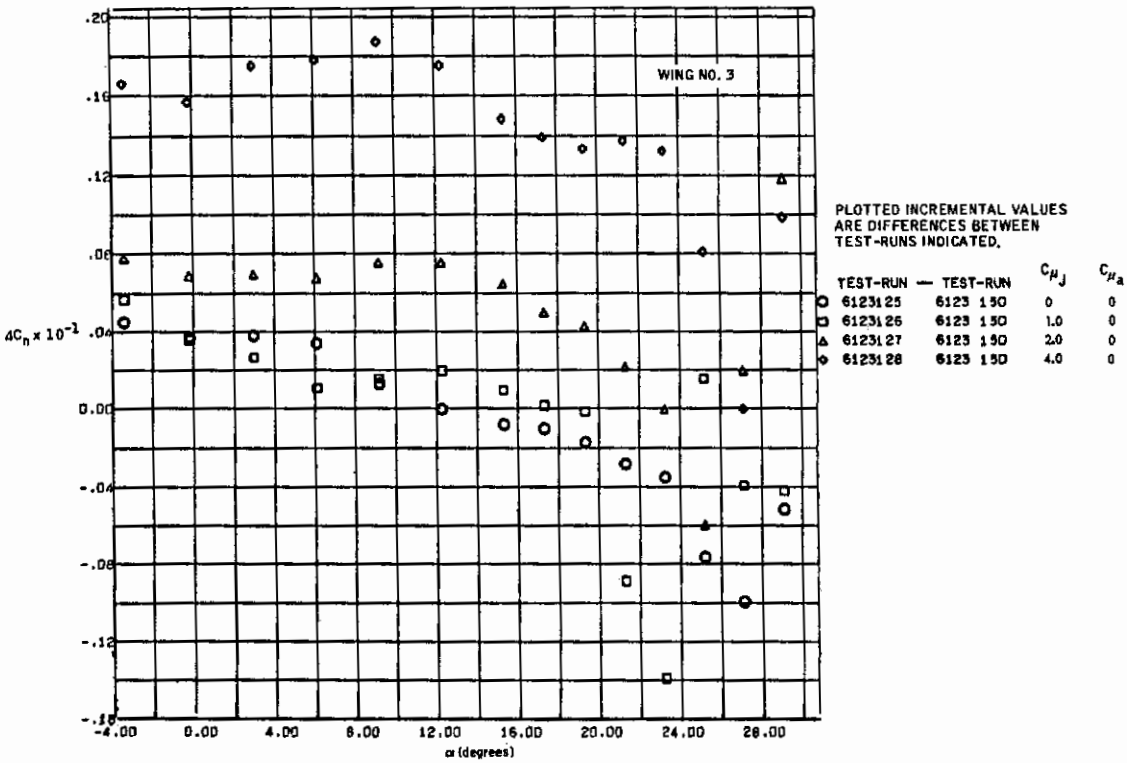

Figure 8.1-2. Effect of Thrust Coefficient on Aileron Effectiveness, Triple-Slotted Flap at 60 Degrees, Yawing Moments, δ_a = ±10 Degrees

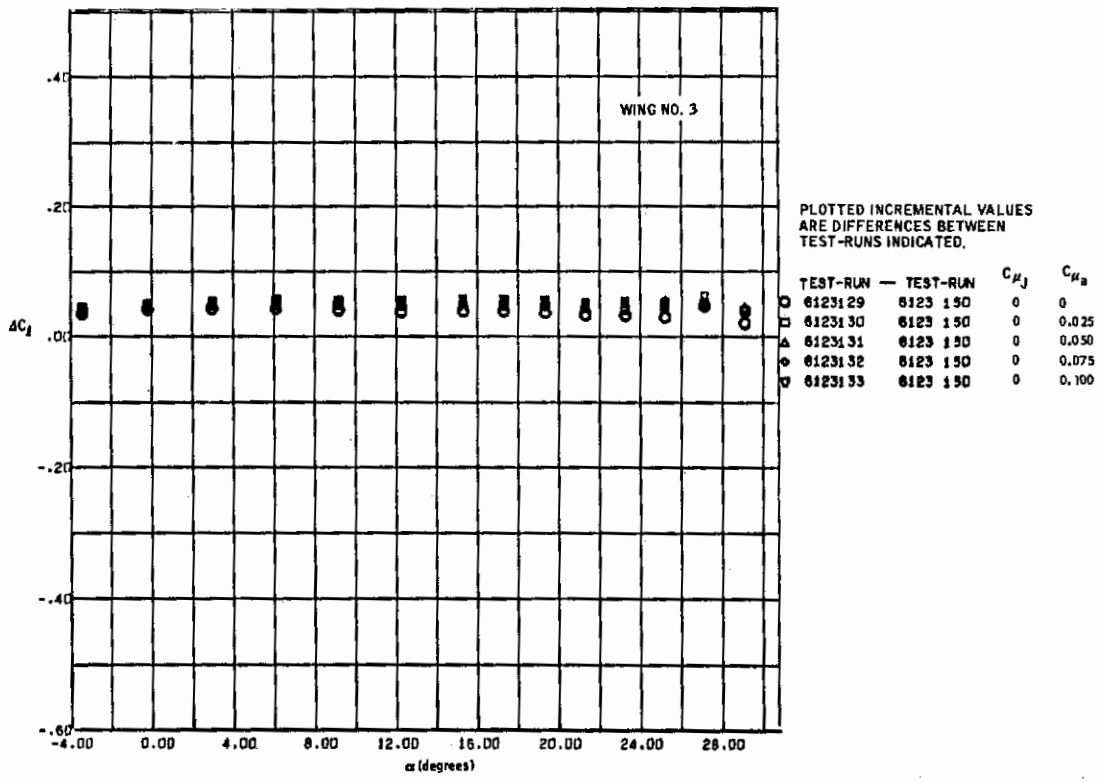

Figure 8.1-3. Effect on BLC Blowing on Aileron Effectiveness, Triple-Slotted Flap at 60 Degrees, Rolling Moments, $\delta_a = \pm 20$ Degrees

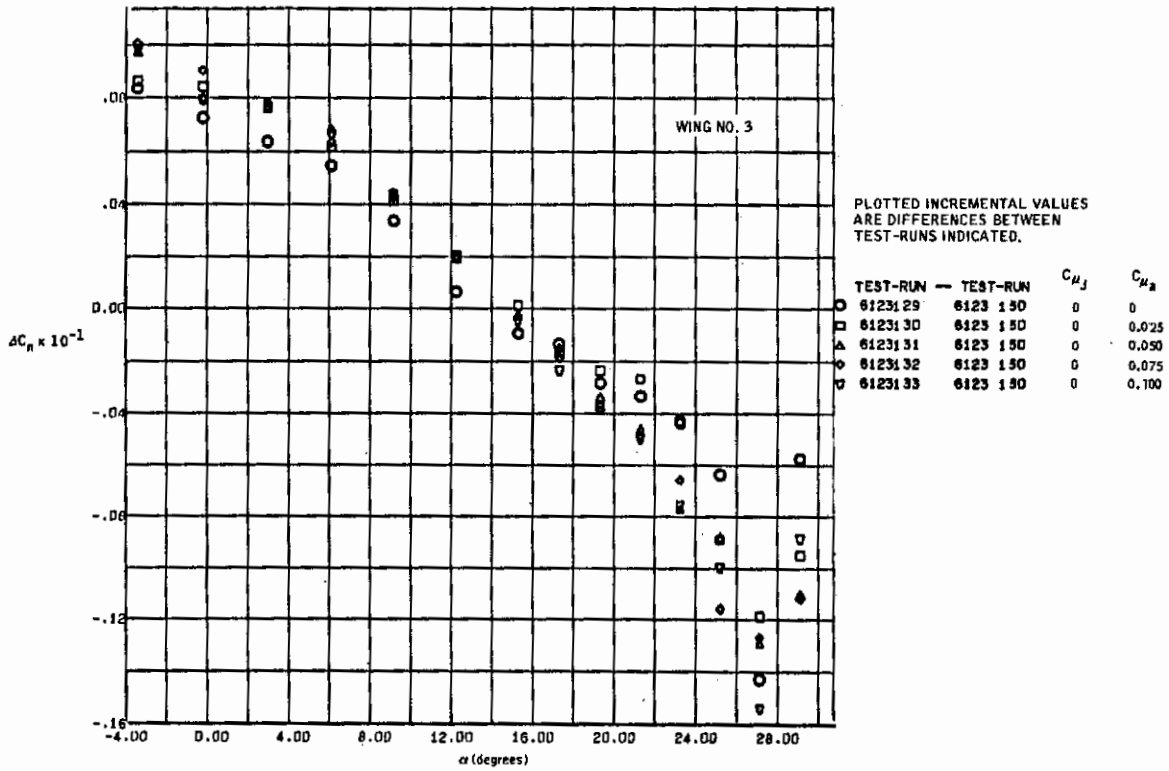

Figure 8.1-4. Effect on BLC Blowing on Aileron Effectiveness, Triple-Slotted Flap at 60 Degrees, Yawing Moments, $\delta_a = \pm 20$ Degrees

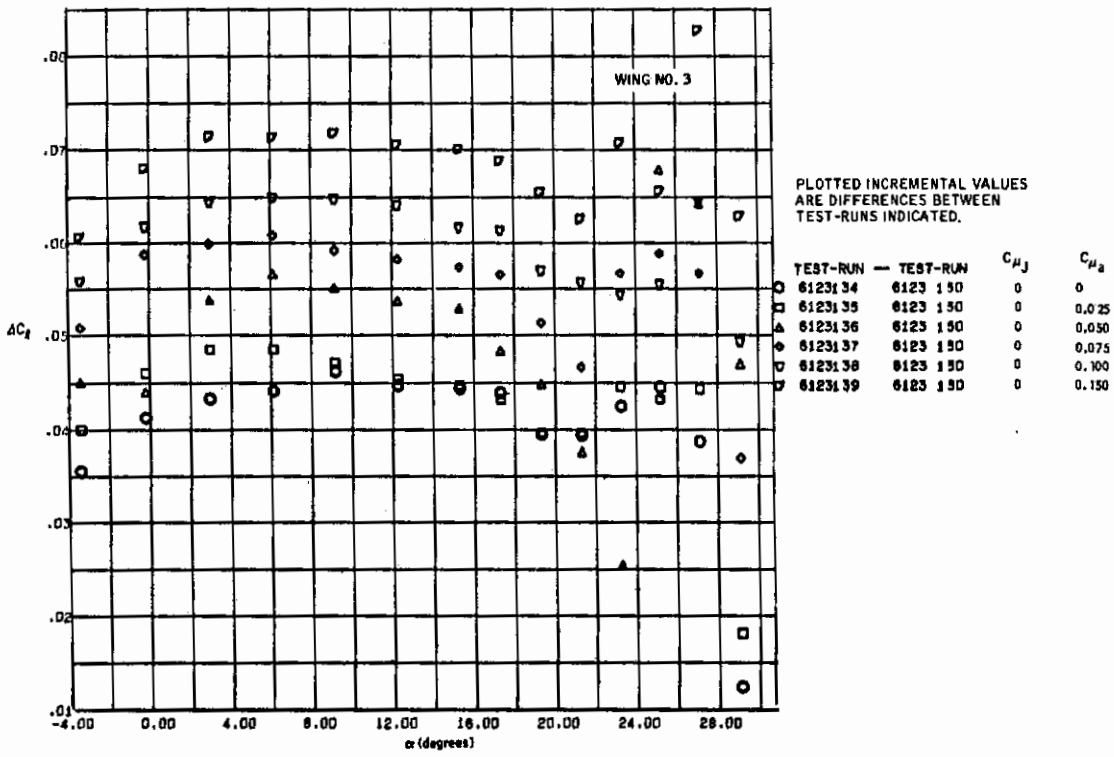

Figure 8.1-5. Effect of BLC Blowing on Aileron Effectiveness, Triple-Slotted Flap at 60 Degrees, Rolling Moments, $\delta_a = \pm 30$ Degrees

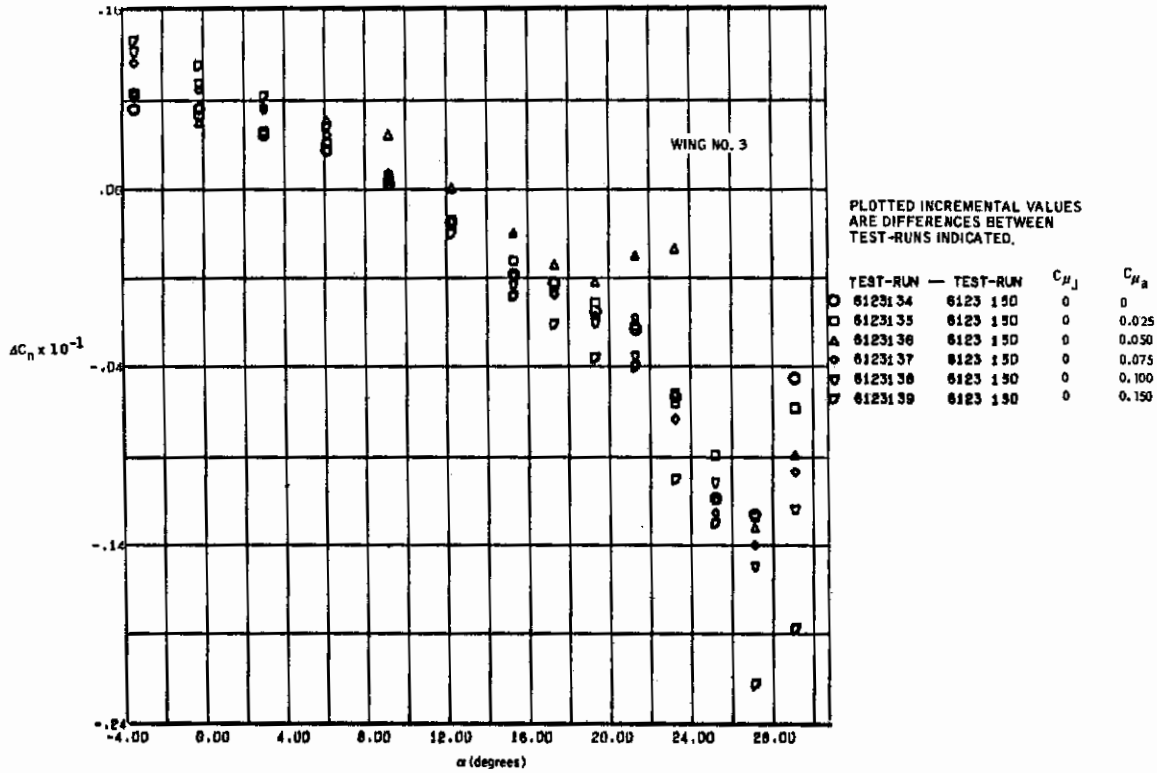

Figure 8.1-6. Effect of BLC Blowing on Aileron Effectiveness, Triple-Slotted Flap at 60 Degrees, Yawing Moments, $\delta_a = \pm 30$ Degrees

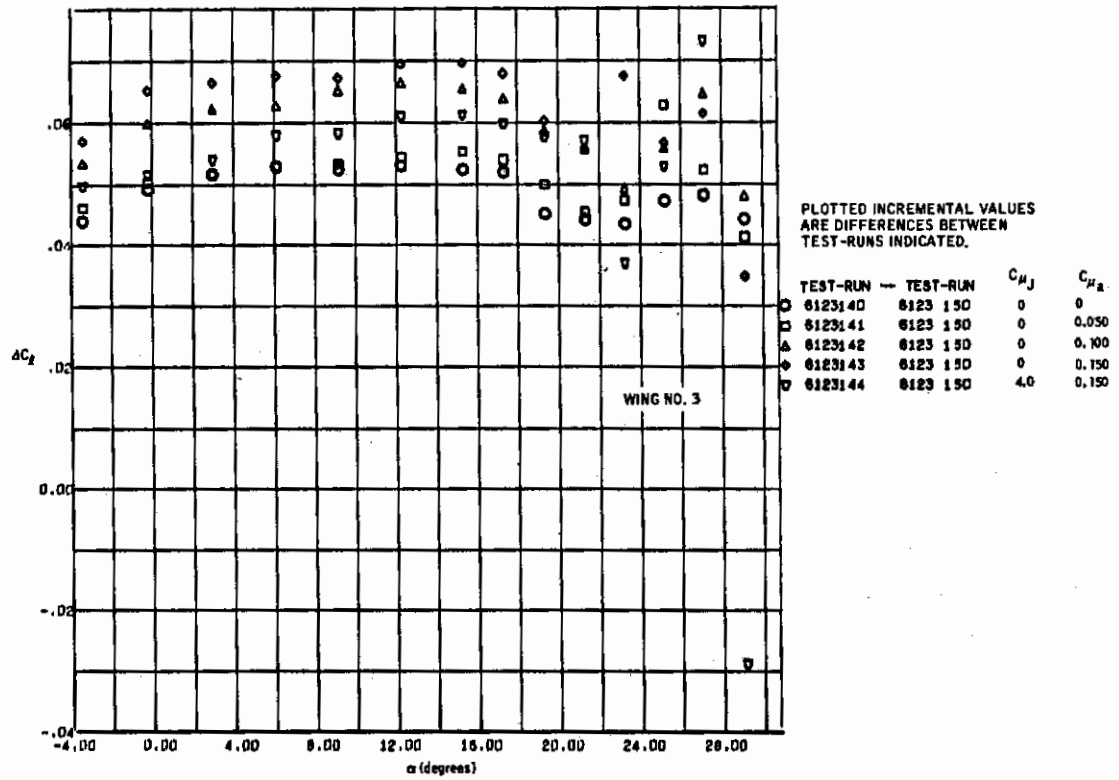

Figure 8.1-7. Effect of BLC Blowing and Thrust Coefficient on Aileron Effectiveness, Rolling Moments, Triple-Slotted Flap at 60 Degrees, δ_a = ±50 Degrees

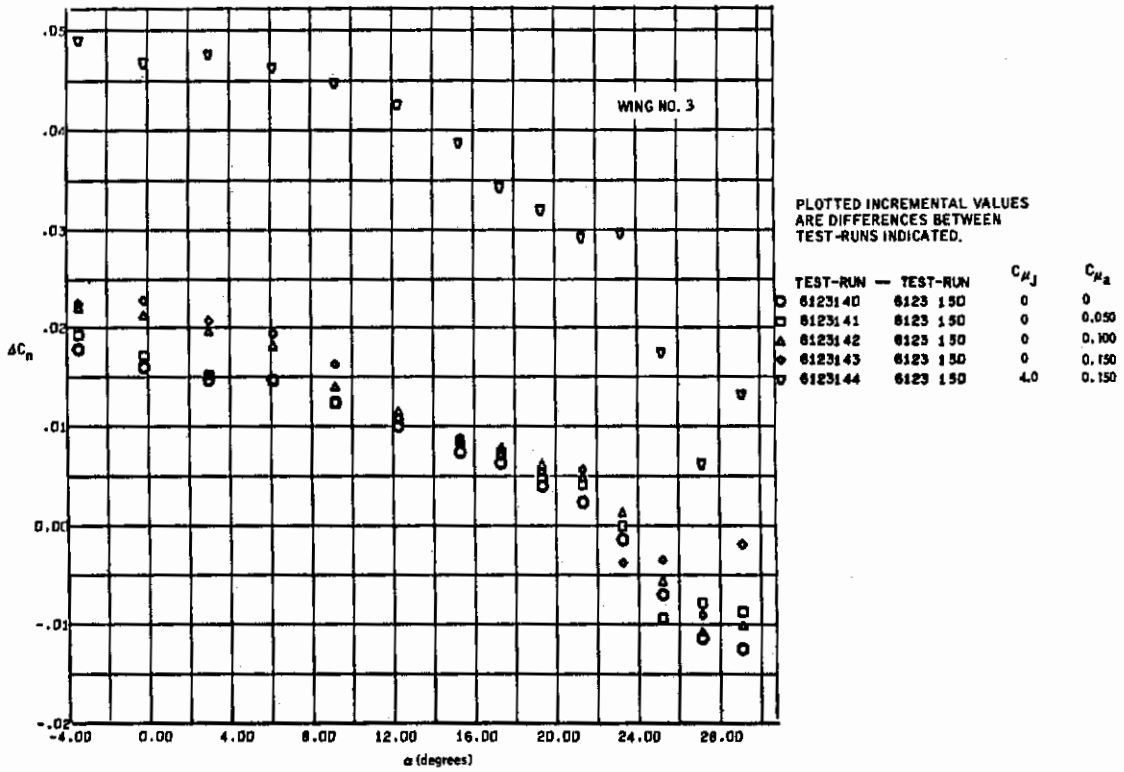

Figure 8.1-8. Effect of BLC Blowing and Thrust Coefficient on Aileron Effectiveness, Yawing Moments, Triple-Slotted Flap at 60 Degrees, δ_a = ±50 Degrees

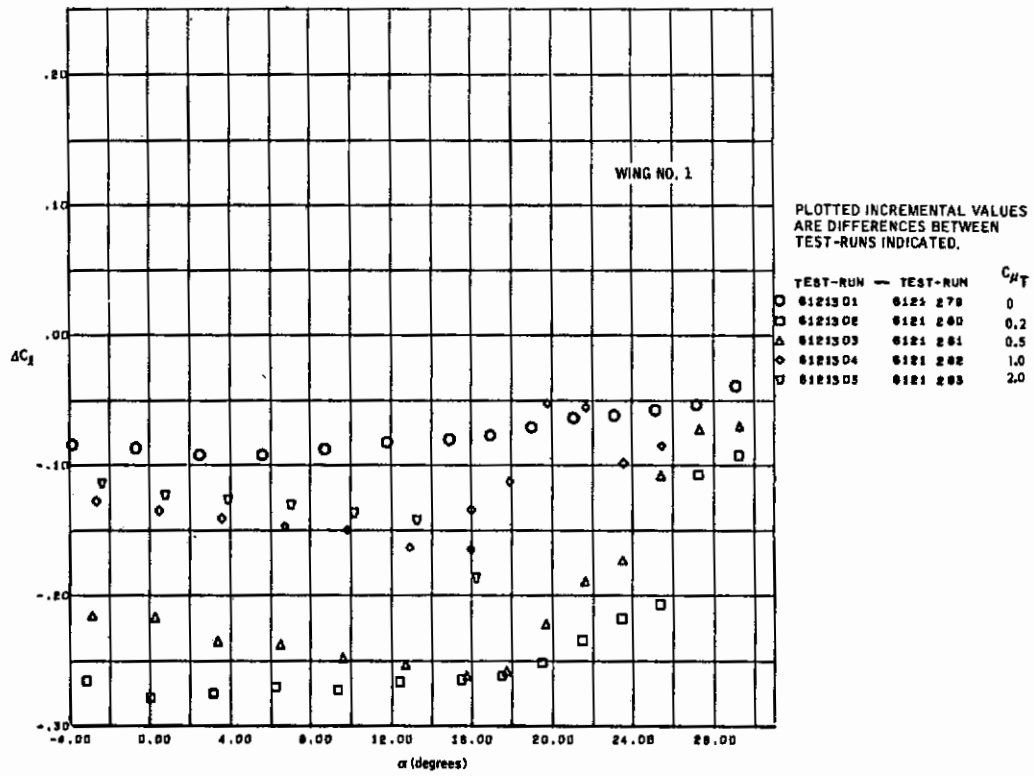

Figure 8.1-9. Spoiler Effectiveness with IBF Plain Flap at 60 Degrees, Rolling Moments, δ_{SP} = 20 Degrees

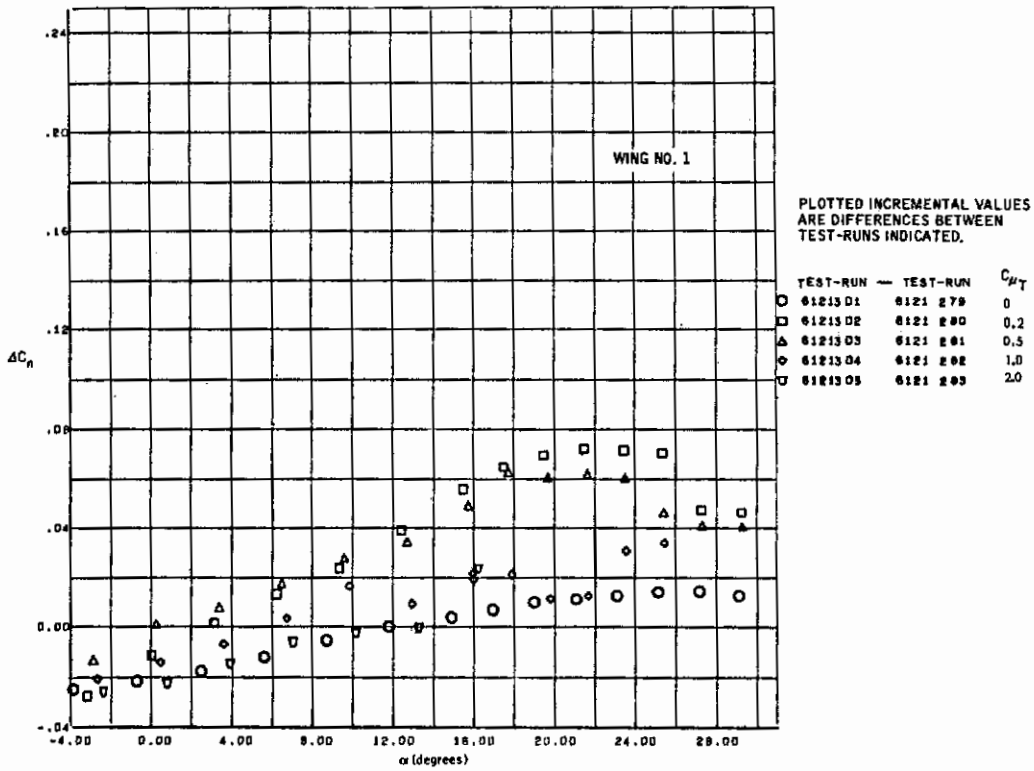

Figure 8.1-10. Spoiler Effectiveness with IBF Plain Flap at 60 Degrees, Yawing Moments, δ_{SP} = 20 Degrees

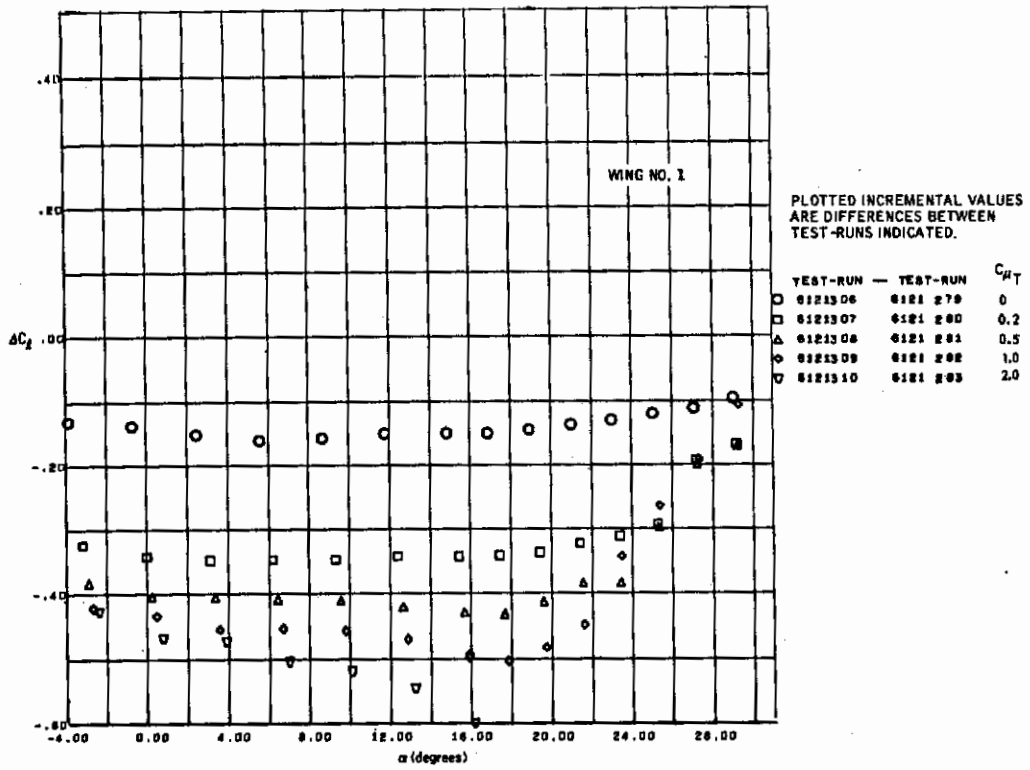

Figure 8.1-11. Spoiler Effectiveness with IBF Plain Flap at 60 Degrees, Rolling Moments, δ_{SP} = 60 Degrees

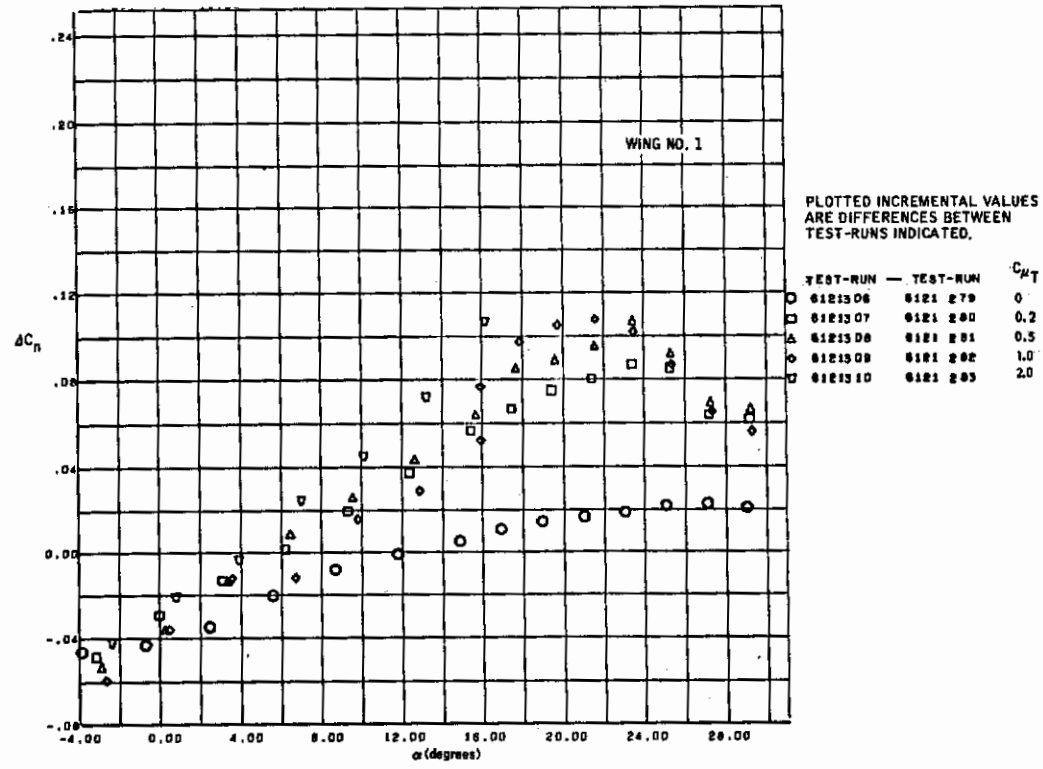

Figure 8.1-12. Spoiler Effectiveness with IBF Plain Flap at 60 Degrees, Yawing Moments, δ_{SP} = 60 Degrees

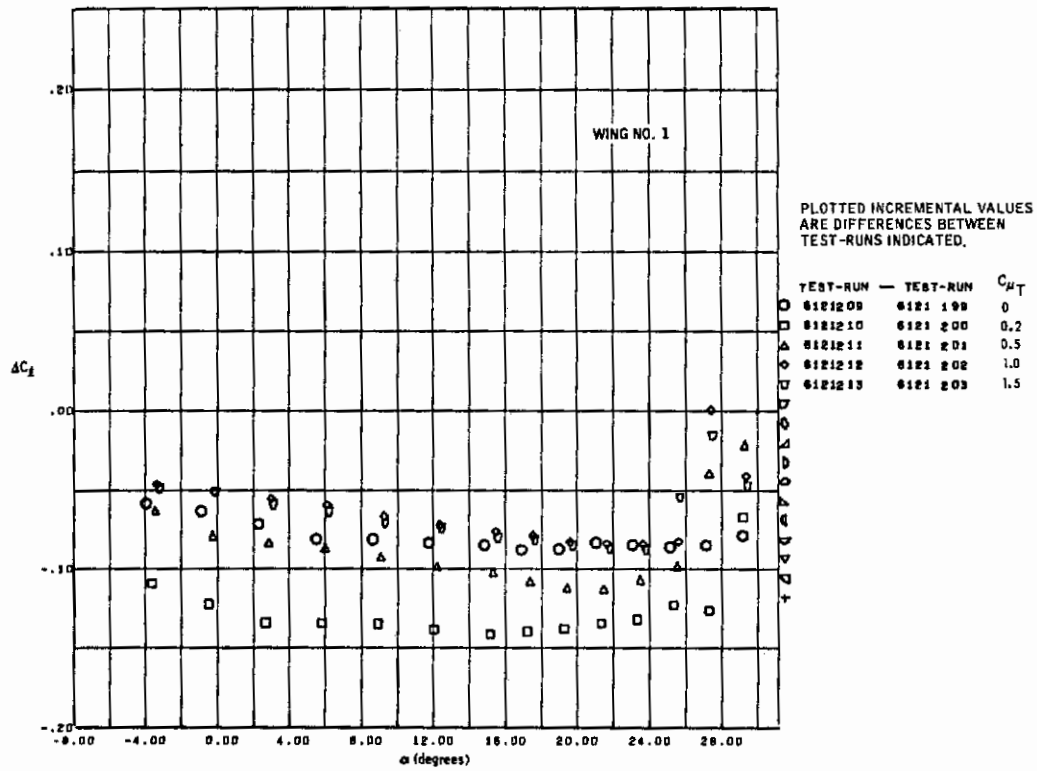

Figure 8.1-13. Spoiler Effectiveness with IBF Single-Slotted Flap at 30 Degrees, Rolling Moments, δ_{SP} = 20 Degrees

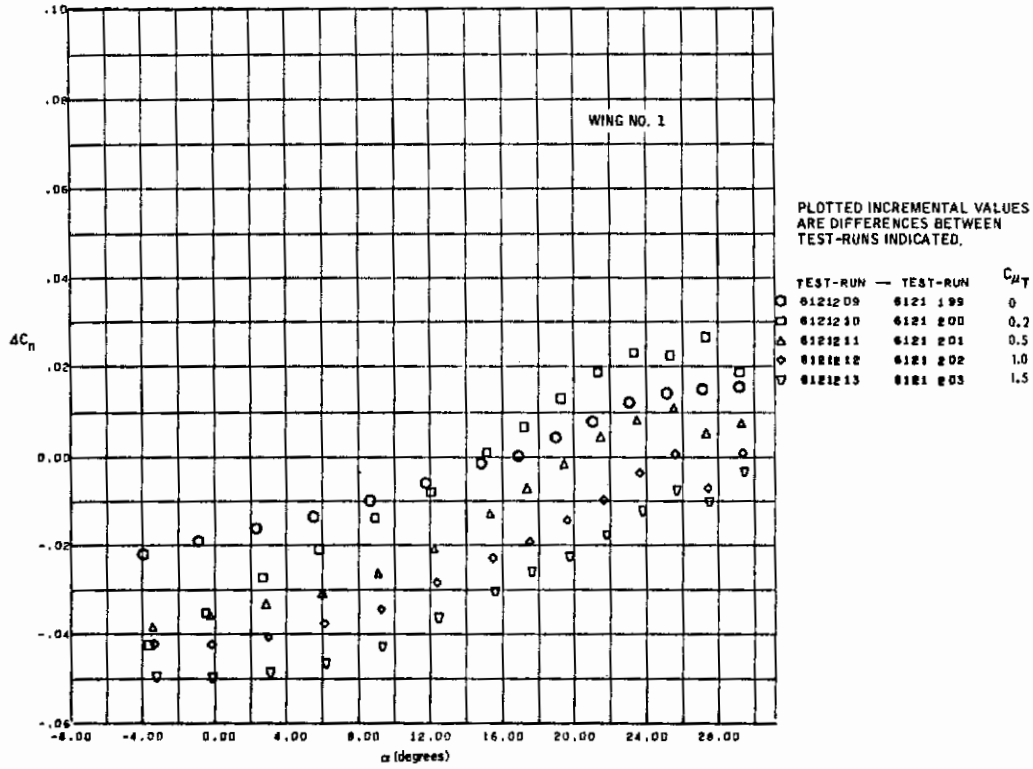

Figure 8.1-14. IBF Spoiler Effectiveness with Single-Slotted Flap at 30 Degrees, Yawing Moments, δ_{SP} = 20 Degrees

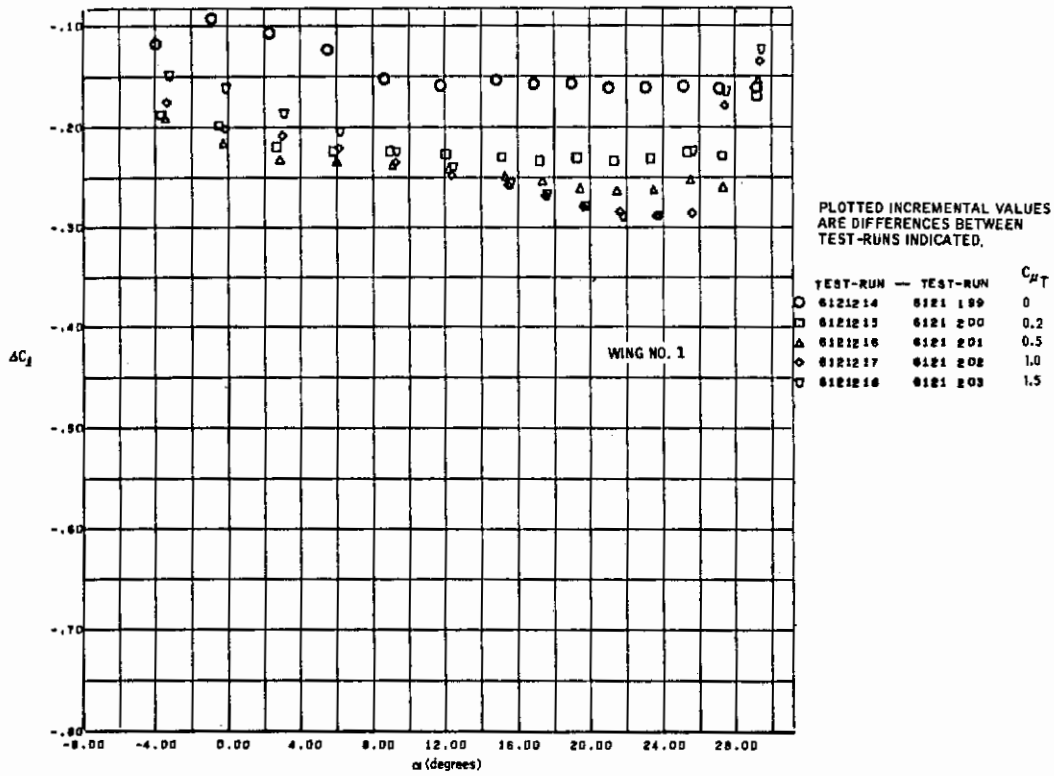

Figure 8.1-15. IBF Spoiler Effectiveness with Single-Slotted Flap at 30 Degrees, Rolling Moments, δ_{SP} = 60 Degrees

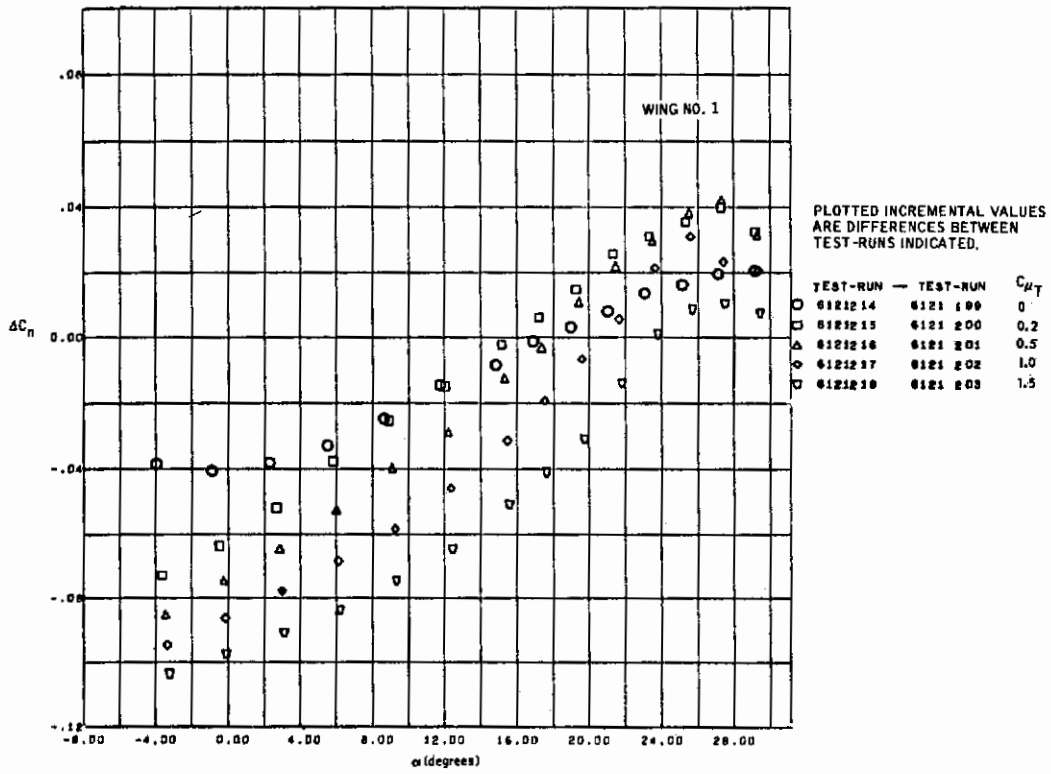

Figure 8.1-16. IBF Spoiler Effectiveness with Single-Slotted Flap at 30 Degrees, Yawing Moments, δ_{SP} = 60 Degrees

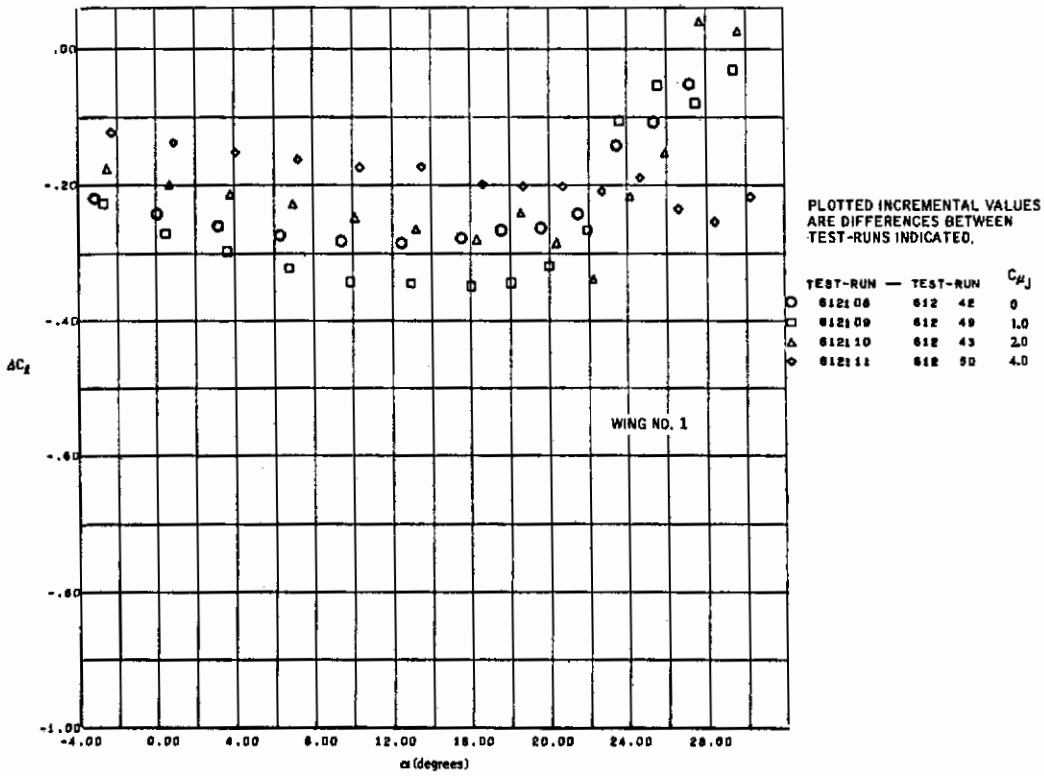

Figure 8.1-17. EBF Spoiler Effectiveness with Triple-Slotted Flap at 60 Degrees, Rolling Moments, δ_{SP} = 20 Degrees

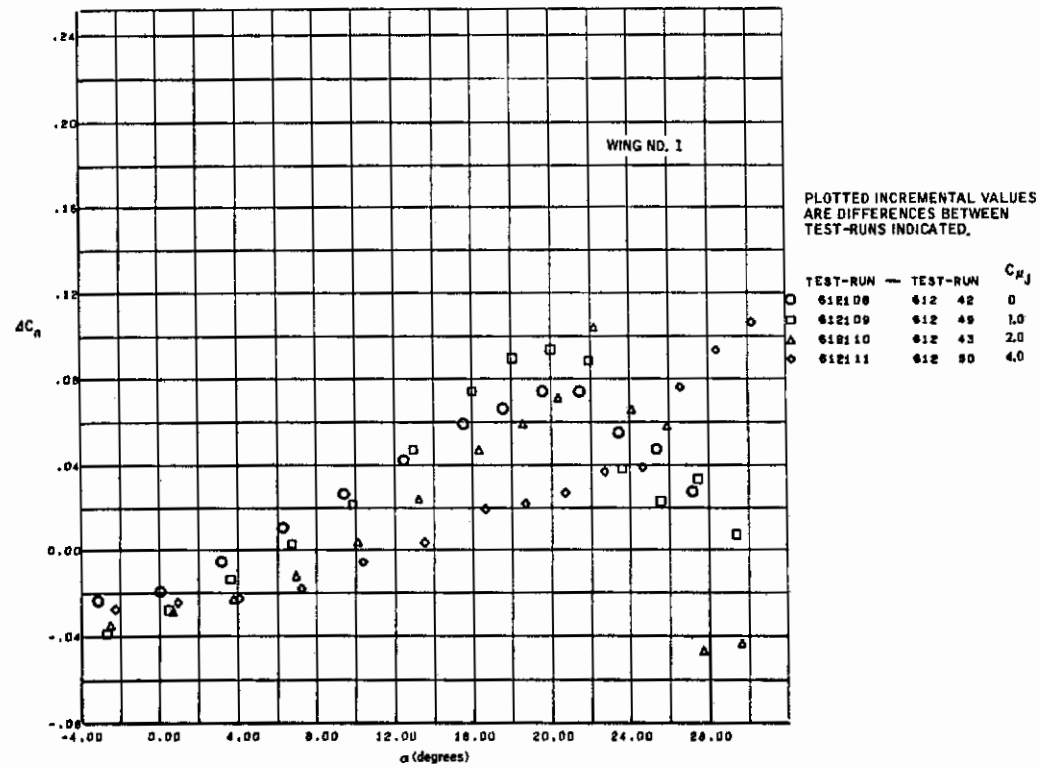

Figure 8.1-18. EBF Spoiler Effectiveness with Triple-Slotted Flap at 60 Degrees, Yawing Moments, δ_{SP} = 20 Degrees

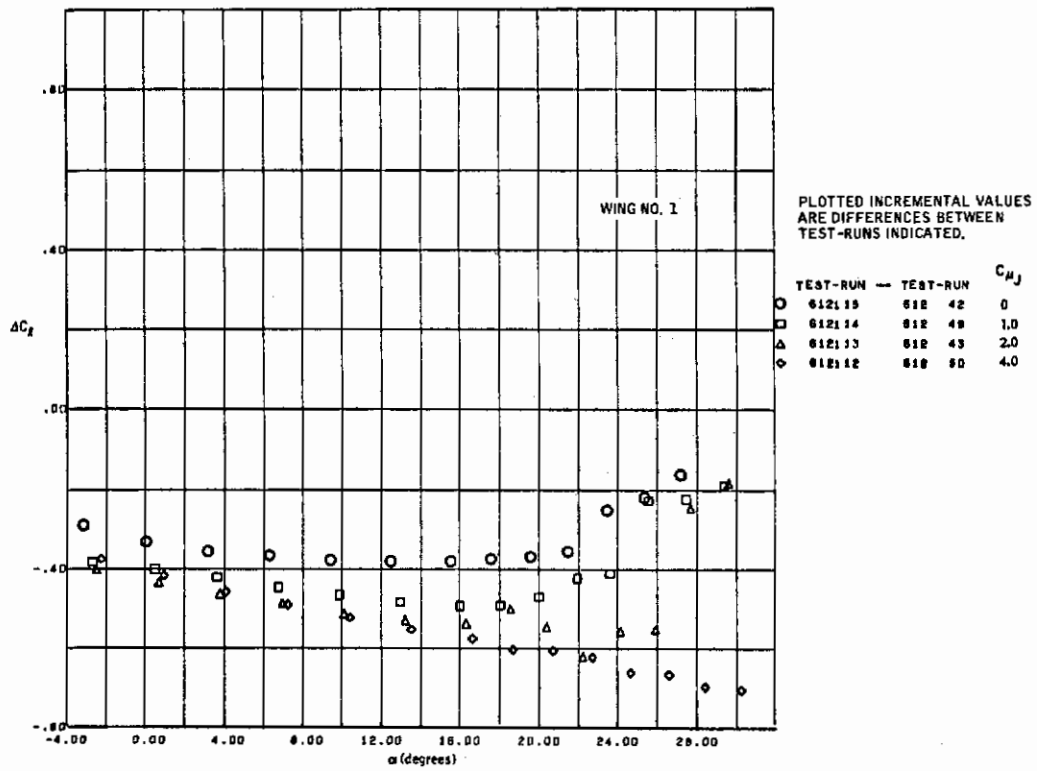

Figure 8.1-19. EBF Spoiler Effectiveness with Triple-Slotted Flap at 60 Degrees, Rolling Moments, δ_{SP} = 60 Degrees

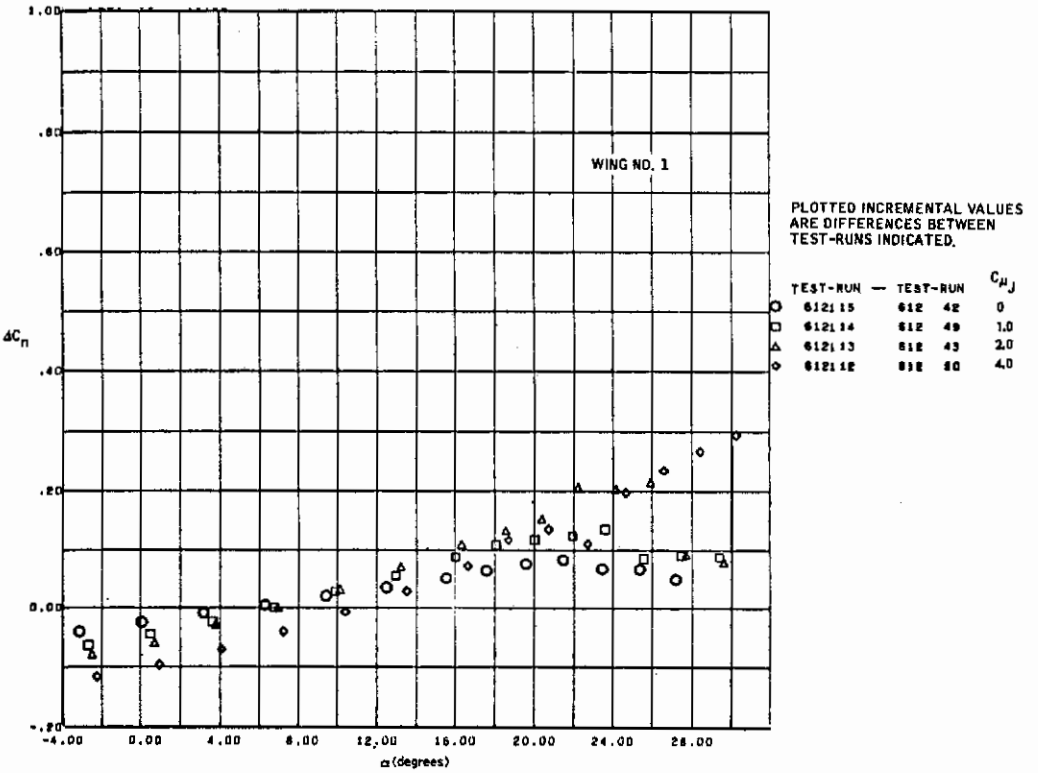

Figure 8.1-20. EBF Spoiler Effectiveness with Triple-Slotted Flap at 60 Degrees, Yawing Moments, δ_{SP} = 60 Degrees

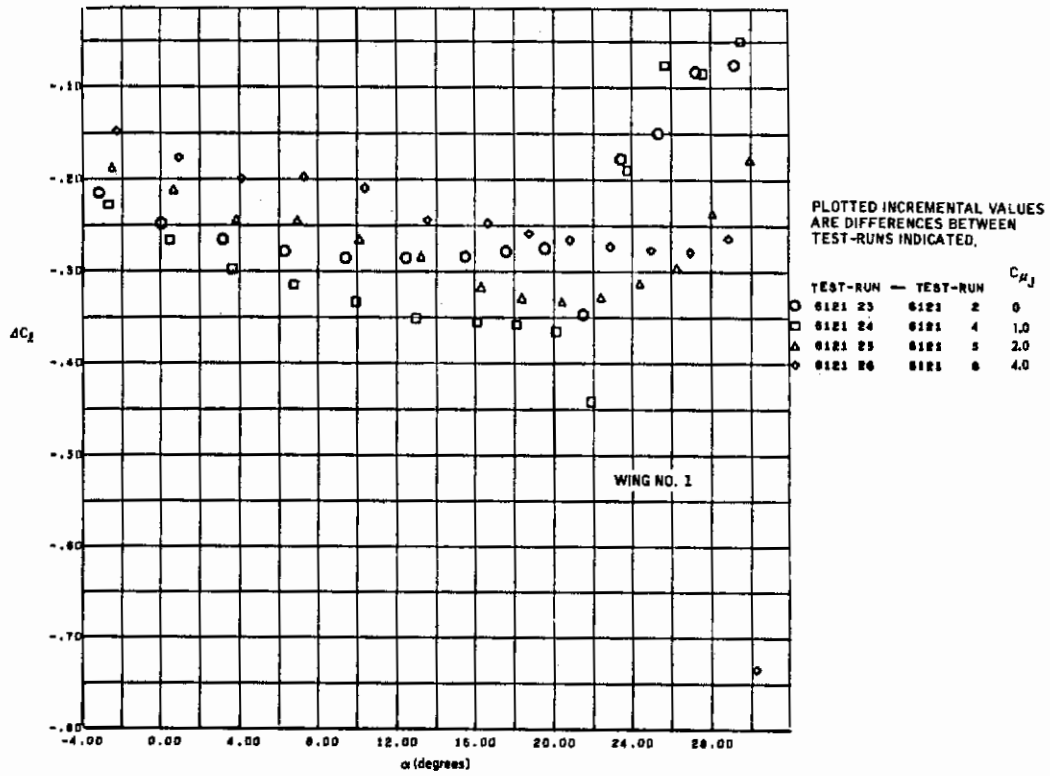

Figure 8.1-21. EBF Spoiler Effectiveness with Triple-Slotted Flap at 60 Degrees, Rolling Moments, δ_{SP} = 20 Degrees

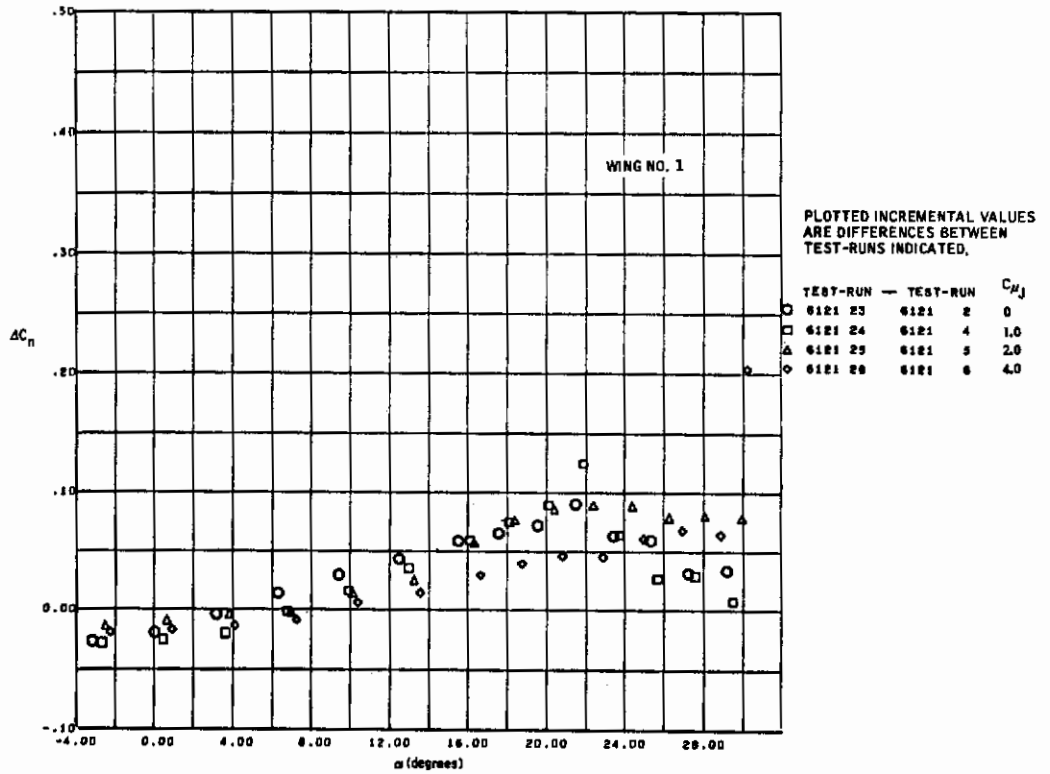

Figure 8.1-22. EBF Spoiler Effectiveness with Triple-Slotted Flap at 60 Degrees, Yawing Moments, δ_{SP} = 20 Degrees

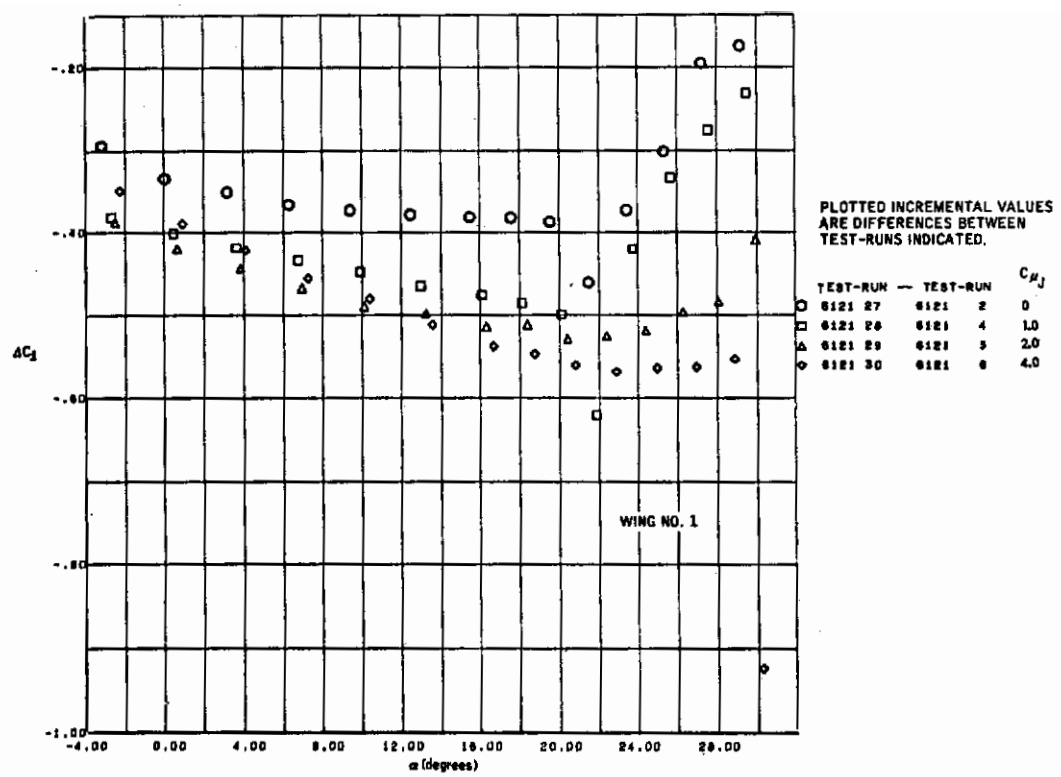

Figure 8.1-23. EBF Spoiler Effectiveness with Triple-Slotted Flap at 60 Degrees, Engine Location B, Rolling Moments, δ_{SP} = 60 Degrees

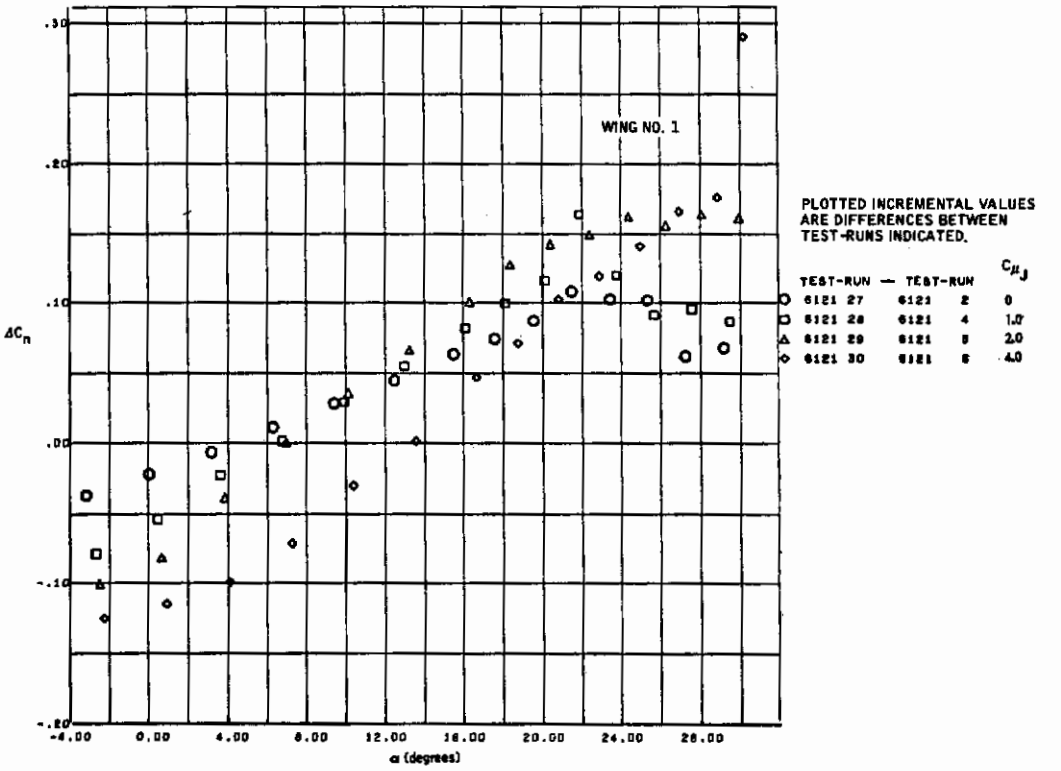

Figure 8.1-24. EBF Spoiler Effectiveness with Triple-Slotted Flap at 60 Degrees, Engine Location B, Yawing Moments, δ_{SP} = 60 Degrees

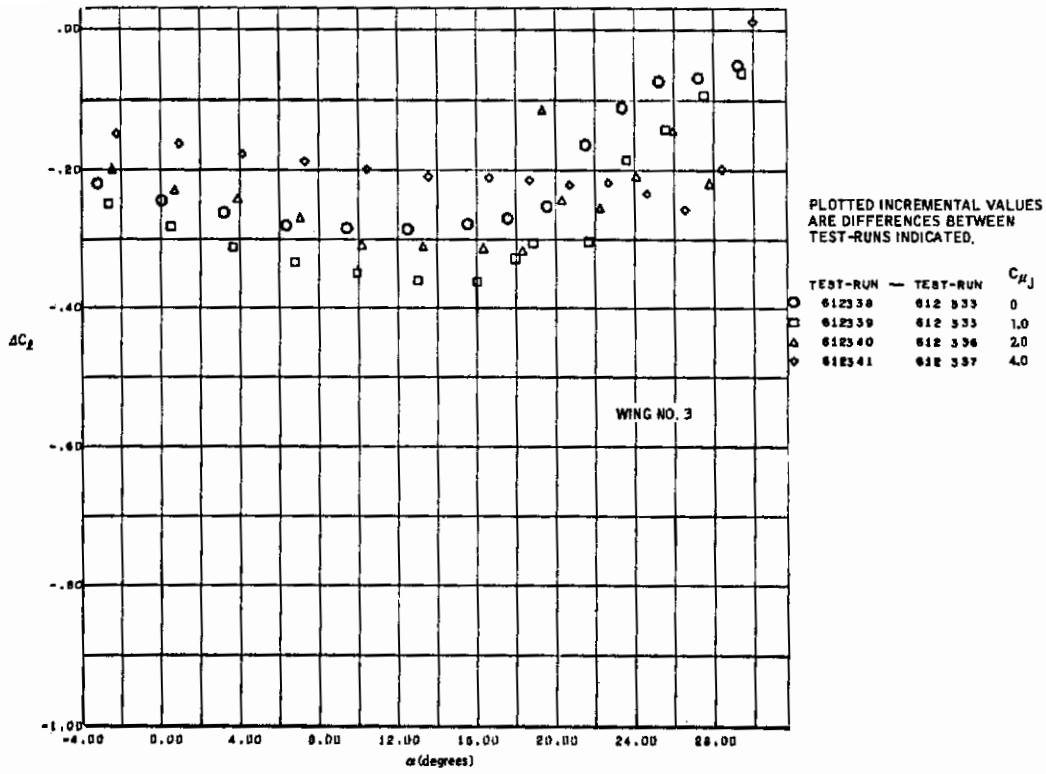

Figure 8.1-25. EBF Spoiler Effectiveness with Triple-Slotted Flap at 60 Degrees, Engine Location D with δ_T = 9 Degrees, Rolling Moments, δ_{SP} = 20 Degrees

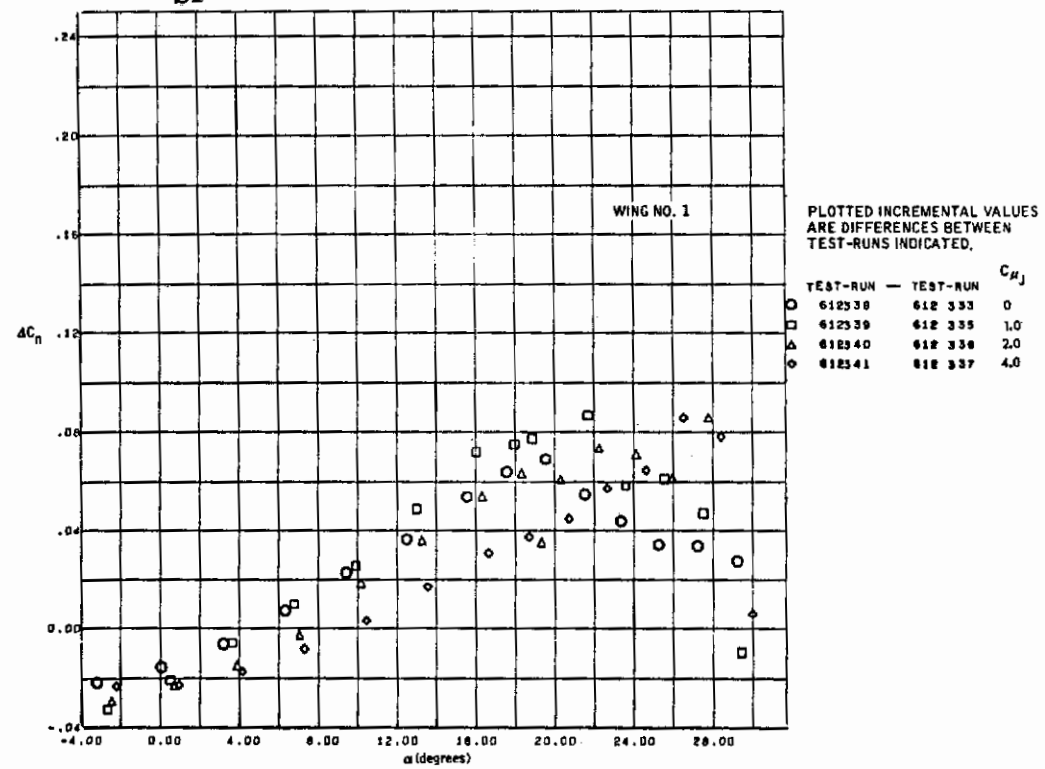

Figure 8.1-26. EBF Spoiler Effectiveness with Triple-Slotted Flap at 60 Degrees, Engine Location D with δ_T = -9 Degrees, Yawing Moments, δ_{SP} = 20 Degrees

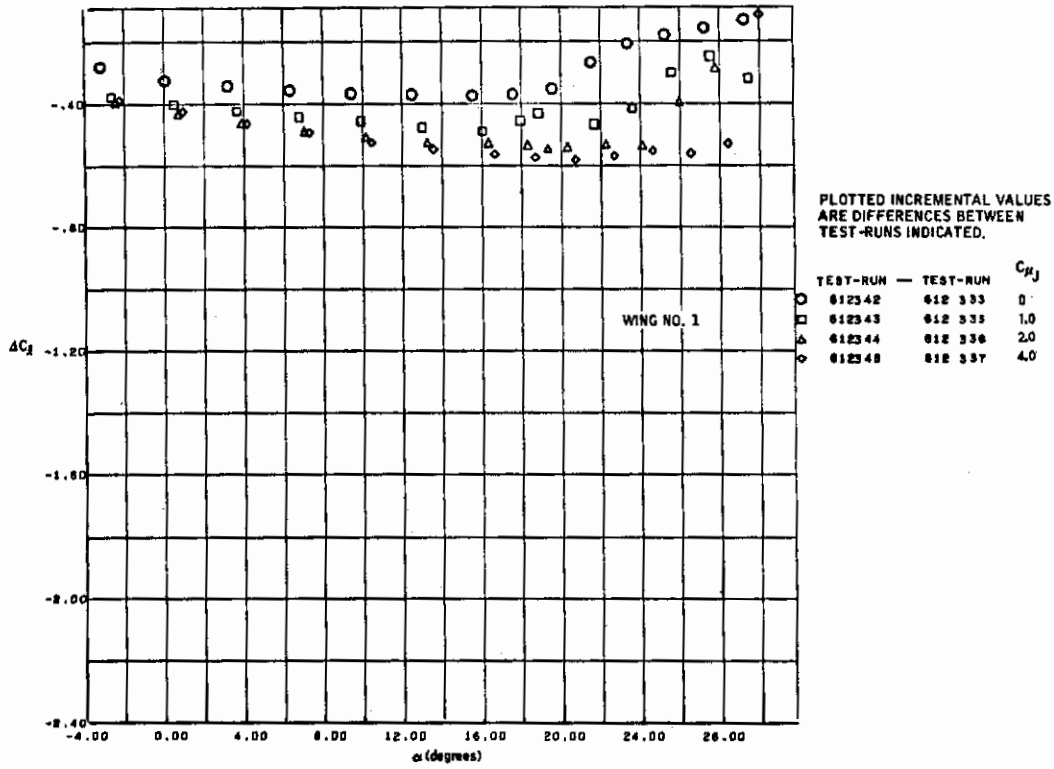

Figure 8.1-27. EBF Spoiler Effectiveness with Triple-Slotted Flap at 60 Degrees, Engine Location D with δ_T = -9 Degrees, Rolling Moments, δ_{SP} = 60 Degrees

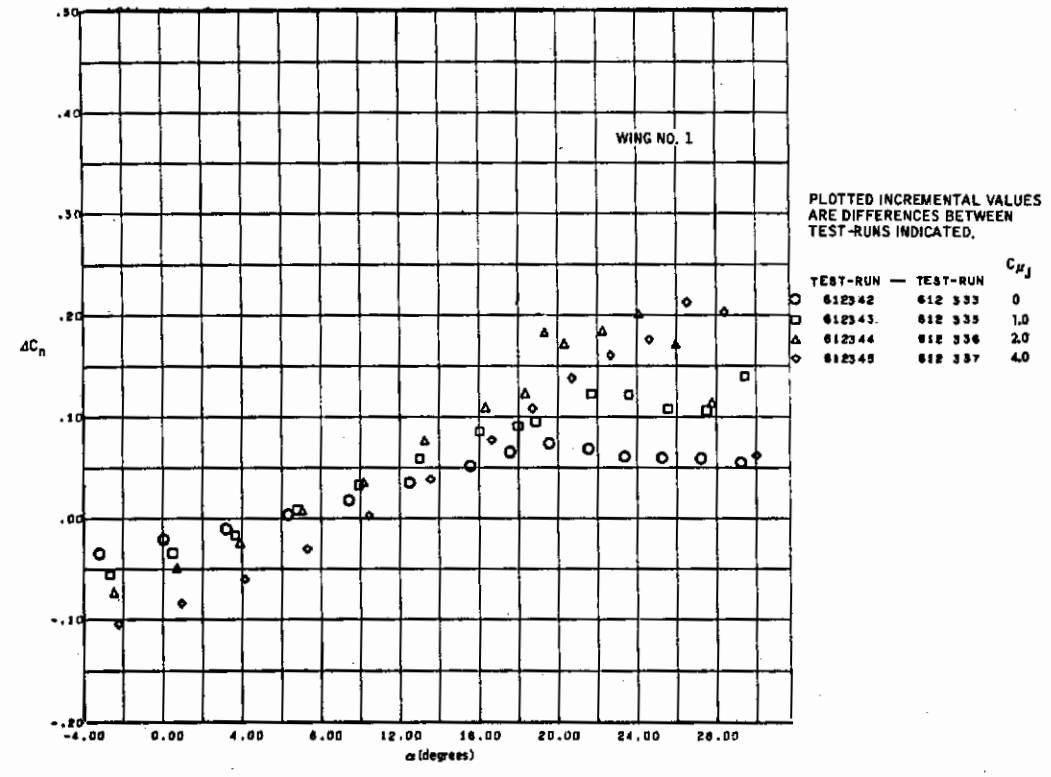

Figure 8.1-28. EBF Spoiler Effectiveness with Triple-Slotted Flap at 60 Degrees, Engine Location D with δ_T = -9 Degrees, Yawing Moments, δ_{SP} = 60 Degrees

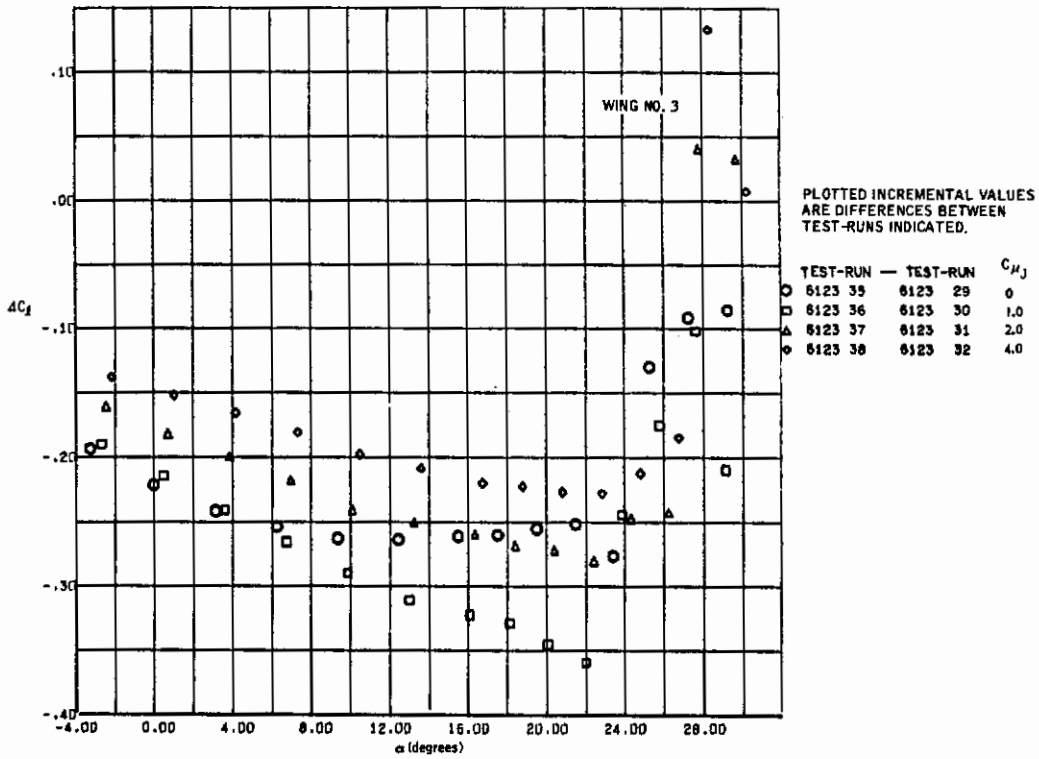

Figure 8.1-29. EBF Spoiler Effectiveness with Triple-Slotted Flap at 60 Degrees, Rolling Moments, δ_{SP} = -20 Degrees

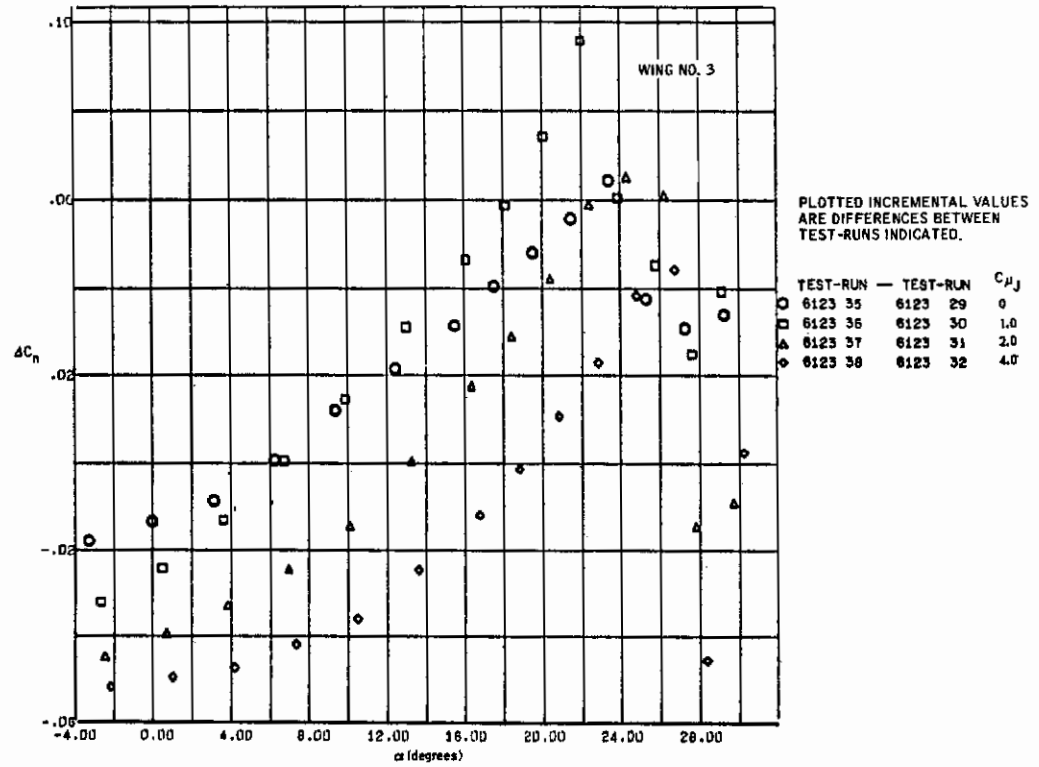

Figure 8.1-30. EBF Spoiler Effectiveness with Triple-Slotted Flap at 60 Degrees, Yawing Moments, δ_{SP} = -20 Degrees

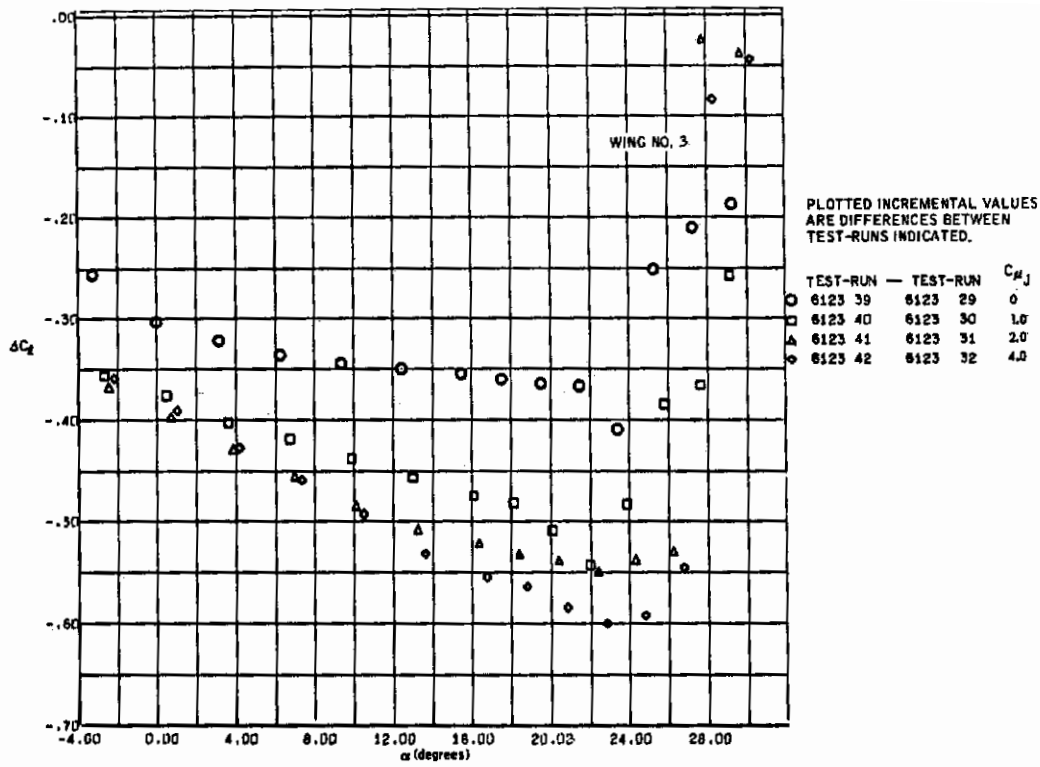

Figure 8.1-31. EBF Spoiler Effectiveness with Triple-Slotted Flap at 60 Degrees, Rolling Moments, δ_{SP} = -60 Degrees

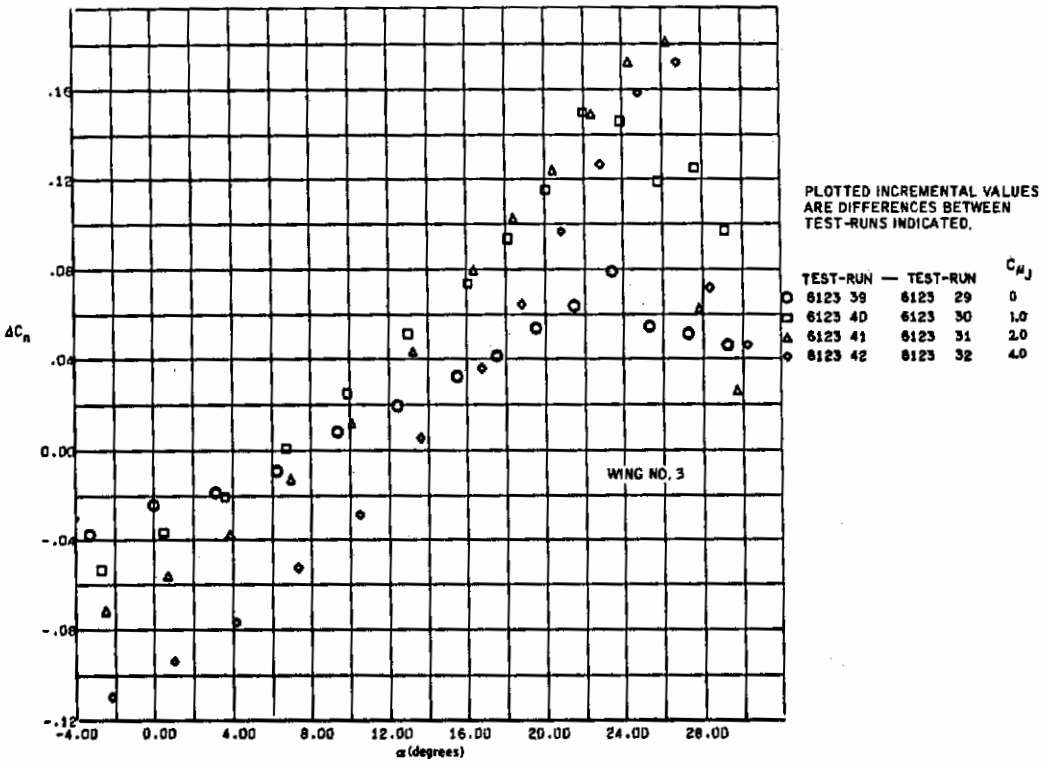

Figure 8.1-32. EBF Spoiler Effectiveness with Triple-Slotted Flap at 60 Degrees, Yawing Moments, δ_{SP} = -60 Degrees

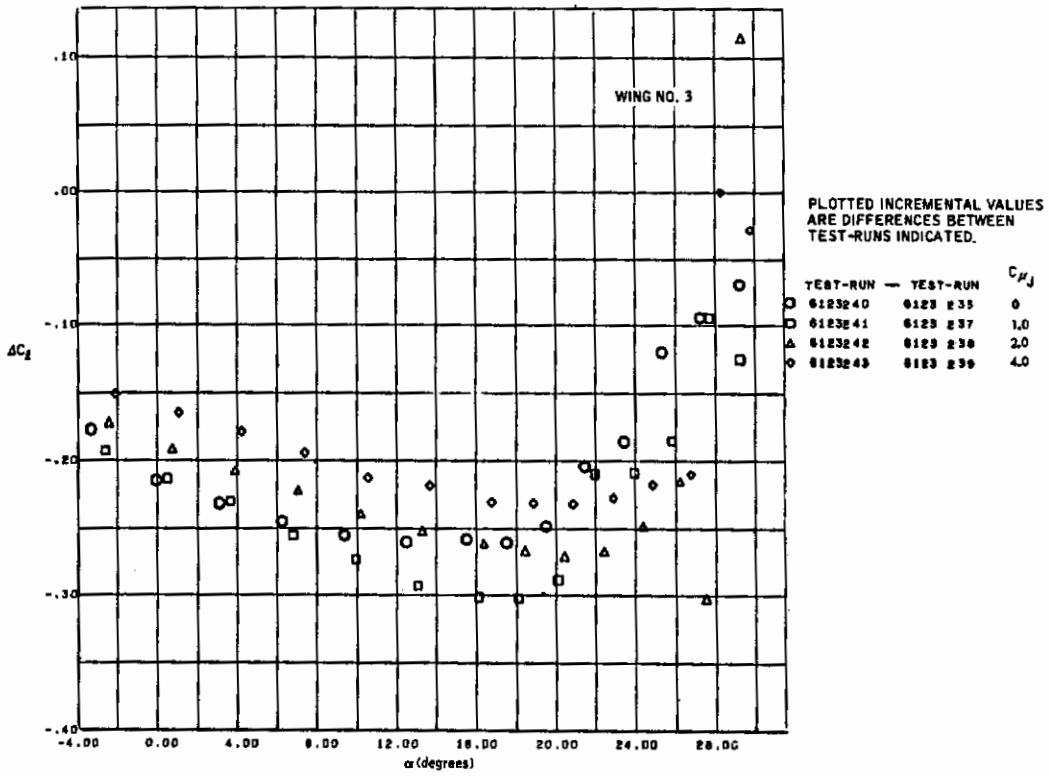

Figure 8.1-33. EBF Spoiler Effectiveness with Triple-Slotted Flap at 60 Degrees, δ_T = -12 Degrees, Rolling Moments, δ_{SP} = 20 Degrees

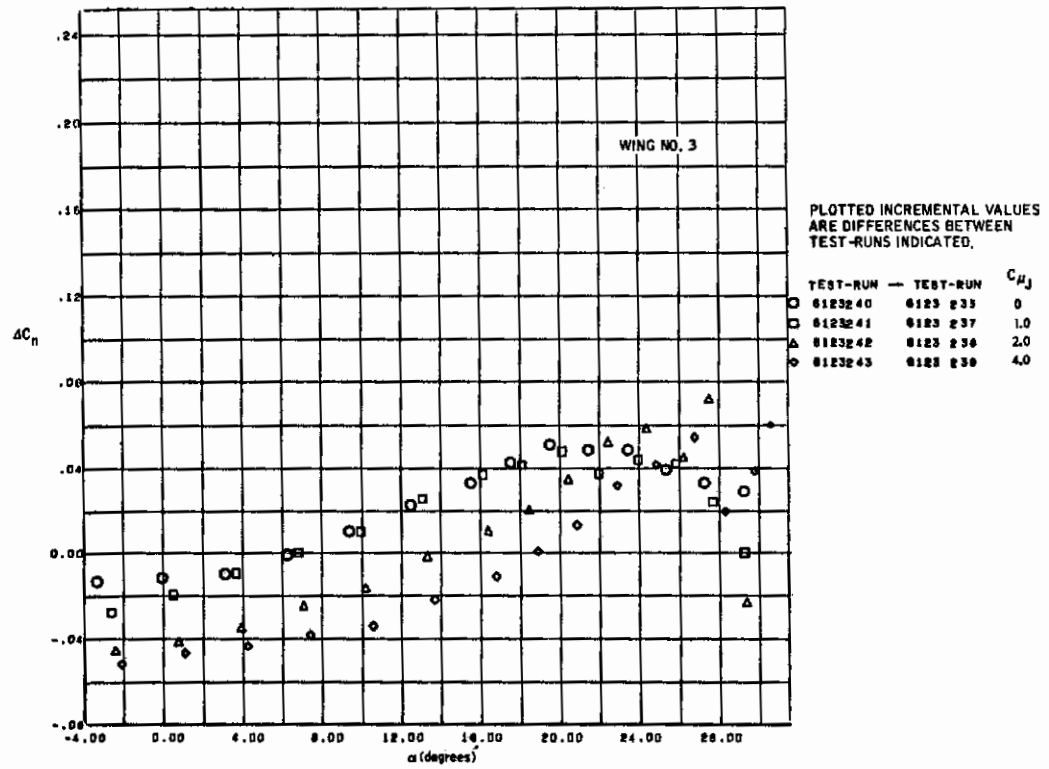

Figure 8.1-34. EBF Spoiler Effectiveness with Triple-Slotted Flap at 60 Degrees, δ_T = -12 Degrees, Yawing Moments, δ_{SP} = 20 Degrees

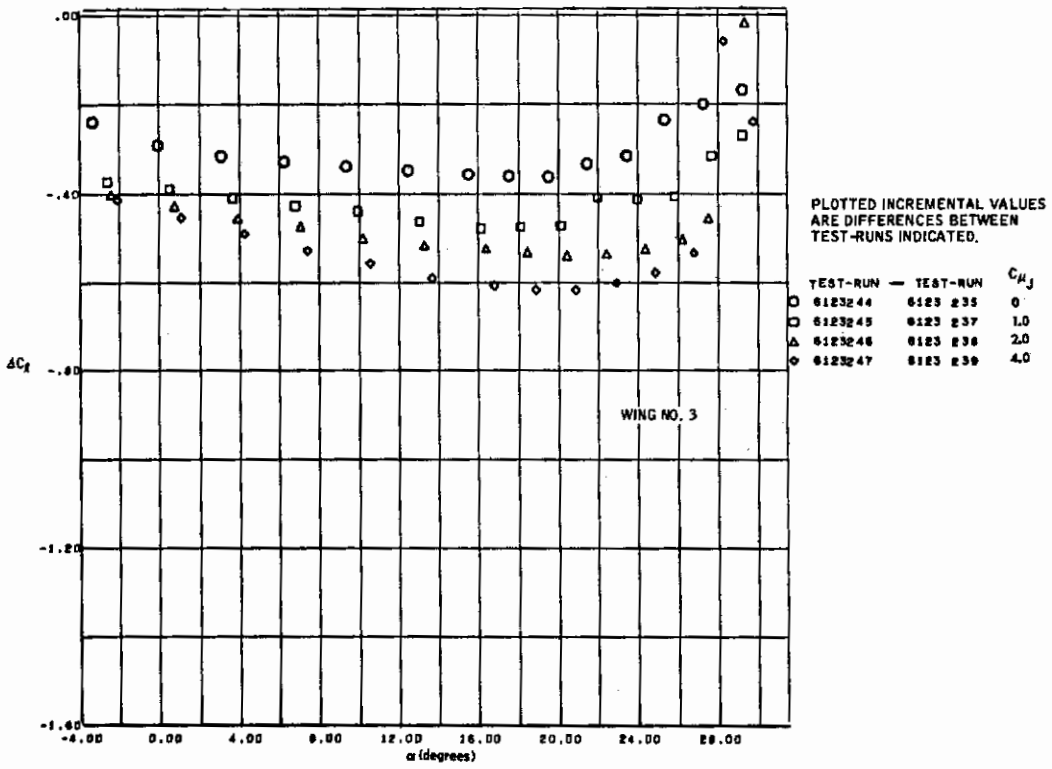

Figure 8.1-35. EBF Spoiler Effectiveness with Triple-Slotted Flap at 60 Degrees, δ_T = -12 Degrees, Rolling Moments, δ_{SP} = 60 Degrees

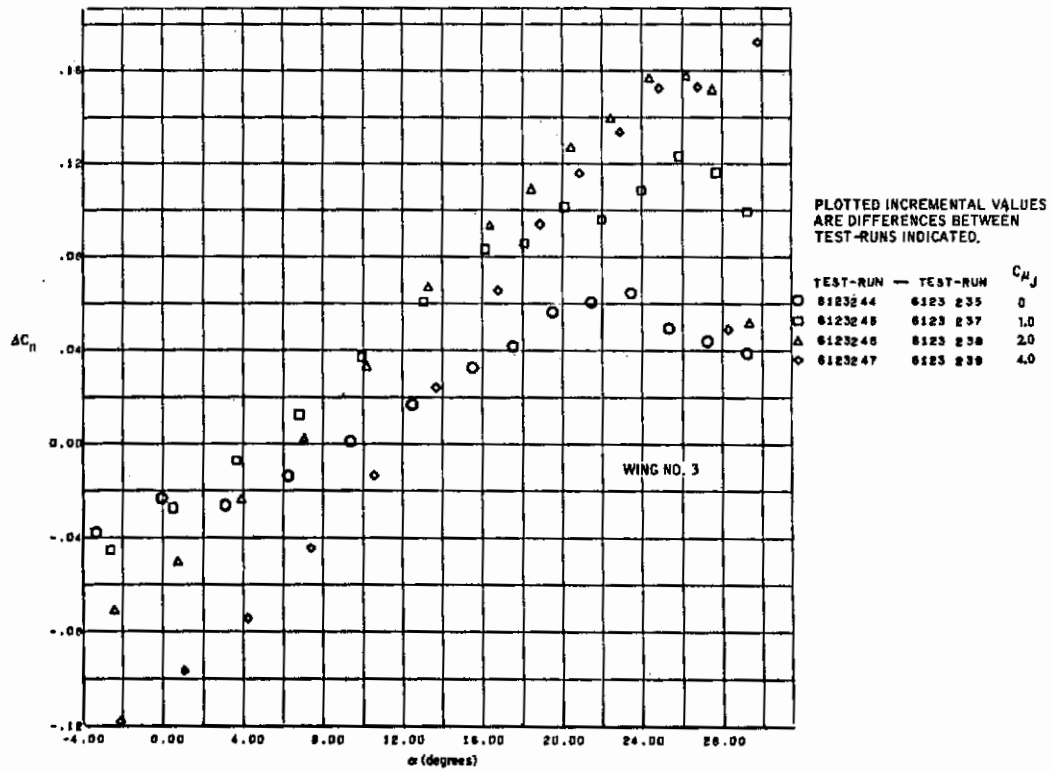

Figure 8.1-36. EBF Spoiler Effectiveness with Triple-Slotted Flap at 60 Degrees, δ_T = -12 Degrees, Yawing Moments, δ_{SP} = 60 Degrees

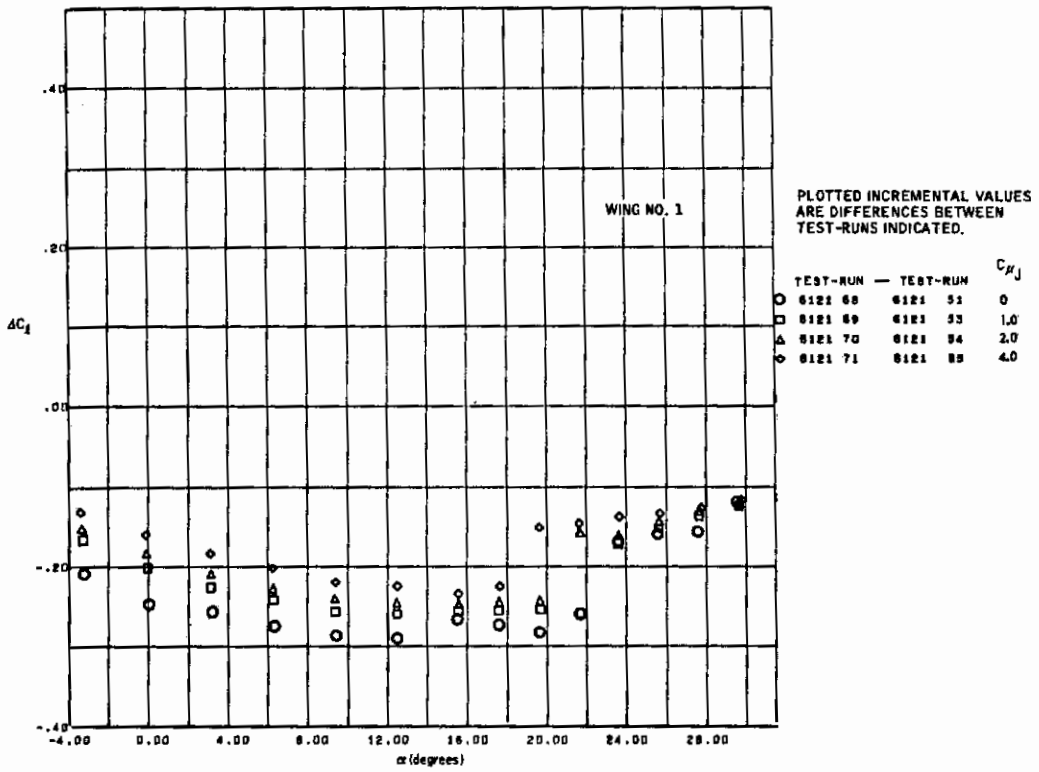

Figure 8.1-37. MF/VT Spoiler Effectiveness with Triple-Slotted Flap at 60 Degrees, δ_T = 30 Degrees, Rolling Moments, δ_{SP} = -20 Degrees

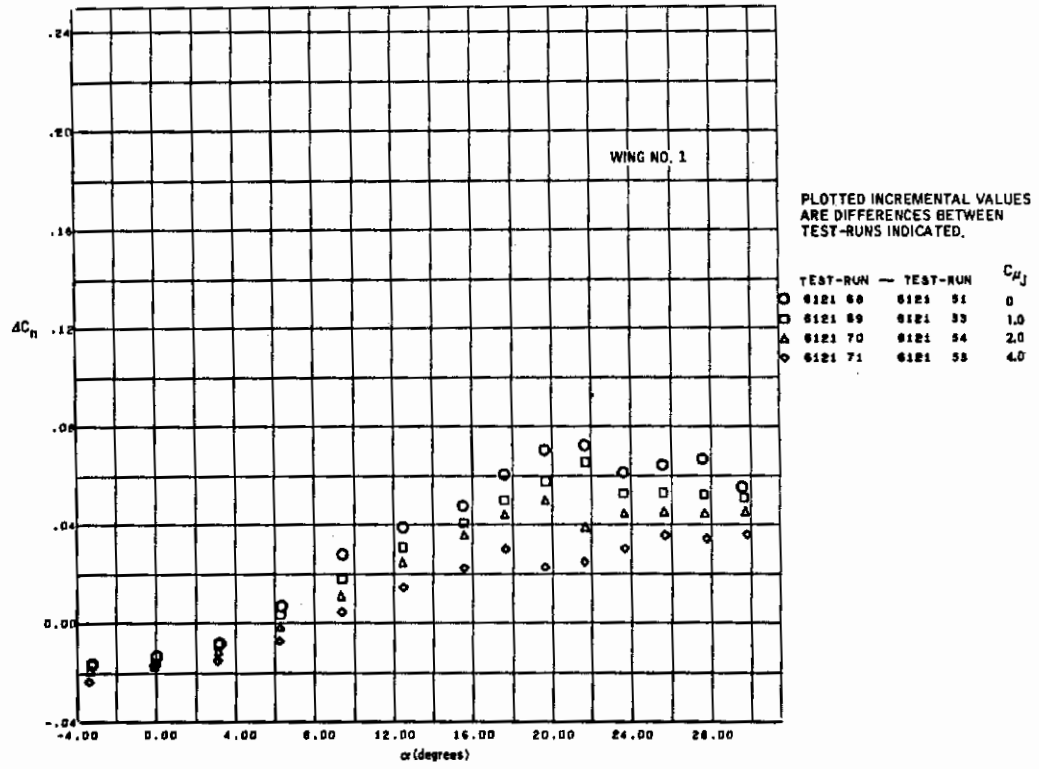

Figure 8.1-38. MF/VT Spoiler Effectiveness with Triple-Slotted Flap at 60 Degrees, δ_T = 30 Degrees, Yawing Moments, δ_{SP} = -20 Degrees

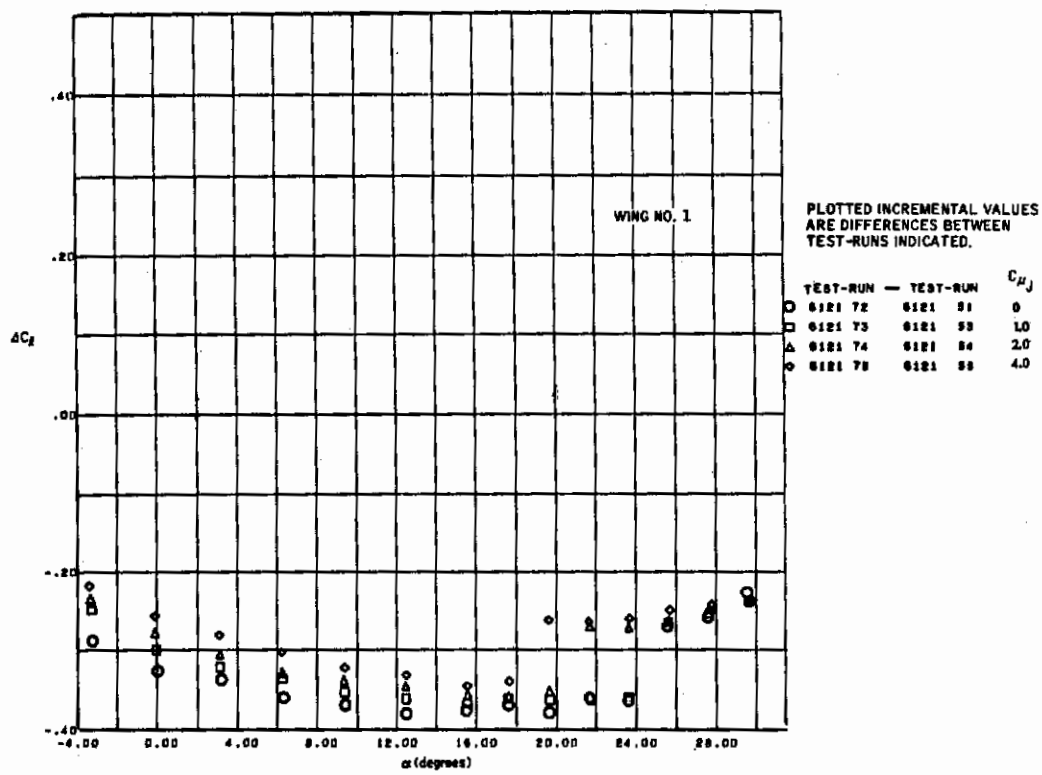

Figure 8.1-39. MF/VT Spoiler Effectiveness with Triple-Slotted Flap at 60 Degrees, δ_T = 30 Degrees, Rolling Moments, δ_{SP} = -60 Degrees

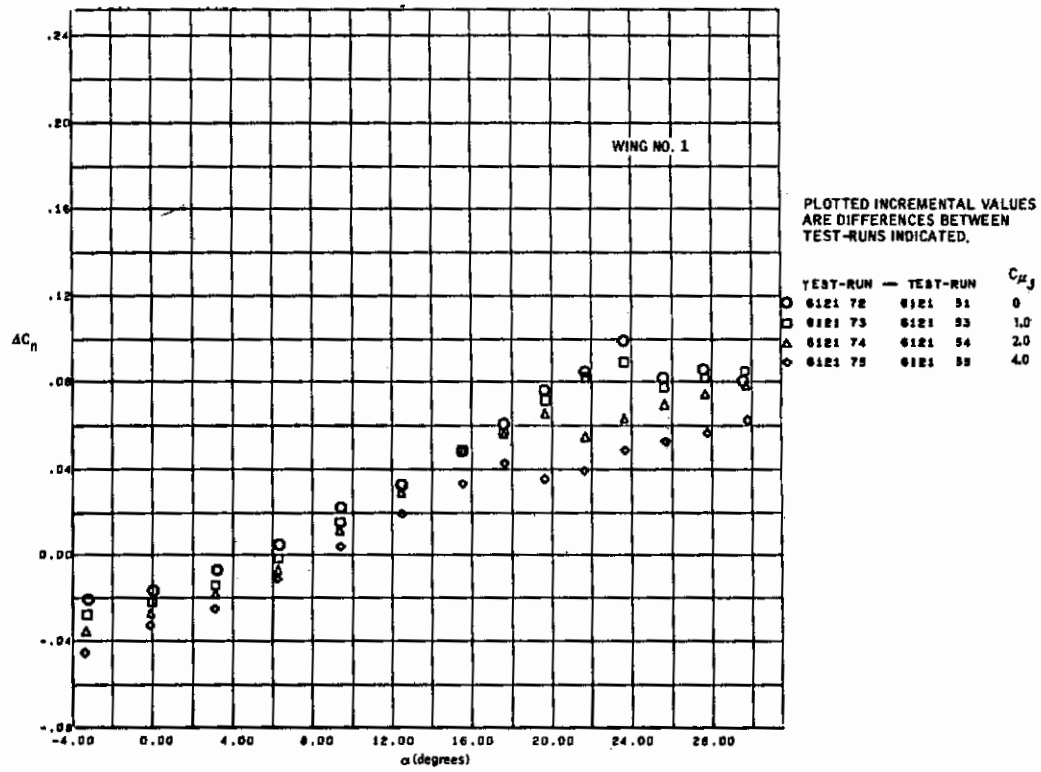

Figure 8.1-40. MF/VT Spoiler Effectiveness with Triple-Slotted Flap at 60 Degrees, δ_T = 30 Degrees, Yawing Moments, δ_{SP} = -60 Degrees

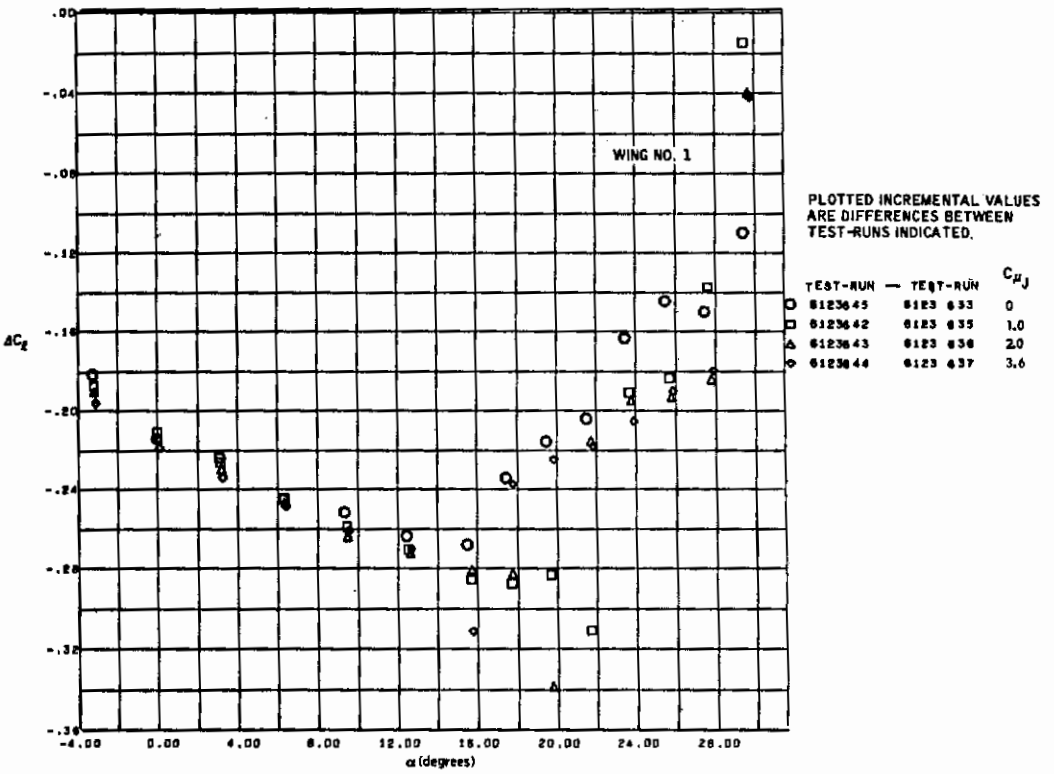

Figure 8.1-41. MF/VT Spoiler Effectiveness with Triple-Slotted Flap at 60 Degrees, δ_T = 60 Degrees, Rolling Moments, δ_{SP} = 20 Degrees

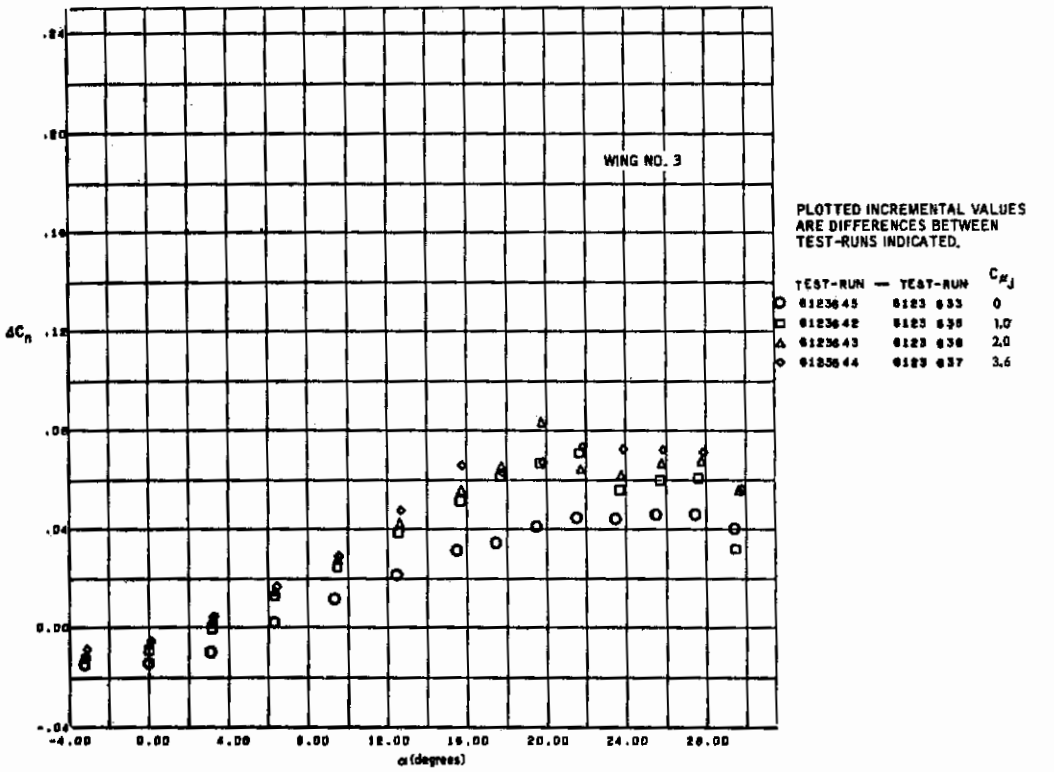

Figure 8.1-42. MF/VT Spoiler Effectiveness with Triple-Slotted Flap at 60 Degrees, δ_T = 60 Degrees, Yawing Moments, δ_{SP} = 20 Degrees

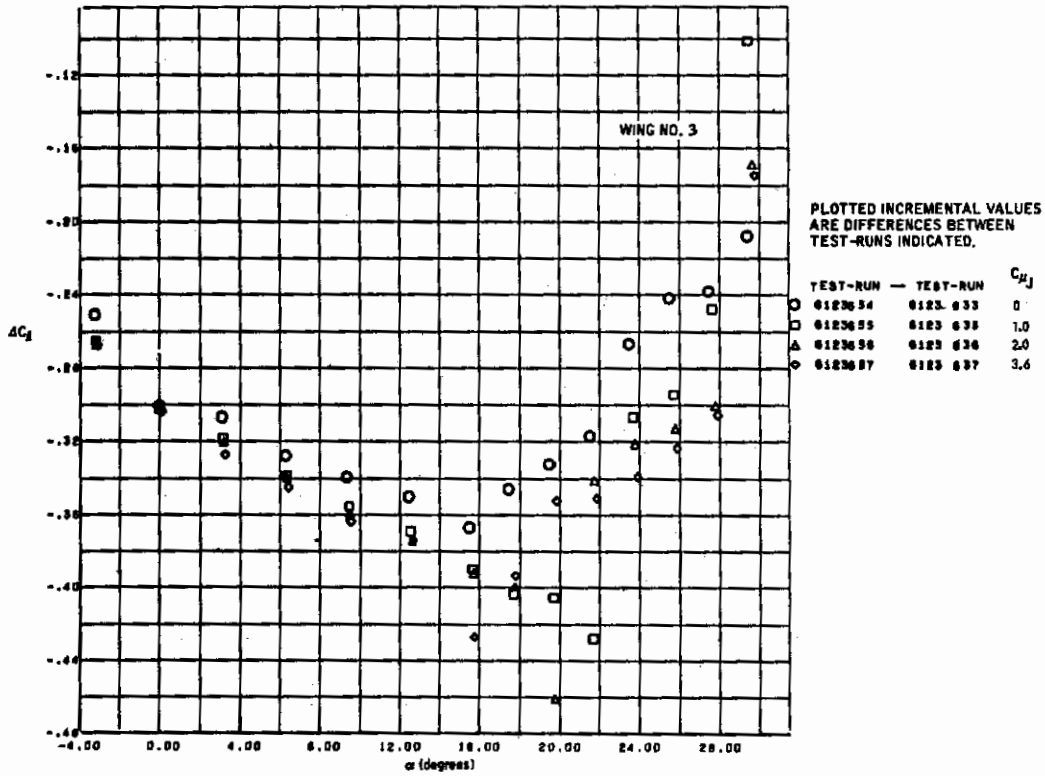

Figure 8.1-43. MF/VT Spoiler Effectiveness with Triple-Slotted Flap at 60 Degrees, δ_T = 60 Degrees, Rolling Moments, δ_{SP} = 60 Degrees

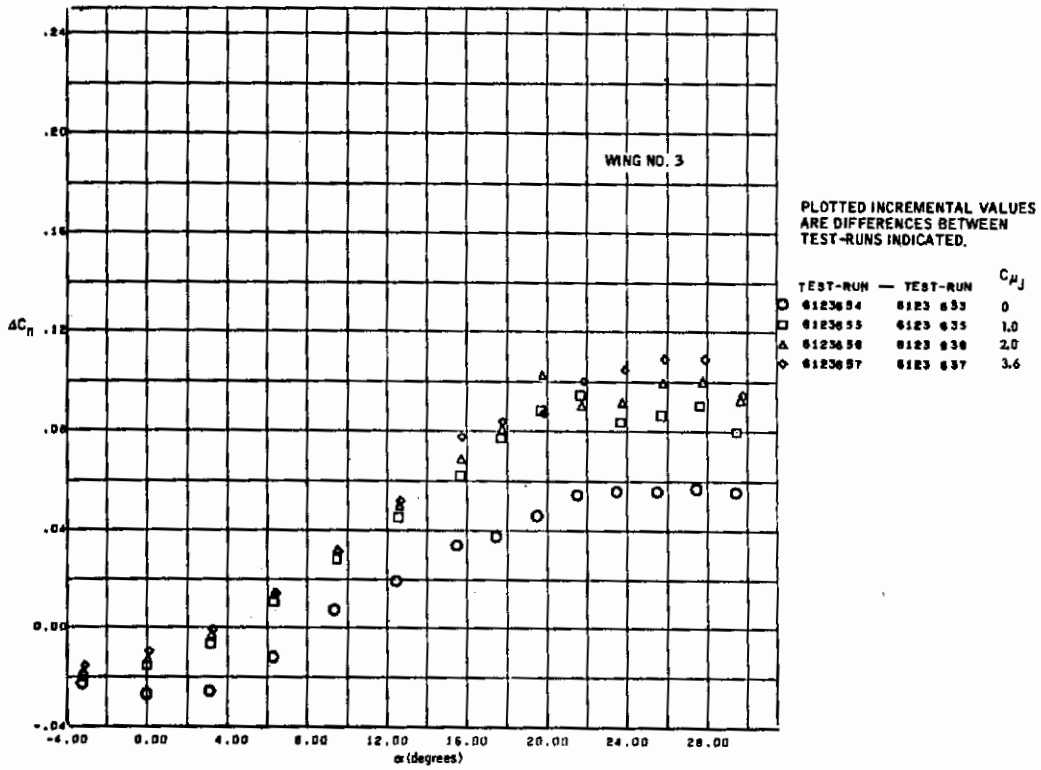

Figure 8.1-44. MF/VT Spoiler Effectiveness with Triple-Slotted Flap at 60 Degrees, δ_T = 60 Degrees, Yawing Moments, δ_{SP} = 60 Degrees

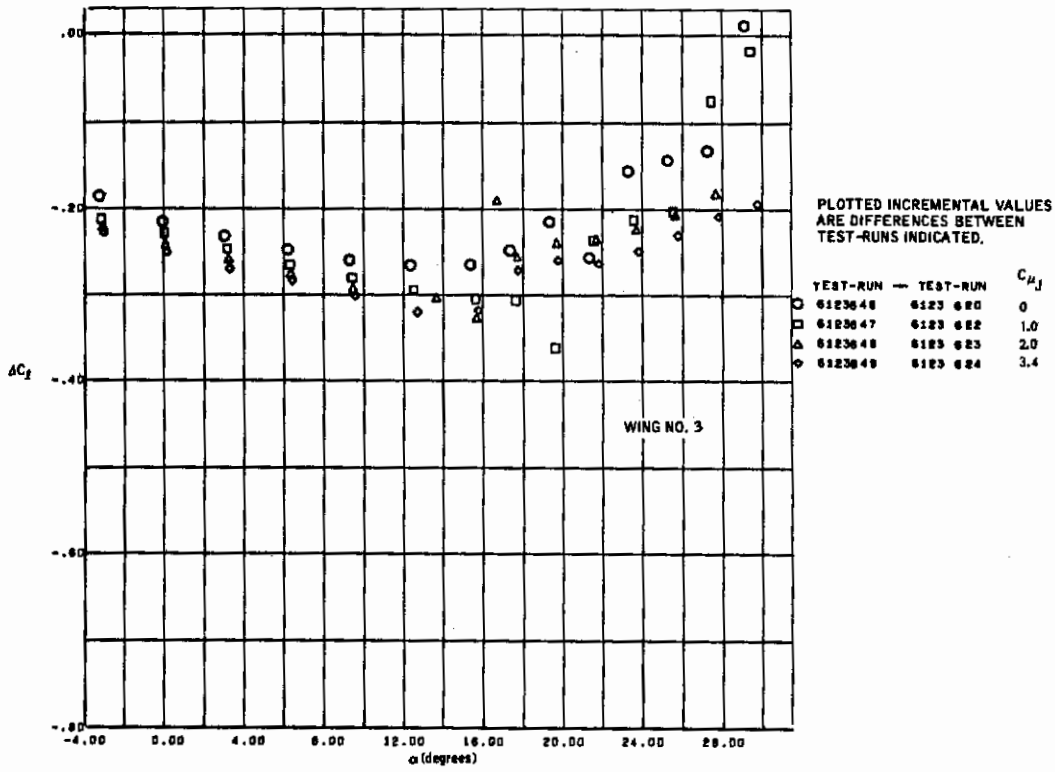

Figure 8.1-45. MF/VT Spoiler Effectiveness with Triple-Slotted Flap at 60 Degrees, δ_T = 90 Degrees, Rolling Moments, δ_{SP} = 20 Degrees

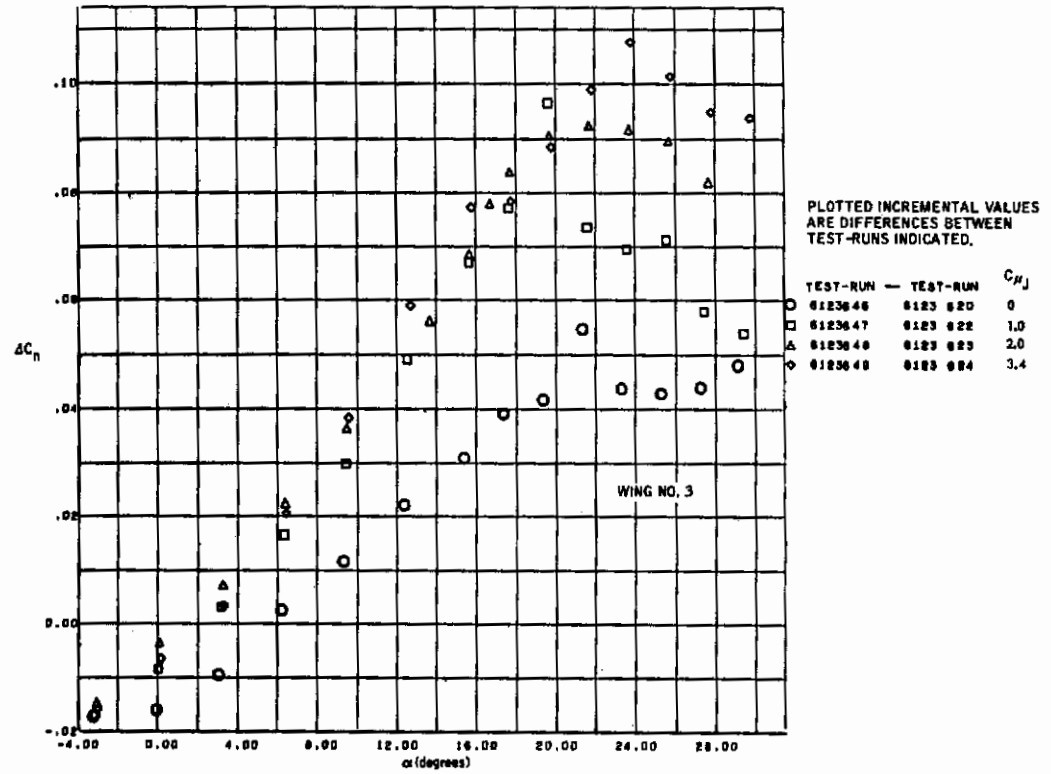

Figure 8.1-46. MF/VT Spoiler Effectiveness with Triple-Slotted Flap at 60 Degrees, δ_T = 60 Degrees, Yawing Moments, δ_{SP} = 20 Degrees

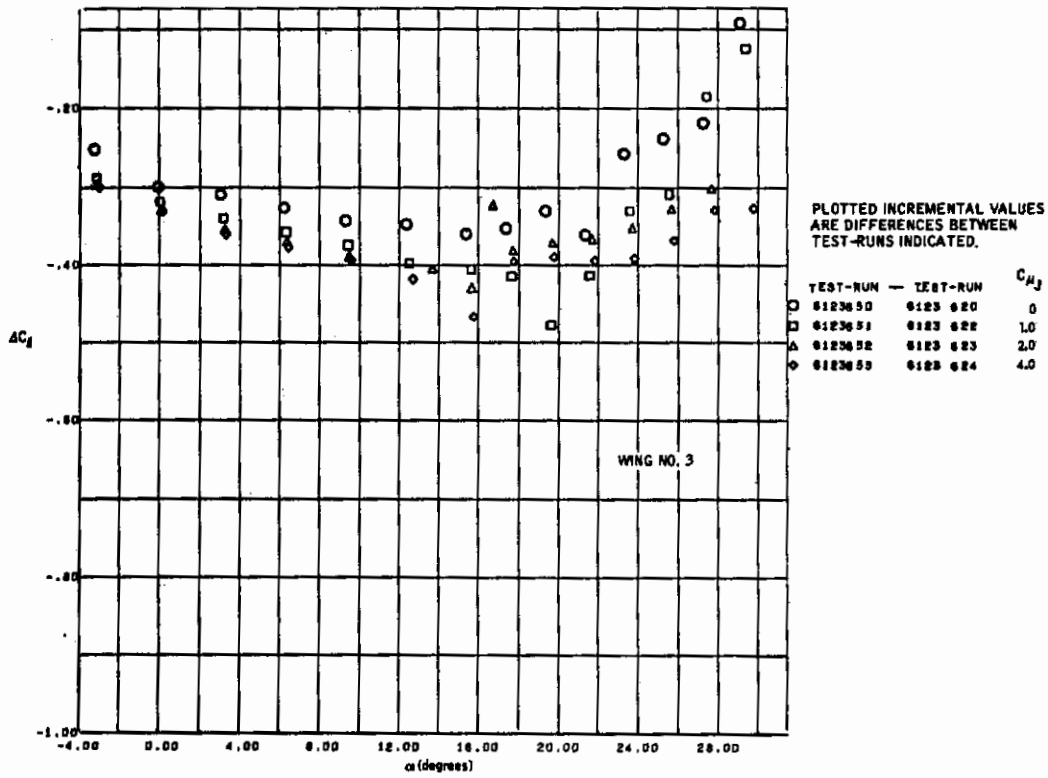

Figure 8.1-47. MF/VT Spoiler Effectiveness with Triple-Slotted Flap at 60 Degrees, δ_T = 90 Degrees, Rolling Moments, δ_{SP} = 60 Degrees

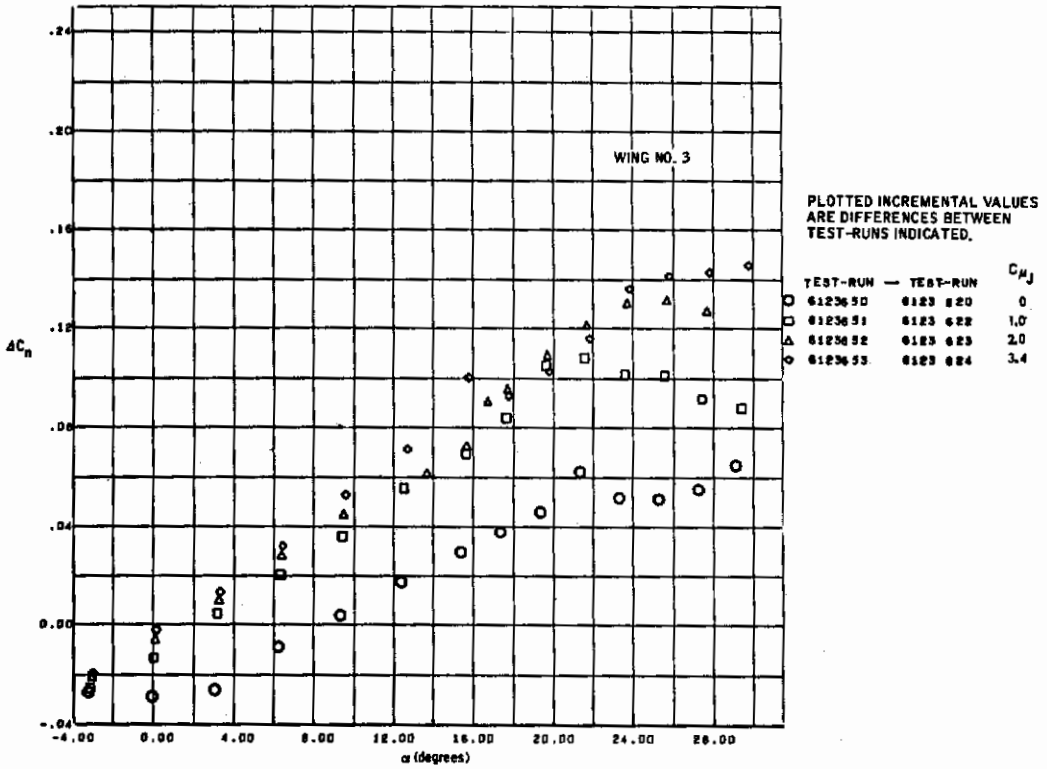

Figure 8.1-48. MF/VT Spoiler Effectiveness with Triple-Slotted Flap at 60 Degrees, δ_T = 90 Degrees, Yawing Moments, δ_{SP} = 60 Degrees

8.2 EMPENNAGE CONTROLS

Elevator and rudder effectiveness, with and without blowing, was obtained from the isolated tail tests, GDLST 611. The full-span, 35-percent-chord elevator was tested at deflection angles from + 10 to -50 degrees. The rudder, on a T-tail, had a 30-percent chord and was tested at deflection angles from 0 to -50 degrees.

Basic data concerning the effects of control surface blowing were obtained from the Convair Digigraphics System and are presented in Figures 8.2-1 through 8.2-6. The lift increment due to blowing is given as a function of angle of attack or sideslip; these increments are from the deflected control surface with no blowing. These figures indicate that the lift increment due to blowing varies with angle of attack and that blowing does not increase the angle of attack for maximum lift.

An attempt was made to determine the blowing momentum coefficient required to obtain theoretical flap lift effectiveness for the elevator control. Theoretical lift effectiveness can be expressed in a number of different forms, but in the DATCOM methodology, potential flow over the flap is considered to be achieved when α_δ reaches its theoretical value. From DATCOM, $(\alpha_\delta)_{theory} = 0.71$ for a 35-percent-chord flap. Values for α_δ were obtained from the test data at the various blowing rates and elevator deflections from the relationship:

$$\alpha_\delta = \frac{\Delta C_L}{C_{L_{\delta_H}} \delta_e}$$

where:

ΔC_L = lift increment due to the elevator

$C_{L_{\alpha_H}}$ = vertical tail lift curve slope with undeflected elevator ($0.0647\ deg^{-1}$)

δ_e = elevator deflection

The data is shown in Figure 8.2-7, where the α_δ values determined from the test data are plotted as functions of elevator blowing momentum coefficient.

Figure 8.2-7 shows that potential flow flap lift increments at the larger elevator deflections were not achieved for blowing rates normally associated with BLC. The elevator blowing slot used for these tests was a rather crude arrangement, and improved performance could possibly be obtained by tailoring the slot geometry. From a practical standpoint, however, control surface blowing becomes less attractive if critical tolerances must be maintained in the blowing systems.

In summary, the preceding sections showed that the large nose-down pitching moments and large changes in downwash angle inherent with the powered-lift systems will require the horizontal tail to be a powerful moment producer for trim. It must also operate over a large angle-of-attack range without stalling, so the need for some means of augmenting tail capabilities is readily apparent. Devices of this category tested during this program were a Krueger type leading-edge flap and elevator blowing. (A lift curve for the Krueger flap was shown in Figure 6.1-4). The Krueger flap was the only device tested that extends stall angle of attack of the control surface, and will be required on the horizontal tail. Since tests of the elevator blowing systems produced inconsistent results, the updated baseline designs have been configured without control surface blowing (at the expense of some increase in horizontal tail size).

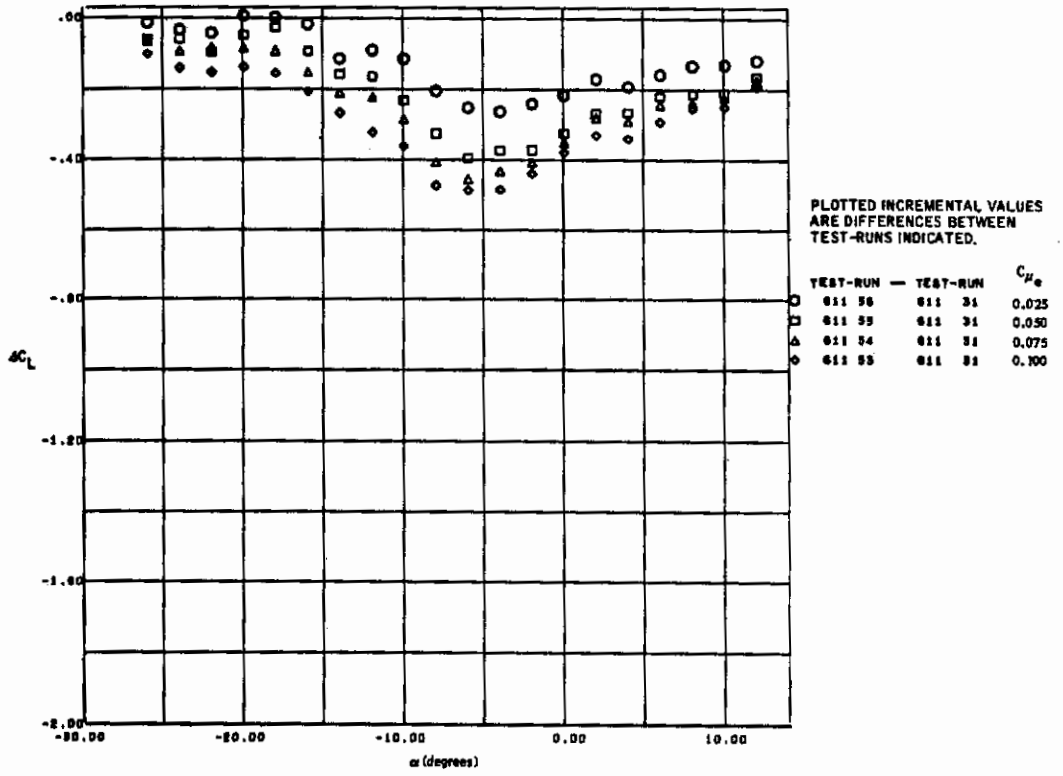

Figure 8.2-1. Effect of BLC Blowing on Elevator Effectiveness, δ_e = -20 Degrees

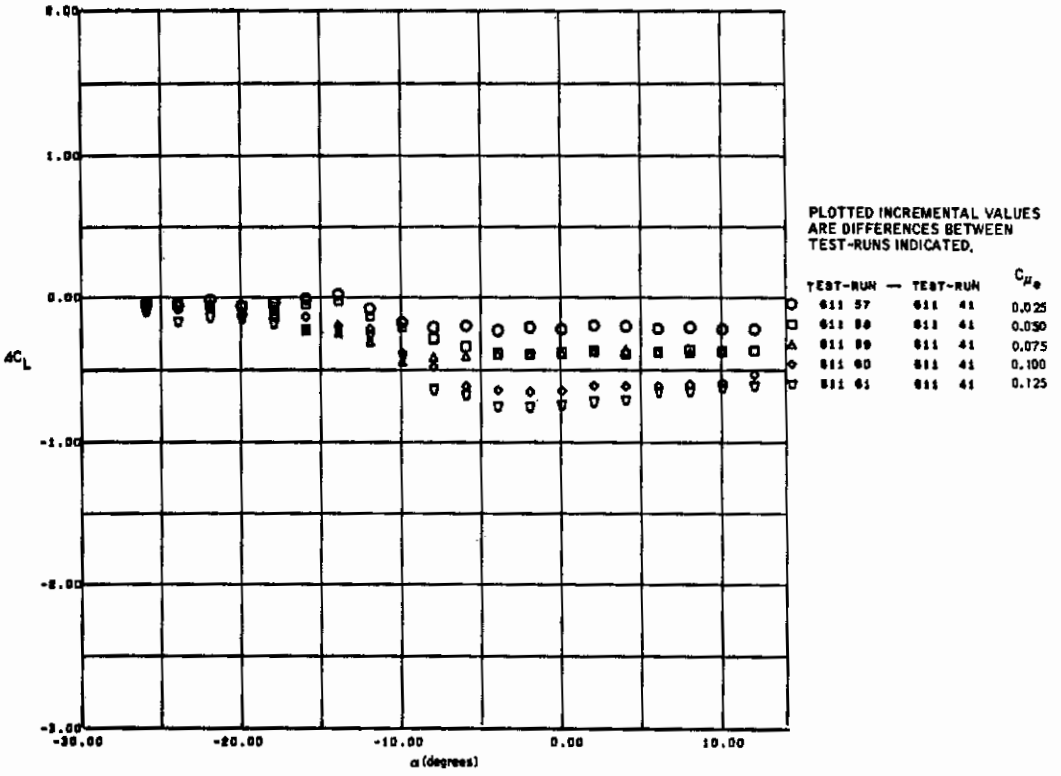

Figure 8.2-2. Effect of BLC Blowing on Elevator Effectiveness, δ_e = -30 Degrees

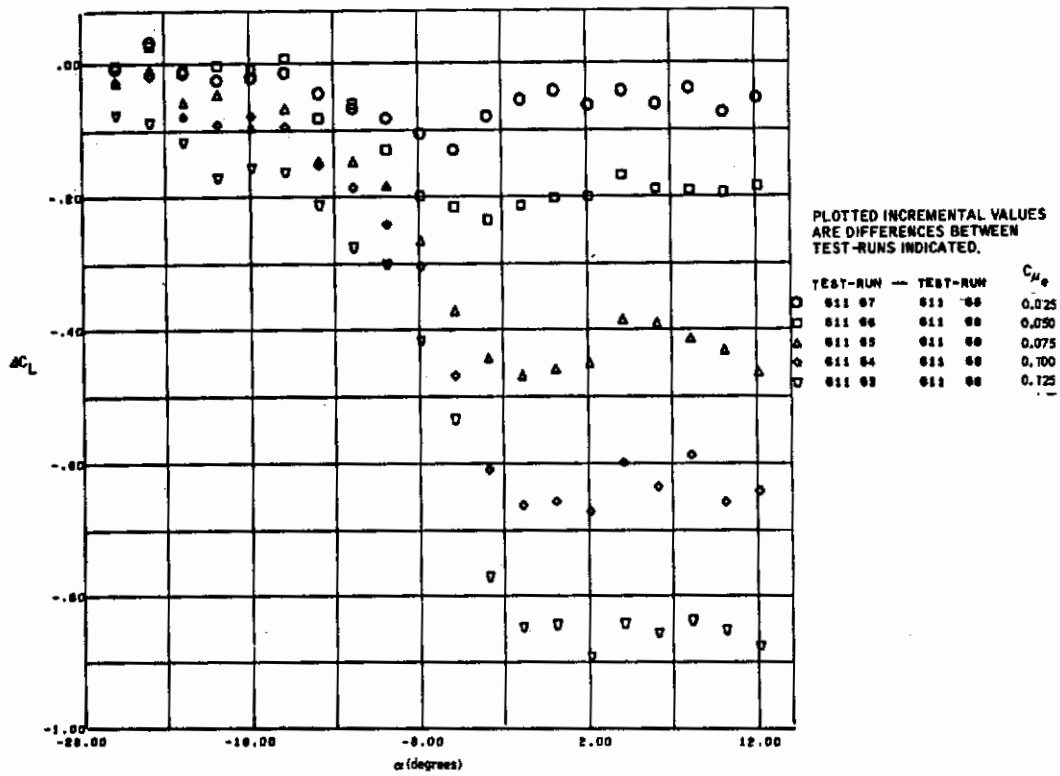

Figure 8.2-3. Effect of BLC Blowing on Elevator Effectiveness, δ_e = -50 Degrees

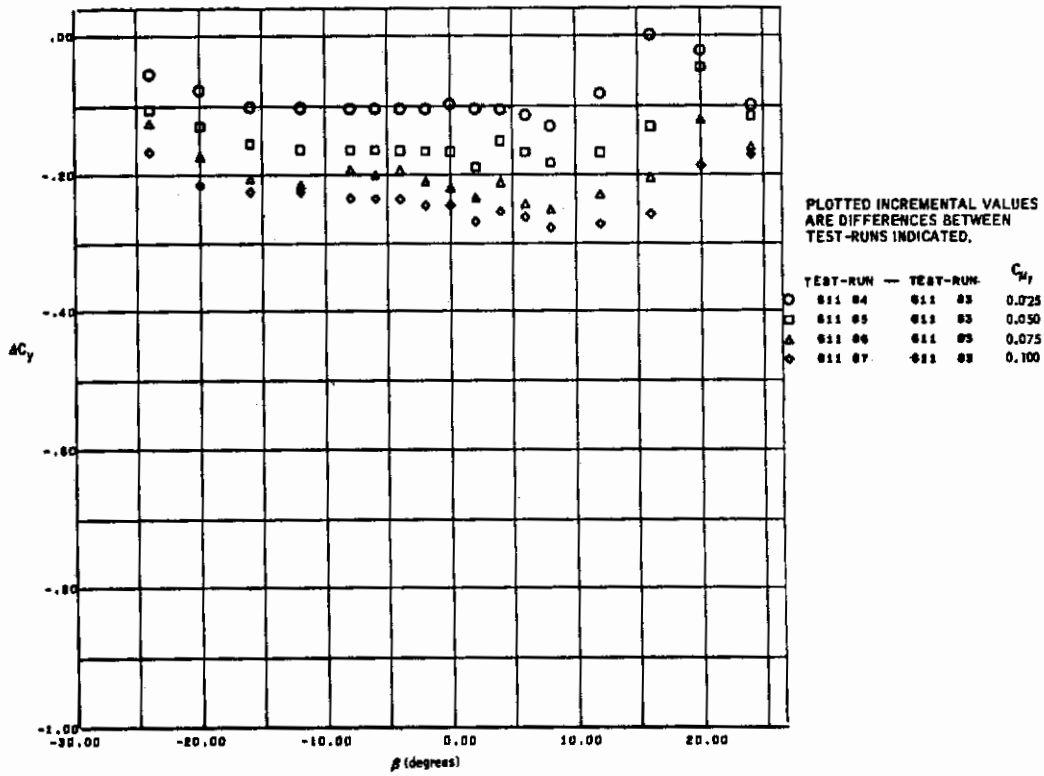

Figure 8.2-4. Effect of BLC Blowing on Rudder Effectiveness, δ_r = -20 Degrees

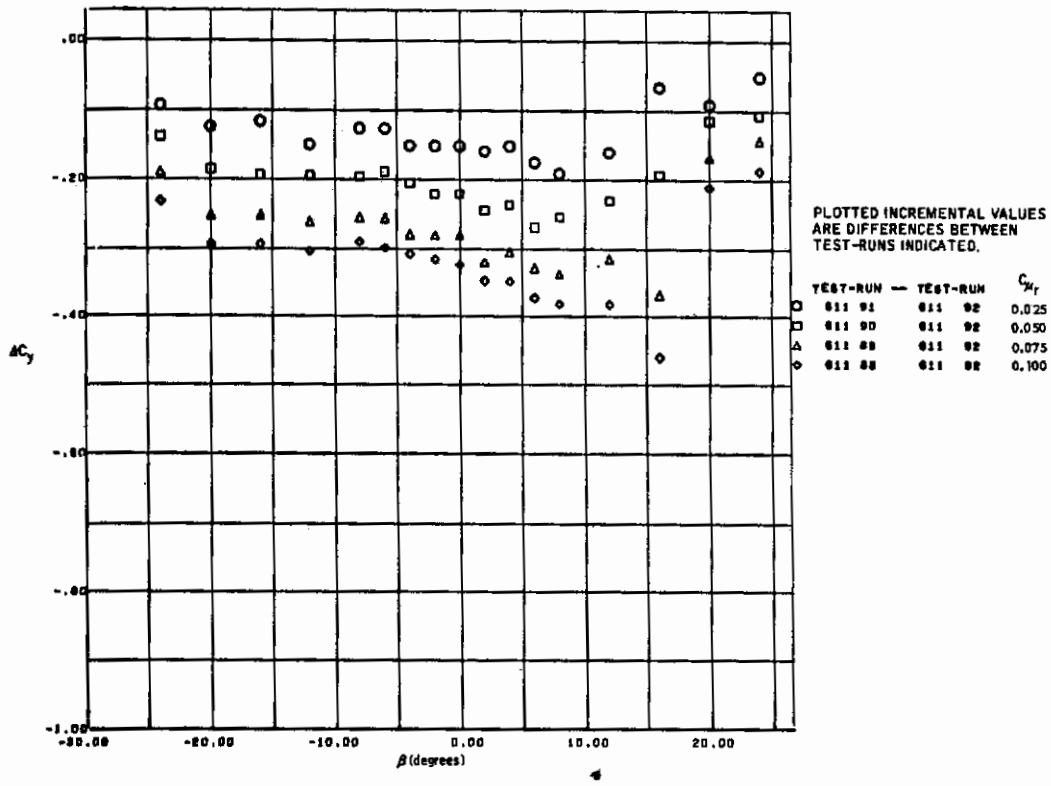

Figure 8.2-5. Effect of BLC Blowing on Rudder Effectiveness, δ_r = -30 Degrees

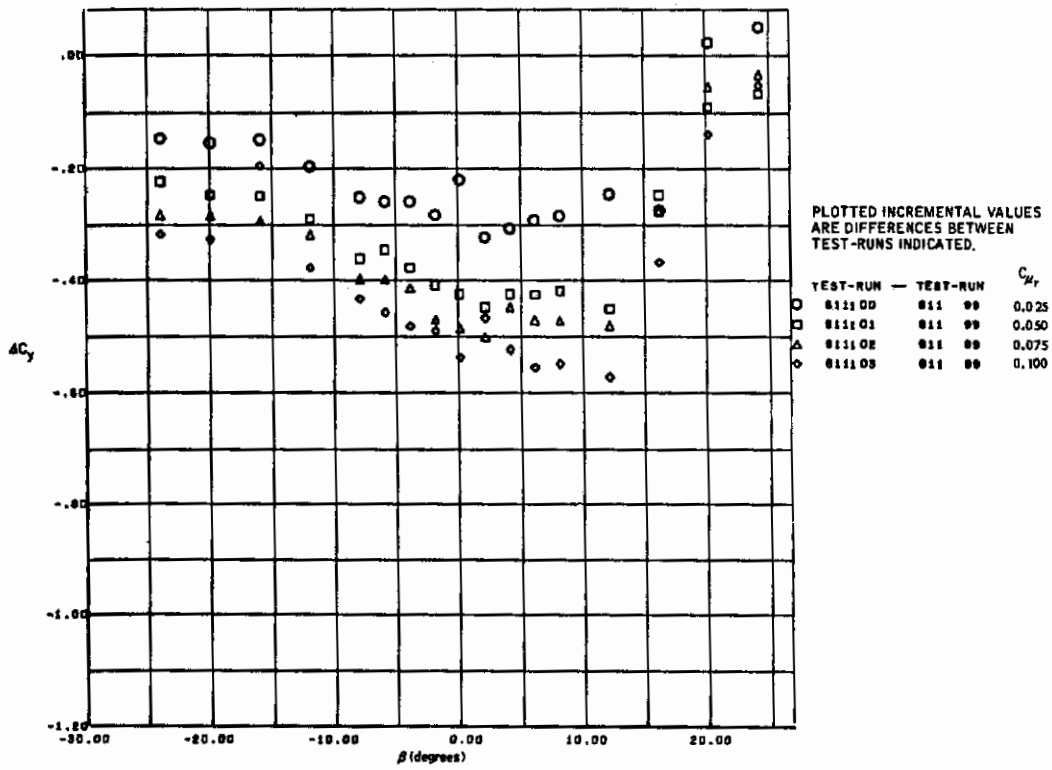

Figure 8.2-6. Effect of BLC Blowing on Rudder Effectiveness, δ_r = -50 Degrees

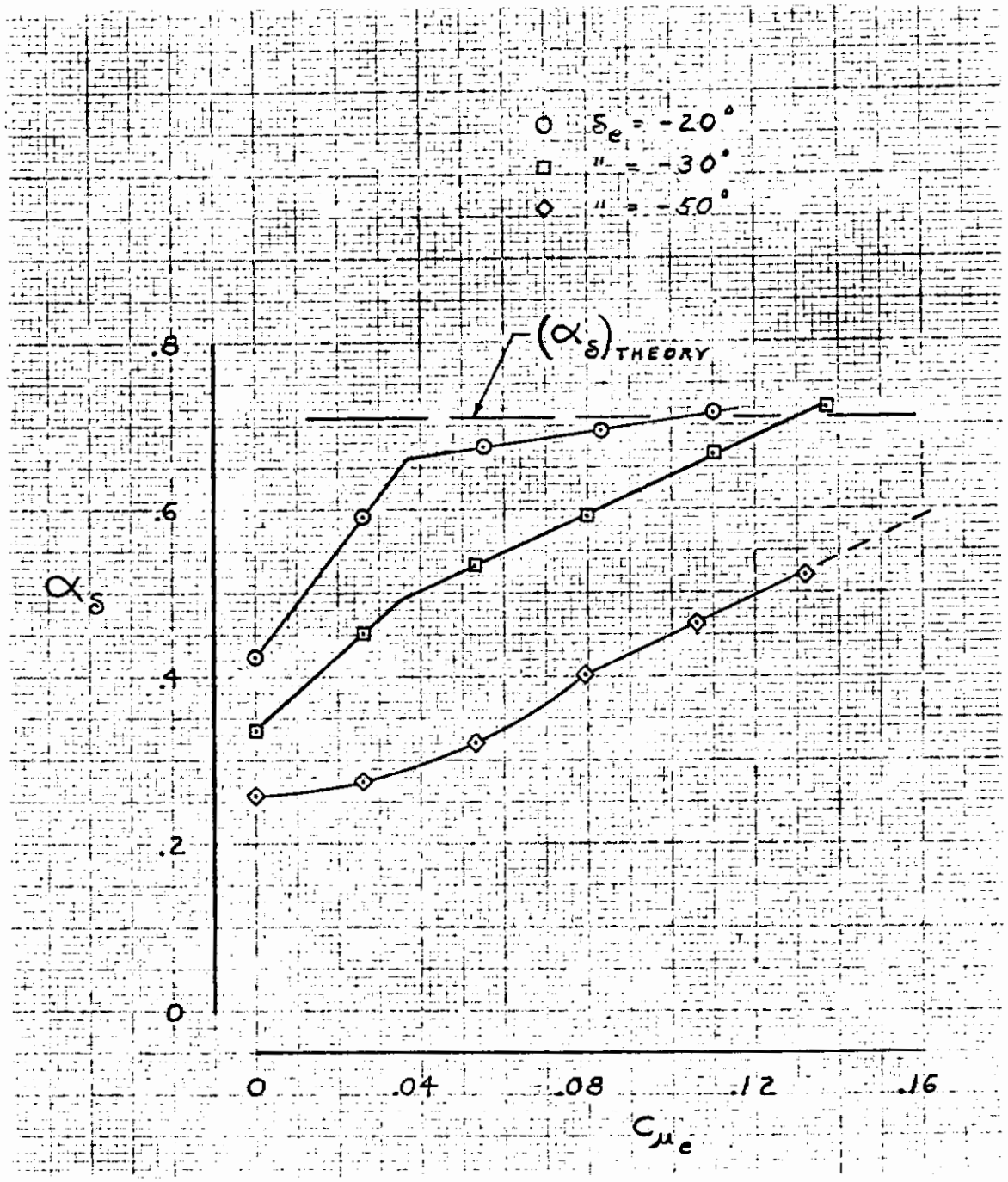

Figure 8.2-7. Blowing Momentum Coefficient Required to Achieve Theoretical Flap Lift Effectiveness, α_H = 0 Degrees

8.3 SPECIAL CONTROL DEVICES

Some limited testing was accomplished with differential leading-edge blowing to evaluate the capability of this scheme to produce rolling and yawing moments. The resulting data is shown in Figures 8.3-1 and 8.3-2. Yawing moments resulting from differential leading-edge blowing are quite small, but large rolling moments can be produced, and it appears that this arrangement would not be a practical solution for controlling engine-out rolling moments.

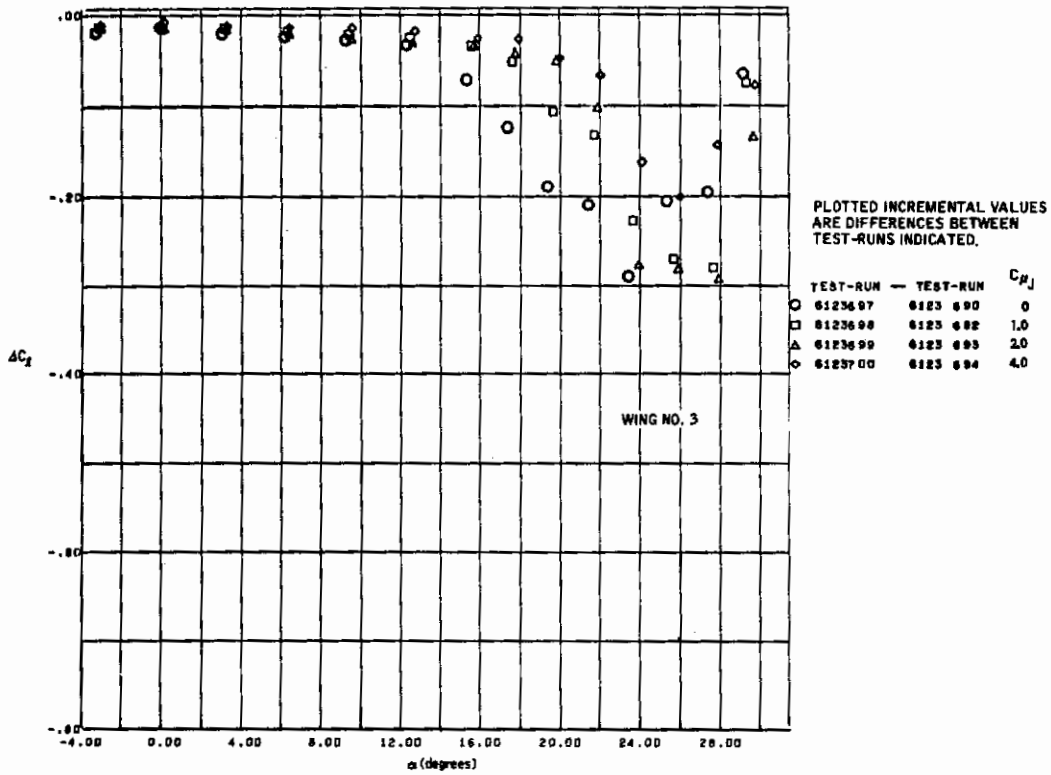

Figure 8.3-1. Effect of Differential Leading-Edge Blowing, Rolling Moments, $C_{\mu_{LE\ left}} = 0$, $C_{\mu_{LE\ right}} = 0.10$

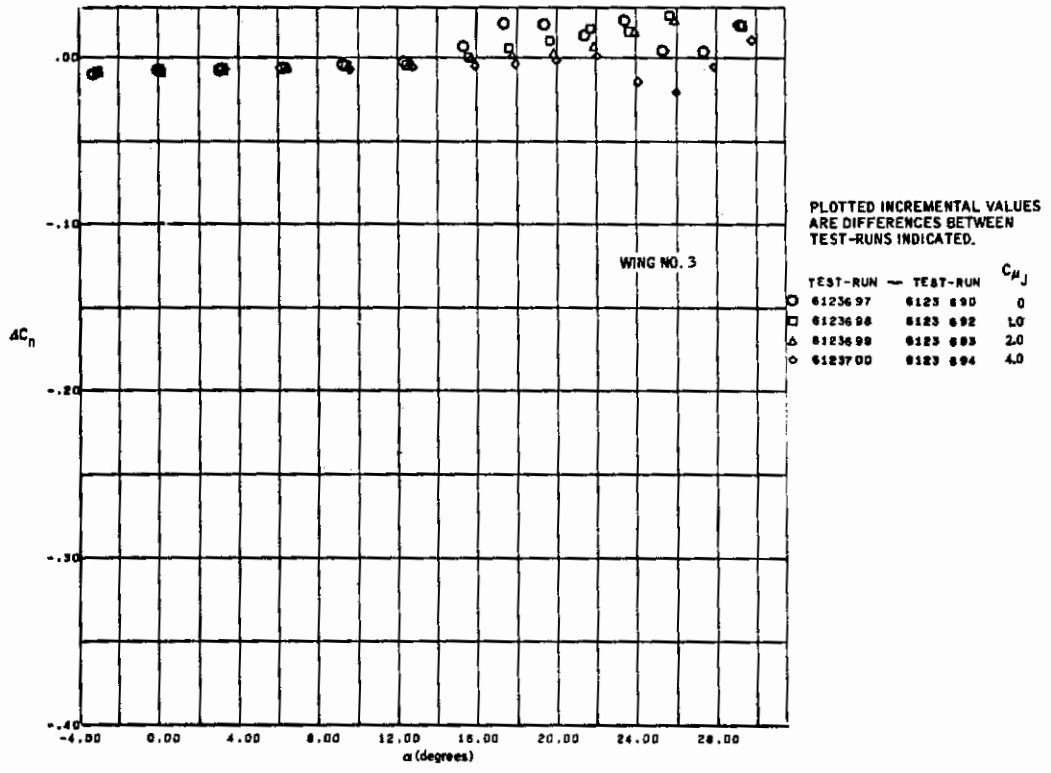

Figure 8.3-2. Effect of Differential Leading-Edge Blowing, Yawing Moments, $C_{\mu_{L\ left}} = 0$, $C_{\mu_{L\ right}} = 0.10$

SECTION 9

ASYMMETRIC POWER EFFECTS

The effects of asymmetric thrust were investigated on the EBF and MF/VT concepts to determine the magnitude of the resulting unbalanced rolling and yawing moments. It was assumed that these moments could be calculated for the IBF concept simply by multiplying the unbalanced force by its appropriate moment arm.

The basic data is shown in Figures 9.0-1 through 9.0-22, in which the incremental rolling and yawing moments between the three- and four-engine cases are shown as a function of angle of attack. The curves also include engine-out data with a lateral control device (usually a spoiler) deflected to its maximum capability. The basic high-lift system used on all configurations was the triple-slotted flap at 60 degrees of deflection. Configuration variables included a variation in wing sweep from 12.5 to 25 degrees for both the EBF and MF/VT concepts. The EBF was also tested with thrust deflectors and with a partial span flap and blown aileron deflected 50 degrees. Primary variable for the MF/VT concept was thrust deflection angle, which was tested at 30, 60 and 90 degrees.

The data shows that the spoiler had more than enough capability to balance engine-out rolling moments on all configurations tested. Actually, only about one-half the rolling moments available from the spoiler would have been required to trim the asymmetric thrust moment. On the EBF configuration, the yawing moment generated by the lateral control was more than adequate to trim the engine-out yawing moments.

Lateral control available from the blown ailerons at 50 degrees of deflection was not sufficient to trim the asymmetric thrust rolling moments (Figure 9.0-9). Figure 9.0-11 indicates that the asymmetric thrust rolling moments are about the same magnitude for partial and full-span flaps.

On the MF/VT concept (Figures 9.0-15 through 9.0-22), directional control requirements are most critical at 30 degrees of thrust deflection. As thrust deflection angle is increased to 90 degrees, however, the engine-out rolling moments become comparable in magnitude to those experienced on the EBF.

As shown in Figure 9.0-23, it was found that the spanwise center of pressure location of the engine-out rolling moment on the EBF is approximately at the spanwise station of the inoperative engine.

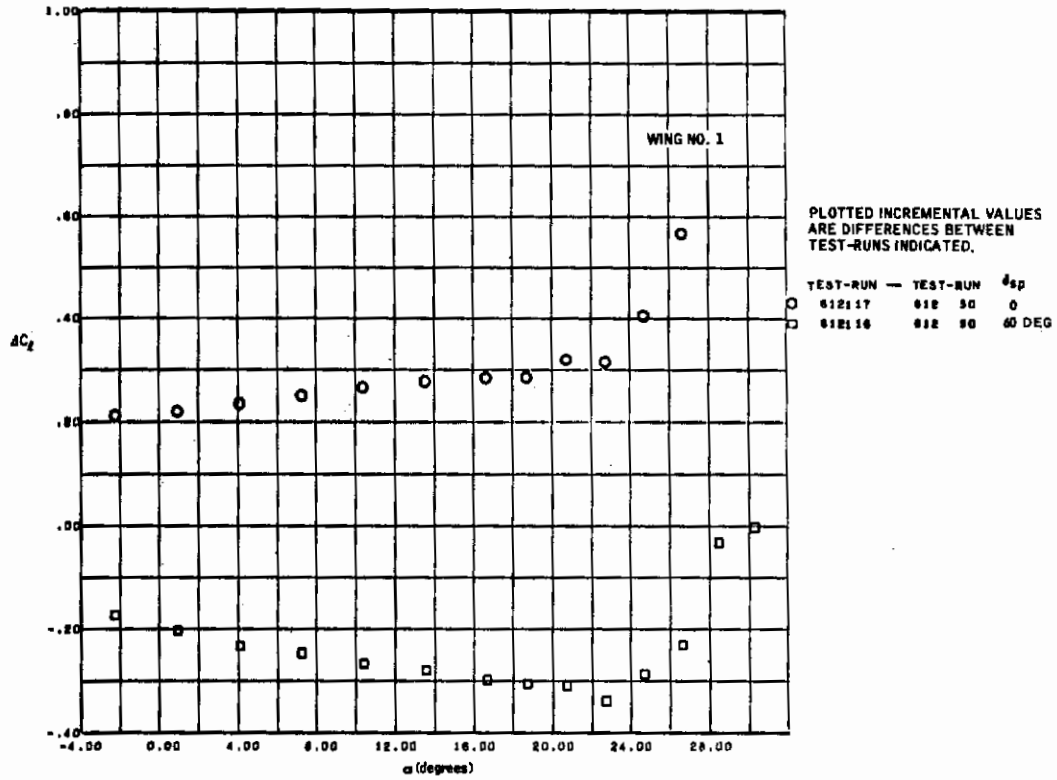

Figure 9.0-1. Engine-Out Rolling Moments with EBF Triple-Slotted Flap at 60 Degrees

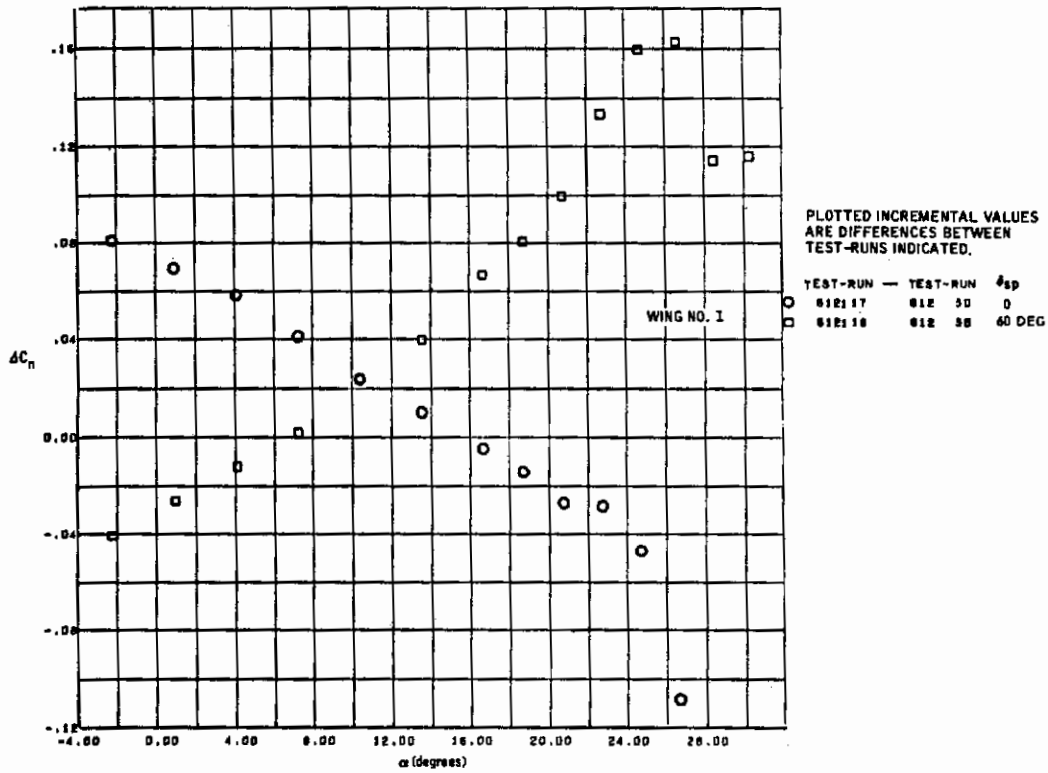

Figure 9.0-2. Engine-Out Yawing Moments with EBF Triple-Slotted Flap at 60 Degrees

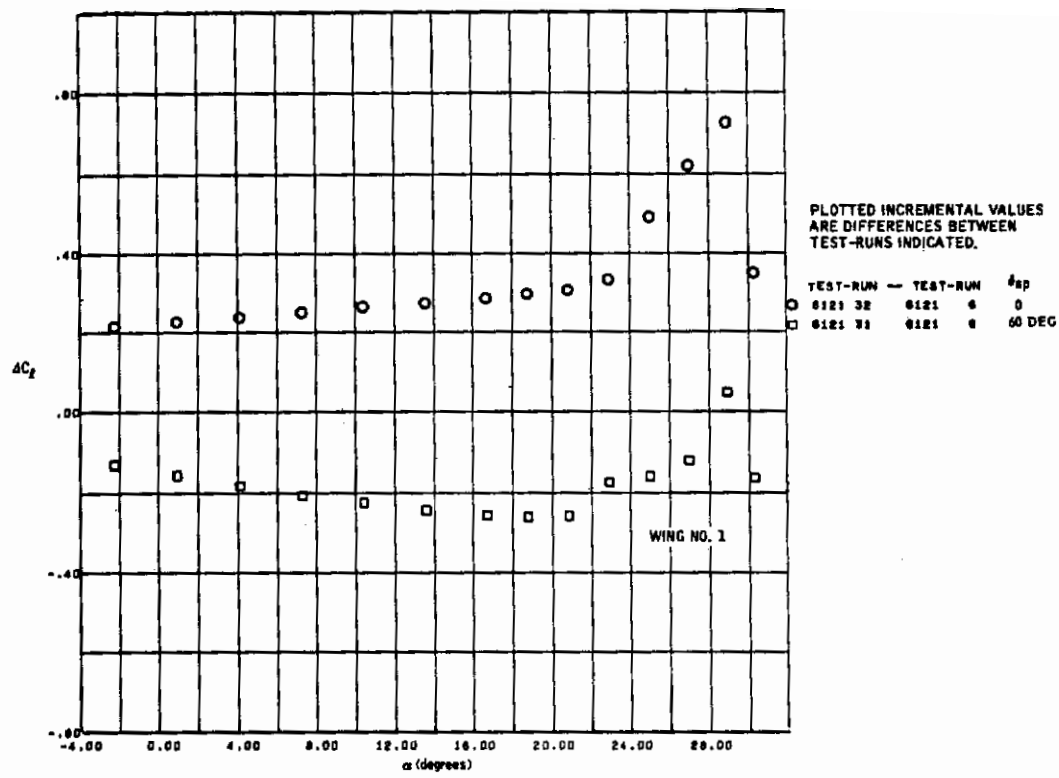

Figure 9.0-3. Engine-Out Rolling Moments with EBF Triple-Slotted Flap at 60 Degrees, Engine Location B

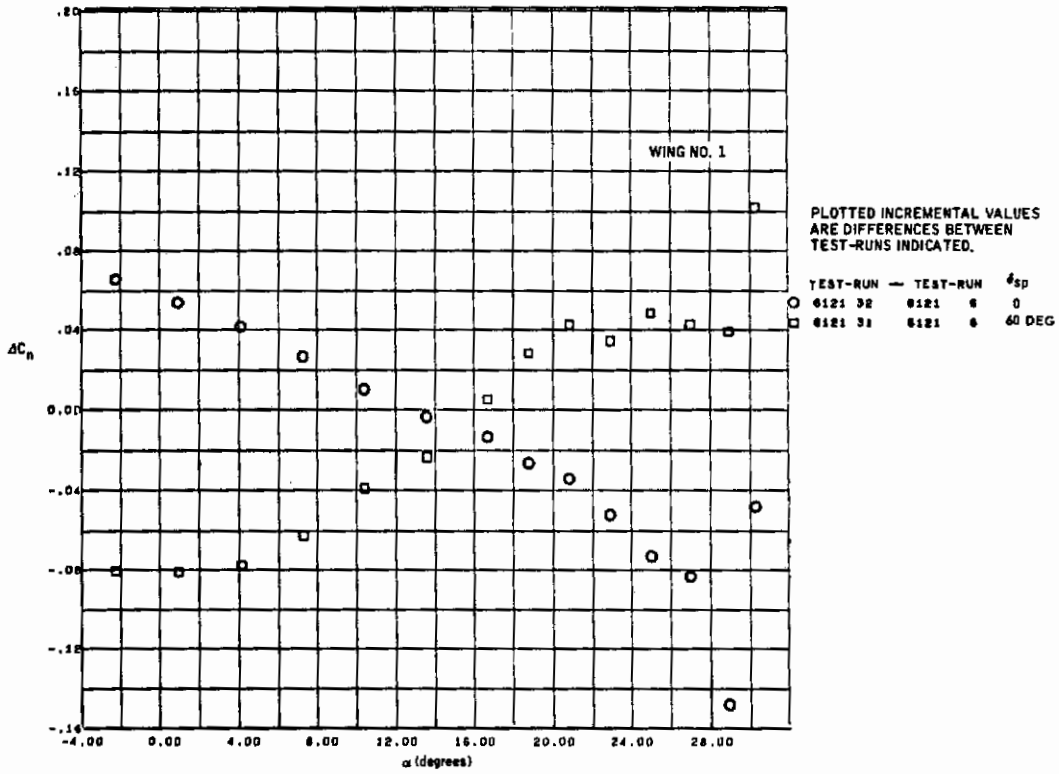

Figure 9.0-4. Inboard Engine-Out Yawing Moments with EBF Triple-Slotted Flap at 60 Degrees, Engine Location B

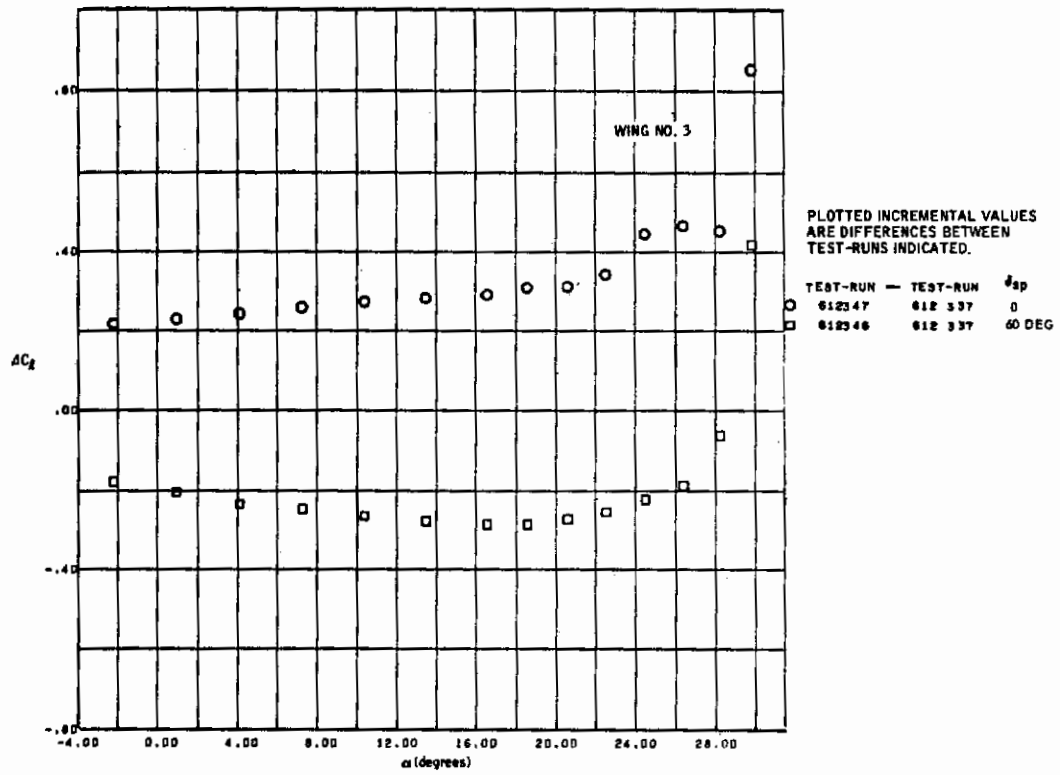

Figure 9.0-5. Engine-Out Rolling Moments with EBF Triple-Slotted Flap at 60 Degrees, δ_T = -9 Degrees

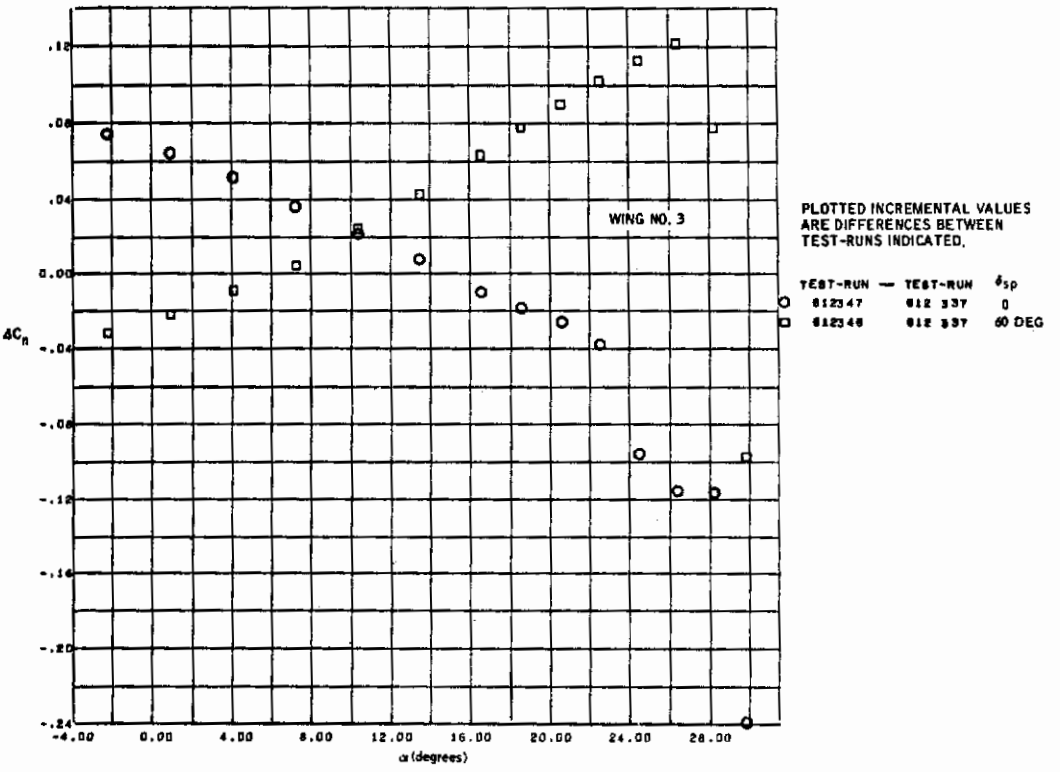

Figure 9.0-6. Engine-Out Yawing Moments with EBF Triple-Slotted Flap at 60 Degrees, δ_T = -9 Degrees

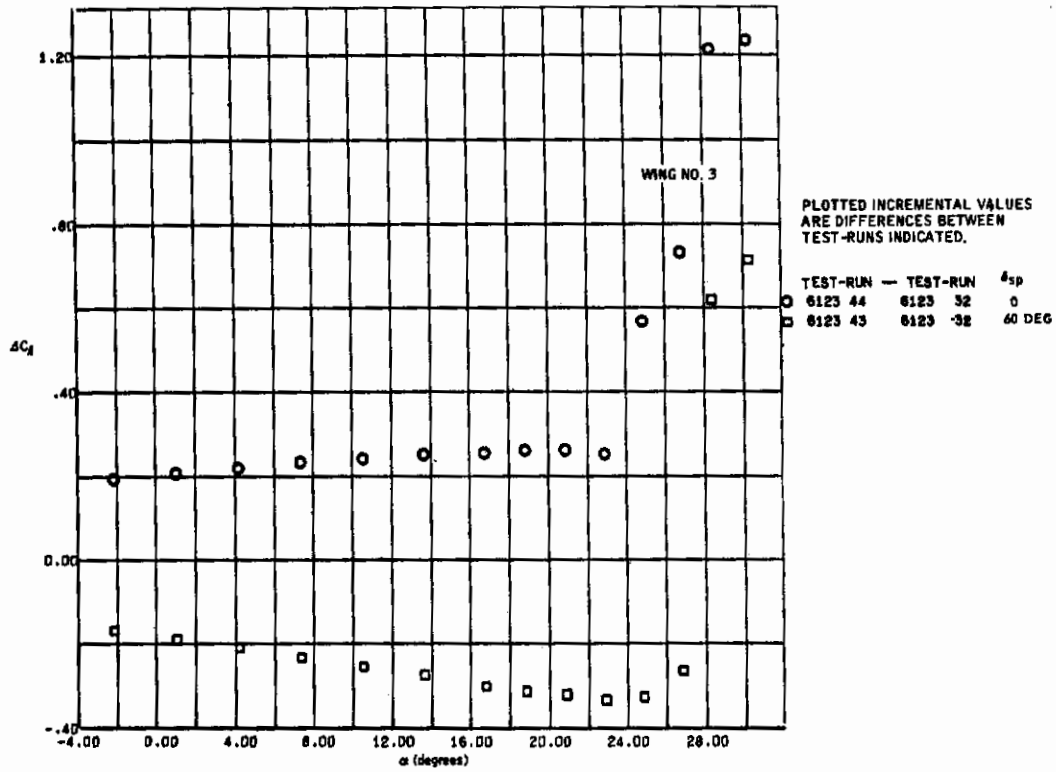

Figure 9.0-7. Engine-Out Rolling Moments with EBF Triple-Slotted Flap at 60 Degrees

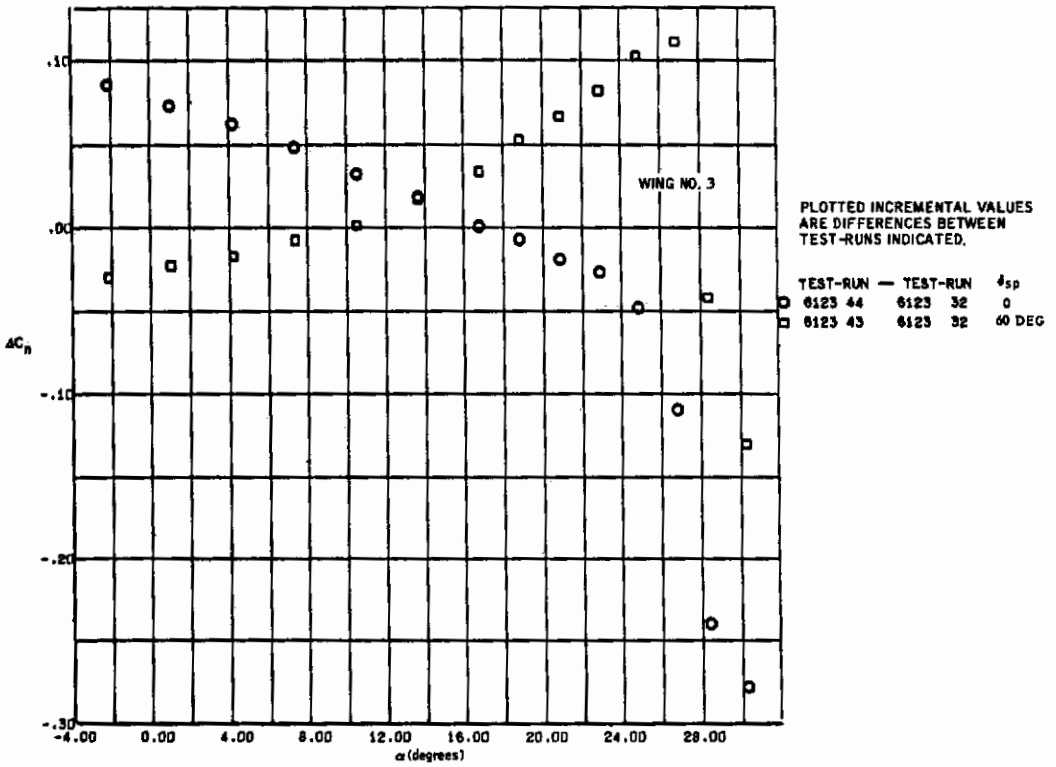

Figure 9.0-8. Engine-Out Yawing Moments with EBF Triple-Slotted Flap at 60 Degrees

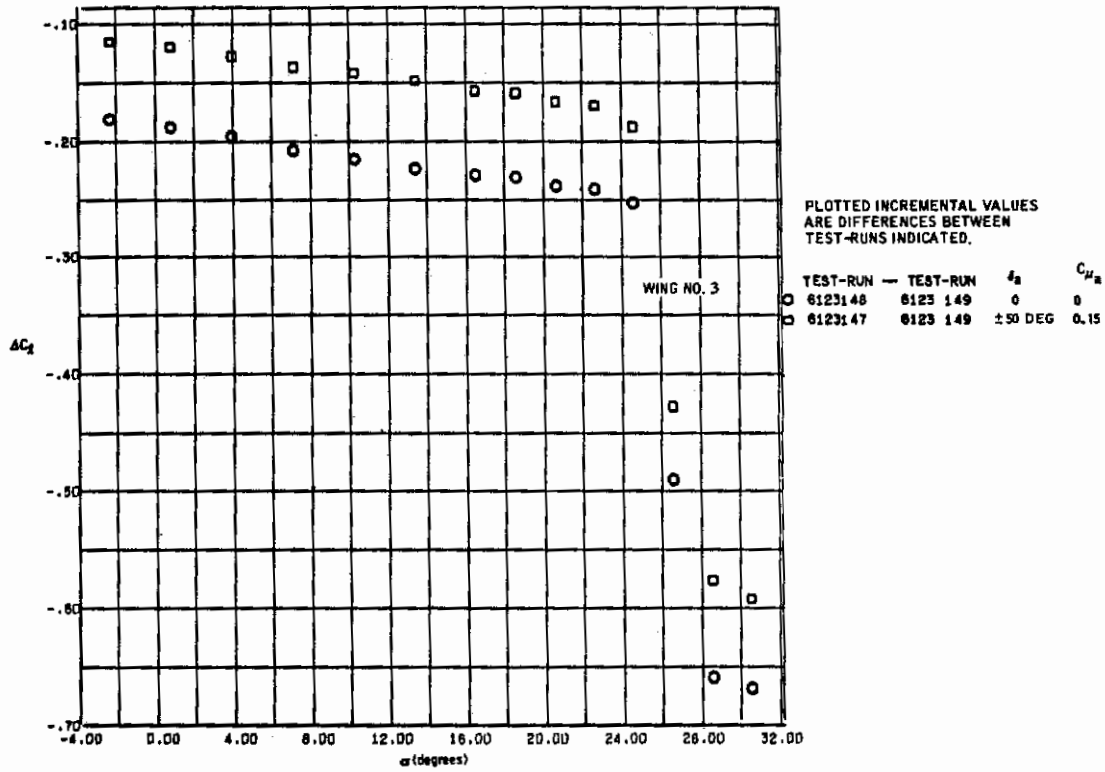

Figure 9.0-9. Engine-Out Rolling Moments with EBF Partial-Span Flap with Aileron, Triple-Slotted Flap at 60 Degrees

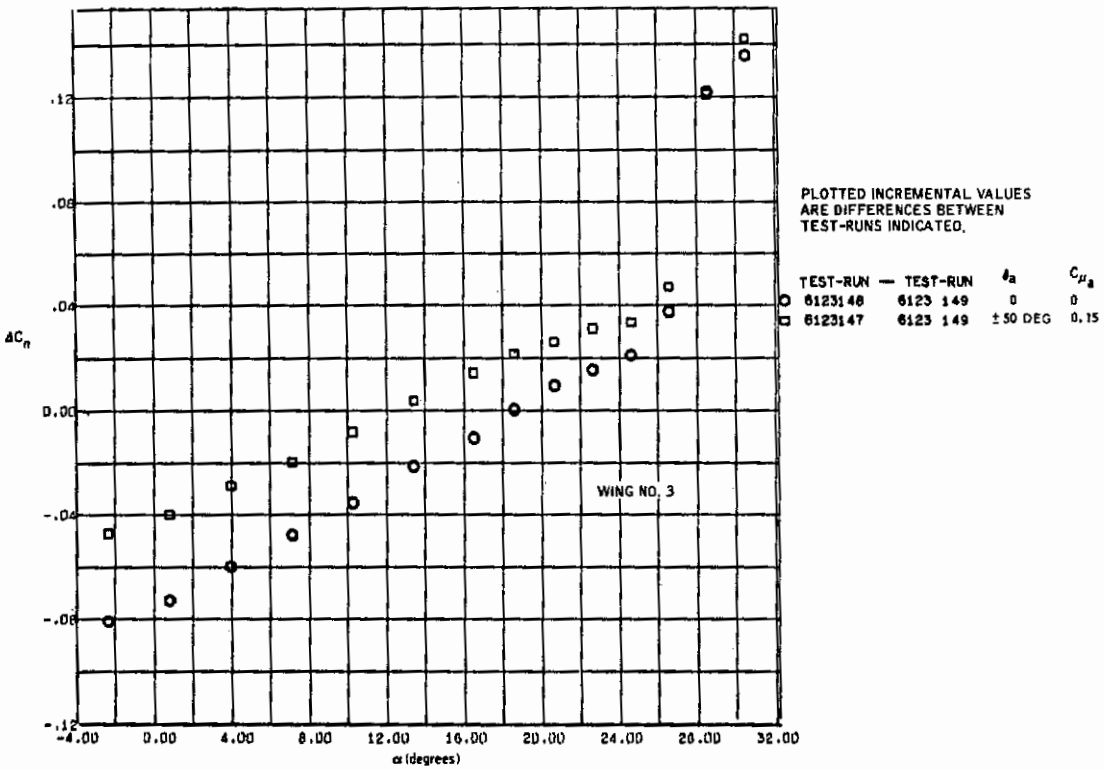

Figure 9.0-10. Engine-Out Yawing Moments with EBF Partial-Span Flap with Aileron, Triple-Slotted Flap at 60 Degrees

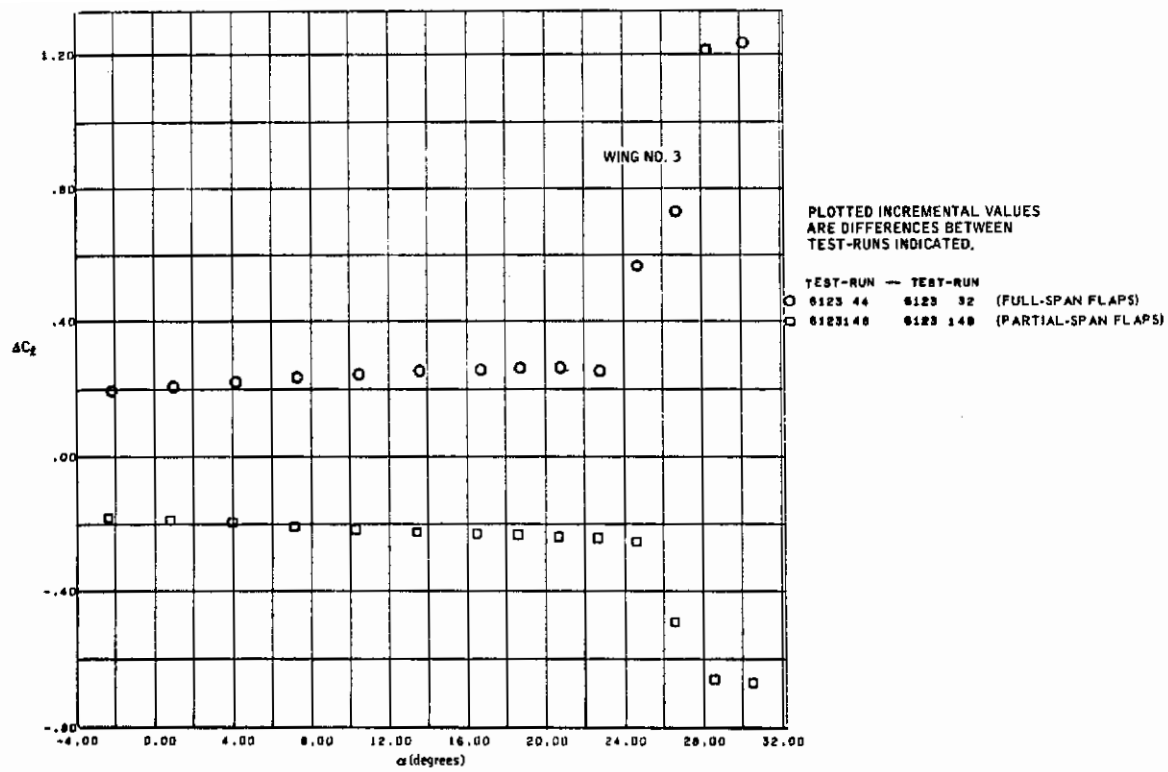

Figure 9.0-11. Comparison of Engine-Out Rolling Moments using Partial- and Full-Span Flaps with EBF Triple-Slotted Flap at 60 Degrees

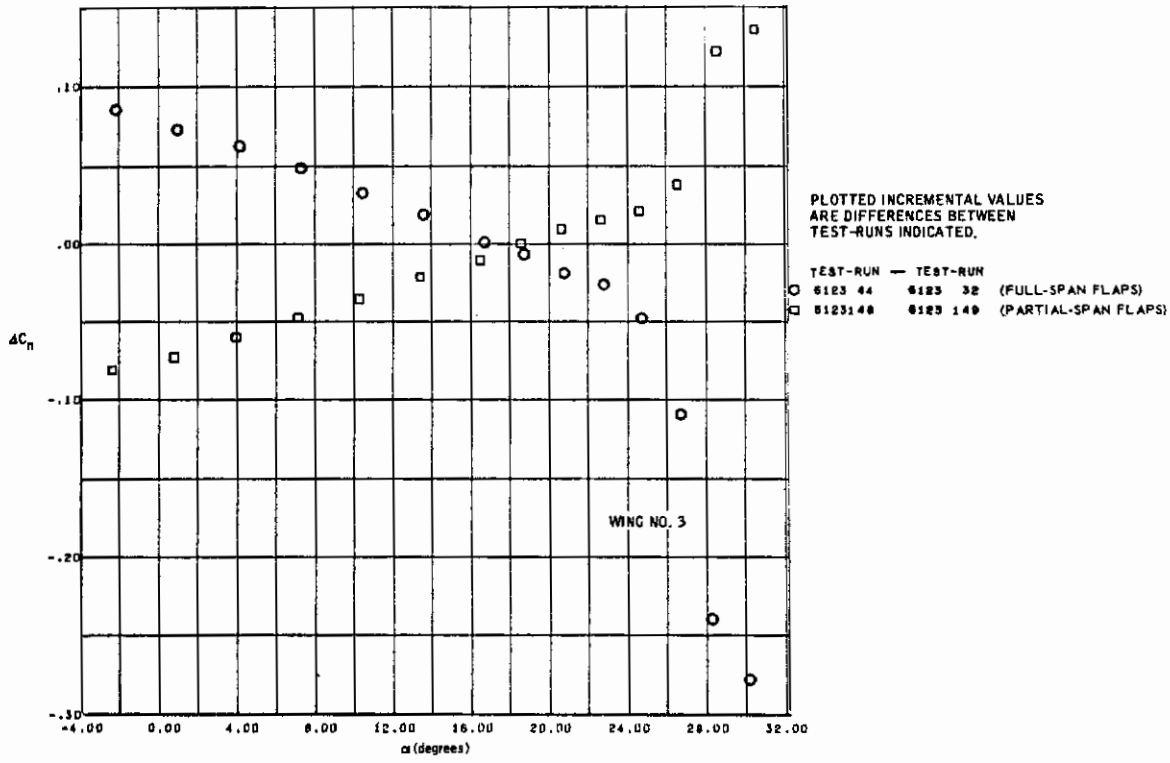

Figure 9.0-12. Comparison of Engine-Out Yawing Moments using Partial- and Full-Span Flaps with EBF Triple-Slotted Flap at 60 Degrees

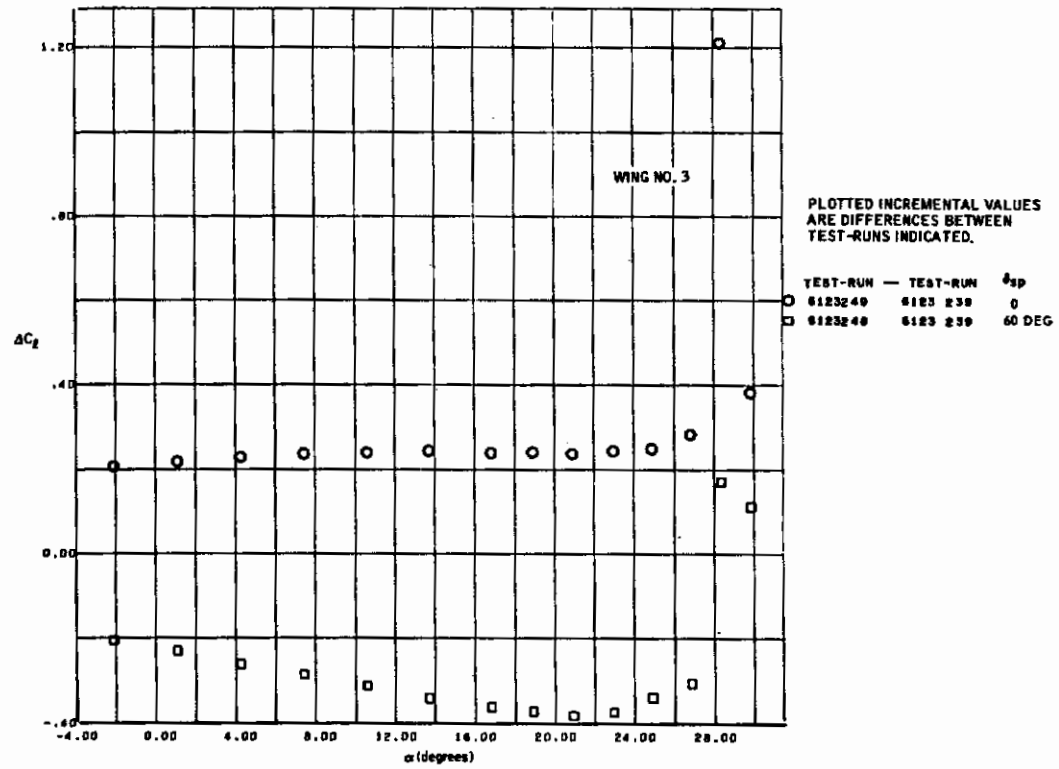

Figure 9.0-13. Engine-Out Rolling Moments with EBF Triple-Slotted Flap at 60 Degrees, δ_T = -12 Degrees

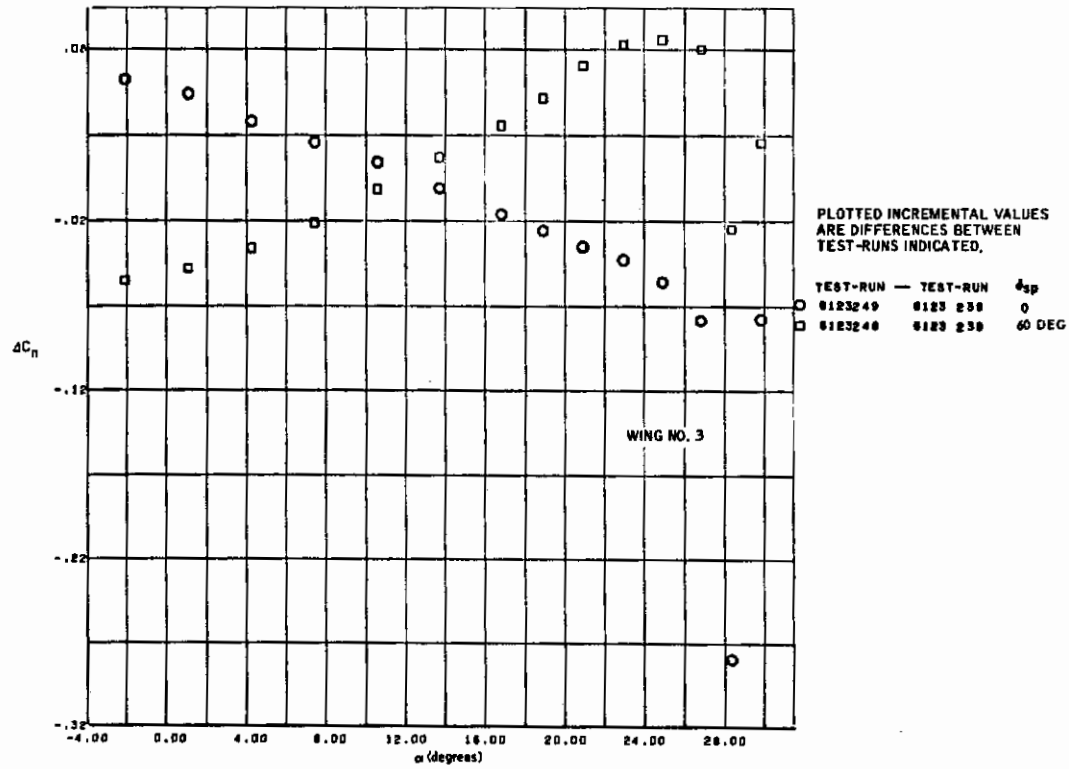

Figure 9.0-14. Engine-Out Yawing Moments with EBF Triple-Slotted Flap at 60 Degrees, δ_T = -12 Degrees

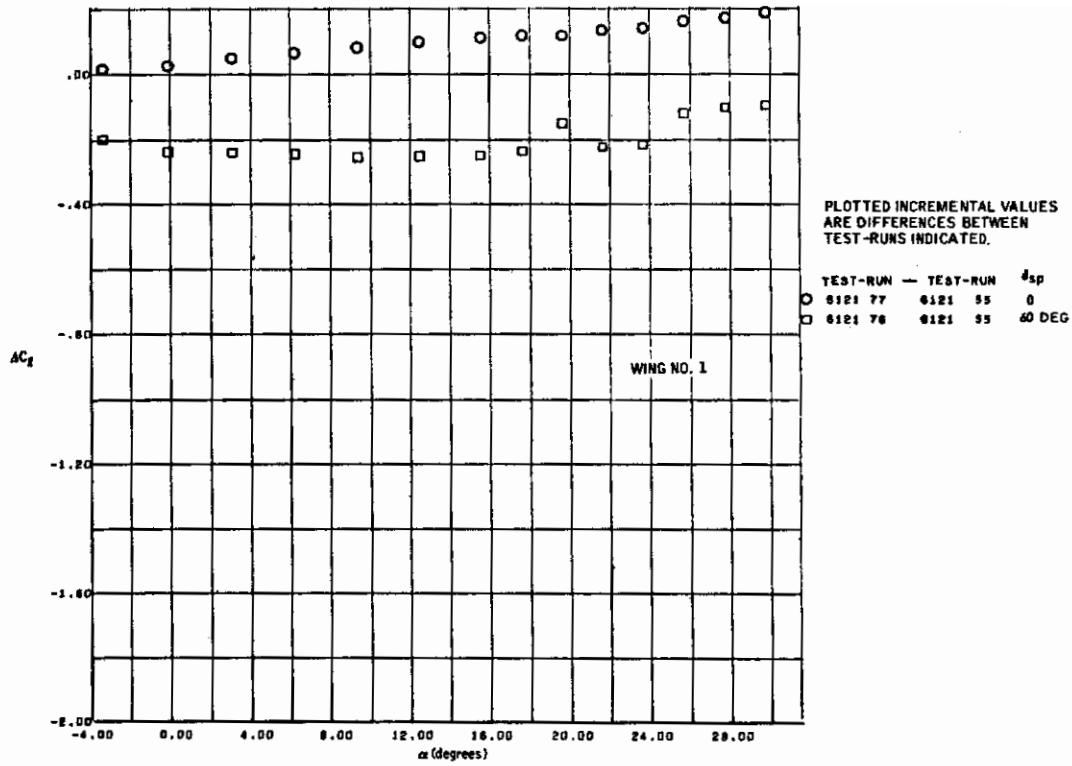

Figure 9.0-15. Engine-Out Rolling Moments with MF/VT Triple-Slotted Flap at 60 Degrees, δ_T = 30 Degrees

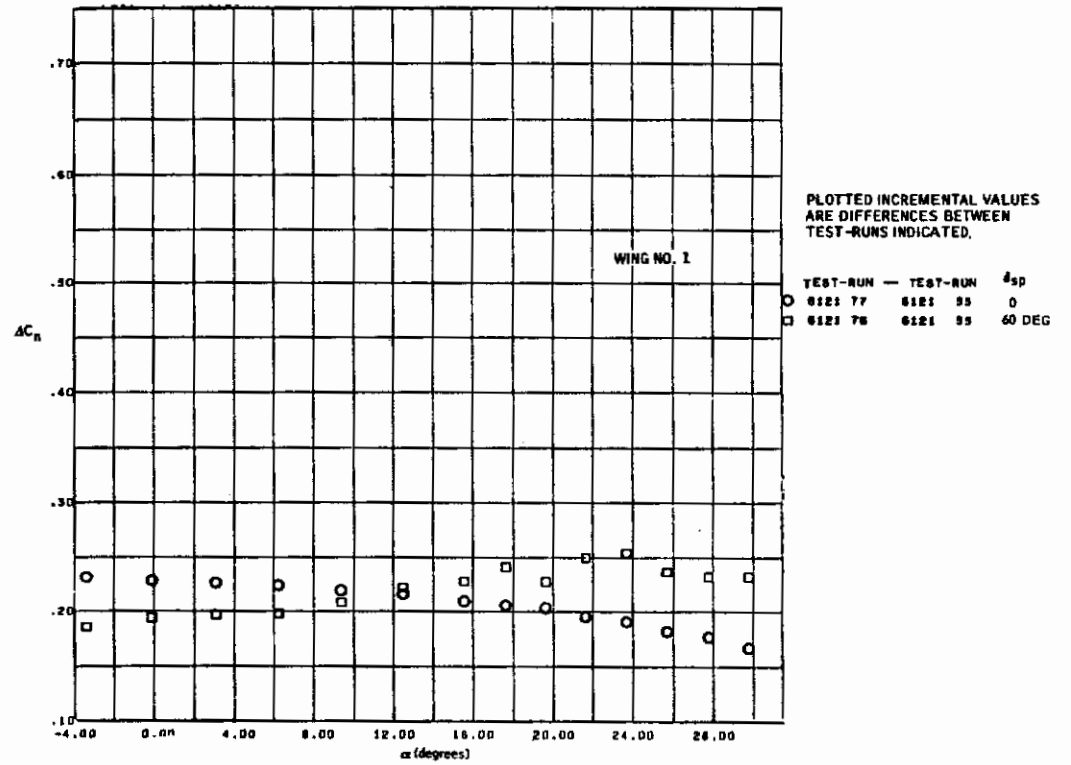

Figure 9.0-16. Engine-Out Yawing Moments with MF/VT Triple-Slotted Flap at 60 Degrees, δ_T = 30 Degrees

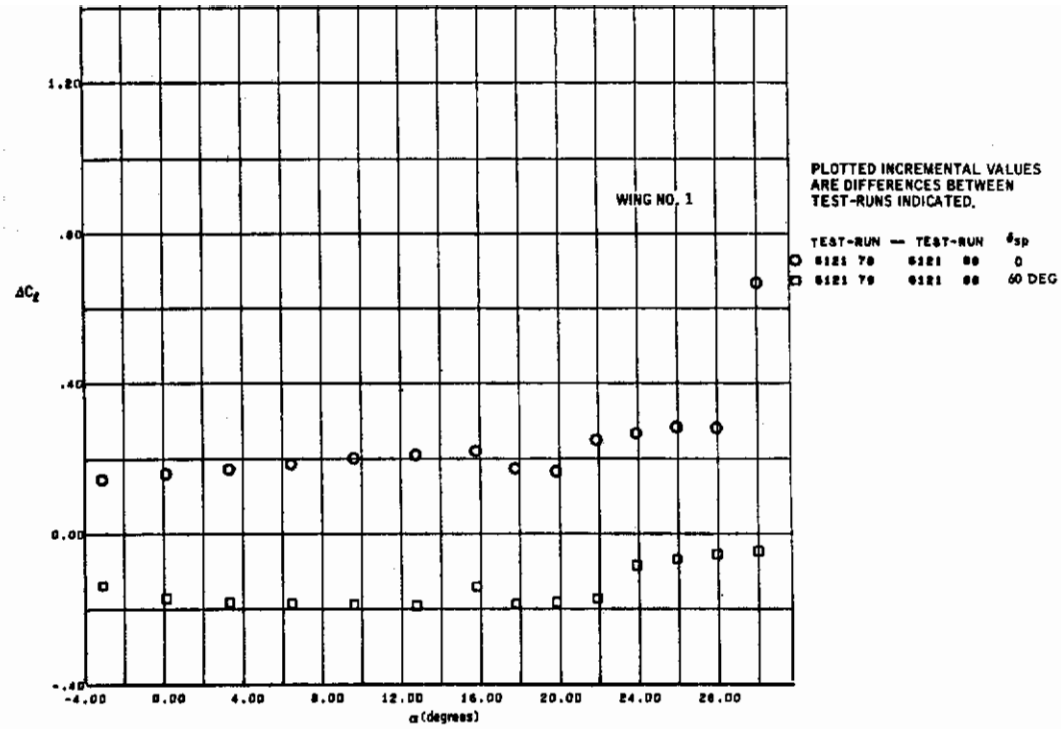

Figure 9.0-17. Engine-Out Rolling Moments with MF/VT Triple-Slotted Flap at 60 Degrees, δ_T = 60 Degrees

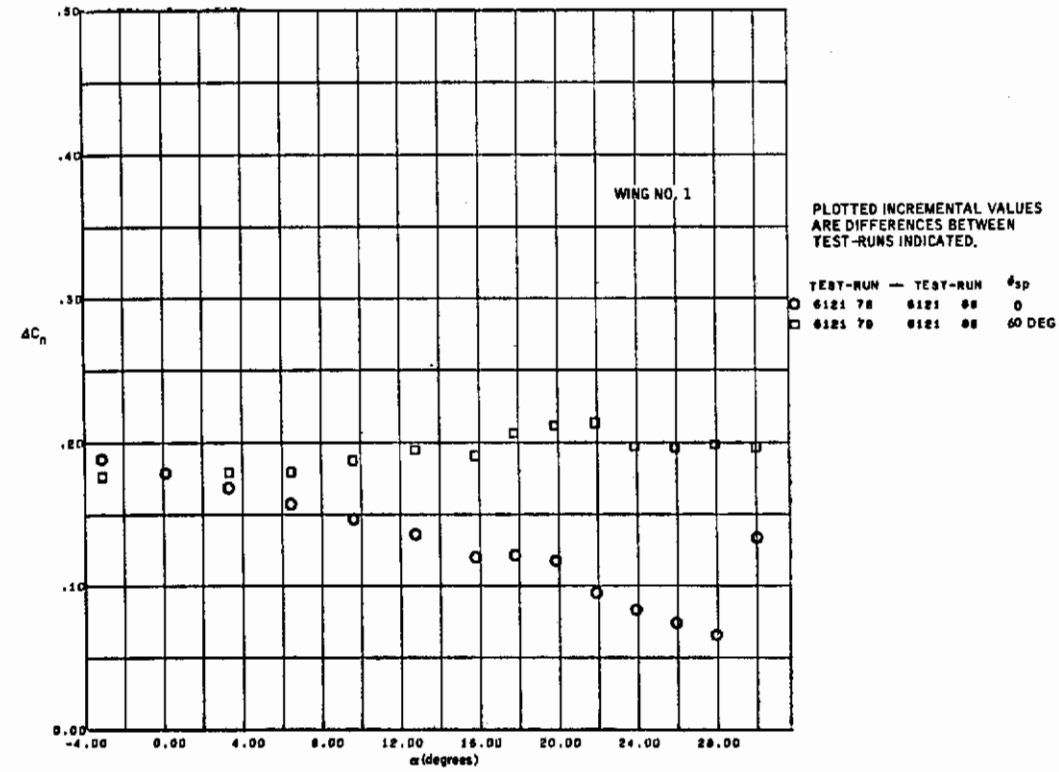

Figure 9.0-18. Engine-Out Yawing Moments with MF/VT Triple-Slotted Flap at 60 Degrees, δ_T = 60 Degrees

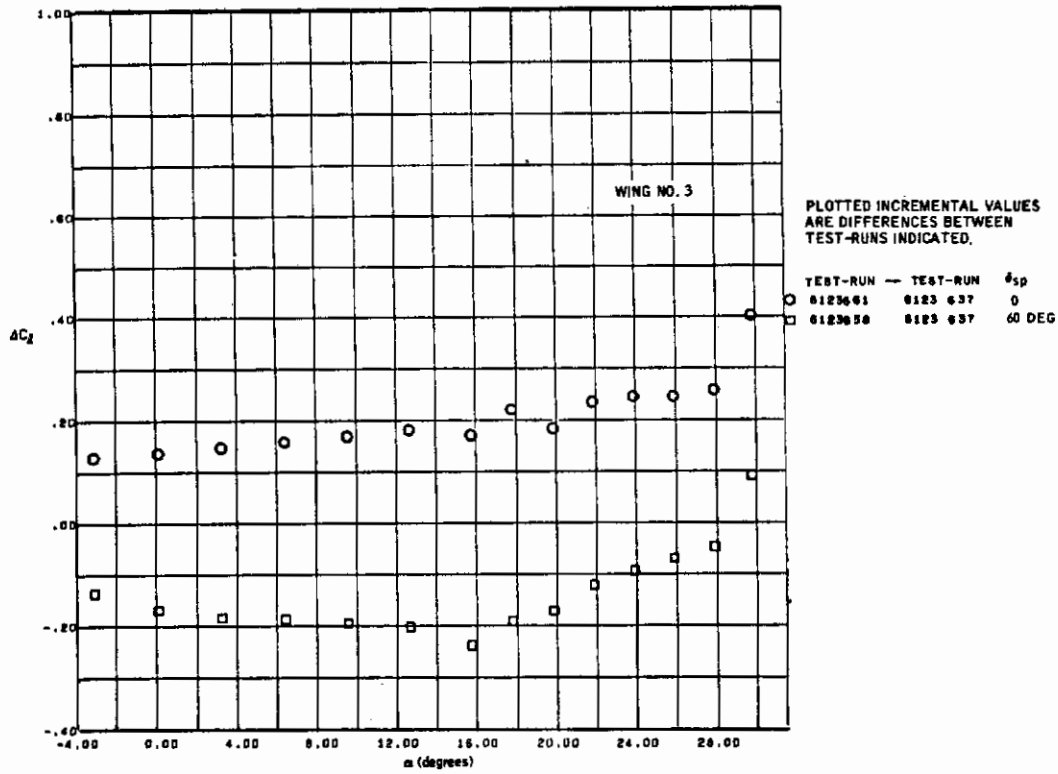

Figure 9.0-19. Engine-Out Rolling Moments with MF/VT Triple-Slotted Flap at 60 Degrees, δ_T = 60 Degrees

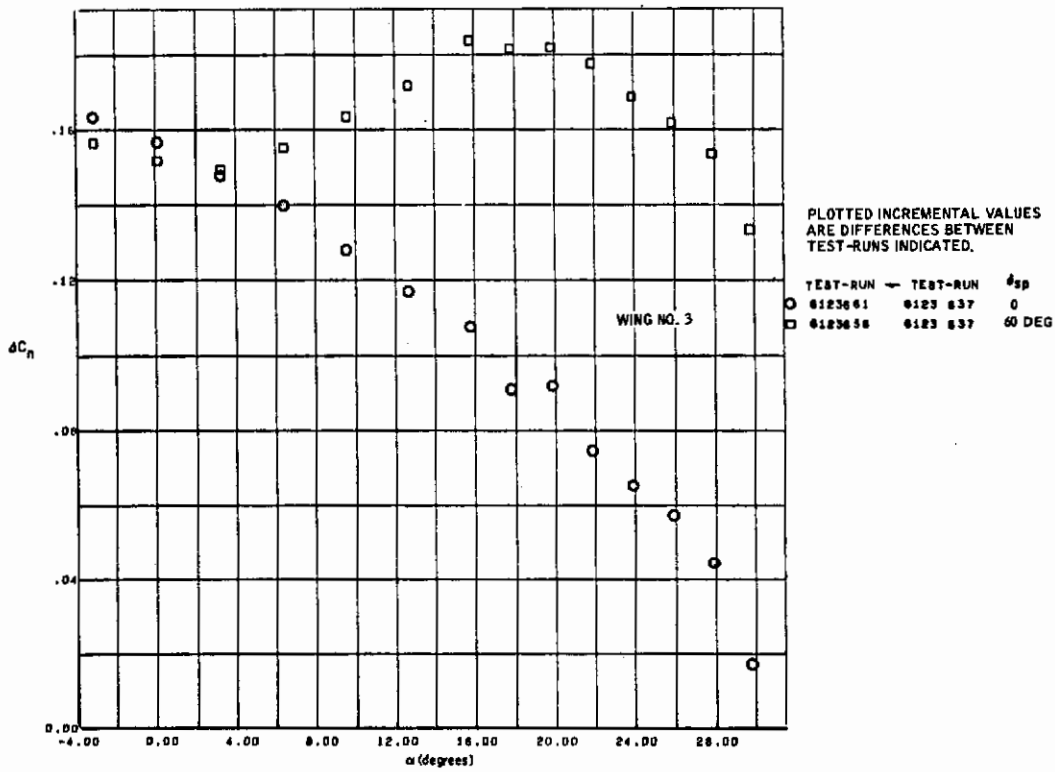

Figure 9.0-20. Engine-Out Yawing Moments with MF/VT Triple-Slotted Flap at 60 Degrees, δ_T = 60 Degrees

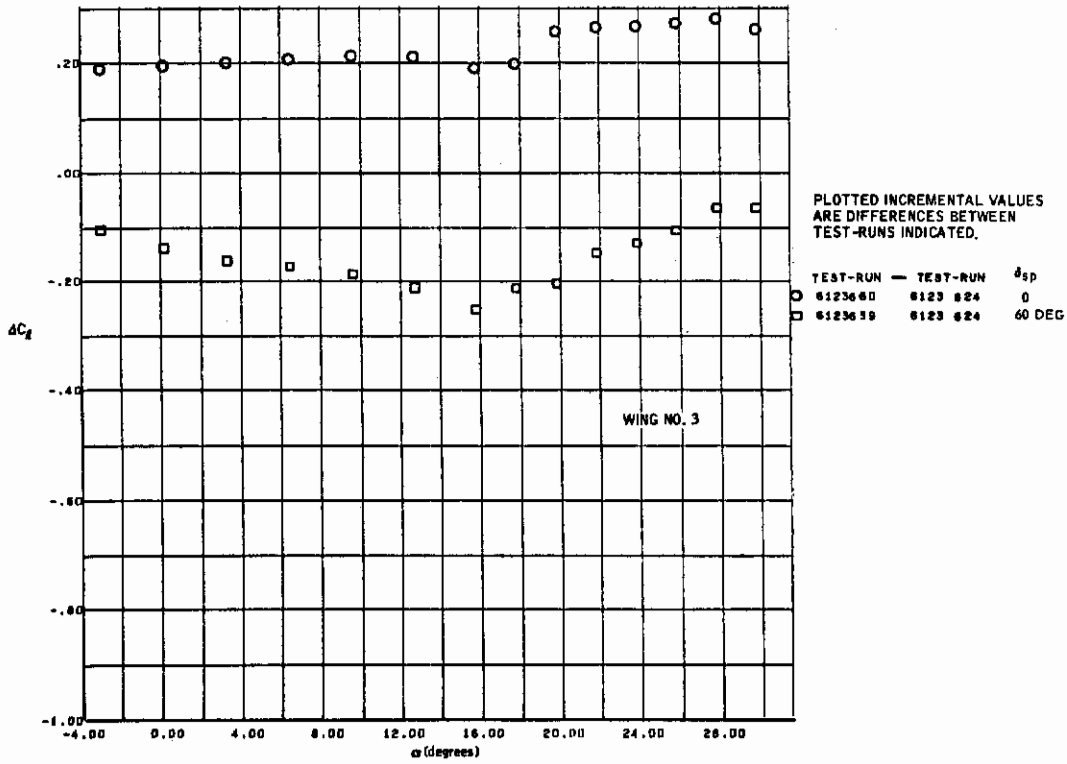

Figure 9.0-21. Engine-Out Rolling Moments with MF/VT Triple-Slotted Flap at 60 Degrees, δ_T = 90 Degrees

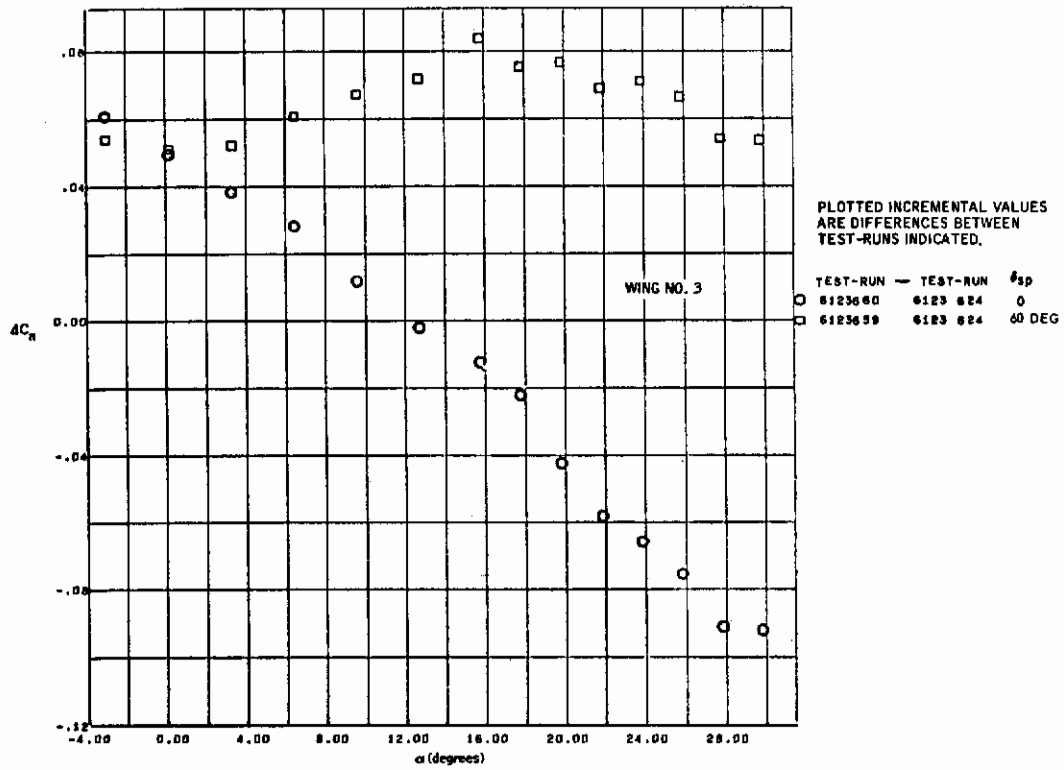

Figure 9.0-22. Engine-Out Yawing Moments with MF/VT Triple-Slotted Flap at 60 Degrees, δ_T = 90 Degrees

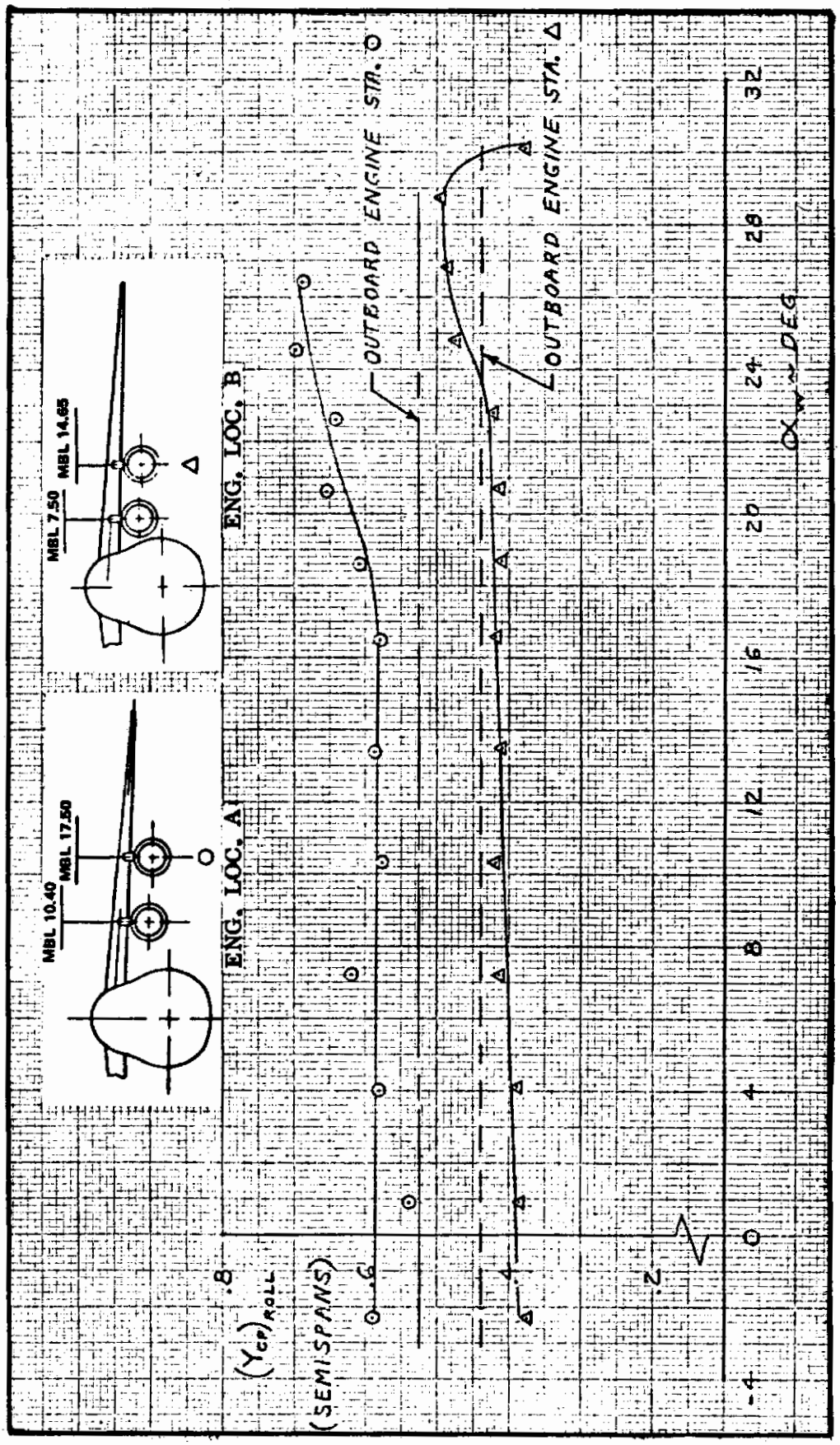

Figure 9.2-23. Effect of Engine Location on Engine-Out Spanwise Center of Pressure (Roll) with EBF Triple-Slotted Flap at 60 Degrees

SECTION 10

GROUND EFFECT

Tests were conducted with the model at varying heights from a moving belt simulation of a ground plane in order to determine the effects of ground interference on lift, drag, and pitching moment for MFVT, EBF, and IBF systems. The model was mounted in an inverted position at a fixed distance above the tunnel floor and the ground plane was lowered from the ceiling to various heights above the wing. Data was recorded for values of height to span ratio between 0.5 and 0.177 (the lower value corresponds to a landing gear and ground clearance limit).

The ground interference tests were conducted with the aspect ratio 8.0, 25 degrees swept wing (Wing No. 3).

The selected test configurations were:

1. MF/VT - Triple and double slotted flaps at 60 and 30 degrees deflection respectively.
2. EBF - Jet momentum coefficients from 0 to 4 with the flap system described above.
3. IBF - Plain flap at 60 degrees deflection.

All configurations were tested with a blown Krueger flap at a fixed momentum coefficient ($C_{\mu_{LE}} = 0.10$).

Effects of ground height on lift for the 60 degree triple slotted system are shown in Figure 10-1. The change in lift coefficient ΔC_{L_G}, due to the ground at a fixed angle of attack is plotted versus the zero ground interference circulation lift coefficient, $C_{L_\infty} - C_{\mu_J} (\sin \alpha + \delta_t)$, is shown for values of ground height to span ratio from 0.5 to 0.177 and for values of C_{μ_J} from 0 to 2.0. The data correlates well with the linear ground interference theory from DATCOM for lift coefficient ≤ 4 at h/b = 0.5 and 0.3, but depart from the linear theory and show negative interference (suckdown) at lift coefficients above 4 for h/b = 0.2 and 0.177. The suckdown effect is nonlinear and is believed due to bound vortex interference effects which reduce the effective dynamic pressure over the model.

Similar trends are indicated in Figures 10-2 and 10-3 for the 30 degree double slotted flap and the 60 degree plain flap, respectively. The data in Figure 10-2 agrees with the linear theory over the entire range shown because of the relatively low values of circulation lift coefficient. On the other hand, the data in Figure 10-3 drops below the linear

theory (h/b = 0.2) for circulation lift coefficients exceeding 4, in a manner similar to that shown in Figure 10-1.

The effect of ground on the angle for maximum lift are shown in Figure 10-4. The variations are for C_{μ_J} equal to 0, 1.0, and 2.0. This data with appropriate information from Figures 10-1, 10-2, or 10-3 can be used to construct the complete lift curve in ground effect indicated in Figure 10-5.

Effects of ground interference on drag for the same three flap configurations are depicted in Figures 10-6 through 10-8. The change in drag coefficient ΔC_{D_G} due to the ground interference is taken at a fixed angle of attack. The drag increment therefore includes the changes in induced drag due to the lift increment ΔC_{L_G} and the reduced downwash angle (or effectively an increased aspect ratio) in the presence of the ground. The data correlates well with the linear theory from DATCOM except at high lift coefficients and low ground heights where nonlinear effects tend to reduce the drag even more than predicted by the linear theory.

Pitching moment increments ΔC_{M_G} at a fixed angle of attack are shown in Figures 10-9 through 10-11 for the three flap configurations. An acceptable theoretical method was not available for comparison. It can be seen, however, that the effect of the ground plane on tail-off pitching moments is quite small.

The effects of the ground height on downwash are shown in Figure 10-12 for a $C_{\mu_J} = 0$ and $1.0 \leq C_{\mu_J} \leq 2.0$, respectively. It is apparent that the effect of ground height on downwash is the major influence on stability and control parameters. Figure 10-12 furnishes a method to determine the ratio $\epsilon_G/\epsilon_\infty$ as a function of ground height and $\alpha/\alpha_{C_{L_{max}}}$ which is the same normalized angle of attack parameter that was used in the Design Compendium (Volume II) to estimate downwash in free air. In this case, however, the value for $\alpha_{C_{L_{max}}}$ is obtained from Figure 10-4 for the appropriate ground height and thrust coefficient.

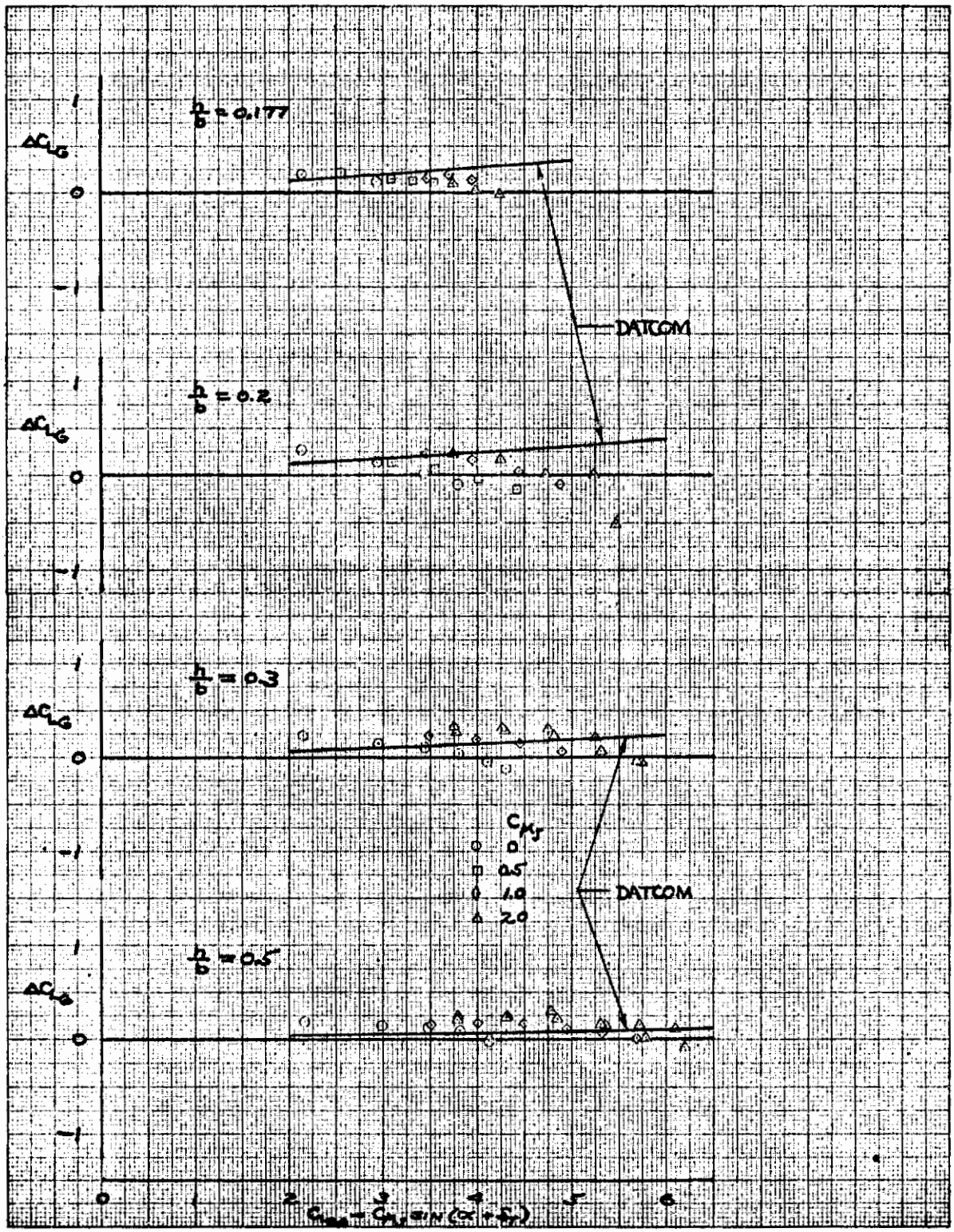

Figure 10-1. Incremental Lift Due To Ground Effect — Wing No. 3, Triple Slotted Flap at 60 Degrees Plus a Leading Edge Flap ($C_{\mu_{LE}}$ = 0.1)

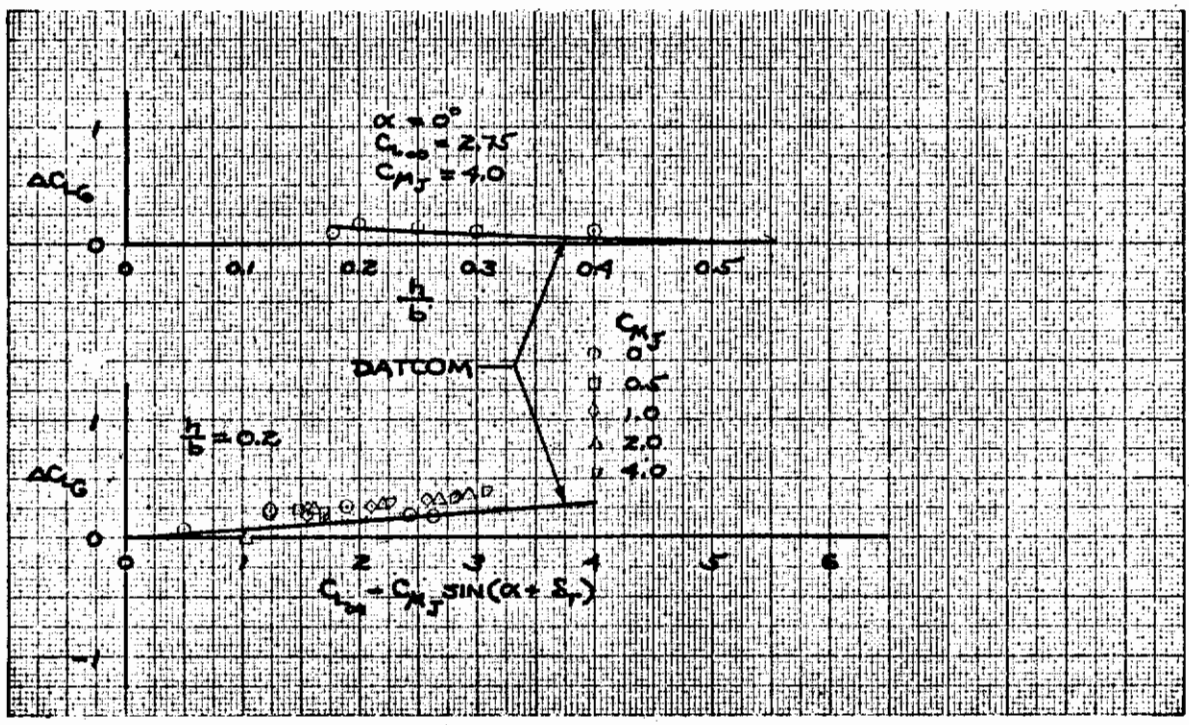

Figure 10-2. Incremental Lift Due to Ground Effect — Wing No. 3, Double Slotted Flap at 30 Degrees Plus a Leading Edge Flap ($C_{\mu_{LE}} = 0.1$)

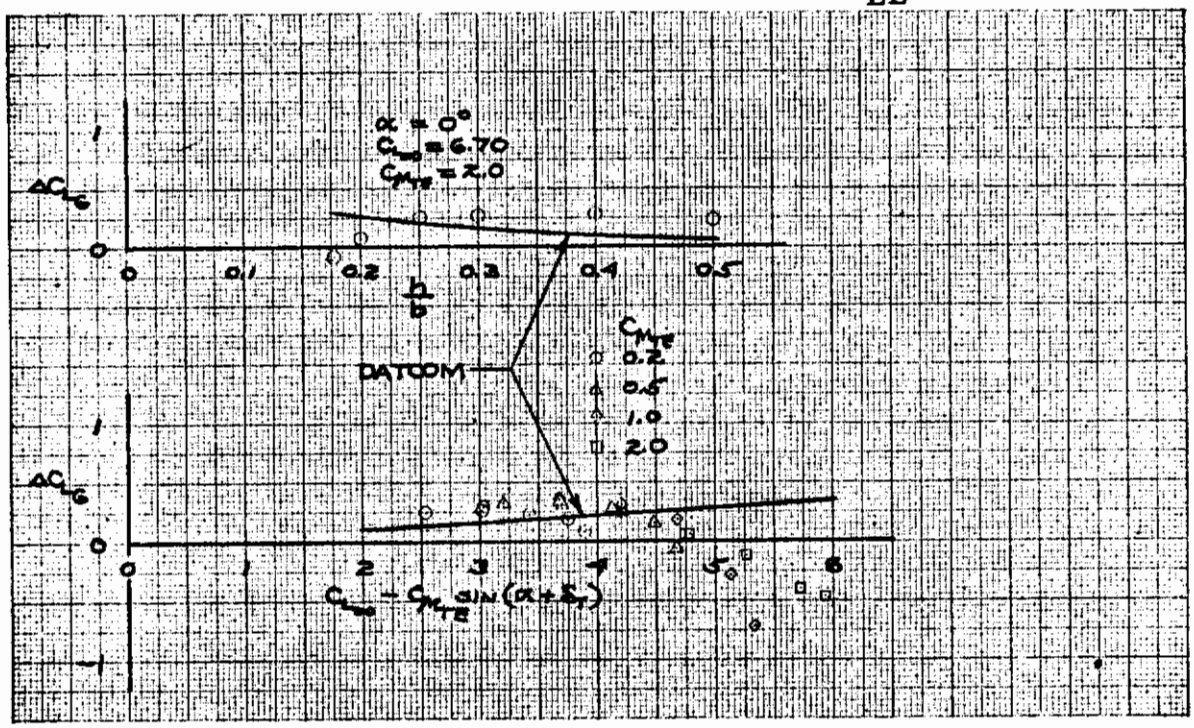

Figure 10-3. Incremental Lift Due to Ground Effect — Wing No. 3, Plain Flap at 60 Degrees Plus a Leading Edge Flap ($C_{\mu_{LE}} = 0.1$)

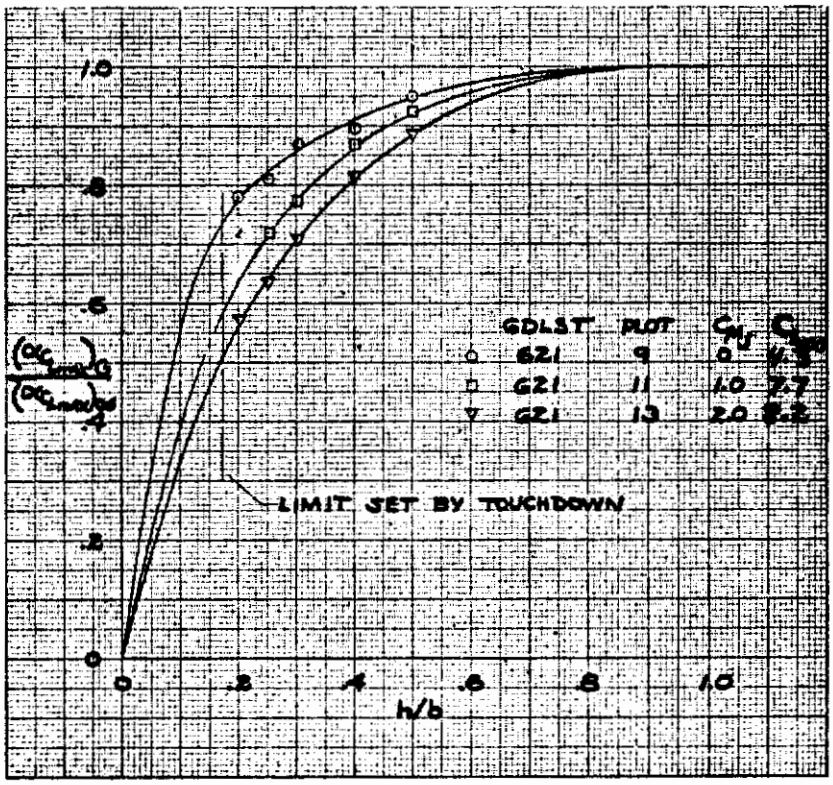

Figure 10-4. Effect of Ground Height on the Angle for Maximum Lift — Wing No. 3, Triple Slotted Flap at 60 Degrees Plus a Leading Edge Flap ($C_{\mu_{LE}}$ = 0.1)

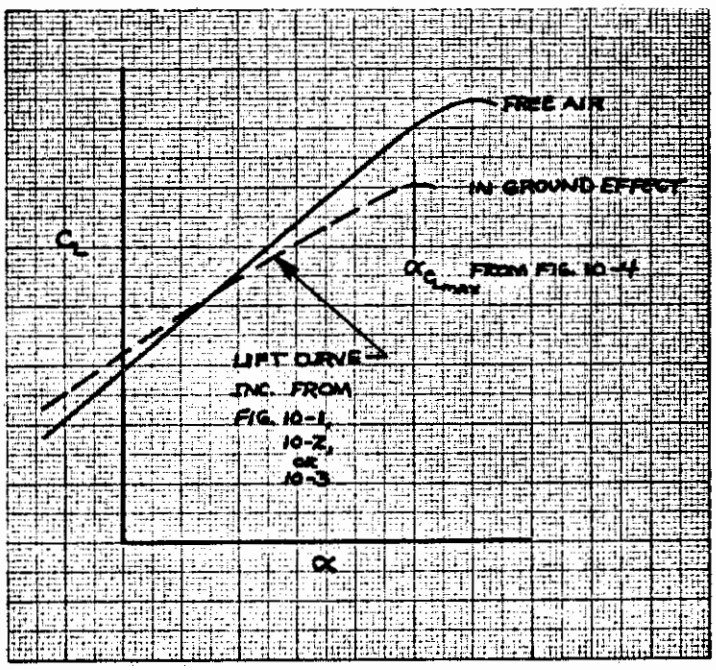

Figure 10-5. Typical Method to Determine Lift Curve in Ground Effect

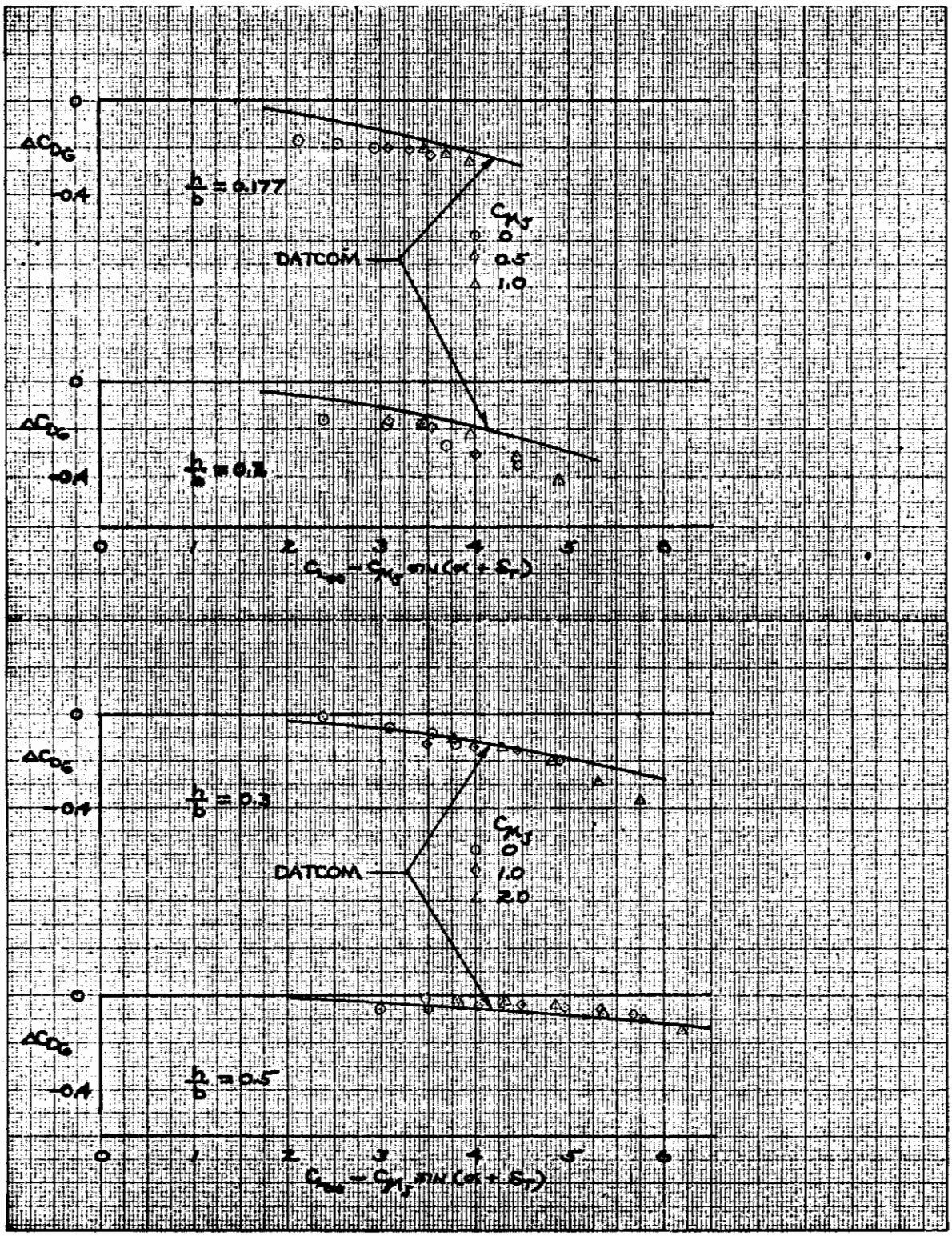

Figure 10-6. Incremental Drag Due to Ground Effect — Wing No. 3, Triple Slotted Flap at 60 Degrees Plus a Leading Edge Flap ($C_{\mu_{LE}} = 0.1$)

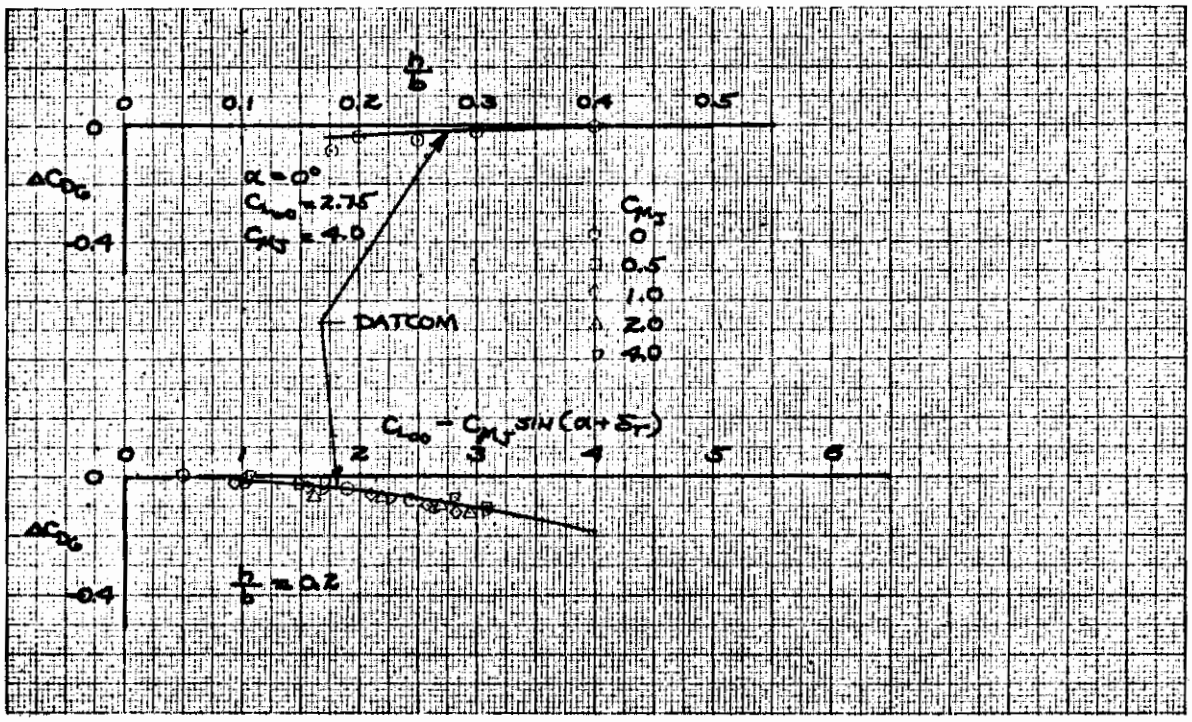

Figure 10-7. Incremental Drag Due to Ground Effect — Wing No. 3, Double Slotted Flap at 30 Degrees Plus a Leading Edge Flap ($C_{\mu_{LE}} = 0.1$)

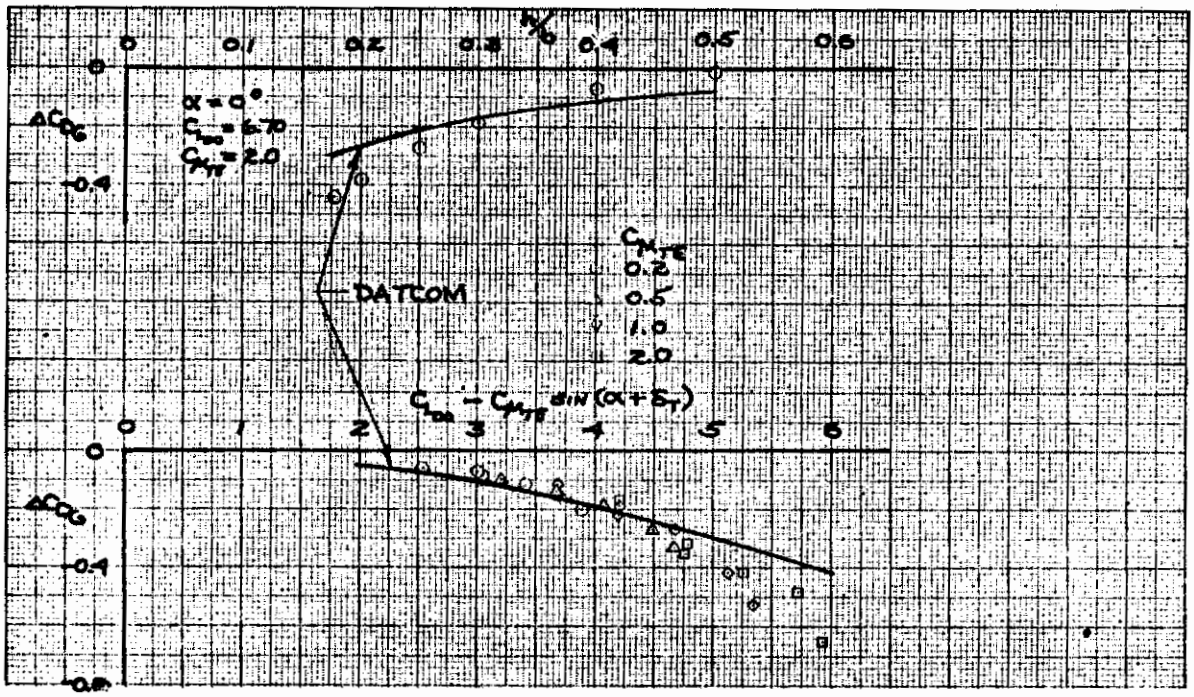

Figure 10-8. Incremental Drag Due to Ground Effect — Plain Flap at 60 Degrees Plus a Leading Edge Flap ($C_{\mu_{LE}} = 0.1$)

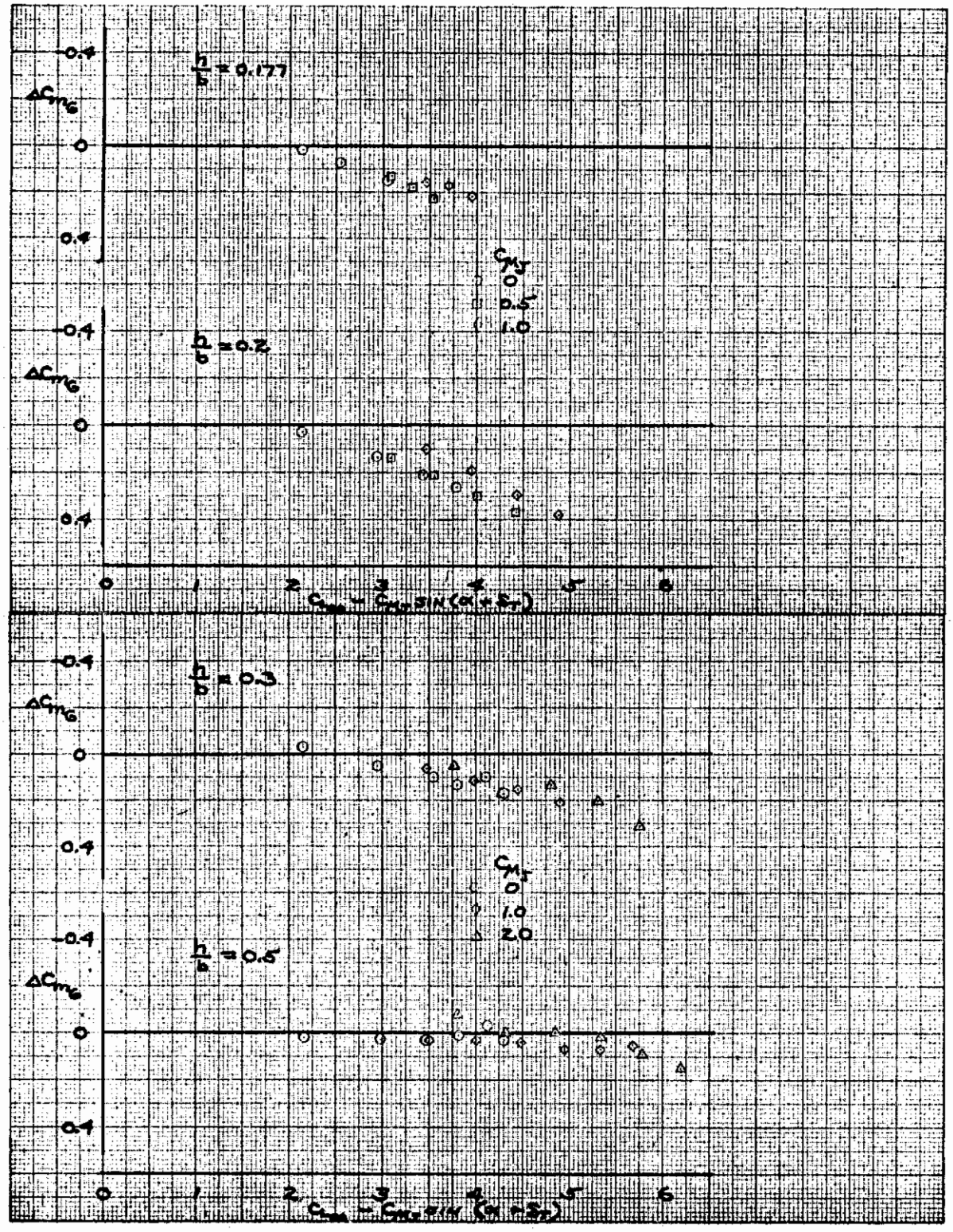

Figure 10-9. Incremental Pitching Moment Due to Ground Effect — Wing No. 3, Triple Slotted Flap at 60 Degrees Plus a Leading Edge Flap ($C_{\mu_{LE}} = 0.1$)

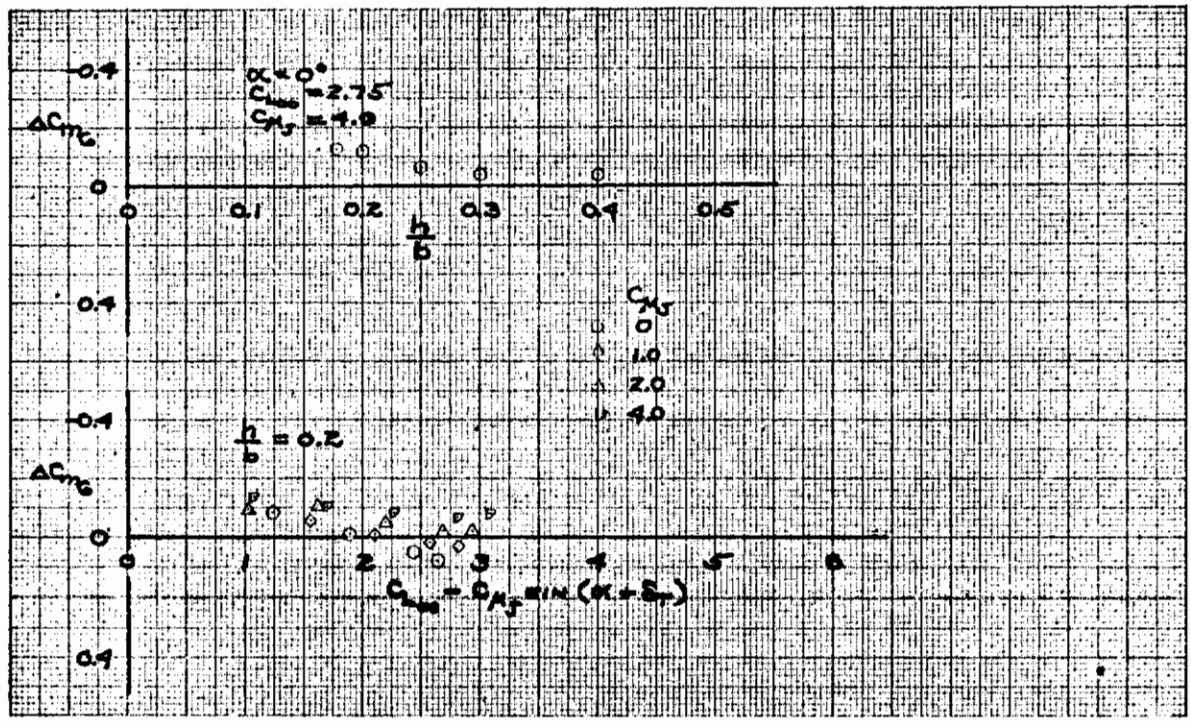

Figure 10-10. Incremental Pitching Moment Due to Ground Effect — Wing No. 3, Double Slotted Flap at 30 Degrees Plus a Leading Edge Flap ($C_{\mu_{LE}} = 0.1$)

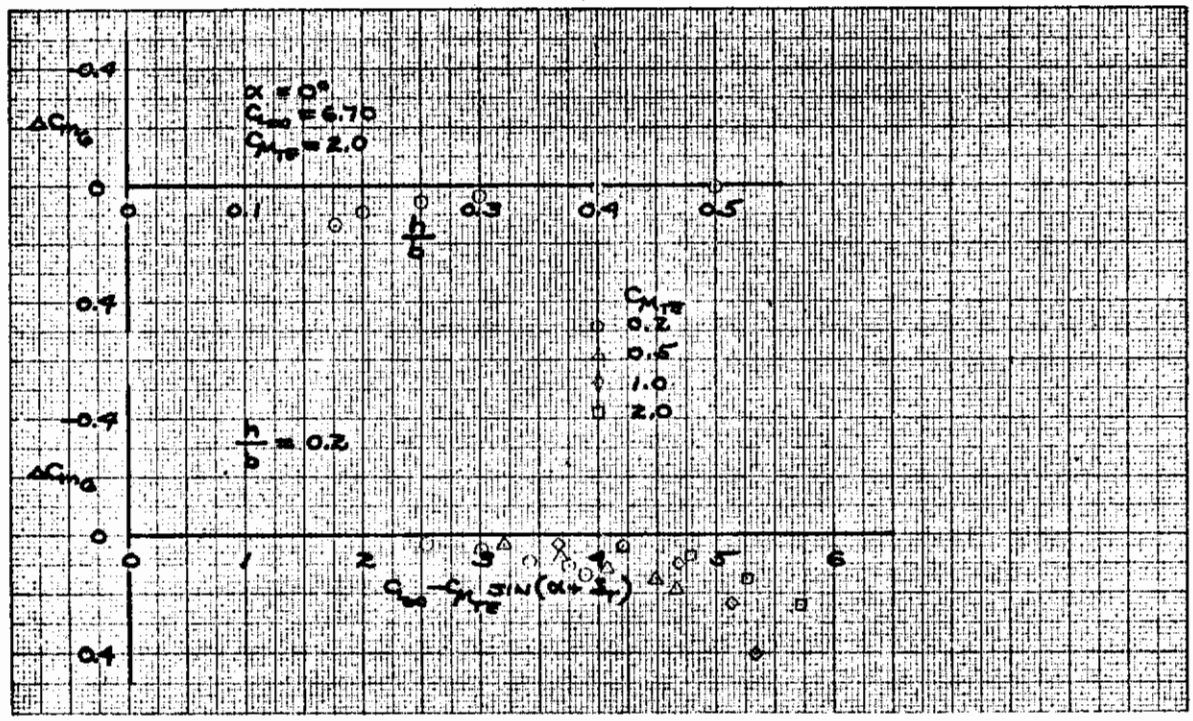

Figure 10-11. Incremental Pitching Moment Due to Ground Effect — Wing No. 3, Plain Flap at 60 Degrees Plus a Leading Edge Flap ($C_{\mu_{LE}} = 0.1$)

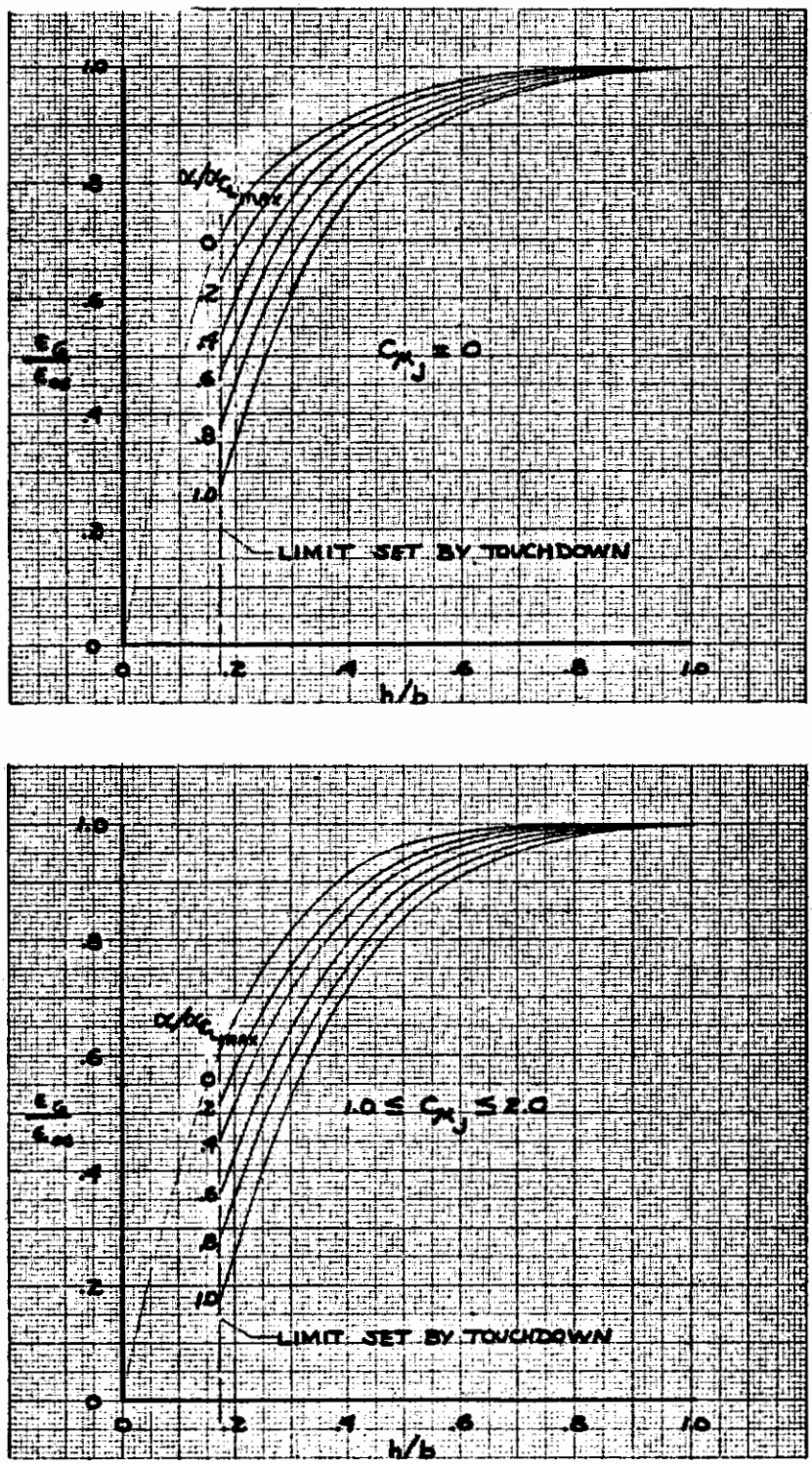

Figure 10-12. Effect of Ground Height on Downwash — Wing No. 3, Triple Slotted Flap at 60 Degrees Plus a Leading Edge Flap ($C_{\mu_{LE}} = 0.1$)

11

CONCLUSIONS AND RECOMMENDATIONS

Investigation of the test data measured in the Convair 8 x 12 ft wind tunnel has substantiated the original confidence in its validity and usefulness. Reproducibility of data made from several repeat runs throughout the tests has been excellent. Recognition of expected trends and good comparisons with predicted results has proven its quality. The moving ground plane testing did in fact prove out that the wall effects were minimal.

The vast amount of data to be analyzed required an efficient systematic procedure to reduce the data into convenient workable form. The interactive graphics computer program used for this task provided a consistent method of unbiased measuring the required parameters associated with the lift and drag curves, as well as measuring the lateral directional derivatives.

The following conclusions are made concerning the aerodynamics and stability and control characteristics of STOL transport.

1. Lift — Trailing edge flap chord, deflection, and nacelle location have a pronounced effect on lift augmentation. The amount of augmentation is directly related to the amount of engine jet stream captured by the trailing edge flap. Furthermore, when the thrust is vectored away from the trailing edge flaps there is little or no lift augmentation produced. Test data indicates very little difference between the EBF and IBF lift effectiveness for similar configuration and blowing rates; that is to say, the amount of augmentation developed from a slotted flap immersed well into the jet stream is nearly the same as that from blowing induced over the upper surface of the deflected flap. The location of powered nacelles was found to have a significant effect on the IBF lift effectiveness. A deterioration in lift was produced by the jet stream cutting the trailing edge jet sheet. Judicious positioning of the engines on the fuselage or deflection of the non-diverted engine thrust would alleviate this problem.

   Idealized jet flapped equations, assuming full jet capture by the flap have been used to compare the test data. There was good agreement in lift effectiveness for the IBF configurations. The exceptions were that it underpredicted (1) lift at high blowing momentum coefficients for IBF and (2) lift for the EBF configurations with flaps having high capture ratio. Leading edge blowing had little effect on lift effectiveness and maximum lift when power was being applied to the trailing edge flaps but did increase max angles of attack. Increases in maximum lift were noted for the power-off cases. Analysis has shown that when power-on partial-span flap data is corrected to full-span by the normal power-off flap span effectiveness, excellent correlation is attained with the full-span flap data.

2. Drag — The induced drag factor measured was consistently lower than what was predicted from lifting line theory. Difficulty in determining the narrow linear portion of the drag curve (C_L^2 vs C_D) has contributed to the lack of any definitive conclusion about induced drag. Thrust recovery was found to be slightly better than that indicated by the static turning angle for the EBF configurations. It was also found to be from 0 to 15% greater than the static turning efficiency for the slotted flaps. The thrust recovery was near optimum for the vectored thrust configurations when the thrust deflection angle equaled the flap deflection.

3. Pitching Moments — The high lift coefficient produced with the three powered lift concepts were accompanied by large nose down pitching moments. On the IBF concept, there were no configuration variables that could be altered to relieve these pitching moments. On the EBF and MF/VT concepts, the pitching moments could be reduced by moving the engines down and forward, but this action also reduced the lift.

4. Horizontal Tail Flow Fields — The extensive amount of wake rake data accumulated during this test program has shown that the downwash behind a wing with a powered lift system is proportional to the aerodynamic lift. Consequently, extremely large downwash angles are to be expected with the lift coefficients at which these powered lift systems operate. It is apparent that the previous comments concerning pitching moments also apply here, i.e., since large downwash angles and pitching moments are inherent with the production of high lift, the configuration must be tailored to eliminate their adverse effects.

5. Lateral-Directional Stability Derivatives — The test data obtained during this program indicate that powered lift systems can have a fairly significant effect on lateral-directional characteristics. A parallel stability derivatives sensitivity study conducted during this program has indicated the magnitude of these changes would not be expected to cause any adverse effect on flying qualities.

6. Control Devices — Lateral control tests have indicated that a satisfactory lateral control system should be attainable with a properly geared spoiler-aileron combination. The ailerons will provide for small, precise bank-angle corrections and the spoilers will provide the gross control power required for rapid bank-angle changes and for arresting engine-out rolling moments.

   Tests with control surface blowing showed erratic results. The configuration design studies have indicated that acceptable longitudinal and directional control can be achieved without resorting to elevator or rudder blowing. The levels of control power required are such that the optimum rudder or elevator control appears to be an unblown surface that would incorporate a passive high lift device such as a slot or double hinge arrangement. A leading edge device is required to extend maximum angle of attack ($C_{L_{max}}$) on the horizontal tail.

Schedule considerations limited the analysis and further study of this extensive collection of data is recommended.

Conclusions have not been drawn as to preference of one system or configuration over another in regards to aerodynamic lift and drag. Generally, the trends and patterns have been noted and explained. The approach taken in the lift and drag analysis furnished satisfactory results and an improved understanding of lift/propulsion concepts. None of the powered lift concepts evaluated could be clearly identified as being superior in producing high lift without also producing large nose down pitching moments.

A recommended approach to the pitching moment problem is to design a configuration that would minimize, or completely eliminate, their adverse affects. The current acceptance of Control Configured Vehicle (CCV) designs indicates this to be a candidate approach. The powered lift concepts developed for the updated baseline configurations should be assessed on a design that utilizes the CCV concept to determine possible improvements in performance and flight characteristics. A canard surface CCV design is the obvious candidate.

REFERENCES

1-1 & 3-1 Eilert, M. B., "Low Speed Wind Tunnel Tests of a Powered 1/20th Scale STOL Tactical Transport Model...," General Dynamics Corporation, GDLST 612, 612-1, 612-3, 612-4, 612-5, 612-6, January 1973.

3-2 Reynolds, H. A., "Two-Dimensional Low Speed Wind Tunnel Test of a 15 Inch Chord by 36 Inch Span Multi-element Airfoil Pressure Model With Leading Edge and Trailing Edge Blowing," General Dynamics Cor-Corporation GDLST 610.

3-3 von der Decken, J., "Aerodynamics of Pneumatic High-Lift Devices" AGARD Lecture Series No. 43, September 1970.

3-4 Hartunian, R. A., "The Finite Aspect Ratio Jet Flap," Cornell Aero Lab Report AI-1190-A-3, October 1959.

3-5 Perry, P. H., "A Review of Some Published Data on the External-Flow Jet Augmented Flap," with Appendix by D. N. Foster, Royal Aircraft Establishment, Tech. Rept. 70240, Dec. 1970.

3-6 Moorhouse, D. J., "A Practical Look at the Stall and High Lift Operation of Externally Blown Flap STOL Transport Configurations," presented at the AGARD Conference on "Fluid Dynamics of Aircraft Stalling," Lisbon, Portugal, April 1972.

3-7 Ramsey, J. C., and Laudeman, E. C., "STOL Tactical Aircraft Investigation State-of-the-Art Design Compendium," General Dynamics Convair Aerospace Division Report CDRL Item 0002-A004, Dec. 1971.

3-8 Strand, T.; Levinsky, E. S.; and Wei, M. H. Y., "Unified Performance Theory for V/STOL Aircraft in Equilibrium Flight, Part I and II," Journal of Aircraft Vol 4 No. 2 and 3, March-April, May-June 1967.

3-9 Carter, A. W., "Effects of a Jet-Exhaust Location on the Longitudinal Aerodynamic Characteristics of a Jet V/STOL Model," NASA TN D-5333.

Unclassified
Security Classification

DOCUMENT CONTROL DATA - R & D

(Security classification of title, body of abstract and indexing annotation must be entered when the overall report is classified)

1. ORIGINATING ACTIVITY (Corporate author) Convair Aerospace Division General Dynamics Corporation San Diego, California 92138	2a. REPORT SECURITY CLASSIFICATION Unclassified 2b. GROUP

3. REPORT TITLE
STOL Tactical Aircraft Investigation
Volume IV - Wind Tunnel Data Analysis

4. DESCRIPTIVE NOTES (Type of report and inclusive dates)
Final Report (7 June 1971 to 31 January 1973)

5. AUTHOR(S) (First name, middle initial, last name)
J. Hebert, Jr., J. C. Ramsey, E. C. Laudeman, C. A. Whitney, N. A. Ponomareff, H. Altman

6. REPORT DATE May 1973	7a. TOTAL NO. OF PAGES 404	7b. NO. OF REFS 10
8a. CONTRACT OR GRANT NO. F33615-71-C-1754 b. PROJECT NO 643A - Task 0001 c. d.	9a. ORIGINATOR'S REPORT NUMBER(S) GDCA-DHG73-001 9b. OTHER REPORT NO(S) (Any other numbers that may be assigned this report) AFFDL TR-73-21-Vol IV	

10. DISTRIBUTION STATEMENT
Approved for Public Release
Distribution Unlimited

11. SUPPLEMENTARY NOTES ----	12. SPONSORING MILITARY ACTIVITY Air Force Flight Dynamics Laboratory (PTA) Wright Patterson AFB, Ohio 45433

13. ABSTRACT Force and rake information measured during 1,087 hours of low speed wind tunnel testing conducted by Convair Aerospace are summarized. Over 2,730 data runs were generated on 242 major configuration variables that covered the following lift/propulsion concepts: Mechanical Flaps Plus Vectored Thrust, Externally Blown Flaps, and Internally Blown Flaps.

Lift data was reduced into three basic terms: power-on to power-off lift curve slope ratio, trailing edge flap lift increment at $\alpha = 0$ degrees, and maximum lift coefficient increment due to the application of power.

These relationships were evaluated as a function of blowing momentum coefficient and correlated for the effects of configurational variations (wing planform, leading and trailing edges, and nacelle location). Drag data was reduced into the form of induced drag factor, minimum profile drag, thrust recovery and then analyzed as a function of blowing momentum coefficient. The pitching moment data analysis compares the flap pitching moment increment among the various configurations.

The downwash data was normalized using aerodynamic lift and subsequently analyzed by comparing downwash intensities at various vertical stations. The static lateral-directional stability derivatives were obtained from linear least-squares curve fits. Control effectiveness data and effects of asymmetric thrust were also obtained by taking increments between the undeflected condition and runs with deflected controls and/or symmetric thrust.

DD FORM 1 NOV 65 1473

Security Classification

Security Classification

14. KEY WORDS	LINK A		LINK B		LINK C	
	ROLE	WT	ROLE	WT	ROLE	WT
1. Externally Blown Flaps						
2. High Lift Systems						
3. Internally Blown Flaps						
4. Mechanical Flaps/Vectored Thrust						
5. Wind Tunnel Data						

☆U.S.Government Printing Office: 1973 — 758-426/90

Security Classification